BEILSTEIN JOURNAL OF NANOTECHNOLOGY

Micro- and nanoscale effects in biological and bioinspired materials and surfaces

Edited by Thies Büscher, Rhainer Guillermo Ferreira, Manuela Rebora and Stanislav Gorb

Imprint

Beilstein Journal of Nanotechnology
www.bjnano.org
ISSN 2190-4286
Email: journals-support@beilstein-institut.de

The *Beilstein Journal of Nanotechnology* is published by the Beilstein-Institut zur Förderung der Chemischen Wissenschaften.

Beilstein-Institut zur Förderung der Chemischen Wissenschaften
Trakehner Straße 7–9
60487 Frankfurt am Main
Germany
www.beilstein-institut.de

BEILSTEIN JOURNAL OF NANOTECHNOLOGY

Functional morphology of cleaning devices in the damselfly *Ischnura elegans* (Odonata, Coenagrionidae)

Silvana Piersanti[1], Gianandrea Salerno[*2], Wencke Krings[3,4], Stanislav Gorb[4] and Manuela Rebora[1]

Full Research Paper

Open Access

Address:
[1]Dipartimento di Chimica, Biologia e Biotecnologie, University of Perugia, Via Elce di Sotto 8, 06121 Perugia, Italy, [2]Dipartimento di Scienze Agrarie, Alimentari e Ambientali, University of Perugia, Borgo XX Giugno, 06121 Perugia, Italy, [3]Department of Cariology, Endodontology and Periodontology, Universität Leipzig, Liebigstraße 12, 04103 Leipzig, Germany and [4]Department of Functional Morphology and Biomechanics, Zoological Institute, Kiel University, Am Botanischen Garten 1–9, 24098 Kiel, Germany

Email:
Gianandrea Salerno[*] - gianandrea.salerno@unipg.it

* Corresponding author

Keywords:
antennae; cuticle; eyes; grooming; legs; resilin

Beilstein J. Nanotechnol. **2024,** *15,* 1260–1272.
https://doi.org/10.3762/bjnano.15.102

Received: 17 July 2024
Accepted: 18 September 2024
Published: 16 October 2024

This article is part of the thematic issue "Micro- and nanoscale effects in biological and bioinspired materials and surfaces".

Associate Editor: J. Lahann

Abstract

Among the different micro- and nanostructures located on cuticular surfaces, grooming devices represent fundamental tools for insect survival. The present study describes the grooming microstructures of the damselfly *Ischnura elegans* (Odonata, Coenagrionidae) at the adult stage. These structures, situated on the foreleg tibiae, were observed using scanning electron microscopy, and the presence and distribution of resilin, an elastomeric protein that enhances cuticle flexibility, were analyzed using confocal laser scanning microscopy. Eye and antennal grooming behavior were analyzed to evaluate the particle removal efficiency in intact insects and in insects with ablated grooming devices. The grooming devices are constituted of long setae from which a concave cuticular lamina develops towards the medial side of the leg. Each seta shows a material gradient of resilin from its basal to the distal portion and from the seta to the cuticular lamina. The removal of the grooming devices induces a strong increase in the contaminated areas on the eyes after grooming. Further studies on insect grooming can provide valuable data on the functional morphology of insect micro- and nanostructures and can represent a starting point to develop advanced biomimetic cleaning tools.

Introduction

Self-grooming, defined as any behavior related to the maintenance and care of body surfaces, is an innate behavior found across a wide range of animal species, from vertebrates to arthropods, with early evolutionary origins (reviews in [1,2]). Despite the distant evolutionary relationship between vertebrates and insects, their grooming behaviors serve multiple and similar purposes, such as body cleaning and disease prevention, distribution of substances across the body surface, maintenance

of sensory organs, and displacement behavior in stressful conditions [3].

In insects, the chitinous exoskeleton, with the epidermis below it, forms the integumentary boundary between internal organs and the external environment. The exoskeleton can perform numerous tasks through the presence of micro- and nanostructures located on its cuticular surface, serving functions from sensory reception to surface adhesion, air retention, food grinding, thermoregulation, and color production (reviews in [4,5]). The insect cuticle is frequently exposed to a variety of inorganic and organic particles, which can disrupt its normal function or hinder essential physiological processes, ultimately decreasing survival rates. As a result, insects dedicate a considerable amount of time to self-grooming to eliminate debris [6,7], parasites [8], and pathogens [9]. This grooming behavior also plays a role in distributing substances across their bodies, such as antimicrobial compounds [10], brochosomes [11], and cuticular lipids [6,12]. Additionally, self-grooming is essential for flight, as it keeps the wings clean [13], and for movement on land, by ensuring the cleanliness of the tarsi and maintaining the adhesion of attachment pads [14-16]. Cleaning behavior plays an exceptionally important role in social insects like ants, for example, to guarantee precise nestmate/non-nestmate discrimination [17] or in mutual grooming [18]. Additionally, grooming plays a pivotal role in maintaining olfactory acuity. Böröczky et al. [19] demonstrated that antennal grooming removes not only foreign chemicals but also excess native cuticular lipids that may interfere with olfaction, thereby maintaining the olfactory sensitivity of the antennae.

In insects, body cleaning devices are typically located on the legs and are associated with complex grooming behaviors that vary greatly across arthropods [20]. Numerous studies on flies [21,22], wasps [23], mantids [24], and crickets [25] indicate that grooming behavior often falls into two distinct clusters. The anterior cluster, predominantly using the forelegs, involves grooming the antennae, head, mesosoma, forelegs, and middle legs. The posterior cluster focuses on cleaning the wings, metasoma, middle legs, and hind legs, and primarily uses the hind legs. A similar behavior is reported in ants, where functional morphology and efficiency of the grooming activity have been largely investigated in old and recent papers [26,27].

The antenna cleaner is usually formed from a modified fore tibia, tibial spurs, and/or fore basitarsus, but its morphology varies greatly among groups [20]. In Hemiptera, antennal grooming involves scraping with the tibial comb complex (tibial comb + fossula) of both forelegs on the antenna, generally followed by grooming the tibial comb complex of one leg using the tarsal hairy pad of the opposite leg [28]. In Lepidoptera, many groups use a comb-like spur on the fore tibia for antennal cleaning [20,29]. In Diptera, tibial grooming combs are found on the ventral apices of the fore tibiae in mosquitoes [22]. In Hymenoptera, one of the fore tibial spurs, called calcar, is highly modified for antennal grooming, and usually the basitarsus is also specialized for this purpose; the two parts acting together form an anatomical cluster called strigil [26,27,30]. In Coleoptera the protibial antennal cleaning organ is the main argument in support of a clade Geadephaga [31].

Studies on insect grooming can provide valuable data on the functional morphology of insect micro- and nanostructures and can enhance our understanding of different insect behavior and evolution (e.g., [32] for Mantodea and [26] for Hymenoptera). Moreover, they can represent the starting point to develop useful biomimetic tools [33]. Studies on grooming devices in Paleoptera (Odonata and Ephemeroptera) are scarce. Except for an old description of odonatan forelegs by St. Quentin [34] and some scattered observations of the grooming behavior in some odonatan species (review in [35]), no detailed study has been performed so far.

This study aims to describe the grooming devices located on the forelegs of a damselfly that are used to clean the head and, especially, the eyes and the antennae. The microstructures were observed using scanning electron microscopy (SEM), and the presence and distribution of resilin, an elastomeric protein that enhances cuticle deformability and flexibility (review in [36]), were analyzed using confocal laser scanning microscopy (CLSM). The eye and antennal grooming behavior of the damselfly *Ischnura elegans* (Vander Linden, 1820) adults (Odonata, Coenagrionidae) was observed and analyzed to evaluate the particle removal efficiency in intact and ablated insects.

Material and Methods

Insects

Ischnura elegans males and females were collected in the field at Centro Ittiogenico del Trasimeno - Sant'Arcangelo (Perugia, Umbria region, Italy), in spring and summer 2023–2024. They were maintained for 2–3 days in a controlled climate chamber (14:10 light–dark rhythm, at a temperature of 25 ± 1 °C and relative humidity of 70 ± 10%) inside net cages (25 cm × 25 cm × 25 cm). *Drosophila melanogaster* flies were used to feed the damselflies. Adult insects of both sexes were used in the study.

Light microscopy

To count the mean number of foretibial grooming structures in males and females, we anaesthetized 13 males and eleven females with carbon dioxide, dissected their forelegs and observed them under a stereomicroscope Leica MZ6 (Leica Microsystem GmbH, Wetzlar, Germany).

To obtain semithin sections, the tibiae of six insects were dissected under the stereomicroscope. Samples were then fixed for 3 h in 2.5% glutaraldehyde in sodium cacodylate buffer (Electron Microscopy Sciences, Hatfield, PA, USA) with a pH of 7.2, repeatedly rinsed in sodium cacodylate buffer and post-fixed for 1 h at 4 °C in 1% osmium tetroxide in sodium cacodylate buffer (Electron Microscopy Sciences). Fixed samples were repeatedly rinsed in the same buffer, dehydrated by using ascending ethanol concentrations, and finally embedded in an Epon–Araldite resin mixture (Sigma-Aldrich). Afterwards, semithin sections of the foretibial grooming structures were cut with a diamond knife using a Leica EM UC6 ultramicrotome, collected on glass slides, stained with 1% methylene blue with sodium borate, and observed and photographed using a KOPPACE microscope camera KP-2100 (KOPPACE, Kepuaisi Science Technology, Shenzhen, China) mounted on a light microscope Leica DMLB (Leica Microsystem GmbH, Wetzlar, Germany).

Scanning electron microscopy

Foretibiae were dissected from anaesthetised specimens (ten males and ten females), fixed for 12 h in 2.5% glutaraldehyde in cacodylate buffer (Electron Microscopy Sciences) at pH 7.2, repeatedly rinsed in the same buffer and dehydrated using ascending ethanol gradients (20%, 50%, 70%, 80%, 95%, and 100%), followed by drying in an oven at 40 °C for three days. Foretibiae of intact and ablated insects used to evaluate the particle removal efficiency were carefully dissected under a stereomicroscope and then dried in an oven at 40 °C for three days. They were not fixed to avoid removing the talc powder present on the grooming structures. The specimens were deposited on aluminum stubs using double-sided adhesive tape. Before the analysis, the samples were sputter-coated with a thin layer of gold (8 nm) using a Q150 T ES (Quorum, Laughton, UK) for 30 s. The samples were then analyzed in a field-emission scanning electron microscope FE SEM LEO 1525 (ZEISS, Oberkochen, Germany) at 5 kV accelerating voltage.

Confocal laser scanning microscopy

A CLSM-based method established by Michels and Gorb [37], to analyze material compositions and their gradients in arthropod cuticle by visualizing autofluorescence, was applied to the foretibial grooming structures. We interpreted the final images and described the material properties of the cuticle as follows: (1) Red areas are likely well-sclerotized, (2) green-to-yellow areas are less sclerotized in comparison to red ones and mechanically stable, but relatively flexible because of the lower degree of sclerotization, and (3) blue areas are rubber-like with a relatively high proportion of resilin-like proteins or unsclerotized chitin. This method has already been widely applied in the literature [37-40].

The insects to be observed were frozen in a conventional lab freezer (ca. −20 °C) for 10 min. The foretibiae were cut from males and females by a scalpel. The specimens were washed in 70% ethanol and then immersed in glycerine (≥99.5%, Carl Roth GmbH & Co. KG, Karlsruhe, Germany). After fixing the specimens in glycerine between a glass slide and a cover slip (Carl Roth GmbH & Co. KG, Karlsruhe, Germany) for ca. 2 h, we visualized them with the CLSM (Zeiss LSM 700, Carl Zeiss Microscopy, Jena, Germany). The CLSM was equipped with four lasers (laser lines: 405, 488, 555, and 639 nm) to excite the sample fluorescence subsequently. Four emission filters transmitting 420–480, ≥490, ≥560, and ≥640 nm were used to visualize different fluorescence emissions of the cuticle components. We have visualized the dorsal and ventral cuticle from the foretibiae of males and females.

Behavior

To describe the grooming behavior, living individuals were observed and video-recorded using a high-speed camera DMK 37BUX287 720×540, 539 FPS, global shutter mounted on a Leica MZ6 (Leica Microsystem GmbH, Wetzlar, Germany) stereomicroscope at 500 FPS. To induce grooming behavior, the insect antennae or eyes were fully covered with pink talc powder (Holi Colors Italia, Calatafimi, Italy) containing irregularly shaped particles (34.5 ± 3.5 µm), previously used in experiments on other insects for the same purpose [28]. In detail, in each experiment, insect antennae or eyes were covered with the powder by gently inserting each antenna or each eye of the live insect into a pipette tip filled with the powder. Video recording began immediately after contamination and continued for 5 min after beginning of the grooming. To describe the grooming behavior, the following parameters and acts (and their duration and frequency) were recorded with the software Solomon coder [41]:

- right foreleg raising and scraping of the right eye, or of the right eye and of the dorsal side of the right antenna with the right tibia (R eye-ant);
- left foreleg raising and scraping of the left eye, or of the left eye and of the dorsal side of the left antenna with the left tibia (L eye-ant);
- right foreleg raising and scraping of the right antenna with the right tibia (R ant);
- left foreleg raising and scraping of the left antenna with the left tibia (L ant);
- head rotation (70–90°) (head rot);
- right tibia running through mouthparts (R tibia cleaning);
- left tibia running through mouthparts (L tibia cleaning); and
- resting between two bouts (resting).

The behavior of four insects with contaminated eyes for a total of 17 bouts and the behavior of four insects with contaminated antennae for a total of eight bouts was analyzed. The behavior recording was stopped when the insect resting time after one bout was longer than 120 s.

The video in Supporting Information File 1 was recorded using a KOPPACE microscope camera KP-2100 (KOPPACE, Kepuaisi Science Technology, Shenzhen, China) mounted on a Leica MZ6 stereomicroscope (Leica Microsystem GmbH, Wetzlar, Germany).

In the experiments with contaminated eyes and with contaminated antennae, in consideration that the data were not normally distributed (Shapiro–Wilk test), to compare the frequency and the duration of forelegs raising and scraping of the eye or of the eye plus the dorsal side of the antennae with the tibiae (Eye-ant), the Mann–Whitney rank sum test was used. The Student *t*-test for independent samples was used to compare the frequency and duration of the other recorded acts (Ant, Tibia cleaning, Head rot) in the experiments with contaminated eyes and with contaminated antennae.

Role of the foretibial cleaning structures and particle removal efficiency

We evaluated particle removal efficiency in experiments with intact and ablated insects, with their foretibial grooming structures artificially removed. To prepare ablated insects, they were anesthetized with carbon dioxide for 60 s, and the tibial grooming structures of the forelegs were carefully cut off with a scalpel blade under the stereomicroscope. The insects were left to recover for 24 h before carrying out the experiments. In each experiment, with intact or ablated insects, antennae or eyes were covered with pink talc powder (Holi Colors Italia, Calatafimi, Italy) as above described. At the beginning of the experiment, just after contamination, and at the end, after 1 h of grooming for the eyes and 10 min of grooming for the antennae, the head of the test insect was observed and photographed. Images of the head and of the forelegs before and after grooming were taken in intact and ablated insects using a KOPPACE microscope camera KP-2100 (KOPPACE, Kepuaisi Science Technology, Shenzhen, China) mounted on a Leica MZ6 stereomicroscope (Leica Microsystem GmbH, Wetzlar, Germany). In some specimens, mouthparts have been dissected and photographed with the same camera and microscope after grooming to evaluate the potential presence of pink powder.

The images of the eyes before and after grooming in intact and ablated insects were analyzed with the software ImageJ to evaluate the difference in areas contaminated with the powder before and after grooming in intact and ablated insects. The antennae of ten intact and ten ablated insects and the eyes of twelve intact and twelve ablated insects were analyzed. The percentage of contaminated area on the eyes of intact and ablated damselflies was compared using the Mann–Whitney Rank Sum Test.

Results

Morphology of the grooming devices

In the distal portion of the fore tibia of both sexes of *Ischnura elegans,* modified setae in the form of flag-shaped structures were visible (Figure 1a,c,d). They are located on the medial side of the tibia, and their number ranged from 7.08 ± 0.27 in males to 6.27 ± 0.24 in females. They measure about 210 µm in length and 44 µm in width and emerge from a well-developed socket (Figure 1b), which gives rise to a long seta, from which a concave cuticular lamina develops towards the medial side of the leg (Figure 1c,d). The border of the cuticular lamina showed indentations and appeared lobate along its medially oriented side (Figure 1c–e). In the cross section, the asymmetrical and concave shape of the grooming structures was clearly visible, with a thin lamina originating from a robust seta (Figure 1f). Dirt particles tended to accumulate inside the flag-shaped structures in correspondence with the concave cuticular lamina (Figure 1d,f). No sexual dimorphism has been observed regarding shape, size, and number of the grooming devices.

The CLSM analyses revealed that each tibial grooming device shows a different relative amount of resilin from its basal to its distal portion and from the hair to the cuticular lamina (Figure 2a,b). The flag-shaped grooming devices are set in a very soft socket, which appears blue, thus indicating a higher amount of resilin or unsclerotized chitin (Figure 2a). The base of the flag is very sclerotized in its basal portion appearing red and yellow, but tends to become richer in resilin or is unsclerotized in its apical portion, where more blue autofluorescence signal is visible (Figure 2a). The cuticular lamina appears blue, thus exhibiting large proportions of resilin or unsclerotized chitin (Figure 2b).

Grooming behavior

The grooming of damselfly eyes and antennae occurred in bouts (Figure 3, Supporting Information File 1). The mean number of bouts before the insect rested for a time longer than 120 s was higher when the eyes were contaminated (4.3 ± 0.9) and lower (1.8 ± 0.5) when the antennae were contaminated (t = 2.6; d.f. = 6; P = 0.043). In each bout, damselflies performed a quick sequence of grooming acts, then stopped for a while before repeating a similar (but not the same) sequence of acts in a new bout (Figure 3). Damselflies cleaned their eyes even in the experiments with only antennal contamination and cleaned their

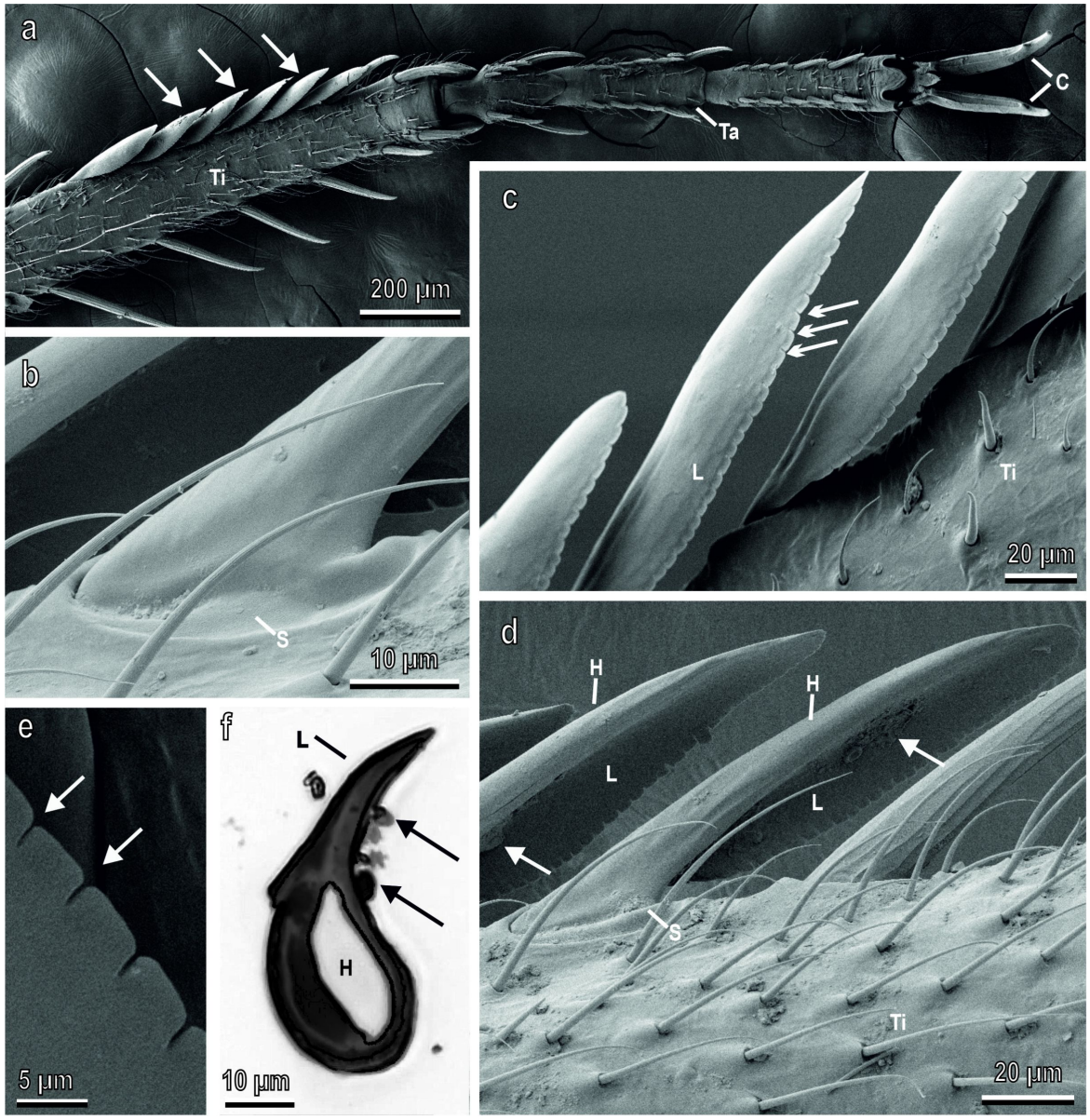

Figure 1: Left foreleg of *Ischnura elegans* (female) in SEM (a–e) and semithin section (f) of a grooming device under a light microscope. (a) Ventral view of tibia (Ti) and tarsus (Ta) showing the tibial grooming devices (arrows) located on the medial side of the tibia. C, claws. (b) Detail of a grooming device emerging from a well-developed socket (S). (c) Detail of the grooming devices observed from the ventral side of the leg. Note the border of the cuticular lamina (L) with indentations (arrows). (d) Grooming devices observed from the dorsal side of the tibia (Ti). Note that each grooming device is constituted of a long hair (H) from which a concave cuticular lamina (L) develops towards the medial side of the leg; arrows indicate the dirt particles accumulated inside the flag-shaped structures in correspondence of the concave cuticular lamina. S, socket. (e) Detail of the border of the cuticular lamina with indentations (arrows). (f) Cross section of a grooming device in its central portion. Note the hair (H) and the concave cuticular lamina (L) collecting dirt particles (arrows).

antennae even in experiments with only eyes contaminated (Figure 3a–f). A sequence of acts of grooming eyes or antennae begins with one or both forelegs raising and scraping (a unidirectional movement from top to bottom) the ipsilateral eye and (afterwards) the ipsilateral antenna (R eye-ant and L eye-ant), with the tibial flag-shaped structures kept in contact first with the eye and afterwards with the dorsal side of the antenna. The action was repeated several times with both legs acting synchronously or with separate movements (Figure 3a–f). A series of eye and antennae scraping was almost always followed by dirt particle cleaning via the running of the tibial grooming structures through mouthparts (R and L tibia cleaning) (Figure 3a–f). Head rotation up to 90° was performed to allow antenna cleaning with the contralateral or ipsilateral tibia (R ant and L

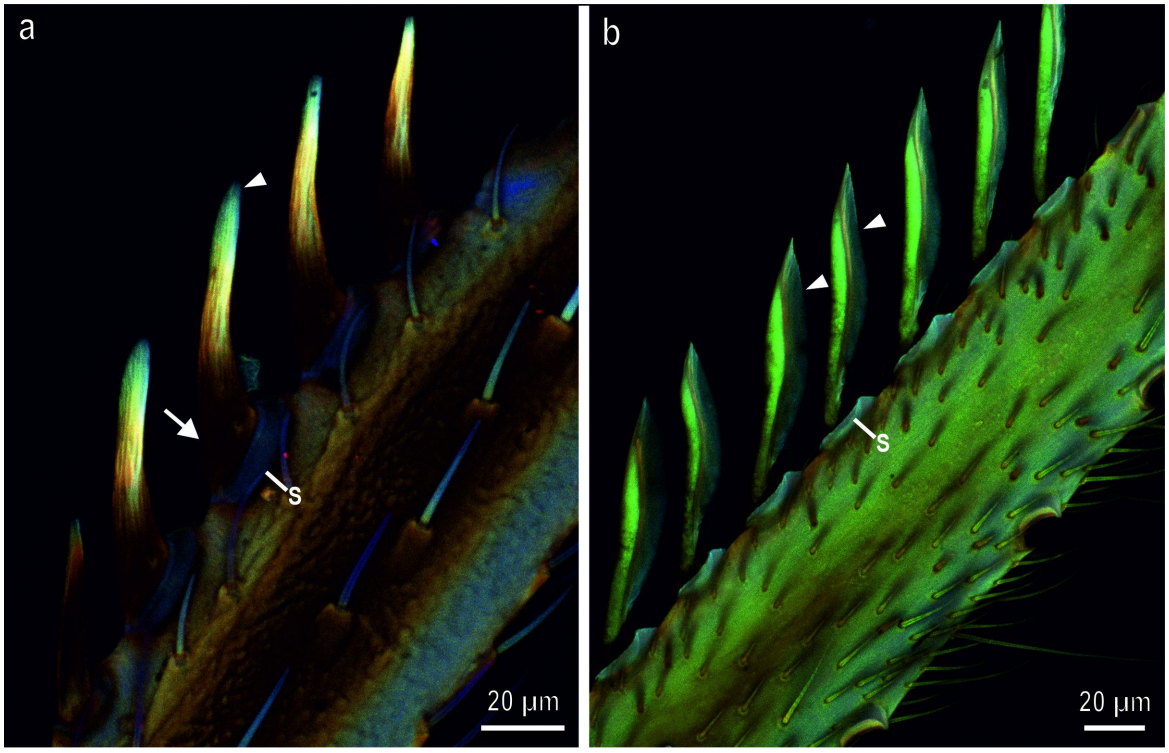

Figure 2: Confocal laser scanning micrographs (maximum intensity projections) showing differences in the autofluorescence composition present in the fore tibal grooming devices of *Ischnura elegans*. Red color indicates chitinous, sclerotized exoskeleton structures, green color indicates chitinous and non- or weakly sclerotized exoskeleton structures, and blue color indicates exoskeleton structures that either contain large proportions of the elastic protein resilin or are unsclerotized. (a) Dorsal view of the tibial grooming devices, revealing strongly sclerotized setae in their basal portion (arrow), which tend to become richer of resilin or unsclerotized and softer in their apical portions which are blue colored (arrow head). Note the soft setal socket (S), which is blue in color. (b) Ventral view of the tibial grooming devices. Note that the cuticular lamina appears blue (arrowhead) owing to either large proportions of resilin or its unsclerotized nature.

ant), in order to reach the side of the antennal surface previously not cleaned with the head in a horizontal position, thus improving the grooming efficiency (Figure 3). The frequency and duration of eye–antennal grooming (R eye-ant plus L eye-ant) (Frequency: $T = 26$; $N = 8$; $P = 0.029$. Duration: $T = 26$; $N = 8$; $P = 0.029$) and of tibia running through the mouthparts (R tibia cleaning plus L tibia cleaning) (Frequency: $t = 2.57$; d.f. = 6; $P = 0.042$. Duration: $t = 2.69$; d.f. = 6; $P = 0.036$) were higher in the experiments with contaminated eyes than in those with contaminated antennae, while there was no significant difference between the frequency ($t = 1.13$; d.f. = 6; $P = 0.302$) and duration ($t = 1.48$; d.f. = 6; $P = 0.189$) of antennal grooming (R ant plus L ant) in the experiments with contaminated eyes and in those with contaminated antennae (Figure 4a,b). There was no significant difference between the frequency ($t = 0.83$; d.f. = 6; $P = 0.439$) and duration ($t = 1.17$; d.f. = 6; $P = 0.287$) of head rotation (head rot) in the experiments with contaminated eyes and in those with contaminated antennae (Figure 4a,b). The mean duration of each bout was about 9.9 ± 2.6 s, when the eyes were contaminated and 4.7 ± 0.4 s, when the antennae were contaminated.

Particle removal efficiency

In the experiments, to evaluate the particle removal efficiency in intact (Figure 5a–c,h,j,k) and ablated (with their foretibial grooming structures artificially removed) (Figure 5d–f,i) insects, we observed that in intact damselflies the particle removal efficiency was very high leading to clean eyes (Figure 5b) and antennae (Figure 5k) after 1 h for the eyes and 10 min for the antennae. The pink powder removed from the eyes or antennae accumulated in correspondence with the flag-shaped structures located on the medial face of the tibia (Figure 5h), particularly in the concave side of the cuticular lamina (Figure 5c). The removal of the grooming devices in ablated insects (Figure 5f,i) induced a strong increase in the percentage of the areas contaminated with the powder on the eyes after grooming (Figure 5e). This percentage was 4.06% of the initial contaminated area in intact damselflies and 42.55% in ablated insects with a significant difference between the two values ($T = 169$; $N = 22$; $P < 0.001$) (Figure 5g).

In some intact specimens, after grooming, dissected mouthparts revealed the presence of pink powder (Figure 6a–e) visible in

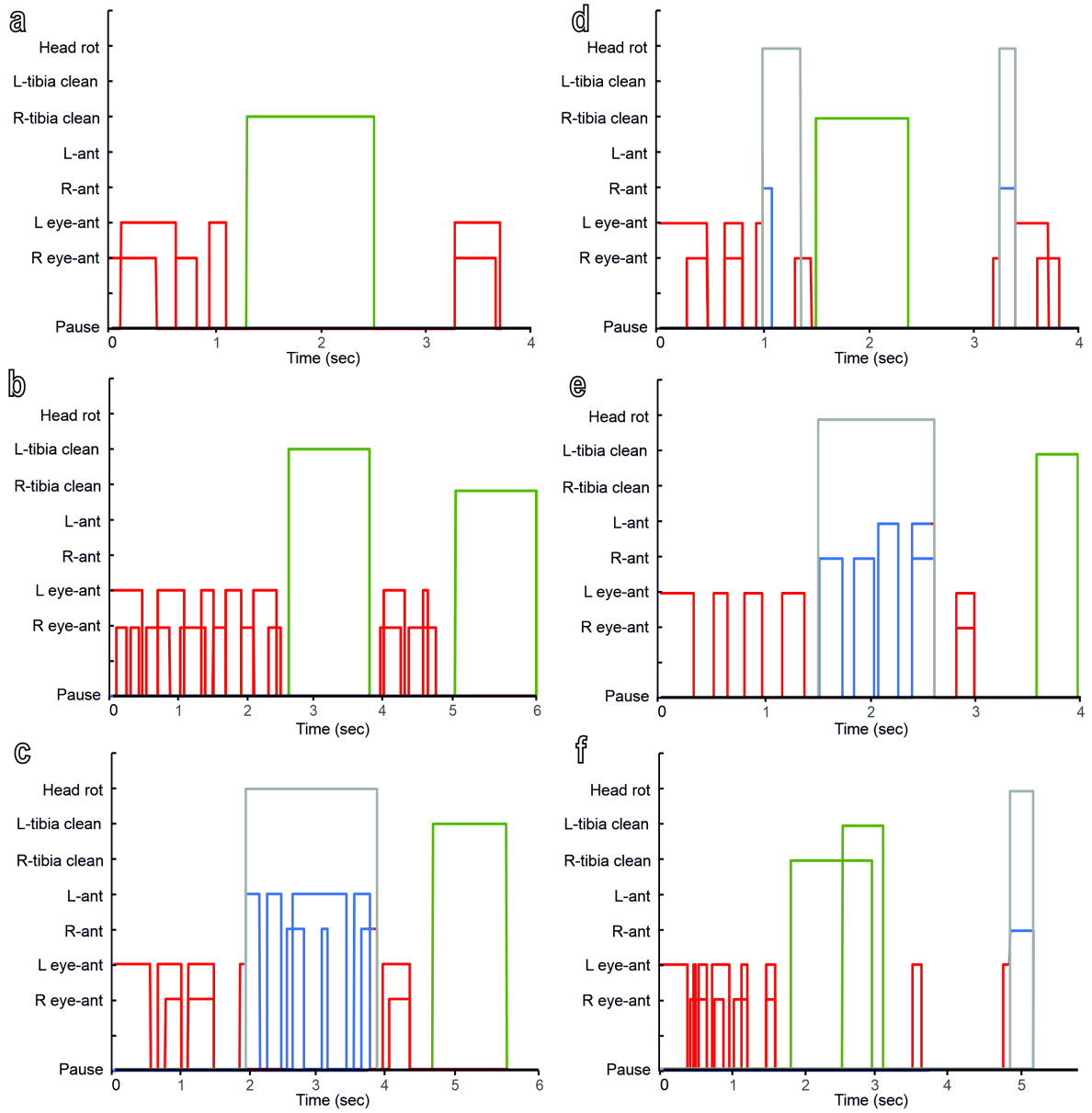

Figure 3: Ethograms of different bouts recorded during the grooming of *Ischnura elegans*. (a) First, (b), second and (c) fifth bout in the grooming of a damselfly with contaminated eyes. (d) First and (e) second bout in the grooming of a damselfly with contaminated antennae. (f) Single bout in the grooming of a damselfly with contaminated antennae. The following acts have been recorded: right foreleg raising and scraping of the right eye or of the right eye and of the dorsal side of the right antenna with the right tibia (R eye-ant); left foreleg raising and scraping of the left eye or of the left eye and of the dorsal side of the left antenna with the left tibia (L eye-ant); right foreleg raising and scraping of the right antenna with the right tibia (R ant); left foreleg raising and scraping of the left antenna with the left tibia (L ant); head rotation (70–90°) (head rot); right tibia running through mouthparts (R tibia cleaning); left tibia running through mouthparts (L tibia cleaning).

particular on the maxillae, especially on the maxillary palps (Figure 6a,b) and on the inner part of the labrum (Figure 6c). Some pink powder was also visible on the mandibular teeth (Figure 6d). The labium (Figure 6e) appeared less involved in tibial cleaning since the presence of pink powder appeared reduced in comparison with the other mouthparts.

Discussion

Among the different micro- and nanostructures of the cuticular surface, grooming devices represent fundamental tools for insect survival. In insects with chewing mouthparts, such as Orthoptera, for instance Grylloblattodea, Dermaptera, Mantodea, and Blattodea, antennal grooming is typically per-

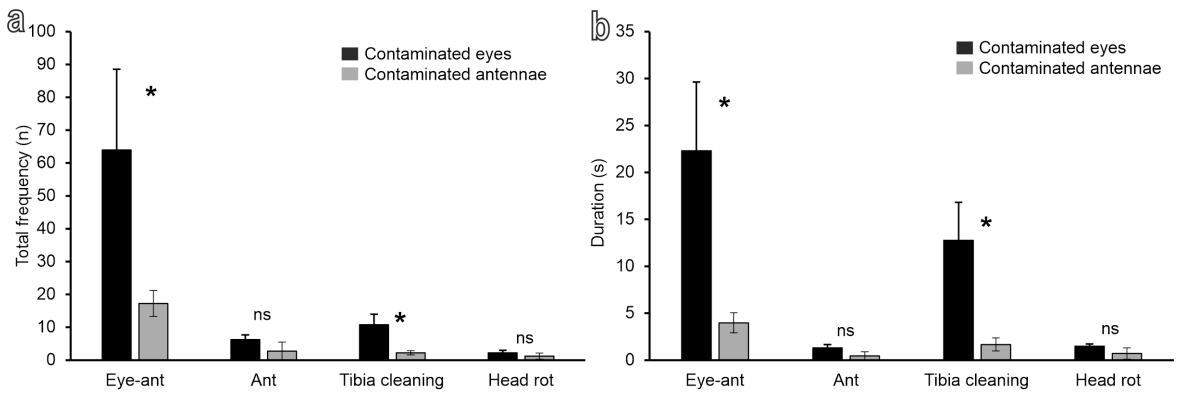

Figure 4: (a) Frequency and (b) duration of the different recorded acts during the grooming of *Ischnura elegans* in the experiments with contaminated eyes and with contaminated antennae. Forelegs raising and scraping of the eye(s) plus the dorsal side of the antennae with the tibiae (Eye-ant). Foreleg raising and scraping of the antennae with the tibiae (Ant). Tibia running through mouthparts (Tibia cleaning). Head rotation (70–90°) (Head rot). The asterisk indicates a significant difference at $p < 0.05$ (Mann–Whitney rank sum test for eye-ant and *t*-test for independent samples for the other acts).

formed using mouthparts to ingest debris [20,42]. These insects clean one antenna at a time by lowering it, then using the ipsilateral foreleg to pull it through the mouthparts from base to tip. This ancestral cleaning pattern has disappeared in insects with more specialized piercing-sucking or siphoning mouthparts, such as Hemiptera, Diptera and Lepidoptera, except the mandibulate archaic moth family Micropterigidae. Hemiptera use their forelegs to scrape their antennae, transferring debris onto the surrounding surface [20]. In contrast, many Hymenoptera employ a combination of techniques, using specialized leg spines to clean their antennae. They pass the antennae through a groove created by the apical tibial spur and the basitarsus of the foreleg, followed by using their mouthparts to clean the tibio-tarsal antenna cleaner [26,27,30,43].

Odonata possess biting mouthparts and ingestion of debris is the most likely strategy, but the behavior involving antennal cleaning with mouthparts cannot be performed owing to the short antennae. Odonata antennae in adults are reduced in size, but they possess different kind of sensilla, such as chemoreceptors [44-47] and thermo-hygroreceptors [44-48], which need frequent cleaning. Furthermore, the need to keep a clean eye surface to guarantee the functioning of the most advanced visual systems among insects ([35], review in [49]) requires the involvement of scraping forelegs with specialized cleaning structures. In our experiments, we could observe a higher frequency and a higher duration of grooming acts when the eyes were contaminated in comparison with antennal contamination, but this is probably due to the higher amount of powder used to contaminate eyes in comparison with that used for antennal contamination. Special attention is devoted by damselflies to their antennae. In particular, they rotate the head up to 90° to allow antenna cleaning with the contralateral or ipsilateral tibia, in order to reach the side of the antennal surface not previously cleaned with the head in horizontal position, thus improving the grooming efficiency. In any case, we could observe that, in each bout, antennae and eyes are always cleaned together, exactly as observed in *Drosophila* where antennal grooming is elicited via mechanoreceptors of Johnston's organ [50]; when legs of *Drosophila* sweep across the antennae, they also sweep across the eyes.

Antennal grooming organs have independently evolved in several insect orders, differing in the morphology and surface complexity of the involved structures [51,52]. These cleaning organs typically consist of modified setae and other cuticular projections that scrape and remove particles, concentrating them for disposal [53]. In *Ischnura elegans*, grooming devices include setae with concave cuticular laminae on the medial side of the tibiae. Each seta emerges from a soft socket either rich in resilin or of unsclerotized chitin, which enables movement at the base, proceeds in a hard base of sclerotized chitin, and ends in a soft tip, either rich in resilin or of unsclerotized chitin. A material gradient from stiff bases to soft tips has also been found in the adhesive hairs of insect leg attachment systems [38,39,54]. This gradient prevents the clustering of adhesive hairs, while the soft tips ensure effective contact between the attachment system and the substrate. Similarly, the material gradient in grooming devices may enhance adhesion to foreign materials for grooming body surfaces. The soft tip and soft lateral cuticular lamina adapt to various surface geometries, while the stiff base prevents clumping of setae. The elasticity of the cuticular lamina of the grooming devices of *I. elegans* enhances the ability of the grooming structures to scrape eyes and antennae removing and collecting debris that accumulated

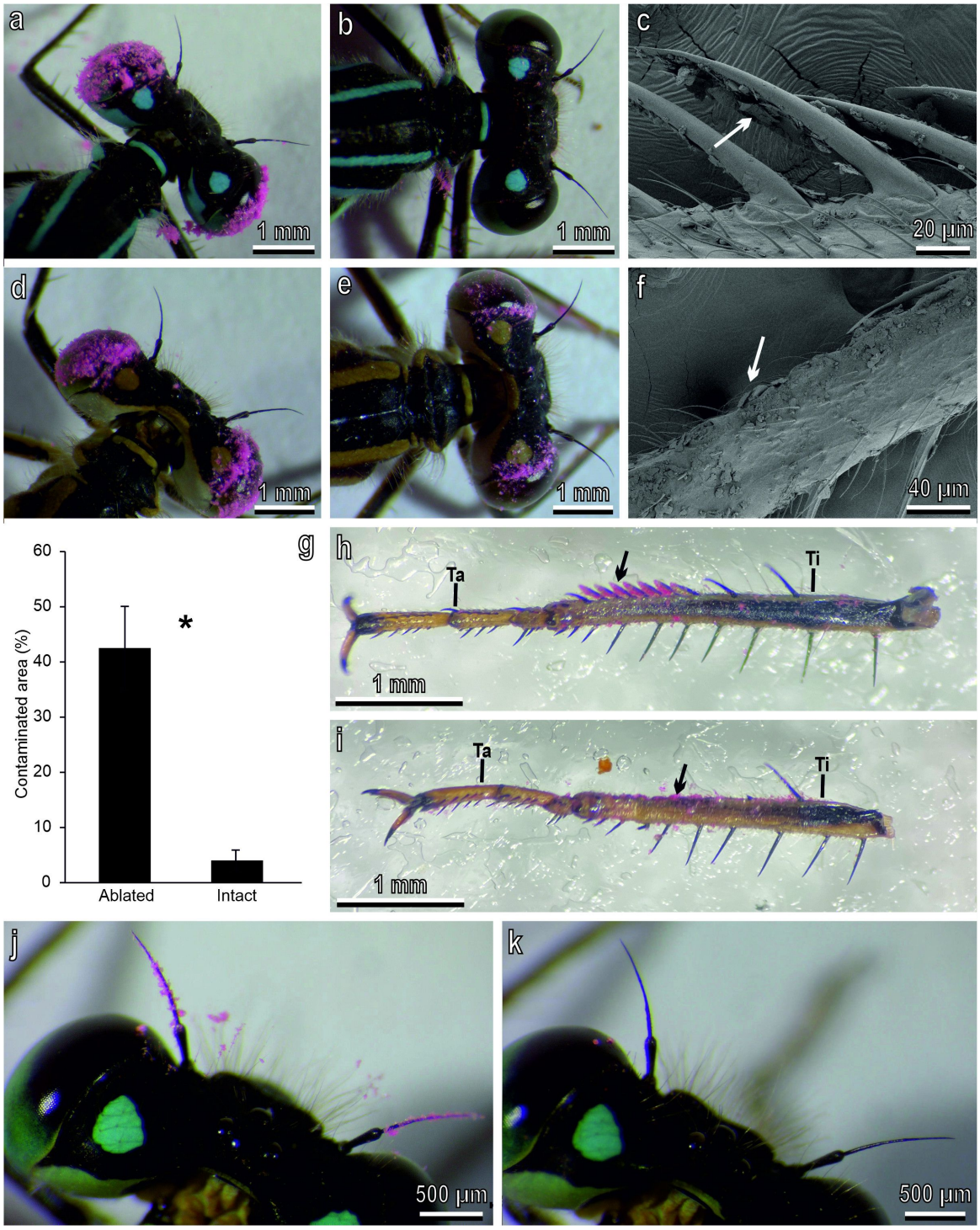

Figure 5: Particle removal efficiency in intact (a–c, h, j, k) and ablated (with the foretibial grooming structures artificially removed) (d–f, i) *Ischnura elegans* (female) under a stereomicroscope (a, b, d, e, h–k) and an SEM (c, f). (a, b) Intact damselflies with eyes contaminated by pink powder, just contaminated (a) and after one hour (b). Note the clean eyes. (c) Detail of the tibial grooming devices with pink powder (arrow) accumulated in correspondence of the concave side of the cuticular lamina. (d, e) Ablated damselflies with eyes contaminated by pink powder, just contaminated (d) and after one hour (e). Note the dirty eyes. (f) Detail of the tibia with the foretibial grooming structures artificially removed with powder (arrow) on the tibial surface. (g) Percentage of contaminated area on the eyes after cleaning of intact and ablated damselflies. The asterisk indicates a significant difference at $p < 0.05$ (Mann–Whitney rank sum test). (h) Tarsus (Ta) and tibia (Ti) with the tibial grooming devices (arrow) collecting pink powder. (i) Tarsus (Ta) and tibia (Ti) of an ablated damselfly. Note that some pink powder (arrow) is visible in correspondence of the grooming devices. (j, k) Intact damselfly with antennae contaminated by pink powder, just contaminated (j) and after (k) 10 min.

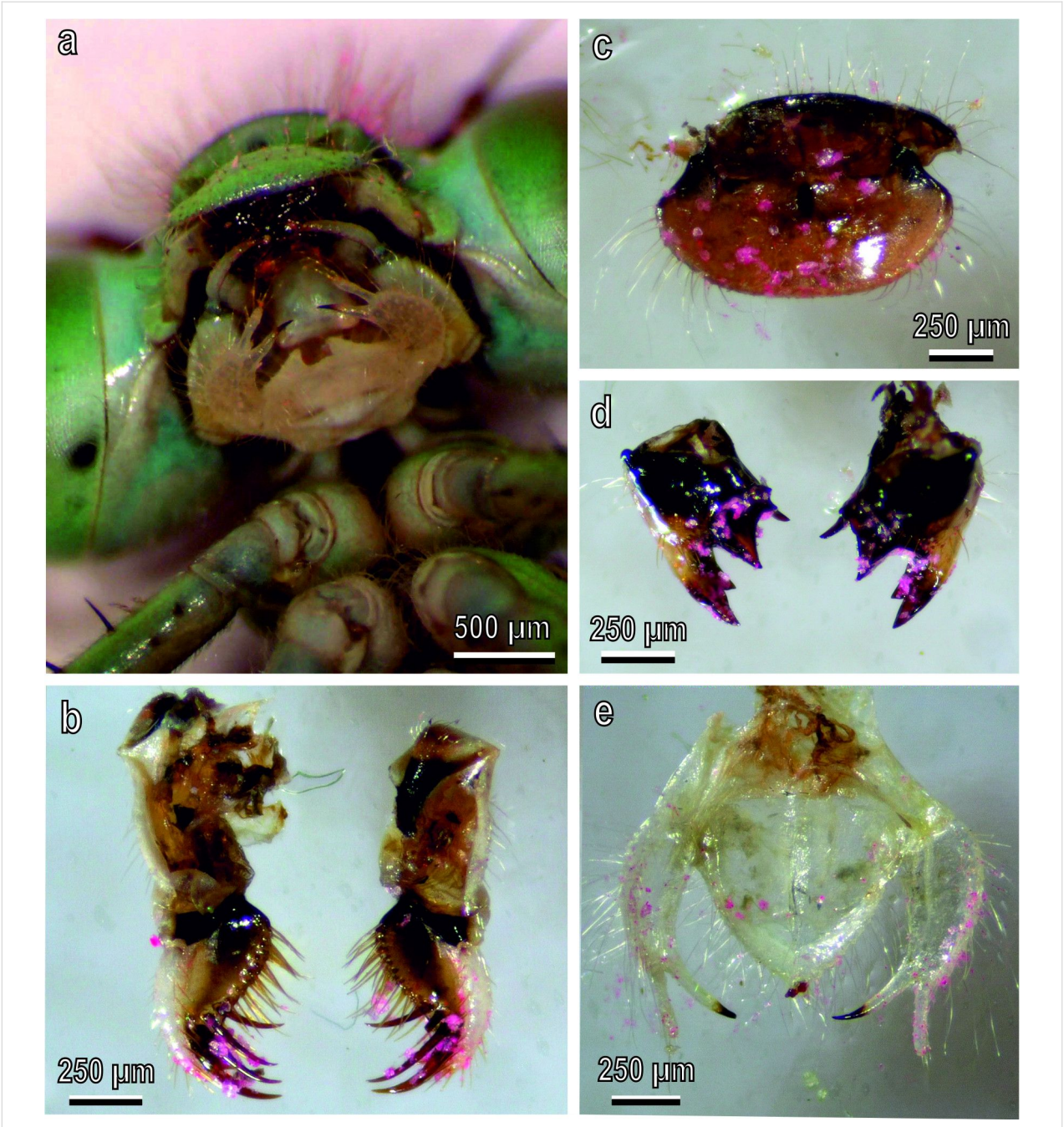

Figure 6: Mouthparts of *Ischnura elegans* dissected immediately after the antennal grooming behavior. (a) Ventral view of mouthparts with pink powder residues. (b) Dorsal view of the maxillae with evident pink powder, particularly on the maxillary palps. (c) Ventral view of the labrum with evident pink powder. (d) Dorsal view of the mandibles with some pink powder on the teeth. (e) Dorsal view of the labium with a reduced presence of pink powder.

inside the flag-shaped structures. The indentations along the lateral border of the lamina can further help in entrapping dirt particles.

The effectiveness of these structures in Odonata grooming is clearly demonstrated in our experiments with ablated insects, where we can observe a strong increase in the percentage of the contaminated areas on the eyes after grooming. In different insect orders, grooming devices are represented by modified setae from which thin cuticular laminae develop on one or on both lateral sides. This is the case of Mantodea, where a femoral brush comprising 100–200 feather- or paddle-shaped setae is present [32]. In Hemiptera, the tibial comb is constituted of a concave cuticular lamina, whose distal border bears a row of

tightly packed digitiform setae with lateral cuticular laminar expansions, which overlap allowing the interdigitations of the setae [28]. The digitiform setae have a gradient of resilin concentration and, therefore, mechanical properties [28]. The interdigitated cuticular laminar expansions overlapping at different heights constitute a very flexible surface because of their high resilin content, which enables them to gently press against the antennal surface to be cleaned, thereby squeezing the debris outwards [28]. Many Hymenoptera bear flattened leg spines specialized for the cleaning of antennae [26,27,55]. A high content of resilin characterizes the inner side of the calcar or the basitarsal comb in the antenna cleaner of different species of Formicidae [56]. Zhang et al. [33], through nanoindentation tests, discovered that the tibial comb of honeybees exhibits a resilin gradient with a stiffness variation spanning nearly two orders of magnitude, ranging from approximately 25 MPa at the tip to around 645 MPa at the base. This gradient enhances the catapult effect, allowing the comb to produce increased inertia that counteracts the initially dominant adhesion, effectively dislodging attached pollen and dust. The same authors also developed an elastomeric bioinspired stiffness-gradient catapult and demonstrated its potential in practical applications, thus confirming that studies on the functional morphology of insect grooming devices can represent a starting point for further investigation of optimal materials design in bioinspired robotic systems.

As observed in our experiments, Odonata clean their grooming devices running their forelegs through the mouthparts. In our observations, we could not detect a special mouthpart involved in collecting particles from the grooming devices since the pink powder can be observed in the distal portion of maxillae, especially on the dentisetae, which are very sclerotized [57], in the mandibles, and in the inner portion of the labrum. In the German cockroach, which possesses chewing mouthparts and achieves antennal debris removal scraping directly the antenna over the glossa, most of the debris are manipulated into the hypopharynx and ingested when grooming is completed [42]. Further studies could clarify the biomechanics of foretibiae cleaning in Odonata. In this regard, it is important to remember that understanding insect grooming may provide insights into routes of entry of pesticides because the oral toxicity of substances that induce grooming (such as insecticides or other chemicals toxic for insects) should increase in insects that include ingestion in their grooming behavior [2].

As reported above, grooming behavior and devices, especially in insects, have been used to investigate phylogeny and evolution because of their low variability within species and relative evolutionary conservatism [26,30,52]. Further investigation of the grooming devices of different Odonata families, which diverged relatively early in their evolution, especially in relation to morphology of their compound eyes, would be interesting in this context.

Supporting Information

Supporting Information File 1

Damselflies' antennal and eye grooming behavior.
[https://www.beilstein-journals.org/bjnano/content/supplementary/2190-4286-15-102-S1.mp4]

Acknowledgements

We are very grateful to Anna Martorel for her help in insect collecting and behavioral observations.

Funding

The study was supported by the European Union – NextGenerationEU under the Italian Ministry of University and Research (MUR) National Innovation Ecosystem grant ECS00000041 – VITALITY. We acknowledge Università degli Studi di Perugia and MUR for support within the project Vitality.

Conflict of Interest

All the authors declare that they have no conflict of interest.

Author Contributions

Silvana Piersanti: conceptualization; investigation; methodology; resources; validation; writing – original draft; writing – review & editing. Gianandrea Salerno: conceptualization; formal analysis; investigation; methodology; resources; supervision; validation; visualization; writing – original draft; writing – review & editing. Wencke Krings: investigation; methodology; writing – review & editing. Stanislav Gorb: conceptualization; investigation; methodology; resources; supervision; validation; writing – original draft; writing – review & editing. Manuela Rebora: conceptualization; funding acquisition; investigation; methodology; resources; supervision; validation; visualization; writing – original draft; writing – review & editing.

ORCID® iDs

Silvana Piersanti - https://orcid.org/0000-0001-7956-9416
Gianandrea Salerno - https://orcid.org/0000-0002-8357-7598
Wencke Krings - https://orcid.org/0000-0003-2158-9806
Stanislav Gorb - https://orcid.org/0000-0001-9712-7953
Manuela Rebora - https://orcid.org/0000-0002-4271-6336

Data Availability Statement

The data that supports the findings of this study is available from the corresponding author upon reasonable request.

References

1. Sachs, B. D. *Ann. N. Y. Acad. Sci.* **1988,** *525,* 1–17. doi:10.1111/j.1749-6632.1988.tb38591.x
2. Zhukovskaya, M.; Yanagawa, A.; Forschler, B. *Insects* **2013,** *4,* 609–630. doi:10.3390/insects4040609
3. Borchelt, P. L. Care of the Body Surface (COBS). In *Comparative Psychology: An Evolutionary Analysis of Animal Behavior;* Denny, M. R., Ed.; John Wiley & Sons: New York, NY, USA, 1980.
4. Gorb, S. N. *Attachment Devices of Insect Cuticle;* Kluwer Academic Publishers: New York, NY, USA, 2001.
5. Schroeder, T. B. H.; Houghtaling, J.; Wilts, B. D.; Mayer, M. *Adv. Mater. (Weinheim, Ger.)* **2018,** *30,* 1705322. doi:10.1002/adma.201705322
6. Szebenyi, A. L. *Anim. Behav.* **1969,** *17,* 641–651. doi:10.1016/s0003-3472(69)80006-0
7. El-Awami, I. O.; Dent, D. R. *Entomol. Exp. Appl.* **1995,** *77,* 81–87. doi:10.1111/j.1570-7458.1995.tb01988.x
8. Vincent, C. M.; Bertram, S. M. *Anim. Behav.* **2010,** *79,* 51–56. doi:10.1016/j.anbehav.2009.10.001
9. Reber, A.; Purcell, J.; Buechel, S. D.; Buri, P.; Chapuisat, M. *J. Evol. Biol.* **2011,** *24,* 954–964. doi:10.1111/j.1420-9101.2011.02230.x
10. Lusebrink, I.; Dettner, K.; Seifert, K. *Naturwissenschaften* **2008,** *95,* 751–755. doi:10.1007/s00114-008-0374-z
11. Rakitov, R.; Gorb, S. N. *Proc. R. Soc. B* **2013,** *280,* 20122391. doi:10.1098/rspb.2012.2391
12. Hefetz, A.; Soroker, V.; Dahbi, A.; Malherbe, M. C.; Fresneau, D. *Chemoecology* **2001,** *11,* 17–24. doi:10.1007/pl00001827
13. Jander, R.; Jander, U. *J. Kans. Entomol. Soc.* **1978,** *51,* 653–665.
14. Clemente, C. J.; Bullock, J. M. R.; Beale, A.; Federle, W. *J. Exp. Biol.* **2010,** *213,* 635–642. doi:10.1242/jeb.038232
15. Hosoda, N.; Gorb, S. N. *Proc. R. Soc. B* **2011,** *278,* 1748–1752. doi:10.1098/rspb.2010.1772
16. Clemente, C. J.; Federle, W. *Bioinspiration Biomimetics* **2012,** *7,* 046001. doi:10.1088/1748-3182/7/4/046001
17. Mizutani, H.; Tagai, K.; Habe, S.; Takaku, Y.; Uebi, T.; Kimura, T.; Hariyama, T.; Ozaki, M. *Insects* **2021,** *12,* 773. doi:10.3390/insects12090773
18. Gordon, D. M. *Ants at work: how an insect society is organized;* Simon and Schuster: New York, NY, USA, 1999.
19. Böröczky, K.; Wada-Katsumata, A.; Batchelor, D.; Zhukovskaya, M.; Schal, C. *Proc. Natl. Acad. Sci. U. S. A.* **2013,** *110,* 3615–3620. doi:10.1073/pnas.1212466110
20. Jander, U. *Z. Tierpsychol.* **1966,** *23,* 199–844. doi:10.1111/j.1439-0310.1966.tb01711.x
21. Dawkins, R.; Dawkins, M. *Anim. Behav.* **1976,** *24,* 739–755. doi:10.1016/s0003-3472(76)80003-6
22. Walker, E. D.; Archer, W. E. *J. Insect Behav.* **1988,** *1,* 97–109. doi:10.1007/bf01052506
23. Thelen, E.; Farish, D. J. *Behaviour* **1977,** *62,* 70–102. doi:10.1163/156853977x00054
24. Zack, S. *Behav. Processes* **1978,** *3,* 97–105. doi:10.1016/0376-6357(78)90037-2
25. Lefebvre, L. *Anim. Behav.* **1981,** *29,* 973–984. doi:10.1016/s0003-3472(81)80050-4
26. Basibuyuk, H. H.; Quicke, D. L. J. *Zool. J. Linn. Soc.* **1999,** *125,* 349–382. doi:10.1111/j.1096-3642.1999.tb00597.x
27. Hackmann, A.; Delacave, H.; Robinson, A.; Labonte, D.; Federle, W. *R. Soc. Open Sci.* **2015,** *2,* 150129. doi:10.1098/rsos.150129
28. Rebora, M.; Salerno, G.; Piersanti, S.; Michels, J.; Gorb, S. *J. Insect Physiol.* **2019,** *112,* 57–67. doi:10.1016/j.jinsphys.2018.12.002
29. ODell, T. M.; Shields, K. S.; Mastro, V. C.; Kring, T. J. *Can. Entomol.* **1982,** *114,* 751–761. doi:10.4039/ent114751-8
30. Basibuyuk, H. H.; Quicke, D. L. J. *Zool. Scr.* **1995,** *24,* 157–177. doi:10.1111/j.1463-6409.1995.tb00397.x
31. Beutel, R. G.; Balke, M.; Steiner, W. E., Jr. *Cladistics* **2006,** *22,* 102–131. doi:10.1111/j.1096-0031.2006.00092.x
32. Ramsay, G. W. *Mantodea (Insecta), with a review of aspects of functional morphology and biology,* Wellington, New Zealand ed.; *Fauna of New Zealand, Number 19*; DSIR Publishing, 1990.
33. Zhang, W.; Jiang, W.; Zhang, C.; Qin, X.; Zheng, H.; Xu, W.; Cui, M.; Wang, B.; Wu, J.; Wang, Z. *Nat. Nanotechnol.* **2024,** *19,* 219–225. doi:10.1038/s41565-023-01524-x
34. von Bigot de Saint Quentin, D. *Zool. Anz.* **1936,** *115,* 225–231.
35. Corbet, P. S. *Dragonflies: Behavior and Ecology of Odonata;* Harley Books: Colchester, UK, 1999.
36. Michels, J.; Appel, E.; Gorb, S. N. *Beilstein J. Nanotechnol.* **2016,** *7,* 1241–1259. doi:10.3762/bjnano.7.115
37. Michels, J.; Gorb, S. N. *J. Microsc. (Oxford, U. K.)* **2012,** *245,* 1–16. doi:10.1111/j.1365-2818.2011.03523.x
38. Peisker, H.; Michels, J.; Gorb, S. N. *Nat. Commun.* **2013,** *4,* 1661. doi:10.1038/ncomms2576
39. Rebora, M.; Michels, J.; Salerno, G.; Heepe, L.; Gorb, E.; Gorb, S. *J. Morphol.* **2018,** *279,* 660–672. doi:10.1002/jmor.20801
40. Rebora, M.; Salerno, G.; Piersanti, S.; Saitta, V.; Morelli Venturi, D.; Li, C.; Gorb, S. *Sci. Rep.* **2023,** *13,* 22101. doi:10.1038/s41598-023-49549-5
41. *Solomon Coder,* Beta 17.03.22; András Péter, 2017, https://solomoncoder.com.
42. Robinson, W. H. Antennal Grooming and Movement Behavior in the German Cockroach, *Blattella germanica* (L.). In *Proceedings of the Second International Conference on Urban Pests,* Edinburgh, UK; 1996; pp 361–369.
43. Jander, R. *Physiol. Entomol.* **1976,** *1,* 179–194. doi:10.1111/j.1365-3032.1976.tb00960.x
44. Rebora, M.; Piersanti, S.; Gaino, E. *Arthropod Struct. Dev.* **2008,** *37,* 504–510. doi:10.1016/j.asd.2008.03.003
45. Rebora, M.; Piersanti, S.; Gaino, E. *Odonatologica* **2009,** *38,* 329–340.
46. Rebora, M.; Salerno, G.; Piersanti, S.; Dell'Otto, A.; Gaino, E. *J. Insect Physiol.* **2012,** *58,* 270–277. doi:10.1016/j.jinsphys.2011.11.018
47. Piersanti, S.; Rebora, M.; Gaino, E. *Odonatologica* **2010,** *39,* 235–241.
48. Piersanti, S.; Rebora, M.; Almaas, T. J.; Salerno, G.; Gaino, E. *J. Insect Physiol.* **2011,** *57,* 1391–1398. doi:10.1016/j.jinsphys.2011.07.005
49. Bybee, S. M.; Johnson, K. K.; Gering, E. J.; Whiting, M. F.; Crandall, K. A. *Org. Diversity Evol.* **2012,** *12,* 241–250. doi:10.1007/s13127-012-0090-6
50. Hampel, S.; Franconville, R.; Simpson, J.; Seeds, A. *eLife* **2015,** *4,* e08758. doi:10.7554/elife.08758
51. Hlavac, T. F. *Psyche* **1971,** *78,* 51–66. doi:10.1155/1971/927545
52. Valentine, B. D. *Coleopt. Bull.* **1973,** *27,* 63–73. doi:10.5962/p.372607
53. Hlavac, T. F. *Ann. Entomol. Soc. Am.* **1975,** *68,* 823–826. doi:10.1093/aesa/68.5.823
54. Salerno, G.; Rebora, M.; Piersanti, S.; Matsumura, Y.; Gorb, E.; Gorb, S. *J. Insect Physiol.* **2020,** *127,* 104117. doi:10.1016/j.jinsphys.2020.104117
55. Schönitzer, K.; Lawitzky, G. *Zoomorphology* **1987,** *107,* 273–285. doi:10.1007/bf00312173

56. Beutel, R. G.; Richter, A.; Keller, R. A.; Hita Garcia, F.; Matsumura, Y.; Economo, E. P.; Gorb, S. N. *J. Morphol.* **2020,** *281,* 737–753. doi:10.1002/jmor.21133
57. Josten, B.; Gorb, S. N.; Büsse, S. *J. Morphol.* **2022,** *283,* 1163–1181. doi:10.1002/jmor.21497

License and Terms

BEILSTEIN JOURNAL OF NANOTECHNOLOGY

A biomimetic approach towards a universal slippery liquid infused surface coating

Ryan A. Faase‡, Madeleine H. Hummel‡, AnneMarie V. Hasbrook, Andrew P. Carpenter and Joe E. Baio*

Full Research Paper

Open Access

Address:
School of Chemical Biological and Environmental Engineering, Oregon State University, Corvallis, OR 97331, USA

Email:
Joe E. Baio* - joe.baio@oregonstate.edu

* Corresponding author ‡ Equal contributors

Keywords:
biocompatibility; biomimetic; blood-contacting; hemocompatibility; non-fouling

Beilstein J. Nanotechnol. **2024,** *15,* 1376–1389.
https://doi.org/10.3762/bjnano.15.111

Received: 04 July 2024
Accepted: 08 October 2024
Published: 08 November 2024

This article is part of the thematic issue "Micro- and nanoscale effects in biological and bioinspired materials and surfaces".

Guest Editor: T. H. Büscher

Abstract

One biomimetic approach to surface passivation involves a series of surface coatings based on the slick surfaces of carnivorous pitcher plants (Nepenthes), termed slippery liquid-infused porous surfaces (SLIPS). This study introduces a simplified method to produce SLIPS using a polydopamine (PDA) anchor layer, inspired by mussel adhesion. SLIPS layers were formed on cyclic olefin copolymer, silicon, and stainless steel substrates, by first growing a PDA film on each substrate. This was followed by a hydrophobic liquid anchor layer created by functionalizing the PDA film with a fluorinated thiol. Finally, perfluorodecalin was applied to the surface immediately prior to use. These biomimetic surface functionalization steps were confirmed by several complimentary surface analysis techniques. The wettability of each surface was probed with water contact angle measurements, while the chemical composition of the layer was determined by X-ray photoelectron spectroscopy. Finally, ordering of specific chemical groups within our PDA SLIPS layer was determined via sum frequency generation spectroscopy. The hemocompatibility of our new PDA-based SLIPS coating was then evaluated by tracking FXII activation, fibrin generation time, clot morphology, and platelet adhesion to the surface. This hemocompatibility work suggests that PDA SLIPS coatings slow or prevent clotting, but the observation of both FXII activation and the presence of adherent and activated platelets at the PDA SLIPS samples imply that this formulation of a SLIPS coating is not completely omniphobic.

Introduction

Clot formation and the overall compatibility of artificial materials within the body remains a common complication of blood contacting surfaces [1-8]. A critical hurdle in reducing the thrombogenicity of a material lies in addressing the intricate layer of protein within blood that adsorbs to any surface it comes into contact with. This layer is responsible for the initia-

tion of host responses such as coagulation or inflammation. To address the body's reaction to these materials, researchers have developed strategies to combat blood clots and bacterial infections in frequently used devices such as tubing, catheters, and grafts [9-15]. Consideration of the coagulation cascade is a crucial part in engineering new materials that interact with blood and reducing the potential for adverse effects. Factor XII, thrombin, and calcium are critical components of the coagulation cascade, and their removal represents a pathway for lowering thrombus formation due to contact with foreign materials. Each of these components has led to different approaches for the removal and or repulsion of these important molecules that control the clotting cascade. The most prominent of the methods are ones that aim to reduce non-specific protein adsorption, increase adhesion resistance, use biomolecules to remove targets of interest, and enhance endothelial cell attachment.

One biomimetic approach to surface passivation involves a series of surface coatings based on the slick surfaces of carnivorous pitcher plants (Nepenthes), termed slippery liquid-infused porous surfaces (SLIPS) [4]. When wetted, the slippery surfaces on the plant cause prey to slide into the bottom of the pitcher-like feature, where they are digested by the plant. Like the pitcher plant surfaces, SLIPS can repel adhesion through the formation of a liquid–liquid interface, unlike more standard surface passivation techniques that consist of a solid–liquid interface [16].

Within a SLIPS coating, a lubricant is anchored to a substrate, creating a smooth liquid layer that is energetically favored to interact with the solid surface. The surface chemistry of the anchoring layer is crucial to the viability of the overall coating as the lubricant must have a greater affinity for the substrate surface than for any foreign surface. Materials coated with SLIPS have demonstrated effectiveness in resisting corrosion, reducing bio-fouling, and preventing icing [1-3,6,8]. There is also evidence that SLIPS are a promising strategy for increasing the biocompatibility of materials [4,11].

SLIPS are generally defined by either a porous or flat solid surface that consists of chemistry that is similar to the pervading liquid [11,17]. The substrate serves an anchor to a lubricant, which provides a smooth liquid layer that provides some sort of resistance to surface adhesion. The liquid is anchored to the surface through van der Waals forces, and capillary forces if there is a rough surface, forces which give way to conditions that are energetically favorable to the retention of the infused liquid as opposed to a foreign one. The preparation of SLIPS substrates include plasma treatments [4,12], acid/base soaks [1,13], anodization [3,14], silane chemistry [18], and polymer multilayers [5,15]. While these methods are effective, there is often a requirement for a specific chemical environment, like a plasma processing step or the growth of an oxide layer. In this investigation, we aim to simplify the fabrication of SLIPS by producing the required lubricant anchor layer through the polymerization of dopamine. This dopamine polymerization step is extremely simple and will form a "sticky" layer to almost any chemistry, thereby, providing a straightforward process to produce a SLIPS layer on almost any substrate.

Over a decade ago, Lee et al. demonstrated that mussels could adhere to virtually any surface through a molecule called polydopamine (PDA) [19]. The power of PDA lies in its ability to coat a thin layer onto any material, from polymers and metals to glass. The authors also demonstrated the modification of the PDA film though the formation of a pseudo self-assembled monolayer [19,20]. In this process, molecules that contain thiol groups attach to the newly formed PDA surface via Michael addition [21-23]. In this work, we take advantage of PDA to cova-

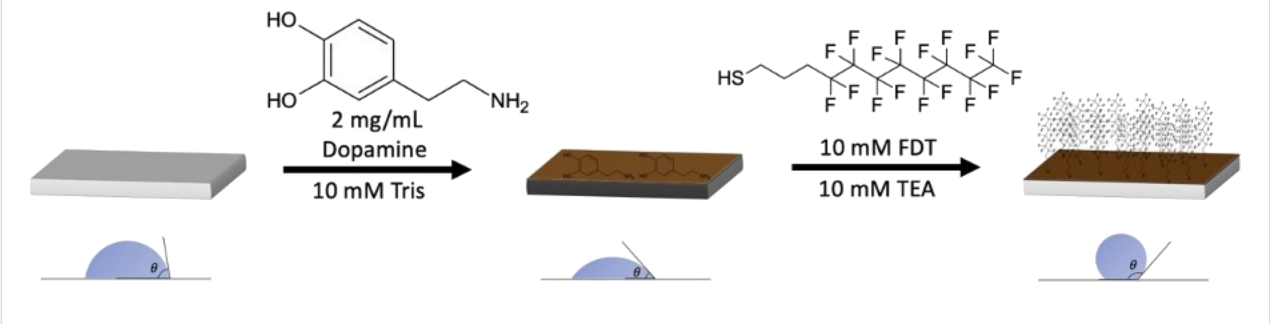

Figure 1: Schematic of PDA–FDT–PFD coating process. The bare substrate, cyclic olefin copolymer (COC, left) is hydrophobic. A layer of polydopamine (PDA) is added to the surface by incubating surfaces overnight with dopamine and Tris. PDA is hydrophilic, so the PDA coating step can be verified through water contact angle measurements. Fluorinated dodecanethiol (FDT) was conjugated to the PDA surface by incubating overnight. FDT is hydrophobic, so this step can be also verified through water contact angle measurements. Not pictured is the addition of perfluorodecalin (PFD) to the surface immediately prior to use.

lently attach fluorinated chains, producing the foundation of a SLIPS material (Figure 1).

In this work we propose and characterize a two-step process, forming a SLIPS layer via a sticky PDA film, to modify the surface of three different materials. To test this combination of PDA and SLIPS we used three distinct materials, cylic olefin copolymer (COC), silicon, and 316 stainless steel (SS) as our substrates. These substrates were first coated with PDA; then, a fluorinated thiol was attached to serve as the anchor for the infused fluid. The resulting surface modifications were then characterized by water contact angle measurements, atomic force microscopy (AFM), sum frequency generation spectroscopy (SFG), and X-ray photoelectron spectroscopy (XPS). Measuring static water contact angles is a straightforward method to determine the relative wettability of a material and allows for a quick check if our surface modifications were successful with a fluid similar to blood [24]. AFM is a technique that provides topographical information through a nanoscale probe [25]. After each successive layer of the coating the topography of the surface will change and can be measured via AFM. SFG is a surface-sensitive non-linear spectroscopic technique, which has the ability to probe vibrational modes at an interface, thereby, providing insight into the order and confirmation of molecules at an interface [26,27]. XPS is a surface-sensitive technique to determine the atomic composition of the outer ca. 10 nm of a surface [28].

As mentioned above, SLIPS represent a novel method of surface passivation that involves trapping a liquid, often an oil, onto a porous surface [4,29]. The result is an antifouling surface that has been proposed to resist adhesion of coagulation factors [4,29]. Yet, the activation of coagulation factors, specifically FXII, and the plasma clotting kinetics on SLIPS surfaces have not been studied previously. Therefore, to assess the hemocompatibity of our newly created PDA-based SLIPS coating, we tested the resistance of the coating to FXII activation, clot formation, clot stability, and platelet adhesion.

FXII activation gives insight into the extent of intrinsic coagulation. On biocompatible surfaces, we would expect to see a lower concentration of activated FXII (FXIIa) than on prothrombogenic surfaces. Platelet adhesion and activation testing describes the tendency of platelets to adhere to a surface, which promotes coagulation. We would expect to see fewer adherent platelets on biocompatible surfaces compared to prothrombogenic surfaces. Fibrin generation time describes the resistance to fibrin formation from fibrinogen and, thus, clot formation. Biocompatible coatings will have a longer fibrin generation time than prothrombogenic coatings. Clot stability, quantified via crosslinking density measurements, provides insight into the ability of a clot to break down. Clots on biocompatible coatings should be less stable (larger fiber diameter and lower crosslinking density) compared to prothrombogenic surfaces.

These assays collectively provide a starting point for understanding the foundation for understanding the behavior of PDA SLIPS when in contact with blood. We anticipate that the PDA SLIPS coating will demonstrate antithrombogenic properties. Therefore, we expect it to exhibit a lower concentration of FXII, decreased platelet adhesion, longer fibrin generation time, and lower clot stability compared to other surfaces.

Experimental

Sample preparation

COC (microfluidic ChipShop, Jena, Germany) was first cut to size, into 1 × 1 cm^2 squares. These COC substrates were cleaned by sequential sonication in DI water and then in a 1:1 mixture of ethanol and acetone for 30 min. Si substrates were fabricated via a diamond-tipped blade in a Disco wafer saw (Disco, Tokyo, Japan) from a silicon wafer cut into 1 × 1 cm^2 substrates. These Si substrates were left overnight to soak in DI water and then sonicated in 20 min intervals with dichloromethane, acetone, and ethanol. 316 SS was purchased from McMaster-Carr (Elmhurst, IL) and ground up to grit 3000 with SiC emery paper and cut by hand into 1 × 1 cm^2 chips. The cut SS substrates were rinsed in DI water and ethanol followed by sonication in a 1:1 mixture of chloroform and methanol for 20 min [30]. All substrates were then dried under a stream of nitrogen and sealed until use. The cleaned substrates were then immersed in dopamine hydrochloride (Sigma-Aldrich, St. Louis, MO) at a concentration of 2 mg/mL for 24 h in a 10 mM Trizma base (Sigma-Aldrich, St. Louis, MO) solution at a pH of 8.5. PDA-coated samples were rinsed with DI and then introduced to a 10 mM aqueous solution of 1*H*,1*H*,2*H*,2*H*-perfluorodecanethiol (FDT) (Sigma-Aldrich, St. Louis, MO) and triethylamine [19]. Following FDT functionalization, the samples were thoroughly rinsed and sonicated in DI water and then sealed under nitrogen until ready to use. Immediately prior to use, the SLIPS formation was completed by adding a layer of liquid perfluorodecalin (PFD) to the surface (Figure 1).

Water contact angle

A custom setup was used similar to one previously described [31]. Static contact angle measurements were conducted with the sessile drop method. Droplets of 5 µL were pipetted onto the surface, and an image was captured. Eight images from two duplicates of each sample type were acquired on a smartphone device and processed in ImageJ (NIH).

Atomic force microscopy

AFM was conducted on a Veeco di Innova instrument in tapping mode. RTESPA-300 (Bruker, Billerica, MA) probes were used with a tip radius of 12 nm, a spring constant of 40 N/m, and a frequency of 300 kHz. A minimum of six images from two different samples were produced with dimensions of 5 × 5 μm at a scan rate of 0.5 Hz. Post processing and analysis of the collected scans included a lowpass filter and took place in the "NanoScope analysis" software.

Sum frequency generation vibrational spectroscopy

The SFG setup used an EKSLPA Nd:YAG laser operated at 50 Hz to generate a fixed visible (532 nm^{-1}) and tunable infrared beam (1000–4000 cm^{-1}). Each beam was overlapped in space and time to produce SFG photons at a spot size of approximately 1 mm. Spectra were collected and offset with a 4 cm^{-1} step size at 200 acquisitions per step. Spectra were collected in an ssp, ppp, and sps polarization combinations (SFG, visible, IR) in a wavenumber range of 1100–1800 cm^{-1}. The spectra were then normalized by dividing the signal by the visible and infrared intensities.

X-ray photoelectron spectroscopy

Spectra were collected on a PHI 5600 system with a hemispherical analyzer and a monochromatic Al Kα (1486.6 eV) X-ray source with an electron flood gun. Scans were collected with a takeoff angle of 55° at a pressure below 3×10^{-9} Torr. A pass energy of 187.5 eV with a step size of 0.8 eV was used for the survey scans, and the high resolution had a pass energy of 23.5 eV and a step size of 0.5 eV/step. Spectra were collected with an X-ray spot size of 400 μm at three different spots for each sample. Analysis and peak fitting took place with CasaXPS (Casa Software Ltd.), where a linear background was used.

Statistical analysis

All statistical analysis was performed using JMP (SAS Institute Inc., Cary, NC). For each test, a one-way ANOVA and a Tukey post-hoc comparison were performed to determine differences between means. For biocompatibility data that was normalized to glass, the error from glass is imbedded in the reported standard deviation. Sample sizes for presented data is included in the figure captions and reported as the mean ± (standard deviation).

Preparation of platelet-poor plasma and washed platelets

Human blood samples were collected from volunteers at Oregon State University Student Health Services in accordance with an approved Institutional Review Board (IRB-2019-0271). Informed consent from four different healthy human donors was obtained prior to venipuncture. Volunteers were above 110 lbs, over the age of 18 years, and had no medication use two weeks prior to the blood draw. Blood samples were processed following the method of McCarty and colleagues [32]. Approximately 15 mL of blood was drawn into sodium citrate Vacutainers. Acid-citrate-dextrose (ACD) was added to the whole blood at a 1:10 volume ratio. Blood was centrifuged at 200*g* for 20 min at room temperature. The supernatant platelet-rich plasma was transferred, and 0.1 μg/mL prostaglandin I2 was added to inhibit platelet activation. Platelet-rich plasma was centrifuged at 1000*g* for 10 min at room temperature. The supernatant platelet-poor plasma (PPP) was transferred and used for fibrin generation studies. The platelet pellet was resuspended in Tyrode's buffer (129 mM NaCl, 20 mM HEPES, 12 mM $NaHCO_3$, 2.9 mM KCl, 1 mM $MgCl_2$, and 0.34 mM Na_2HPO_4), and 0.1 μg/mL prostaglandin I2 was added. The platelets were centrifuged at 1000*g* for 10 min, the supernatant was discarded, and pelleted platelets were resuspended in Tyrode's buffer. Platelets were counted using a hemocytometer and the platelet solution was diluted to a concentration of 1×10^8 platelets/mL [33,34].

FXIIa assay

Wells of interest of a nontreated 96-well polystyrene were blocked with 300 μL 1% bovine serum albumin (BSA) in Milli-Q water for 2 h at 37 °C. After 2 h, the wells were rinsed three times with Milli-Q water. Plates were coated immediately prior to use. FXIIa assays were performed using methods adapted from Bates and colleagues [33]. A solution of FXII (200 nM), prekallikrein (PK) (50 nM), and high-molecular-weight kininogen (HMWK) (50 nM) in vacuum-filtered and degassed buffer (25 mM HEPES pH 7.4, 150 mM NaCl, and 0.1% BSA) was prepared, and 120 μL was added to each well of a 96-well plate blocked with BSA. After incubation for 60 min, 90 μL of protein solution was removed and added to a new plate containing 5 μL 4.7mM soybean trypsin inhibitor (Sigma). 5 μL of chromogenic substrate S-2302 (Chromogenix) was added to each well and the absorbance was measured at 405 nm every 1 min for 60 min using a FlexStation 3 microplate reader (Molecular Devices). A standard curve was used to determine the concentration of FXIIa from the measured OD. A BSA-blocked well was used as a negative control and glass was used as a positive control. Three separate experiments were performed for a total sample size of 18.

Clot turbidity analysis

Wells of interest of a non-treated polystyrene 96-well plate were blocked with 300 μL 1% BSA in Milli-Q water for 2 h at 37 °C. After 2 h, wells were rinsed three times with Milli-Q

water. Plates were coated immediately prior to use. Fibrin generation experiments were performed on a FlexStation 3 (Molecular Devices) using methods adapted from Bates et al. and Sask et al. [33,35]. 50 µL of PPP from fresh human blood samples from two donors was added to wells with or without surfaces, along with 50 µL buffer (25 mM HEPES pH 7.4, 150 mM NaCl). Plasma was then recalcified with 50 µL 25 mM $CaCl_2$. Absorbance measurements were taken every 1 min for 60 min at 405 nm. Three separate experiments were performed for a total sample size of 18 per donor. Fibrin generation time was defined as the time to reach a 5% increase over the baseline absorbance value. 5% is a sufficient threshold to overcome the noise floor of the data [33].

Clot morphology

Wells of interest of a non-treated 96-well polystyrene were blocked with 300 µL 1% BSA in Milli-Q water for 2 h at 37 °C. After 2 h, wells were rinsed three times with Milli-Q water. Plates were coated immediately prior to use. Clots were prepared using the same method as turbidity analysis, but clots were allowed to form for five times the fibrin generation time to ensure samples were fully clotted. Fibrin clots and surfaces were removed from wells and fixed in 1% paraformaldehyde and 2.5% glutaraldehyde in 0.1 M sodium cacodylate buffer overnight. Samples were then rinsed twice in 0.1 M cacodylate buffer for 15 min each. Samples were dehydrated in a graded series of ethanol (10%, 30%, 50%, 70%, 90%, 95%, and 100%) for 10–15 min each, followed by critical point drying (Electron Microscopy Sciences). Samples were sputter-coated with gold/palladium (Cressington 108A) and imaged on a scanning electron microscope (SEM) (FEI Quanta 600F). ImageJ was used to measure fiber diameter and clot density. Clot density was determined by drawing a line through the image and counting the number of times a fiber crosses the line [36]. The diameter of ten fibers per spot per sample were measured. Three lines of 4 µm in length were drawn per spot per sample. Two samples per sample group were analyzed and the experiment was repeated twice.

Platelet adhesion and activation

10^8 platelets/mL in Tyrode's buffer were incubated on surfaces in a 96-well plate for 2 h at 37 °C. Surfaces were rinsed with Tyrode's buffer five times to remove nonadherent and loosely bound platelets. The samples were then fixed and prepared for SEM using the same method as for the clots. At least three spots per sample and two samples per sample group were imaged. Blood from two donors was used, and the experiment was repeated twice. ImageJ was used to count the number of adherent platelets and calculate average cell area. The average cell area describes where on average platelets fall on the spectrum of activation. Inactive discoid platelets have a smaller area than active spread platelets, at approximately 2–10 μm^2 and 20–50 μm^2, respectively.

Results and Discussion

The overall goal was to, first, demonstrate that we can produce a universal coating that mimics the pitcher plant SLIPS by using the sticky chemistry provide by mussels (PDA) and, then, to test the biocompatibility of the layer. To assess our coating strategy, we used several complimentary surface analysis techniques to characterize our biomimetic surfaces. The wettability of each surface was probed with water contact angle measurements, while the chemical composition of the layer was determined by XPS. Surface roughness was evaluated using AFM to confirm successful formation of a porous structure. Finally, ordering of specific chemical groups within our PDA SLIPS layer was explored via SFG spectroscopy.

Initially, each functionalization step was assessed through static water contact angle measurements, the results of which can be found in Figure 2. The observed static water contact angles taken from the three different bare substrates varied slightly, with COC as the most hydrophobic one because of its hydrocarbon chemical structure. As these substrates were functionalized with PDA, all three substrates became more wettable. The final functionalization layer (FDT) then coated the surface with

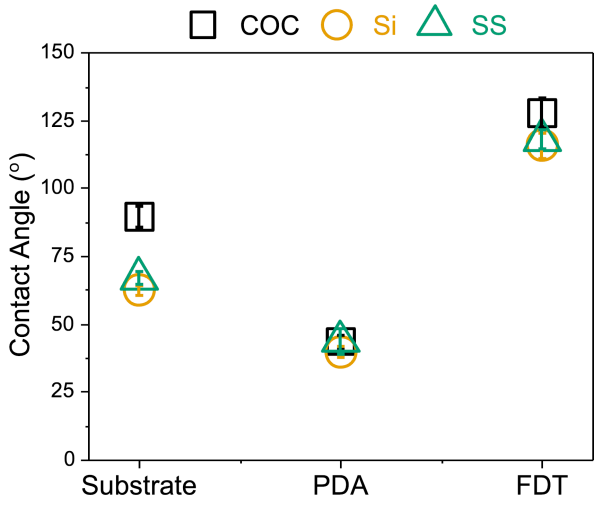

Figure 2: Contact angle measurements during the development of SLIPS coatings. Plot of the static water contact angles for each layer of the coating across the three substrates. Black squares represent COC, yellow circles show Si, and green triangles denote SS. Points are reported as the mean with the bars representative of the standard deviation for a sample size of n = 16. The bare substrate, COC (left), is hydrophobic. A layer of polydopamine (PDA) was added to the surface by incubating surfaces overnight with dopamine and Tris. PDA is hydrophilic, so the PDA coating step can be verified via the water contact angle. Fluorinated dodecanethiol (FDT) was conjugated to the PDA surface by incubating overnight. FDT is hydrophobic, so this step can be verified also with water contact angle measurements.

electronegative fluorine groups, thereby, creating a more hydrophobic surface [37].

The static water contact angle values collected from the three substrates were (89.3 ± 3.7)° for bare COC, (62.2 ± 1.9)° for Si, and (66.8 ± 2.5)° for SS (Figure 2), all of which were consistent with what was expected [38-41]. The experimental contact angles for substrates following the next functionalization step, the addition of PDA, were (43.3 ± 2.5)° for COC, (39.6 ± 2.1)° for Si, and (43.4 ± 4.7)° for SS, which was also in agreement with other values reported for PDA-coated substrates [19]. The final layer of the coating involved covalently attaching the fluorinated thiol, FDT, to the newly formed PDA film. The reported values for the final layer are (127.6 ± 5.6)° for COC, (115.6 ± 4.5)° for Si, and (117.8 ± 3.5)° for SS.

This dramatic increase in observed hydrophobicity was expected as the fluorine groups in the FDT chains decrease the wettability of the layer. Additionally, a two-tailed *t*-test demonstrated that for each successive functionalization, the contact angles were significantly different from the previous layer ($p < 0.05$). The contact angles from the PDA-coated COC and SS samples were not considered significantly different from one another, and there was neither a statistical difference between the water contact angles observed for the SS and Si samples coated with FDT. However, all substrates coated with the final layer of FDT exhibited water contact angles that exceeded 110°, indicating that we produced of a material with low surface energy suitable for SLIPS on all three substrates [17].

Both theoretical and XPS-determined compositions of all three substrates (COC, Si, and SS) functionalized with the PDA–FDT film are reported in Table 1. The atomic compositions for the final layer of the coating were consistent across the three substrates and are similar, thereby, confirming that we were successful with both the PDA and FDT functionalization steps. XPS survey and high-resolution C 1s spectra collected from PDA–FDT-coated substrates can be found in Figure 3. All survey spectra (Figure 3a,c,e) are nearly identical across the three substrates, which suggests a uniform FDT coating across the three different sample types. High-resolution C 1s spectra (Figure 3b,d,f) yield peak envelopes made up of four distinct peaks. These four peaks from high to low binding energies, correspond to C–C/C–H bonds (285 eV), C=O bonds (288 eV),

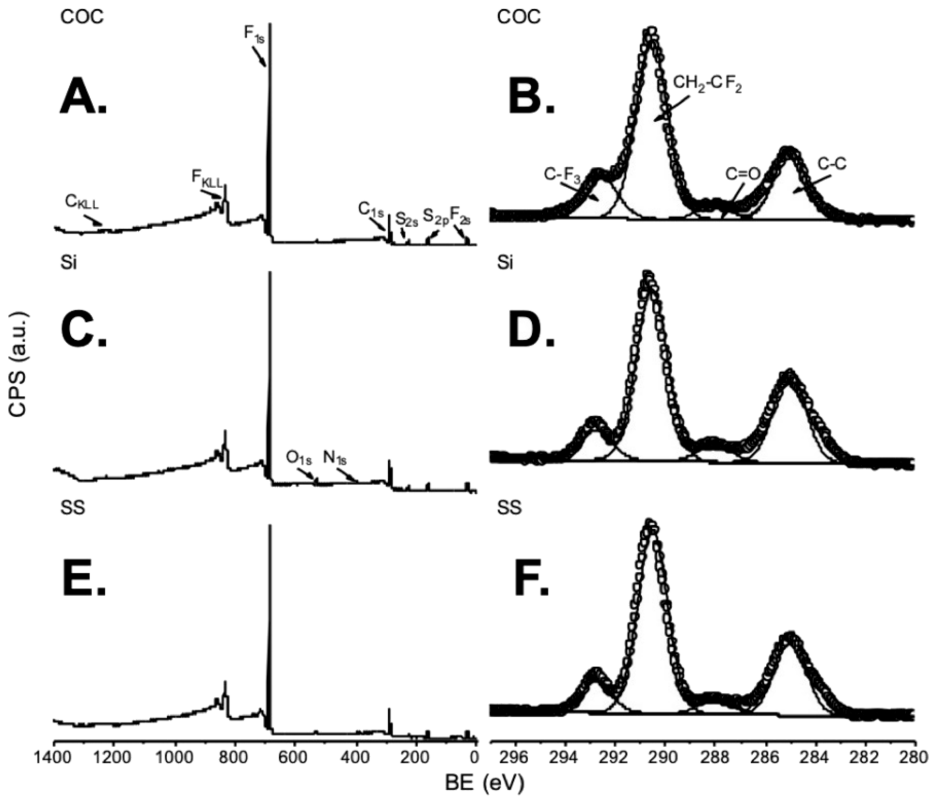

Figure 3: Survey and high-resolution scans of the final layer of the SLIPS coating. (A, C, E) Plots of XPS survey spectra and (B, D, F) high-resolution C 1s scans from the final layer of the coating. The first row (A, B) are the scans for the coating on COC, second row (C, D) on Si, and the final row (E, F) on SS. There are no unexpected peaks in the survey spectrum across all substrates. In the C 1s high-resolution scan, C–C carbon can be found at 285 eV and the fluorinated groups, CF2 and CF3, are observed at 290.6 and 293 eV, respectively. See Supporting Information File 1 for high-resolution S 2p XPS spectra.

and two peaks related to fluorinated species (CF_2 at 290.6 eV and CF_3 at 293 eV) [28,42]. The C–C and C=O peaks likely stem from the PDA layer, while the fluorinated species can be attributed to the FDT layer covalently attached the PDA film. This covalent attachment is also confirmed by the XPS S 2p high-resolution spectra (Supporting Information File 1), which exhibited the same peak envelope across all the three substrates and were representative of a covalent carbon-sulfur bond [43].

Table 1: Compositions (atom %) of the final layer of the coating with FDT (n = 3) on each of the three different substrates. Theoretical compositions are listed for comparison in the first column.

% Atomic composition FDT (n = 3)				
element	theoretical	COC	SI	SS
C 1s	37.9	35.2 (2.5)	41.2 (0.5)	38.2 (0.4)
N 1s	0	0 (0.0)	1.4 (0.2)	0.6 (0.1)
S 2p	3.4	5 (1.2)	4.2 (0.2)	4.7 (0.3)
O 1s	0	0.4 (0.2)	2.8 (0.2)	1.5 (0.3)
F 1s	58.6	59.2 (4.0)	50.5 (0.7)	55.1 (0.4)

AFM highlighted the level of roughness at each stage of the coating to show a rougher topography for the final layer. Results for each layer of the coating are shown in Supporting Information File 1, Figure S1 and reported as root mean square roughness (Rq), a useful metric for comparing surface roughness. The final layer with FDT should increase the surface roughness as only a monolayer is expected to bond. The final value layer of the coating that contains FDT showed Rq values of 70.5 ± 23.5 nm for COC, 46.9 ± 26 nm for Si, and 47.8 ± 20.7 nm for SS (Supporting Information File 1, Table S1). A two-tailed t-test showed that the increase in roughness after each successive coating was significantly different compared to the previous layer, suggesting successful attachment of a porous matrix onto a variety of different substrates. The roughness of all samples with the final layer of the coating were not significantly different from one another, suggesting universal attachment of the SLIPS porous component.

The final structure of oxidative polymerization for dopamine into PDA is not fully agreed upon [20,44,45]. Therefore, information about the presence and ordering of specific chemical groups within the substrate–PDA–FDT layers was provided by SFG spectra collected from the COC–PDA–FDT sample (Figure 4). The stretching region between 1100 and 1850 cm^{-1} contains modes related to specific molecular groups within each layer of the coating. This includes, but is not limited to, C=O carbonyl stretchings from PDA, ring deformations from COC and PDA, and CF_3 stretchings from FDT. Within the SFG spectra, the carbonyl stretching that stems from the oxidized surface of both COC and PDA was observed at 1730 cm^{-1}. Additionally, a ring deformation was observed as a broad peak at around 1600 cm^{-1}. This likely originates from ring structures present in both COC and PDA. The feature observed at 1400 cm^{-1} was not readily assigned; however, it was the sole vibrational mode observed for COC in this region and is likely a contribution from order in the bulk. A final mode was assigned to the CF_3 asymmetric stretching at 1370 cm^{-1} [46].

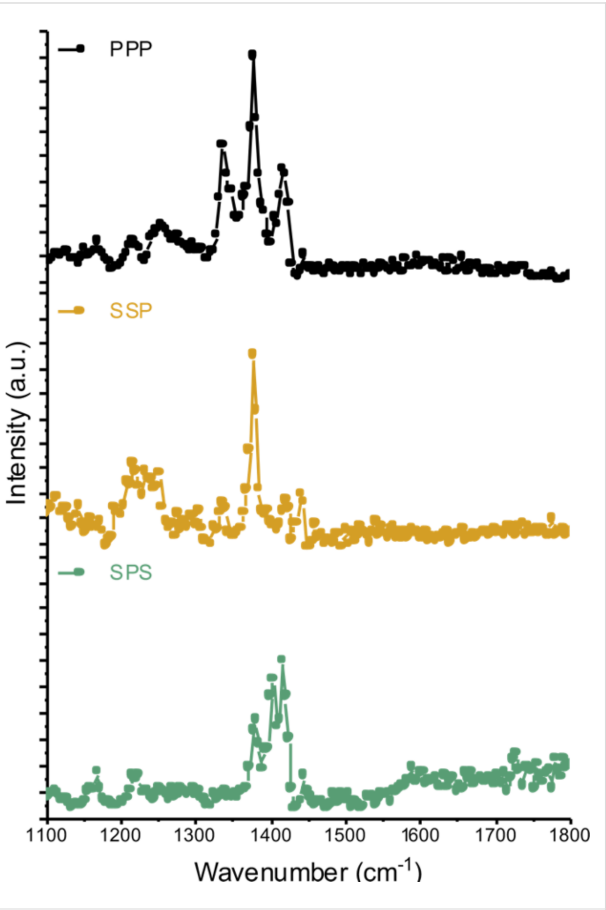

Figure 4: SFG spectra of the final layer in the SLIPs coating. SFG spectra from 1100 to 1800 cm^{-1} from a COC substrate coated with PDA–FDT. The top spectra were collected in ppp, the middle spectra in ssp, and the bottom spectra in sps polarization combinations.

Observed changes across the SFG spectra collected with different polarization combinations provide information about the orientation of molecular bonds at the interface [26,27]. Here, by collecting SFG spectra from the COC–PDA–FDT sample with ppp, ssp, and sps combinations, we acquired info about the general orientation of both the polymerized dopamine molecules and FDT after being bound to the surface. The CF_3 asymmetric stretching, specifically in sps, at 1400 cm^{-1} provides evidence that the FDT molecule was oriented out of the interfacial plane. The modes at 1600 cm and 1730 cm^{-1} indicate ring de-

formation and carbonyl stretching, respectively. The presence of the ring deformation peak at 1600 cm^{-1} in the SPS spectrum suggests that the ring lies in the interfacial plane. This also holds true for the carbonyl stretching at 1730 cm^{-1}. Additionally, these modes are not observed in SSP, which further demonstrated that the ring structure and carbonyl groups of PDA lie in the interfacial plane or parallel to the surface. This would support the theory of π–π stacking proposed by Lynge et al., where PDA aggregates form and are joined together through π stacking [45].

As mentioned earlier, quantification of the activation of intrinsic coagulation on SLIPS surfaces have not been fully investigated. For biomaterials, the intrinsic pathway has been shown to activate upon exposure, whereas in vivo the extrinsic pathway dominates [47]. Thus, in this investigation we took one of our newly created PDA SLIPS samples (PDA–FDT–PFD on COC) and characterized it in terms of FXII activation, fibrin generation time, clot morphology, and platelet adhesion and activation. Previously, Badv et al. hypothesized that the prolonged clotting time they observed on a SLIPS-coated catheter was due to reduced activation of the contact system, which implied a lower concentration of FXIIa on their surfaces [18]. Additionally, it has been shown that FXII activation is reduced at hydrophilic surfaces [48], potentially due to trapping of a liquid layer, which reduced protein adhesion. While activation is decreased on hydrophilic surfaces, it is elevated on negatively charged surfaces like glass [49].

FXIIa concentration was determined at each step of our surface modification process. In this work, we used BSA-coated surfaces as a negative control and glass as a positive control. We expected to observe less activation of FXII on PDA SLIPS surfaces compared to untreated surfaces, such as negatively charged glass and COC, because of the prospective omniphobic properties aiding in protein adhesion resistance. FXII did not autoactivate in neat buffer on all PDA SLIPS surfaces but did autoactivate on glass surfaces (Figure 5). A three times increase in FXII activation on bare glass compared to BSA was reported previously, which is consistent with what we observed here [33]. We detected a ≈65% increase in FXII activation on PDA–FDT–PFD compared to BSA and a ≈40% reduction in FXII activation on PDA–FDT–PFD compared to glass. This suggests that there is FXII coming down onto the surface of our coating and activating, though to a lesser degree than on glass. However, we observed no difference in FXII activation between PDA and glass, which is unsurprising given that both surfaces are hydrophilic. There was also no observed difference in FXII activation between COC and PDA–FDT–PFD, suggesting COC exhibits an intrinsic coagulation behavior similar to that of PDA–FDT–PFD.

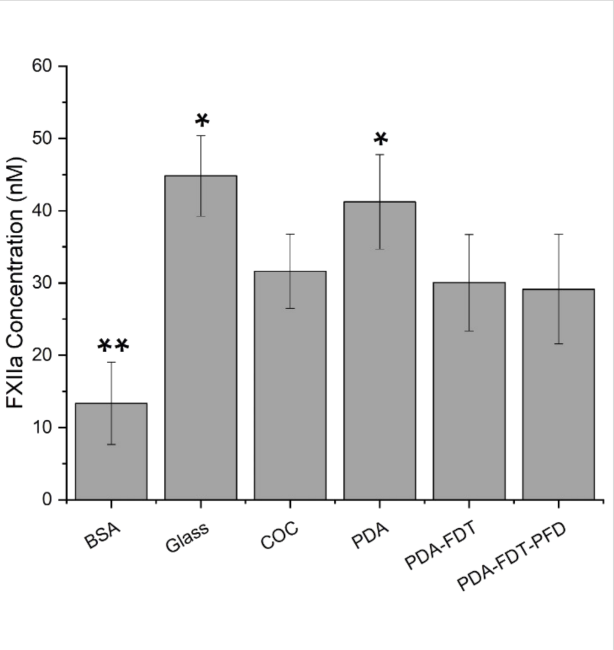

Figure 5: FXIIa concentration after 1 h incubation with HMWK and PK on surfaces. Error bars indicate standard deviation, n = 18. COC, PDA–FDT and PDA–FDT–PFD activated 50% less FXII than PDA and glass, but 100% more than BSA. Single asterisk (*) and double asterisk (**) indicate significantly higher or lower activation, respectively (α = 0.05).

Next, we tracked the fibrin generation kinetics of PPP across all our experimental and control surfaces (Figure 6). The observed range of fibrin generation time of 5–30 min was consistent with those reported previously using similar methods of turbidimetric quantification on other experimental surfaces [33,50]. We observed that plasma clotted 2.5× slower on PDA–FDT–PFD than glass and there was no significant difference between PDA–FDT–PFD, BSA, or COC. The observed differences in FXII activation between BSA and PDA–FDT–PFD, combined with the lack of observed differences in plasma clotting time, would suggest that PDA–FDT–PFD induces an antithrombogenic pathway that is different than the typical intrinsic coagulation behavior.

Previously, SLIPS coatings were observed to resist platelet adhesion in whole blood and platelet-rich plasma adhesion assays [4,10]. However, no work has been done previously in a purified platelet system, which allows for identifying the specific interactions between platelets and surfaces independent of protein adsorption or other events that may take place within whole blood and plasma studies. In our purified platelet system, we observed a 150% increase in adherent platelets on PDA–FDT–PFD compared to BSA and a 50% decrease in adherent platelets on PDA–FDT–PFD compared to glass (Figure 7). This suggests that the SLIPS coating is not completely omniphobic as adherent cells are observed.

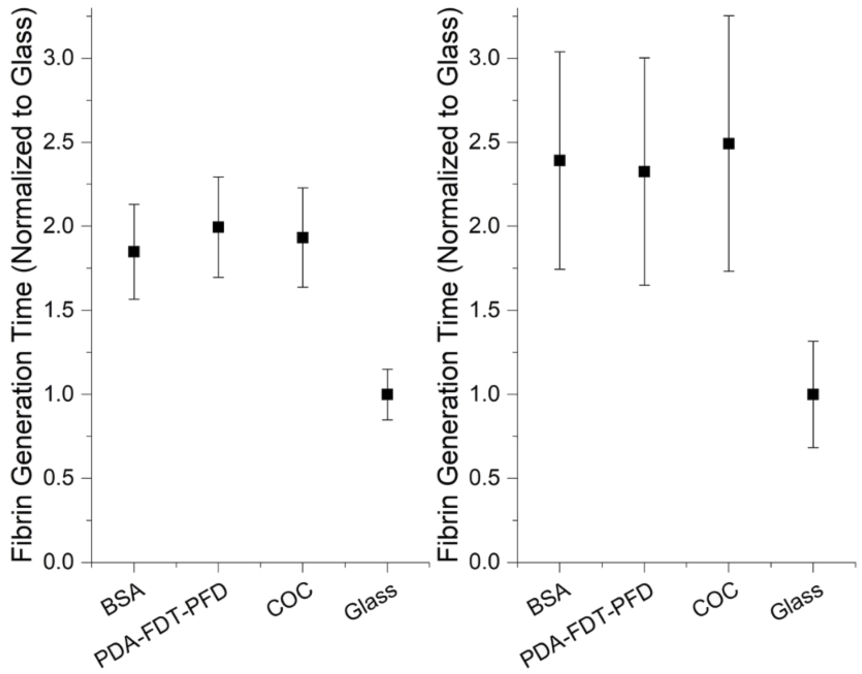

Figure 6: Fibrin generation time on modified surfaces for two donors, A1 (left) and A3 (right). Data was normalized to glass and combined for three runs. Error bars represent standard deviation. Recalcified citrated plasma was incubated with the surfaces at 37 °C. OD was measured every 1 min for 60 min. PPP clotted approximately 2.5 times slower on PDA–FDT–PFD than on glass in all runs, and there was no difference between PDA–FDT–PFD and BSA or COC. Fibrin generation time was defined as the time to reach a 5% increase in OD over the baseline. PDA–FDT–PFD clotted significantly slower than glass for both donors and all runs ($\alpha = 0.05$).

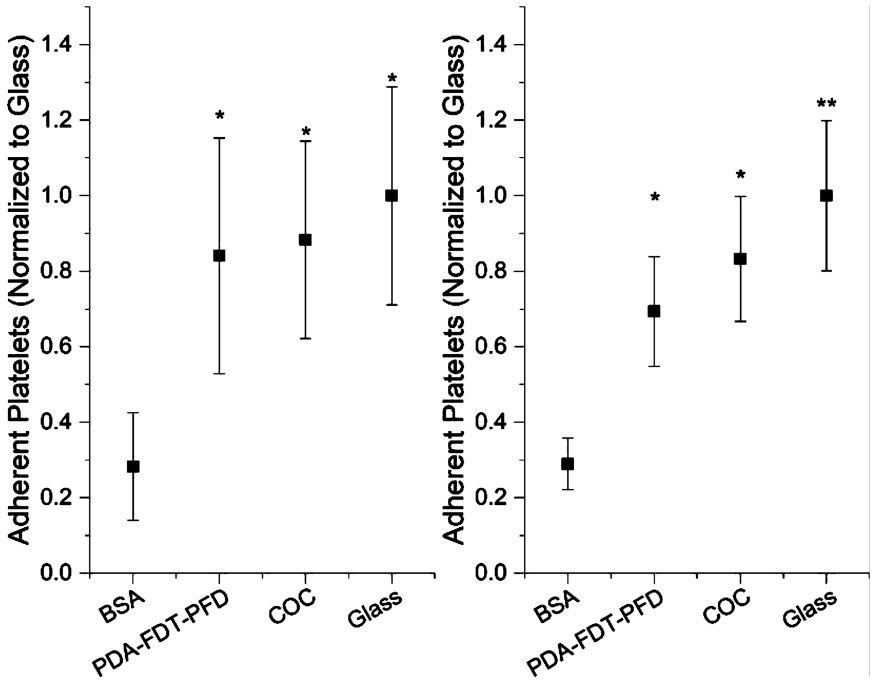

Figure 7: Adherent platelets per 3520 μm^2 surface area for two donors, A1 (left) and A3 (right). Surfaces were incubated with 10^8 platelets/mL in Tyrode's buffer for 90 min. Platelets were counted using SEM. For each donor and each run, two samples per sample group and three spots per sample were imaged. There was approximately 150% lower adhesion to BSA-coated surfaces than to all other surfaces. There was no difference in platelet adhesion between PDA–FDT–PFD, COC, and glass for donor A1, and glass had a significantly higher platelet adhesion than PDA–FDT–PFD and COC for donor A3.

Fibrin generation time was determined on BSA, glass, bare COC, and PDA–FDT–PFD. We expected to observe a longer fibrin generation time on PDA–FDT–PFD than on glass and COC because of the hypothesized antithrombogenic behavior due to omniphobicity of SLIPS. PPP clotted approximately 2.5 times slower on PDA–FDT–PFD than on glass for all runs, and there was no difference between PDA–FDT–PFD and BSA or COC (Figure 6). Contrastingly, previous studies investigating SLIPS-induced fibrin polymerization found a significant reduction compared to bare surfaces [4]. There was significant variation between donors and between runs, but the trends remained consistent. Differences between runs were not of interest, so data was normalized to the fibrin generation time on glass. Samples were isolated from three distinct draws from each of two donors for a total sample size of 14 per sample per donor.

Clot fiber diameter and crosslinking density measurements were taken from SEM micrographs. Representative SEM micrographs are shown in Figure 8. Less stable clots exhibit larger fiber diameters and more porous fibrin networks. Therefore, PDA–FDT–PFD was expected to produce clots with larger fiber diameters and less crosslinked networks compared to the bare glass and COC surfaces. Data was normalized to glass, and PDA–FDT–PFD yielded an approximately 20% higher fiber diameter and 25% lower clot density than glass (Figure 9). PDA–FDT–PFD also led to significantly higher fiber diameter

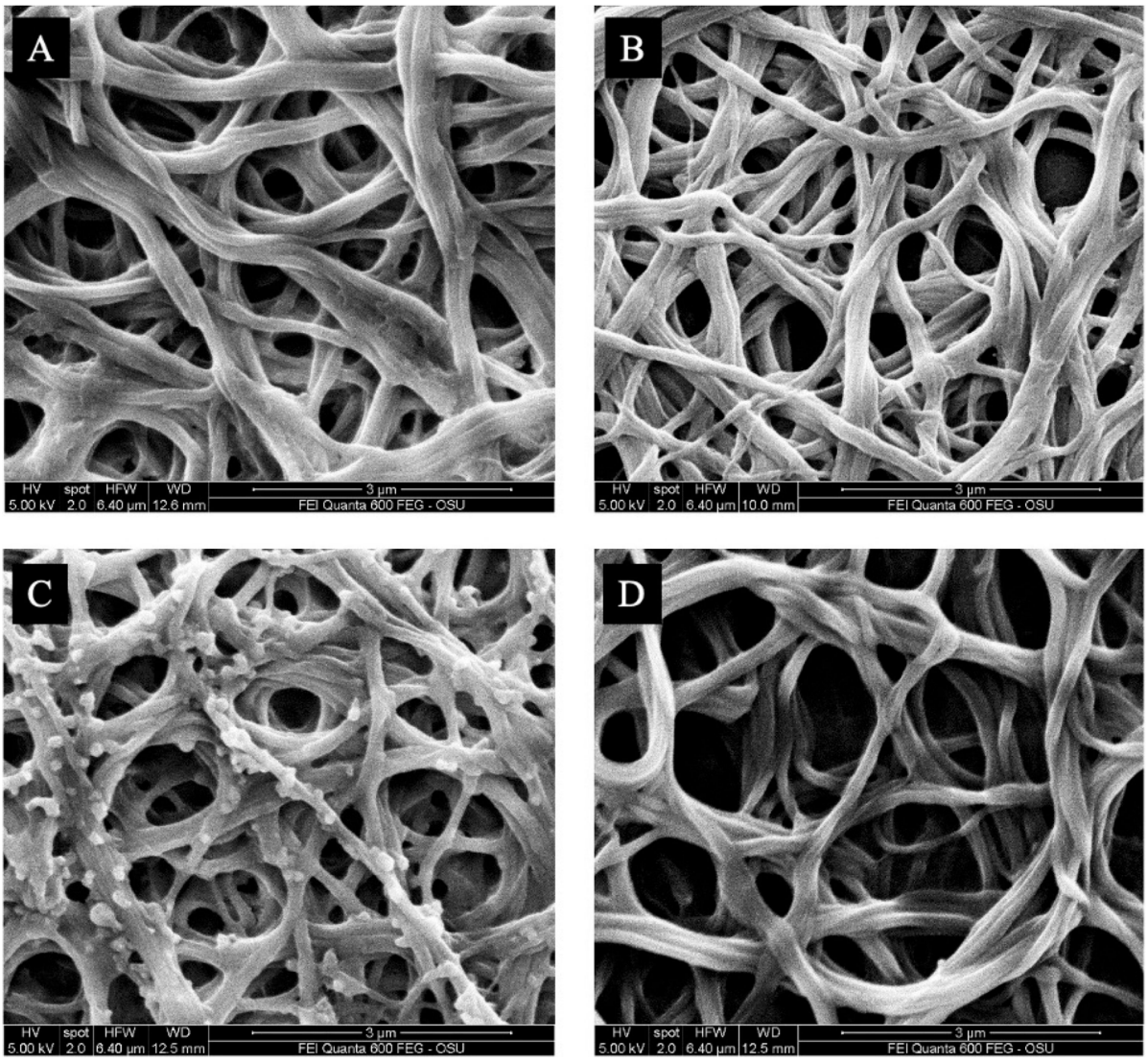

Figure 8: Representative SEM micrographs of clotted plasma on (A) BSA, (B) glass, (C) COC, and (D) PDA–FDT–PFD. Recalcified citrated PPP was incubated with the surfaces for at least ten times the clotting time. All micrographs are from donor A1.

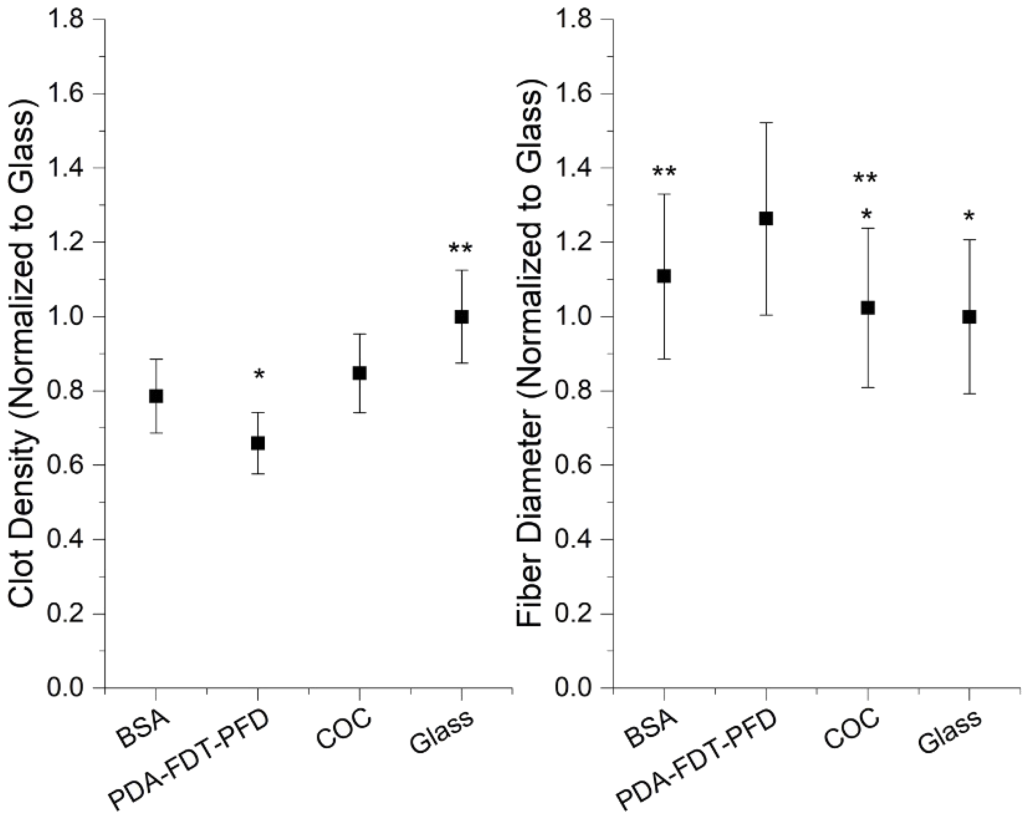

Figure 9: Clot morphology assessed using SEM after incubation of recalcified PPP on surfaces. Data are from a single donor. (Left) Fiber diameter, measured on ten fibers (n = 60). (Right) Clot density, defined as the number of times a fiber crosses a line of fixed length. Three lines were drawn per spot (n = 18). PDA–FDT–PFD yielded significantly higher fiber diameter and lower clot density than glass, COC and BSA (α = 0.05).

and lower clot density than BSA and COC, suggesting that clots formed on PDA–FDT–PFD are less stable and easier to break down than clots formed on glass, COC, and BSA [36]. Similar surface-induced thrombus properties were observed in other SLIPS applications, where, in comparison to untreated surfaces, SLIPS-treated surfaces under dynamic blood flow yielded significantly lower thrombi weights [4].

Finally, platelet adhesion was quantified from SEM micrographs. As mentioned earlier, SLIPS surfaces have been shown to resist platelet adhesion because of their omniphobic properties [4,10]. Therefore, we expected to observe little to no adherent platelets on the PDA–FDT–PFD surfaces. To test this, purified platelets were incubated with surfaces for 90 min, rinsed three times, fixed, and dehydrated in preparation for imaging. The horizontal field width was set to 64 µm, the surface area for analysis was 3520 μm^2 (Figure 10), and data was normalized to glass. There was approximately 150% lower adhesion to BSA-coated surfaces than to all other surfaces. There was no difference in platelet adhesion between PDA–FDT–PFD, COC, and glass for donor A1. However, glass exhibited significantly higher platelet adhesion than PDA–FDT–PFD and COC for donor A3 (Figure 7).

Combined, these biocompatibility assays demonstrate that this formulation of a SLIPS coating is not completely omniphobic as FXII activated on the surface and platelets adhered to the coating. The observed prolonged fibrin generation time in PPP, however, suggests that SLIPS could still exhibit antithrombogenic behavior. The FXII assay and platelet adhesion studies were performed in a purified system to gather information on isolated surface interactions, whereas the fibrin generation study was performed using PPP to investigate comprehensive hematologic behavior of the surfaces. This suggests that the SLIPS coating could have a high affinity for a passivating blood protein or low affinity for an active procoagulant. More work on specific coagulation factor adsorption and activation, such as thrombin, fibrinogen, and complement system proteins is needed to fully characterize the surface. Studies on FXII and platelet adhesion in plasma and whole blood models would provide more insight into observed activation in a purified system.

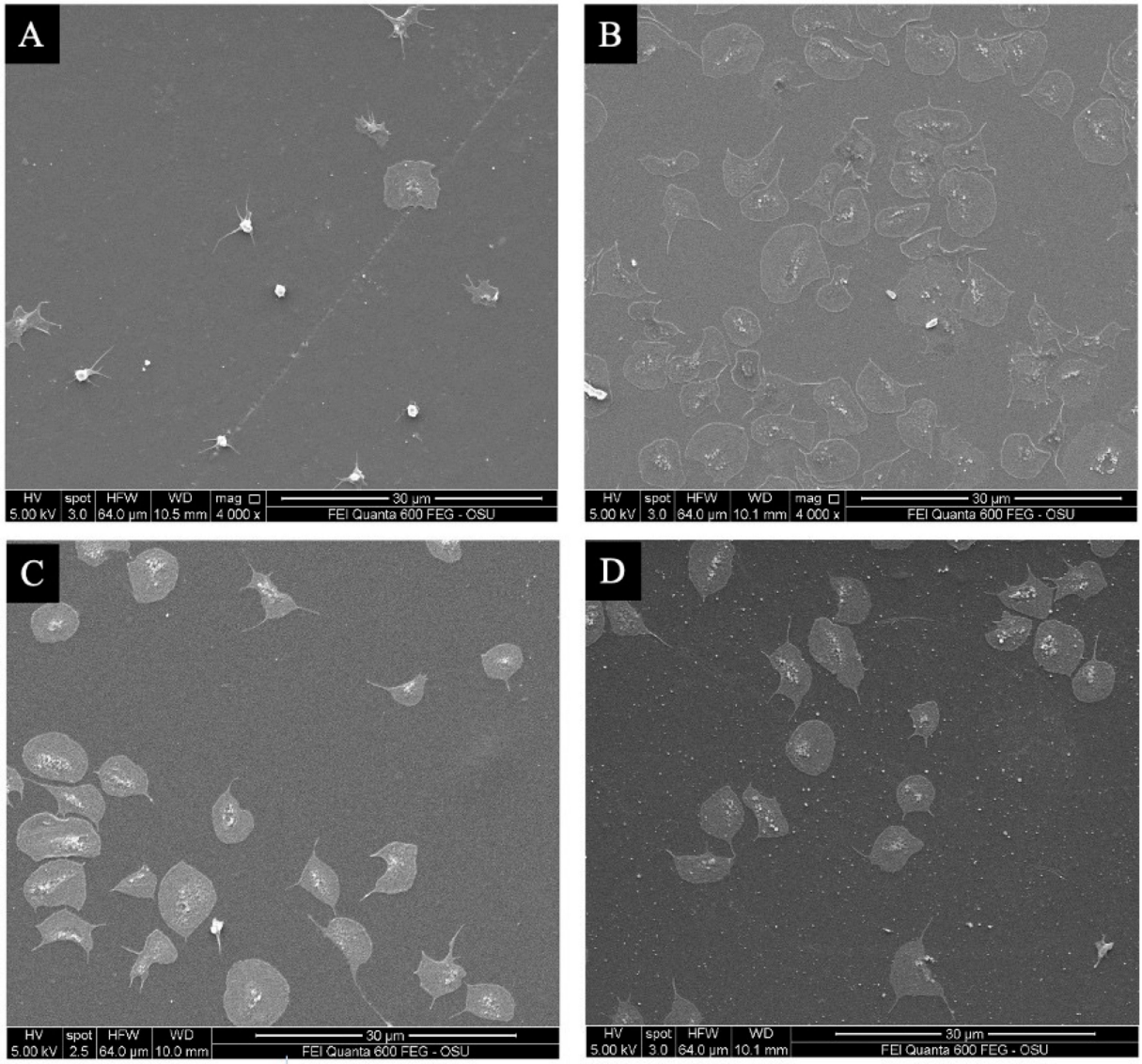

Figure 10: Representative SEM micrographs of adherent platelets on (A) BSA, (B) glass, (C) COC, and (D) PDA–FDT–PFD. Surfaces were incubated with 10^8 platelets/mL in Tyrode's buffer for 90 min.

Supporting Information

Supporting Information File 1

Additional figures and table.
[https://www.beilstein-journals.org/bjnano/content/supplementary/2190-4286-15-111-S1.pdf]

Author Contributions

Ryan A. Faase: conceptualization; data curation; formal analysis; investigation; methodology; writing – original draft. Madeleine H. Hummel: conceptualization; data curation; formal analysis; investigation; methodology; writing – original draft. AnneMarie V. Hasbrook: conceptualization; data curation; formal analysis; investigation; methodology; writing – original draft. Andrew P. Carpenter: conceptualization; data curation; formal analysis; investigation; methodology; supervision; writing – original draft. Joe E. Baio: conceptualization; funding acquisition; methodology; project administration; supervision; writing – review & editing.

ORCID® iDs

AnneMarie V. Hasbrook - https://orcid.org/0009-0007-1554-8115
Andrew P. Carpenter - https://orcid.org/0000-0003-1020-1706
Joe E. Baio - https://orcid.org/0000-0002-9692-689X

Data Availability Statement

The data that supports the findings of this study is available from the corresponding author upon reasonable request.

References

1. Xiao, L.; Li, J.; Mieszkin, S.; Di Fino, A.; Clare, A. S.; Callow, M. E.; Callow, J. A.; Grunze, M.; Rosenhahn, A.; Levkin, P. A. *ACS Appl. Mater. Interfaces* **2013,** *5,* 10074–10080. doi:10.1021/am402635p
2. Amini, S.; Kolle, S.; Petrone, L.; Ahanotu, O.; Sunny, S.; Sutanto, C. N.; Hoon, S.; Cohen, L.; Weaver, J. C.; Aizenberg, J.; Vogel, N.; Miserez, A. *Science* **2017,** *357,* 668–673. doi:10.1126/science.aai8977
3. Wilson, P. W.; Lu, W.; Xu, H.; Kim, P.; Kreder, M. J.; Alvarenga, J.; Aizenberg, J. *Phys. Chem. Chem. Phys.* **2013,** *15,* 581–585. doi:10.1039/c2cp43586a
4. Leslie, D. C.; Waterhouse, A.; Berthet, J. B.; Valentin, T. M.; Watters, A. L.; Jain, A.; Kim, P.; Hatton, B. D.; Nedder, A.; Donovan, K.; Super, E. H.; Howell, C.; Johnson, C. P.; Vu, T. L.; Bolgen, D. E.; Rifai, S.; Hansen, A. R.; Aizenberg, M.; Super, M.; Aizenberg, J.; Ingber, D. E. *Nat. Biotechnol.* **2014,** *32,* 1134–1140. doi:10.1038/nbt.3020
5. Manna, U.; Raman, N.; Welsh, M. A.; Zayas-Gonzalez, Y. M.; Blackwell, H. E.; Palecek, S. P.; Lynn, D. M. *Adv. Funct. Mater.* **2016,** *26,* 3599–3611. doi:10.1002/adfm.201505522
6. Deng, R.; Shen, T.; Chen, H.; Lu, J.; Yang, H.-C.; Li, W. *J. Mater. Chem. A* **2020,** *8,* 7536–7547. doi:10.1039/d0ta02000a
7. Epstein, A. K.; Wong, T.-S.; Belisle, R. A.; Boggs, E. M.; Aizenberg, J. *Proc. Natl. Acad. Sci. U. S. A.* **2012,** *109,* 13182–13187. doi:10.1073/pnas.1201973109
8. Liu, Y.; Tian, Y.; Chen, J.; Gu, H.; Liu, J.; Wang, R.; Zhang, B.; Zhang, H.; Zhang, Q. *Colloids Surf., A* **2020,** *588,* 124384. doi:10.1016/j.colsurfa.2019.124384
9. Rungraeng, N.; Hoo Yoon, S.; Li, Y.; Jun, S. *Trans. ASABE* **2015,** 861–867. doi:10.13031/trans.58.10939
10. Yuan, S.; Luan, S.; Yan, S.; Shi, H.; Yin, J. *ACS Appl. Mater. Interfaces* **2015,** *7,* 19466–19473. doi:10.1021/acsami.5b05865
11. Howell, C.; Grinthal, A.; Sunny, S.; Aizenberg, M.; Aizenberg, J. *Adv. Mater. (Weinheim, Ger.)* **2018,** *30,* 1802724. doi:10.1002/adma.201802724
12. Alcaire, M.; Lopez-Santos, C.; Aparicio, F. J.; Sanchez-Valencia, J. R.; Obrero, J. M.; Saghi, Z.; Rico, V. J.; de la Fuente, G.; Gonzalez-Elipe, A. R.; Barranco, A.; Borras, A. *Langmuir* **2019,** *35,* 16876–16885. doi:10.1021/acs.langmuir.9b03116
13. Tuo, Y.; Zhang, H.; Chen, W.; Liu, X. *Appl. Surf. Sci.* **2017,** *423,* 365–374. doi:10.1016/j.apsusc.2017.06.170
14. Prado, L. H.; Anastasiou, E.; Virtanen, S. *Mater. Lett.* **2021,** *296,* 129892. doi:10.1016/j.matlet.2021.129892
15. Kratochvil, M. J.; Welsh, M. A.; Manna, U.; Ortiz, B. J.; Blackwell, H. E.; Lynn, D. M. *ACS Infect. Dis.* **2016,** *2,* 509–517. doi:10.1021/acsinfecdis.6b00065
16. He, M.; Gao, K.; Zhou, L.; Jiao, Z.; Wu, M.; Cao, J.; You, X.; Cai, Z.; Su, Y.; Jiang, Z. *Acta Biomater.* **2016,** *40,* 142–152. doi:10.1016/j.actbio.2016.03.038
17. Villegas, M.; Zhang, Y.; Abu Jarad, N.; Soleymani, L.; Didar, T. F. *ACS Nano* **2019,** *13,* 8517–8536. doi:10.1021/acsnano.9b04129
18. Badv, M.; Jaffer, I. H.; Weitz, J. I.; Didar, T. F. *Sci. Rep.* **2017,** *7,* 11639. doi:10.1038/s41598-017-12149-1
19. Lee, H.; Dellatore, S. M.; Miller, W. M.; Messersmith, P. B. *Science* **2007,** *318,* 426–430. doi:10.1126/science.1147241
20. Lee, H. A.; Park, E.; Lee, H. *Adv. Mater. (Weinheim, Ger.)* **2020,** *32,* 1907505. doi:10.1002/adma.201907505
21. Huang, N.; Zhang, S.; Yang, L.; Liu, M.; Li, H.; Zhang, Y.; Yao, S. *ACS Appl. Mater. Interfaces* **2015,** *7,* 17935–17946. doi:10.1021/acsami.5b04597
22. Liu, X.; Gu, W.; Wang, K.; Zhang, W.; Xia, C.; Shi, S. Q.; Li, J. *Cellulose* **2019,** *26,* 7223–7236. doi:10.1007/s10570-019-02609-4
23. Shahkaramipour, N.; Lai, C. K.; Venna, S. R.; Sun, H.; Cheng, C.; Lin, H. *Ind. Eng. Chem. Res.* **2018,** *57,* 2336–2345. doi:10.1021/acs.iecr.7b05025
24. Huhtamäki, T.; Tian, X.; Korhonen, J. T.; Ras, R. H. A. *Nat. Protoc.* **2018,** *13,* 1521–1538. doi:10.1038/s41596-018-0003-z
25. Kumar, B. R.; Rao, T. S. *Dig. J. Nanomater. Biostructures* **2012,** *7,* 1881–1889.
26. Baio, J. E.; Weidner, T.; Brison, J.; Graham, D. J.; Gamble, L. J.; Castner, D. G. *J. Electron Spectrosc. Relat. Phenom.* **2009,** *172,* 2–8. doi:10.1016/j.elspec.2009.02.008
27. Weidner, T.; Castner, D. G. *Phys. Chem. Chem. Phys.* **2013,** *15,* 12516. doi:10.1039/c3cp50880c
28. Vickerman, J. C.; Gilmore, I. S., Eds. *Surface Analysis – The Principal Techniques,* 2nd ed.; Wiley: Chichester, UK, 2009. doi:10.1002/9780470721582
29. Wong, T.-S.; Kang, S. H.; Tang, S. K. Y.; Smythe, E. J.; Hatton, B. D.; Grinthal, A.; Aizenberg, J. *Nature* **2011,** *477,* 443–447. doi:10.1038/nature10447
30. Volný, M.; Elam, W. T.; Ratner, B. D.; Turecek, F. *J. Biomed. Mater. Res., Part B* **2007,** *80B,* 505–510. doi:10.1002/jbm.b.30624
31. Lamour, G.; Hamraoui, A.; Buvailo, A.; Xing, Y.; Keuleyan, S.; Prakash, V.; Eftekhari-Bafrooei, A.; Borguet, E. *J. Chem. Educ.* **2010,** *87,* 1403–1407. doi:10.1021/ed100468u
32. McCarty, O. J. T.; Larson, M. K.; Auger, J. M.; Kalia, N.; Atkinson, B. T.; Pearce, A. C.; Ruf, S.; Henderson, R. B.; Tybulewicz, V. L. J.; Machesky, L. M.; Watson, S. P. *J. Biol. Chem.* **2005,** *280,* 39474–39484. doi:10.1074/jbc.m504672200
33. Bates, N. M.; Puy, C.; Jurney, P. L.; McCarty, O. J. T.; Hinds, M. T. *Cardiovasc. Eng. Tech.* **2020,** *11,* 448–455. doi:10.1007/s13239-020-00474-y
34. Khalifehzadeh, R.; Ciridon, W.; Ratner, B. D. *Acta Biomater.* **2018,** *78,* 23–35. doi:10.1016/j.actbio.2018.07.042
35. Sask, K. N.; Berry, L. R.; Chan, A. K. C.; Brash, J. L. *Langmuir* **2012,** *28,* 2099–2106. doi:10.1021/la203821g
36. Hethershaw, E. L.; Cilia La Corte, A. L.; Duval, C.; Ali, M.; Grant, P. J.; Ariëns, R. A. S.; Philippou, H. *J. Thromb. Haemostasis* **2014,** *12,* 197–205. doi:10.1111/jth.12455
37. Dalvi, V. H.; Rossky, P. J. *Proc. Natl. Acad. Sci. U. S. A.* **2010,** *107,* 13603–13607. doi:10.1073/pnas.0915169107
38. Williams, R.; Goodman, A. M. *Appl. Phys. Lett.* **1974,** *25,* 531–532. doi:10.1063/1.1655297
39. Chang, S.-H.; Hsiao, Y.-C. *Polymers (Basel, Switz.)* **2017,** *9,* 545. doi:10.3390/polym9100545
40. Song, J.-W.; Zeng, D.-L.; Fan, L.-W. *J. Colloid Interface Sci.* **2020,** *561,* 870–880. doi:10.1016/j.jcis.2019.11.070
41. Hwang, S.-J.; Tseng, M.-C.; Shu, J.-R.; Her Yu, H. *Surf. Coat. Technol.* **2008,** *202,* 3669–3674. doi:10.1016/j.surfcoat.2008.01.016
42. Militello, M. C.; Gaarenstroom, S. W. *Surf. Sci. Spectra* **1999,** *6,* 141–145. doi:10.1116/1.1247908
43. Brizzolara, R. A. *Surf. Sci. Spectra* **1996,** *4,* 96–101. doi:10.1116/1.1247810

44. Ryu, J. H.; Messersmith, P. B.; Lee, H. *ACS Appl. Mater. Interfaces* **2018,** *10,* 7523–7540. doi:10.1021/acsami.7b19865
45. Lynge, M. E.; van der Westen, R.; Postma, A.; Städler, B. *Nanoscale* **2011,** *3,* 4916. doi:10.1039/c1nr10969c
46. Tyrode, E.; Johnson, C. M.; Rutland, M. W.; Day, J. P. R.; Bain, C. D. *J. Phys. Chem. C* **2007,** *111,* 316–329. doi:10.1021/jp063912h
47. Weber, M.; Steinle, H.; Golombek, S.; Hann, L.; Schlensak, C.; Wendel, H. P.; Avci-Adali, M. *Front. Bioeng. Biotechnol.* **2018,** *6,* 99. doi:10.3389/fbioe.2018.00099
48. Zhuo, R.; Siedlecki, C. A.; Vogler, E. A. *Biomaterials* **2006,** *27,* 4325–4332. doi:10.1016/j.biomaterials.2006.04.001
49. Stavrou, E.; Schmaier, A. H. *Thromb. Res.* **2010,** *125,* 210–215. doi:10.1016/j.thromres.2009.11.028
50. Stevens, K. N. J.; Aldenhoff, Y. B. J.; van der Veen, F. H.; Maessen, J. G.; Koole, L. H. *J. Biomed. Biotechnol.* **2007,** *2007,* 1–10. doi:10.1155/2007/29464

License and Terms

BEILSTEIN JOURNAL OF NANOTECHNOLOGY

Ultrablack color in velvet ant cuticle

Vinicius Marques Lopez*[1], Wencke Krings[2,3], Juliana Reis Machado[4], Stanislav Gorb[2] and Rhainer Guillermo-Ferreira[1]

Full Research Paper

Open Access

Address:
[1]Lestes Lab, Federal University of Triângulo Mineiro, Uberaba, Minas Gerais, Brazil, [2]Department of Functional Morphology and Biomechanics, Kiel University, Am Botanischen Garten 1–9, 24098 Kiel, Germany, [3]Department of Cariology, Endodontology and Periodontology, Universität Leipzig, Liebigstraße 12, 04103 Leipzig, Germany and [4]Institute of Biological and Natural Sciences, Federal University of Triângulo Mineiro, Uberaba, Minas Gerais, Brazil

Email:
Vinicius Marques Lopez* - ovinicius.lopez@gmail.com

* Corresponding author

Keywords:
animal coloration; biophotonics; Hymenoptera; insects; Mutillidae; superblack; surface

Beilstein J. Nanotechnol. **2024,** *15,* 1554–1565.
https://doi.org/10.3762/bjnano.15.122

Received: 20 July 2024
Accepted: 12 November 2024
Published: 02 December 2024

This article is part of the thematic issue "Micro- and nanoscale effects in biological and bioinspired materials and surfaces".

Associate Editor: K. Ariga

Abstract

We studied the ultrastructure of the ultrablack cuticle in *Traumatomutilla bifurca*, an enigmatic and visually striking species of velvet ants (Hymenoptera, Mutillidae). Using a combination of scanning electron microscopy (SEM), transmission electron microscopy (TEM), confocal laser scanning microscopy (CLSM), and optical spectroscopy, we conducted a comprehensive analysis of the cuticle to elucidate its unique optical properties. SEM imaging provided a detailed surface morphology, while TEM provided insights into the internal structure. CLSM showed that the cuticle exhibits no autofluorescence. Our findings reveal a highly specialized cuticle, characterized by microstructures that effectively minimize reflectance and enhance light absorption. Optical spectrometry confirmed the ultrablack nature of the cuticle, with the measured reflectance approaching minimal levels across a broad spectrum of wavelengths. Therefore, our study contributes to a deeper understanding of ultrablack biological materials and their potential applications in biomimetics.

Introduction

The phenomenon of highly absorptive colors, also known as ultrablack, has risen considerable interest in recent years because of its potential applications in various fields, including optics, camouflage, and solar energy harvesting [1,2]. These colors are characterized by their ability to reflect an exceptionally low amount of visible light. Inspired by several biological examples observed in some organisms, scientists are committed to unraveling the mechanisms underlying the development of

ultrablack technical surfaces, seeking to replicate such structures in synthetic and natural materials with equivalent properties [3-8].

Ultrablack colors are a rare spectacle among animals. These colors with high absorption are formed in nature by a sophisticated arrangement of microstructures (i.e., structures visible under microscope) alongside pigment depositions in underlying tissues [9,10]. For instance, in male peacock spiders (Figure 1A), ultrablack pigmentation originates from the interaction of light with arrays of microlenses on the cuticle or overlapping brush-like scales positioned just above a densely pigmented absorbing layer. Similar phenomena can be observed in butterflies [11,12], birds [13], and snakes [14,15]. This intricately structured setup prolongs the light's exposure to the melanized integument, thereby augmenting light absorption by the pigment [10]. Consequently, ultrablack colors exhibit an extraordinarily low reflectance across ultraviolet and visible (UV–vis) spectrum wavelengths, often falling below 0.5% of the incident light [10,13].

The ultrablack surfaces found in certain organisms present a remarkable adaptation shaped by selective pressures in their respective environments. For example, combining conspicuous visual cues with ultrablack colors may provide heightened internal visual contrast, thus highlighting sexually selected colors in peacock spiders [10,13] (Figure 1A) and birds-of-paradise (Figure 1B). Likewise, ultrablack colors may offer thermoregulatory and disruptive advantages to vipers (Figure 1C) and assist butterflies in predator evasion (Figure 1D) [9,15]. Therefore, the parallel between ultrablack colors in animals underscores the convergent evolution of anti-

Figure 1: Examples of ultrablack colors in animals within their natural habitats. (A) Peacock spider (*Maratus tasmanicus*, Araneae: Salticidae) (© 2021 Henning Kallies), (B) bird-of-paradise (*Lophorina niedda*, Passeriformes: Paradisaeidae) (© 2022 Jes Lefcourt), (C) Gaboon viper (*Bitis rhinoceros*, Squamata: Viperidae) (By Justin Philbois), and (D) butterfly (*Catonephele numilia,* Lepidoptera: Papilionidae). Figures A and B were reproduced from https://www.inaturalist.org/observations/95228671 and https://www.inaturalist.org/observations/13984541, respectively, with permission from the respective authors. This content is not subject to CC BY 4.0. Figures C and D were reproduced from https://www.inaturalist.org/observations/131996241 and https://www.inaturalist.org/photos/17218853, respectively (published by iNaturalist, distributed under the terms of the Creative Commons CC0 1.0 Universal license).

reflective mechanisms as an important strategy for survival and reproductive success across diverse habitats and ecological contexts.

The evolution of ultrablack colors in animals highlights nature's ingenuity in achieving structurally assisted absorption to reduce specular reflectance. This demonstrates how organisms have developed sophisticated mechanisms to modulate the interaction between light and biological surfaces, resulting in highly absorptive and minimally reflective colors. These adaptations play a role in animal survival and reproductive success, offering substantial adaptive advantages within their respective habitats.

Velvet ants (Hymenoptera: Mutillidae) are wasps that exhibit a wide range of colors, usually contrasting with black integument. Their coloration is considered to be aposematic, that is, colors that ward off predators, but also may have some function in camouflage and protection against solar radiation [16]. Although hymenopterans (sawflies, bees, wasps, and ants) are one of the most diverse animal groups, few studies have addressed the mechanisms behind their coloration. Here, we present the discovery of the ultrablack cuticle in the velvet ant *Traumatomutilla bifurca* (Klug, 1821), a feature previously unreported in the Hymenoptera.

Materials and Methods

Study species

Traumatomutilla bifurca (Hymenoptera: Mutillidae) is a species widely distributed in Brazil, primarily in Brazilian savanna and Caatinga areas [17]. Distinguished by its black integument adorned with contrasting patterns of black and white setae along its body (Figure 2), this species exhibits behavior akin to other females of the family. Frequently observed walking on exposed sandy soil, often in aggregations of bees (personal observation), *T. bifurca* also occurs in forested habitats adjoining open landscapes. Demonstrating remarkable mobility, it covers significant distances in pursuit of hosts on the ground. While sightings may occur throughout the day, peak activity typically coincides with the early morning and late afternoon, during periods of subdued sunlight (personal observations). For subsequent analyses, we utilized female specimens collected from Caatinga regions in Pernambuco, Brazil (09°19'44.2''S, 42°33'30''W) in February 2022. The specimens were preserved in absolute alcohol.

Scanning electron microscopy (SEM)

To investigate the internal characteristics of cuticle cross sections, we prepared the samples by sectioning, allowing for the visualization of the underlying structures. Prior to SEM imaging, a thin layer of gold–palladium, 10 nm thick, was applied to the samples. We utilized a Hitachi S-4800 SEM, operating at 3 kV. Images were captured at different magnifications, starting at 15,000× and adjusted as needed.

Transmission electron microscopy (TEM)

TEM was utilized to examine the internal cuticle morphology at high resolution at a nanometer scale. The apparatus was configured to operate at 50 kV with a minimum vacuum column pressure of 5.10–2.00 hPa. For sample preparation, transversely sectioned *T. bifurca* specimens were fixed in Karnovsky fixative solution + 0.1% ruthenium red for 12 h. Following buffer washing, a post-fixative solution (osmium tetroxide + 0.1% ruthenium red) was applied at room temperature. After rinsing with alcohol, dehydration proceeded through sequential baths of 70%, 90%, and three changes of 100% alcohol. The material (meso and metasoma) was embedded in epoxy resin, and the molds were polymerized at 60 °C. After block trimming, ultrathin sections (60 to 80 nm) were obtained using a Leica EM UC7 ultramicrotome (EM UC7, Leica Biosystems, Solms, Germany) and contrasted with osmium tetroxide.

Confocal laser scanning microscopy (CLSM)

The capacity of insect cuticle to emit autofluorescence at various wavelengths is extensively documented, influenced by material composition, degree of sclerotization, and the presence of resilin [18]. Insect cuticle with protein-dominated regions, which can include resilin, an elastic protein present in arthropod cuticles, or unsclerotized chitin exhibits autofluorescence when excited with a laser of 405 nm wavelength. Regions with a low degree or high degree of sclerotization emit autofluorescence when excited with lasers of 488 nm (low degree) or 555 and 639 nm wavelengths (both high degree).

For documentation of the natural autofluorescence, cuticle was cut and arranged on glass slides. Each piece was enclosed by multiple reinforcement rings and then filled with glycerine (99.5% or higher purity, water-free, Carl Roth GmbH & Co. KG, Karlsruhe, Germany) and covered with a glass slip. Following the method described in [10], we documented the samples using a Zeiss LSM 700 confocal laser scanning microscope (Carl Zeiss Microscopy GmbH, Jena, Germany). Four stable solid-state lasers emitting at 405, 488, 555, and 639 nm wavelengths were utilized. Specific bandpass or longpass emission filters (ranging from 420–480 nm, 490 nm or higher, 560 nm or higher, and 640 nm or higher) were employed accordingly. After scanning, the autofluorescence images were combined (using maximum intensity projection) with Zeiss Efficient Navigation (ZEN) software (Carl Zeiss MicroImaging GmbH, Jena, Germany). We assigned blue to the autofluorescence signal from the 405 nm laser, green to the 488 nm laser, and red (50% saturation) to both the 555 and 639 nm lasers.

Figure 2: Velvet ants (*Traumatomutilla bifurca*, Hymenoptera: Mutillidae) in their natural habitats. The images highlight the dark integument with contrasting patterns of black and white setae. The photos depicted in Figure 2 were adapted (cropped) from https://www.inaturalist.org/photos/62624578, https://www.inaturalist.org/photos/62624589, https://www.inaturalist.org/photos/62624582, and https://www.inaturalist.org/photos/62624568 (© 2020 shrike2, published by iNaturalist, distributed under the terms of the Creative Commons Attribution-Non Commercial 4.0 International License, https://creativecommons.org/licenses/by-nc/4.0/). This content is not subject to CC BY 4.0.

Optical spectrometry

Reflectance spectra measurements were conducted using a high-resolution optical fiber spectrometer (Flame; Ocean Insight, Inc., Dunedin, FL, USA), equipped with a DH-2000-BAL light source (Ocean Insight, Inc.) and an optical fiber probe consisting of a 400 µm detector and a light guide. Spectral luminance was controlled using a Spectralon® standard that reflects 99% of light in the UV–vis spectrum. A standard distance of 5 mm was maintained between the fiber probe and both the Spectralon standard and the sample. This distance was determined using the scale provided on the Ocean Insight holder, ensuring consistency across all measurements. Spectra were obtained with normal incidence, covering the spectral range from 300 to 800 nm, with light focused on two parts of the body, namely, the black thorax and the black spot on the metasoma. For each analyzed individual (N = 3), five replicates were

measured for each analyzed body part, totaling to 60 reflectance spectra.

The average reflectance spectra of the ultrablack colors of the velvet ant female were then compared with spectra from animal species with the lowest reflectance in nature, that is, the butterfly *Troides helena* (Papilionidae), the peacock spider *Maratus karrie* (Araneae: Salticidae), and the bird-of-paradise *Drepanornis bruijnii* (Passeriformes: Paradisaeidae). The spectra of these species were obtained from data provided in [10,12], and species with the highest absorbance in the UV–vis spectrum were selected.

Thermal images

This experimental protocol was adapted from [15]. For the thermal images, a velvet ant specimen was carefully positioned on a polystyrene plate, serving as a thermal insulator, and covered with a layer of sand measuring 2 cm in thickness. Using a Fluke TiS75+ Thermal Camera, thermal images were captured before, during, and after a controlled heating process induced by a thermal lamp positioned 10 cm away. Prior to initiating the experiment, the female specimen was photographed, and subsequent images were taken at 1 min and 2 min intervals during the heating process. Throughout the experiment, the ambient temperature was meticulously maintained at a controlled 24 °C.

Results

Our results indicate that the cuticle reflectance of *T. bifurca* females closely resembles the spectra of other animal species with ultrablack coloration (Figure 3). The ultrablack colors in *T. bifurca* are less reflective compared to the butterfly *T. helena* and are similar to those seen in peacock spiders and birds-of-paradise (Figure 3).

The primary characteristic of the ultrablack cuticle is its pronounced black coloration, as evidenced by the photographs and CLSM images. This intense black color is likely attributed to the presence of melanin. Interestingly, unlike the melanin de-

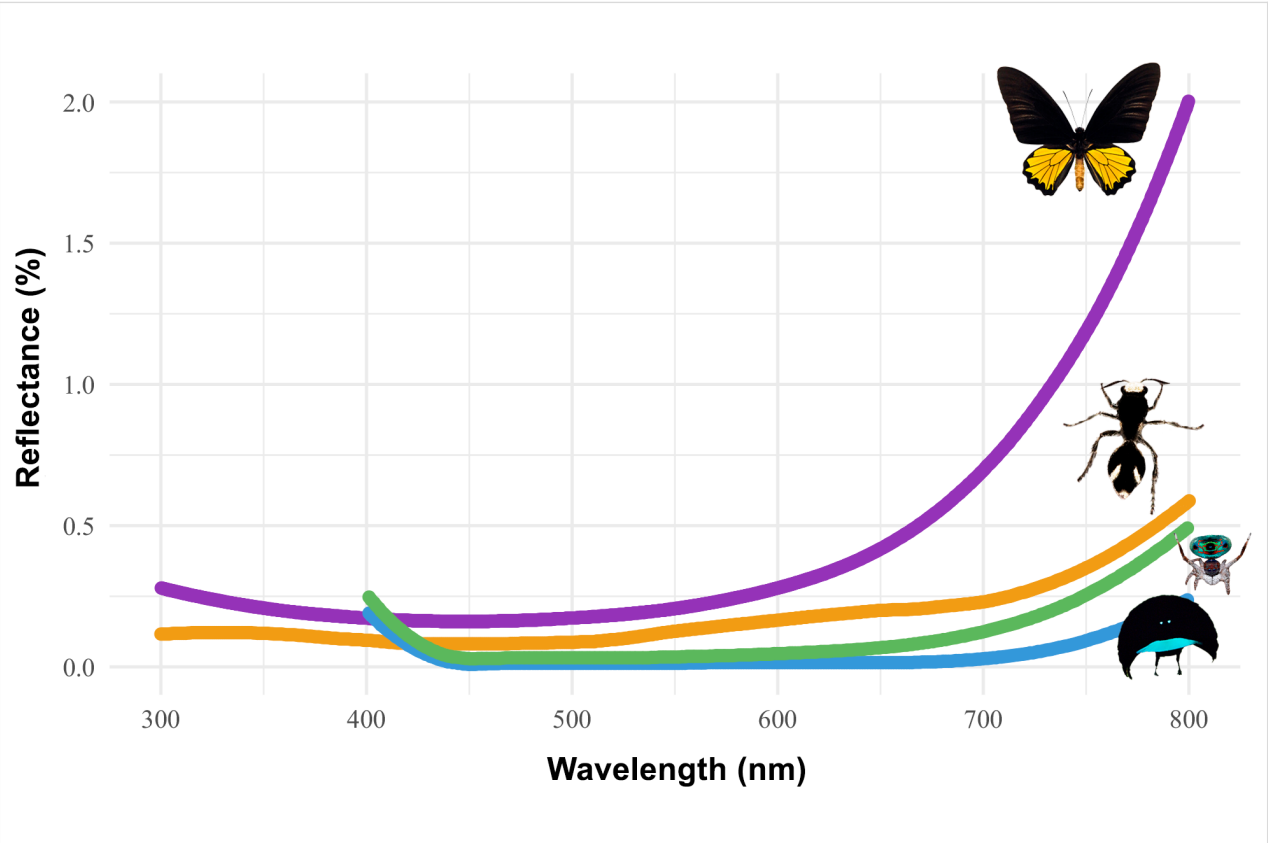

Figure 3: Reflectance spectra of ultrablack colors in the velvet ant *Traumatomutilla bifurca* (Hymenoptera: Mutillidae) (orange line) (original data), the butterfly *Troides helena* (Lepidoptera: Papilionidae) (purple line), the peacock spider *Maratus karrie* (Araneae: Salticidae) (green line), and the bird-of-paradise *Drepanornis bruijnii* (Passeriformes: Paradisaeidae) (blue line). The spectra of the spider and bird were obtained from [10] and that of the butterfly was obtained from [12]. The spectra of *T. bifurca* are derived from our study. The illustrations of velvet ant and bird-of-paradise were created using Adobe Photoshop. Butterfly image is from Insectpedia - stock.adobe.com. This content is not subject to CC BY 4.0. The image of the peacock spider was reproduced from https://www.inaturalist.org/observations/160699324 (© 2022 Donna Newton, published by iNaturalist, distributed under the terms of the Creative Commons Attribution-Non Commercial 4.0 International License, https://creativecommons.org/licenses/by-nc/4.0/). This content is not subject to CC BY 4.0.

scribed in *Hermetia illucens* [19], the melanin in *T. bifurca* does not exhibit autofluorescence. This distinction and the fact that all other structural features serve to enhance this fundamental black coloration are noteworthy.

SEM analysis of the cuticle surface in *T. bifurca* reveals a dense covering of spines and setae (Figure 4). The setae display nanostructures in the form of grooves and are hollow (Figure 4D). No morphological distinction was observed between white and black setae (Figure 4A).

The cuticle is composed of overlapping lamellae with connective pillars and underlying layers (Figure 5). The SEM and TEM images of the *T. bifurca* cuticle reveal that the cuticle sculpturing and setae together with the black pigment may facilitate structural light absorption (Figure 5). The setae in Figure 4,

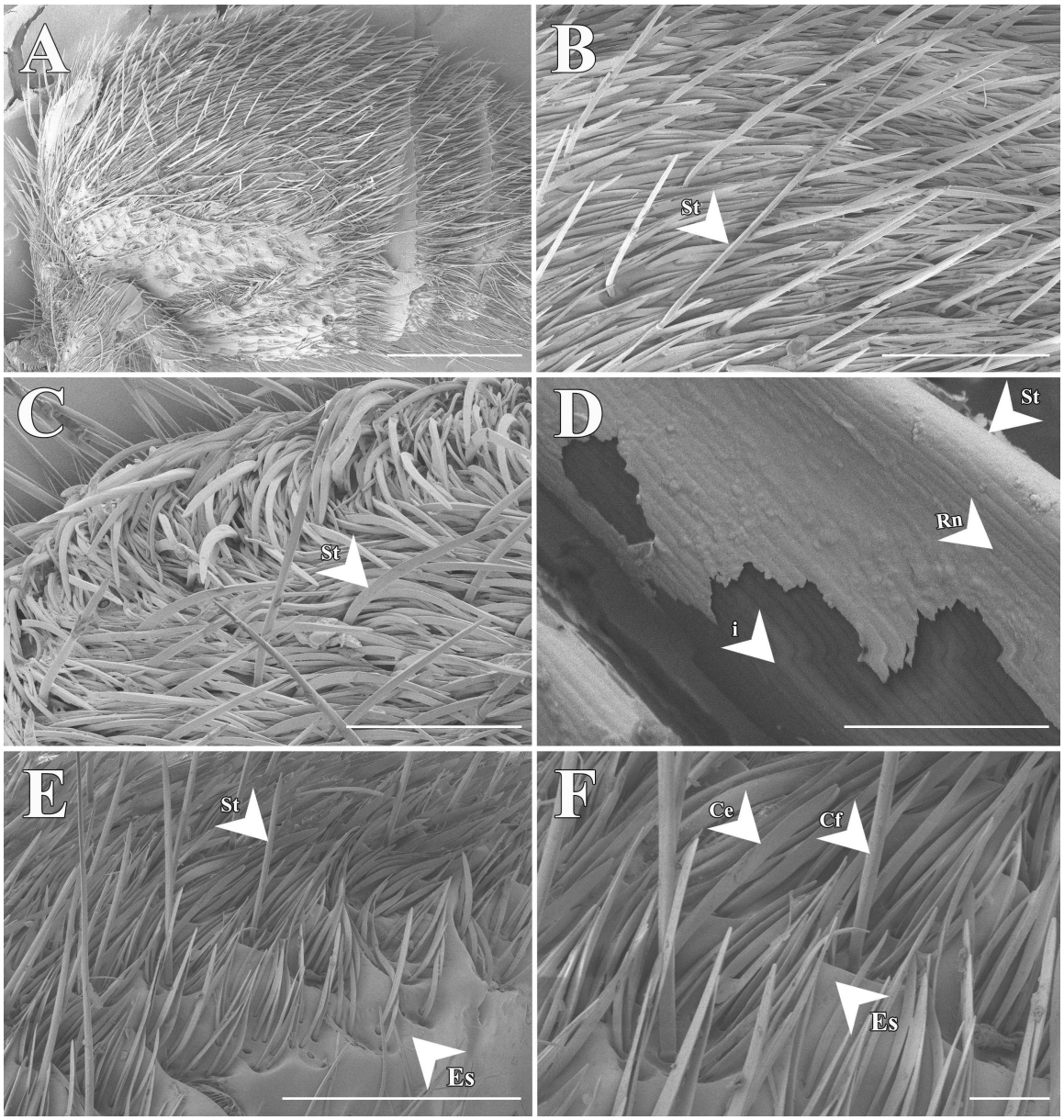

Figure 4: Scanning electron microscopy (SEM) images of the cuticle surface of *Traumatomutilla bifurca* (Hymenoptera: Mutillidae). It exhibits a dense covering of spines and setae (A–F). The setae display an arrangement of slightly flattened filamentous structures (B, C, E, and F). The setae feature grooved nanostructure and are hollow (D), with no morphological distinction between white (B and C) and black (E and F) setae. Legend: St = setae; Rn = grooves on the bristles; i = hollow interior of the setae; Es = surface sculpturing; Ce = slightly flattened setae; Cf = spines. Scale bars: 1 mm in A, 400 µm in B, 200 µm in C, 4 µm in D, and 500 µm in E, 100 µm in F.

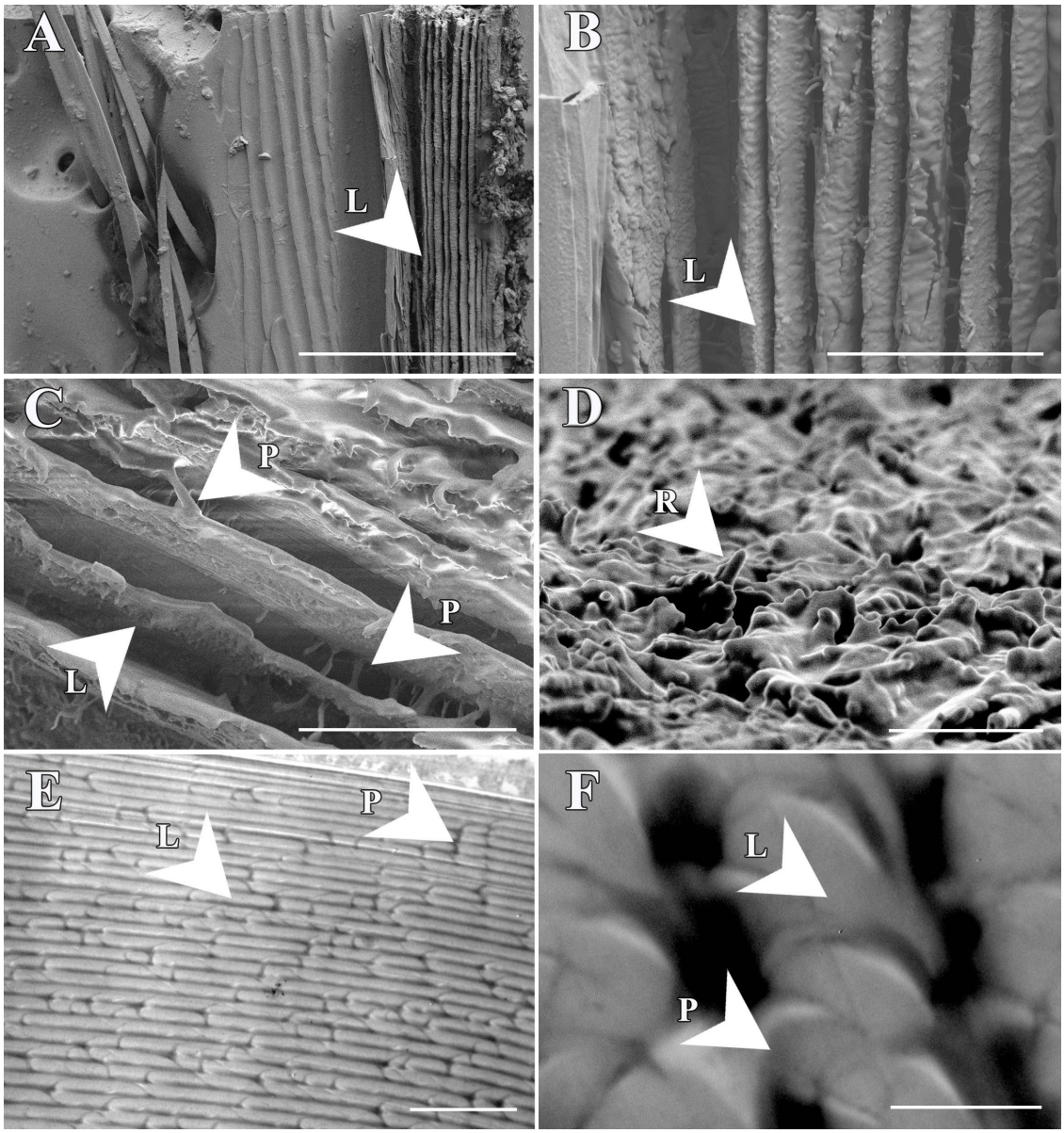

Figure 5: Scanning (A–D) and transmission (E and F) electron microscopy images of the cuticle structure of *Traumatomutilla bifurca* (Hymenoptera: Mutillidae). There is a complex structural arrangement of lamellar units (C and D), stacked on top of each other (E and F). There are also dark transverse bands that interconnect two consecutive longitudinal bands of the same lamellae (arrow), or of two separate lamellae (A and B). Legend: L = lamellae; P = pillars; R = rugosity of chitin fibers embedded in a protein matrix. Scale bars: 100 µm in A, 20 µm in B, 15 µm in C, 3 µm in D, 5 µm in E and 1 µm in F.

with their grooved nanostructures and hollow interiors, and the stacked lamellae (see L in Figure 5) are integral to the structures represented in Figure 6, where setae and lamellae likely enhance light absorption through multiple scattering and increased path length as light interacts with the cuticular protrusions and lamellar layers. Additionally, iterative scattering and absorption occur between the cuticular protrusions and the underlying layer with presumable absorptive properties (Figure 6). This process increases the path length through lamellae, leading to more efficient absorption, as evidenced by CLSM images of the target species (Figure 7).

Thermal imaging results indicate that *T. bifurca* was consistently 2 °C cooler than the ambient temperature (Figure 8). Furthermore, no thermal differences were observed between areas with white hair and ultrablack cuticle (Figure 8). This is

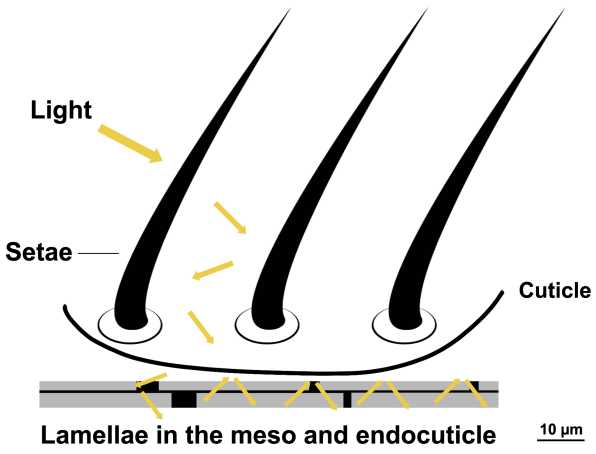

Figure 6: Scheme illustrating the functionality of the surface structure in *Traumatomutilla bifurca* (Hymenoptera: Mutillidae). Proposed mechanisms of structurally assisted absorption by surface sculpturing and setae, as light (yellow arrows) traverses through the dark pigmented cuticle and into the absorbing layer. Additionally, there is multiple scattering between protrusions and iterative absorption as light traverses through the cuticle at each lamella. Thus, the increased path length of light through lamellae may cause enhanced absorption.

the evidence that the color plays a secondary role in thermobiology of this animal; rather, the isolation properties of the hair cover are decisive for thermoregulation function.

Discussion

The results suggest that the velvet ant *Traumatomutilla bifurca* possesses an ultrablack, structurally intricate antireflective coloration. The ultrablack coloration is produced by structurally assisted light guiding and absorption due to complex arrangements of microstructures at the cuticle surface above absorptive lamellae. The surface microstructure of the ultrablack cuticle (setae and microsculpturing) bear some structural resemblance to the ultrablack surfaces in other animals [10,13]. Moreover, there are lamellae underneath the epicuticle, stacked on top of each other and interconnected by columns. This kind of structure can also be found in another wasp, the oriental hornet *Vespa orientalis* (Hymenoptera, Vespidae) [20-22], however, it does not result in ultrablack colors.

The structures of *T. bifurca* may act as a light-trapping mechanism and can enhance absorption by 5% compared to a flat surface. The dense layer of black epicuticular setae further enhances ultrablack coloration. Ishay and collaborators [22] suggested that longitudinal chitinous plates would be interconnected by dark transverse and longitudinal absorptive bands. These are often rods of chitin embedded in a protein matrix [23]. The authors also suggested that there is a proteinaceous filling material, which tends to leach out during preparation of the specimens for SEM, leaving behind empty lacunae.

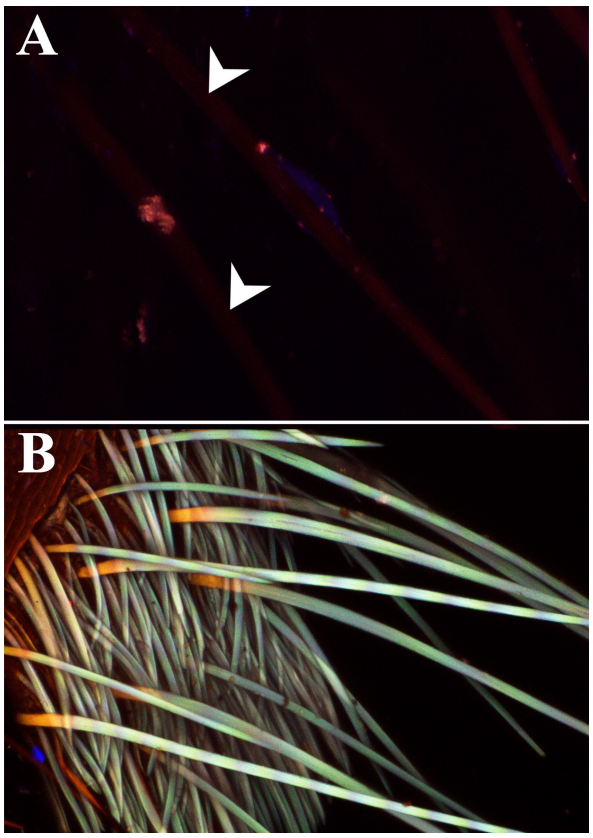

Figure 7: Confocal laser scanning microscopy micrographs (maximum intensity projections) showing different types of autofluorescence exhibited by the cuticle. Blue regions contain resilin or some other proteins, while green, orange, and red structures represent different degrees of sclerotization. Black regions are presumably melanized. (A) The cuticle of the velvet ant *Traumatomutilla bifurca* shows no autofluorescence, while black setae show a very low signal (white arrows). (B) The autofluorescence in the white setae is whitish, which means that all of the wavelengths are present in the signal.

Modelled reflectance of *V. orientalis* suggests that this layered structure contributes to the overall antireflective properties of the cuticle by increasing the effective surface area available for light absorption [20]. Although this system in *V. orientalis* is coupled with xanthopterins to absorb light, the similar structure in *T. bifurca* is most probably coupled with melanin as in other velvet ants [24].

Similar cases of white–black structural colors can be observed in other insect groups. For instance, the tiger mosquito *Aedes albopictus* (Diptera: Culicidae) exhibits black and white scales with micro- and nanostructures that turn transparent scales into superwhite and melanized scales into superblack [25]. Melanin pigments can produce a black color with visible reflections, such as in shiny fur and feathers. The degree of such visible reflections depends on the surface structure. Ultrablack color lacks this gloss and instead displays a matte black appearance

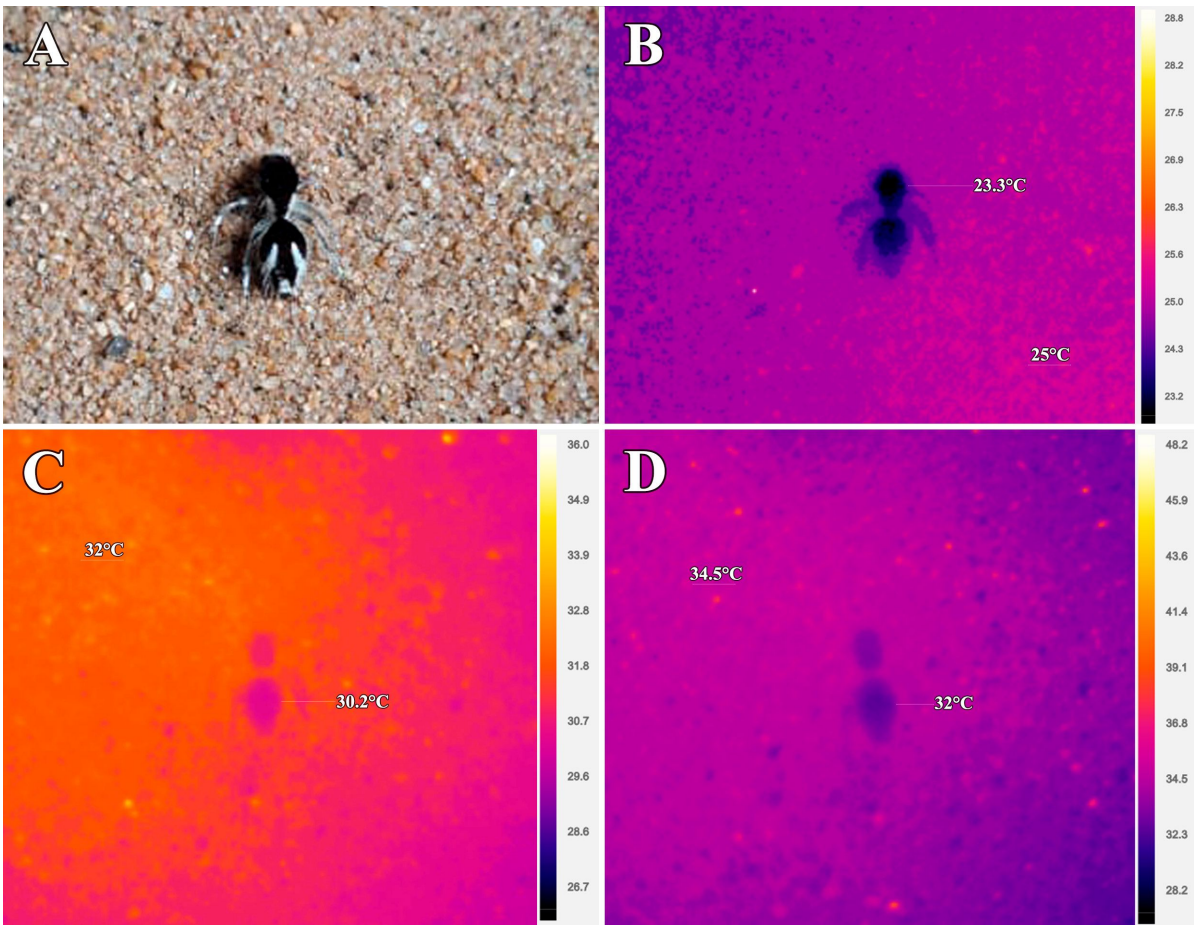

Figure 8: Thermal images of a female *Traumatomutilla bifurca* (Hymenoptera: Mutillidae). (A) Visible spectrum image, (B) thermal image of the animal before heating, (C) thermal image after 1 min of heating, and (D) thermal image after 2 min of heating.

due to the presence of (often hierarchical) surface microstructures. For example, in the beetle *Alaus oculatus* (Coleoptera: Elateridae), there are two large dorsal circular spots known as eyespots. Within these spots, fixed setae are present in a concave structure, and the underlying cuticle features a microstructured topography [26]. These concave structures scatter light and enhance absorption by melanin, serving as an antireflective feature and creating ultrablack colors [26]. In another beetle species, *Euprotaetia inexpectata* (Coleoptera: Scarabaeidae), a complex ultrastructure consisting of randomly oriented anisotropic micropillars accounts for its significant absorptivity [27].

Peacock spiders feature microstructures in specific body regions that exhibit ultrablack coloration with high absorbance. Interestingly, these microstructures are absent in other dark body areas with lower UV–vis absorbance [10]. These microstructures scatter light across the absorptive cuticle, further aided by brush-like scales that serve as an anti-reflective coating [10]. Similarly, birds-of-paradise display ultrablack coloration attributed to microstructures found in the barbules of their feathers, yielding a similar effect [13]. West African Gaboon vipers exhibit dorsal patches of black scales with microscale leaf-like elevations and nanoscale ridges that result in ultrablack colors [14,15]. These examples suggest that microstructure-assisted ultrablack colors are naturally selected and may have evolved convergently across animal groups, including velvet ants.

In addition to their role in color production, submicrometer-sized structures, when randomly distributed in size and position on (or in) a transparent material, can enhance light scattering. This scattering can intensify white coloration; however, when the underlying material is black, as in *T. bifurca*, these structures can contribute to the enhancement of ultrablack coloration by amplifying light absorption. Future studies should investigate this phenomenon in greater detail, exploring how variations in the distribution and organization of such microstructures influence the absorption efficiency and potential adaptive

significance of ultrablack coloration in different ecological contexts.

The role of ultrablack colors in nature is still a topic of debate, with limited evidence regarding the selective pressures driving their evolution. Recent studies propose that ultrablack coloration may enhance visual signals from bright colors in peacock spiders and birds-of-paradise, traits that are sexually selected [10,13]. However, in velvet ants, sexual behavior in most species remains largely unexplored, and the sparse evidence suggests little correlation between female coloration and male preference [28]. As a result, an alternative hypothesis regarding the evolution and function of ultrablack colors in velvet ants is the amplification of antipredatory visual signals.

Female velvet ants are renowned for their effective defenses against predators. Given their characteristics and life habits, such as diurnal activity, striking colors, and inability to fly, it is expected that they would be frequent targets for predators. However, there is limited observational and experimental evidence documenting interactions between velvet ants and insectivorous predators [29,30]. Observations indicate that while bufonid toads may initially prey on female velvet ants, they tend to avoid them in subsequent encounters [29,30]. Conversely, birds and lizards, which are known predators of defended insects such as bees and wasps, exhibit caution and generally avoid interacting with female velvet ants [30,31]. Therefore, this behavior suggests that the colors of velvet ants, closely linked to their defense mechanisms, such as cuticle hardness and their painful sting, may function as an honest warning signal to potential predators.

Thermal imaging suggests that the body temperature of *T. bifurca* in a range of ambient temperatures generally remains below ambient temperature. There is evidence indicating that structures like the long white setae in Thistledown velvet ants (*Dasymutilla gloriosa*) in the Desert Mimicry Ring may play a role in thermal regulation [32]. Additionally, previous studies have suggested a potential association between dark colors in velvet ants and photoprotection [16]. In this case, the dark cuticle would function as a radiation filter to prevent ultraviolet radiation from reaching the cells underneath. This protection may derive from melanin [16], and the tile-shaped cuticular lamellae that might protect from the damage of exposure to UV light [33]. Our findings do not provide compelling evidence regarding the thermal implications of ultrablack colors in *T. bifurca*, even though the wasps were always 2 °C below ambient temperatures. Surprisingly, the white setae did not exhibit distinct thermal behavior compared to the dark colors. Furthermore, the analysis of setae ultrastructures revealed no significant differences among them. Therefore, future investigations should address not only the thermal implications of ultrablack colors compared to other velvet ants with non-ultrablack dark colors, but also the thermal properties of white setae.

Another potential function of the sculptured cuticle is resistance to high forces. Velvet ants are known as “indestructible insects” not only because most predators fear their panful stings and venom, but also because of their hard exoskeleton [29,30]. The sculptured cuticle may have a similar structure and force-resisting mechanisms as other wasps [34]. In some wasp species, the sculpturing of the cuticle and the lamellae terraces may form an accordion-like structure that increase resistance to fractures and high pressures [34].

Ultrablack coloration has garnered significant interest in recent years because of its potential applications across various fields, including optics, camouflage, and solar energy capture. Characterized by their remarkable ability to reflect an exceptionally low amount of light across a broad spectrum of wavelengths in the UV–vis range, these surfaces have drawn inspiration from natural occurrences observed in certain organisms. Scientists are actively engaged in deciphering the underlying mechanisms behind the development of these ultrablack surfaces, with the goal of replicating such structures in synthetic materials possessing analogous properties [3,5,6,15].

In conclusion, the study of ultrablack coloration in animals, such as *T. bifurca*, reveals the intricate interplay between structural microfeatures and pigment absorption that results in these remarkably absorptive surface. Especially, this kind of wasp-inspired technology may have its application in increasing efficiency of solar panels [20]. Further research is needed to uncover the mechanisms and functional roles of ultrablack coloration in velvet ants, as well as to determine which other Hymenopteran species exhibit this fascinating color trait.

Supporting Information

Supporting Information File 1

Spectrum obtained from females of *Traumatomutilla bifurca*.
[https://www.beilstein-journals.org/bjnano/content/supplementary/2190-4286-15-122-S1.rar]

Acknowledgements

We thank Alberto Borba for his invaluable assistance with the TEM images, Vivina S. Ferreira and Herbeson Ovidio de Jesus Martins for their support with field collections, Felipe Henrique Datto-Liberato for his kind help with the images, and Victor

Hugo Martins Machado for generously providing the thermal lamp used in our experiment. Finally, we extend our heartfelt gratitude to Henning Kallies (Figure 1A), Jes Lefcourt (Figure 1B), Justin Philbois (Figure 1C), Manuel Ortiz (Figure 1D) and Nicole Desnoyers (Figure 2) for generously granting permission to use their photographs in this manuscript. This work is based on the doctoral thesis of the first author (V. M. Lopez, "Evolutionary ecology of antipredator coloration in velvet ants (Hymenoptera: Mutillidae)," University of São Paulo, 2024).

Funding

This study was supported by the National Council for Scientific and Technological Development - CNPq (proc.142299/2020-0) and Minas Gerais State Research Support Foundation - FAPEMIG (proc. APQ-05401-23). RGF thanks CNPq (Proc. 312847/2022-0) for a productivity grant. We thank the Public Prosecutor's Office of Minas Gerais (MPMG, through the Regional Coordination of Environmental Prosecutor's Offices of the Paranaíba and Lower Grande River Watersheds) for constant support.

Conflict of Interest

There are no conflicts to declare.

Author Contributions

Vinicius Marques Lopez: conceptualization; formal analysis; funding acquisition; investigation; methodology; visualization; writing – original draft; writing – review & editing. Wencke Krings: formal analysis; investigation; methodology; validation; writing – review & editing. Juliana Reis Machado: investigation; methodology; writing – review & editing. Stanislav Gorb: conceptualization; formal analysis; funding acquisition; methodology; supervision; visualization; writing – review & editing. Rhainer Guillermo-Ferreira: conceptualization; formal analysis; funding acquisition; methodology; supervision; visualization; writing – original draft; writing – review & editing.

ORCID® iDs

Vinicius Marques Lopez - https://orcid.org/0000-0001-9445-6540
Wencke Krings - https://orcid.org/0000-0003-2158-9806
Stanislav Gorb - https://orcid.org/0000-0001-9712-7953

Data Availability Statement

All data that supports the findings of this study is available in the published article and/or the supporting information of this article.

References

1. Dou, S.; Xu, H.; Zhao, J.; Zhang, K.; Li, N.; Lin, Y.; Pan, L.; Li, Y. *Adv. Mater. (Weinheim, Ger.)* **2021,** *33,* 2000697. doi:10.1002/adma.202000697
2. Mattos, B. D.; Jäntti, N.; Khakalo, S.; Zhu, Y.; Miettinen, A.; Parkkonen, J.; Khakalo, A.; Rojas, O. J.; Ago, M. *Adv. Funct. Mater.* **2023,** *33,* 2304867. doi:10.1002/adfm.202304867
3. Mizuno, K.; Ishii, J.; Kishida, H.; Hayamizu, Y.; Yasuda, S.; Futaba, D. N.; Yumura, M.; Hata, K. *Proc. Natl. Acad. Sci. U. S. A.* **2009,** *106,* 6044–6047. doi:10.1073/pnas.0900155106
4. Han, Z.; Li, B.; Mu, Z.; Yang, M.; Niu, S.; Zhang, J.; Ren, L. *Nanoscale Res. Lett.* **2015,** *10,* 344. doi:10.1186/s11671-015-1052-7
5. Xiao, P.; Yang, W.; Qiu, N.; Li, S.; Ni, F.; Zhang, C.; Gu, J.; Kuo, S.-W.; Chen, T. *Nano Lett.* **2022,** *22,* 9343–9350. doi:10.1021/acs.nanolett.2c02385
6. Gopal, L.; Sudarshan, T. *Surf. Eng.* **2023,** *39,* 636–640. doi:10.1080/02670844.2023.2248705
7. Wei, W.; Li, M.; Han, Y.; Wu, M.; Yan, J.; Liu, M.; Chen, Y. *Adv. Opt. Mater.* **2022,** *10,* 2101854. doi:10.1002/adom.202101854
8. Zhao, B.; Shi, X.; Khakalo, S.; Meng, Y.; Miettinen, A.; Turpeinen, T.; Mi, S.; Sun, Z.; Khakalo, A.; Rojas, O. J.; Mattos, B. D. *Nat. Commun.* **2023,** *14,* 7875. doi:10.1038/s41467-023-43594-4
9. Stavenga, D. G.; Foletti, S.; Palasantzas, G.; Arikawa, K. *Proc. R. Soc. B* **2006,** *273,* 661–667. doi:10.1098/rspb.2005.3369
10. McCoy, D. E.; McCoy, V. E.; Mandsberg, N. K.; Shneidman, A. V.; Aizenberg, J.; Prum, R. O.; Haig, D. *Proc. R. Soc. B* **2019,** *286,* 20190589. doi:10.1098/rspb.2019.0589
11. Vukusic, P.; Sambles, J. R.; Lawrence, C. R. *Proc. R. Soc. London, Ser. B* **2004,** *271,* S237–S239. doi:10.1098/rsbl.2003.0150
12. Davis, A. L.; Nijhout, H. F.; Johnsen, S. *Nat. Commun.* **2020,** *11,* 1294. doi:10.1038/s41467-020-15033-1
13. McCoy, D. E.; Feo, T.; Harvey, T. A.; Prum, R. O. *Nat. Commun.* **2018,** *9,* 1. doi:10.1038/s41467-017-02088-w
14. Spinner, M.; Gorb, S. N.; Balmert, A.; Bleckmann, H.; Westhoff, G. *PLoS One* **2014,** *9,* e91087. doi:10.1371/journal.pone.0091087
15. Spinner, M.; Kovalev, A.; Gorb, S. N.; Westhoff, G. *Sci. Rep.* **2013,** *3,* 1846. doi:10.1038/srep01846
16. Lopez, V. M.; Azevedo Tosta, T. A.; da Silva, G. G.; Bartholomay, P. R.; Williams, K. A.; Guillermo-Ferreira, R. *J. Therm. Biol.* **2021,** *100,* 103030. doi:10.1016/j.jtherbio.2021.103030
17. Bartholomay, P.; Williams, K.; Luz, D.; Cambra, R.; de Oliveira, M. L. *Insecta Mundi* **2019,** *0709,* 1–37.
18. Michels, J.; Gorb, S. N. *J. Microsc. (Oxford, U. K.)* **2012,** *245,* 1–16. doi:10.1111/j.1365-2818.2011.03523.x
19. Rebora, M.; Salerno, G.; Piersanti, S.; Saitta, V.; Morelli Venturi, D.; Li, C.; Gorb, S. *Sci. Rep.* **2023,** *13,* 22101. doi:10.1038/s41598-023-49549-5
20. Plotkin, M.; Hod, I.; Zaban, A.; Boden, S. A.; Bagnall, D. M.; Galushko, D.; Bergman, D. J. *Naturwissenschaften* **2010,** *97,* 1067–1076. doi:10.1007/s00114-010-0728-1
21. Ishay, J. S.; Pertsis, V. *J. Electron Microsc.* **2002,** *51,* 401–411. doi:10.1093/jmicro/51.6.401
22. Ishay, J. S.; Kirshboim, S.; Steinberg, D.; Kalicharan, D.; Jongebloed, W. L. *Comp. Biochem. Physiol., Part A: Mol. Integr. Physiol.* **1998,** *120,* 661–670. doi:10.1016/s1095-6433(98)10084-3
23. Giraud-Guille, M. M.; Bouligand, Y. Chitin-Protein Molecular Organization in Arthropod. In *Chitin in Nature and Technology;* Muzzarelli, R.; Jeuniaux, C.; Gooday, G. W., Eds.; Springer US: Boston, MA, 1986; pp 29–35. doi:10.1007/978-1-4613-2167-5_5
24. Hines, H. M.; Witkowski, P.; Wilson, J. S.; Wakamatsu, K. *PLoS One* **2017,** *12,* e0182135. doi:10.1371/journal.pone.0182135

25. Rebora, M.; Salerno, G.; Piersanti, S.; Kovalev, A.; Gorb, S. N. *Beilstein J. Nanotechnol.* **2023,** *14,* 496–508. doi:10.3762/bjnano.14.41
26. Wong, V. L.; Marek, P. E. *PeerJ* **2020,** *8,* e8161. doi:10.7717/peerj.8161
27. Parisotto, A.; Vogler-Neuling, V. V.; Steiner, U.; Saba, M.; Wilts, B. D. *Mater. Today Adv.* **2023,** *19,* 100399. doi:10.1016/j.mtadv.2023.100399
28. VanderSal-Jensen, N. D.; Crews, S. C.; Gillespie, R. G. *Invertebr. Biol.* **2016,** *135,* 200–210. doi:10.1111/ivb.12128
29. Mergler, C. J.; Gall, B. G. *Ethol. Ecol. Evol.* **2021,** *33,* 15–24. doi:10.1080/03949370.2020.1789747
30. Gall, B. G.; Spivey, K. L.; Chapman, T. L.; Delph, R. J.; Brodie, E. D., Jr.; Wilson, J. S. *Ecol. Evol.* **2018,** *8,* 5852–5862. doi:10.1002/ece3.4123
31. Manley, D. G.; Sherbrooke, W. C. *Southwest Nat.* **2001,** *46,* 221–222. doi:10.2307/3672534
32. Wilson, J. S.; Sidwell, J. S.; Forister, M. L.; Williams, K. A.; Pitts, J. P. *Biol. Lett.* **2020,** *16,* 20200242. doi:10.1098/rsbl.2020.0242
33. Ishay, J. S.; Joseph, Z.; Galushko, D. V.; Bergman, D. J. *Curr. Nanosci.* **2005,** *1,* 125–156. doi:10.2174/1573413054065321
34. Mora-Castro, R.; Hernández-Jiménez, M.; Sáenz-Arce, G.; Porras-Peñaranda, J.; Hanson-Snortum, P.; Avendaño-Soto, E. *Sci. Rep.* **2020,** *10,* 1418. doi:10.1038/s41598-020-58301-2

License and Terms

BEILSTEIN JOURNAL OF NANOTECHNOLOGY

Natural nanofibers embedded in the seed mucilage envelope: composite hydrogels with specific adhesive and frictional properties

Agnieszka Kreitschitz*[1,2,§] and Stanislav N. Gorb[2]

Review

Open Access

Address:
[1]University of Wrocław, Department of Plant Developmental Biology, ul. Kanonia 6/8, 50-328 Wrocław, Poland and [2]Kiel University, Department of Functional Morphology and Biomechanics, Am Botanischen Garten 9, D-24098 Kiel, Germany

Email:
Agnieszka Kreitschitz* - agnieszka.kreitschitz@uwr.edu.pl;
Stanislav N. Gorb - sgorb@zoologie.uni-kiel.de

* Corresponding author
§ Phone: +48 71 375 40 91

Keywords:
adhesion; cellulose; friction; hydrogel; mucilage envelope; seeds

Beilstein J. Nanotechnol. **2024,** *15,* 1603–1618.
https://doi.org/10.3762/bjnano.15.126

Received: 27 August 2024
Accepted: 22 November 2024
Published: 13 December 2024

This article is part of the thematic issue "Micro- and nanoscale effects in biological and bioinspired materials and surfaces".

Associate Editor: J. Lahann

Abstract

The increasing interests in natural, biodegradable, non-toxic materials that can find application in diverse industry branches, for example, food, pharmacy, medicine, or materials engineering, has steered the attention of many scientists to plants, which are a known source of natural hydrogels. Natural hydrogels share some features with synthetic hydrogels, but are more easy to obtain and recycle. One of the main sources of such hydrogels are mucilaginous seeds and fruits, which produce after hydration a gel-like, transparent capsule, the so-called mucilage envelope. Mucilage serves several important biological functions, such as supporting seed germination, protecting seeds against pathogens and predators, and allowing the seed to attach to diverse surfaces (e.g., soil or animals). The attachment properties of mucilage are thus responsible for seed dispersal. Mucilage represents a hydrophilic, three-dimensional network of polysaccharides (cellulose, pectins, and hemicelluloses) and is able to absorb large amounts of water. Depending on the water content, mucilage can behave as an efficient lubricant or as strong glue. The current work attempts to summarise the achievements in the research on the mucilage envelope, primarily in the context of its structure and physical properties, as well as biological functions associated with these properties.

Introduction

The definition of hydrogels describes them as hydrophilic, three-dimensional (3D), polymeric networks able to absorb huge amounts of water [1-3]. This term refers perfectly to the mucilage envelope produced by many fruits and seeds (diaspores) of diverse plant taxa [4-9]. Mucilage is considered as a natural hydrogel and shares specific features with synthetic hydrogels [2,9-11]. Hydrogels are 3D networks of polymers (i.e., polysaccharides in plant seeds) interacting via chemical

bonds (ionic and covalent), physical interactions (hydrogen bonds), or van der Waals forces [3,11,12].

The ability to produce the mucilage envelope is a widespread feature in diverse plant groups (mosses, ferns, gymnosperms, and dicotyledons) as well as plant organs (roots, leaves, flowers, seeds, and fruits) [4-6]. Among the various substances produced by diaspores, mucilage at the macroscale can be very easy to perceive without any special equipment. Macroscopically observable mucilage is often a transparent, gel-like capsule formed around the diaspore after hydration with water (Figure 1).

At the microscale mucilage exhibits, before hydration, successive layers formed by adcrustation in the mucilaginous cells of the seed/fruit coat (the outermost covering of the diaspore) [6,13]. Mucilage is often composed of three types of polysaccharides, which are typical components found in the plant cell wall. It exhibits modified secondary cell wall, where pectins are the dominating component, while hemicelluloses and cellulose fibrils constitute the lesser part of its composition [14-16]. The nanoscale level of the spatial organisation of mucilage observed with scanning electron microscopy (SEM) reveals the complexity of the mucilage with special features, such as 3D organisation of polysaccharides in a net-like structure [7,13].

In the last years, the mucilage produced by plant diaspores became of high interest in diverse sectors, such as medicine, cosmetics, food, biomedicine, pharmaceutics, nanomaterials, and bioinspired nanotechnology [11,17-20]. Mucilage is a natural, biodegradable, non-toxic plant product, odourless, colourless, and tasteless [11,21]. Its chemical composition and special physical properties allow many applications of mucilage, for example, as thickening and structuring (gel-forming) agent, emulsifier or stabiliser for food products, scaffold for tissue regeneration, additive in formation of medicinal tablets, and for gels and wound dressings [15,18,20-22].

Mucilage is a complex mixture of polysaccharides, that is, pectins, hemicelluloses, and cellulose fibrils, which are derivatives of the modified secondary cell wall with its special properties. Among these properties, one of the most important ones is the ability to accumulate a large amount of water [2,6,16,23]. This is connected to many ecological advantages for the dias-

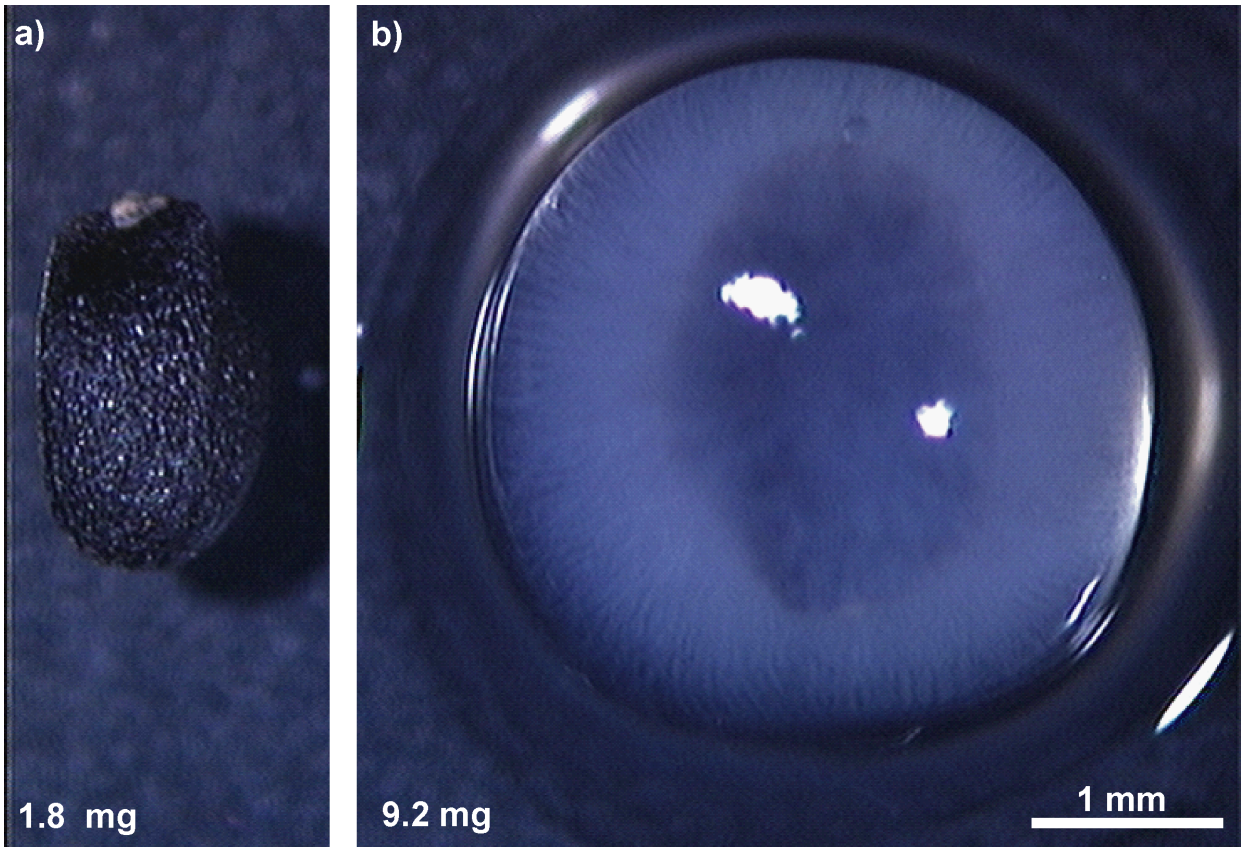

Figure 1: *Ocimum basilicum*. (a) Dry seed and (b) seed after hydration with visible mucilage envelope. The mucilage envelope accumulates water and keeps it around the seed. Note the mass increase after hydration.

pores. The mucilage supports seed germination, dispersal, and various interactions with other organisms. It protects diaspores against digestion, pathogens, harvesting by ants, and osmotic stress [4-6,10,24,25].

Depending on the hydration level, mucilage exhibits distinct physical properties, which are also connected with its biological functions. In a fully hydrated state, it demonstrates very low friction, important for example, in endozoochoric diaspore dispersal [26-28]. Hydrated mucilage can very strongly adhere to surfaces (e.g., stone or glass) when completely dried out after contact, with pull-off forces reaching values around 6.5 N [29]. Such strong adhesion can enable seed attachment to the soil, preventing removal and damage by other organisms [16,30], or to animal bodies, promoting epizoochory [31-33]. These distinct physical features make mucilage also an important substrate for pharmaceutical, biomedical, and food industries [11,15,19-21].

Here, we briefly review the basic composition and structure of mucilage, its frictional and adhesive properties, and ecological aspects associated with these properties. We also summarise and discuss the results of our studies from the last few years conducted on mucilage envelopes and summarise them to demonstrate the current state of knowledge on this topic (Figure 2).

Review

Spatial structure of the mucilage – from pressed layers to a 3D network

Substances with gel character (slime, mucus, and mucilage) are ubiquitous in nature and are produced by diverse organisms such as bacteria, plants representing diverse groups (algae, ferns, and higher plants), and animals (fishes, frogs, and jellyfish). They can be important in different ways for the organisms (locomotion, reproduction, and defence) [34,35],

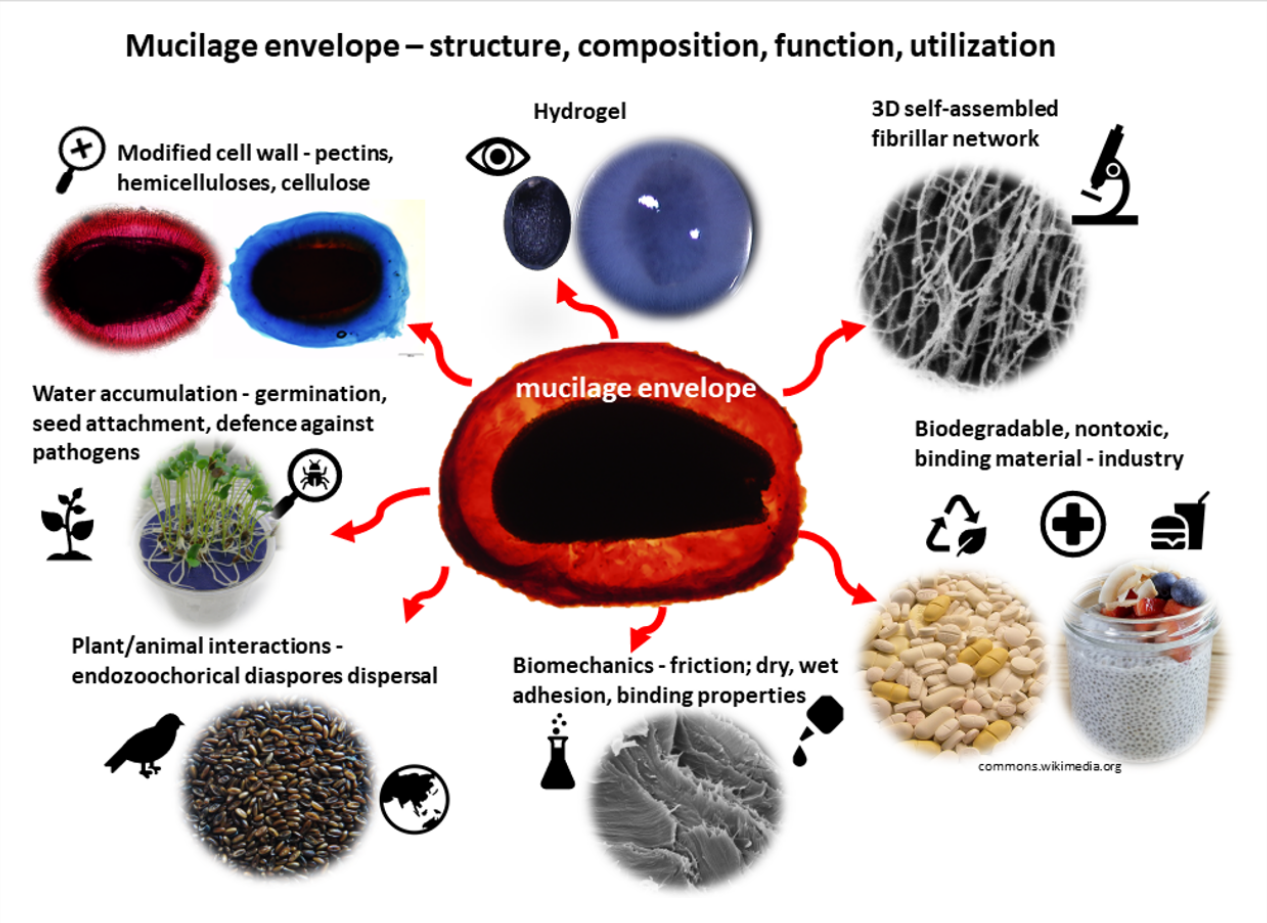

Figure 2: Structure, composition, function, properties, and exploitation of the seed mucilage envelope. The photo of Chia pudding with coconut milk and berries was adapted from https://www.flickr.com/photos/197996902%40N06/52774529156/, ("Chia pudding with coconut milk and berries (KETO, LCHF, Low Carb, Gluten free, FIT)", © Ewelina Podrez-Siama, published via Flickr, distributed under the terms of the Creative Commons Attribution 2.0 Generic License, https://creativecommons.org/licenses/by/2.0). The photo depicting pills was adapted from https://commons.wikimedia.org/wiki/File:Tablets_pills_medicine_medical_waste.jpg ("Various unused tablets collected to be treated as medical waste", © Pöllö, published via Wikimedia Commons, distributed under the terms of the Creative Commons Attribution 3.0 Generic License, https://creativecommons.org/licenses/by/3.0/).

but one of their most significant functions is their ability to absorb water [6,11,15,17,18]. One of such gel-like natural materials studied intensively over the last years is the diaspore (seeds and fruits) mucilage envelope produced by different plants (monocotyledons and dicotyledons) [2,4,6,16,22,36,37]. The mucilage envelope can be described as nanoscale 3D self-assembled fibrillar network, which is able to entrap water and to form a so-called molecular gel after hydration [8,22,38].

Mucilage, which is produced by the mucilaginous cells of diaspores in a form of densely packed layers, has the ability of loosening its structure after hydration into an easily accessible 3D fibrillar network [7,13,14,39] (Figure 3 and Figure 4 below). One of the key components of this network are, in general, cellulose fibrils, which constitute a kind of skeleton for other polysaccharides (pectins and hemicelluloses); however, there is also almost purely pectic seed mucilages without cellulose fibrils and mucilage dominated by hemicelluloses [6,7]. This self-organising nature and the natural composition makes the mucilage envelope a perfect material for diverse studies and a model for the production of synthetic gels or gel-like substances with properties resembling those of hydrogels [11,22].

Cellulose nanofibrils (CNFs) have been of interest for diverse industry branches because of their natural origin and biodegradability. They are used, for example, for paper production, as food additives, in biofilms, and in the production of packing materials and aerogels [15,18,20-22]. However, little is known about the structural properties of CNFs, and they require proper characterisation of their micro- and nanostructures. In the last years, SEM visualisation, combined with the critical point drying (CPD) procedure, has been widely used in nanostructural studies of diverse hydrogel-like samples, containing cellulose fibrils, or biofilms [7,40,41]. The CPD method allows one to maintain the original 3D ultrastructure of the samples without collapsing after dehydration [40,41]. When hydrated hydrogel-like CNFs are gently dried using CPD, the result is an aerogel-like material [41,42] with extremely interesting frictional properties [43].

The cell wall is a typical part of plant cells, and its basic chemical composition includes cellulose, hemicelluloses, and pectic polysaccharides [44-47]. Cellulose is a linear polymer composed of β-1,4-linked D-glucose [47]. The cellulose chains are held together by intramolecular hydrogen bonds, forming cellulose microfibrils, whose diameter can vary across species from 2.2–3.6 nm [48-51], over 3–4 nm [52], to even 30 nm of average width [53]. Microfibrils are typical of primary cell walls, while the next higher level of organisation are macrofibrils [54], specific for secondary cell walls [47,55,56].

Cell wall architecture has been studied in many cases on the primary cell wall of parenchymatous, root tip, or epidermal cells [54,57-59]. Visualisation of the secondary cell wall was previously carried out for tracheary elements of xylem [60-62]. The microfibrils of the primary cell wall are rather thin (2–3 nm), which makes their differentiation from other polysaccharides (pectins and hemicelluloses) rather difficult. The size of the microfibrils of the secondary cell wall (20–30 nm) [53] makes their observation easier, particularly using high-resolution microscopy techniques, such as atomic force microscopy (AFM), transmission electron microscopy (TEM), SEM, or cryo-SEM [45,57,63-66]. Very often, the procedures for preparing mucilage envelope samples can destroy and/or influence the organisation of polysaccharides, making the analysis of spatial structure of the mucilage impossible. The complicated preparation procedures and analysis give us often an information limited to just one factor, for example, to specific chemical composition or topology (AFM, FTIR, or Raman microscopy) [45]. Ideally, the comparison of data from diverse visualisation techniques can provide us with reliable results about the 3D organisation of the polysaccharides within the mucilage envelope.

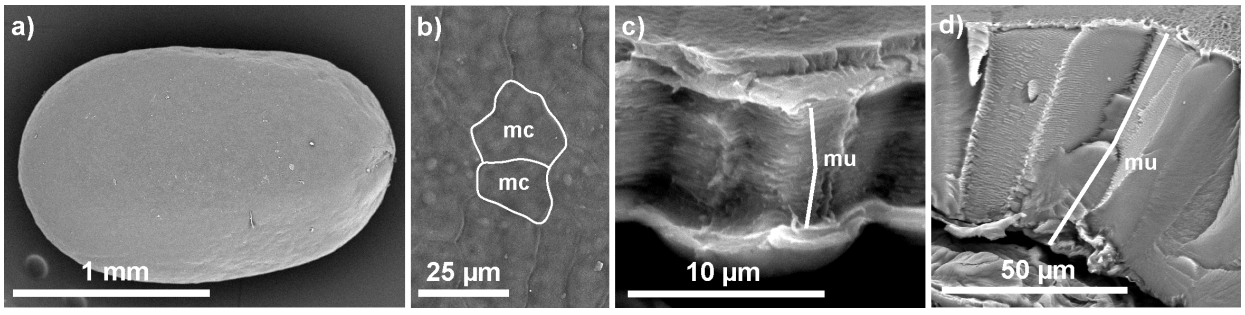

Figure 3: *Salvia hispanica* dry seed. (a) The whole seed is covered with mucilaginous cells. (b) The mucilaginous cells (mc) can have irregular shape (white outlines). (c, d) Cross fractures through the mucilaginous cells; a very thick mucilage deposit (mu) composed of many thin layers is visible in the dry stage of the mucilaginous cell wall.

CPD is a technique used for diverse biological samples (plants, animals, and microorganisms) that are very fragile and contain water. CPD allows for drying of samples without deforming them or collapsing the structure. This technique is very effective for sample imagining in TEM and SEM [7,41,67,68]. CPD minimises the negative pressure differences during drying. The comparison of CPD and air-drying techniques of plant material, for example, parenchymatic cells [69] and the mucilage envelope [7,13], clearly showed advantages of the CPD method. During air-drying, the mucilage envelope changes from its initial form (a soft hydrated gel) into a thin, compressed, crust-like layer [7]. Similarly, parenchymatic cells were completely flattened [69] after air-drying. CPD-dried mucilage envelope preserves its 3D structure and form [7,13]. Another example of the advantages of CPD are studies of TEMPO-oxidised cellulose nanofibrils (TCNFs). In these structural studies, freeze-drying and critical point drying techniques were applied to preserve the open fibril structure of gel-like TCNFs. The result of gently drying the hydrated CNFs was an aerogel-like material with large surface area [41]. The freeze-drying process causes the formation of ice crystals, which destroy the delicate ultrastructure of the studied material [70].

As mentioned before, the mucilage envelope represents a special type of secondary cell wall, where non-cellulosic polysaccharides dominate (pectins and hemicelluloses) and cellulose is a minor, but nevertheless important, skeletal component [2,6,7,71]. The cellulose fibrils appear as an important structural element in the seed mucilage envelope for plants from diverse genera, such as *Artemisia annua*, *A. ballerieri*, *A. campestris* (Asteraceae), *Arabidopsis thaliana*, *Capsella bursa-pastoris*, *Lepidium sativum* (Brassicaceae), *Ocimum basilicum*, *Salvia hispanica* (chia), *Salvia sclarea* (Lamiaceae), or even in such an exotic genus like *Commicarpus* (Nyctaginaceae) [4-7,72,73]. The observation of the mucilage envelope is easily possible at the macroscale with the naked eye. The hydration of the seed causes the formation of a transparent gel-like envelope surrounding the diaspore [7,73,74] (Figure 1), which is easily observable. Air-drying of hydrated mucilage causes water evaporation and its compression to a transparent, thin layer tightly adhering to substrates (stone or glass). In this form of mucilage, long, tangled or parallel organised cellulose fibrils can be recognised under the high magnification of a SEM [7,13,73]. The observation of the 3D nanoscale organisation of the mucilage envelope requires critical point drying, as discussed above (Figure 4). From CPD+SEM visualisations, the probable localisation of mucilage polysaccharides has been deduced based on their shape, thickness, and position in the complex netlike structure [7]. The revealed architecture of the mucilage envelope [7] resembles the known structure of cell walls [57,74-78]. The long, unbranched fibrils (main chains) are cellulose fibrils building the main skeleton of examined mucilage. Their average size ranges from 20.8 nm in *Arabidopsis thaliana*, over 32.7 nm in *Salvia hispanica*, to 57.3 nm in *Ocimum basilicum* [7]. TEM and SEM [45,65,78,79] showed the size of cellulose microfibrils in a range of 3–50 nm, depending on cell wall type. This wide range of size can be also a result of bundles formed by cellulose fibrils (Figure 4h) [80]. The results of our research [7,13] confirmed the diversity of cellulose fibril sizes in the mucilage envelope of different taxa and also the presence of cellulose bundles (Figure 4).

Another interesting and effective method to visualise mucilage hydrogels in three dimensions at the nanoscale is freezing-drying (lyophilisation). Samateh et al. [8] used the mucilaginous seeds of *Ocimum basilicum* and *Salvia hispanica* to study the 3D organisation of mucilage (called there *molecular gel*). The lyophilisation allowed for carefully removing the water from the mucilage while preserving the polysaccharide fibrils in the extended state. SEM imagining of *S. hispanica* mucilage revealed the network of fibrils extending from the seed surface into all directions. The diameters of these fibrils were estimated to be around 50 nm (in SEM) and around 20 nm (in TEM) [8]. Our results for the related species *Salvia sclarea* showed a mean values of 32.7 nm (range 24.7–44.2 nm) for the main chains (cellulose fibrils) and 18.4 nm (range 14.1–23.8 nm) for the cross-links (pectin and hemicellulose chains) [7]. One difference can be seen when comparing both methods. In our studies, we observed small granules covering the fibrils. We supposed that they are proteins that are natural elements of the cell wall and the mucilage envelope [7,13,16]. Samateh et al. [8] did not detect them. This can be a result of the prior treatment, such as dehydration in alcohol series before CPD (possibly an effect of the protein denaturation), or due to differences in chemical composition between the taxa studied.

Critical point drying in studies of natural samples containing cellulose fibrils [40,41,81], other polysaccharides (cell wall, mucilage, and envelope) [7,13], and synthetic hydrogels [82] maintained the 3D network of the studied materials. During drying, the hydrogen bonds undergo reformation, which may cause the mechanical collapse of the spatial structure.

Frictional properties

One of the important features of hydrogels [83-87] is their ability to decrease friction in contact. The frictional properties of hydrogels depend on their chemical composition [26,27,88,89], on monomer and cross-linking concentrations, and on the type of substrate surface [88].

Hydrogels with their low friction are crucial in biomedical applications or for drug delivery [38,83,86,88]. The diaspore

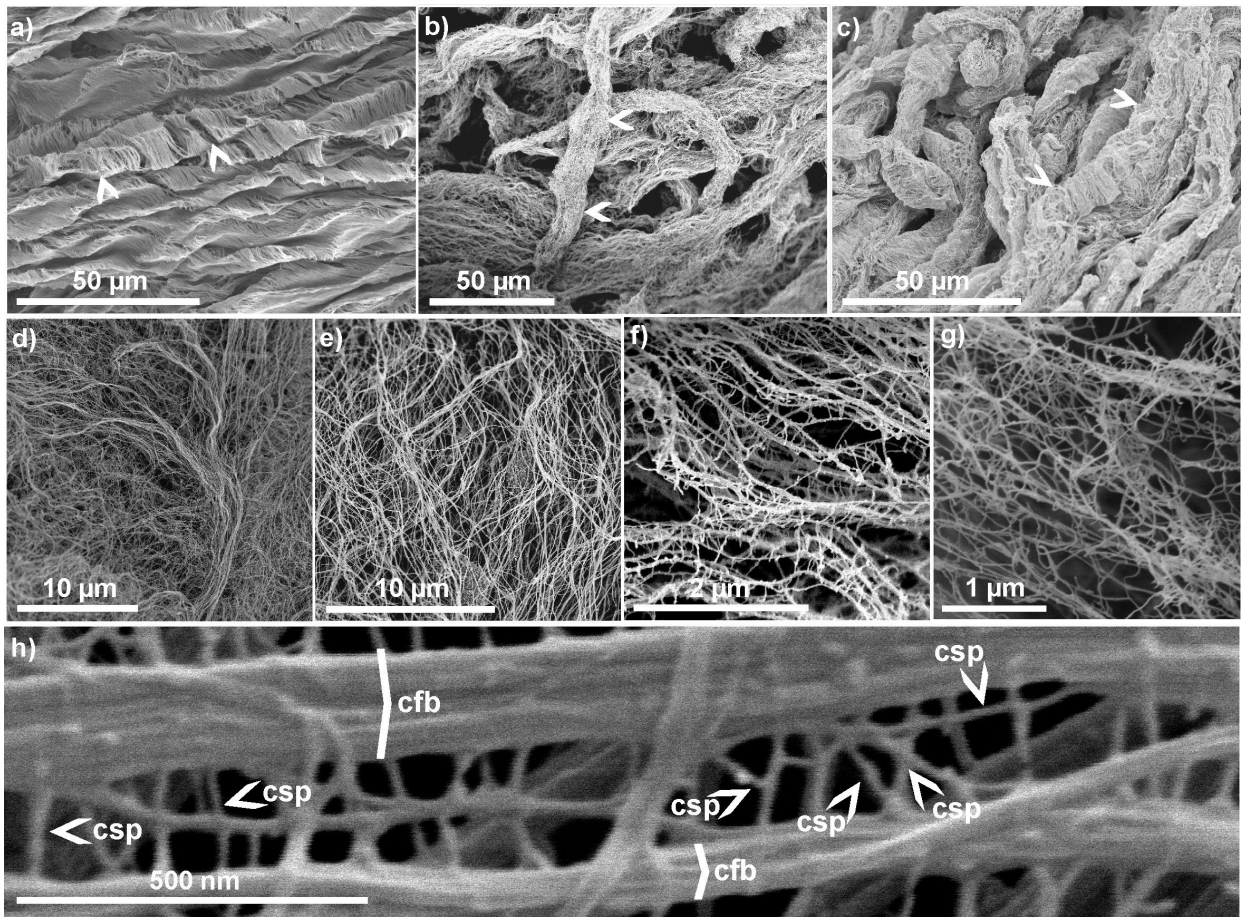

Figure 4: Mucilage envelope after hydration and critical point drying, visualised in SEM. (a) *Ocimum basilicum*. (b) *Salvia sclarea*. (c) *Commicarpus helenae*. (d) *Artemisia annua*. (e) *Ocimum basilicum*. (f) *Salvia sclarea*. (g) *Plantago psyllium*. (h) *Ocimum basilicum*. (a–c) Mucilaginous cell walls after hydration and subsequent mucilage expansion can present a tubular form. (d–g) After complete expansion of the envelope, the mucilaginous polysaccharides (pectins, hemicelluloses, and cellulose fibrils) form a netlike 3D structure. (h) High-magnification image showing cellulose fibril bundles (cfb), which form the main (unbranched) skeleton, while pectins and hemicelluloses (csp – cross-linking polysaccharides) are the cross-linkers. This structure is typical of diverse taxa from different plant groups and represents a characteristic 3D netlike architecture of a hydrogel.

mucilage is regarded as a natural hydrogel [38] because of its capacity to absorb water and to form specific netlike spatial architecture of interlaced polysaccharides (see above). The most important polysaccharides of the mucilage with hydrophilic characters are pectins and hemicelluloses. The former are composed of negatively charged galacturonic acid residues responsible for the high hydration ability of pectins [90] and are the main component of mucilage in diverse taxa of such genera as *Artemisia*, *Arabidopsis, Lepidium,* and *Linum* (Figure 5a–c) [5,6,90]. Among hemicelluloses, heteroxylans are extremely hydrophilic components, which dominate the seed mucilage in *Plantago* taxa [2,91]. Another important component of the mucilage is cellulose (Figure 5a,d–f). Its ability to bind water is not as great as that of pectins, but it plays an important structural role and can interact with other polysaccharides in mucilage, forming the 3D network [7]. The ability of a hydrogel or mucilage to absorb water is due to the presence of hydrophilic groups, such as carboxyl or hydroxyl groups. At the same time, hydrogels are insoluble in water because of their cross-linked network structure [38,92]. Two main physical properties of mucilage, friction and adhesion, are directly connected with the amount of water present in the hydrogel. Depending on the hydration degree of mucilage, it can behave as super lubricant [93,94] or super glue [29].

Friction of the hydrated mucilage envelope

Many plant hydrogels possess very good lubricating properties, sometimes better than those of artificially produced substances [94]. Some of them reveal even super low friction, that is, frictional coefficients (μ) below 0.01 [95]. Exemplary values are $\mu < 0.03$ in the seed mucilage of quince fruits [96], $\mu = 0.003$ in polysaccharides extracted from red microalgae [97], and $\mu = 0.005$ in mucilage of the water plant *Brassenia schreberi* [94]. *Ocimum basilicum* seed mucilage also

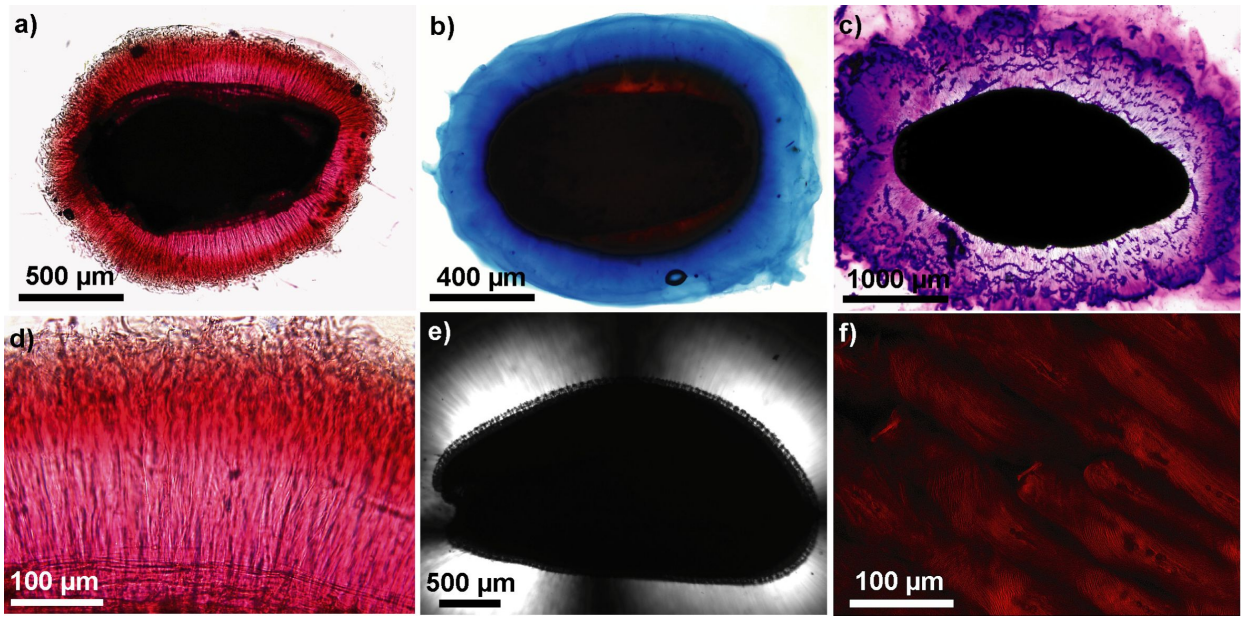

Figure 5: Staining of basic mucilage components. (a) *Artemisia annua* – pectins stained with ruthenium red. Delicate cellulose fibrils are visible stretching radially from the seed surface. (b) *Capsella bursa-pastoris* – pectins stained with alcian blue. (c) *Plantago ovata* mucilage is rich in hemicelluloses but comprises also pectins – staining with crystal violet. (d) *Artemisia annua* – magnification of the mucilage envelope. Delicate cellulose fibrils, stretching from the seed surface, are imbedded in the mass of pectins. (e) *Lepidium sativum* – polarisation microscopy image of cellulose fibrils demonstrating the presence of crystalline cellulose shining white. (f) *Ocimum basilicum* – fluorescence microscopy image of the mucilage stained with direct red. Cellulose fibrils are stained red (compare with Figure 5a).

exhibits super lubricity with a friction coefficient of 0.003 [94,98].

Experimental tests with mucilaginous diaspores after seed hydration demonstrate how the frictional properties of these diaspores change before and after contact with water and subsequent mucilage formation. The friction coefficient of dry flax diaspores was reported to be in the range of 0.499–1.073 measured on diverse substrates [99]. In our experiments, we obtained values between 0.25 and 0.31 on a glass surface [26]. The situation changed visibly after hydration. The mucilage envelope is very slippery, and the lowest friction coefficient occurs in the fully hydrated state, just at the end of the mucilage envelope formation. The measured friction coefficient values ranged from 0.039 to 0.055 (*Linum usitatissimum* (flax) seed mucilage) [26]. Flax seeds produce pectic mucilage, which is rich in rhamnogalacturonan I (pectin) and arabinoxylan (hemicellulose) [100,101]. The mixture of these polysaccharides gives the flax mucilage viscous properties [101]. Another example is the cellulosic mucilage of *Plantago lanceolata*. Plantain cellulose mucilage contains pectins, hemicellulose, and cellulose fibrils [27,102]. However, the content of cellulose in this mucilage is relatively low [27]. The cellulose fibrils here play an important role in helping to attach the mucilage to the seed surface and in preventing it against the loss from the seed [7,27]. The friction coefficient of *P. lanceolata* dry seeds ranged from 0.4 to 0.5 on a glass surface; for hydrated seeds with freshly formed mucilage, it ranged from 0.05 to 0.08 [27].

Another example of ultralow friction coefficient on glass was measured for *Ocimum basilicum* mucilage with a mean value of 0.003 [94]. The mucilage composition of *O. basilicum* differs clearly from those of *L. usitatissimum* and *P. ovata*. In *O. basilicum,* it is dominated by two hemiceluloses, glucomannan (43%) and xylan (24.29%) [94,103], but also contains a few percent of glucan [94,103] and arabinogalactan [94]. The mucilage of basil seeds also contains pectins, cellulose fibrils, and starch grains [7]. The cellulose fibrils here constitute a scaffold for other polysaccharides [7]. Friction measurements were also carried out with dry basil seeds, as well as with hydrated and dried (vacuum freeze-drying) seeds. The friction coefficient of dry seeds was ten times larger (0.02) than that of hydrated seeds with mucilage (0.002). The ultralow friction coefficient of basil mucilage was explained by the specific mucilage composition, that is, the presence of abundant OH groups in the polysaccharide molecules, a 3D network microstructure forming cross-linking sheets, and the presence of water [94]. The authors observed that a thin layer of basil mucilage was adsorbed at the glass surface because of the abundant OH groups. This layer prevented the mucilage from the direct contact with the glass, which finally resulted in ultralow friction [94]. Water, which forms hydration layers, one

adsorbed at the mucilage surface and the other one at the glass surface, plays important role in ultralow friction [94]. During sliding, the hydration layers act as lubricant reducing friction [88,94].

We suppose that an important factor regarding ultralow friction is the presence of cellulose fibrils as the structural element reinforcing the mucilage. During the friction measurements on flax and plantain seeds, we observed that the pectic flax mucilage adhered to the glass plate and was almost lost. This probably happened because of the lack of cellulose fibrils in flax as it rarely occurred in cellulosic plantain mucilage [26,27]. Cellulose fibrils constitute a kind of scaffold for other components of mucilage; because of the interactions among all polysaccharides in the envelope they can remain on the seed surface [7]. We observed the lowest friction of mucilage just after hydration. In time series of measurements, the friction increased. The water loss from the mucilage caused an increase of its stiffness and adhesive properties [26]. The decreasing hydration level and the increasing viscosity of flax mucilage play an important role in the friction increase. The viscoelastic properties of mucilage in diverse flax lines were studied and showed that the proportion between xylan (hemicellulose) and uronic acid residues (pectin) can influence the viscosity of mucilage. A higher proportion of xylan leads to an increase of mucilage viscosity [104]. This feature is presumably responsible for the stronger adherence of the mucilage to the seed surface [101] and for higher friction [26]. The friction coefficient of *Linum usitatissimum* (0.039) [26] was slightly higher than that of *Ocimum basilicum* (0.003) [94], and both values can be considered as ultralow friction.

Zhang et al. [94] assumed that with an increasing shear rate the viscosity decreases, and the polysaccharide organisation in the mucilage becomes more ordered. This presumably causes easy sliding of *Ocimum basilicum* mucilage. It can be summarised that different factors influence the frictional properties of mucilage, namely, chemical composition, viscosity, network structure, and water amount.

One of the important roles of the mucilage envelope is the protection of the diaspore against damage by digestive organs of animals [28]. It can be expected that mucilaginous seeds with ultralow friction better fulfil their biological role than mucilaginous seeds with just low friction, which was demonstrated in our experiment with pigeons (see below).

Friction after chemical and thermal treatments

The antimicrobial activity of seed mucilage was previously described for *Linum usitatissimum* [105,106], *Salvia hispanica* [106,107], and *Lallemantia royleana* [108]. However, the mucilage extracted from diverse seeds, such as *Ocimum basilicum*, *Cydonia oblonga*, *Lepidium sativum* [109], and the abovementioned flax and chia, are also popular substrates for the production of biofilms or the encapsulation of medical substances. A very important advantage of diaspore mucilages are their antimicrobial properties [105,106,110,111].

Phenolic compounds are secondary plant metabolites, which demonstrate a wide range of structures, from simple molecules to polymeric compounds. They can be produced in diverse plant organs, such as seeds, fruits, flowers, and leaves, and are involved in the defence of the plant against herbivore animals, fungi, and viruses [112,113]. Phenolic compounds are very abundant substances in seeds, playing an important role in their development and maturation. They are accumulated in most cases in the seed coat [113] and can be released after hydration and accumulated in the mucilage envelope as in case of *Ocimum basilicum* [98] or *Lallemantia royleana* (balangu shirazi) seeds [108].

Phenolic molecules in the seed mucilage of *Ocimum basilicum* were detected in a very small amount, which raises questions about their role. The experiment answering this question can be an oxidation process of phenols, which happens at increased temperature (40 °C) [98]. One can suppose that the increase of the temperature within the mucilage envelope in the natural environment can happen spontaneously. The mucilage envelope can act as a lens focusing the light and locally increasing temperature [4]. The temperature increase possibly activates enzymes involved in the germination processes [5]. This could happen to *Ocimum basilicum* seeds (as well as to seeds of other plant taxa) under natural conditions. The direct consequence of the temperature increase is the oxidation of phenolic molecules and the accumulation at the air–water interface of the mucilage envelope. This process also has an influence on the frictional properties of basil seed mucilage. As our experiments showed, the oxidised mucilage demonstrated a higher friction coefficient than the fresh mucilage envelope. This result can be explained by stronger chemical interactions between the phenolic layer formed at the mucilage surface and the acrylic glass used for the friction measurements. In this way, the protective function of phenolic molecules, which are concentrated on the mucilage surface, can be maximised [98]. Thus, we assume that increased concentration of phenolic compounds at the mucilage interface has an important antimicrobial function for the seed. The mucilage envelope supports the germination through speeding it up, but also protects the seeds against pathogens probably also by the presence of these phenolic substances [72,98].

As we have mentioned above, natural polysaccharide-based hydrogels obtained from seed mucilage of flax, plantain, chia, basil, and quince found broad application in various fields, such as food, agriculture, and medicine [20,114,115]. Diverse other substances and systems with antimicrobial activity (antibiotics, essential oils, phenolics, and metal nanoparticles) can be incorporated into the mucilage hydrogels, which after some additional modifications can be used for the production of biofilms, encapsulation, or lubricants with medical application [106,110,111,116,117]. Our findings may also help to design pathogen-resistant lubricating biomaterials with low friction, which can be achieved in rather simply way by adding phenolic substances to the medical hydrogels [98].

Adhesive properties

Seed dispersal is a crucial factor for many plants, allowing for the genetic continuity as well as for occupying new habitats. Through diverse mechanisms developed by the plants, seeds can be dispersed at a local scale (in the vicinity of mother plant) or transported over longer distances between islands or continents [28,118]. Plants developed diverse morphological mechanisms for the diaspore transport. One of the ways of promoting long-distance dispersal is the proper interaction between the plant diaspores and animals [118-120]. Epizoochory is the way of diaspore transport on animals due to the presence of interlocking structures or sticky viscous substances, which allow for attachment to the animal body [118,119,121].

The mucilage envelope is one of the factors enabling short- and long-distance dispersal of diaspores. Many authors working on mucilaginous seeds supposed that the mucilage envelope can support epizoochoric ways of seed dispersal [29,31-33]. However, direct experimental support of the mucilage role in epizoochory (e.g., epiornitochory) is only scarcely documented in the literature like, for example, the dispersion of fruits of *Adenostemma brasilianum* [121] or the human-mediated dispersal of *Plantago asiatica* seeds [122]. The mucilage envelope reveals its adhesive properties in a hydrated state. However, just after the seed hydration and mucilage envelope formation, the adhesion force is very low. With the loss of water, adhesion increases and determines the attachment potential of the diaspore to animal bodies [27,28]. Another factor regarding mucilage adhesion is the mucilage type determined by its chemical composition. Depending on the mucilage chemical composition, the measured adhesion strength was higher for flax mucilage (dominated by pectins) (91 mN) than for plantain (32 mN) (pectins and some cellulose). We suppose that cellulose fibrils are involved rather in the mucilage stability than in the adhesion process itself [26,27,29]. However, more detailed studies including mucilages with higher content of cellulose (*Ocimum basilicum*, *Salvia hispanica*, and *Lepidium sativum*) gave us further insight into seed mucilage adhesion mechanisms (see below).

Adhesion of the hydrated mucilage

Biological functions of hydrated mucilage have been described for diverse diaspores. Adhesion under wet conditions appears just after hydration. The mucilage envelope is formed within a few minutes and causes adherence to soil particles. The mass of the diaspore is increasing because of the accumulated water and attached soil particles [123-125]. The total mass increase after the contact of mucilaginous seed to dry soil can increase from 24 times as in *Alyssum minus* [123] to 68 times as in *Lepidium perfoliatum* [123], or even up to 75 times in *Capsella bursa-pastoris* [126]. This mass increase, as well as the adherence of the mucilage to the substrate, may prevent the diaspores from being removed during flooding, water erosion, and/or surface run-off [30,127,128]. Pan et al. [36] tested the effect of erosive surface flow on seeds attached by wet mucilage to the substrate; they summarised that wet (as well as dry) mucilage allowed most species to stay anchored to the substrate. However, the adhesion strength of hydrated mucilage is much lower than that of the dried mucilage envelope [26,27,29]. Yet, the adhesive properties seem to be strong enough for keeping the seed anchored to the soil. A resistance of mucilaginous diaspores against run-off water was also observed in *Helianthemum violaceum* (pectic mucilage) and *Fumana ericifolia* (cellulose mucilage) [30]. The study revealed that this process did not depend on the amount of mucilage produced by the seeds and neither on the chemical composition of the mucilage.

The protective role of the hydrated, viscous mucilage envelope was noted in some studies concerning animal–diaspore interactions. It was observed that mucilage prevents diaspores from predation, because of its viscous character. Seeds with hydrated mucilage are very unwieldy for granivore insects (e.g., ants) collecting seeds [25,129]. Pan et al. [129] observed that workers of harvester ants *Pogonomyrmex subdentatus* were sticking temporarily with their mandibles to mucilaginous seeds or abandoned them. The authors supposed that the mucilage may glue their mouthparts together. Moreover, the sand particles, sticking to the mucilage envelope and camouflaging them, can be an additional factor preventing the seed collection by granivore insects [25,130].

Another example of such sticky traps is described regarding false chinch bugs (*Nysius raphanus*) entrapped by flax seeds covered by the mucilage envelope. These insects stuck on the mucilage when it was dried out [25]. Roberts et al. [131] observed nematodes entrapped by *Capsella bursa-pastoris* seed mucilage. However, in this case, a kind of protocarnivory was

supposed, where the dead nematodes could potentially serve as a nutrient source for developing seedlings [131].

The specific chemical composition and spatial structure of the mucilage as well as its adhesive properties, which appear after hydration, are not only important for their biological functions, but also crucial regarding technological applications [17,20]. Adhesion is essential in industrial sectors including medicine, bioengineering, cosmetics, food, and pharmacy [17,20,114,132-134]. Natural polymers present in the seed mucilage are the most attractive source among diverse hydrogels, particularly because of their high biodegradability, non-toxicity, and non-irritability. They also demonstrate attractive bioadhesive properties because of the presence of many carboxyl or hydroxyl groups of polysaccharides, which are the main component of mucilage [17,133,134]. Hydrogels can adhere to diverse inorganic and organic materials under wet conditions [133,135]. Mucilage hydrogels have also the ability to regenerate these properties after rehydration. It was observed that the dried mucilage of *Salvia hispanica* after rehydration fully preserved its adhesive potential and macroscopic structure. This property makes chia mucilage a possible additive ingredient in food production [136].

Adhesion of the hydrated mucilage dried in contact

Strong permanent adhesion of some plant parts is a well-known phenomenon. English Ivy (*Hedera helix* L.) is a climbing plant able to grow on diverse vertical substrates (trees, walls, and rocks). The plant as many other epiphytes developed attachment roots, which produce a glue-like substance allowing for strong attachment to the substrate [137-139]. This material is composed of pectic polysaccharides and arabinogalactan protein [140]. This glue-like substance is secreted also by other climbing plants (*Parthenocissus quinquefolia* and *Campsis radicans*), which develop special organs, such as tendrils, supporting them in attachment to the substrates [141]. Quantification of the adhesive properties of plant root hairs was done experimentally to give an idea about the adhesive power of the plant. Adventitious roots of *Hedera helix* reached a maximal adhesion (F_{max}) of 7.07 N, tendrils of *Parthenocissus quinquefolia* (Virginia Creeper) were on the second position with 14.03 N, and the maximal measured value belongs to the tendrils of *Campsis radicans,* namely, 25.18 N [142]. The sea grass (*Posidonia oceanica*) root hairs can also generate strong adhesion under sea water conditions [143-145].

Attachment pads or roots are special organs organised in clusters and supporting the whole plant body climbing on the substrate. In contrast, the seed mucilage envelope is produced by individual diaspores and ensures the diaspore dispersal success or attachment to the ground. Adhesion of hydrated diaspore mucilage reaches values of micronewtons and, as long as water is present in the mucilage, the diaspore can be removed from surfaces (animal fur or feathers). However, even in the fully hydrated state, the mucilage is sticky to ensure the first contact to the surface. Losing the water from mucilage causes stronger adhesion [26,27]; finally, dry mucilage can be strongly cemented to the substrate (glass, soil, or animals) [29]. The results of our studies on adhesive force measurements of dried-in-contact seed mucilage gave us rather unexpected results. The mucilage (of individual seed samples) demonstrated adhesive properties even better than the commercial UHU glue (UHU GmbH & Co. KG, Bühl, Germany). The maximal adhesion (F_{max}) of the mucilage ranged from 2.03 to 6.22 N [29]. We also tested adhesion of *Plantago ovata* husk (a seed coat covering the seed, built of mucilaginous cells), which reached 37.4 N; the corresponding control samples of UHU glue reached 30.4 N [29].

In our experiments, we observed that the adhesive properties of the mucilage depend on the chemical composition of mucilage, the amount of mucilage produced by the diaspore, the shape and size of the diaspore, and the fractions of polysaccharides and their chemical structure (presence or absence of branched molecules). The spatial structure of the mucilage depends on the presence of side chains attached to the main polysaccharide chain [7,13,23,101]. The mucilage of *Plantago ovata* is composed of highly branched arabinoxylan with side chains that are rich in sites with the affinity to form hydrogen bonds [146]. The diaspores of this taxon also produce an abundant mucilage envelope, which demonstrates strong adhesive properties (5.74 N) [29]. In contrast, *Plantago lanceolata* produces a small mucilaginous envelope, which contains a high amount of unsubstituted xylan backbone making this mucilage less susceptible to bonding with substrates [91] and relatively lowly adhesive (2.03 N) [29].

Cellulose fibrils are present in the mucilage envelope of many plant taxa (e.g., *Ocimum* sp. or *Salvia* sp. *Lepidium* sp.). The highest adhesion of cellulosic mucilage was measured in *Ocimum basilicum* (6.22 N). Basil mucilage comprises thick cellulose fibrils [7]. Cellulose in the form of CNFs is very often used as an additive in the production of, for example, paper and biofilms [41,147,148] because CFNs have many unique properties, such as high mechanical strength (higher than that of steel and alloys, <2 GPa) [149]. Therefore, it was assumed that cellulose fibrils are responsible for the strong mechanical resistance of the mucilage.

Another important physical factor strongly influencing the attachment of mucilaginous seeds to the substrate is the temper-

ature. LoPresti et al. [37] stated that mucilage dried at high temperatures requires, on average, only 33% of the force required to dislodge seeds dried in the refrigerator or at room temperature. It can be supposed that the high temperatures destroy the polysaccharide structure and other important chemical bonds responsible for the interaction between mucilage and substrate. Also, very recent studies involving computer simulations demonstrated the influence of different temperatures on hydrophobic–polar and hydrogen bond interactions within the mucilage envelope [150].

The adhesive strength is expressed as the maximum force per unit area [29,149]; hence, the contact area affects the measured adhesion force. In interspecific comparisons of over fifty species, attachment strength was strongly correlated with the mucilage volume (contact area). Seeds with larger mucilage envelope were attached stronger to the substrate presumably because of the higher contact area [36,129]. It cannot be excluded that many other factors (pH, temperature, humidity, or substrate type) can also influence the adhesive properties of the mucilage envelope.

The role of mucilage envelope in the seeds dispersal

Fruits and seeds exhibit diverse mechanisms allowing for successful dispersal. Animals contribute in the dispersal of plant diaspores, spreading them over short or long distances [120,151-154]. One of the most effective ways of seed transport by animals is endozoochory. The seeds are ingested, pass through the animal digestive system, and are finally defecated in another place [155-157]. Among diverse animals, birds are an important vector for seeds dispersal particularly on long distances. This strategy can be a strong specialisation of invasive plants, which diaspores are transported to new habitats and quickly start their colonisation [120,152,153,158]. Some factors promote seeds dispersal via endozoochory, that is, a small size and a high number of seeds produced by the plant [159], as well as the presence of mechanisms improving seeds resistance to digestion [154,160]. One of such adaptation, supporting the seeds passage through the digestive system, is the presence of the mucilage envelope. Because of the high slipperiness [26,27], the mucilage envelope should facilitate the passage of the seeds through the bird guts.

As observed in our experiments, from 18900 tested mucilaginous seeds of six plant taxa that were fed to pigeons (*Columa livia domestica*), 841 seeds recovered. From 8100 of non-mucilaginous control seeds of three taxa, only eight recovered. Many seeds were viable and able to germinate. The highest count of seeds was obtained for three *Plantago* taxa (*P. lanceolata*, *P. psyllium*, and *P. ovata*). The result of our studies revealed that the presence of the mucilage envelope supports the endozoochoric transport by birds [28]. The taxa from the genus *Plantago* are distributed on all continents. Many of them exist also as single-island endemics, and this fact is connected with the role of migratory birds as endozoochoric seed dispersers [161]. The ability of mucilage formation helps the diaspores transportation in both dispersal ways, that is, epi- and endozoochoric. *Plantago* seeds were identified in droppings of diverse birds, such as house sparrow (*Passer domesticus*), bullfinch (*Pyrrhula* sp.), greenfinch (*Chloris* sp.), grey partridge (*Perdix perdix*), and racing pigeons (*Columba livia*) [162-166]. This fact also supports the dispersal of *Plantago* seeds via endozoochory.

In our second experiment with the mucilage envelope mechanically removed from the seed surface of three *Plantago* taxa [167] only nine seeds from 8100 seeds fed to pigeons recovered, but none of them germinated. The data from both experiments demonstrate clearly the important role of the mucilage envelope in preventing damage from the digestive system of birds and, thus, in endozoochoric seed dispersal [28,167].

Seeds of non-mucilaginous plants like *Amaranthus retroflexus* and *Chenopodium album* were also found in the droppings of, for example, grey partridge (*Perdix perdix* L.). Approximately 0.3% of the ingested seeds passed the digestive system undamaged, and some of them were able to germinate [158]. In our studies, we tested 2700 *Amaranthus albus* seeds, four of which recovered, and three of them germinated [28]. Such non-mucilaginous seeds are also able to pass the pigeons' digestive system, but more likely very sporadically. However, even only a few such seeds surviving the way through the birds' digestive system can have the chance to germinate and to make the first step in the colonisation of a new habitat.

The presence of the mucilage envelope is not the only feature responsible for endozoochoric seeds dispersal. In case of frugivory (fruits dispersal by birds), the dispersed fruits possess some distinct features simplifying their dispersal, among them signalling colour, edible parts, and relatively small size (less than 20 mm) [151]. The fruits can also be equipped with mucilage-like material (hemiparasitic mistletoe *Viscum album*). In mistletoe, the mucilage (viscin) is rather abundant and very sticky, allowing for attachment to tree branches. Diverse birds, such as *Turdus viscivorus* (Mistle Trush), *Bombycilla garrulus* (Bohemian Waxwing), and *Sylvia atricapilla* (Eurasian Blackcap), are known consumers of mistletoe fruits. A number of 16 to 18 fruits can be eaten and pass the digestive system in only 15–20 min. This makes the long distance dispersal of seeds

very effective [168]. In their study on long distance seeds dispersal by birds, Viana et al. [169] observed that migratory birds transported seeds over hundreds of kilometres, thus being responsible for the seeds dispersal from the mainland to oceanic islands. Up to 1.2% of the studied birds carried seeds in the guts, and some of the seeds remained viable. If we take into consideration billions of seasonal migratory birds, their effect on seeds transportation over long distances can be rather substantial [169].

Conclusion

Taking into account that many plants all over the world are able to produce seed/fruit mucilage, we have a natural source of non-toxic, biodegradable hydrogels. The mucilage envelopes of diverse diaspores share many common features, but also demonstrate some differences in their chemical composition and physical character. All the special properties of the mucilaginous envelope (specific composition and 3D architecture, low friction at strong hydration, and high adhesion at low hydration) makes it an important material in diverse industrial applications. Taxa whose mucilage has been studied rather well are *Linum usitatissimum*, *Ocimum basilicum*, *Plantago ovata*, *Salvia hispanica*, and *Lepidium sativum*. However, the number of plant taxa with seeds/fruits able to produce the mucilage envelope and waiting for exploration is huge (mucilaginous seeds/fruits are produced in about 110 different families). Thus, we expect more exciting research on this topic in the near future.

Acknowledgements

We would like to thank to Joachim Oesert (University of Kiel) for his technical help in CPD and SEM preparations.

Funding

The studies were supported by the Short Term Scientific Mission, COST Action TD0906 (COST-STSM-ECOST-STSM-TD0906-020513-030288), by the German Academic Exchange Office (DAAD) (grant No. 323/A/10/02617), German Science Foundation (DFG) - the Short Stay Program No. GZ: GO 995/21-1, AOBJ: 611170 and funding from the European Union's Horizon 2020 research and innovation program under the Marie Skłodowska-Curie grant No 702293 – MuCellWall to A.K., and the grant GO 995/43-1 from German Science Foundation (DFG) to S.N.G. The funders did not take part in study design, data collection and analysis, decision of publishing, or any preparation of the manuscript.

ORCID® iDs

Agnieszka Kreitschitz - https://orcid.org/0000-0002-3045-843X
Stanislav N. Gorb - https://orcid.org/0000-0001-9712-7953

Data Availability Statement

Data sharing is not applicable as no new data was generated or analyzed in this study.

References

1. Coviello, T.; Matricardi, P.; Marianecci, C.; Alhaique, F. *J. Controlled Release* **2007,** *119,* 5–24. doi:10.1016/j.jconrel.2007.01.004
2. Phan, J. L.; Burton, R. A. New Insights into the Composition and Structure of Seed Mucilage. In *Annual Plant Reviews online;* Roberts, J. A., Ed.; Wiley Online Library, 2018; Vol. 1, pp 63–104. doi:10.1002/9781119312994.apr0606
3. Peppas, N. A.; Hoffman, A. S. 1.3.2E - Hydrogels. In *Biomaterials Science,* 4th ed.; Wagner, W. R.; Sakiyama-Elbert, S. E.; Zhang, G.; Yaszemski, M. J., Eds.; Biomaterials Science; Academic Press, 2020; pp 153–166. doi:10.1016/b978-0-12-816137-1.00014-3
4. Grubert, M. *Acta Biol. Venez.* **1974,** *8,* 315–551.
5. Kreitschitz, A. Biological properties of fruit and seed slime envelope – how to live, fly, and not die. In *Functional Surfaces in Biology. Little structures with big effects;* Gorb, S. N., Ed.; Springer: Dordrecht, Netherlands, 2009; Vol. 1, pp 11–30. doi:10.1007/978-1-4020-6697-9_2
6. Western, T. L. *Seed Sci. Res.* **2012,** *22,* 1–25. doi:10.1017/s0960258511000249
7. Kreitschitz, A.; Gorb, S. N. *PLoS One* **2018,** *13,* e0200522. doi:10.1371/journal.pone.0200522
8. Samateh, M.; Pottackal, N.; Manafirasi, S.; Vidyasagar, A.; Maldarelli, C.; John, G. *Sci. Rep.* **2018,** *8,* 7315. doi:10.1038/s41598-018-25691-3
9. Sacco, P.; Lipari, S.; Cok, M.; Colella, M.; Marsich, E.; Lopez, F.; Donati, I. *Gels* **2021,** *7,* 47. doi:10.3390/gels7020047
10. Tsai, A. Y.-L.; McGee, R.; Dean, G. H.; Haughn, G. W.; Sawa, S. *Plant Cell Physiol.* **2021,** *62,* 1847–1857. doi:10.1093/pcp/pcab099
11. Cakmak, H.; Ilyasoglu-Buyukkestelli, H.; Sogut, E.; Ozyurt, V. H.; Gumus-Bonacina, C. E.; Simsek, S. *Food Hydrocolloids Health* **2023,** *3,* 100131. doi:10.1016/j.fhfh.2023.100131
12. Hennink, W. E.; van Nostrum, C. F. *Adv. Drug Delivery Rev.* **2002,** *54,* 13–36. doi:10.1016/s0169-409x(01)00240-x
13. Kreitschitz, A.; Gorb, S. N. *Flora (Jena)* **2017,** *229,* 9–22. doi:10.1016/j.flora.2017.02.010
14. Haughn, G. W.; Western, T. L. *Front. Plant Sci.* **2012,** *3,* 64. doi:10.3389/fpls.2012.00064
15. Soukoulis, C.; Gaiani, C.; Hoffmann, L. *Curr. Opin. Food Sci.* **2018,** *22,* 28–42. doi:10.1016/j.cofs.2018.01.004
16. Tsai, A. Y.-L.; Kunieda, T.; Rogalski, J.; Foster, L. J.; Ellis, B. E.; Haughn, G. W. *Plant Physiol.* **2017,** *173,* 1059–1074. doi:10.1104/pp.16.01600
17. Tosif, M. M.; Najda, A.; Bains, A.; Kaushik, R.; Dhull, S. B.; Chawla, P.; Walasek-Janusz, M. *Polymers (Basel, Switz.)* **2021,** *13,* 1066. doi:10.3390/polym13071066
18. Lutz, T. M.; Kimna, C.; Casini, A.; Lieleg, O. *Mater. Today Bio* **2022,** *13,* 100203. doi:10.1016/j.mtbio.2022.100203
19. López-Díaz, A. S.; Méndez-Lagunas, L. L. *Food Rev. Int.* **2023,** *39,* 6677–6706. doi:10.1080/87559129.2022.2123501
20. Goksen, G.; Demir, D.; Dhama, K.; Kumar, M.; Shao, P.; Xie, F.; Echegaray, N.; Lorenzo, J. M. *Int. J. Biol. Macromol.* **2023,** *230,* 123146. doi:10.1016/j.ijbiomac.2023.123146
21. Kučka, M.; Ražná, K.; Harenčár, Ľ.; Kolarovičová, T. *Nutraceuticals* **2022,** *2,* 253–269. doi:10.3390/nutraceuticals2040019

22. Bahú, J. O.; de Andrade, L. R. M.; de Melo Barbosa, R.; Crivellin, S.; da Silva, A. P.; Souza, S. D. A.; Cárdenas Concha, V. O.; Severino, P.; Souto, E. B. *Bioengineering* **2022,** *9,* 376. doi:10.3390/bioengineering9080376
23. Macquet, A.; Ralet, M.-C.; Kronenberger, J.; Marion-Poll, A.; North, H. M. *Plant Cell Physiol.* **2007,** *48,* 984–999. doi:10.1093/pcp/pcm068
24. Yang, X.; Baskin, J. M.; Baskin, C. C.; Huang, Z. *Perspect. Plant Ecol. Evol. Syst.* **2012,** *14,* 434–442. doi:10.1016/j.ppees.2012.09.002
25. LoPresti, E. F.; Pan, V.; Goidell, J.; Weber, M. G.; Karban, R. *Ecology* **2019,** *100,* e02809. doi:10.1002/ecy.2809
26. Kreitschitz, A.; Kovalev, A.; Gorb, S. N. *Acta Biomater.* **2015,** *17,* 152–159. doi:10.1016/j.actbio.2015.01.042
27. Kreitschitz, A.; Kovalev, A.; Gorb, S. N. *Beilstein J. Nanotechnol.* **2016,** *7,* 1918–1927. doi:10.3762/bjnano.7.183
28. Kreitschitz, A.; Haase, E.; Gorb, S. N. *Sci. Nat.* **2021,** *108,* 2. doi:10.1007/s00114-020-01709-7
29. Kreitschitz, A.; Kovalev, A.; Gorb, S. N. *Int. J. Mol. Sci.* **2021,** *22,* 1443. doi:10.3390/ijms22031443
30. Engelbrecht, M.; Bochet, E.; García-Fayos, P. *Biol. J. Linn. Soc.* **2014,** *111,* 241–251. doi:10.1111/bij.12198
31. Ryding, O. *Syst. Geogr. Plants* **2001,** *71,* 503–514. doi:10.2307/3668696
32. Dale, E.; de Lange, P.; Burns, B. *N. Z. J. Ecol.* **2017,** *41,* 226–233. doi:10.20417/nzjecol.41.27
33. Azevedo, I. H. F.; Braz, D. M. *Flora (Jena)* **2018,** *240,* 48–57. doi:10.1016/j.flora.2017.12.011
34. Rühs, P. A.; Bergfreund, J.; Bertsch, P.; Gstöhl, S. J.; Fischer, P. *Soft Matter* **2021,** *17,* 3022–3036. doi:10.1039/d1sm00142f
35. Hanaoka, K.; Ohno, H.; Wada, N.; Ueno, S.; Goessler, W.; Kuehnelt, D.; Schlagenhaufen, C.; Kaise, T.; Irgolic, K. J. *Chemosphere* **2001,** *44,* 743–749. doi:10.1016/s0045-6535(00)00291-5
36. Pan, V. S.; Girvin, C.; LoPresti, E. F. *Ann. Bot. (Oxford, U. K.)* **2022,** *129,* 817–830. doi:10.1093/aob/mcac045
37. LoPresti, E. F.; Stessman, M. E.; Warren, S. E.; Toll, K. *J. Ecol.* **2023,** *111,* 525–536. doi:10.1111/1365-2745.14044
38. Ogbonnaya, M.; Popoola, A. P. I. *AIMS Mater. Sci.* **2023,** *10,* 1045–1076. doi:10.3934/matersci.2023056
39. Arsovski, A. A.; Haughn, G. W.; Western, T. L. *Plant Signaling Behav.* **2010,** *5,* 796–801. doi:10.4161/psb.5.7.11773
40. Kang, K.-Y.; Hwang, K.-R.; Park, J.-Y.; Lee, J.-P.; Kim, J.-S.; Lee, J.-S. *Polymers (Basel, Switz.)* **2018,** *10,* 676. doi:10.3390/polym10060676
41. Ketola, A. E.; Leppänen, M.; Turpeinen, T.; Papponen, P.; Strand, A.; Sundberg, A.; Arstila, K.; Retulainen, E. *RSC Adv.* **2019,** *9,* 15668–15677. doi:10.1039/c9ra01447k
42. Lu, Y.; Gao, R.-N.; Xiao, S.; Yin, Y.; Liu, Q.; Li, J. Cellulose based aerogels: Processing and morpholog. In *Biobased Aerogels: Polysaccharide and Protein–based Materials;* Thomas, S.; Pothan, L. A.; Mavelil–Sam, R., Eds.; Green Chemistry; Royal Society of Chemistry: Croydon, U.K., 2018; pp 25–41. doi:10.1039/9781782629979-00025
43. Schaber, C. F.; Kreitschitz, A.; Gorb, S. N. *ACS Appl. Mater. Interfaces* **2018,** *10,* 37566–37574. doi:10.1021/acsami.8b05972
44. Beck, C. B. Structure and development of the cell wall. *An introduction to plant structure and development: Plant anatomy for the twenty–first century;* Cambridge University Press, 2005; pp 57–80. doi:10.1017/cbo9781139165365.005
45. Sarkar, P.; Bosneaga, E.; Auer, M. *J. Exp. Bot.* **2009,** *60,* 3615–3635. doi:10.1093/jxb/erp245
46. Houston, K.; Tucker, M. R.; Chowdhury, J.; Shirley, N.; Little, A. *Front. Plant Sci.* **2016,** *7,* 984. doi:10.3389/fpls.2016.00984
47. Cosgrove, D. J. *Plant Physiol.* **2022,** *189,* 1246–1277. doi:10.1093/plphys/kiac184
48. Kennedy, C. J.; Cameron, G. J.; Šturcová, A.; Apperley, D. C.; Altaner, C.; Wess, T. J.; Jarvis, M. C. *Cellulose* **2007,** *14,* 235–246. doi:10.1007/s10570-007-9116-1
49. Xu, P.; Donaldson, L. A.; Gergely, Z. R.; Staehelin, L. A. *Wood Sci. Technol.* **2007,** *41,* 101–116. doi:10.1007/s00226-006-0088-3
50. Wohlert, M.; Benselfelt, T.; Wågberg, L.; Furó, I.; Berglund, L. A.; Wohlert, J. *Cellulose* **2022,** *29,* 1–23. doi:10.1007/s10570-021-04325-4
51. Cosgrove, D. J. *Curr. Opin. Plant Biol.* **2014,** *22,* 122–131. doi:10.1016/j.pbi.2014.11.001
52. Jarvis, M. C. *Philos. Trans. R. Soc., A* **2018,** *376,* 20170045. doi:10.1098/rsta.2017.0045
53. Caffall, K. H.; Mohnen, D. *Carbohydr. Res.* **2009,** *344,* 1879–1900. doi:10.1016/j.carres.2009.05.021
54. Ding, S.-Y.; Himmel, M. E. *J. Agric. Food Chem.* **2006,** *54,* 597–606. doi:10.1021/jf051851z
55. Lyczakowski, J. J.; Bourdon, M.; Terrett, O. M.; Helariutta, Y.; Wightman, R.; Dupree, P. *Front. Plant Sci.* **2019,** *10,* 1398. doi:10.3389/fpls.2019.01398
56. Donaldson, L. *Wood Sci. Technol.* **2007,** *41,* 443–460. doi:10.1007/s00226-006-0121-6
57. McCann, M. C.; Roberts, K. *J. Exp. Bot.* **1994,** *45,* 1683–1691. doi:10.1093/jxb/45.special_issue.1683
58. Satiat-Jeunemaifre, B.; Martin, B.; Hawes, C. *Protoplasma* **1992,** *167,* 33–42. doi:10.1007/bf01353578
59. Fujino, T.; Sone, Y.; Mitsuishi, Y.; Itoh, T. *Plant Cell Physiol.* **2000,** *41,* 486–494. doi:10.1093/pcp/41.4.486
60. Fahlén, J.; Salmén, L. *Biomacromolecules* **2005,** *6,* 433–438. doi:10.1021/bm040068x
61. Zimmermann, T.; Thommen, V.; Reimann, P.; Hug, H. J. *J. Struct. Biol.* **2006,** *156,* 363–369. doi:10.1016/j.jsb.2006.06.007
62. Lacayo, C. I.; Malkin, A. J.; Holman, H.-Y. N.; Chen, L.; Ding, S.-Y.; Hwang, M. S.; Thelen, M. P. *Plant Physiol.* **2010,** *154,* 121–133. doi:10.1104/pp.110.155242
63. Marga, F.; Grandbois, M.; Cosgrove, D. J.; Baskin, T. I. *Plant J.* **2005,** *43,* 181–190. doi:10.1111/j.1365-313x.2005.02447.x
64. Ding, S.-Y.; Liu, Y.-S.; Zeng, Y.; Himmel, M. E.; Baker, J. O.; Bayer, E. A. *Science* **2012,** *338,* 1055–1060. doi:10.1126/science.1227491
65. Zhang, T.; Mahgsoudy-Louyeh, S.; Tittmann, B.; Cosgrove, D. J. *Cellulose* **2014,** *21,* 853–862. doi:10.1007/s10570-013-9996-1
66. Pfaff, S. A.; Wang, X.; Wagner, E. R.; Wilson, L. A.; Kiemle, S. N.; Cosgrove, D. J. *Cell Surf.* **2022,** *8,* 100089. doi:10.1016/j.tcsw.2022.100089
67. Smith, M. E.; Finke, E. H. *Invest. Ophthalmol.* **1972,** *11,* 127–132.
68. Hawkins, D. M.; Ellis, E. A.; Stevenson, D.; Holzenburg, A.; Reddy, S. M. *J. Mater. Sci.* **2007,** *42,* 9465–9468. doi:10.1007/s10853-007-1806-4

69. Ménard, D.; Blaschek, L.; Kriechbaum, K.; Lee, C. C.; Serk, H.; Zhu, C.; Lyubartsev, A.; Nuoendagula; Bacsik, Z.; Bergström, L.; Mathew, A.; Kajita, S.; Pesquet, E. *Plant Cell* **2022,** *34,* 4877–4896. doi:10.1093/plcell/koac284
70. Nordestgaard, B. G.; Rostgaard, J. *J. Microsc. (Oxford, U. K.)* **1985,** *137,* 189–207. doi:10.1111/j.1365-2818.1985.tb02577.x
71. Griffiths, J. S.; North, H. M. *New Phytol.* **2017,** *214,* 959–966. doi:10.1111/nph.14468
72. Kreitschitz, A. *Seed Sci. Res.* **2012,** *22,* 177–189. doi:10.1017/s0960258512000098
73. Kreitschitz, A.; Gorb, S. N. *S. Afr. J. Bot.* **2023,** *160,* 376–383. doi:10.1016/j.sajb.2023.07.030
74. Zhou, Z.; Xing, J.; Zhao, J.; Liu, L.; Gu, L.; Lan, H. *Plant Growth Regul.* **2022,** *97,* 185–201. doi:10.1007/s10725-021-00702-y
75. Carpita, N. C.; Gibeaut, D. M. *Plant J.* **1993,** *3,* 1–30. doi:10.1111/j.1365-313x.1993.tb00007.x
76. Cosgrove, D. J. *Nat. Rev. Mol. Cell Biol.* **2005,** *6,* 850–861. doi:10.1038/nrm1746
77. Cosgrove, D. J.; Jarvis, M. C. *Front. Plant Sci.* **2012,** *3,* 204. doi:10.3389/fpls.2012.00204
78. Somerville, C.; Bauer, S.; Brininstool, G.; Facette, M.; Hamann, T.; Milne, J.; Osborne, E.; Paredez, A.; Persson, S.; Raab, T.; Vorwerk, S.; Youngs, H. *Science* **2004,** *306,* 2206–2211. doi:10.1126/science.1102765
79. Carpita, N. C.; Defernez, M.; Findlay, K.; Wells, B.; Shoue, D. A.; Catchpole, G.; Wilson, R. H.; McCann, M. C. *Plant Physiol.* **2001,** *127,* 551–565. doi:10.1104/pp.010146
80. Song, B.; Zhao, S.; Shen, W.; Collings, C.; Ding, S.-Y. *Front. Plant Sci.* **2020,** *11,* 479. doi:10.3389/fpls.2020.00479
81. Peng, Y.; Gardner, D. J.; Han, Y. *Cellulose* **2012,** *19,* 91–102. doi:10.1007/s10570-011-9630-z
82. Zhang, J.; Peppas, N. A. *J. Biomater. Sci., Polym. Ed.* **2022,** *13,* 511–525. doi:10.1163/15685620260178373
83. Gong, J. P.; Osada, Y. *Prog. Polym. Sci.* **2002,** *27,* 3–38. doi:10.1016/s0079-6700(01)00037-5
84. Guilherme, M. R.; Aouada, F. A.; Fajardo, A. R.; Martins, A. F.; Paulino, A. T.; Davi, M. F. T.; Rubira, A. F.; Muniz, E. C. *Eur. Polym. J.* **2015,** *72,* 365–385. doi:10.1016/j.eurpolymj.2015.04.017
85. Ma, L.; Chai, C.; Wu, W.; Qi, P.; Liu, X.; Hao, J. *Carbohydr. Polym.* **2023,** *305,* 120544. doi:10.1016/j.carbpol.2023.120544
86. Geurds, L.; Xu, Y.; Stokes, J. R. *Biotribology* **2021,** *25,* 100162. doi:10.1016/j.biotri.2021.100162
87. Kaur, P.; Agrawal, R.; Pfeffer, F. M.; Williams, R.; Bohidar, H. B. *J. Polym. Environ.* **2023,** *31,* 3701–3718. doi:10.1007/s10924-023-02859-1
88. Shoaib, T.; Espinosa-Marzal, R. M. *Colloids Interfaces* **2020,** *4,* 54. doi:10.3390/colloids4040054
89. Gorges, H.; Kovalev, A.; Gorb, S. N. *Acta Biomater.* **2024,** *184,* 286–295. doi:10.1016/j.actbio.2024.06.045
90. Willats, W. G. T.; McCartney, L.; Knox, J. P. *Planta* **2001,** *213,* 37–44. doi:10.1007/s004250000481
91. Phan, J. L.; Tucker, M. R.; Khor, S. F.; Shirley, N.; Lahnstein, J.; Beahan, C.; Bacic, A.; Burton, R. A. *J. Exp. Bot.* **2016,** *67,* 6481–6495. doi:10.1093/jxb/erw424
92. Ahmed, E. M. *J. Adv. Res.* **2015,** *6,* 105–121. doi:10.1016/j.jare.2013.07.006
93. Li, J.; Liu, Y.; Luo, J.; Liu, P.; Zhang, C. *Langmuir* **2012,** *28,* 7797–7802. doi:10.1021/la300957v
94. Zhang, L.; Liu, Y.; Chen, Z.; Liu, P. *Colloids Surf., A* **2016,** *489,* 454–460. doi:10.1016/j.colsurfa.2015.11.019
95. Erdemir, A. Superlow friction. In *Encyclopedia of Tribology;* Wang, Q. J.; Chung, Y. W., Eds.; Springer: Boston, MA, 2013; pp 3397–3400. doi:10.1007/978-0-387-92897-5_221
96. Hakala, T. J.; Saikko, V.; Arola, S.; Ahlroos, T.; Helle, A.; Kuosmanen, P.; Holmberg, K.; Linder, M. B.; Laaksonen, P. *Tribol. Int.* **2014,** *77,* 24–31. doi:10.1016/j.triboint.2014.04.018
97. Arad, S. (M.).; Rapoport, L.; Moshkovich, A.; van Moppes, D.; Karpasas, M.; Golan, R.; Golan, Y. *Langmuir* **2006,** *22,* 7313–7317. doi:10.1021/la060600x
98. Lee, K.; Kreitschitz, A.; Lee, J.; Gorb, S. N.; Lee, H. *ACS Appl. Mater. Interfaces* **2020,** *12,* 42531–42536. doi:10.1021/acsami.0c12357
99. Coşkuner, Y.; Karababa, E. *J. Food Eng.* **2007,** *78,* 1067–1073. doi:10.1016/j.jfoodeng.2005.12.017
100. Fedeniuk, R. W.; Biliaderis, C. G. *J. Agric. Food Chem.* **1994,** *42,* 240–247. doi:10.1021/jf00038a003
101. Naran, R.; Chen, G.; Carpita, N. C. *Plant Physiol.* **2008,** *148,* 132–141. doi:10.1104/pp.108.123513
102. Cowley, J. M.; O'Donovan, L. A.; Burton, R. A. *Sci. Rep.* **2021,** *11,* 12692. doi:10.1038/s41598-021-92114-1
103. Naji-Tabasi, S.; Razavi, S. M. A.; Mohebbi, M.; Malaekeh-Nikouei, B. *Food Hydrocolloids* **2016,** *52,* 350–358. doi:10.1016/j.foodhyd.2015.07.011
104. Wannerberger, K.; Nylander, T.; Nyman, M. *Acta Agric. Scand.* **1991,** *41,* 311–319. doi:10.1080/00015129109439914
105. Czemplik, M.; Zuk, M.; Kulma, A.; Kuc, S.; Szopa, J. GM flax as a source of effective antimicrobial compounds. In *Science against Microbial Pathogens: Communicating Current Research and Technological Advances;* Méndez–Vilas, A., Ed.; Formatex Research Center: Norristown, 2011; pp 1216–1224.
106. Cacciatore, F. A.; Maders, C.; Alexandre, B.; Barreto Pinilla, C. M.; Brandelli, A.; da Silva Malheiros, P. *Food Microbiol.* **2022,** *108,* 104116. doi:10.1016/j.fm.2022.104116
107. Xing, X.; Hsieh, Y. S. Y.; Yap, K.; Ang, M. E.; Lahnstein, J.; Tucker, M. R.; Burton, R. A.; Bulone, V. *Carbohydr. Polym.* **2017,** *175,* 231–240. doi:10.1016/j.carbpol.2017.07.059
108. Behbahani, B. A.; Fooladi, A. A. I. *Int. J. Biol. Macromol.* **2018,** *114,* 882–889. doi:10.1016/j.ijbiomac.2018.03.177
109. Behrouzian, F.; Razavi, S. M. A.; Phillips, G. O. *Bioact. Carbohydr. Diet. Fibre* **2014,** *3,* 17–28. doi:10.1016/j.bcdf.2014.01.001
110. Jouki, M.; Yazdi, F. T.; Mortazavi, S. A.; Koocheki, A. *Food Hydrocolloids* **2014,** *36,* 9–19. doi:10.1016/j.foodhyd.2013.08.030
111. Luo, M.; Cao, Y.; Wang, W.; Chen, X.; Cai, J.; Wang, L.; Xiao, J. *Food Hydrocolloids* **2019,** *87,* 783–791. doi:10.1016/j.foodhyd.2018.09.010
112. Cheynier, V. *Phytochem. Rev.* **2012,** *11,* 153–177. doi:10.1007/s11101-012-9242-8
113. Corso, M.; Perreau, F.; Mouille, G.; Lepiniec, L. *Plant Sci.* **2020,** *296,* 110471. doi:10.1016/j.plantsci.2020.110471
114. Amiri, M. S.; Mohammadzadeh, V.; Yazdi, M. E. T.; Barani, M.; Rahdar, A.; Kyzas, G. Z. *Molecules* **2021,** *26,* 1770. doi:10.3390/molecules26061770
115. Qiao, Z.; Zhang, K.; Liu, H.; Roh, Y.; Kim, M. G.; Lee, H. J.; Koo, B.; Lee, E. Y.; Lee, M.; Park, C. O.; Shin, Y. *Adv. Healthcare Mater.* **2024,** *13,* 2303244. doi:10.1002/adhm.202303244

116. Kurd, F.; Fathi, M.; Shekarchizadeh, H. *Food Biosci.* **2019,** *32,* 100475. doi:10.1016/j.fbio.2019.100475
117. Tang, Y.; Xu, H.; Wang, X.; Dong, S.; Guo, L.; Zhang, S.; Yang, X.; Liu, C.; Jiang, X.; Kan, M.; Wu, S.; Zhang, J.; Xu, C. *J. Nanobiotechnol.* **2023,** *21,* 300. doi:10.1186/s12951-023-02025-8
118. Sorensen, A. E. *Annu. Rev. Ecol. Syst.* **1986,** *17,* 443–463. doi:10.1146/annurev.es.17.110186.002303
119. Fahn, A.; Werker, E. Anatomical mechanisms of seed dispersal. In *Seed biology;* Kozlovsky, T. T., Ed.; Academic Press: New York, 1972; Vol. I, pp 151–221. doi:10.1016/b978-0-12-424301-9.50010-3
120. Nathan, R.; Schurr, F. M.; Spiegel, O.; Steinitz, O.; Trakhtenbrot, A.; Tsoar, A. *Trends Ecol. Evol.* **2008,** *23,* 638–647. doi:10.1016/j.tree.2008.08.003
121. Dosil Hiriart, F. D.; Katinas, L.; Segura, L. N. *N. Z. J. Bot.* **2023,** 1–16. doi:10.1080/0028825x.2023.2278622
122. Abe, N.; Koyama, K.; Okamoto, A.; Katayama, K.; Kato, Y.; Mimura, N.; Okoshi, S.; Tanaka, Y. *Sustainability* **2022,** *14,* 6909. doi:10.3390/su14116909
123. Sun, Y.; Tan, D. Y.; Baskin, C. C.; Baskin, J. M. *Aust. J. Bot.* **2012,** *60,* 439–449. doi:10.1071/bt11314
124. Deng, W.; Iannetta, P. P. M.; Hallett, P. D.; Toorop, P. E.; Squire, G. R.; Jeng, D.-S. *Biorheology* **2013,** *50,* 57–67. doi:10.3233/bir-130627
125. Karamismailoğlu, M. C. *Biol. Diversity Conserv.* **2018,** *11,* 60–64.
126. Deng, W.; Jeng, D.-S.; Toorop, P. E.; Squire, G. R.; Iannetta, P. P. M. *Ann. Bot. (Oxford, U. K.)* **2012,** *109,* 419–427. doi:10.1093/aob/mcr296
127. Gutterman, Y. Seed Dispersal and Seed Predation of Plant Species in the Negev Desert. In *Seed Germination in Desert Plants;* Gutterman, Y., Ed.; Springer: Berlin, Heidelberg, 1993; pp 79–144. doi:10.1007/978-3-642-75698-6_3
128. Jiao, J.; Han, L.; Jia, Y.; Lei, D.; Wang, N.; Li, L. *SpringerPlus* **2013,** *2,* S9. doi:10.1186/2193-1801-2-s1-s9
129. Pan, V. S.; McMunn, M.; Karban, R.; Goidell, J.; Weber, M. G.; LoPresti, E. F. *Funct. Ecol.* **2021,** *35,* 2448–2460. doi:10.1111/1365-2435.13881
130. Fuller, P. J.; Hay, M. E. *Ecology* **1983,** *64,* 960–963. doi:10.2307/1937217
131. Roberts, H. R.; Warren, J. M.; Provan, J. *Sci. Rep.* **2018,** *8,* 10120. doi:10.1038/s41598-018-28564-x
132. Li, Z.; Yu, C.; Kumar, H.; He, X.; Lu, Q.; Bai, H.; Kim, K.; Hu, J. *Gels* **2022,** *8,* 682. doi:10.3390/gels8100682
133. Yan, Y.; Xu, S.; Liu, H.; Cui, X.; Shao, J.; Yao, P.; Huang, J.; Qiu, X.; Huang, C. *Colloids Surf., A* **2020,** *593,* 124622. doi:10.1016/j.colsurfa.2020.124622
134. Kharaziha, M.; Scheibel, T.; Salehi, S. *Prog. Polym. Sci.* **2024,** *150,* 101792. doi:10.1016/j.progpolymsci.2024.101792
135. Sadat Hosseini, M.; Kamali, B.; Nabid, M. R. *Int. J. Biol. Macromol.* **2022,** *203,* 93–104. doi:10.1016/j.ijbiomac.2022.01.031
136. Brütsch, L.; Stringer, F. J.; Kuster, S.; Windhab, E. J.; Fischer, P. *Food Funct.* **2019,** *10,* 4854–4860. doi:10.1039/c8fo00173a
137. Melzer, B.; Steinbrecher, T.; Seidel, R.; Kraft, O.; Schwaiger, R.; Speck, T. *J. R. Soc., Interface* **2010,** *7,* 1383–1389. doi:10.1098/rsif.2010.0140
138. Tay, J. Y. L.; Zotz, G.; Gorb, S. N.; Einzmann, H. J. R. *Front. For. Glob. Change* **2021,** *4,* 764357. doi:10.3389/ffgc.2021.764357
139. Tay, J. Y. L.; Kovalev, A.; Zotz, G.; Einzmann, H. J. R.; Gorb, S. N. *Am. J. Bot.* **2022,** *109,* 874–886. doi:10.1002/ajb2.16000
140. Huang, Y.; Wang, Y.; Tan, L.; Sun, L.; Petrosino, J.; Cui, M.-Z.; Hao, F.; Zhang, M. *Proc. Natl. Acad. Sci. U. S. A.* **2016,** *113,* E3193–E3202. doi:10.1073/pnas.1600406113
141. Bowling, A. J.; Vaughn, K. C. *Protoplasma* **2008,** *232,* 153–163. doi:10.1007/s00709-008-0287-x
142. Steinbrecher, T.; Danninger, E.; Harder, D.; Speck, T.; Kraft, O.; Schwaiger, R. *Acta Biomater.* **2010,** *6,* 1497–1504. doi:10.1016/j.actbio.2009.10.003
143. Zenone, A.; Alagna, A.; D'Anna, G.; Kovalev, A.; Kreitschitz, A.; Badalamenti, F.; Gorb, S. N. *Mar. Environ. Res.* **2020,** *160,* 105012. doi:10.1016/j.marenvres.2020.105012
144. Zenone, A.; Badalamenti, F.; Alagna, A.; Gorb, S. N.; Infantes, E. *Front. Mar. Sci.* **2022,** *8,* 788448. doi:10.3389/fmars.2021.788448
145. Zenone, A.; Kovalev, A.; Badalamenti, F.; Gorb, S. N. *Restor. Ecol.* **2024,** *32,* e14084. doi:10.1111/rec.14084
146. Yu, L.; Stokes, J. R.; Yakubov, G. E. *Carbohydr. Polym.* **2021,** *269,* 118318. doi:10.1016/j.carbpol.2021.118318
147. Delgado-Aguilar, M.; González Tovar, I.; Tarrés, Q.; Alcalá, M.; Pèlach, M. À.; Mutjé, P. *BioResources* **2015,** *10,* 5345–5355. doi:10.15376/biores.10.3.5345-5355
148. Hu, F.; Zeng, J.; Cheng, Z.; Wang, X.; Wang, B.; Zeng, Z.; Chen, K. *Carbohydr. Polym.* **2021,** *254,* 117474. doi:10.1016/j.carbpol.2020.117474
149. Zhang, W.; Wang, R.; Sun, Z.; Zhu, X.; Zhao, Q.; Zhang, T.; Cholewinski, A.; Yang, F. (K.); Zhao, B.; Pinnaratip, R.; Forooshani, P. K.; Lee, B. P. *Chem. Soc. Rev.* **2020,** *49,* 433–464. doi:10.1039/c9cs00285e
150. Sionkowski, P.; Kruszewska, N.; Kreitschitz, A.; Gorb, S. N.; Domino, K. *Entropy* **2024,** *26,* 380. doi:10.3390/e26050380
151. Kay, Q. O. N. Edible fruits in a cool climate: the evolution and ecology of endozoochory in the European flora. In *Fruit and seed production: Aspects of development, environmental physiology and ecology;* Marshall, C.; Grace, J., Eds.; Society for Experimental Biology Seminar Series; Cambridge University Press, 1992; pp 217–250. doi:10.1017/cbo9780511752322.012
152. Willson, M. F.; Traveset, A. The ecology of seed dispersal. In *Seeds: the ecology of regeneration in plant communities;* Fenner, M., Ed.; CABI Publishing: Wallingford U.K., 2000; pp 85–110. doi:10.1079/9780851994321.0085
153. Schaefer, H. M.; Ruxton, G. D. Animals as seed dispersers. In *Plant–animal communication;* Schaefer, H. M.; Ruxton, G. D., Eds.; Oxford, online edn; Oxford Academic, 2011; pp 48–67. doi:10.1093/acprof:osobl/9780199563609.003.0003
154. Picard, M.; Chevalier, R.; Barrier, R.; Boscardin, Y.; Baltzinger, C. *J. Veg. Sci.* **2016,** *27,* 987–998. doi:10.1111/jvs.12418
155. van der Pijl, L. *Principles of Dispersal in Higher Plants;* Springer: Berlin, Heidelberg, New York, 1982. doi:10.1007/978-3-642-87925-8
156. Jordano, P. Fruits and frugivory. In *Seeds: the ecology of regeneration in plants communities;* Fenner, M., Ed.; CABI Publishing: Wallingford U.K.; pp 125–165. doi:10.1079/9780851994321.0125
157. Trabelcy, B.; Izhaki, I.; Gerchman, Y. *J. Ecol.* **2022,** *110,* 526–539. doi:10.1111/1365-2745.13836
158. Orłowski, G.; Czarnecka, J. *Pol. J. Ecol.* **2009,** *57,* 191–196.
159. Henrik Bruun, H.; Poschlod, P. *Oikos* **2006,** *113,* 402–411. doi:10.1111/j.2006.0030-1299.14114.x
160. Pakeman, R. J.; Digneffe, G.; Small, J. L. *Funct. Ecol.* **2002,** *16,* 296–304. doi:10.1046/j.1365-2435.2002.00625.x

161. Iwanycki Ahlstrand, N.; Havskov Reghev, N.; Markussen, B.; Bruun Hansen, H. C.; Eiriksson, F. F.; Thorsteinsdóttir, M.; Rønsted, N.; Barnes, C. J. *Ecol. Evol.* **2018,** *8,* 6812–6826. doi:10.1002/ece3.4195
162. Eber, G. *Z. Wiss. Zool., Abt. A, B* **1962,** *167,* 338–394.
163. Cavers, P. B.; Bassett, I. J.; Crompton, C. W. *Can. J. Plant Sci.* **1980,** *60,* 1269–1282. doi:10.4141/cjps80-180
164. Orłowski, G.; Czarnecka, J.; Goławski, A.; Karg, J.; Panek, M. *J. Ornithol.* **2016,** *157,* 61–73. doi:10.1007/s10336-015-1248-8
165. Lovas-Kiss, Á.; Vizi, B.; Vincze, O.; Molnár V., A.; Green, A. J. *J. Ecol.* **2018,** *106,* 1714–1723. doi:10.1111/1365-2745.12913
166. Lovas-Kiss, Á.; Sánchez, M. I.; Wilkinson, D. M.; Coughlan, N. E.; Alves, J. A.; Green, A. J. *Ecography* **2019,** *42,* 956–967. doi:10.1111/ecog.04065
167. Kreitschitz, A.; Hasse, E.; Gorb, S. N. *Seed Sci. Res.* **2024,** in press.
168. Heide–Jørgensen, H. S. www.viscum.dk, 2015; https://viscum.dk/wp-content/uploads/2020/12/Viscum_2015_english_small.pdf (accessed Aug 22, 2024).
169. Viana, D. S.; Gangoso, L.; Bouten, W.; Figuerola, J. *Proc. R. Soc. B* **2016,** *283,* 20152406. doi:10.1098/rspb.2015.2406

License and Terms

BEILSTEIN JOURNAL OF NANOTECHNOLOGY

Biomimetic nanocarriers: integrating natural functions for advanced therapeutic applications

Hugo Felix Perini‡, Beatriz Sodré Matos‡, Carlo José Freire de Oliveira and Marcos Vinicius da Silva*

Perspective

Open Access

Address:
Department of Immunology, Microbiology and Parasitology. Biological and Natural Sciences Institute. Federal University of Triângulo Mineiro. Uberaba, Minas Gerais, Brazil

Email:
Marcos Vinicius da Silva* - marcos.silva@uftm.edu.br

* Corresponding author ‡ Equal contributors

Keywords:
cancer; drug delivery; human health; mimetics; nanotechnology

Beilstein J. Nanotechnol. **2024,** *15,* 1619–1626.
https://doi.org/10.3762/bjnano.15.127

Received: 22 July 2024
Accepted: 28 November 2024
Published: 16 December 2024

This article is part of the thematic issue "Micro- and nanoscale effects in biological and bioinspired materials and surfaces".

Guest Editor: T. H. Büscher

Abstract

Biomimetic nanocarriers, engineered to mimic the characteristics of native cells, offer a revolutionary approach in the treatment of various complex human diseases. This strategy enhances drug delivery by leveraging the innate properties of cellular components, thereby improving biocompatibility and targeting specificity. Biomimetic nanocarriers demonstrate significant advancements in drug delivery systems against cancer therapy, Alzheimer's disease, autoimmune diseases, and viral infections such as COVID-19. Here, we address the therapeutic applications of biomimetic nanocarriers and their promising strategy for personalized medicine.

Introduction

Human exposure to nanoparticles has naturally occurred for millennia, with a notable intensification following the industrial revolution [1]. The foundational concept of modern nanotechnology, introduced by Richard Feynman in 1959 during an American Physical Society meeting [1,2], involves the manipulation of matter at the atomic level. The term "nanometer" was initially proposed by Richard Zsigmondy in the context of measuring gold colloids. Nanotechnology is generally defined as the manipulation of matter on a nanoscale, typically ranging from 1 to 100 nm [2]. At this scale, nanoparticles can effectively interact with DNA and protein molecules [3,4].

Matter can exhibit distinct physical, chemical, and biological properties at the nanoscale compared to the macroscale, with significant differences in key characteristics. The National Nanotechnology Initiative (NNI) emphasizes that nanomaterials hold promising potential across various fields of knowledge [1,5]. Materials such as liposomes, nanoparticles, polymer–drug conjugates, inorganic noble metals, and quantum dots may improve therapeutical characteristics as demonstrated in Figure 1-1.

In the field of drug delivery, properties such as size, surface-to-volume ratio, and biocompatibility have driven the develop-

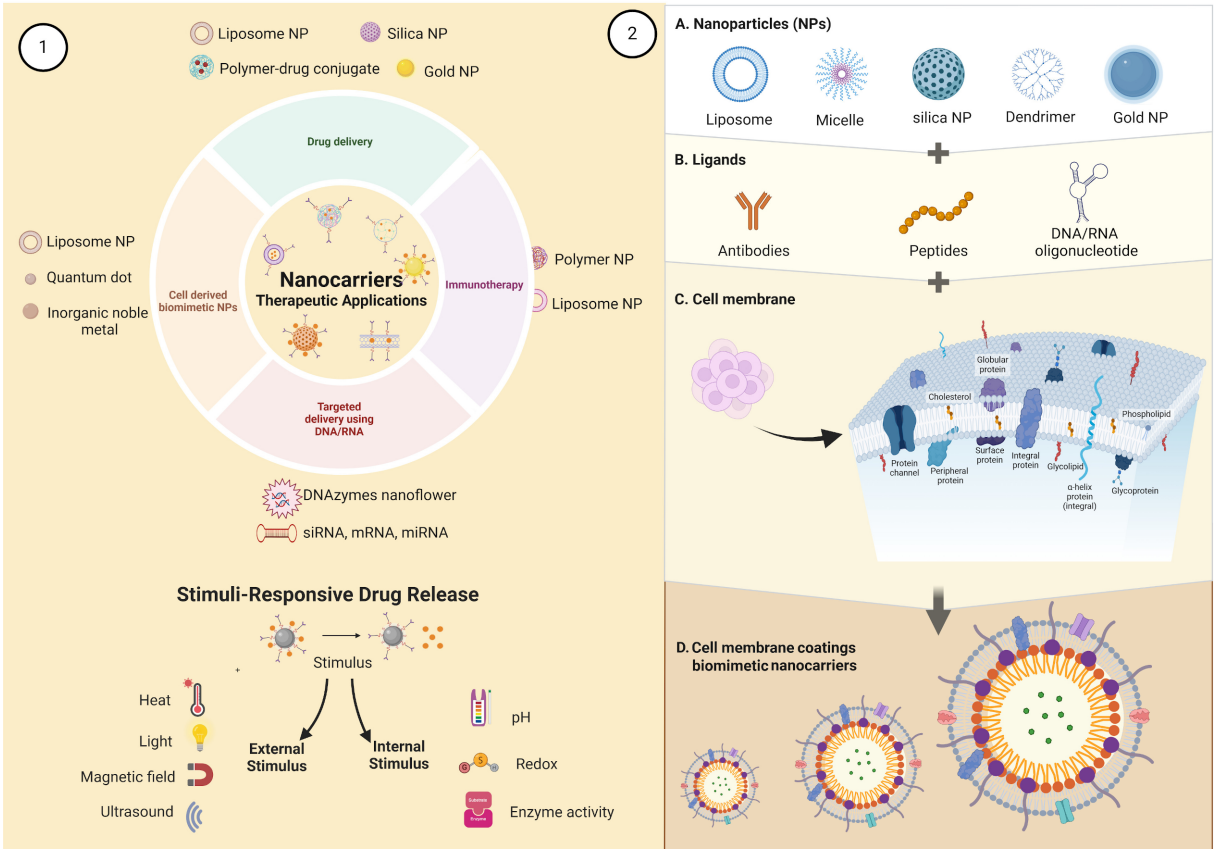

Figure 1: Schematic of biomimetic nanocarriers. Nanoparticles (NPs) used as nanocarriers in therapeutic applications such as drug delivery, immunotherapy, targeted delivery, biomimetic-derived NPs, and stimuli-responsive drug release (1). Coated NPs for improving biological activity through biomimetic biomembranes (2): Most used materials for creating nanoparticles (A), binders used for delivery and binding to target cells (B), characteristics of cell membranes (C), and biomimetic nanocarriers (D). Created in BioRender. Sodré, B. (2024) https://BioRender.com/n85g617. This content is not subject to CC BY 4.0.

ment of nanoscale-based devices [6-9]. Nanocompounds offer a strategic approach to addressing or at least improving the application of organic and inorganic compounds with activity against various diseases [10-12]. Faced with a physiological stimulus, the carrier decouples from the transported product and releases it at a specific interaction site (Figure 1-1). However, some challenges are encountered by these compounds such as: loss of stability, low efficiency in crossing biological barriers, inadequate efficacy in reaching target active molecules, and poor biodistribution [13,14]. Nanocarriers are employed to transport raw materials, which can be vesicles or solid nanoparticles [15]. Despite the significant advancements nanocarriers have brought to medical sciences, particularly in cancer treatment, several challenges remain for their widespread application. Issues such as cytotoxicity, difficulties in management, encapsulation, and in vivo release pose barriers to the application of nanocarriers [16,17].

In this context, biomimetic strategies using natural components emerge as revolutionary tools to overcome these challenges. The utilization of cellular components or parts thereof, such as macromolecules or membranes, can enhance drug delivery and therapeutic efficiency in the human body, representing a new opportunity for personalized therapies [12,18,19]. Here, we explored the implications of biomimetic nanostructured carriers and their applications in human health.

Biomimetic Nanocarriers

The principle of biomimetic nanocarriers involves coating nanoscale carriers with materials capable of replicating the characteristics or functions of native cells [19]. Nanoparticle coating involves obtaining nanoparticles (Figure 1-2A), which can be organic or inorganic in structure (Figure 2A), and conjugating them with functional ligands (Figure 1-2B) or biological structures, such as cell membranes (Figure 1-2C), which mask the nanocarriers and enhance biological activity (Figure 1-2D) [20]. This mimetic surface helps the device to mask epitopes potentially recognized by the immune system, thereby enhancing their biocompatibility. Additionally, the selectivity for targets and the circulation time of these carriers are im-

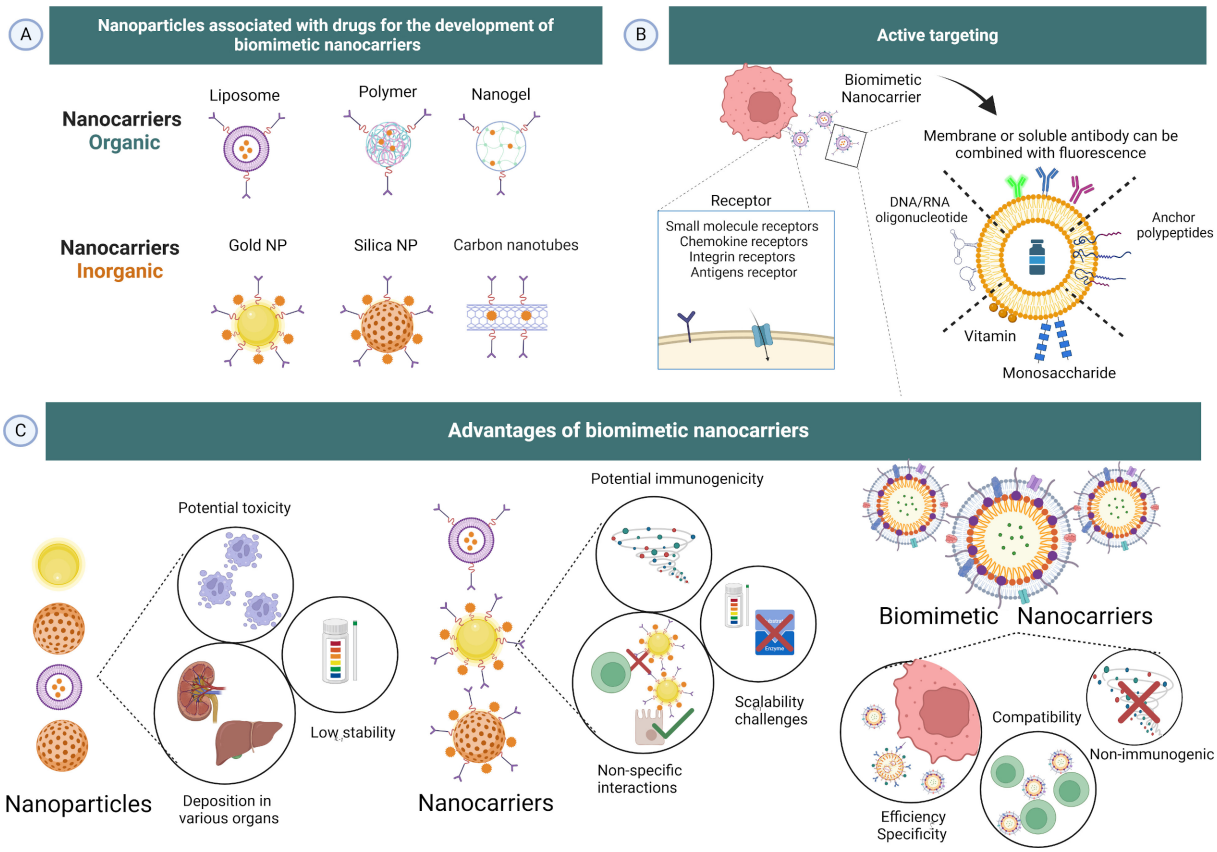

Figure 2: Action of biomimetic nanocarriers. Inorganic and organic nanoparticles with transport function (A); target with potential binding sites for drug delivery; (B) and coated nanocarriers improve functional activity and carrier efficiency (C). Created in BioRender. Sodré, B. (2024) https://BioRender.com/c20d446. This content is not subject to CC BY 4.0.

proved [19,21-25]. Various cellular components such as extracellular vesicles, leukocyte and red blood cell membranes are beneficial for developing bioinspired devices. Specific targets, including peptides, aptamers, proteins, and viral capsids, may also be utilized in the production of nature-inspired synthetics as demonstrated in Figure 2B [22-26]. Indeed, the co-incubation of nanoparticles with cellular components creates an environment conducive to the absorption of proteins by the nanoparticles, thereby facilitating the connection of these structures [21-23].

The obtention of biomimetic nanocarriers can be achieved through two fundamental approaches: the synthetic engineering of biologically based components and the utilization of existing elements such as viral and bacterial vectors [27-29]. Drug delivery can occur through passive or active targeting mechanisms. In the passive strategy, coated nanocarriers can traverse permeable vessels (as observed in tumors, for example) and exhibit tropism toward specific pathological targets based on the size, surface charge, and physicochemical properties of the nanostructure. The active strategy involves surface coating with specific ligands which interact with elevated levels of target-specific receptors. Both delivery systems aim to achieve responsive drug release directly at the therapeutic target (Figure 2B) [19,30]. Therefore, a crucial step in constructing efficient biomimetic-based nanocarriers is understanding the fundamental building blocks, size, shape, and biological properties to mimic real cells and enable their internalization [31,32].

One efficient strategy for producing biomimetic nanocarriers involves camouflage with biological membranes. The phospholipids, anchored proteins, fatty acids, and other compounds present in these membranes not only confer cell-like properties to the carriers but also prevent immune recognition, extend circulation time, and enhance target mimicry, such as that of cancer cells [33]. Coating particles with membranes has been well-described for nanoparticles, and this process entails three steps: obtaining membrane-derived vesicles from a cellular source (1); generating the nanoparticles (2); and fusing the vesicles with the particles (3) [34-37].

Obtaining membrane vesicles requires the lysis of donor cells, necessitating an adequate number of cells [37]. Cells may be sourced from specific tissues or clonally expanded in the laboratory. Once sufficient cells are available, membrane vesicle isolation begins. Target cells are subjected to freeze–thaw cycles or hypotonic environments to induce cell lysis and release intracellular components [38,39]. The resulting product is then washed in a buffer solution containing protease inhibitors to eliminate cellular debris [40]. Subsequent sonication yields vesicles of 1 to 2 μm, and size homogenization can be achieved using a micro-extruder with a nanoscale membrane [41].

Once membrane vesicles are prepared, fusion with the nanocarrier can be accomplished by several methods [20,42]. Bath sonication disrupts membranes by forming cavitation bubbles, allowing them to reassemble around the nanocarrier. Optimizing this process requires adjusting exposure time, wave frequency, and temperature control [36,43]. However, due to vesicle fragmentation and reassembly, achieving uniform size can be challenging [44]. Electroporation involves exposing vesicles in a microfluidic device to an electric field, creating membrane pores for nanocarrier incorporation. Key parameters, including pulse voltage and exposure time, can be optimized to improve efficiency. Though costly, this method is suitable for industrial applications [34,45].

Another strategy exploits electrostatic charges of nanocarriers and membrane vesicles. Opposite charges (negative for vesicles and positive for carriers) foster electrostatic attraction, leading to spontaneous synthesis [46-48]. The process depends on electrostatic and hydrophobic interactions, where modulation of the carrier charge determines the strength of interaction and conjugation efficiency with the membrane vesicle [49,50]. A common technique for merging cellular membranes and carriers is coextrusion through polyester or polycarbonate membranes with various pore sizes [51,52]. In this method, mechanical extrusion forces the nanocarriers into the membrane vesicles. This approach yields product uniformity and preserves membrane protein layers, though it involves increased material waste and costs [34,35,53]. Regardless of the membrane-masking technique, various cell types can enhance the efficiency of delivery systems, including immune cells (phagocytes, lymphocytes, and NK cells) [54], erythrocytes [55], platelets [56], cancer cells [57] and hybrid membrane constructs [58].

Regarding materials for coating nanoparticles, a variety of hydrophilic polymers are available [30]. The most prevalent technique involves the use of polyethylene glycol (PEG). It provides biological protection against proteolysis and improved biocompatibility, metabolism, and drug absorption by the mononuclear phagocytic system due to its hydrophilic barrier [59]. Although PEG-coated nanostructures exhibit promising physicochemical properties, they have shown limitations; studies point to cases of hypersensitivity in PEGylated vaccines [60,61]. Potential adverse immune reactions have also been reported [59,61].

Nanocarriers have evolved into intricate chemical structures that include specific functionalities, allowing them to preferentially target sites of interest with their payload while minimizing immune clearance (Figure 2C) [62]. In studies on the anticancer activity of polylactic glycolic acid (PLGA) nanoparticles coated with membranes, Zhang et al. (2021) tested nanoparticles loaded with gambogic acid and coated with red-blood-cell-derived membranes in colorectal cancer cells. They demonstrated a reduction in phagocytosis, increasing the circulation time of the nanoparticles due to the coating [63]. A similar study with nanoparticles coated with cytotoxic T lymphocyte membranes for the treatment of gastric cancer showed a reduction in macrophage uptake compared to other membrane types [64]. Other studies on nanoparticles loaded with the antitumor molecule bufalin and covered with platelet membranes demonstrated their ability to evade macrophage uptake and enhance binding to target cancer cells. Together, these results confirm the ability of biomimetic coated nanostructures to evade the immune system, enabling prolonged circulation time and, consequently, sustained and controlled release of potential associated drugs [21].

To overcome these limitations and enhance coating efficiency, the decoration of nanostructures with functional ligands increases their biological interactions. Decreasing nonspecific interactions and immunogenicity is one of the main solutions that biomimetics addresses (Figure 2C). This approach has demonstrated that complex nanocarrier drug delivery systems need to exhibit compatible surfaces with target cells to enhance their functional capabilities [19].

Biomimetic Nanocarriers in Human Health

The field of nanocarriers for drug delivery in cancer therapy has been extensively studied in the pursuit of biocompatible components with high specificity. In this context, the integration of synthetic compounds such as nanoparticles with natural components, including membranes from various cell types (e.g., erythrocytes, leukocytes, stem cells, tumor components) or other biocomponents (e.g., platelets), can enhance the functionality of carriers and meet the requirements for human applications [19].

The cellular membranes of cancer cells exhibit adhesion molecules crucial to cancer development and metastasis. Heterotypic or homotypic adhesive interactions through selectins, E-cadherins, Thomsen–Friedenreich (TF) antigens, the immunoglobulin superfamily (Ig-SF), and the interaction of SIRP-α with CD47 inhibit the phagocytosis of these cells, thus preventing their capture by dendritic cells [62,65,66]. Nanocarriers associated with cancer treatment offer numerous advantages, including immune evasion, targeting behavior, specific site accumulation, targeted delivery of drugs or genes, and reduced side effects. Studies involving inorganic nanocarriers with cell membrane coatings (CMC-NPs) have highlighted the importance of the homotypic behavior of CMC-NPs in delivering active therapeutic agents to specific sites, promoting immune evasion of CD47 cells by blocking binding with SIRP-α, preventing its phosphorylation, and thereby restoring the phagocytosis of cancer cells by macrophages. Additional studies have demonstrated that coated nanocarriers, such as PLGA NPs and silica NPs, enhance interactions with dendritic cells, leading to antitumor responses [25,26].

In a similar study with CMC-NPs composed of C-phycocyanin (C-PC) and a CD59-specific binding peptide (CD59sp), the antitumor activity of the C-PC/CMC-CD59sp nanoparticle was demonstrated by inhibiting proliferation through negative regulation of cyclin D1, halting the G0/G1 cell cycle in HeLa and SiHa cervical cancer cells [67,68]. Biomimetic-specific targets provide opportunities for personalized cancer therapies [10-12].

Coated nanocarriers have also been employed in treating other diseases, such as Alzheimer's disease. Current medications for Alzheimer's face the challenge of the blood–brain barrier (BBB), which includes the blood–brain, cerebrospinal fluid–brain, and blood–cerebrospinal fluid barriers. These barriers exhibit high selectivity in drug delivery due to their protective mechanism against harmful endogenous and exogenous substances through transcellular pathways. The BBB selectively permits molecules smaller than 400 Da with specific shapes, ionization states, and lipophilicity, thereby excluding macromolecular drugs and those with nonpermissive characteristics at the barrier [69].

Polymeric nanoparticles, as well as those based on lipids and inorganic materials, are extensively studied for Alzheimer's disease treatment due to their tissue selectivity, potential circulation time, encapsulation capacity, and, importantly, their ability to enhance BBB penetration. Studies have shown that polymeric biomimetic nanoparticles carrying proteins can penetrate the brain parenchyma and release active agents, demonstrated by the increased accumulation of 3D6-Fab antibody fragments in the brains of mouse models, and reducing Aβ1-42 aggregation, which is linked to dementia and neuronal loss [70].

Focusing on BBB compatibility, lipid-based nanoparticles demonstrate high potential in facilitating drug delivery. Macrophage membrane-coated liposomes co-modified with the RVG29 peptide and triphenylphosphine cation have shown improved targeting of brain neuronal mitochondria, as evidenced by fluorescence intensities identified in brain homogenates, and reduced Aβ1 deposition, demonstrating the ability of the nanocomposite to cross the BBB [71]. Inorganic nanoparticles exhibit unique optical, magnetic, and chemical properties and stability. Gold nanoparticles (AuNPs) with polyoxometalate and the peptides POMD and LPFFD (AuNPs@POMD-pep) have shown inhibition of Aβ1 aggregation and Aβ-induced cytotoxicity. However, the inherent toxicity of this formulation, challenges in particle digestion, and the potential for triggering immune reactions remain limiting factors [72,73].

Biomimetic nanocarriers coated with membranes from various cell types have also been applied in treating autoimmune diseases, such as rheumatoid arthritis, to optimize and enhance drug accumulation and delivery to specific sites. Studies with platelet membrane-coated nanoparticles loaded with the immunosuppressant FK506 have demonstrated increased delivery to inflammation sites and reduced symptoms such as redness and inflammation in the hind limbs of mice [27,74].

In the treatment of COVID-19, biomimetic nanocarriers have also been used to optimize anti-inflammatory and antiviral treatments. Tan et al. (2021) employed lopinavir (LPV), an antiviral drug, in polymeric nanoparticles coated with macrophage membranes (PLGA-LPV@M). This biomimetic nanocarrier demonstrated the ability to inherit the antigenic profile of macrophages, enabling the absorption of pro-inflammatory substances, increasing medication accumulation at the infection site, and reducing the adverse effects of the free medication [75]. Additionally, in tests with mice treated with PLGA-LPV@M, a 60% of improvement survival was observed compared to the control group (saline treated). Untreated animals rapidly lost weight and none survived for more than five days. This data demonstrates the effective therapeutic effect of biomimetic structures [75].

In addition to direct applications, interactions with the immune system targets also demonstrated the efficiency of biomimetic nanocarrier applications. To address the characteristic cytokine storm (as observed in COVID-19 disease), studies have developed nanocarriers containing squalene, adenosine, and vitamin E (SQAD/VitE) [76]. The anti-inflammatory properties of adenosine and the ability of squalene to prolong blood circu-

lation time provide improved bioavailability and drug delivery. Additionally, the capacity of these nanocarriers to react with reactive oxygen species at inflammation sites offers an anti-inflammatory response, reducing tissue damage [76,77].

Within this scope, manganese dioxide nanocarriers have been studied to address a challenge in chemodynamical therapy (CDT): the high presence of reducing species (GSH) inhibit the therapeutic effects of CDT in tumors [78]. By releasing metal cations in the early stages to consume the reducing substances, these nanocarriers enhance therapeutic efficacy of CDT. This mechanism has also been applied to amphiphilic nanoparticles and ROS-responsive poly(α-l-lysine) nanoparticles, which are developed and used to encapsulate antibiotics, achieving both antibacterial and antioxidant functionalities [79,80].

Conclusion

Biomimetic nanocarriers represent a promising strategy for the treatment of several clinically relevant and challenging human diseases. This study demonstrates that mimicking cell membranes, particularly those of immune system cells, offers significant benefits by reducing the degradation of biomaterials by the host. The use of biocompatible coatings not only enhances treatment efficacy but also paves the way for increasingly personalized therapeutic approaches. This strategy holds substantial potential for achieving high efficiency in treating diseases that currently lack a cure.

Acknowledgements

The authors are grateful to the Fundação Coordenação de Aperfeiçoamento de Pessoal de Nível Superior (CAPES), the Conselho Nacional de Desenvolvimento Científico e Tecnológico (CNPq), and the Fundação de Amparo à Pesquisa do Estado de Minas Gerais (FAPEMIG). The graphical abstract was created in BioRender. Sodré, B. (2024) https://BioRender.com/q48u348. This content is not subject to CC BY 4.0.

Funding

This work was supported by the Fundação de Amparo à Pesquisa do Estado Minas Gerais (FAPEMIG – funding number: RED-00198-23 and RED-00224-23) and by the Conselho Nacional de Desenvolvimento Científico e Tecnológico (CNPq Bench fee Lv2).

Author Contributions

Hugo Felix Perini: conceptualization; investigation; methodology; writing – original draft; writing – review & editing. Beatriz Sodré Matos: conceptualization; investigation; visualization; writing – original draft; writing – review & editing. Carlo José Freire de Oliveira: conceptualization; funding acquisition; visualization; writing – original draft; writing – review & editing. Marcos Vinicius da Silva: conceptualization; funding acquisition; project administration; supervision; visualization; writing – original draft; writing – review & editing.

ORCID® iDs

Hugo Felix Perini - https://orcid.org/0000-0003-1988-7273
Beatriz Sodré Matos - https://orcid.org/0000-0002-0342-1017
Carlo José Freire de Oliveira - https://orcid.org/0000-0003-2211-7333
Marcos Vinicius da Silva - https://orcid.org/0000-0002-2966-7621

Data Availability Statement

Data sharing is not applicable as no new data was generated or analyzed in this study.

References

1. Grumezescu, A. M.; Holban, A. M. *Nanoengineering in the Beverage Industry;* Woodhead Publishing: Duxford, U.K., 2020; Vol. 20. doi:10.1016/c2017-0-02394-7
2. Bayda, S.; Adeel, M.; Tuccinardi, T.; Cordani, M.; Rizzolio, F. *Molecules* **2019,** *25,* 112. doi:10.3390/molecules25010112
3. Dacoba, T. G.; Olivera, A.; Torres, D.; Crecente-Campo, J.; Alonso, M. J. *Semin. Immunol.* **2017,** *34,* 78–102. doi:10.1016/j.smim.2017.09.007
4. Cui, J.; Piotrowski-Daspit, A. S.; Zhang, J.; Shao, M.; Bracaglia, L. G.; Utsumi, T.; Seo, Y.-E.; DiRito, J.; Song, E.; Wu, C.; Inada, A.; Tietjen, G. T.; Pober, J. S.; Iwakiri, Y.; Saltzman, W. M. *J. Controlled Release* **2019,** *304,* 259–267. doi:10.1016/j.jconrel.2019.04.044
5. National Nanotechnology Initiative (NNI). "What is nanotechnology?". https://www.nano.gov/about-nanotechnology (accessed July 25, 2024).
6. Alqosaibi, A. I. *Saudi J. Biol. Sci.* **2022,** *29,* 103298. doi:10.1016/j.sjbs.2022.103298
7. Zhang, Y.; Lin, S.; Fu, J.; Zhang, W.; Shu, G.; Lin, J.; Li, H.; Xu, F.; Tang, H.; Peng, G.; Zhao, L.; Chen, S.; Fu, H. *J. Appl. Microbiol.* **2022,** *133,* 1273–1287. doi:10.1111/jam.15640
8. Zhao, X.; Zhao, R.; Nie, G. *Nat. Protoc.* **2022,** *17,* 2240–2274. doi:10.1038/s41596-022-00713-7
9. Wicki, A.; Witzigmann, D.; Balasubramanian, V.; Huwyler, J. *J. Controlled Release* **2015,** *200,* 138–157. doi:10.1016/j.jconrel.2014.12.030
10. Alhomaidi, E.; Jasim, S. A.; Amin, H. I. M.; Lima Nobre, M. A.; Khatami, M.; Jalil, A. T.; Hussain Dilfy, S. *IET Nanobiotechnol.* **2022,** *16,* 284–294. doi:10.1049/nbt2.12096
11. Jasim, S. A.; Patra, I.; Opulencia, M. J. C.; Hachem, K.; Parra, R. M. R.; Ansari, M. J.; Jalil, A. T.; Al-Gazally, M. E.; Naderifar, M.; Khatami, M.; Akhavan-Sigari, R. *Nanotechnol. Rev.* **2022,** *11,* 2483–2492. doi:10.1515/ntrev-2022-0143
12. da Silva, D. A.; De Luca, A.; Squitti, R.; Rongioletti, M.; Rossi, L.; Machado, C. M. L.; Cerchiaro, G. *J. Inorg. Biochem.* **2022,** *226,* 111634. doi:10.1016/j.jinorgbio.2021.111634
13. Akulo, K. A.; Adali, T.; Moyo, M. T. G.; Bodamyali, T. *Polymers (Basel, Switz.)* **2022,** *14,* 2359. doi:10.3390/polym14122359
14. Madhi, Z. S.; Shallan, M. A.; Almaamuri, A. M.; Alhussainy, A. A.; AL-Salih, S. S. S.; Raheem, A. K.; Alwan, H. J.; Jalil, A. T. *J. Drug Delivery Sci. Technol.* **2022,** *78,* 103948. doi:10.1016/j.jddst.2022.103948

15. Shaw, D. S.; Honeychurch, K. C. *Biosensors* **2022,** *12,* 675. doi:10.3390/bios12090675
16. Yih, T. C.; Al-Fandi, M. *J. Cell. Biochem.* **2006,** *97,* 1184–1190. doi:10.1002/jcb.20796
17. Jiang, W.; Kim, B. Y.; Rutka, J. T.; Chan, W. C. *Expert Opin. Drug Delivery* **2007,** *4,* 621–633. doi:10.1517/17425247.4.6.621
18. Rao, L.; Yu, G.-T.; Meng, Q.-F.; Bu, L.-L.; Tian, R.; Lin, L.-S.; Deng, H.; Yang, W.; Zan, M.; Ding, J.; Li, A.; Xiao, H.; Sun, Z.-J.; Liu, W.; Chen, X. *Adv. Funct. Mater.* **2019,** *29,* 10.1002/adfm.201905671. doi:10.1002/adfm.201905671
19. Al-Hetty, H. R. A. K.; Kadhim, M. S.; Al-Tamimi, J. H. Z.; Ahmed, N. M.; Jalil, A. T.; Saleh, M. M.; Kandeel, M.; Abbas, R. H. *Emergent Mater.* **2023,** *6,* 1–13. doi:10.1007/s42247-023-00453-8
20. Safdar, A.; Wang, P.; Muhaymin, A.; Nie, G.; Li, S. *J. Controlled Release* **2024,** *373,* 128–144. doi:10.1016/j.jconrel.2024.07.013
21. Wang, H.; Wu, J.; Williams, G. R.; Fan, Q.; Niu, S.; Wu, J.; Xie, X.; Zhu, L.-M. *J. Nanobiotechnol.* **2019,** *17,* 60. doi:10.1186/s12951-019-0494-y
22. Siegler, E. L.; Kim, Y. J.; Chen, X.; Siriwon, N.; Mac, J.; Rohrs, J. A.; Bryson, P. D.; Wang, P. *Mol. Ther.* **2017,** *25,* 2607–2619. doi:10.1016/j.ymthe.2017.08.010
23. Zhang, Q.; Dehaini, D.; Zhang, Y.; Zhou, J.; Chen, X.; Zhang, L.; Fang, R. H.; Gao, W.; Zhang, L. *Nat. Nanotechnol.* **2018,** *13,* 1182–1190. doi:10.1038/s41565-018-0254-4
24. Hu, C.-M. J.; Zhang, L.; Aryal, S.; Cheung, C.; Fang, R. H.; Zhang, L. *Proc. Natl. Acad. Sci. U. S. A.* **2011,** *108,* 10980–10985. doi:10.1073/pnas.1106634108
25. Wang, Y.; Zhang, K.; Qin, X.; Li, T.; Qiu, J.; Yin, T.; Huang, J.; McGinty, S.; Pontrelli, G.; Ren, J.; Wang, Q.; Wu, W.; Wang, G. *Adv. Sci.* **2019,** *6,* 1900172. doi:10.1002/advs.201900172
26. Gan, J.; Du, G.; He, C.; Jiang, M.; Mou, X.; Xue, J.; Sun, X. *J. Controlled Release* **2020,** *326,* 297–309. doi:10.1016/j.jconrel.2020.07.008
27. Kunde, S. S.; Wairkar, S. *Int. J. Pharm.* **2021,** *598,* 120395. doi:10.1016/j.ijpharm.2021.120395
28. Mendanha, D.; Vieira de Castro, J.; Ferreira, H.; Neves, N. M. *J. Controlled Release* **2021,** *337,* 482–493. doi:10.1016/j.jconrel.2021.07.047
29. Drotleff, S.; Lungwitz, U.; Breunig, M.; Dennis, A.; Blunk, T.; Tessmar, J.; Göpferich, A. *Eur. J. Pharm. Biopharm.* **2004,** *58,* 385–407. doi:10.1016/j.ejpb.2004.03.018
30. Chen, L.; Hong, W.; Ren, W.; Xu, T.; Qian, Z.; He, Z. *Signal Transduction Targeted Ther.* **2021,** *6,* 225. doi:10.1038/s41392-021-00631-2
31. He, Z.; Zhang, Y.; Feng, N. *Mater. Sci. Eng., C* **2020,** *106,* 110298. doi:10.1016/j.msec.2019.110298
32. Jin, K.; Luo, Z.; Zhang, B.; Pang, Z. *Acta Pharm. Sin. B* **2018,** *8,* 23–33. doi:10.1016/j.apsb.2017.12.002
33. Salmaso, S.; Mastrotto, F.; Roverso, M.; Gandin, V.; De Martin, S.; Gabbia, D.; De Franco, M.; Vaccarin, C.; Verona, M.; Chilin, A.; Caliceti, P.; Bogialli, S.; Marzaro, G. *J. Controlled Release* **2021,** *340,* 318–330. doi:10.1016/j.jconrel.2021.11.006
34. Chugh, V.; Vijaya Krishna, K.; Pandit, A. *ACS Nano* **2021,** *15,* 17080–17123. doi:10.1021/acsnano.1c03800
35. Moshrefiravasjani, R.; Kamrani, A.; Nazari, N.; Jafari, F.; Nasiri, H.; Jahanban-esfahlan, R.; Akbari, M. *Pathol., Res. Pract.* **2024,** *254,* 155083. doi:10.1016/j.prp.2023.155083
36. Bang, K.-H.; Na, Y.-G.; Huh, H. W.; Hwang, S.-J.; Kim, M.-S.; Kim, M.; Lee, H.-K.; Cho, C.-W. *Cancers* **2019,** *11,* 807. doi:10.3390/cancers11060807
37. Su, J.; Sun, H.; Meng, Q.; Yin, Q.; Zhang, P.; Zhang, Z.; Yu, H.; Li, Y. *Adv. Funct. Mater.* **2016,** *26,* 7495–7506. doi:10.1002/adfm.201603381
38. Xie, W.; Deng, W.-W.; Zan, M.; Rao, L.; Yu, G.-T.; Zhu, D.-M.; Wu, W.-T.; Chen, B.; Ji, L.-W.; Chen, L.; Liu, K.; Guo, S.-S.; Huang, H.-M.; Zhang, W.-F.; Zhao, X.; Yuan, Y.; Dong, W.; Sun, Z.-J.; Liu, W. *ACS Nano* **2019,** *13,* 2849–2857. doi:10.1021/acsnano.8b03788
39. Krishnamurthy, S.; Gnanasammandhan, M. K.; Xie, C.; Huang, K.; Cui, M. Y.; Chan, J. M. *Nanoscale* **2016,** *8,* 6981–6985. doi:10.1039/c5nr07588b
40. Yang, J.; Teng, Y.; Fu, Y.; Zhang, C. *Int. J. Nanomed.* **2019,** *14,* 5061–5071. doi:10.2147/ijn.s202910
41. Chhabria, V.; Beeton, S. *Nanomedicine (London, U. K.)* **2016,** *11,* 2797–2807. doi:10.2217/nnm-2016-0180
42. Alimohammadvand, S.; Kaveh Zenjanab, M.; Mashinchian, M.; Shayegh, J.; Jahanban-Esfahlan, R. *Biomed. Pharmacother.* **2024,** *177,* 116951. doi:10.1016/j.biopha.2024.116951
43. He, W.; Frueh, J.; Wu, Z.; He, Q. *Langmuir* **2016,** *32,* 3637–3644. doi:10.1021/acs.langmuir.5b04762
44. Chen, G.; Roy, I.; Yang, C.; Prasad, P. N. *Chem. Rev.* **2016,** *116,* 2826–2885. doi:10.1021/acs.chemrev.5b00148
45. Kim, K.; Lee, W. G. *J. Mater. Chem. B* **2017,** *5,* 2726–2738. doi:10.1039/c7tb00038c
46. van Weerd, J.; Karperien, M.; Jonkheijm, P. *Adv. Healthcare Mater.* **2015,** *4,* 2743–2779. doi:10.1002/adhm.201500398
47. Dąbkowska, M.; Ulańczyk, Z.; Łuczkowska, K.; Rogińska, D.; Sobuś, A.; Wasilewska, M.; Olszewska, M.; Jakubowska, K.; Machaliński, B. *J. Nanobiotechnol.* **2021,** *19,* 258. doi:10.1186/s12951-021-00984-4
48. Bäumer, N.; Scheller, A.; Wittmann, L.; Faust, A.; Apel, M.; Nimmagadda, S. C.; Geyer, C.; Grunert, K.; Kellmann, N.; Peipp, M.; Kailayangiri, S.; Gutierrez Suburu, M. E.; Strassert, C. A.; Schenk, M.; Greune, L.; Rüter, C.; Dersch, P.; Hartmann, W.; Rossig, C.; Neri, D.; Müller-Tidow, C.; Schwöppe, C.; Schliemann, C.; Khandanpour, C.; Lenz, G.; Berdel, W. E.; Bäumer, S. *J. Hematol. Oncol.* **2022,** *15,* 171. doi:10.1186/s13045-022-01390-5
49. Wang, X.; Wang, X.; Bai, X.; Yan, L.; Liu, T.; Wang, M.; Song, Y.; Hu, G.; Gu, Z.; Miao, Q.; Chen, C. *Nano Lett.* **2019,** *19,* 8–18. doi:10.1021/acs.nanolett.8b02638
50. Fan, L.; Jin, L.; Tang, T.; Zheng, Y.; Chen, Z.; Lin, H.; Ding, C.; Wang, T.; Chen, H.; Guo, Y.; Xu, C.; Zhou, H.; Wu, X.; Fu, X.; Yan, F.; Mao, Z.; Chen, G. *Theranostics* **2024,** *14,* 283–303. doi:10.7150/thno.90370
51. Omrani, M.; Beyrampour-Basmenj, H.; Jahanban-Esfahlan, R.; Talebi, M.; Raeisi, M.; Serej, Z. A.; Akbar-Gharalari, N.; Khodakarimi, S.; Wu, J.; Ebrahimi-kalan, A. *Mol. Cell. Biochem.* **2024,** *479,* 679–691. doi:10.1007/s11010-023-04756-6
52. Vijayan, V.; Uthaman, S.; Park, I.-K. *Polymers (Basel, Switz.)* **2018,** *10,* 983. doi:10.3390/polym10090983
53. Zhai, Y.; Su, J.; Ran, W.; Zhang, P.; Yin, Q.; Zhang, Z.; Yu, H.; Li, Y. *Theranostics* **2017,** *7,* 2575–2592. doi:10.7150/thno.20118
54. Rao, L.; He, Z.; Meng, Q.-F.; Zhou, Z.; Bu, L.-L.; Guo, S.-S.; Liu, W.; Zhao, X.-Z. *J. Biomed. Mater. Res., Part A* **2017,** *105,* 521–530. doi:10.1002/jbm.a.35927
55. Chen, M.; Liu, A.; Chen, B.; Zhu, D.-M.; Xie, W.; Deng, F.-F.; Ji, L.-W.; Chen, L.-B.; Huang, H.-M.; Fu, Y.-R.; Liu, W.; Wang, F.-B. *Nanoscale* **2019,** *11,* 12388–12396. doi:10.1039/c9nr01805k

56. Sun, M.; Miyazawa, K.; Pendekanti, T.; Razmi, A.; Firlar, E.; Yang, S.; Shokuhfar, T.; Li, O.; Li, W.; Sen Gupta, A. *Nanoscale* **2020,** *12,* 21255–21270. doi:10.1039/d0nr03633a
57. Palminteri, M.; Dhakar, N. K.; Ferraresi, A.; Caldera, F.; Vidoni, C.; Trotta, F.; Isidoro, C. *Nanotheranostics* **2021,** *5,* 197–212. doi:10.7150/ntno.53888
58. Wang, R.; Wang, X.; Zhao, H.; Li, N.; Li, J.; Zhang, H.; Di, L. *J. Controlled Release* **2024,** *365,* 331–347. doi:10.1016/j.jconrel.2023.11.033
59. Hyldbakk, A.; Hansen, T.; Hak, S.; Borgos, S. E. F. *J. Controlled Release* **2024,** *366,* 611–620. doi:10.1016/j.jconrel.2024.01.016
60. Ran, R.; Middelberg, A. P. J.; Zhao, C.-X. *Colloids Surf., B* **2016,** *148,* 402–410. doi:10.1016/j.colsurfb.2016.09.016
61. Kozma, G. T.; Mészáros, T.; Berényi, P.; Facskó, R.; Patkó, Z.; Oláh, C. Z.; Nagy, A.; Fülöp, T. G.; Glatter, K. A.; Radovits, T.; Merkely, B.; Szebeni, J. *Vaccine* **2023,** *41,* 4561–4570. doi:10.1016/j.vaccine.2023.06.009
62. Guido, C.; Maiorano, G.; Cortese, B.; D'Amone, S.; Palamà, I. E. *Bioengineering* **2020,** *7,* 111. doi:10.3390/bioengineering7030111
63. Zhang, Z.; Qian, H.; Yang, M.; Li, R.; Hu, J.; Li, L.; Yu, L.; Liu, B.; Qian, X. *Int. J. Nanomed.* **2017,** *12,* 1593–1605. doi:10.2147/ijn.s127256
64. Zhang, L.; Li, R.; Chen, H.; Wei, J.; Qian, H.; Su, S.; Shao, J.; Wang, L.; Qian, X.-P.; Liu, B. *Int. J. Nanomed.* **2017,** *12,* 2129–2142. doi:10.2147/ijn.s126016
65. Serati-Nouri, H.; Mahmoudnezhad, A.; Bayrami, M.; Sanajou, D.; Tozihi, M.; Roshangar, L.; Pilehvar, Y.; Zarghami, N. *J. Drug Delivery Sci. Technol.* **2021,** *66,* 102902. doi:10.1016/j.jddst.2021.102902
66. Nummelin, S.; Kommeri, J.; Kostiainen, M. A.; Linko, V. *Adv. Mater. (Weinheim, Ger.)* **2018,** *30,* 1703721. doi:10.1002/adma.201703721
67. Jiang, L.; Wang, Y.; Zhu, F.; Liu, G.; Liu, H.; Ji, H.; Zheng, S.; Li, B. *J. Cancer (Wyoming, Aust.)* **2019,** *10,* 92–104. doi:10.7150/jca.27462
68. Wang, Y.; Jiang, L.; Yin, Q.; Liu, H.; Liu, G.; Zhu, G.; Li, B. *J. Cancer (Wyoming, Aust.)* **2017,** *8,* 3001–3013. doi:10.7150/jca.21059
69. Pardridge, W. M. *NeuroRx* **2005,** *2,* 3–14. doi:10.1602/neurorx.2.1.3
70. Xie, J.; Gonzalez-Carter, D.; Tockary, T. A.; Nakamura, N.; Xue, Y.; Nakakido, M.; Akiba, H.; Dirisala, A.; Liu, X.; Toh, K.; Yang, T.; Wang, Z.; Fukushima, S.; Li, J.; Quader, S.; Tsumoto, K.; Yokota, T.; Anraku, Y.; Kataoka, K. *ACS Nano* **2020,** *14,* 6729–6742. doi:10.1021/acsnano.9b09991
71. Han, Y.; Gao, C.; Wang, H.; Sun, J.; Liang, M.; Feng, Y.; Liu, Q.; Fu, S.; Cui, L.; Gao, C.; Li, Y.; Yang, Y.; Sun, B. *Bioact. Mater.* **2021,** *6,* 529–542. doi:10.1016/j.bioactmat.2020.08.017
72. Zhong, X.; Na, Y.; Yin, S.; Yan, C.; Gu, J.; Zhang, N.; Geng, F. *Molecules* **2023,** *28,* 2336. doi:10.3390/molecules28052336
73. Gao, N.; Sun, H.; Dong, K.; Ren, J.; Qu, X. *Chem. – Eur. J.* **2015,** *21,* 829–835. doi:10.1002/chem.201404562
74. He, Y.; Li, R.; Liang, J.; Zhu, Y.; Zhang, S.; Zheng, Z.; Qin, J.; Pang, Z.; Wang, J. *Nano Res.* **2018,** *11,* 6086–6101. doi:10.1007/s12274-018-2126-5
75. Tan, Q.; He, L.; Meng, X.; Wang, W.; Pan, H.; Yin, W.; Zhu, T.; Huang, X.; Shan, H. *J. Nanobiotechnol.* **2021,** *19,* 173. doi:10.1186/s12951-021-00926-0
76. Dormont, F.; Brusini, R.; Cailleau, C.; Reynaud, F.; Peramo, A.; Gendron, A.; Mougin, J.; Gaudin, F.; Varna, M.; Couvreur, P. *Sci. Adv.* **2020,** *6,* eaaz5466. doi:10.1126/sciadv.aaz5466
77. Li, S.; Liu, X.; Liu, G.; Liu, C. *Viruses* **2023,** *15,* 596. doi:10.3390/v15030596
78. Lin, F.; Qin, Y.; Sun, J.; Liu, Y.; Yang, S.; Zheng, S.; Yin, L.; Li, D.; Cui, L.; Li, G.; Qiu, Z.; Liu, Z. *J. Mater. Chem. B* **2024,** *12,* 12062–12072. doi:10.1039/d4tb01819b
79. Peng, N.; Du, Y.; Yu, G.; Zhang, C.; Cai, Q.; Tang, H.; Liu, Y. *Langmuir* **2022,** *38,* 13139–13149. doi:10.1021/acs.langmuir.2c01857
80. Wang, Y.; Li, Y.; Liu, W.; Li, C.; Duo, X.; Meng, X.; Feng, Y. *Macromol. Biosci.* **2024,** *24,* 2300580. doi:10.1002/mabi.202300580

License and Terms

BEILSTEIN JOURNAL OF NANOTECHNOLOGY

Orientation-dependent photonic bandgaps in gold-dust weevil scales and their titania bioreplicates

Norma Salvadores Farran[1,2], Limin Wang[1], Primoz Pirih[*1] and Bodo D. Wilts[*1]

Full Research Paper

Open Access

Address:
[1]Department for Chemistry and Physics of Materials, University of Salzburg, Jakob-Haringer-Str. 2a, 5020 Salzburg, Austria and
[2]Current address: Institute of Materials Science and Technology, Vienna Technical University, 1060 Vienna, Austria

Email:
Primoz Pirih[*] - primoz.pirih@plus.ac.at;
Bodo D. Wilts[*] - bodo.wilts@plus.ac.at

* Corresponding author

Keywords:
animal coloration; photonic crystal; polarization conversion; sol–gel replication; weevil

Beilstein J. Nanotechnol. **2025,** *16,* 1–10.
https://doi.org/10.3762/bjnano.16.1

Received: 04 July 2024
Accepted: 19 December 2024
Published: 02 January 2025

This article is part of the thematic issue "Micro- and nanoscale effects in biological and bioinspired materials and surfaces".

Guest Editor: T. H. Büscher

Abstract

The scales of the gold-dust weevil *Hypomeces squamosus* are green because of three-dimensional diamond-type chitin–air photonic crystals with an average periodicity of about 430 nm and a chitin fill fraction of about 0.44. A single scale usually contains one to three crystallites with different lattice orientations. The reciprocal space images and reflection spectra obtained from single domains indicated a partial photonic bandgap in the wavelength range from 450 to 650 nm. Light reflected from {111}-oriented domains is green-yellow. Light reflected from blue, {100}-oriented domains exhibits polarization conversion, rotating the angle of linearly polarized light. The overall coloration, resulting from the reflections from many scales, is close to uniformly diffuse because of the random orientation of the domains. Using titania sol–gel chemistry, we produced negative replicas that exhibited a 70 to 120 nm redshift of the bandgap, depending on the lattice orientation. The wavelength shift in {100} orientation is supported by full-wave optical modeling of a dual diamond network with an exchanged fill fraction (0.56) of the material with the refractive index in the range of 1.55 to 2.00. The study suggests that the effective refractive index of titania in the 3D lattice is similar to that in sol–gel films. The study demonstrates the potential of replicating complex biophotonic structures using the sol–gel technique. Optimization of the sol–gel process could lead to customizable photonic bandgaps that might be used in novel optical materials.

Introduction

Animal coloration is produced by means of absorption, scattering, luminescence, and interference. The latter is achieved when light interacts with a material having a periodically changing refractive index. Interference produces structural colors that may be quite saturated and angle-dependent (iridescent). Structurally colored materials feature refractive index

variations in one, two, or three dimensions [1,2]. In particular, three-dimensional (3D) photonic crystals are characterized by a photonic bandgap that prohibits light of certain wavelengths from propagating through (specific) orientations of the material [3]. A complete photonic bandgap, where propagation of light waves in a certain wavelength band is prohibited, is generally not possible with biological photonic crystals, as the refractive index contrast (approx. 1.55) between chitin and air is too low to achieve this condition [4,5].

The intriguing properties of photonic bandgap materials extend beyond coloration, as they can be used for manipulating light in key optical technologies such as lasers [6], light-emitting diodes [7], and light guides [8]. For applications in the visible spectral range, the periodicity needs to be in the range of a few hundreds of nanometers [9]. This periodicity is challenging to engineer using, for example, block copolymers [10,11], lithography, or laser etching [12,13], but it can be routinely found in animal integuments.

Biomimetic approaches using templates from natural structures offers a possible alternative. The scales of many beetles and weevils contain diamond photonic crystals [14-16] that may serve as a template for materials with a complete photonic bandgap, provided that the refractive index contrast of the template is increased [15,17,18]. Birds, butterflies, beetles, and, particularly, weevils produce many interesting quasi- and highly ordered photonic structures [14,19-22] that may be used as an inspiration for optical engineering. Indeed, single diamond photonic networks are one of the most efficient naturally occurring 3D photonic crystal structures. They can also be described using triply periodic minimal surface (TPMS) models, where a minimal surface separates two volumes with differing refractive indices. The diamond TPMS structure is special as it provides optimal diffraction efficiency and can form photonic bandgaps even with lower refractive index contrasts (i.e., with refractive index contrasts above 2.1) [15,17]. This makes these structures rather interesting for their use as templates. The work of Galusha and colleagues demonstrated a double-imprint templating process to create a positive titania replica of beetle scales with high refractive index. This showed the effectiveness of a sol–gel process at relatively low temperature (130 °C) in replicating complex biological structures and obtaining photonic crystals with desired optical properties [23,24].

In this work, we characterized natural photonic crystals found in the scales of the gold-dust weevil, *Hypomeces squamosus* (Coleoptera: Curculionidae; Herbst 1795), a pest of several crops [25-27]. We investigated the properties of photonic structures in the scales using reflected light microscopy and spectroscopy. Brillouin zones inferred from the reciprocal space images indicated that the scales are composed of one to three randomly oriented domains of single diamond network photonic crystals. The domains in lattice orientation {100} exhibited polarization conversion. The structure inferred from optical measurements was confirmed using conventional and focused ion beam scanning electron microscopy (FIB-SEM). By averaging the reciprocal space images obtained from different lattice orientations, we obtained a uniform diffuse green scatterogram, confirming the mechanism producing the dull, unsaturated overall coloration found on the gold-dust weevil and several other weevils [19,21,28]. Subsequently, using plasma etching, we removed the scale cortex and made negative titania replicas of exposed photonic crystals using a sol–gel chemistry approach [14,24]. The increased refractive index contrast and the increased fill fraction of the replicas resulted in a redshift, which was confirmed with full-wave modeling. Full-wave modeling further suggested that the titania replicated from a 3D template has a similar refractive index as the titania thin layers obtained with a sol–gel process, suggesting a similar porosity despite the more complicated geometry. The work further supports the use of biological photonic structures for synthesizing novel optical devices.

Results

Appearance and structure of the scales

The body and the elytra of the gold-dust weevil *Hypomeces squamosus* are covered with iridescent scales (Figure 1). The scales on the wings and body appear mostly greenish, while the scales on the legs are more bluish (Figure 1a). The elytral scales are flat, about 70 µm long and about 50 µm wide. Several parallel lines are visible on the upper side of the scales at high magnification in an optical microscope, and the broken scale stalks are visible on the lower side (Figure 1b).

Single scales, imaged with the 20× (NA = 0.60) objective and full-aperture illumination, appear rather uniformly colored (Figure 1b). Reflectance spectra measured with a modified reflected light microscope (see Methods section) feature peaks between 450 and 600 nm (Figure 1c), regardless of which scale side is facing upwards. The reflectance amplitudes are markedly higher than that of a diffuse reference standard, indicating directional reflection. The scales immersed in refractive index oils appeared yellowish because of a presence of a blue-absorbing pigment (Supporting Information File 1, Figure S1). Maximal transmission was achieved with the oil with refractive index 1.56, indicating that the scales are composed of chitin and an undetermined short-wavelength absorbing pigment. To investigate whether the origin of the coloration is structural, we examined the external and internal structure of intact and plasma-etched elytral scales using scanning electron microscopy (Figure 2). Using a focused ion beam electron microscope, we

Figure 1: The gold-dust weevil *Hypomeces squamosus*. (a) A macro photo of the weevil with extended depth of field. (b) Epi-reflectance microscope image of two scales, upper (left) and lower side (right) facing upwards (average scale length 67 ± 7 µm, N = 10). (c) Reflectance spectra of several single scales, measured with the 20× (NA = 0.60) objective and normalized against a white diffusive standard. Scale bars: (a) 1 mm and (b) 10 µm.

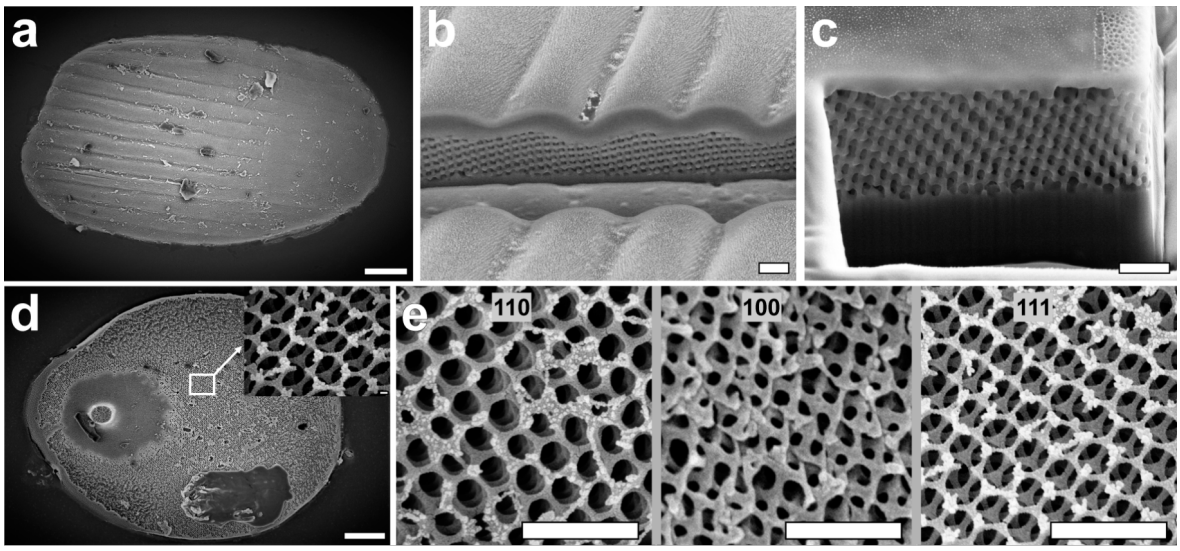

Figure 2: Structural characterization of the scales. (a) SEM image of an intact scale with the upper lamina facing upwards. (b, c) Cross-sectional images of an intact scale show a thin cortex wrapping around a chitin–air network with a 3D periodic nanostructure; the undulating upper cortex layer is thicker in (b) than the flat lower cortex layer in (c). (d) SEM image of the lower surface of an etched scale. (e) Different lattice orientations of the 3D nanostructure found in etched scales. The structure is strongly reminiscent of single diamond-type photonic networks [15]. Scale bars: (a, d) 10 µm, inset 100 nm, (b, c) 1 µm, and (e) 2 µm.

exposed the diamond lattice chitinous network underneath the cortex of intact scales (Figure 2b,c). The upper cortex is ≈1 µm thick and has undulations spaced about 5 µm apart (Figure 2b), which were visible in the light microscopy images (Figure 1b). The lower cortex is thinner (≈0.5 µm) and flat (Figure 2c).

From the FIB-SEM cuts, we estimated the chitin fill fraction of the chitin network to be 0.44 ± 0.06. By adjusting the power and duration of the argon plasma etching, we were able to selectively etch the lower cortex of the scales (Figure 2d), revealing the underlying chitin network (Figure 2d,e). The etched scales showed different lattice domains that had a reduced chitin fill fraction due to etching. From the 2D Fourier transform of the {111}-oriented domains, whose first spatial frequency peaks were in a symmetric hexagonal pattern, we estimated a single-diamond unit cell size of 427 ± 4 nm (Supporting Information File 1, Figure S3). The transition between differently oriented domains is continuous (Supporting Information File 1, Figure S5).

Spatial distribution of reflectance

Previous work on single diamond network photonic crystals has shown that their orientation and nature can be identified using reciprocal k-space imaging [28]. To see whether the gold-dust weevil scales contain diamond photonic crystal networks, we performed reciprocal space imaging using a 50× (NA = 0.95)

objective. The real space images with full-aperture illumination have shown a uniform green tint of the scales. With the illumination aperture fully closed, the real space images revealed domains with distinct blueish, greenish, and yellowish tints (Figure 3a).

By illuminating a single domain with full-aperture illumination and inserting the Bertrand lens into the detection pathway, we obtained reciprocal space images (Figure 3b). The domains oriented close to the {111} direction produced reciprocal space images with a greenish or yellowish central hexagon shape (Figure 3b II,VII), while the domains close to {110} orientation produced images with two partially visible hexagons (Figure 3b I,III,VIII). The domains close to the {100} orientation exhibited a square-shaped blue zone in the center of the reciprocal space image, corresponding to the X-symmetry point (Figure 3b V). Overall, the domains in the scales seem to be oriented randomly. Additional measurements are presented in Supporting Information File 1, Figure S6.

Reciprocal space imaging also allows one to map the bandgap diagram. For this, we measured reflectance spectra in the reciprocal space using full-aperture illumination from a domain that was almost perfectly {100}-oriented (Figure 3d). The spectrum measured in the image center, close to the X-symmetry point, has a peak around 440 nm, whereas the spectra measured at the diagonals close to the rim, approaching L-symmetry points, have peaks around 500 nm (Figure 3e). The reflectance peak from the L-symmetry point, measured from a {111}-oriented domain, was about 550 nm (not shown here). The polarization dependence of reflections is shown in Supporting Information File 1, Figure S2. In brief, while the {111}-oriented domains retained the polarization angle, the light reflected from {100}-oriented domains exhibited polarization conversion, similarly to the case shown in [16]. The polarization contrast (i.e., the ratio of maximal to minimal peak reflectance) was lower for the blue domain than for the green domain. The polarization conversion angle depended on the exact orientation of the domain.

Titania replicas exhibit a redshift

Diamond-type photonic crystals are arguably one of the most sophisticated structures of photonics research [14,28,29], but the refractive index of chitin (n = 1.55, see also [4]) in intact insect scales is too low to allow for the formation of a complete

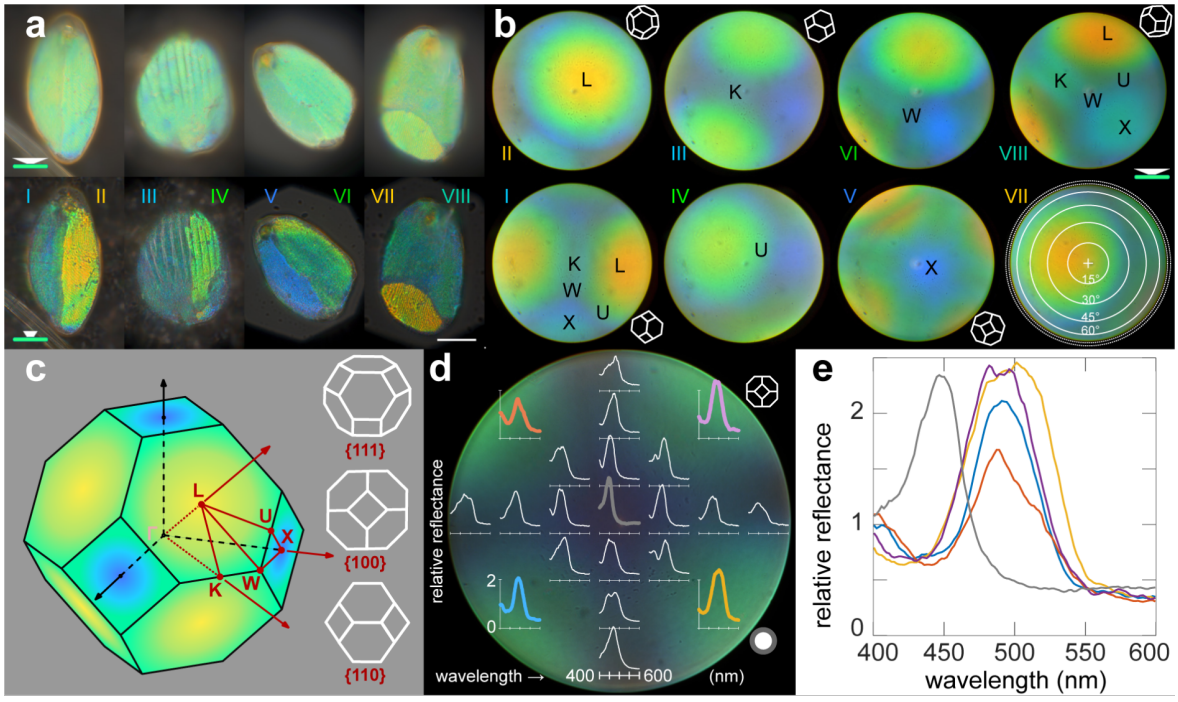

Figure 3: Real and reciprocal space images and directional reflectance spectra. (a) Light microscopy images of four scales, each with two domains, illuminated with large-aperture (top row) and with small-aperture (bottom row) illumination, revealing the differently colored domains. (b) Reciprocal space images obtained by illuminating the domains shown in (a) with small-field, full-aperture illumination reveal the first Brillouin zone with indicated symmetry points. See Supporting Information File 1, Figure S6, for more examples. (c) A schematic representation of the first Brillouin zone of a diamond network (left) and the isometric projections of the high-symmetry points (right). (d, e) Directional reflectance spectra measured from the reciprocal image of a {100}-oriented domain. Polarization properties of the same domain are shown in Supporting Information File 1, Figure S2. Reflectance spectra were normalized against a white diffusive standard. Roman numerals indicate the domains corresponding between (a) and (b). Scale bar: (a) 20 µm. The rim of the reciprocal space images (b, d) corresponds to 71° (NA = 0.95). Symmetry points in (b, c) are indicated with letters (LUXWK). The white circle in (d) approximates the collection area of the *XY*-translatable fiber.

bandgap, hindering photonic applications. The diamond networks in insect scales are, however, ideal templates for transferring these complex geometries, which cannot be otherwise synthesized, into media with higher refractive index. Plasma etching is an effective way to open the beetle scales and make them accessible to the chemical environment used for biotemplating. To show the potential of the gold-dust weevil scales for biotemplating, we plasma-etched the scales and produced (imperfect) negative replicas of the diamond-based photonic structure via an established titania-based sol–gel process [24], followed by the removal of the chitinous template. The elemental composition of the original scales and the replicas (Supporting Information File 1, Table S1) shows that nitrogen is absent in the replicas, indicating that the cleaning procedure, despite its relatively low maximal temperature (130 °C) satisfactorily removed the template's original material from the replica.

We obtained two different types of replicas differing in color; the first type was orange, and the second type was greenish-blue, as shown in Figure 4. The real space and reciprocal space images are shown in Figure 4a,b. The green replica was roughly {100}-oriented, and the orange replica was roughly {111}-oriented. SEM images shown in Figure 4d,e confirmed the successful replication with an increased fill fraction, compared to the original material (Figure 2); the two fill fractions, f, were expected to be conserved but exchanged (i.e., titania $f \approx 0.56$ and void $f \approx 0.44$).

The obtained reflectance spectra of the green and the orange replica (Figure 4e) have peaks and bandwidths (FWHM) of 550 ± 50 and 625 ± 150 nm, respectively. The comparison with the spectra of the original scales with similar domain orientations (blue 440 nm, green 550 nm) indicate a redshift of the peak reflectance of about 110 and 125 nm, for the {100}- and {111}-oriented domains, respectively. The spectra of replicated domains that were less ideally oriented are shown in Supporting Information File 1, Figure S4. The redshift is consistent both with a higher refractive index contrast and with an increase of the fill fraction.

Modeling confirms an increase of refractive index contrast

Full-wave simulations of a {100}-oriented diamond photonic crystal with a range of refractive indices (Figure 4f) show that the reflectivity (i.e., the angle-integrated reflectance) of the idealized diamond structure with fill fraction $f = 0.44$, illuminated with a plane wave, peaks at about 440 nm, and that a shift to 540 nm is expected for a negative replica ($f = 0.56$) at the refractive index $n = 1.90$, with a concomitant approx. 25%

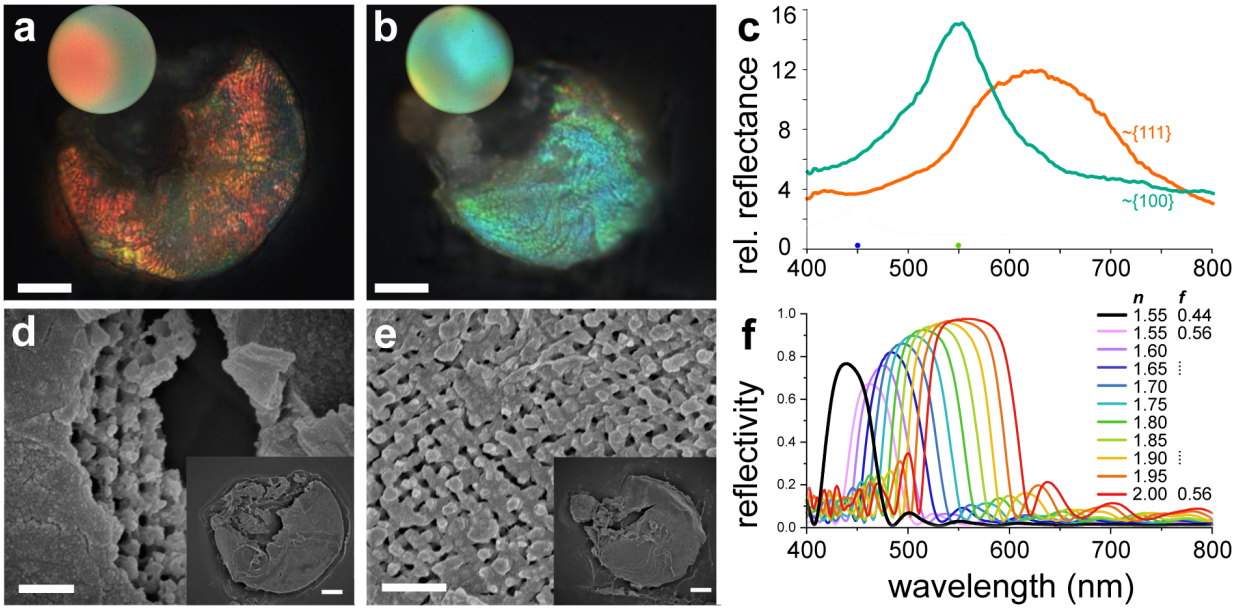

Figure 4: Structural properties of negative titania diamond scale replicas, optical measurements, and optical modeling. (a, b) Real space microscopy images, the insets show the associated reciprocal space images. (c) Reflectance spectra of the replicas. (d, e) High-magnification SEM images, obtained from the same replicas as shown in panels (a, b). (f) Full-wave optical modeling of the {100} orientation of a single diamond network photonic crystal with refractive index $n = 1.55$ and fill fraction $f = 0.44$, and the negative replica with fill fraction $f = 0.56$, in the refractive index range $n = 1.55$–2.00. Scale bars: (a, b) 10 µm, (d, e) 1 µm (in the insets 10 µm). The rim of the reciprocal space image in the insets of (a, b) corresponds to 71° (NA = 0.95).

increase of peak reflectivity (from ≈0.75 to ≈0.95). The increase of reflectivity shown by modeling is consistent with the measured peak reflectance in original and templated scales (original: <10, template: >10, referred to a diffuse white standard (Figure 1 and Figure 4c). The measured spectra, both of the native templates and the replica, are broader than those produced by the idealized model.

Discussion

The scales are not just a simple covering for the gold-dust weevil; they are, in fact, a complex photonic system. The green hue of the scales arises from the interaction of light with the three-dimensional diamond-type chitin–air photonic crystal structures present within the scales (Figures 1–3). This diamond network, with a unit cell constant of approximately 430 nm and a chitin fill fraction of slightly less than a half, interacts with incident light in a way that results in angle-dependent coloration and polarization on a microscopic level (Figure 3 and Supporting Information File 1, Figure S2). This phenomenon is similar to what has been previously observed in other weevils that possess diamond-type photonic crystals [14,15,30] with similar chitin filling fractions [31,32] and unit cell dimensions [15]. The elytral scales are not uniform, as they can contain single or multiple crystallites with varying lattice orientations under a structured enveloping cortex. Each crystallite contributes to the overall optical properties of the scale (Figure 3). The crystallites can feature different orientations, which has strong consequences for interference and, thus, the resulting color [3,5].

The domains oriented roughly along the {100} direction exhibit polarization conversion (Supporting Information File 1, Figure S2 and [16]). This property is indeed interesting from a materials science perspective, but it is unlikely that polarization conversion would give an adaptive advantage in biological signaling, as the polarization signal is scrambled by multiple crystallite orientations and across the scales. Indeed, we observed virtually no noticeable effect on iridescence when using a polarizer and/or analyzer at the macrophotographic scale; however, a subtle iridescent effect on the elytral scales was observed in a particular experimental setting, using a (small aperture) stereomicroscope, either with a ring illuminator or an arbitrarily placed point source. With the ring illuminator, the scales facing the objective appeared predominantly blue-green speckled, while, among the scales seen at grazing angles, less scales appeared blue and more turned yellowish (subtly seen in Figure 1a, more pronounced in Supporting Information File 1, Figure S7). A pointillist macroscopic coloration effect by a changing periodicity has been shown for cuticular multilayers [33], but to our knowledge never conclusively for photonic crystals (for a review, see [21]). The iridescence effect was reversed when we turned the animal to the side (not shown); hence, the effect is likely not due to the material composition or lattice periodicity differences between the scales at the top and the side of the elytrae.

Given the randomness of the lattice orientations in the scales of the gold-dust weevil, the iridescence observed in slanted scales is possibly due to the photonic crystals' finite dimensions and due to the optical effects caused by the enveloping cortex. Moreover, under an extended illumination source, iridescence vanished, and the weevil appeared uniformly diffuse bright green and dull (i.e., without specularity). We simulated the effect of color mixing by averaging the narrow- and whole-aperture-illuminated reciprocal space images and obtained a uniform green far-field reflectance profile (Supporting Information File 1, Figure S7), as shown experimentally previously [15,19]. We, hence, conclude that under natural illumination, the weevil's intricate photonic effects average out into a uniform green. Diffuse coloration is not uncommon in nature and is achieved either by quasi-ordered and disordered structures [19,20], by employing pigments [34], by randomization of orientations of photonic structures [21,35], or by a combination of these mechanisms [36]. It seems that the additive pointillistic mixing of ordered domains observed in the gold-dust weevil and other weevils is quite good at reducing the specular surface reflections, especially when compared with multilayered cuticles [21].

We employed biotemplating to create negative replicas of weevil scales using well-established titania sol–gel chemistry [37]. These replicas, while maintaining the intricate structure of the original scales, exhibited a redshift of the photonic bandgap of 70 to 120 nm, depending on the orientation (Figure 4). This peak shift can be attributed to the difference in refractive index between chitin, the primary component of the original scales, and titania, the material used for the replica, and the increase of the fill fraction.

The measured reflectance spectra, both of the native templates and the replicas, are broader than those produced by the idealized model. This difference is partially attributed to the measurement geometry: While the model assumes a plane wave, in the experiment, the source is extended, and the light collection is either having a large but finite angle in real space, or a small angle in the reciprocal space. Further, in the experiment, the lattice orientation is never exactly in the {100} orientation.

Taking into account the general arrangement of the investigated material, many factors (e.g., local periodicity imperfections, optical crosstalk between crystallites, and optical effects of the lamina, or, in the case of replicas, depth-dependent etching)

may additionally scramble the measured spectra. Comparing the experiments and the model, we therefore suggest that the employed templating procedure produced a titania photonic crystal with an effective refractive index likely in the range of 1.75–1.90 (Figure 4). This is, to our knowledge, the first rough estimation of the refractive index for titania in a 3D lattice, which indicates that with the templating process employed here, the 3D geometry did not significantly increase the porosity of titania.

Our estimate for the effective refractive index of titania in the 3D lattice is in the range reported for pure titania thin films (1.95–2.55 [38], 1.72–2.03 [39]), hybrid silica/titania thin films (1.95 [40], 1.50–1.95 [41] and hybrid organotitania (1.75–2.05 [42], 1.55–1.65 [43]). This is lower than the tabulated values of titania prepared by, for example, layer deposition (2.10 [44], 2.40 [45], see also [46,47]), but higher than that of pure silica replicas (1.50 [18]). This is not unexpected as the effective refractive index of titania thin films produced by sol–gel synthesis varies because of porosity, depending on the specific process, chemicals, and reaction conditions [41]. A higher annealing temperature seems to have a large influence on reducing the porosity of thin films, while, during templating, it unfortunately introduces lattice breakage and shrinkage. Therefore, a calcination process at high temperatures is likely not the best option for pure titania [24], although it seems to work better for silica [18]. The replication process used here had a modestly high temperature step (130 °C). Raising the temperature slightly might increase the effective refractive index of titania before lattice degradation occurs. If the process could be additionally tuned by, for example, varying process times and chemical compositions (including hybrid sol/gels), a further reduction of porosity might lead to the closing of the photonic bandgap at the effective refractive index of about 2.1 [17].

Conclusion

The gold-dust weevil's scales house a complex photonic system that influences coloration and light interaction through a three-dimensional diamond-type chitin–air photonic crystal structure. While the individual scales appear bright and of saturated color, the resulting overall coloration under an extended light source is uniformly green with a very low specularity. The synthesis of negative replicas using titania sol–gel chemistry demonstrates its potential for producing materials with length scales found in nature. The observed redshift in the replicas indicates the possibility of tuning optical properties by varying the replication material. Optimizing the existing sol–gel procedures using, for example, (i) a double inversion process, (ii) other materials that would produce a higher refractive index contrast, or (iii) materials with non-linear optical properties [48-50] would be an interesting future research direction.

Experimental

Light microscopy

The image of the whole animal was taken with a stereomicroscope (Stereo Discovery V20, Zeiss, Oberkochen, Germany). For microscopy and spectroscopy, we used a Zeiss Axioscope 5 with an epi-illumination attachment equipped with the field and aperture stops and a linear polarizer (0–90°). The observation path included a Bertand lens and a fully rotatable linear analyzer. The objectives used were from the EC Epiplan-Neofluar series [5×, 10×, 20×, 50×, and 100×] with apertures [NA = 0.13, 0.30, 0.60, 0.95, and 0.95], respectively. For reciprocal space imaging, we used the 50× and 100× objectives. The 100× objective has a smaller minimal illumination spot (field), but a bigger minimal aperture (angle of the illumination cone), and produces a smaller reciprocal image size than the 50× objective. We, therefore, used the latter on single-domain scales and with small illumination apertures (Supporting Information File 1, Figure S7), and the former for reciprocal space spectroscopy (Figure 3, Supporting Information File 1, Figure S2). Images were acquired with a RGB camera (DFK 38UX304, pixel pitch 3.45 µm, The Imaging Source, Bremen, Germany) and processed with ImageJ/Fiji [51]. Extended depth-of-field images (Figure 1, Supporting Information File 1, Figure S7) were processed from image stacks with Helicon Focus (HeliconSoft, Kharkiv UA).

Spectroscopy

Reflectance spectra were collected via a side port (part 425146-9031, Zeiss) installed below the standard tube lens. The side port was modified to fit a 30 mm cage system holding an *XY* translator (ST1XY-S/M, Thorlabs, 6 mm travel) holding a light fiber at the focal plane of the side port's tube lens. The light was reflected to the side via a slide-in mirror and focused by the tube lens on a 200 µm fiber (FC-UVIR200, Avantes, Apeldoorn NL EU) attached to a CCD spectrometer (AvaSpec-ULS2048XL-EVO, Avantes). The measurement spot could be translated using the micrometer screws, whose readings were calibrated using reverse illumination and a mirror in the object plane. For spectroscopy of reciprocal space images (Figure 3, Supporting Information File 1, Figure S2), we used the 100× (NA = 0.95) objective. For spectroscopy of real space images (Figure 1), we used the 20× (NA = 0.60) objective. A white diffuse reference tile (WS-2, Avantes) was used as the reference for spectroscopy measurements. Illumination was provided by a xenon or a halogen light source.

Electron microscopy

Top-view images of single scales were acquired with a Zeiss Ultra Plus 55 scanning electron microscope (Zeiss, Oberkochen, Germany) using an in-lens secondary electron

detector at 5 kV acceleration voltage. The scales and replicas were attached to an aluminum holder via a conductive carbon tape. These samples were coated with gold using a Sputter Coater 108 (Cressington Scientific Instruments, Watford, UK). The settings were: sputter time 120 s, current 40 mA, and background pressure 0.08 mbar. Cross-sectional images of single scales were recorded using a focused ion beam scanning electron microscope (Scios2, Thermo Fisher Scientific, Waltham, MA, USA) using an Everhart–Thornley detector and an in-lens secondary electron detector at 5 kV acceleration voltage. These samples were coated with gold using a Cressington 208 HR sputter coater. Elemental analysis was performed with 8 kV acceleration voltage, using an EDX detector attached to the Zeiss SEM (X-Max silicon drift energy-dispersive spectrometer, detector area 50 mm^2, Oxford Instruments, UK).

Lattice periodicity

The lattice periodicity was estimated from SEM images using ImageJ/Fiji [51]. Briefly, SEM images were calibrated using the annotated scale bar and converted from 8-bit to float. Domains with a consistent hexagon appearance were cropped to a square and windowed using a circular Gaussian-smoothed mask. We analyzed images whose 2D Fourier transforms had six symmetric and sharp amplitude peaks. The periodicity k of the orientation {111} was estimated as the average of the distances of the three unique peaks from the DC point, and the nearest neighbor distance $2k/\sqrt{3}$ was multiplied with $\sqrt{2}$ to obtain the unit cell size.

Preparation of titania replicas

Individual scales were scraped off from the elytra and transferred to a glass slide. Scales were etched using an argon plasma etching device (Emitech K1050X, Quorum, Laughton, UK). The settings were: etching time 36 min, power 50 W, argon pressure 0.9 mbar. Negative titania replicas were fabricated from the etched scales using a sol–gel chemistry protocol modified from ([24]). Briefly, titania sol was synthesized by adding 2 mL of hydrolyzed titanium ethoxide to a pre-mixed solution containing 1.6 mL of concentrated trifluoroacetic acid (99%) and 0.4 mL of concentrated hydrocloric acid (12 M). After stirring the mixture for 20 min, 4 mL of ethanol was added to adjust the viscosity of the solution. Titania sol was formed by stirring the mixture continuously for 24 h. Two drops of 1 µL of titania sol were dripped onto the etched weevil scales at opposing points and a glass slide was placed on top to ensure even infiltration via capillary forces. To solidify the sol and evaporate the residual solvent, the scales were heated in an oven at 100 °C for 20 min. Then, the top slide was removed. The scale template was removed by acid etching, using drops of a 3:1 mixture of concentrated nitric and hydrochloric acids, followed by heating at 130 °C for 15 min. The replicas were then cleaned using deionized water. Titanium(IV) ethanolate (33–35% TiO_2), tetraethyl orthosilicate (TEOS 98%), and the standard chemicals (trifluoroacetic acid, nitric acid (68%, technical), hydrochloric acid (35%, technical), and perchloric acid (60%)) were purchased from VWR (Vienna, Austria).

Full-wave photonic modeling

Light scattering by the single diamond network nanostructure was simulated with the three-dimensional finite-difference time-domain (FDTD) method, using Ansys Lumerical 2024 R1 (Ansys Inc., Canonsburg, PA, USA). The diamond nanostructures were approximated via an idealized single diamond network approximated by triply periodic minimal surface model from its level-set equation [52]. Diamond geometries were set up in a rectangular simulation box with two lateral directions. While the in-plane boundaries had periodic boundary conditions, the boundary along the incident light directions had a perfectly matched layer (PML) boundary. The diamond geometry used to simulate the scale response had a lattice parameter of 400 nm and a solid fill fraction of 0.44, with a refractive index of cuticular chitin [4]. Simulations of the negative template had the inverse network with a solid fill fraction of 0.56 and a refractive index between 1.55 and 2.00. Light, with wavelengths of 400–800 nm, was incident in normal direction onto the structure that was oriented along the [100] direction. The angle-integrated reflectivity was obtained from a monitor placed above the light source spanning the entire simulation box area.

Supporting Information

Supporting Information File 1

Material characterization, polarization properties, lattice estimation, additional microscopy and spectroscopy.
[https://www.beilstein-journals.org/bjnano/content/supplementary/2190-4286-16-1-S1.pdf]

Acknowledgements

We thank Viola Bauernfeind and Ullrich Steiner (Adolphe Merkle Institute) for technical support with the FIB-SEM, Gregor Zickler (PLUS) for technical support with the SEM, and the three anonymous reviewers for the helpful feedback on the manuscript.

Funding

We acknowledge the start-up funding from the University of Salzburg.

Author Contributions

Norma Salvadores Farran: formal analysis; investigation; validation; visualization; writing – original draft; writing – review & editing. Limin Wang: conceptualization; formal analysis; investigation; methodology; supervision; writing – original draft; writing – review & editing. Primoz Pirih: conceptualization; formal analysis; investigation; supervision; visualization; writing – original draft; writing – review & editing. Bodo D. Wilts: conceptualization; formal analysis; investigation; project administration; resources; supervision; writing – original draft; writing – review & editing.

ORCID® iDs

Limin Wang - https://orcid.org/0000-0002-8849-9621
Primoz Pirih - https://orcid.org/0000-0003-1710-444X
Bodo D. Wilts - https://orcid.org/0000-0002-2727-7128

Data Availability Statement

The data that supports the findings of this study is available from the corresponding author upon reasonable request.

References

1. Kinoshita, S.; Yoshioka, S. *ChemPhysChem* **2005,** *6,* 1442–1459. doi:10.1002/cphc.200500007
2. Srinivasarao, M. *Chem. Rev.* **1999,** *99,* 1935–1962. doi:10.1021/cr970080y
3. Joannopoulos, J. D.; Johnson, S. G.; Winn, J. N.; Meade, R. D. *Photonic Crystals: Molding the Flow of Light,* 2nd ed.; Princeton University Press: Princeton, 2008. doi:10.1515/9781400828241
4. Leertouwer, H. L.; Wilts, B. D.; Stavenga, D. G. *Opt. Express* **2011,** *19,* 24061–24066. doi:10.1364/oe.19.024061
5. Saba, M.; Wilts, B. D.; Hielscher, J.; Schröder-Turk, G. E. *Mater. Today: Proc.* **2014,** *1,* 193–208. doi:10.1016/j.matpr.2014.09.023
6. Zhang, J. P.; Chu, D. Y.; Wu, S. L.; Ho, S. T.; Bi, W. G.; Tu, C. W.; Tiberio, R. C. *Phys. Rev. Lett.* **1995,** *75,* 2678–2681. doi:10.1103/physrevlett.75.2678
7. Wierer, J. J., Jr.; David, A.; Megens, M. M. *Nat. Photonics* **2009,** *3,* 163–169. doi:10.1038/nphoton.2009.21
8. Chow, E.; Lin, S. Y.; Johnson, S. G.; Villeneuve, P. R.; Joannopoulos, J. D.; Wendt, J. R.; Vawter, G. A.; Zubrzycki, W.; Hou, H.; Alleman, A. *Nature* **2000,** *407,* 983–986. doi:10.1038/35039583
9. Vats, N.; John, S.; Busch, K. *Phys. Rev. A* **2002,** *65,* 043808. doi:10.1103/physreva.65.043808
10. Vukovic, I.; Voortman, T. P.; Merino, D. H.; Portale, G.; Hiekkataipale, P.; Ruokolainen, J.; ten Brinke, G.; Loos, K. *Macromolecules* **2012,** *45,* 3503–3512. doi:10.1021/ma300273f
11. Dolan, J. A.; Wilts, B. D.; Vignolini, S.; Baumberg, J. J.; Steiner, U.; Wilkinson, T. D. *Adv. Opt. Mater.* **2015,** *3,* 12–32. doi:10.1002/adom.201400333
12. Yao, P.; Schneider, G. J.; Prather, D. W.; Wetzel, E. D.; O'Brien, D. J. *Opt. Express* **2005,** *13,* 2370–2376. doi:10.1364/opex.13.002370
13. Li, J.; Herman, P. R.; Kitaev, V.; Wong, S.; Ozin, G. A. *Appl. Phys. Lett.* **2005,** *87,* 141106. doi:10.1063/1.2077857
14. Galusha, J. W.; Richey, L. R.; Gardner, J. S.; Cha, J. N.; Bartl, M. H. *Phys. Rev. E* **2008,** *77,* 050904. doi:10.1103/physreve.77.050904
15. Wilts, B. D.; Michielsen, K.; Kuipers, J.; De Raedt, H.; Stavenga, D. G. *Proc. R. Soc. B* **2012,** *279,* 2524–2530. doi:10.1098/rspb.2011.2651
16. Wu, X.; Rodríguez-Gallegos, F. L.; Heep, M.-C.; Schwind, B.; Li, G.; Fabritius, H.-O.; von Freymann, G.; Förstner, J. *Adv. Opt. Mater.* **2018,** *6,* 1800635. doi:10.1002/adom.201800635
17. Yablonovitch, E. *J. Phys.: Condens. Matter* **1993,** *5,* 2443–2460. doi:10.1088/0953-8984/5/16/004
18. Van Opdenbosch, D.; Johannes, M.; Wu, X.; Fabritius, H.; Zollfrank, C. *Photonics Nanostruct. - Fundam. Appl.* **2012,** *10,* 516–522. doi:10.1016/j.photonics.2012.02.006
19. Pouya, C.; Stavenga, D. G.; Vukusic, P. *Opt. Express* **2011,** *19,* 11355–11364. doi:10.1364/oe.19.011355
20. Bermúdez-Ureña, E.; Kilchoer, C.; Lord, N. P.; Steiner, U.; Wilts, B. D. *iScience* **2020,** *23,* 101339. doi:10.1016/j.isci.2020.101339
21. Seago, A. E.; Brady, P.; Vigneron, J.-P.; Schultz, T. D. *J. R. Soc., Interface* **2009,** *6,* S165–S184. doi:10.1098/rsif.2008.0354.focus
22. Parisotto, A.; Steiner, U.; Cabras, A. A.; Van Dam, M. H.; Wilts, B. D. *Small* **2022,** *18,* 2200592. doi:10.1002/smll.202200592
23. Galusha, J. W.; Richey, L. R.; Jorgensen, M. R.; Gardner, J. S.; Bartl, M. H. *J. Mater. Chem.* **2010,** *20,* 1277–1284. doi:10.1039/b913217a
24. Galusha, J. W.; Jorgensen, M. R.; Bartl, M. H. *Adv. Mater. (Weinheim, Ger.)* **2010,** *22,* 107–110. doi:10.1002/adma.200902852
25. Chellappan, M.; Divya, K. K.; Viswanathan, A.; Mohan, L. K. Pests and Their Management in Rubber. In *Trends in Horticultural Entomology;* Mani, M., Ed.; Springer; pp 1477–1488. doi:10.1007/978-981-19-0343-4_63
26. Hutacharern, C.; Sabhasri, B. *Z. Angew. Entomol.* **1985,** *99,* 170–174. doi:10.1111/j.1439-0418.1985.tb01975.x
27. Waite, G. K. Pests and pollinators of mango. In *Tropical fruit pests and pollinators: Biology, economic importance, natural enemies and control;* Peña, J. E.; Sharp, J. L.; Wysoki, M., Eds.; CABI Publishing: Wallingford, UK, 2002; pp 103–129. doi:10.1079/9780851994345.0103
28. Wilts, B. D.; Michielsen, K.; De Raedt, H.; Stavenga, D. G. *J. R. Soc., Interface* **2012,** *9,* 1609–1614. doi:10.1098/rsif.2011.0730
29. Maldovan, M.; Thomas, E. L. *Nat. Mater.* **2004,** *3,* 593–600. doi:10.1038/nmat1201
30. Galusha, J. W.; Jorgensen, M. R.; Richey, L. R.; Gardner, J. S.; Bartl, M. H. *Proc. SPIE* **2009,** *7401,* 74010G. doi:10.1117/12.824181
31. Djeghdi, K.; Steiner, U.; Wilts, B. D. *Adv. Sci.* **2022,** *9,* 2202145. doi:10.1002/advs.202202145
32. Chang, Y.; Ogawa, Y.; Jacucci, G.; Onelli, O. D.; Tseng, H.-Y.; Vignolini, S. *Adv. Opt. Mater.* **2020,** *8,* 2000432. doi:10.1002/adom.202000432
33. Schultz, T. D.; Bernard, G. D. *Nature* **1989,** *337,* 72–73. doi:10.1038/337072a0
34. Stavenga, D. G. *J. Exp. Biol.* **2023,** *226,* jeb245221. doi:10.1242/jeb.245221
35. Jessop, A.-L.; Pirih, P.; Wang, L.; Patel, N. H.; Clode, P. L.; Schröder-Turk, G. E.; Wilts, B. D. *J. R. Soc., Interface* **2024,** *21,* 20240185. doi:10.1098/rsif.2024.0185
36. Kilchoer, C.; Pirih, P.; Steiner, U.; Wilts, B. D. *J. Exp. Biol.* **2019,** *222,* jeb213306. doi:10.1242/jeb.213306

37. Bartl, M. H.; Galusha, J. W.; Jorgensen, M. R. Oxide-Based Photonic Crystals from Biological Templates. In *Functional Metal Oxide Nanostructures;* Wu, J.; Cao, J.; Han, W.-Q.; Janotti, A.; Kim, H.-C., Eds.; Springer Series in Materials Science; Springer New York: New York, NY, U.S.A., 2011; pp 175–207. doi:10.1007/978-1-4419-9931-3_9
38. Mosaddeq-ur-Rahman, M.; Yu, G.; Soga, T.; Jimbo, T.; Ebisu, H.; Umeno, M. *J. Appl. Phys.* **2000,** *88,* 4634–4641. doi:10.1063/1.1290456
39. Rantala, J. T.; Kärkkäinen, A. H. O. *Opt. Express* **2003,** *11,* 1406–1410. doi:10.1364/oe.11.001406
40. Zięba, M.; Wojtasik, K.; Tyszkiewicz, C.; Gondek, E.; Nizioł, J.; Suchanek, K.; Wojtasik, M.; Pakieła, W.; Karasiński, P. *Materials* **2021,** *14,* 7125. doi:10.3390/ma14237125
41. Antonello, A.; Brusatin, G.; Guglielmi, M.; Bello, V.; Mattei, G.; Zacco, G.; Martucci, A. *J. Nanopart. Res.* **2011,** *13,* 1697–1708. doi:10.1007/s11051-010-9923-4
42. Himmelhuber, R.; Gangopadhyay, P.; Norwood, R. A.; Loy, D. A.; Peyghambarian, N. *Opt. Mater. Express* **2011,** *1,* 252–258. doi:10.1364/ome.1.000252
43. Wang, F.; Luo, Z.; Qing, S.; Qiu, Q.; Li, R. *J. Alloys Compd.* **2009,** *486,* 521–526. doi:10.1016/j.jallcom.2009.06.195
44. Sarkar, S.; Gupta, V.; Kumar, M.; Schubert, J.; Probst, P. T.; Joseph, J.; König, T. A. F. *ACS Appl. Mater. Interfaces* **2019,** *11,* 13752–13760. doi:10.1021/acsami.8b20535
45. Jolivet, A.; Labbé, C.; Frilay, C.; Debieu, O.; Marie, P.; Horcholle, B.; Lemarié, F.; Portier, X.; Grygiel, C.; Duprey, S.; Jadwisienczak, W.; Ingram, D.; Upadhyay, M.; David, A.; Fouchet, A.; Lüders, U.; Cardin, J. *Appl. Surf. Sci.* **2023,** *608,* 155214. doi:10.1016/j.apsusc.2022.155214
46. Palik, E. D. *Handbook of optical constants of solids;* Academic Press, 1998; Vol. 3.
47. Refractive index database. https://refractiveindex.info/?shelf=main&book=TiO2 (accessed Oct 14, 2024).
48. Verstraete, C.; Mouchet, S. R.; Verbiest, T.; Kolaric, B. *J. Biophotonics* **2019,** *12,* e201800262. doi:10.1002/jbio.201800262
49. Vogler-Neuling, V. V.; Talts, Ü.-L.; Ferraro, R.; Weigand, H.; Finco, G.; Winiger, J.; Benedek, P.; Kusch, J.; Karvounis, A.; Wood, V.; Leuthold, J.; Grange, R. *Adv. Photonics Res.* **2024,** *5,* 2400058. doi:10.1002/adpr.202400058
50. Mouchet, S. R.; Verstraete, C.; Kaczmarek, A. M.; Mara, D.; van Cleuvenbergen, S.; Van Deun, R.; Verbiest, T.; Maes, B.; Vukusic, P.; Kolaric, B. *J. Biophotonics* **2019,** *12,* e201800470. doi:10.1002/jbio.201800470
51. Schindelin, J.; Arganda-Carreras, I.; Frise, E.; Kaynig, V.; Longair, M.; Pietzsch, T.; Preibisch, S.; Rueden, C.; Saalfeld, S.; Schmid, B.; Tinevez, J.-Y.; White, D. J.; Hartenstein, V.; Eliceiri, K.; Tomancak, P.; Cardona, A. *Nat. Methods* **2012,** *9,* 676–682. doi:10.1038/nmeth.2019
52. Wohlgemuth, M.; Yufa, N.; Hoffman, J.; Thomas, E. L. *Macromolecules* **2001,** *34,* 6083–6089. doi:10.1021/ma0019499

License and Terms

BEILSTEIN JOURNAL OF NANOTECHNOLOGY

Better together: biomimetic nanomedicines for high performance tumor therapy

Imran Shair Mohammad[*1], Gizem Kursunluoglu[2], Anup Kumar Patel[1], Hafiz Muhammad Ishaq[*3], Cansu Umran Tunc[2,4], Dilek Kanarya[2], Mubashar Rehman[5], Omer Aydin[2,6,7,8] and Yin Lifang[9]

Review

Open Access

Beilstein J. Nanotechnol. **2025,** *16,* 1246–1276.
https://doi.org/10.3762/bjnano.16.92

Received: 22 January 2025
Accepted: 15 July 2025
Published: 05 August 2025

This article is part of the thematic issue "Micro- and nanoscale effects in biological and bioinspired materials and surfaces".

Guest Editor: T. H. Büscher

Address:
[1]Department of Radiology, City of Hope National Medical Center, 1500 East Duarte Rd., Duarte, California 91010, USA, [2]Nanothera Lab, Drug Application and Research Center (ERFARMA), Erciyes University, 38039, Kayseri, Turkey, [3]Faculty of Veterinary and Animal Sciences, Muhammad Nawaz Shareef University of Agriculture, Multan 66000, Pakistan, [4]Utah Center for Nanomedicine, University of Utah, Salt Lake City, UT, 84112, USA, [5]Department of Pharmacy, Quaid-i-Azam University, Islamabad 45320, Pakistan, [6]Department of Biomedical Engineering, Erciyes University, 38039, Kayseri, Turkey, [7]Nanotechnology Research and Application Center (ERNAM), Erciyes University, Kayseri 38039, Turkey, [8]Clinical Engineering Research and Implementation Center (ERKAM), Erciyes University, Kayseri 38040, Turkey and [9]Department of Pharmaceutics, School of Pharmacy, China Pharmaceutical University, Nanjing 211198, PR China

Email:
Imran Shair Mohammad[*] - imohammad@coh.org;
Hafiz Muhammad Ishaq[*] - drhafizishaq@hotmail.com

* Corresponding author

Keywords:
biomimetic nanoparticles; homotypic binding; nanomaterials; targeted drug delivery; tumor therapy

Abstract

The emergence of nanotechnology offers a promising avenue for enhancing cancer treatment outcomes. In this context, biomimetic nanoparticles have emerged as an exciting frontier in the field of biomedicine. These nanoparticles can emulate essential biological functions, drawing from an abundant reservoir of cellular capabilities. This includes engaging in biological binding, precise homing to tumor sites, and interaction with immune cells. These inherent traits endow biomimetic nanoparticles with a suite of intelligent features, including biocompatibility, low immunogenicity, reduced toxicity, immune evasion, prolonged circulation, homotypic binding, enhanced tumor targeting, and the capability of precise delivery. By integrating biologically inspired coatings derived from cell membranes with nanoparticle cores, these carriers become highly versatile vessels for encapsulating a wide array of therapeutic agents. As a result, they are being extensively harnessed for the precise delivery of drugs and genes, underpinning numerous biomedical applications. This discussion delves into the challenges and opportunities presented by biomimetic nanoparticles and

offers a comprehensive exploration of their fundamentals and recent breakthroughs, with an eye towards clinical translation. By bridging the gap between scientific innovation and clinical utility, biomimetic nanoparticles hold great promise for advancing the field of cancer treatment.

Introduction

Cancer is a complex disease, which involves numerous cells and their crosstalk with surrounding environment, including immunosuppression in T cells via PD-1/PD-L1 axis, recruitment of stem cells via CXCR4/CXCL2 chemokine axis, maturation of immune cells via membrane interactions, and various other physical/chemical interactions, uncover the emergence of cell membrane-based drug delivery systems [1,2]. Cancer treatment has been revolutionized, yet cancer is treated with traditional methods, that is, chemotherapy, radiotherapy, and surgical intervention, accompanied by several lethal implications along with low solubility, poor bioavailability, and fatal off-target effects [3,4]. In addition, the escalation of new glitches such as drug sensitivity in tumor cells has been reduced due to the emergence of multidrug resistance (MDR) by various factors, including ATP-dependent drug efflux, selective stress of drugs, altered DNA repair mechanisms, cellular heterogeneity, recurrence, and altered metabolic responses inevitably leads to treatment failure [5-7]. Anyhow, an early detection of cancer enhances treatment success and increases survival. However, monotherapies proved limited therapeutic efficacy. Thus, an effective multiple cancer therapeutic regimen has been employed to successfully eradicate tumors [8]. To overcome these discrepancies, an efficient, biocompatible, nontoxic, non-immunogenic and precisely targeted drug delivery system is desirable [9].

Conventional non-targeted delivery systems result in off-targeting as they also affect healthy cells and organs. Therefore, there is an ultimate need to produce suitable carriers, which can reduce the side effects and toxicity, while achieving high therapeutic efficacy. Consequently, the use of nanoparticles (NPs) has been proven a great breakthrough in the field of cancer treatment. NPs, smaller than 100 nm, show unique physicochemical and biological properties, and incredible potential of being therapeutic agent carriers for biomedical applications [10,11]. They are capable to deliver a range of therapeutics including genes, vaccines, biological macromolecules, hydrophobic/hydrophilic drugs, and proteins to certain organs such as brain, liver, spleen, lungs, arterial walls for both immediate and sustained release. Their degradation and release kinetics can be controlled or manipulated by different methods and incorporation or conjugation of specific materials. Importantly, they mainly focus on different biomaterials, drug release behavior, targeting ability, and surface modifications [12-15].

A variety of nanoparticles have been researched including liposomes, polymer NPs, solid lipid NPs, and hybrid NPs [16]. Nanoscale drug carriers with the advantage of high penetration, long circulation, and significant targetability have been employed for the treatment of various fatal diseases such as cancer, Alzheimer's, stroke, and diabetes [17-19]. However, the development of optimum NP drug carriers is still critical as they all come with several limitations. For example, liposomes can carry hydrophilic drugs that quickly eliminate from the system. Also, metal or polymeric NPs face poor biodegradability, which enriches them in kidney and liver tissues for longer than required, causing toxic effects while showing inadequate efficacy at the desired site [20,21].

Biomimetic NPs potentially fit in this scenario. These are specialized NPs, where the surface is designed with natural biocompatible biomaterials that can mimic the structure and functions of the natural cells to improve targetability, enhance biocompatibility, and increase retention time with minimum undesired immune reaction [22]. Importantly, efficient tracking and profound interactions within complex biological environments can be achieved by using biomimetic NPs with prolonged circulation time, summarized in Figure 1.

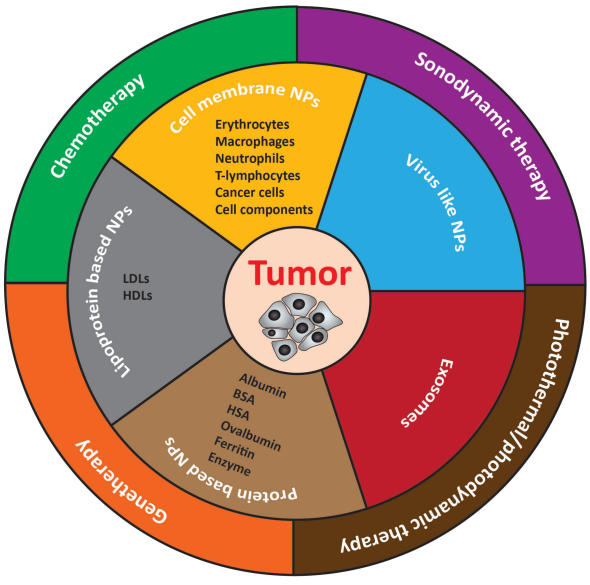

Figure 1: Types and antitumor application of biomimetic nanomedicines.

Moreover, research in NP-mediated drug delivery has been shifted to focus on the use of cell-derived cancer therapies/engineered or live cells for cancer therapies and immunomodulation. In terms of drug discovery and delivery, various strategies have been developed including cell-based drug delivery, which provides a promising platform to enhance therapeutic drug delivery, increase efficacy, reduce off-targeting and side effects of the therapeutic regimen. By utilizing recent advances in micro/nanotechnology and molecular pharmaceutics, potent bioinspired cell-based therapeutics could be obtained by genetic engineering, endocytosis, chemical bioconjugation, and physical modifications (Figure 2) [23]. More precisely, cell membranes or whole cells, which could exploit homotypic targeting mechanism and exosomes, are being employed to deliver anticancer/immune modulating drugs or vaccine delivery [2,24]. The cell or biomimetic NPs can alter biological functions via various pathways and can be effectively used in targeting and manipulating their action site to achieve desired therapeutic effects. Thus, it is critical to explore and understand the types, targeting mechanism, immune responses, and therapeutic outcomes of such NPs. Unlike previous reports, here, we provide an up-to-date review of recent advances in biomimetic nanomedicines with a specific focus on their types and recent advancements only for cancer treatment.

This review focuses on the recent advancements in biomimetic nanomedicines engineered with various biomaterials, emphasizing their interactions with different types of tumors and tumor microenvironment (TME). It presents the role of biomimetic nanoparticles in developing targeted cancer therapies by selectively eliminating the tumor cells, sparing healthy tissues, and possibly stimulating the immune system. The review explores biomimetic nanodrug delivery systems as antitumor immunotherapy, including antigen/adjuvant delivery and tumor antigen-specific T-cell targeting strategies. It also summarizes the characteristics of biomimetic drug delivery nanocarriers designed from different cell types, their modification with specific ligands for precise and enhanced tumor targeting and TME responsiveness. Finally, by integrating nature-inspired architec-

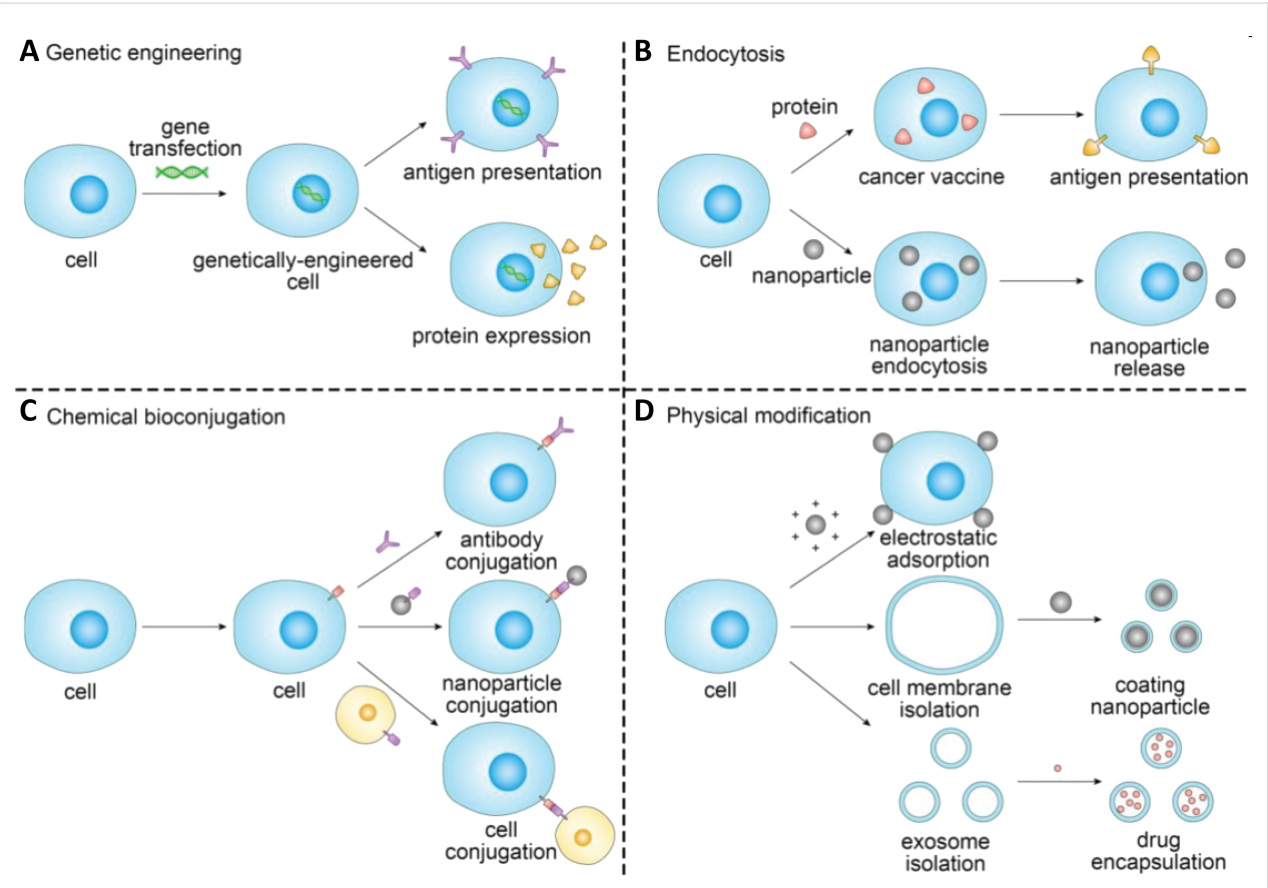

Figure 2: Schematic of the representative strategies of engineering cells for cancer immunotherapy. The cells used for drug delivery and cancer immunotherapy involve erythrocytes, platelets, leukocytes, cancer cells and stem cells. Figure 2 was reproduced from [23] (© 2019 X. Xu et al., published by Ivyspring International Publisher, distributed under the terms of the Creative Commons Attribution 4.0 International License, https://creativecommons.org/licenses/by/4.0).

tures, these smart, multifunctional biomimetic nanoparticles offer a promising path to overcome current therapeutic challenges and revolutionize precision oncology.

Review

1 Types of biomimetic nanoparticles

1.1 Cell membrane-camouflaged nanoparticles

Cell membranes have emerged as an ideal strategy to protect synthetic nanoparticles during circulation. Cell membrane-coated biomimetic nanoparticles act like source cells with significant biomedical properties including biocompatibility, low toxicity, and potent targetability. They are recognized as "own" by the immune system and are not phagocytosed, thus increasing circulation and retention time [25].

1.1.1 Erythrocytes. Erythrocytes (red blood cells, RBCs) are the most abundant form of cells in the blood and an excellent candidate for long-time circulation of drug carriers. Among all eukaryotic cells, they are easiest to use for biomedical applications as they lack mature DNA and other organelles [26]. There are various methods to load agents inside or attach onto the surface of RBCs by either chemical or physical methods such as (A) hypotonic presealing, (B) hypotonic loading, (C) electroporation, and (D) surface coupling (Figure 3). Generally, RBC membranes can be separated by hypotonic treatment to remove intracellular components (Figure 3A,B). Erythrocyte drug loading has been demonstrated by encapsulating artemether as a model drug and using different modifications of the hypotonic methods [27]. When exposed to a hypotonic solution, water enters the erythrocytes, an equilibrium is established as substances enter and leave the swollen RBCs. A hypotonic solution is prepared by dissolving a relatively higher amount of the drug. Drug loading can be enhanced by carrying out the process at 0 °C as the fatty acid chains in the membrane solidify and pores remain open for a longer period. In contrast, storage of erythrocytes at 0 °C before drug loading prevents pore formation, leading to lowered drug loading. Finally, the tonicity of the solution is raised to attain isotonic conditions, and the rising temperature leads to the resealing of RBCs. It was also observed that optimum drug loading is achieved at a certain tonicity level. Therefore, artemether loading was higher when using 0.6% NaCl hypotonic solution than when using 0.3% NaCl solution [28]. Drugs can also be loaded in erythrocytes by electroporation (Figure 3C). Although electroporation is an easy and feasible loading method, its scale-up is challenging [29]. Many researchers have attached drugs, therapeutic proteins, or drug-loaded nanoparticles onto the surface of RBCs to transfer innate characteristics of RBCs to the nanoparticles (Figure 3D) [30].

1.1.2 Macrophages. Macrophages are a critical part of the TME. They are specific type of immune cells that can recognize healthy somatic cells as "own" cells and exogenous particles, cancer cells, and pathogens as "foreign" and phagocytose them [31]. Therefore, macrophage membranes could be used to escape the reticuloendothelial system (RES), target cancer cells and pathogens, and enhance tumor accumulation. Recently, Huang et al. reported macrophage membrane-coated targeted NPs for tumor inhibition and macrophage polarization. They incorporated methyltransferase like 14 (METTL14) and RS09 inside the macrophages and then functionalized the surface with DSPE-PEG2000-cRGD. METTL14 significantly inhibits the

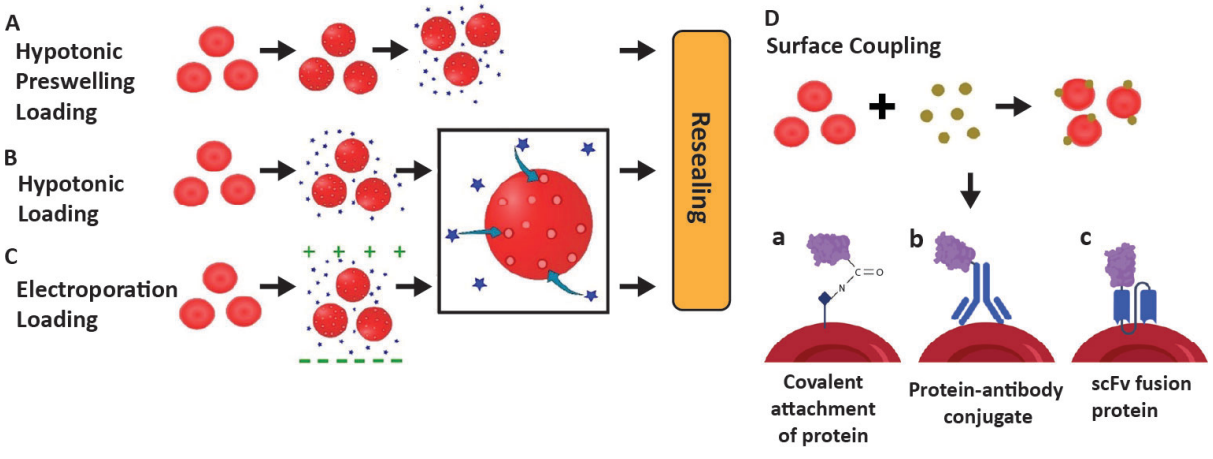

Figure 3: Drug loading strategies in erythrocytes. (A) Preswelling in hypotonic solution containing an excess of the drug, (B) drug loading in hypotonic solution containing an excess of the drug, (C) electroporation-mediated drug loading in isotonic solution containing an excess of the drug, and (D) hitchhiking drug or drug carrier attached on the surface of erythrocyte. Panels a–c represent three different methods of RBCs coupling with therapeutic proteins. Figure 3 D was reproduced from [30] (© 2021 J. S. Brenner et al., published by Annual Reviews, distributed under the terms of the Creative Commons Attribution 4.0 International License, https://creativecommons.org/licenses/by/4.0).

tumor growth in vitro, downregulates TICAM2, and inhibits the macrophage polarization by the Toll-like receptor 4 pathway. The combinatory NPs induce antitumor M1 macrophage polarization, and cRGD modification further enhances tumor accumulation [32].

In another study, Hou et al. employed M1-type macrophages and loaded them with sorafenib (SF) to develop lipid nanoparticles (M1/SLNPs). The M1/SLNPs showed an increase in tumor accumulation and enhanced the SF tumor targeting efficacy. Furthermore, they increased the ratio of M1-type macrophages, CD3+CD4+T cells, and CD3+CD8+T cells in the tumor tissues, indicating the reversal of immunosuppressive TMEs (Figure 4) [33]. Interestingly, Xue et al. applied magnetothermal (MHT) antitumor therapy because of minimal invasiveness, high efficiency, and better tissue penetration. They developed small Fe@Fe_3O_4-DHCA nanoparticles (≈14 nm) and coated them with macrophages (RAW267.4 cells) for magnetic resonance imaging (MRI) and MHT of solid tumors. The Fe@Fe_3O_4-DHCA NPs showed accumulation in tumor cells resulting in enhanced MRI and MHT performance in vitro. Furthermore, RAW267.4-loaded with Fe@Fe_3O_4-DHCA demonstrated efficiency in vivo. Thus, Fe@Fe_3O_4-DHCA nanoparticles showed great application potential for tumor diagnosis and therapy [34].

1.1.3 Neutrophils. Neutrophils are among the most abundant and frontline phagocytes among the white blood cells [35]. Neutrophils are the first to appear at the site of inflammation and easily cross different biological barriers such as blood–tissue barrier, blood–brain barrier (BBB) or blood–tumor barrier (BTB). Therefore, neutrophil membrane-coated nanoparticles have been successfully employed to cross biological barriers to target cancer cells. The neutrophil membranes enhanced circulation life, efficiently targeted tumors, and inhibited growth by photodynamic therapy. Neutrophil membrane-coated celastrol-loaded PEG-PLGA nanoparticles were prepared to treat pancreatic cancer, where drug delivery is limited by the blood–pancreas barrier. The nanoparticles successfully crossed the barrier, accumulated selectively in pancreatic cancer cells, inhibited tumor growth and its metastasis to the liver [36]. Similarly, neutrophil membrane-coated PLGA nanoparticles were used for the combination of near-IR imaging and photodynamic therapy of hepatocellular carcinoma [37].

1.1.4 T lymphocytes (T cells). T cells are highly specific and more actively identify foreign bodies, including cancer cells. In

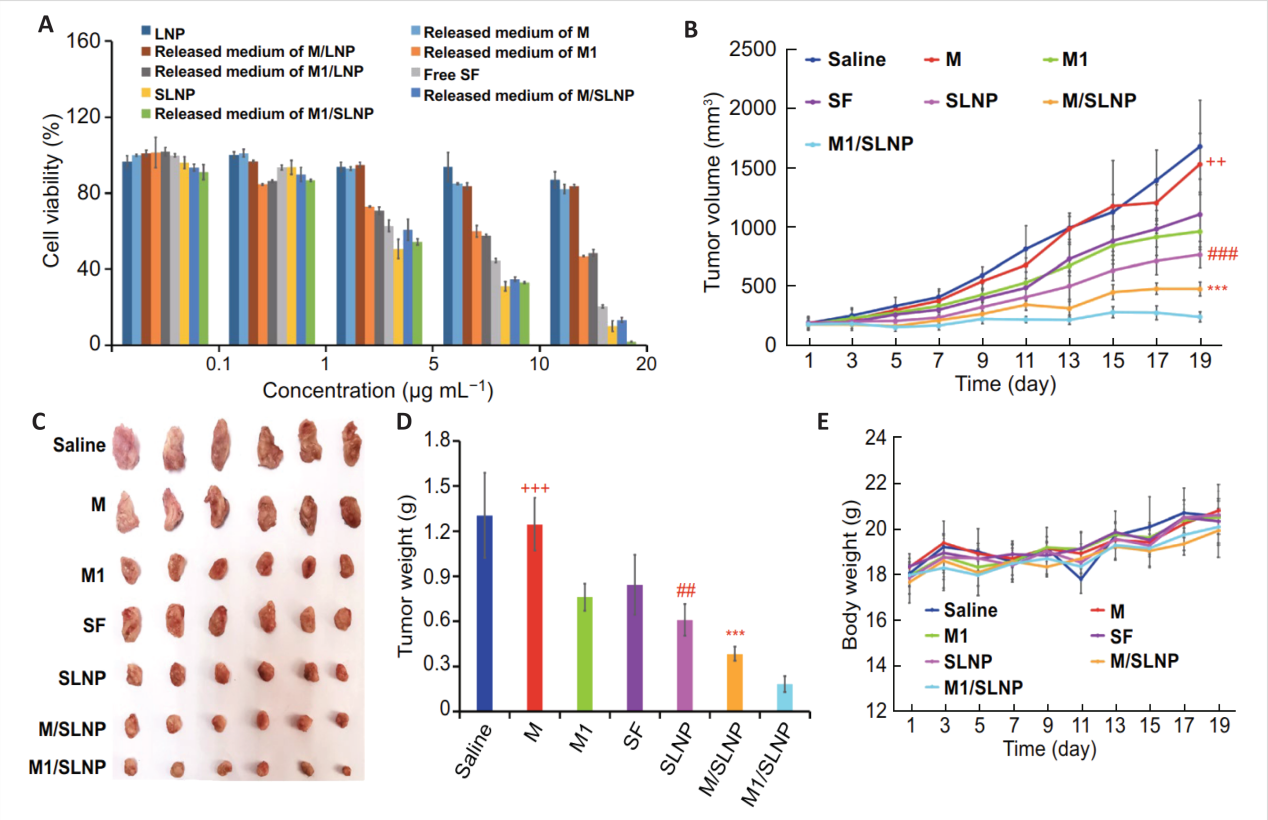

Figure 4: In vitro and in vivo antitumor efficacy of M1/SLNP. (A) Cell viability in Hepa1-6 cells, (B–D) changes in tumor volume and weights, and (E) body weight changes in Hepa1-6 tumor bearing mice. Figure 4 was reproduced from [33] (© 2021 T. Hou et al., published by Springer Nature, distributed under the terms of the Creative Commons Attribution 4.0 International License, https://creativecommons.org/licenses/by/4.0).

addition to directly killing cancer cells, T cells organize the immune response by recruiting other immune cells and also prevent the immune response from overreacting [38]. Therefore, T cells are the most extensively studied immune cells in cancer immunotherapy [39]. Kang et al. have developed T lymphocyte membrane-coated nanoparticles that can target cancer by T cell-associated proteins and kill cancer by cytotoxic agents loaded in the nanoparticles. Unlike T cells, the T lymphocyte membrane-coated nanoparticles are resistant to immunosuppressive and apoptotic signaling [40]. In recent years, the applications of T cell-mediated cancer cell targeting have expanded. One example is intravenous administration of T cell membrane-coated nanoparticles directed to the cancerous organ by an externally applied magnetic field, followed by immune cell membrane-mediated cancer targeting. This strategy led to accelerated accumulation of nanomedicine in the tumor with minimal off-target exposure [41]. Wayteck et al. have prepared liposomes that can hitchhike on cells to the tumor site and get separated to perform their cytotoxic activity [42].

1.1.5 Cancer cells. Cancer cells establish their own mechanism to escape immune response [43]. They are tightly bound by surface proteins to hinder the penetration of drugs and drug carriers. In addition, cancer cell membranes express specific receptors and antigens that help them recognize and target through a homotypic binding mechanism [44,45]. Therefore, cancer cell membranes are also extensively explored to localize nanomedicines to cancer cells. Cancer cell membrane-coated nanoparticles can enter the cancer cells simply by fusion. The membrane coating is fused with the cancer cell membrane and delivers the payload inside the cytosol [46]. A distinctive characteristic of cell membrane-coated nanocarriers is that they include carbohydrates, proteins, and lipids, in addition to being biocompatible [47]. For this reason, cancer membranes are also preferred for vaccine delivery [48]. Some researchers incorporated RBC membrane components into cancer cell membranes to form a hybrid membrane, which facilitates simultaneously circulation in blood after intravenous administration and fusion with cancer cells to deliver payload intracellularly (hybrid cell membrane). However, the cell membrane-coated nanoparticles targeting efficiency is not universal as it does not always result in successful targeting, may be due to host–donor mismatch or intra-patient differences in cancer cell expression. This problem could be solved by using patient-derived cancer membranes for personalized cancer treatment [49].

1.1.6 Cell component platelets. Platelets lack a nucleus and are the smallest of all blood components. They circulate freely in the body and can reach deep tissues. Importantly, platelets are reported to activate and specifically bind to cancer cells [50]. Therefore, platelets have been used to load cytotoxic drugs for prolonged circulation in blood, escape immune response, and reach the tumor site [51]. Due to their small size, platelet-based NPs can be made as small as 175 nm [52]. Notably, they can be stored at −80 °C while preserving their cytotoxic and targeting functions [53]. Tang et al. have prepared Janus platelet microrobots that use asymmetrically surface-attached urea enzyme to drive them through the body fluids. The asymmetrical catalysis of urea to ammonia acts as a gas jet to propel the microrobots to the desired site of action [54].

1.2 Lipoprotein-based biomimetic nanoparticles

Lipoproteins are complex structures with a lipid core, usually cholesterol esters and triglycerides, surrounded by a monolayer of phospholipids and apolipoproteins [55]. Lipoproteins include, among others, low-density lipoprotein (LDL) and high-density lipoprotein (HDL). Due to the hydrophobic core and prolonged circulation, they have been used in drug delivery. The lipid core of the lipoprotein tend to load a variety of lipophilic drug molecules [56,57], while the apolipoproteins guide the formation of lipoproteins, provide structural integrity, activate or inhibit lipoprotein metabolism, and act as ligands for lipoprotein receptors. Moreover, they play an important role in tumor regulation and progression, as they are potent and specific inhibitors of 3-hydroxy-3-methylglutaryl coenzyme A reductase, the rate-limiting enzyme of the mevalonate metabolic pathway [58]. The use of statins, drugs that lower plasma lipoprotein levels, has been shown to reduce the risk of certain types of cancer [59,60].

1.2.1 Low-density lipoprotein (LDL). Lipoproteins can load small molecular drugs (including chemotherapeutic agents), nucleic acids, and other macromolecules [61]. LDL was the first lipoprotein used for drug delivery and imaging applications. The particles are smaller than 50 nm and are characterized by surface apolipoprotein B-100. The uptake of LDL inside the cells occurs mainly via receptor-mediated endocytosis by a structurally similar receptor family, similar to LDL receptor proteins including LDL receptor-related protein (LRP or megalin), very-low density lipoprotein (vLDL) receptor, and apolipoprotein E receptor-2 (ApoER2) [62]. After uptake, LDL is phagocytosed to form lysosomes. However, lysosomes can degrade most drugs, which limits their applications [63,64]. Zhu et al. proposed reconstituted LDL nanoparticles to prevent acidic degradation. They added fatty acids to encapsulate drugs in the lipid core because fatty acids are not degraded in the lysosome and can safeguard the payload [64].

1.2.2 High-density lipoprotein (HDL). HDL plays an important role in cancer regulation due to its effect on immunomodulation, and anti-inflammatory and antioxidant action to suppress tumor growth [65]. Additionally, HDL can modulate the tumor

microenvironment and reverse cholesterol transportation to cancer cells to limit their growth [66]. Consequently, HDL has been reported as a therapeutic agent to alleviate certain types of cancers. Recently, Rink et al. have prepared HDL nanoparticles that target SCARB1, inhibit cholesterol uptake, and induce ferroptosis of the cancer cells [67]. HDL presents many features that make it ideal for drug delivery applications including biocompatibility and biodegradability, long circulation, hydrophobic core, and small size. The main lipoprotein of HDL is alpha apolipoprotein (apo A-I and apo A-II) that can bind SR-BI receptors overexpressed on cancer cells. Unlike LDL, HDL is transported directly into the cytosol bypassing lysosomal degradation [68]. Reconstituted HDL (rHDL) is now developed by changing the chemical composition or morphology to optimize drug delivery. When loaded with chemotherapeutic agents, rHDL shows outstanding active targeting and anticancer activities [57]. Moreover, rHDL showed potential to co-load hydrophobic paclitaxel and hydrophilic doxorubicin in apo A-I targeted rHDL nanoparticles. These nanoparticles showed superior antitumor activity in vitro and in vivo [69]. Previously, rHDL combined with a hydrophilic polymeric core and a magnetic core for imaging applications [70,71].

Cholesterol has been associated as a key player in the emergence of many diseases including medulloblastoma. HDL nanoparticles have been prepared to treat medulloblastoma by disrupting the cholesterol signaling pathway (Figure 5). The HDL nanoparticles were successfully taken up by the medulloblastoma cells (DAOY) and hedgehog-driven Ewing sarcoma cells. Results showed that HDL nanoparticles induce efflux of cholesterol to lower its intracellular level and induce tumor cell death by disrupting cholesterol signaling [72]. Therefore, HDL nanoparticles not only an effective drug carrier with inherent targeting ability but can also act as a therapeutic agent against cholesterol-dependent diseases.

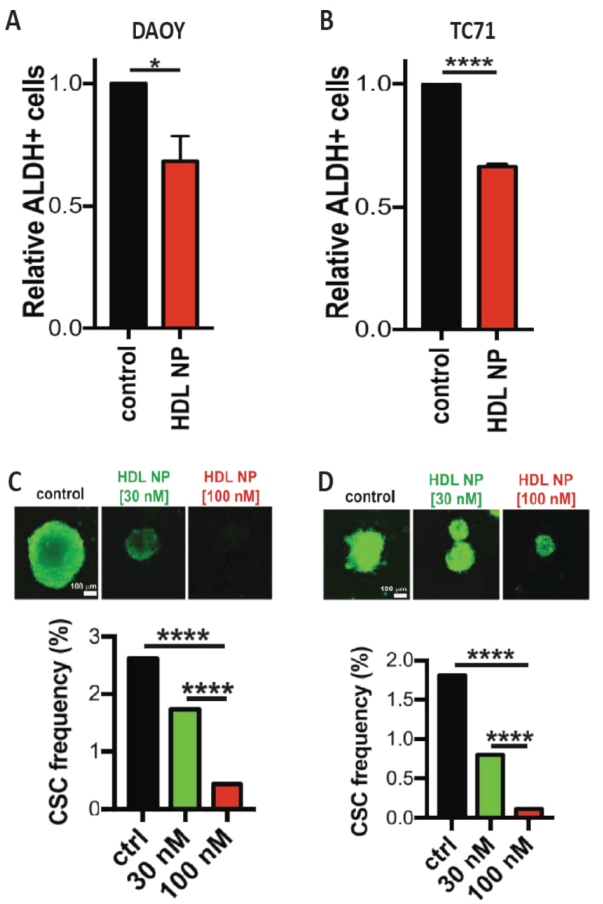

Figure 5: Cancer stem cell depletion with HDL NPs. (A, B) DAOY and TC71 cells were treated with or without HDL NPs depicting the proportion of ALDH+ cells relative to control, (C, D) DAOY or TC71 cells seeded in the presence or absence of HDL NPs to assess sphere formation. Figure 5 was adapted from [72] (© 2018 J. B. Bell et al., published by Springer Nature, distributed under the terms of the Creative Commons Attribution 4.0 International License, https://creativecommons.org/licenses/by/4.0).

1.3 Protein-based biomimetic nanoparticles

Peptides and proteins are essential to maintain hemostasis by binding various biomolecules circulating in blood. They not only maintain the electrolyte and osmotic pressure but also deliver a variety of molecules across the body [73,74]. Peptides possess different functional groups on their surface that can act as a template for various NPs, mostly for diagnostic or multifunctional theranostic applications.

1.3.1 Albumin. Albumin is a major protein present in blood and widely studied for drug–protein interaction and nanoparticle corona formation studies. Due to its immunocompatibility, long half-life, and abundance of binding sites it is considered safe for drug delivery applications. In fact, albumin-conjugated drugs are already used in clinical practice [75]. Albumin molecules can be used as a template to surface-decorate inorganic/metallic nanoparticles by biomineralization. In this method, the thiol group at the albumin surface acts as scaffold for synthesis of nanoparticles [76]. The thiol groups are protonated at neutral pH and can entrap Au(III) ions. When the pH is changed to basic (≈12), Au(III) is reduced to Au and gold nanoparticles are formed [77]. Synthesis of albumin-templated nanomaterials depends upon many factors. Yang et al. produced ceria nanoparticles, nanoclusters, and nanochains by changing molar concentration, time of reaction, and temperature. They found that size and morphology of the nanomaterials can be optimized by careful tuning of switchable ionic redox systems (Ce^{3+}/Ce^{4+}), the unique structure of protein, and reducible disulfide groups [78-80].

1.3.2 Bovine serum albumin. Bovine serum albumin (BSA) is widely used in biomedical applications such as supplemental

growth media and protein standards. BSA was used as a template for the synthesis of organic–inorganic hybrid nanoparticles. BSA has some immunogenic effects and is therefore used in immunotherapy and analytic bioassay applications [78,81-83].

1.3.3 Human serum albumin. Human serum albumin (HSA) has biomedical applications as HAS-templated NPs exhibit immune escape, enhanced stability, and high drug loading [84-87]. HSA NPs can load drugs and contrast agents directly and prolong their circulation [88]. Furthermore, cancer cells overexpress albumin receptors on their surface. Therefore, albumin nanoparticles have an intrinsic ability to target cells by fusion to the surface proteins [89].

Just like drug–protein binding in vivo, nanoparticles can adsorb plasma proteins at their surface in blood circulation and form a corona, which can alter their biodistribution, cell uptake, and intracellular degradation [90]. Thus, as the protein corona increases, albumin proteins affect nanoparticle fate in vivo. As albumin is the most abundant protein in the blood, precoating with albumin has been shown to prevent adsorption of other plasma proteins and degradation of nanoparticles in vivo [91,92].

1.3.4 Ovalbumin. Ovalbumin (OVA) is a major component of egg white and a readily available protein for drug delivery applications. It forms crosslinked gels and responds to changes in pH and temperature [93]. To escape the RES, ovalbumin nanoparticles are conjugated with polyethylene glycol. Controlling the PEG/OVA ratio allows for fine-tuning of critical physical properties, such as particle size, elasticity, and mesh size [94]. Like BSA, ovalbumin can activate an immune response and the presence of endotoxin contaminants activates macrophages and dendritic cells [95]. Therefore, ovalbumin nanoparticles are generally limited to immunotherapeutic applications.

1.3.5 Ferritin-based biomimetic nanoparticles. Ferritin is an iron transport protein and possesses a hollow cage-like structure, which offers high drug loading. Initially, ferritin was only used as a template to develop diagnostic agents [96]. Later, it was used to encapsulate a wide range of therapeutic agents. Importantly, ferritin receptors are overexpressed in cancer cells and serve as a platform for active targeting by using ferritin nanoparticles. Bellini et al. synthesized ferritin nanoparticles for in vitro and in vivo targeting of cancer cells [97]. As ferritin is prepared by genetic engineering, it can be genetically modified to recombinant ferritin. This property was exploited to design redox and pH dual-responsive ferritin nanoparticles. In drug-loaded mesoporous silica nanoparticles, ferritin was used as a gating material. It covered the pores to prevent drug release and opened only when activated by redox or pH stimuli [98]. Similarly, recombinant ferritin can be used as a carrier of macromolecules such as enzymes by electrostatic interaction with the negatively charged interior of the ferritin cage [99].

1.3.6 Enzyme-based biomimetic nanoparticles. Enzymes are biological catalysts and proteins by nature. Multienzymes are complex structures in which enzymes that perform sequential functions of a metabolic pathway are noncovalently associated with each other. The multifunctional enzyme complexes inspired researchers to design multienzyme complexes of their own choice. Initially, multiple enzymes were co-loaded in liposomes to perform different steps of a metabolic pathway [100]. Later, this strategy has evolved into the development of artificial organelles, which contain enzymes for a complex cascade reaction. Artificial organelles consist of capsosomes with a polymeric shell containing multiple liposomes, where each liposome may carry a certain type of enzyme. The capsosomes can efficiently enter the cell, and the enzymes exert their specific activities intracellularly [101]. More recently, the microfluidic spray technique was used to load alcohol oxidase and catalase into hollow hydrogel microspheres. The microfluidic spray technique provided excellent control over the number, type, and spatial control of the enzyme. The enzyme cascade was successfully applied to reduce the alcohol levels as an alternative antidot for alcohol intoxication [102].

1.4 Exosome-based biomimetic nanoparticles

Exosomes are endogenous extracellular vehicles released by most of the cells. These phospholipid bilayer nanovesicles are surface-enriched with proteins accounting for their dynamic and prominent roles in immune escape, cell–cell communication, and specific cell uptake [103]. They are small in size (30–150 nm), bypass biological barriers, and are efficiently taken up by cells due to their surface markers [104]. The International Society for Extracellular Vesicles has set out guidelines on the purity of extracellular vesicles depending upon intended applications [105]. Through exosomes, donor cells can transfer exogenous substances, such as proteins, mRNAs, microRNAs (miRNAs), and lipids, to recipient cells. Consequently, these naturally equipped nanocarriers have been used for drug delivery [106].

Exosomes are usually isolated from biological samples by centrifugation, size exclusion chromatography, ultrafiltration, immune affinity, and commercial kits [107]. Microfluidic devices are now aiding the separation of exosomes by acoustic cell separation [108,109]. The drugs can be either directly load in exosomes or exosomes are sliced to remove contents and reassembled [110]. The interaction between exosomes and host cells is very complex involving recognition, binding, cellular

uptake, and intracellular transport. These steps are specific to different types of target cells and determine the fate of exosomes [107]. Moreover, they offer prolonged circulation, excellent target specificity, and intracellular delivery without degradation. Exosomes have also been used to deliver chemotherapeutic agents, nucleic acids, macromolecules, and diagnostic agents. Thus, exosomes are ideal delivery vehicles for therapeutic treatments that should be specific to the targeting sites with low toxicity to other organs, high encapsulation and delivery efficiencies. They protect the payload while in circulation and maintain a steady release profile [111].

1.5 Virus-like particles

Virus or virus subunits have long been used as vaccines for the protection against various diseases. Nanotechnology has advanced this field by facilitating the safe delivery of vaccines and improving their immunogenicity [112]. The presence of viral nucleic acids has been a key concern in medical applications, which limits the use of viruses in living organisms. Virus-like particles are multimeric nanoparticles consisting of viral proteins but lack viral genetic material. Thus, they lack pathogenicity but offer virus-associated specific tissue targeting and intracellular delivery of payload [113]. For example, Dashti et al. reported a novel method to encapsulate guest proteins in murine polyoma virus capsomeres; the virus capsomere was prepared by expression of viral protein in recombinant *Escherichia coli*. Then the virus capsomere was transferred to a dialysis bag and allowed to self-assemble into nanoparticles in assembly buffer. The virus-like particles efficiently protected the payload and successfully delivered multiple proteins directly into cytosol of the cells [114] and induced a strong immune response due to the presence of viral epitopes. Plant virus-like particles have been used to treat canine oral melanoma using radio-immunotherapy (Figure 6).

Bacteriophages are also widely used for drug delivery applications. M13 phage is the most extensively studied phage for targeted drug delivery. In a recent study, the DNA of the M13 phage was modified to encode for SPARC binding peptide and cathepsin B cleavage peptide. Then, superparamagnetic iron oxide nanoparticles were covalently bonded to cathepsin B expressed on M13 phages to track their intracellular delivery [115]. Excellent control of shape, size, and genetic modification makes virus-like particles an excellent opportunity for safe and effective delivery of payload to an intended site.

2 Biomedical applications of biomimetic nanoparticles

2.1 Chemotherapy

In recent years, the development of novel chemotherapeutics and their delivery vehicles has received great attention. The delivery strategies can significantly improve chemotherapeutics efficacy and significantly overcome poor bioavailability, adverse effects, and resistance. Nevertheless, drug delivery is still facing many challenges, including non-specific targeting, rapid clearance, limited accumulation at tumor sites, and a set of biological barriers that need to be passed. So far, scientists have put great effort into fabricating smart nanomaterials that could achieve targeted drug delivery [116-119]. In biological systems, drug delivery systems interact with different body structures as well as physiologic environments. Thus, the structures of drug carriers must be constructed in a way that allows them to elude immune recognition and overcome barriers via effective bio-interfacing.

Within the scope of biomimetic nanomedicine for chemotherapeutic delivery, RBC-mimicking nanoparticles have been investigated extensively, as they are predominant cells in circulation, RBC membrane isolation is relatively easy, and they express various surface receptors that help immunocompatibility, immune evasion, and long half-life. RBC-mimicking nanostructures were investigated and successfully used for different tumor targeting and treatment applications [120-123]. In this respect, drug nanocrystals coated with RBC membrane and modified with a tumor-targeting peptide was successfully used for targeted therapy of glioma [124]. The peptide-modified nanosystem showed increased drug accumulation and enhanced therapeutic activity both in subcutaneous and orthotopic tumor models [125,126]. Another study regarding targeted therapy and improved drug delivery to the brain used the dual modification of RBC-coated lipid nanoparticles with T7 peptide, a ligand of transferrin receptor, and NGR peptide, a ligand of CD13 [127]. Dual modification with the peptides yielded the ability to overcome the BBB and target the glioma. In another study, RBC-covered graphene oxide quantum dots (GTDC@M) were investigated regarding the targeted therapy of metastatic breast cancer (Figure 7) [128]. The nanosystem was modified with TAT (T) and RGD (R) peptides for targeted delivery of the chemotherapeutics gamabufotalin (C) and doxorubicin (DOX) in triple-negative breast cancer (TNBC), resulting in potent inhibition of tumor growth and breast cancer metastasis. RBC membrane was also conjugated with gold nanostars to control the release with near-infrared irradiation. Also, RBC and platelet hybrid membrane-coated gold nanostars achieved targeted delivery to melanoma cells while avoiding macrophage phagocytosis [129].

Although RBC-camouflage nanomedicines are feasible biomimetic nanoplatforms, other cell membrane-coated drug delivery systems also provide promising therapeutic strategies [130-132]. Nanomaterials camouflaged with cancer cell membrane (CCM) have been used for a number of theranostic appli-

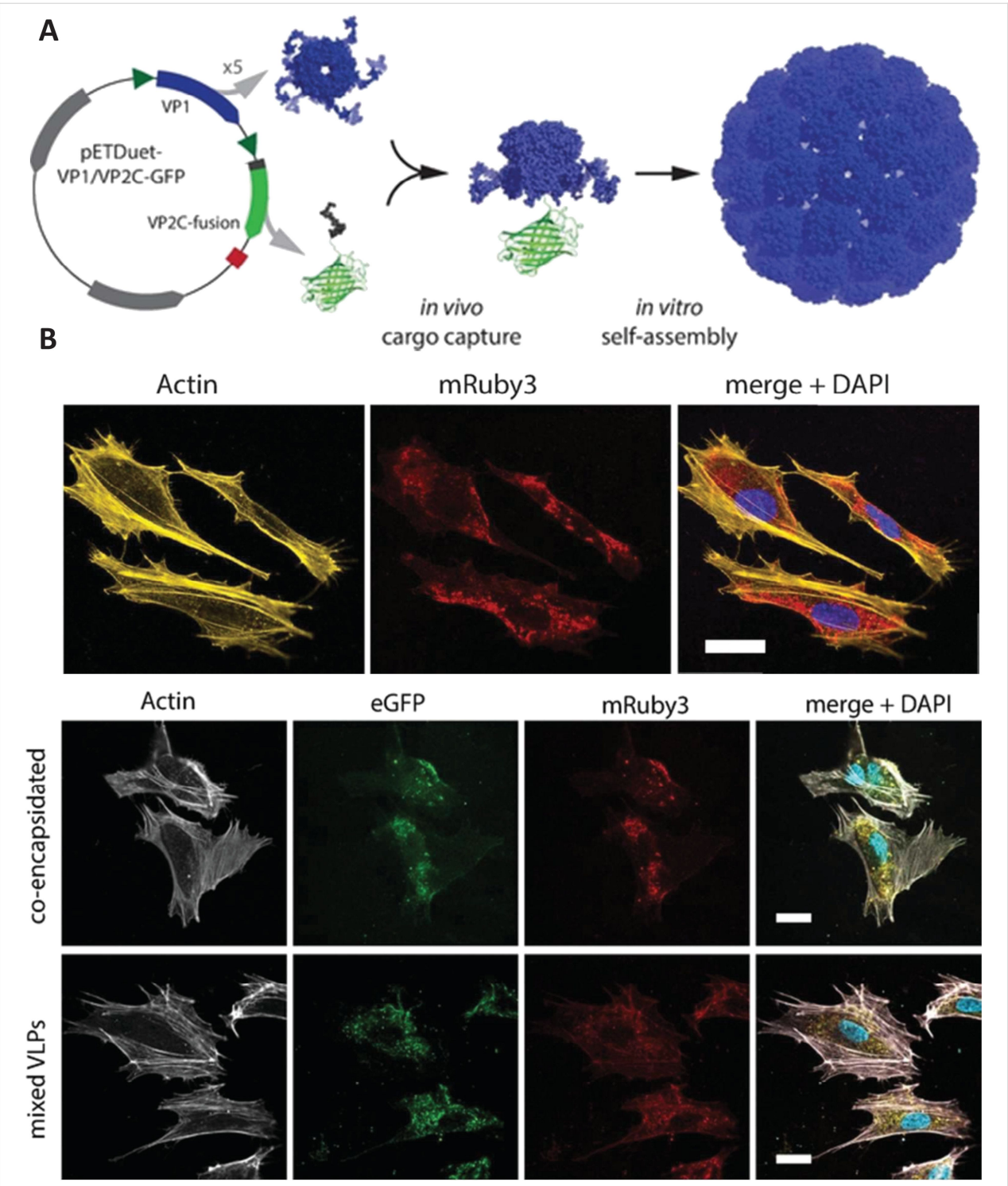

Figure 6: Schematic presentation of (A) cargo capture and self-assembly of virus-like particles, (B) cellular uptake of mRuby3-loaded VLPs, and (C) co-delivery of cargo proteins to HUVECs cells incubated with VLPs co-encapsulating GFP and mRuby3, or with a mixture of VLPs separately encapsulating the fluorescent proteins. Figure 6 was reprinted with permission from [114], Copyright 2018 American Chemical Society. This content is not subject to CC BY 4.0.

cations [133,134]. Rao et al. showed that CCM-coated nanoparticles displayed excellent targeting ability when the nanoparticle-coating membrane matched with the tumor (host) [49]. In this study, a CCM coating of gelatin nanoparticles was employed against head and neck squamous cell carcinoma. The nanoparticles coated with patient-derived CCM provide effec-

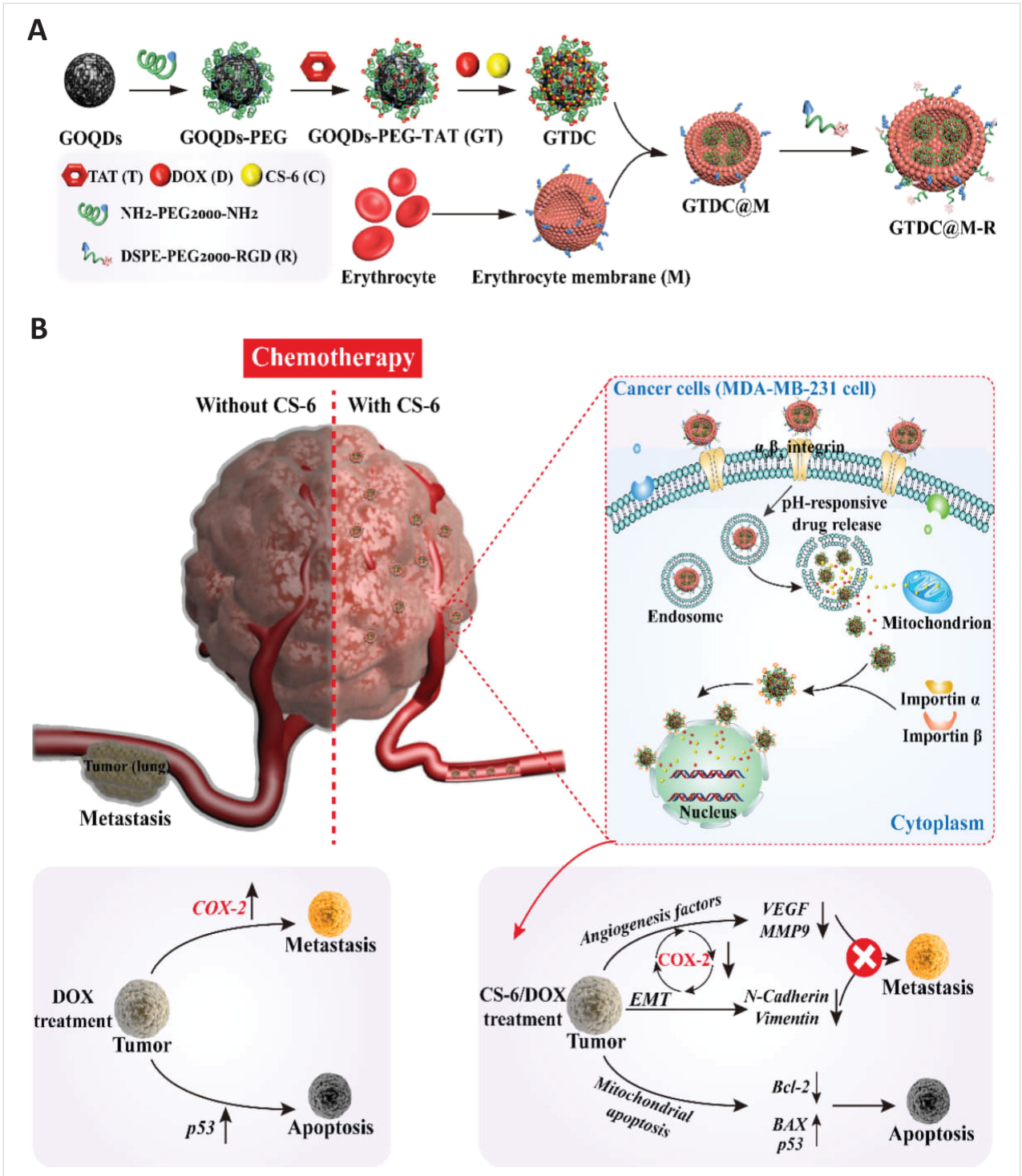

Figure 7: (A) Preparation of TAT and RGD modified RBC-covered graphene oxide quantum dot nanoparticles and (B) inhibition of tumor growth and metastasis mediated by the nanosystem and its proposed molecular mechanism. Figure 7 was reprinted from [128], *Acta Biomaterialia*, vol. 113, by J. Fan; B. Liu; Y. Long; Z. Wang; C. Tong; W. Wang; P. You; X. Liu, "Sequentially-targeted biomimetic nano drug system for triple-negative breast cancer ablation and lung metastasis inhibition", Pages 554–569, Copyright (2020), with permission from Elsevier. This content is not subject to CC BY 4.0.

tive targeting of the tumor in patient-derived tumor cells animal models through homologous targeting. In another study, the homologous targeting effect was successfully utilized to deliver doxorubicin (DOX), mefuparib hydrochloride (MHP) and poly(ADP-ribose) polymerase inhibitor in MCF7-tumor bearing mice [46]. In that study, a PEGylated-lipid nanoparticle

(PEG-liposome) with a mesoporous silica nanoparticle core (LM) was prepared, and then the nanosystem was coated with CCM (CCM@LM). The biomimetic nanomedicine showed high internalization in a way similar to an enveloped virus. The PEGylation of the inner cavity provided subcellular localization of payload in the nucleus subsequent to cellular internalization. The whole nanosystem demonstrated a significant antitumor activity. Shao et al. established X-ray-responsive CCM-covered mesoporous organosilica nanoparticles for the controlled release of DOX [135]. The drug-loaded nanoparticle was camouflaged with 4T1 membrane, and the biomimetic system showed prolonged circulation, enhanced tumor accumulation, and release of DOX under low-dose radiation. Furthermore, Mohammad at al. exploited homotypic mechanisms to enhance the therapeutic efficacy of chemotherapeutics in lung cancer MDR cell lines. They isolated different cell membranes (RBCs, 4T1, LO2, and A549-T) and constructed cell membrane-camouflaged biogenic nanoparticles to deliver antitumor paclitaxel and MDR-modulator disulfiram. Consequently, the MDR cancer cell membrane-coated nanoparticles (A549/T CM-HNPs) selectively recognized the source cells and increased the cellular internalization up to nine-fold via homotypic binding. Moreover, the A549/T CM-HNPs sensitized MDR cells to PTX by suppressing the P-gp activity 3.2-fold and induced apoptosis (70%) in homologous A549/T cells [45] (Figure 8).

Kong et al. developed biomimetic oxygen-carrying NPs and conjugated ultrasmall nanozyme on their surface; they further coated the NPs with bone marrow stromal cell membrane to target and successfully deplete leukemic cells in bone marrow and prevent homing of AML. Furthermore, the cell membrane acted as CXR4 antagonist to block the CXCR4/CXCL12-mediated homing of leukemia cells to the bone marrow and infiltration into other organs like the liver and spleen [136] (Figure 9).

Ke et al. altered the tumor glucose supply and metabolic pathways by designing RGD-modified, RBC membrane-coated glucose oxidase (Gox) and DOX metal organic framework bioreactors (RGD-mGZD). The RGD-mGZD NPs preferentially targeted the tumor site consuming the intratumoral oxygen and glucose to starve the tumor cells. At the same time DOX was released by the decomposition of the metal organic framework in acidic TME to induce chemotherapeutic effects and synergistically kill the tumor cells [137]. The immunosuppressive TME considerably attenuated the chemotherapeutic effect of various anticancer drugs. Therefore, reprogramming of TME and targeting tumor-associated macrophages (TAMs) could be a promising strategy to enhance chemotherapeutic efficacy. In this respect, Wang et al. synthesized bioengineered cancer cell membrane-coated, gemcitabine-loaded PLGA dual targeting NPs (PG@KMCM) for pancreatic cancer treatment. The PG@KMCM efficiently delivered gemcitabine to pancreatic cancer cells and TAMs simultaneously and potentiated the antitumor effect. Moreover, in combination with PD-L1, the PG@KMCM reprogrammed the immunosuppressive TME by eliminating the PD-L1 macrophages and therefore downregulating PD-L1 expression [138] (Figure 10).

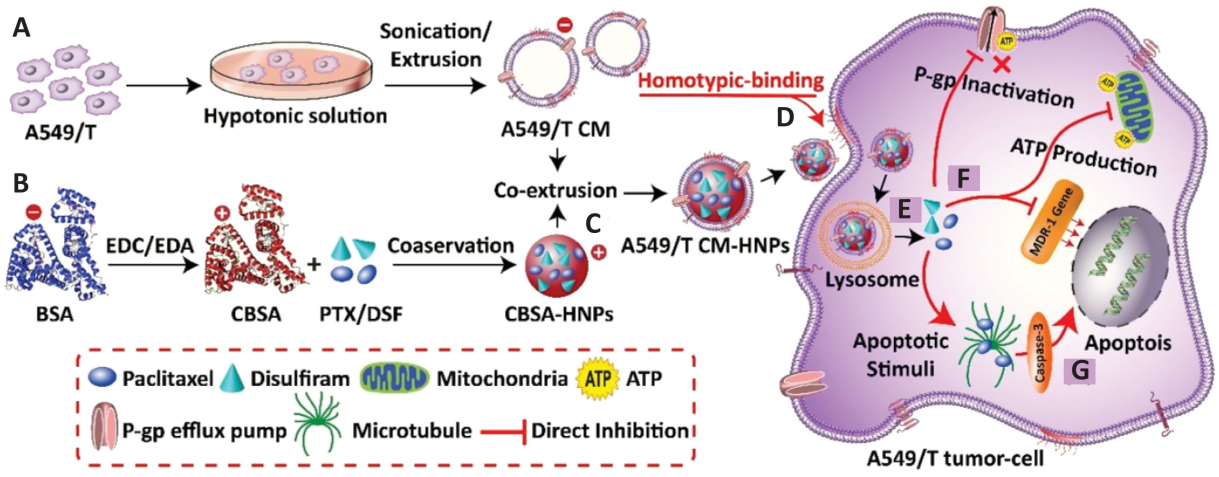

Figure 8: (A) Hypotonic treatment of taxol resistant A549/T cells to obtain A549/T cell membrane vesicles, (B) synthesis of cationic bovine serum albumin (CBSA), (C) hybrid nanoparticles (CBSA-HNPs) generation by sonication and co-extrusion, (D) A549/T CM-HNPs targeting via homotypic-binding mechanism, releasing (E) paclitaxel and disulfiram, and (F) inhibited ATP concentration, downregulated MDR-1 gene, and therefore suppressed P-gp activity and increased intracellular PTX to induce (G) caspase-3-dependent MDR tumor cell apoptosis. Figure 8 was reproduced from [45] (©2020 Mohammad et al., published by MDPI, distributed under the terms of the Creative Commons Attribution 4.0 International License, https://creativecommons.org/licenses/by/4.0).

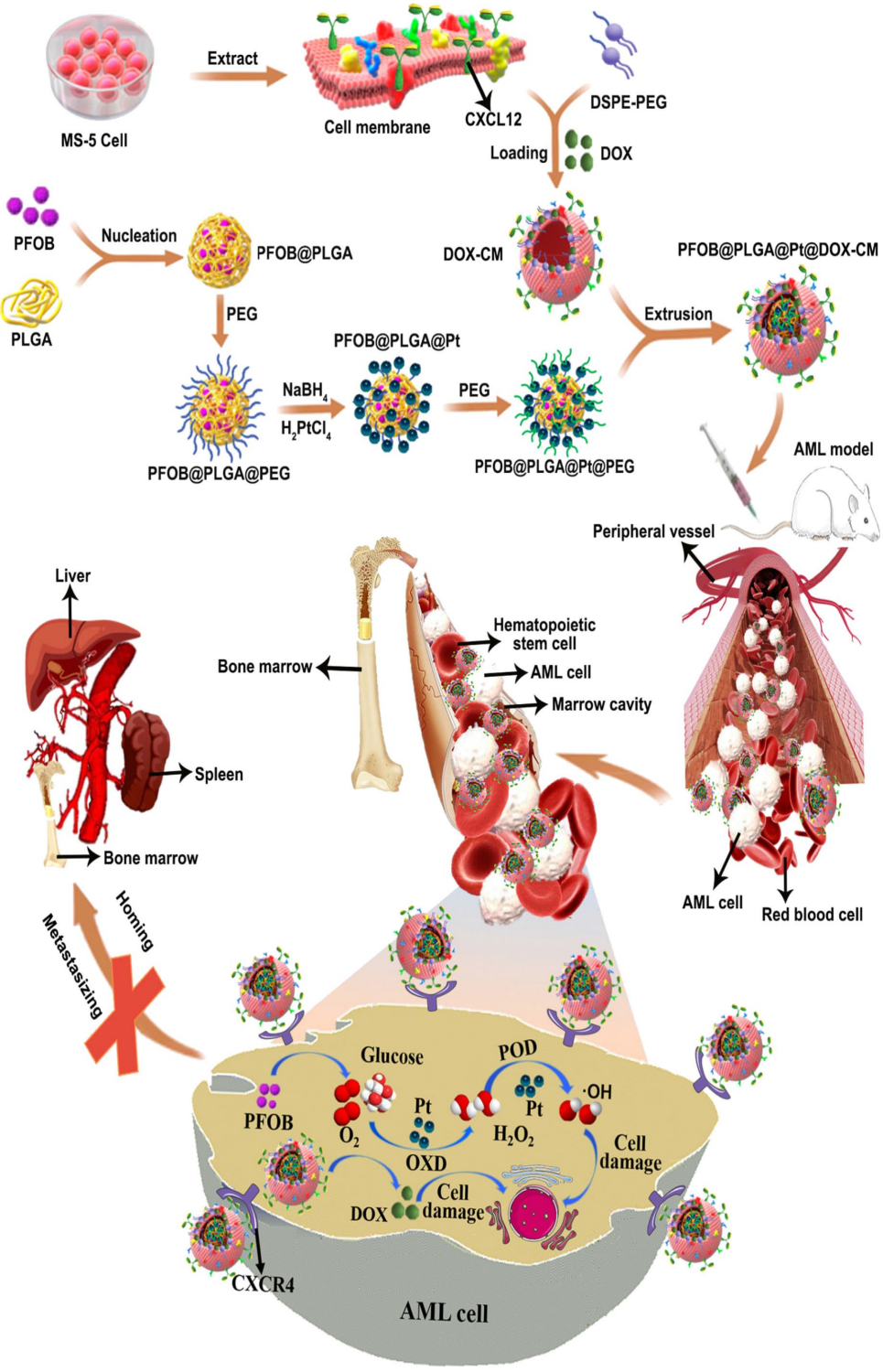

Figure 9: Schematic representation of biomimetic PFOB@PLGA@Pt@DOX-CM for anti-leukemia efficacy via chemotoxicity and excessive ROS generation to induce leukemia cell apoptosis. Furthermore, PFOB@PLGA@Pt@DOX-CM accumulate in the bone marrow and act as CXCR4 antagonists to block the leukemia cell-stroma adhesive interactions and prevent infiltration of AML cells to other normal organs, such as liver and spleen. Figure 9 was reproduced from [136] (© 2022 F. Kong et al., published by Elsevier B.V. on behalf of KeAi Communications Co. Ltd., distributed under the terms of the Creative Commons Attribution-NonCommercial-NoDerivatives 4.0 International License, https://creativecommons.org/licenses/by-nc-nd/4.0/). This content is not subject to CC BY 4.0.

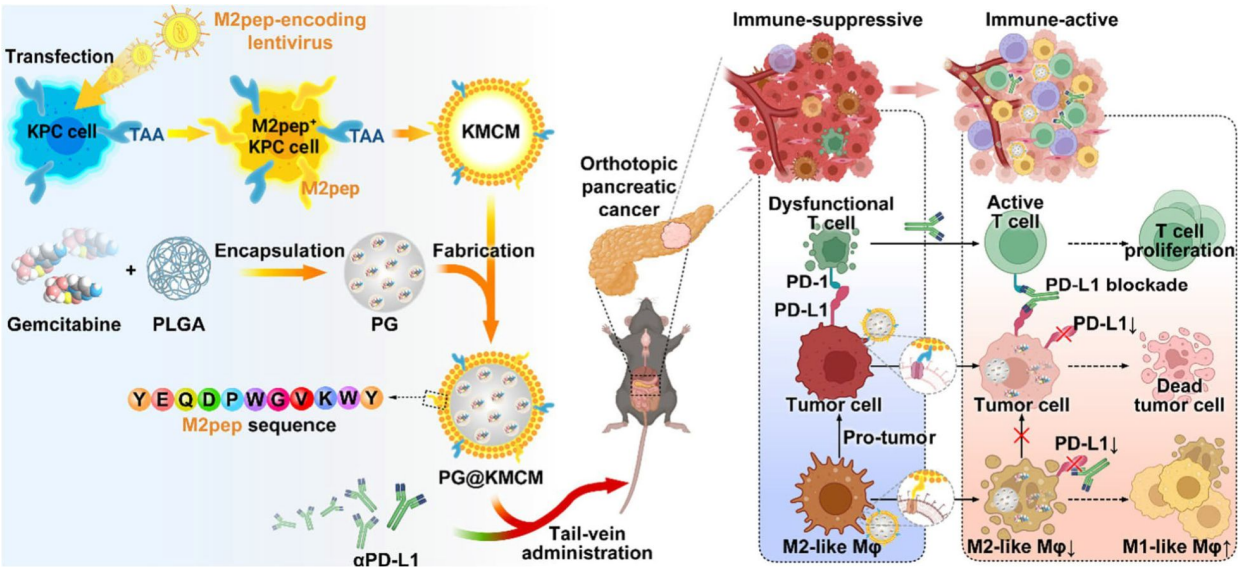

Figure 10: Fabrication of dual targeting PG@KMCM for chemoimmunotherapy in pancreatic cancer. Figure 10 was reproduced from [138] (© 2022 Wang et al., published by BMC (part of Springer Nature), distributed under the terms of the Creative Commons Attribution 4.0 International License, https://creativecommons.org/licenses/by/4.0).

Similarly, to attenuate the immunosuppressive TNBC TME, Li et al. constructed CRT-overexpressed tumor cell membrane-coated biomimetic NPs by encapsulating epirubicin (EPI), Gox, and hemin in ZIF-8 nanoparticles (mEHGZ). EPI induced immunogenic cell death (ICD), Gox and hemin initiated ROS generation, and the CRT membrane gave an "eat me" signal to dendritic cells (DCs) to invoke the tumor immunity cycle. Thus, the ICD effect promoted maturation of DCs and increased the infiltration of cytotoxic T lymphocytes at the tumor site, thus, reversing the immunosuppressive TME. Notably, mEHGZ in combination with anti-PD-L1 antibody dramatically reduced tumor growth and lung metastasis [139] (Figure 11).

To increase the chemotherapeutic drug delivery, Zhao et al. combined magnetite and DOX encapsulated in 6 BSA subunit to design a BSA magnetite nanotorpedo (BMNT). The BMNT significantly stops the leakage of DOX and prolonged its half-life in blood circulation to achieve efficient antitumor efficacy [140]. Against glioma, Du et al. designed hydrazone bond-conjugated DOX-manganese dioxide (MnO_2) NPs coated with C6 cell membrane (MnO_2-DOX-C6). MnO_2 promoted the decomposition of H_2O_2 to produce oxygen and increase the ROS via a Fenton-like reaction. Interestingly, the C6 membrane coating allowed MnO_2-DOX to target the glioma cells by homologous targeting and enhanced glioma cells apoptosis [141]. To improve the antitumor efficacy and bioavailability of chemotherapeutics, Gao et al. exploited albumin-mediated transportation and developed a biomimetic prodrug by modifying camptothecin with different fatty acid chain lengths. The series of in vitro and in vivo experiments confirmed the potent antitumor efficacy of CPT18C-HAS without obvious adverse effects [142]. It was reported that TNBC patients showed higher shear wave elasticity (SWE) α-SMA expression in tumor tissues than non-TNBC patients, which directly correlates to the neoadjuvant treatment efficacy. To confirm this phenomenon, Zheng et al. constructed TNBC membrane-coated, artesunate-loaded PLGA NPs (231M-ARS@PLGA) to regulate the SWE stiffness via cancer-associated fibroblast (CAF) inhibition. In the MDA-MB 231 and E0771 orthotopic tumor models, 231M-ARS@PLGA reduced the SWE stiffness and tumor hypoxia, which potently enhanced the antitumor effects of OTX and PD1 inhibitor. Importantly, single-cell sequencing demonstrated two main CAFs (extracellular matrix and wound-healing CAFs) that produce extracellular matrix could influence the tumor SWE stiffness as well as the antitumor effect of drugs. Moreover, biomimetic NPs reduced the CAF status, which in turn attenuates tumor hypoxia by increasing inflammatory blood vessels and oxygen transport capacity. This confirmed the role of CAFs on SWE stiffness and antitumor efficacy, which could be employed in clinical theranostics through non-invasive SWE imaging (Figure 12) [143].

2.2 Gene therapy

In order to achieve efficient delivery, the drug carriers must not degrade or be identified by nucleases and immune cells. Also, they need to pass multiple biological barriers and achieve high accumulation at the disease site with maximum internalization and endosomal escape [144]. In a recent study, Walweel et al.

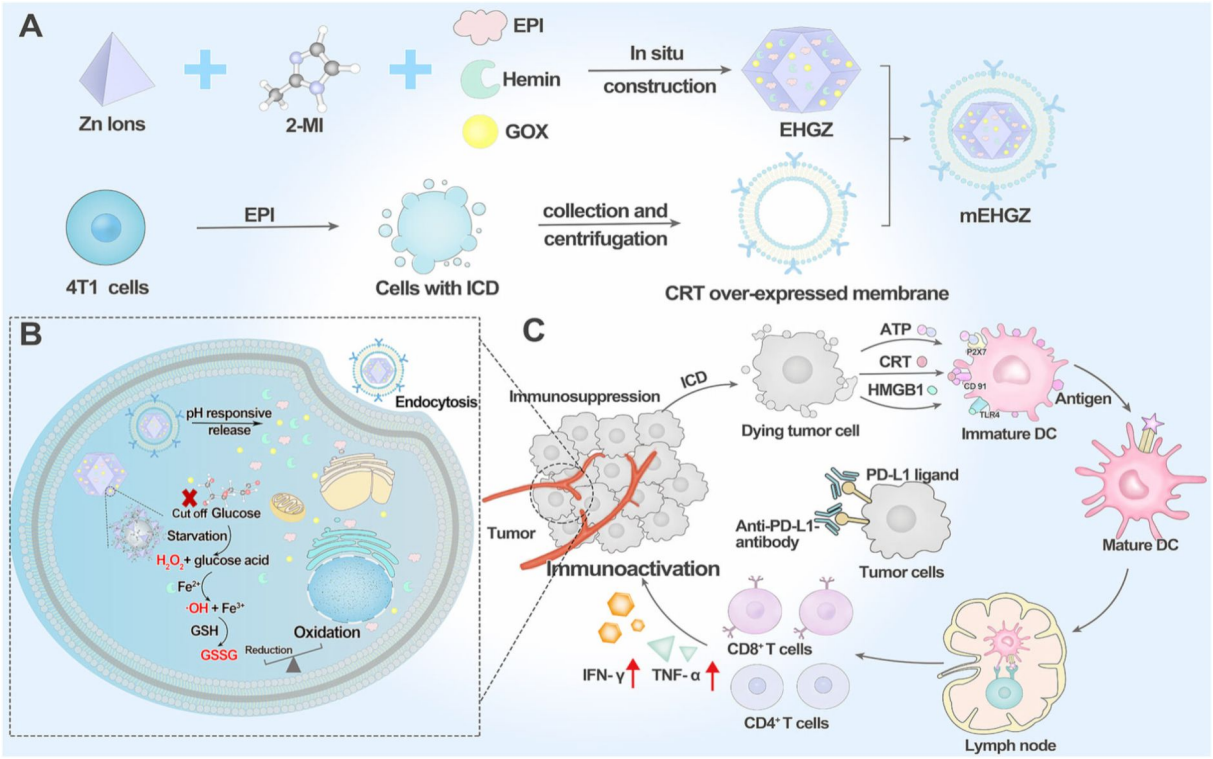

Figure 11: Self-amplified biomimetic nanosystem to induce ICD and activate an immune microenvironment to enhance the therapeutic effects of anti-PD-L1 antibody. (A) Preparation of CRT over-expressed tumor cell membrane coated EPI, Gox and hemin in ZIF-8 loaded mEHGZ NPs and (B) underlying mechanism (C) to create an immunosupportive microenvironment to boost the therapeutic effect of anti-PD-L1 antibody. Figure 11 was reproduced from [139] (© 2023 Z. Li et al., published by Elsevier B.V. on behalf of KeAi Communications Co. Ltd., distributed under the terms of the Creative Commons Attribution-NonCommercial-NoDerivatives 4.0 International License, https://creativecommons.org/licenses/by-nc-nd/4.0/). This content is not subject to CC BY 4.0.

engineered a novel cationic star copolymer to deliver LC3 siRNA efficiently into TNBC cells. The polycationic structure provided strong electrostatic condensation with siRNA and enabled proton sponge-mediated endosomal escape, ensuring cytoplasmic release of the gene cargo. These LC3siRNA-loaded nanoparticles (LC3siRNA-NPs) exhibited pH-responsive behavior, enhanced cellular uptake, and potent suppression of autophagy. In vitro and in vivo experiments demonstrated that co-administration with doxorubicin significantly inhibited tumor growth and induced apoptosis, highlighting the system's promise for overcoming chemoresistance in TNBC [145]. The success of efficient drug delivery to achieve considerable therapeutic outcomes highly depends on various critical structural parameters including charge, shape, and size [146]. Importantly, various problems exist associated with exogenous siRNA/genes, including easy degradation, short circulation time, immune clearance, low accumulation, and inability to penetrate the target cell membrane [147,148]. Gene therapy paves new ways in the treatment of incurable diseases by effective gene regulation strategies, such as a three-layer core–shell biomimetic nanostructure fabricated to overcome limitations in siRNA delivery to glioblastoma (Figure 13). The three-layer shell consisted of polyethyleneimine (PEI)-siRNA complex in the core, citraconic anhydride grafted poly-L-lysine (PLL-CA) in the middle, and an outer layer of angiopep-2-decorated RBC membrane (Ang-RBCm). The RBC membrane allowed for longer circulation of NPs, without being recognized by the immune system. While further modification of the membrane with angiopep-2 provided enhanced BBB penetration. The inner PLL-CA cavity provided charge conversion in the acidic compartments of the tumor by proton sponge effects, resulting in NP escape from the acidic endosomes. Meanwhile, the outer RBC membrane shell is disrupted and accelerates the release of siRNA into the cytoplasm [149,150]. In contrast, Li et al. synergistically delivered a miR-144/451a cluster by constructing chitosan NPs (CAs) camouflaged with macrophage membranes for oral squamous cell carcinoma (OSCC) treatment. It was demonstrated that CAs coloaded with miR-144-MEXO/CA-miR-451a NPs significantly reduced the viability, migration, and invasion of OSCC cells; also, they substantially reduced the CAB39 and MIF expression in OSCC cells [151].

The targeted pH-responsive biomimetic nanodelivery system displayed high therapeutic efficacy with minimal side effects in

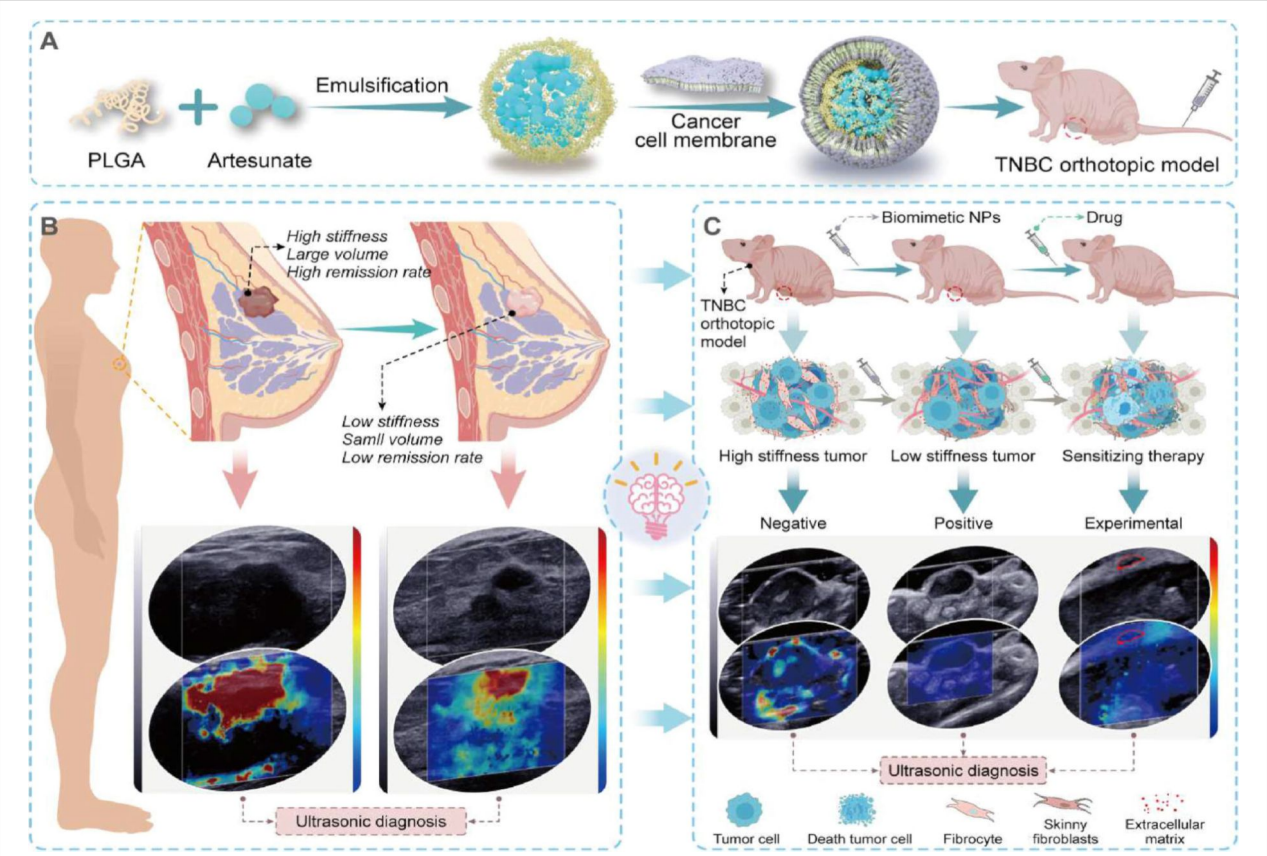

Figure 12: Schematic illustration of (A) fabrication of biomimetic NPs and (B, C) the mechanism by which shear wave elasticity imaging can predict TNBC treatment efficacy in MDA-MB-231 and E0771 orthotopic tumor models. Figure 12 was reproduced from [143] (© 2023 D. Zheng et al., published by Elsevier B. V. on behalf of KeAi Communications Co. Ltd.), distributed under the terms of the Creative Commons Attribution 4.0 International License, https://creativecommons.org/licenses/by/4.0).

orthotopic human glioblastoma-bearing animals. In one study, a worm-like nanostructure coated with RBC membrane for siRNA delivery has also been demonstrated. Herein, RBC membrane was modified with RGD peptide to achieve active targeting ability and a pH-dependent charge conversion strategy was involved to accomplish effective siRNA release [152]. In another example of RBC camouflaged particle, amphiphilic copolymer of PLGA-PEI was coated with RBC membrane to transfect endothelial cells with plasmid DNA for EGFR expression [153]. In another approach, CCM-based biomimetic nanomedicine for siRNA delivery has also been reported [154]. CCM-coated poly(β-amino ester) was successfully applied for siRNA delivery, resulting in cancer cell targeting, inhibition of PKL1 gene expression, and the induction of apoptosis in cancer cells. Besides the membrane coating strategy, a DNA nanotechnology-based nanosystem, which is inspired by holliday junction molecules, was demonstrated [155]. DNA tiles mimicking the holliday junction molecule structure were conjugated with gold nanoparticles and successfully used for the delivery of a neutral antisense oligonucleotide, morpholino, for silencing HER2 and ERα genes in breast cancer.

Within gene therapy applications, bioinspired tumor-homing nanomedicines have also been demonstrated for combinational therapies. Macrophage–CCM hybrid-coated PLGA was used to deliver siRNA against fibrinogen-like protein 1 and metformin, a metabolic immunomodulator for both gene therapy and immunosuppressive tumor microenvironment [156]. Other combinational therapy strategies using biomimetic nanoplatforms were reported with co-delivery of nucleic acid drugs and chemotherapeutics [157-159], and combinational gene therapy and photothermal therapy [160]. Recently, Liang et al. developed novel stealth and MMP2-activated biomimetic nanoparticles by using MMP2-responsive peptides to bind with miR-126-3p and then further camouflaged with RBC membrane (REMAIN). Due to the natural RBC membrane, REMAIN showed extended circulation, low toxicity, better biocompatibility, and immune escape; they induced the apoptosis of lung cancer cells, in vitro and in vivo [161].

Furthermore, Yang et al, inspired by human bone marrow mesenchymal stem cells, developed a biomimetic zeolitic imidazolate framework-8 to navigate herpes simplex virus type I thymi-

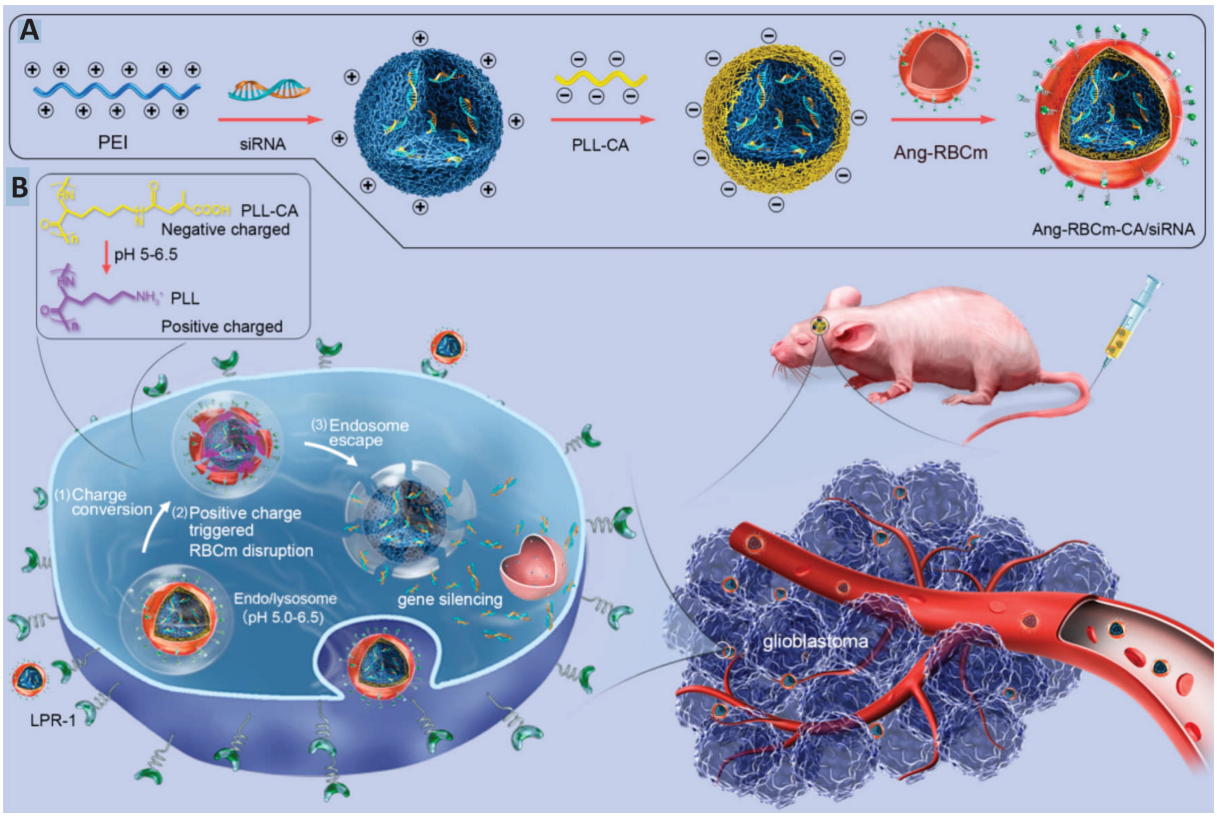

Figure 13: (A) preparation of Arg-RBCm-CA/siRNA and (B) pH-dependent siRNA release mechanism and overcoming BBB. Figure 13 was reprinted with permission from [149], Copyright 2020 American Chemical Society. This content is not subject to CC BY 4.0.

dine kinase-encoded plasmids and ganciclovir for lung cancer treatment. The biomimetic NPs showed long circulation and enhanced tumor accumulation, and significantly inhibited the tumor. These biological bomb structures killed the transfected as well surrounding lung cancer cells by a "bystander effect" and efficiently suppressed lung cancer [162].

2.3 Photothermal/photodynamic therapy

Photothermal therapy (PTT), a new class of cancer treatment that uses heat absorbed by light-absorbing materials, is a non-invasive method with certain advantages, including reduced toxicity and strong anti-tumor efficacy [163-165]. The working principle of PTT is based on the conversion of absorbed light energy into heat, resulting in photoablation, which leads to cell damage and death [166]. Overall, PTT presents great potential in improving recovery time and better outcomes in cancer treatment [163,167]. To enhance the therapeutic efficiency of PTT, biomimetic NPs have been developed by camouflaging the PTT particles with different cell membranes to allow them to be used in cancer diagnosis and treatment. The biomimetic PTT NPs diffuse into tumor tissues and are engulfed by the cancer cells; then light is applied to heat up the tissue by using PTT, destroying cancer cells. Previously, RBC membrane coating increased and improved the effect of PTT by prolonging blood circulation and enabling precise tumor homing. It was observed that RBC membrane-coated NPs significantly improve PTT effects and reduce tumor with 100% survival up to 45 days [168-170].

In another study, Wu et al. employed "disassembly–reassembly" technology to obtain reconstituted RBCs (rRBCs) for a membrane-coated delivery platform. It was found that the rRBC membrane improved stability, circulation time, and immune escape after removing the endogenous proteins and lipids on the membrane. After synthesizing biomimetic rRBC membrane, the IR780 (NIR) fluorescence dye was loaded as a photosensitizer for PTT to generate biomimetic "IR780-rRBC" NPs. The anti-tumor effect of IR780-rRBC was also evaluated. After laser treatment, the tumor temperatures in mice treated with IR780-rRBC and IR780-rRBC NPs increased up to 60 and 70 °C, respectively. Importantly, following photothermal therapy in R780-RBC and IR780-rRBC groups, a significant necrosis in the tumor and a noticeable suppression in the tumor volume were observed [171]. Li et al. developed hybrid nanovesicles (TT3-oCB NP-EXOs) with enhanced second near-infrared (NIR-II, 900–1700 nm) fluorescence and PTT, consisting of

tumor cell-derived exosomes (EXO) and TT3-oCB nanoparticles. The TT3-oCB NP-EXOs showed promising and stable photothermal conversion capacity under 808 nm irradiation to be used as biomimetic NPs for NIR-II fluorescence imaging-guided PTT of tumors. The TT3-oCB NP-EXOs demonstrated prolonged blood circulation and enhanced tumor uptake in vitro and in vivo [172].

In addition to the direct ablation of tumor cells, photothermal therapy also elicits immune responses, which could be used to treat metastatic tumors by producing tumor-associated antigens [173,174]. Therefore, combining PTT and immunotherapy is thought to be ideal for efficient anticancer immunotherapy [175-177]. Recently, inorganic photothermal transducing agents coated with antibodies/peptides have been successfully applied for combined cancer therapy. This biomimetic nanosystem comprised $FePSe_3$ modified with chitosan, CT26 cancer cell membrane (CCM), and anti-PD-1 peptide (APP) for PTT-immunotherapy. To improve the immunotherapeutic effects, the anti-PD-1 peptide was covalently bound to the chitosan-stabilized $FePSe_3$ nanosheets. Under NIR laser irradiation, the photothermal effects produced by $FePSe_3$-APP-CCM not only killed cancer cells but also induced intense immune responses both in vitro and in vivo [175].

In another report, Wei et al. developed a cancer cell membrane-coated homotypic targeting gold nanocage, m@Au-D/B NCs, loaded with DOX and l-buthionine sulfoximine (BSO) for promising anticancer combination therapy by eliciting ferroptosis and immune responses. DOX and BSO induced ferroptosis by glutathione consumption and ROS generation. Moreover, the gold nanocages evoked PTT and photochemical catalysis, generating more ROS under NIR irradiation. At the same time, the m@Au-D/B NCs-associated PTT and ROS generation could repolarize TAMs and initiate the release of proinflammatory cytokines, as well as significantly inhibit tumor growth at minimum toxicity [178]. In order to downregulate heat shock protein (HSP) expression, Shu et al. constructed 4T1 cell membrane-coated biocompatible mesoporous Prussian blue nanoparticles (PBLM@CCM NPs) loaded with lonidamine (LN) and DL-menthol. The PBLM@CCM NPs selectively delivered LN to reduce HSP and overcome heat endurance in PTT by inhibiting intracellular ATP production. Furthermore, the PBLM@CCM NPs allowed for photoacoustic imaging and produced heat to promote the phase change of DL-menthol for ultrasound imaging [179].

It was observed that cancer stem cells (CSCs) are the key to cancer metastasis, recurrence, and chemotherapeutic resistance. To inhibit CSCs, Liu et al. designed MnO_x-loaded polydopamine (MnO_x/PDA) nanobombs with chemodynamic, photodynamic, photothermal, and biodegradation properties. The MnO_x/PDA nanobombs directly target the CSCs in the TME by generating hyperthermia, hypoxia, and oxidative stress. Furthermore, macrophage membrane-coated MnO_x/PDA targeted and synergistically inhibited tumor volume up to 70.8% in colorectal cancer tumor model [180], as shown in Figure 14.

In terms of antitumor immunotherapy, the immunosuppressive TME and inferior drug targeting are major challenges. To address these, Zhao et al. developed myeloid-derived suppressor cell (MDSC) membrane-coated camouflage gold nanorods covered with silica dioxide and then coated them with manganese dioxide (MnO_2) to obtain GNRs@SiO_2@MnO_2@MDSCs (GSMM). GSMM actively targeted MDSCs and the localized surface plasmon resonance of GNRs developed in the NIR-II window via the MnO_2 layer coating, conveying NIR-II photothermal and photoacoustic imaging to GSMM; also Mn^{2+} release could be used for magnetic resonance imaging. The Mn^{2+} catalyzed the reaction of H_2O_2 into ·OH for chemodynamic therapy (CDT) to activate the cGAS-STING mechanism and the secretion of interferon type I, proinflammatory cytokines, and chemokines. Furthermore, the PDT and CDT-mediated ICD of tumor cells further enhanced the antitumor immunity via exposure of CRT, HMGB1, and ATP [181], as shown in Figure 15.

The inter- and intra-individual heterogeneities of tumors and TME and the differences between heterotopic and orthotopic tumors limit the translational potential of nanoplatforms in accurate tumor therapy [182,183]. To address this Wu et al., used head and neck squamous cell carcinoma (HNSCC) cell membranes and patient-derived cell membranes to surface-modify gold NPs (Au@C-CCM or Au@C NP) and evaluated the antitumor efficacy in subcutaneous xenograft, tongue orthotopic xenograft, immune competent primary and distal tumor models, as well as patient-derived xenograft models. It was observed that Au@C-CCM produced up to 44.2% photothermal conversion for primary HNSCC therapy, inducing immunotherapy to inhibit tumor metastasis via photothermal therapy-mediated ICD. Furthermore, due to the homologous targeting mechanism, the homologous CCM-coated NPs demonstrated distinct tumor ablation in all four models, indicating efficient antitumor therapy [184]. Regarding the most malignant and high-MDR pancreatic ductal adenocarcinoma (PDAC), Zhang et al. designed TME-responsive PDAC cell line-camouflaged gold nanocages (AuNCs) to simultaneously deliver the chemotherapeutic GEM and a nitrogen oxide (NO) donor (L-Arg) for efficient tumor homing and reduced chemoresistance. The high intracellular level of glutathione cleaved the disulfide bond and triggered the release of GEM. Also, the

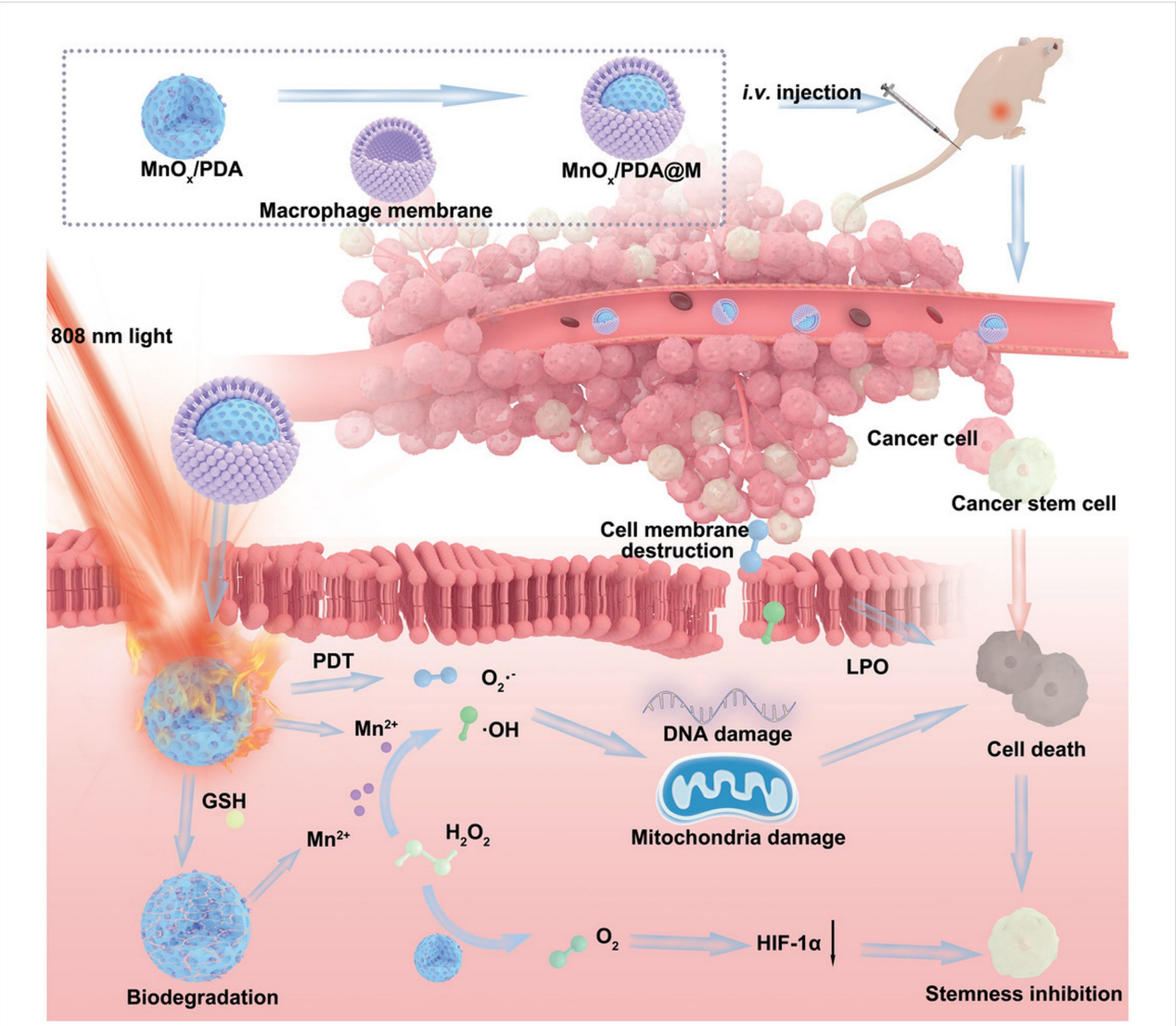

Figure 14: Macrophage membrane-coated MnO_x/PDA nanobombs for antitumor therapy with chemodynamic, photodynamic, photothermal, and biodegradation properties. Figure 14 was reproduced from [180], S. Liu et al., "Biomimetic Nanobomb for Synergistic Therapy with Inhibition of Cancer Stem Cells", *Small*, with permission from John Wiley and Sons. Copyright © 2022 Wiley-VCH GmbH. This content is not subject to CC BY 4.0.

elevated ROS level activated L-Arg and generated NO, facilitating GEM to penetrate PDAC tumor tissues by vasodilation and normalization of blood vessels to induce potent antitumor effects. Importantly, the AuNCs not only served as a photothermal agent but also generated significant photoacoustic signals to monitor drug accumulation and distribution inside the tumor cells [185], as shown in Figure 16.

Photodynamic therapy (PDT) is one of the most important therapy types that can be used alone or in combination with other traditional treatment methods in cancer treatment [186]. Compared to traditional cancer treatment methods, PDT is considered to be very advantageous due to its very low intervention level. The process of producing reactive oxygen species is based on various biochemical reactions that occur when light-sensitive agents, called photosensitizers, interact with light of the appropriate wavelength [187]. Photosensitive agents transfer this absorbed energy to the molecules in the living microenvironment through two different types of mechanisms. In type-1 reactions, the high-energy photosensitizer can directly react with an electron-donating substrate to form superoxide anion radicals. In type-2 reactions, the energy of the high-energy photosensitizer is transferred directly to ground state oxygen $^3O_2$ in the environment, producing highly reactive singlet oxygen $^1O_2$. The production of singlet oxygen and superoxide anions using any of these two mechanisms create a toxic effect on cells through damaging lipids, proteins, and nucleic acids. Accordingly, cell death and cell destruction result [188-191].

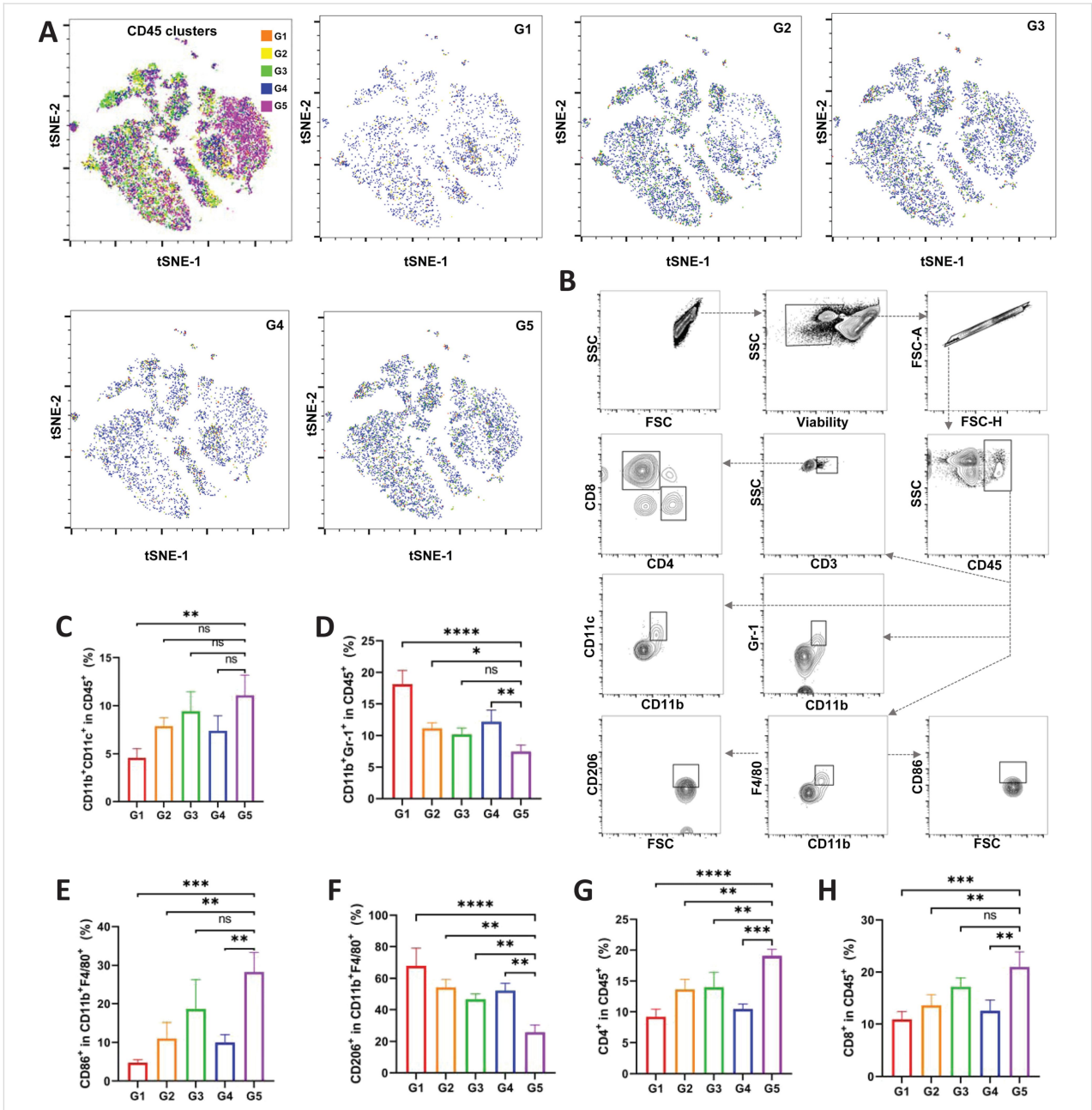

Figure 15: Myeloid-derived suppressor cell membrane-coated camouflage gold nanorods covered with silica and manganese dioxide (GNRs@SiO_2@MnO_2@MDSCs, GSMM) and TME after different treatments. (A) Mass cytometry of CD45+ tumor-infiltrating leukocytes. The t-distribution stochastic neighbor embedding (t-SNE) plot of CD45+ tumor-infiltrating leukocytes of a total 25 samples (pooled data) (left panel: overlaid with color-coded clusters) and density t-SNE plots of CD45+ tumor-infiltrating leukocytes in different treatment groups (G1: PBS, G2: PBS + laser, G3: GSM + laser, G4: GSMM, G5: GSMM + laser). (Laser irradiation was conducted at 4 h post-injection of nanoparticles with a 1064 nm laser for consecutive 5 min, 0.6 W/cm^2). (B) Schematic gating strategy for the identification of various immune cell populations in a B16F10 xenograft model. Flow cytometric quantification of (C) CD11b+CD11c+ dendritic cells, (D) CD11b+Gr-1+ MDSCs, (E) CD86+CD11b+F4/80+ M1 macrophages, (F) CD206+CD11b+F4/80+ M2 macrophages, and (G) CD4+ T cells, H) CD8+ T cells in tumor tissues. Figure 15 was reproduced from [181] (© 2023 Y. Zhao et al., published by Elsevier B.V. on behalf of KeAi Communications Co. Ltd., distributed under the terms of the Creative Commons Attribution-NonCommercial-NoDerivatives 4.0 International License, https://creativecommons.org/licenses/by-nc-nd/4.0/). This content is not subject to CC BY 4.0.

To date, numerous NPs have been studied to increase the concentration of photosensitizers and to ensure their accumulation at the tumor site. At the same time, studies on liposomes, dendrimers, silver, and gold nanoparticles have been carried out to improve the phototoxic properties of photosensitizers. PDT is applied to cancer types characterized by no therapeutic efficacy or lacking effective therapeutic targets. In a study conducted by Zhang et al., PDT, PTT, and the anticancer agent DOX have

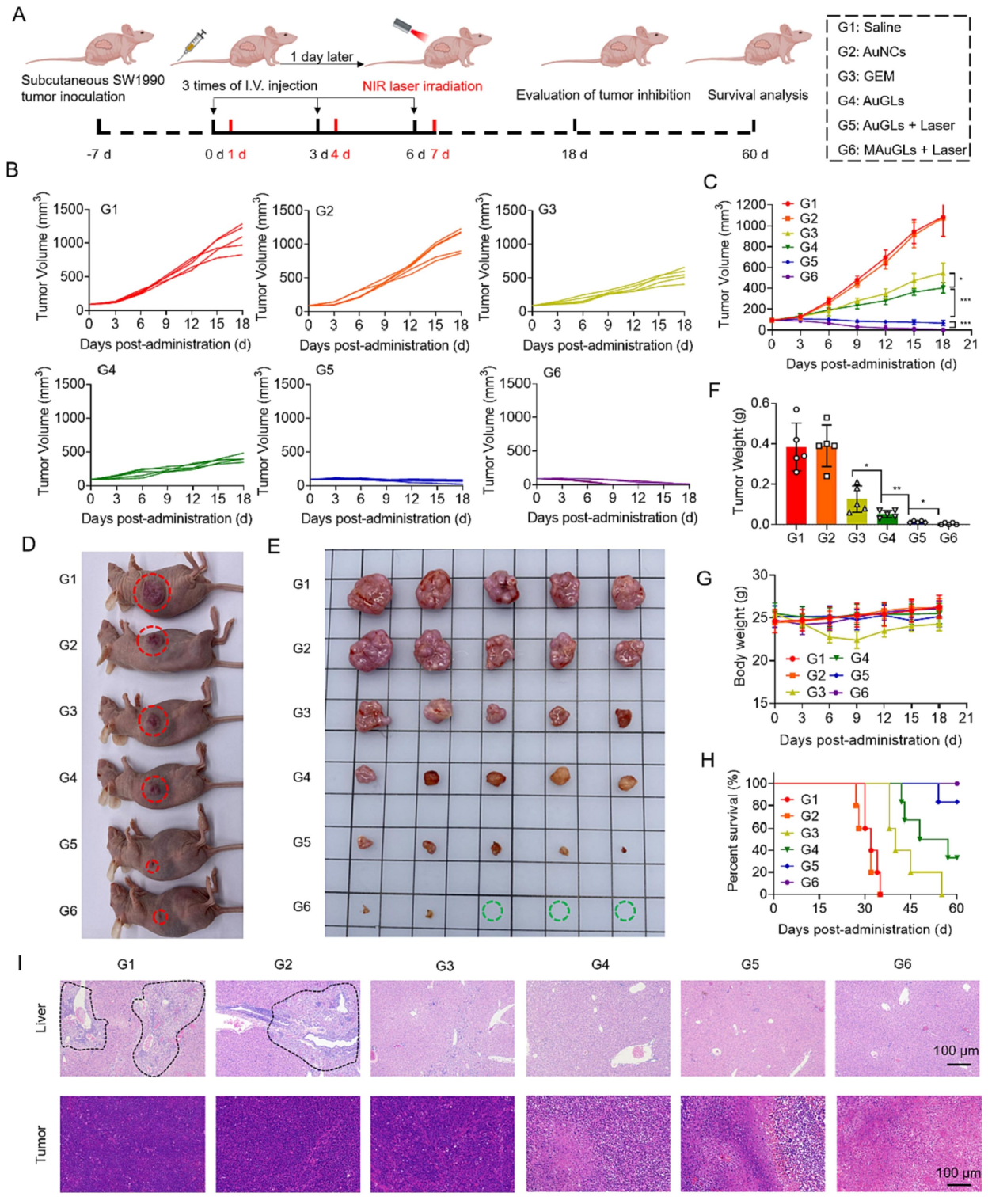

Figure 16: Antitumor efficacy of TME responsive PDAC cell line camouflaged gold nanocages. (A) Schematic illustration of the design of the experiments, (B, C) relative tumor growth curves until day 18, (D) image of the tumor-bearing mice on day 18, (E) excised tumors on day 18, (F) weights of excised tumors on day 18, (G) changes in body weights of tumor-bearing mice within 18 days, (H) survival graph up to 60 days, and (I) H&E staining of livers and tumors of the mice. The black dashed lines indicated the metastatic tumors in the livers. Figure 16 was reprinted from [185], *Journal of Controlled Release*, vol. 354, by F. Zhang; Q. Hu; B. Li; Y. Huang; M. Wang; S. Shao; H. Tang; Z. Yao; Y. Ping; T. Liang, "A biomimetic nanodrug for enhanced chemotherapy of pancreatic tumors", Pages 835–850, Copyright (2023), with permission from Elsevier. This content is not subject to CC BY 4.0.

been applied in combination on TNBC, and a novel biomimetic platform has been developed with leukocyte-platelet hybrid membrane and dendritic large pore mesoporous silicon nanoparticles, LPHM and DLMSNs, respectively. IR780 and DOX have been co-loaded into the DLMSNs to carry DLMSNs-DOX-IR780 (DDI) NPs. The leukocyte/platelet hybrid membrane was coated with DDI NPs to prepare the final biomimetic platform, LPHM-DDI NPs. These NPs showed superior TNBC targeting ability and very high PTT/PDT performance in vitro and in vivo. After NIR laser irradiation with the synergistic effect of PDT and PTT, cytotoxicity was observed in TNBC cells after treatment with LPHM-DDI NPs. Furthermore, tumor growth and recurrence were effectively suppressed in the TNBC mouse model. This suggests that PTT/PDT provides a promising biomimetic nanoplatform as a combination therapy against TNBC [192]. In a similar study, platelet-mimetic NPs have been used to create more effective PDT therapy. Van Straten et al. developed platelet-mimetic PLGA NPs encapsulating verteporfin as the photosensitizer, which shifted the absorption peak from 682 to 712 nm, allowing for better absorption in deeper tissues. Thus, platelet-mimetic PLGA NPs achieved higher accumulation in tumor tissues in comparison with control and RBC membrane-coated NPs. Furthermore, the platelet-mimetic PLGA NPs exhibited significant tumor ablation without causing any side effects under NIR irradiation [187].

Recently, PDT received great attention due to its ability to induce ICD. In this respect, Wu et al. developed multifunctional MPCO biomimetic NPs (4T1Mem@PGA-Ce6/Ola) to codeliver the photosensitizer chlorin e6 (Ce6) and olaparib (Ola) with the function of preventing DNA repair. The nanoplatform demonstrated efficient tumor homing, and Ce6 and Ola induced synergistic antitumor efficacy under laser irradiation. Furthermore, MPCO activated the cyclic guanosine monophosphate–adenosine monophosphate synthase–interferon gene stimulator signaling (cGAS-STING) pathway to produce cytokines. The damage-associated molecular patterns induced by ICD can work with these cytokines to recruit and stimulate the maturation of dendritic cells and induce a systemic antitumor immune response [193].

2.4 Sonodynamic therapy

Sonodynamic therapy (SDT) is a non-invasive therapeutic strategy that enables tumor cells to be killed by activation of photosensitive compounds [194]. It is also an anti-cancer method working through localized light transmission derived from PDT. The combination of PTT and SDT shows great promise for synergistic antitumor therapy. In SDT, the tumor site is exposed to focused ultrasound (FUS), which offers improved tissue penetration and reduces potential off-target effects [195]. Deep tissue penetration of SDT can overcome the inherent deficiency of PTT in targeting deeper tumors. In some applications, FUS may offer a wider variety of applications regarding focus and tumor coverage. Similar to photosensitizers, FUS activates “sonosensitizers” that selectively accumulate in tumor cells and generate ROS. In addition, SDT can be integrated with different FUS approaches. For example, FUS can be administered i.v. to permeabilize cell membranes and increase drug delivery through transient openings in the blood–brain or blood–tumor barriers. Injected contrast agents can be placed [176]. Moreover, the accumulation of sonosensitizers in tumor cells can be enriched with enhanced permeability and retention (EPR) effect.

Zhang et al. took advantage of the ability of the macrophage membrane coating to target the tumor and avoid the RES. As shown in Figure 17, compared to ICG-labeled CAu-BMSNs, the ICG-labeled N@CAu-BMSNs showed a significantly high NIR-II fluorescence signal in tumors, confirming active targeting and RES evasion of the macrophage membrane. Also, the macrophage membrane-coated biomimetic nanosystem demonstrated an excellent synergistic antitumor effect of SDT/CO treatment to effectively suppress tumor growth, relapse, and metastasis to the lung. The strategy based on sonodynamic/CO therapy and IDO signal inhibition is a promising approach against tumor recurrence and lung metastasis in clinical trials [196].

In another study, a triple therapy combining PTT, SDT, and anti-PD-1 immunotherapy, guided by multimodal imaging to treat 4T1 tumors in mice model (Figure 18) [197]. The authors used PLGA-based biomimetic nanoparticles (CHINPs) coated with 4T1 cancer cell membranes and loaded with ultrasound- and laser-responsive agents (HMME and SPIO). These biomimetic nanoparticles actively targeted homologous 4T1 tumors, enabled precise tumor targeting, and eliminated primary tumors by multiple imaging-guided PTT/SDT treatment, exposing tumor antigens, and enhancing immune responses by boosting $CD8^+$ T cells and reducing Tregs. Anti-PD-1 antibodies further strengthened T cell activity by blocking immune checkpoints, leading to improved tumor control and reduced metastasis.

Aydin et al. developed a novel FUS-responsive biomimetic nanoparticle system by coating gold nanocones (AuNCs) with B16F10 melanoma cell membranes (CCM@AuNCs). These nanoparticles exhibited strong homologous targeting toward melanoma cells, enabling enhanced accumulation and might facilitate mechanical ablation upon therapeutic FUS exposure. Following activation, this approach may promote the release of tumor-associated antigens and potentially enhance immune cell

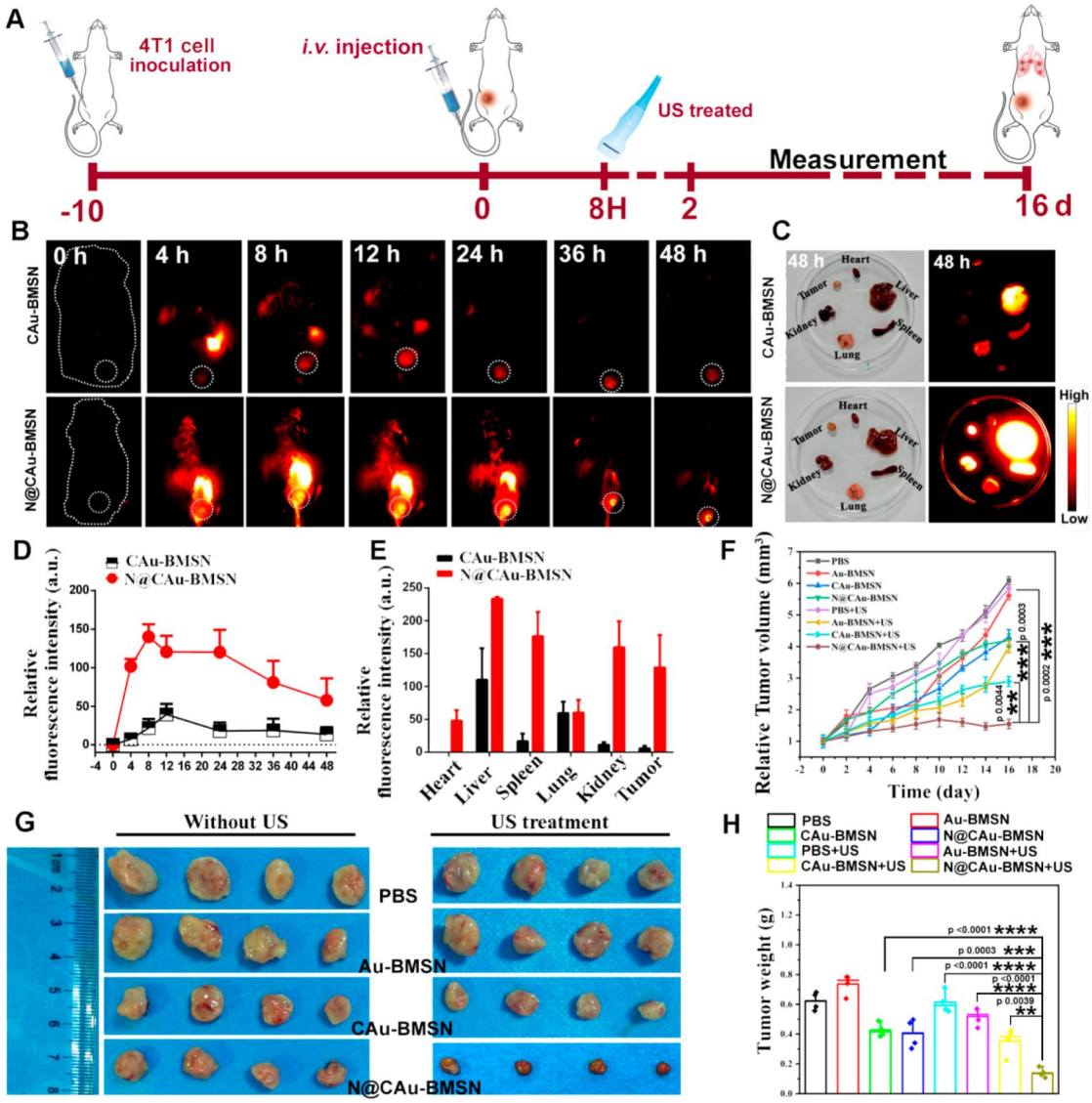

Figure 17: (A) Schematic representation of an in vivo study of N@CAu-BMSNs, (B) NIR-II fluorescence imaging of ICG-labeled CAu-BMSNs or N@CAu-BMSNs at different time points after i.v. injection, (C) ex vivo biodistribution in tumor and major organs isolated from 4T1-tumor-bearing mice after 48 h of ICG-labeled CAu-BMSN or N@CAu-BMSN injection, respectively, (D, E) fluorescence intensity of tumor and major organs after intravenous injection at different time points, (F) tumor volume change of mice after receiving US treatment, (G) tumor images, and (H) average tumor weight of mice after US treatments. Figure 17 was reprinted with permission from [196], Copyright 2020 American Chemical Society. This content is not subject to CC BY 4.0.

infiltration into the TME. Such a strategy might represent a promising platform for melanoma-targeted FUS-assisted immunotherapy [198].

Another biomimetic nanoplatform study concerned the resistance of cancer cells to SDT. Feng et al. have introduced a biomimetic nanoplatform based on hollow mesoporous titanium dioxide nanoparticles (HMTNPs) with autophagy inhibitor (hydroxychloroquine sulfate, HCQ) loading and cancer cell membrane (CCM) coating (Figure 19) [199]. Due to the functionalization of the biomimetic surface, CCM-HMTNPs/HCQ are able to evade macrophage phagocytosis and actively recognize tumors with their homologous targeting ability. Subsequently, HCQ released in response to ultrasound stimulation has the ability to block autophagic flux and cut off the nutrient supply derived from damaged organelles, which is expected to abolish the cells' resistance to SDT. Thus, the study demonstrated a new therapeutic route to target autophagy in SDT.

Conclusion and Future Perspectives

Our comprehensive review has underscored the remarkable potential of biomimetic NPs in the realm of drug delivery.

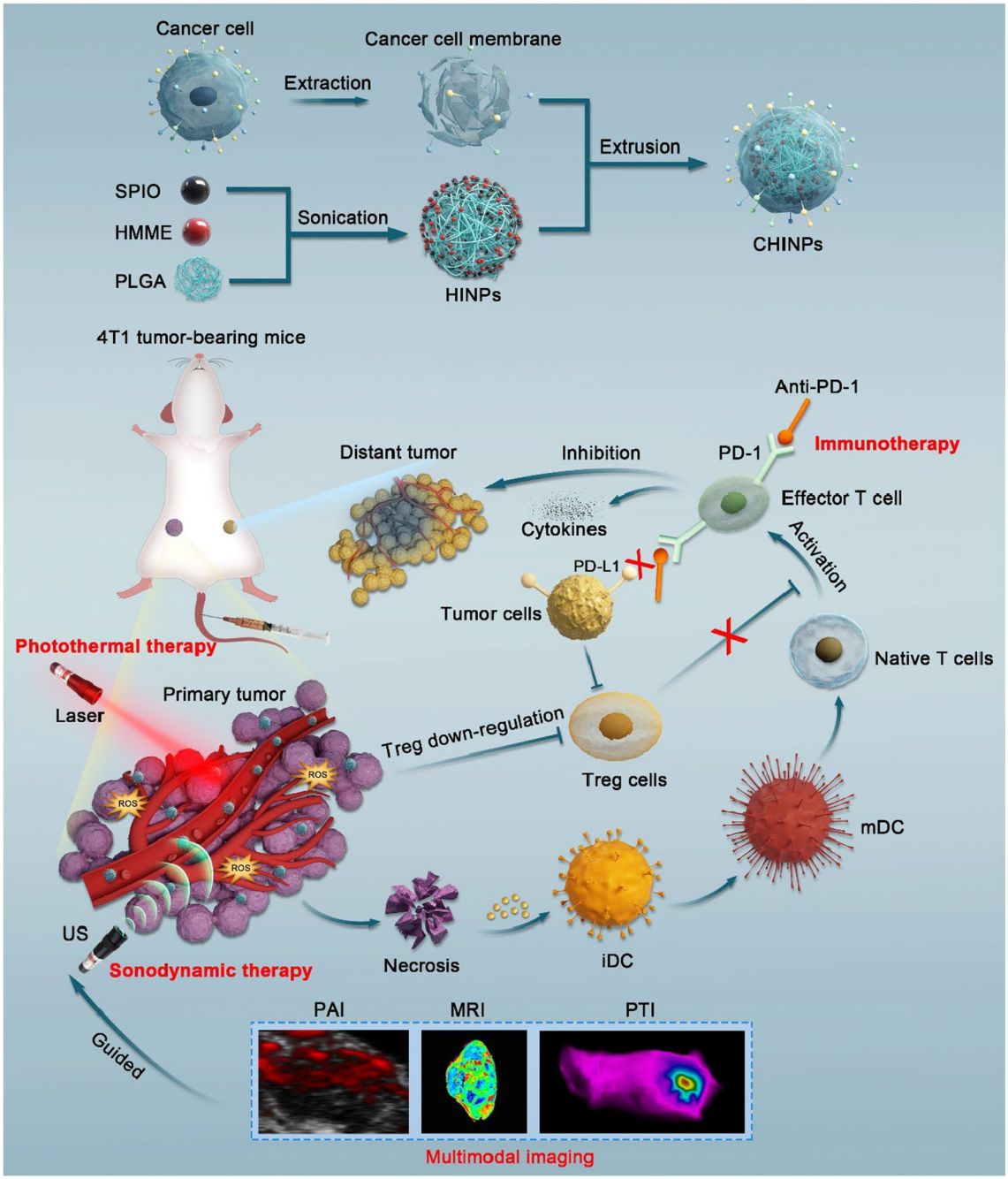

Figure 18: Illustration of CHINPs synthesis and combined effects of PTT/SDT enhanced anti-PD-1 against primary and distant tumor. Figure 18 was reproduced by [197] (© 2022 X. Lin et al., published by BMC (part of Springer Nature), distributed under the terms of the Creative Commons Attribution 4.0 International License, https://creativecommons.org/licenses/by/4.0).

These biomimetic NPs exhibit a unique amalgamation of distinct biochemical functionalities, heightened biocompatibility, augmented bioavailability through evasion of immune responses, and precise targeting, thereby limiting premature clearance en route to designated sites of action. Also, by integrating or fabricating biomaterials onto the surface of nanoparticles, they mimic the biological features and functions of native cells. Therefore, it is evident that biomimetic NPs represent a promising avenue for clinical translation.

However, the deployment of biomimetic NPs in clinical applications is not devoid of formidable challenges that warrant meticulous attention. The issues surrounding the selection of the most appropriate cell membrane type and source, the scalability

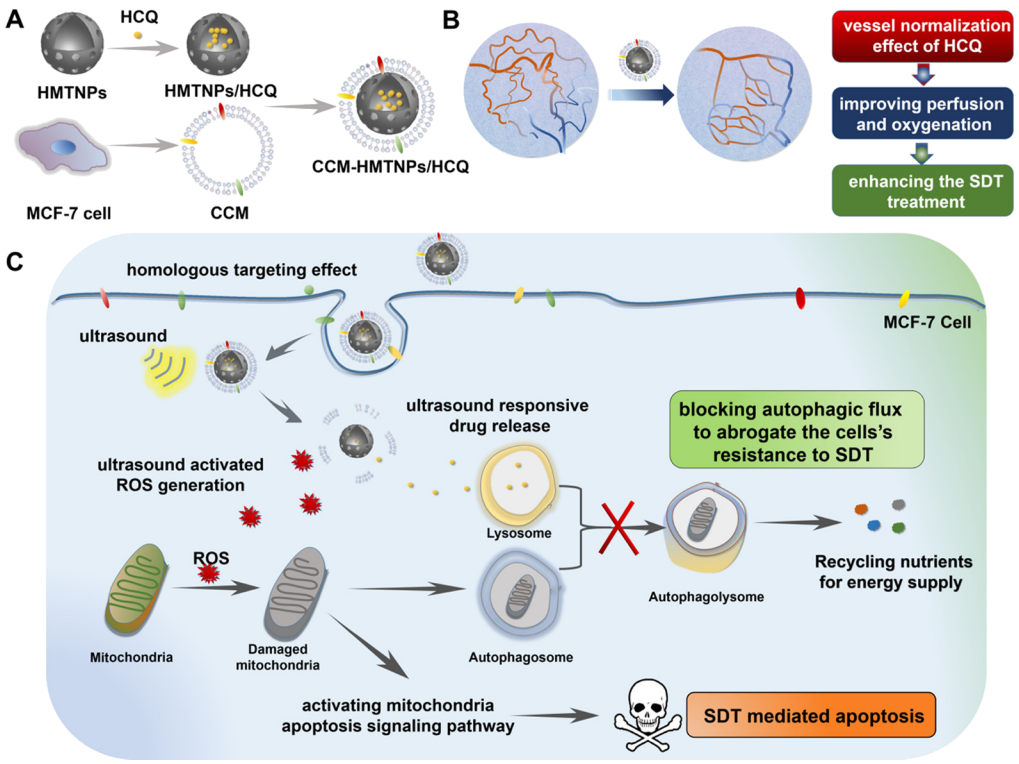

Figure 19: SDT mechanism of CCM-HMTNPs/HCQ via autophagy regulation in breast cancer treatment. Figure 19 was reprinted with permission from [199], Copyright 2019 American Chemical Society. This content is not subject to CC BY 4.0.

Table 1: Summary of practical benefits and challenges of biomimetic nanoparticles in comparison to conventional nanoparticles.

Aspect	Biomimetic nanoparticles	Conventional nanoparticles
immune evasion	* mimic natural cell membranes	
targeting specificity	* high target specificity via cell membrane proteins and natural ligands	
circulation time	* long retention time mimicking natural cells (e.g., RBC membrane)	
biocompatibility and toxicity	* improved biocompatibility	
drug loading and therapeutic efficacy	* ability to load various cargos, including drugs and siRNA	* good drug payload and solubility
manufacturing complexity	* complex preparation of cell membranes and coating steps	
stability and storage	* biological materials may degrade during storage	* longer shelf life under standard conditions
safety/immunogenicity risk	* dependent on cell source and patient variability	* known side effect profiles, particularly for approved drugs
clinical translation	* limited progression to clinical usage despite promising preclinical results	* some clinically approved nanoparticle therapies (e.g., nab-paclitaxel)
regulatory approval	* complex classification and limited precedent	* familiar to regulatory bodies with established frameworks

and reproducibility of manufacturing processes, post-fabrication sterilization methods, long-term stability and storage conditions, the development of personalized biomimetic NPs, concerns related to cross-reactivity, regulatory approval hurdles, and the economic feasibility of large-scale production must be considered.

We anticipate that sustained efforts in the advancement of cutting-edge technologies and a concerted approach to address these multifaceted challenges will herald a transformative paradigm shift in the field of novel drug delivery systems. Such advancements hold the promise of revolutionizing the way therapeutics are designed, formulated, and administered, ultimately enhancing the efficacy and precision of drug delivery and thus benefiting both scientific and medical communities alike.

Funding

Omer Aydin Ph.D. recognizes the support of the TUBITAK 2247-D National Early-Stage Researchers Program (#121C221).

Conflict of Interest

The authors declare that they have no known competing financial interests or personal relationships that could have appeared to influence the work reported in this paper.

Author Contributions

Imran Shair Mohammad: writing – original draft. Gizem Kursunluoglu: writing – review & editing. Anup Kumar Patel: writing – review & editing. Hafiz Muhammad Ishaq: writing – original draft. Cansu Umran Tunc: writing – original draft. Dilek Kanarya: writing – review & editing. Mubashar Rehman: writing – original draft. Omer Aydin: writing – original draft. Yin Lifang: supervision.

ORCID® iDs

Imran Shair Mohammad - https://orcid.org/0000-0002-1351-0216
Gizem Kursunluoglu - https://orcid.org/0000-0002-9407-4662
Anup Kumar Patel - https://orcid.org/0000-0003-0840-0781
Cansu Umran Tunc - https://orcid.org/0000-0002-8555-1340
Dilek Kanarya - https://orcid.org/0000-0001-8984-0142
Omer Aydin - https://orcid.org/0000-0002-9028-8786

Data Availability Statement

Data sharing is not applicable as no new data was generated or analyzed in this study.

References

1. Lin, X.; Kang, K.; Chen, P.; Zeng, Z.; Li, G.; Xiong, W.; Yi, M.; Xiang, B. *Mol. Cancer* **2024,** *23,* 108. doi:10.1186/s12943-024-02023-w
2. Yaman, S.; Chintapula, U.; Rodriguez, E.; Ramachandramoorthy, H.; Nguyen, K. T. *Cancer Drug Resist.* **2020,** *3,* 879–911. doi:10.20517/cdr.2020.55
3. Ayana, G.; Ryu, J.; Choe, S.-w. *Micromachines* **2022,** *13,* 1508. doi:10.3390/mi13091508
4. Sharma, M.; Bakshi, A. K.; Mittapelly, N.; Gautam, S.; Marwaha, D.; Rai, N.; Singh, N.; Tiwari, P.; Agarwal, N.; Kumar, A.; Mishra, P. R. *J. Controlled Release* **2022,** *346,* 43–70. doi:10.1016/j.jconrel.2022.04.007
5. Zhang, M.; Du, Y.; Wang, S.; Chen, B. *Drug Des., Dev. Ther.* **2020,** *14,* 5495–5503. doi:10.2147/dddt.s282368
6. Mohammad, I. S.; He, W.; Yin, L. *Crit. Rev. Ther. Drug Carrier Syst.* **2020,** *37,* 473–509. doi:10.1615/critrevtherdrugcarriersyst.2020025052
7. Mohammad, I. S.; He, W.; Yin, L. *Biomed. Pharmacother.* **2018,** *100,* 335–348. doi:10.1016/j.biopha.2018.02.038
8. Li, T.; Qin, X.; Li, Y.; Shen, X.; Li, S.; Yang, H.; Wu, C.; Zheng, C.; Zhu, J.; You, F.; Liu, Y. *Front. Bioeng. Biotechnol.* **2020,** *8,* 371. doi:10.3389/fbioe.2020.00371
9. Sushnitha, M.; Evangelopoulos, M.; Tasciotti, E.; Taraballi, F. *Front. Bioeng. Biotechnol.* **2020,** *8,* 627. doi:10.3389/fbioe.2020.00627
10. Karthik, K. K.; Cheriyan, B. V.; Rajeshkumar, S.; Gopalakrishnan, M. *Biomed. Technol.* **2024,** *6,* 61–74. doi:10.1016/j.bmt.2023.12.001
11. Azimizonuzi, H.; Ghayourvahdat, A.; Ahmed, M. H.; Kareem, R. A.; Zrzor, A. J.; Mansoor, A. S.; Athab, Z. H.; Kalavi, S. *Cancer Cell Int.* **2025,** *25,* 26. doi:10.1186/s12935-024-03610-z
12. Tunç, C. Ü.; Aydin, O. *J. Drug Delivery Sci. Technol.* **2022,** *74,* 103603. doi:10.1016/j.jddst.2022.103603
13. Tunc, C. U.; Kursunluoglu, G.; Akdeniz, M.; Kutlu, A. U.; Han, M. I.; Yerer, M. B.; Aydin, O. *ACS Mater. Au* **2023,** *3,* 483–491. doi:10.1021/acsmaterialsau.3c00033
14. Aydin, O.; Youssef, I.; Yuksel Durmaz, Y.; Tiruchinapally, G.; ElSayed, M. E. H. *Mol. Pharmaceutics* **2016,** *13,* 1413–1429. doi:10.1021/acs.molpharmaceut.6b00147
15. Zahin, N.; Anwar, R.; Tewari, D.; Kabir, M. T.; Sajid, A.; Mathew, B.; Uddin, M. S.; Aleya, L.; Abdel-Daim, M. M. *Environ. Sci. Pollut. Res.* **2020,** *27,* 19151–19168. doi:10.1007/s11356-019-05211-0
16. Tundisi, L. L.; Ataide, J. A.; Costa, J. S. R.; Coêlho, D. d. F.; Liszbinski, R. B.; Lopes, A. M.; Oliveira-Nascimento, L.; de Jesus, M. B.; Jozala, A. F.; Ehrhardt, C.; Mazzola, P. G. *Colloids Surf., B* **2023,** *222,* 113043. doi:10.1016/j.colsurfb.2022.113043
17. Tuteja, J.; Sand, A. Role of nanomedicine for targeted drug delivery in life-threatening diseases. In *Nanobiotechnology for the Livestock Industry;* Pratap Singh, R.; Adetunji, C. O.; Singh, R. I.; Singh, J.; Solanki, P. R.; Singh, K. R. B., Eds.; Elsevier: Amsterdam, Netherlands, 2023; pp 189–217. doi:10.1016/b978-0-323-98387-7.00004-5
18. Liu, R.; Luo, C.; Pang, Z.; Zhang, J.; Ruan, S.; Wu, M.; Wang, L.; Sun, T.; Li, N.; Han, L.; Shi, J.; Huang, Y.; Guo, W.; Peng, S.; Zhou, W.; Gao, H. *Chin. Chem. Lett.* **2023,** *34,* 107518. doi:10.1016/j.cclet.2022.05.032
19. Kar, R.; Dhar, R.; Mukherjee, S.; Nag, S.; Gorai, S.; Mukerjee, N.; Mukherjee, D.; Vatsa, R.; Chandrakanth Jadhav, M.; Ghosh, A.; Devi, A.; Krishnan, A.; Thorat, N. D. *ACS Biomater. Sci. Eng.* **2023,** *9,* 577–594. doi:10.1021/acsbiomaterials.2c01329
20. Shakeel, A.; Dash, S.; Kumar, V. K.; Mohanty, S. Role of Polymeric Nanomaterial in Regenerative Medicine and Stem Cell Biology. *Biomimetic Biomaterials for Tissue Regeneration and Drug Delivery;* Springer: Singapore, 2022; pp 75–98. doi:10.1007/978-981-16-4566-2_4
21. Sriwidodo; Umar, A. K.; Wathoni, N.; Zothantluanga, J. H.; Das, S.; Luckanagul, J. A. *Heliyon* **2022,** *8,* e08934. doi:10.1016/j.heliyon.2022.e08934

22. Chen, L.; Hong, W.; Ren, W.; Xu, T.; Qian, Z.; He, Z. *Signal Transduction Targeted Ther.* **2021,** *6,* 225. doi:10.1038/s41392-021-00631-2
23. Xu, X.; Li, T.; Shen, S.; Wang, J.; Abdou, P.; Gu, Z.; Mo, R. *Theranostics* **2019,** *9,* 7889–7905. doi:10.7150/thno.38583
24. Vijayan, V.; Uthaman, S.; Park, I.-K. Cell Membrane Coated Nanoparticles: An Emerging Biomimetic Nanoplatform for Targeted Bioimaging and Therapy. In *Biomimetic Medical Materials: From Nanotechnology to 3d Bioprinting;* Noh, I., Ed.; Springer: Singapore, 2018; pp 45–59. doi:10.1007/978-981-13-0445-3_3
25. Li, B.; Wang, F.; Gui, L.; He, Q.; Yao, Y.; Chen, H. *Nanomedicine (London, U. K.)* **2018,** *13,* 2099–2118. doi:10.2217/nnm-2018-0017
26. Zhang, F.; Li, F.; Lu, G.-H.; Nie, W.; Zhang, L.; Lv, Y.; Bao, W.; Gao, X.; Wei, W.; Pu, K.; Xie, H.-Y. *ACS Nano* **2019,** *13,* 5662–5673. doi:10.1021/acsnano.9b00892
27. Aghili, Z. S.; Magnani, M.; Ghatrehsamani, M.; Nourian Dehkordi, A.; Mirzaei, S. A.; Banitalebi Dehkordi, M. *Sci. Rep.* **2024,** *14,* 9381. doi:10.1038/s41598-024-60103-9
28. Riaz, M. I.; Sarwar, H. S.; Rehman, M.; Gohar, U. F.; Raza, S. A.; Siddique, M. I.; Shahnaz, G.; Sohail, M. F. *Braz. J. Pharm. Sci.* **2019,** *55,* e17680. doi:10.1590/s2175-97902019000117680
29. Lucas, A.; Lam, D.; Cabrales, P. *Drug Delivery* **2019,** *26,* 433–442. doi:10.1080/10717544.2019.1591544
30. Brenner, J. S.; Mitragotri, S.; Muzykantov, V. R. *Annu. Rev. Biomed. Eng.* **2021,** *23,* 225–248. doi:10.1146/annurev-bioeng-121219-024239
31. Oishi, Y.; Manabe, I. *Int. Immunol.* **2018,** *30,* 511–528. doi:10.1093/intimm/dxy054
32. Huang, X.; Wang, L.; Guo, H.; Zhang, W. *Bioact. Mater.* **2023,** *23,* 69–79. doi:10.1016/j.bioactmat.2022.09.027
33. Hou, T.; Wang, T.; Mu, W.; Yang, R.; Liang, S.; Zhang, Z.; Fu, S.; Gao, T.; Liu, Y.; Zhang, N. *Nano-Micro Lett.* **2021,** *13,* 6. doi:10.1007/s40820-020-00531-0
34. Xue, F.; Zhu, S.; Tian, Q.; Qin, R.; Wang, Z.; Huang, G.; Yang, S. *J. Colloid Interface Sci.* **2023,** *629,* 554–562. doi:10.1016/j.jcis.2022.08.186
35. Xiang, H.; Yang, R.; Tu, J.; Xi, Y.; Yang, S.; Lv, L.; Zhai, X.; Zhu, Y.; Dong, D.; Tao, X. *Biomed. Pharmacother.* **2023,** *157,* 113992. doi:10.1016/j.biopha.2022.113992
36. Cao, X.; Hu, Y.; Luo, S.; Wang, Y.; Gong, T.; Sun, X.; Fu, Y.; Zhang, Z. *Acta Pharm. Sin. B* **2019,** *9,* 575–589. doi:10.1016/j.apsb.2018.12.009
37. Zhang, Z.; Li, D.; Cao, Y.; Wang, Y.; Wang, F.; Zhang, F.; Zheng, S. *Int. Immunopharmacol.* **2021,** *99,* 107624. doi:10.1016/j.intimp.2021.107624
38. Neeve, S. C.; Robinson, B. W.; Fear, V. S. *Clin. Transl. Immunol.* **2019,** *8,* e1076. doi:10.1002/cti2.1076
39. Farhood, B.; Najafi, M.; Mortezaee, K. *J. Cell. Physiol.* **2019,** *234,* 8509–8521. doi:10.1002/jcp.27782
40. Kang, M.; Hong, J.; Jung, M.; Kwon, S. P.; Song, S. Y.; Kim, H. Y.; Lee, J.-R.; Kang, S.; Han, J.; Koo, J.-H.; Ryu, J. H.; Lim, S.; Sohn, H. S.; Choi, J.-M.; Doh, J.; Kim, B.-S. *Adv. Mater. (Weinheim, Ger.)* **2020,** *32,* 2003368. doi:10.1002/adma.202003368
41. Mühlberger, M.; Janko, C.; Unterweger, H.; Schreiber, E.; Band, J.; Lehmann, C.; Dudziak, D.; Lee, G.; Alexiou, C.; Tietze, R. *J. Magn. Magn. Mater.* **2019,** *473,* 61–67. doi:10.1016/j.jmmm.2018.10.022
42. Wayteck, L.; Dewitte, H.; De Backer, L.; Breckpot, K.; Demeester, J.; De Smedt, S. C.; Raemdonck, K. *Biomaterials* **2016,** *77,* 243–254. doi:10.1016/j.biomaterials.2015.11.016
43. George, A. P.; Kuzel, T. M.; Zhang, Y.; Zhang, B. *Comput. Struct. Biotechnol. J.* **2019,** *17,* 484–497. doi:10.1016/j.csbj.2019.03.015
44. Narain, A.; Asawa, S.; Chhabria, V.; Patil-Sen, Y. *Nanomedicine (London, U. K.)* **2017,** *12,* 2677–2692. doi:10.2217/nnm-2017-0225
45. Shair Mohammad, I.; Chaurasiya, B.; Yang, X.; Lin, C.; Rong, H.; He, W. *Pharmaceutics* **2020,** *12,* 950. doi:10.3390/pharmaceutics12100950
46. Nie, D.; Dai, Z.; Li, J.; Yang, Y.; Xi, Z.; Wang, J.; Zhang, W.; Qian, K.; Guo, S.; Zhu, C.; Wang, R.; Li, Y.; Yu, M.; Zhang, X.; Shi, X.; Gan, Y. *Nano Lett.* **2020,** *20,* 936–946. doi:10.1021/acs.nanolett.9b03817
47. Lei, W.; Yang, C.; Wu, Y.; Ru, G.; He, X.; Tong, X.; Wang, S. *J. Nanobiotechnol.* **2022,** *20,* 45. doi:10.1186/s12951-022-01251-w
48. He, H.; Guo, C.; Liu, W.; Chen, S.; Wang, X.-Y.; Yang, H. *MedComm: Biomater. Appl.* **2022,** *1,* e22. doi:10.1002/mba2.22
49. Rao, L.; Yu, G.-T.; Meng, Q.-F.; Bu, L.-L.; Tian, R.; Lin, L.-S.; Deng, H.; Yang, W.; Zan, M.; Ding, J.; Li, A.; Xiao, H.; Sun, Z.-J.; Liu, W.; Chen, X. *Adv. Funct. Mater.* **2019,** *29,* 1905671. doi:10.1002/adfm.201905671
50. Sarkar, S.; Alam, M. A.; Shaw, J.; Dasgupta, A. K. *Pharm. Res.* **2013,** *30,* 2785–2794. doi:10.1007/s11095-013-1097-1
51. Xu, P.; Zuo, H.; Chen, B.; Wang, R.; Ahmed, A.; Hu, Y.; Ouyang, J. *Sci. Rep.* **2017,** *7,* 42632. doi:10.1038/srep42632
52. Díaz, A.; Saxena, V.; González, J.; David, A.; Casañas, B.; Carpenter, C.; Batteas, J. D.; Colón, J. L.; Clearfield, A.; Delwar Hussain, M. *Chem. Commun.* **2012,** *48,* 1754–1756. doi:10.1039/c2cc16218k
53. Wu, Y.-W.; Huang, C.-C.; Changou, C. A.; Lu, L.-S.; Goubran, H.; Burnouf, T. *J. Biomed. Sci. (London, U. K.)* **2020,** *27,* 45. doi:10.1186/s12929-020-00633-2
54. Tang, S.; Zhang, F.; Gong, H.; Wei, F.; Zhuang, J.; Karshalev, E.; Esteban-Fernández de Ávila, B.; Huang, C.; Zhou, Z.; Li, Z.; Yin, L.; Dong, H.; Fang, R. H.; Zhang, X.; Zhang, L.; Wang, J. *Sci. Rob.* **2020,** *5,* eaba6137. doi:10.1126/scirobotics.aba6137
55. Feingold, K. R. Introduction to Lipids and Lipoproteins. In *Endotext;* Feingold, K. R.; Ahmed, S. F.; Anawalt, B.; Blackman, M. R.; Boyce, A.; Chrousos, G.; Corpas, E.; de Herder, W. W.; Dhatariya, K.; Dungan, K.; Hofland, J.; Kalra, S.; Kaltsas, G.; Kapoor, N.; Koch, C.; Kopp, P.; Korbonits, M.; Kovacs, C. S.; Kuohung, W.; Laferrère, B.; Levy, M.; McGee, E. A.; McLachlan, R.; Muzumdar, R.; Purnell, J.; Rey, R.; Sahay, R.; Shah, A. S.; Singer, F.; Sperling, M. A.; Stratakis, C. A.; Trence, D. L.; Wilson, D. P., Eds.; MDText.com, Inc.: South Dartmouth, MA, USA, 2000.
56. Gupta, A.; Sharma, R.; Kuche, K.; Jain, S. *Int. J. Pharm.* **2021,** *596,* 120272. doi:10.1016/j.ijpharm.2021.120272
57. Mei, Y.; Tang, L.; Xiao, Q.; Zhang, Z.; Zhang, Z.; Zang, J.; Zhou, J.; Wang, Y.; Wang, W.; Ren, M. *J. Mater. Chem. B* **2021,** *9,* 612–633. doi:10.1039/d0tb02139c
58. Longo, J.; Freedland, S. J.; Penn, L. Z.; Hamilton, R. J. *Prostate Cancer Prostatic Dis.* **2022,** *25,* 650–656. doi:10.1038/s41391-022-00557-y
59. Riscal, R.; Skuli, N.; Simon, M. C. *Mol. Cell* **2019,** *76,* 220–231. doi:10.1016/j.molcel.2019.09.008
60. Peltomaa, A. I.; Talala, K.; Taari, K.; Tammela, T. L. J.; Auvinen, A.; Murtola, T. J. *Cancers* **2022,** *14,* 2920. doi:10.3390/cancers14122920

61. Gilmore, S. F.; He, W.; Rasley, A.; Fischer, N. O. Strategies for Functionalizing Lipoprotein-Based Nanoparticles. *Control of Amphiphile Self-Assembling at the Molecular Level: Supra-Molecular Assemblies with Tuned Physicochemical Properties for Delivery Applications;* ACS Symposium Series, Vol. 1271; American Chemical Society: Washington, DC, USA, 2017; pp 131–150. doi:10.1021/bk-2017-1271.ch006
62. Di, L.; Maiseyeu, A. *Drug Delivery* **2021,** *28,* 408–421. doi:10.1080/10717544.2021.1886199
63. Wu, F.; Wuensch, S. A.; Azadniv, M.; Ebrahimkhani, M. R.; Crispe, I. N. *Mol. Pharmaceutics* **2009,** *6,* 1506–1517. doi:10.1021/mp900081y
64. Zhu, C.; Pradhan, P.; Huo, D.; Xue, J.; Shen, S.; Roy, K.; Xia, Y. *Angew. Chem.* **2017,** *129,* 10535–10538. doi:10.1002/ange.201704674
65. Ossoli, A.; Wolska, A.; Remaley, A. T.; Gomaraschi, M. *Biochim. Biophys. Acta, Mol. Cell Biol. Lipids* **2022,** *1867,* 159068. doi:10.1016/j.bbalip.2021.159068
66. Zhao, T.-J.; Zhu, N.; Shi, Y.-N.; Wang, Y.-X.; Zhang, C.-J.; Deng, C.-F.; Liao, D.-F.; Qin, L. *J. Cell. Physiol.* **2021,** *236,* 7853–7873. doi:10.1002/jcp.30412
67. Rink, J. S.; Lin, A. Y.; McMahon, K. M.; Calvert, A. E.; Yang, S.; Taxter, T.; Moreira, J.; Chadburn, A.; Behdad, A.; Karmali, R.; Thaxton, C. S.; Gordon, L. I. *bioRxiv* **2020,** 155242. doi:10.1101/2020.06.16.155242
68. Mooberry, L. K.; Sabnis, N. A.; Panchoo, M.; Nagarajan, B.; Lacko, A. G. *Front. Pharmacol.* **2016,** *7,* 466. doi:10.3389/fphar.2016.00466
69. Rui, M.; Xin, Y.; Li, R.; Ge, Y.; Feng, C.; Xu, X. *Mol. Pharmaceutics* **2017,** *14,* 107–123. doi:10.1021/acs.molpharmaceut.6b00732
70. Banik, B.; Wen, R.; Marrache, S.; Kumar, A.; Kolishetti, N.; Howerth, E. W.; Dhar, S. *Nanoscale* **2018,** *10,* 366–377. doi:10.1039/c7nr06295h
71. Nandwana, V.; Ryoo, S.-R.; Kanthala, S.; McMahon, K. M.; Rink, J. S.; Li, Y.; Venkatraman, S. S.; Thaxton, C. S.; Dravid, V. P. *Chem. Mater.* **2017,** *29,* 2276–2282. doi:10.1021/acs.chemmater.6b05357
72. Bell, J. B.; Rink, J. S.; Eckerdt, F.; Clymer, J.; Goldman, S.; Thaxton, C. S.; Platanias, L. C. *Sci. Rep.* **2018,** *8,* 1211. doi:10.1038/s41598-017-18100-8
73. Negussie, A. B.; Dell, A. C.; Davis, B. A.; Geibel, J. P. *Cells* **2022,** *11,* 1712. doi:10.3390/cells11101712
74. Mohammad, I. S.; He, W.; Yin, L. *Pharm. Res.* **2018,** *35,* 77. doi:10.1007/s11095-018-2370-0
75. An, F.-F.; Zhang, X.-H. *Theranostics* **2017,** *7,* 3667–3689. doi:10.7150/thno.19365
76. Matei, I.; Buta, C. M.; Turcu, I. M.; Culita, D.; Munteanu, C.; Ionita, G. *Molecules* **2019,** *24,* 3395. doi:10.3390/molecules24183395
77. Yao, Y.; Li, P.; He, J.; Wang, D.; Hu, J.; Yang, X. *ACS Appl. Mater. Interfaces* **2021,** *13,* 28650–28661. doi:10.1021/acsami.1c05669
78. Yang, Z.; Luo, S.; Zeng, Y.; Shi, C.; Li, R. *ACS Appl. Mater. Interfaces* **2017,** *9,* 6839–6848. doi:10.1021/acsami.6b15442
79. Jolley, C. C.; Uchida, M.; Reichhardt, C.; Harrington, R.; Kang, S.; Klem, M. T.; Parise, J. B.; Douglas, T. *Chem. Mater.* **2010,** *22,* 4612–4618. doi:10.1021/cm100657w
80. Hart, C.; Abuladel, N.; Bee, M.; Kreider, M. C.; CVitan, A. C.; Esson, M. M.; Farag, A.; Ibeh, T.; Kalivas, E. N.; Larco, D.-M.; Walker Long, A.; Lymperopoulos, L.; Mendel, Z.; Miles, N.; Zareba, C. M.; Schwabacher, J. C.; Slucher, H.; Vinals, J.; Heddleston, J. M.; Li, W.; Fox, D. M.; Hartings, M. R. *Dalton Trans.* **2017,** *46,* 16465–16473. doi:10.1039/c7dt03275g
81. Zhao, R.; Jiang, M. *bioRxiv* **2020,** 397455. doi:10.1101/2020.11.25.397455
82. Zhu, Y.; Xue, J.; Chen, W.; Bai, S.; Zheng, T.; He, C.; Guo, Z.; Jiang, M.; Du, G.; Sun, X. *J. Controlled Release* **2020,** *322,* 300–311. doi:10.1016/j.jconrel.2020.03.045
83. Si, X.; Song, X.; Xu, K.; Zhao, C.; Wang, J.; Liu, Y.; He, S.; Jin, M.; Li, H. *Microchem. J.* **2019,** *149,* 104050. doi:10.1016/j.microc.2019.104050
84. Chen, F.; Mao, M.; Wang, J.; Liu, J.; Li, F. *Talanta* **2020,** *209,* 120509. doi:10.1016/j.talanta.2019.120509
85. Borlan, R.; Tatar, A.-S.; Soritau, O.; Maniu, D.; Marc, G.; Florea, A.; Focsan, M.; Astilean, S. *Nanotechnology* **2020,** *31,* 315102. doi:10.1088/1361-6528/ab8b90
86. Lu, W.; Wang, S.; Liu, R.; Guan, Y.; Zhang, Y. *Acta Biomater.* **2021,** *126,* 249–258. doi:10.1016/j.actbio.2021.03.010
87. Shahabadi, N.; Zendehcheshm, S.; Khademi, F. *Biotechnol. Rep.* **2021,** *30,* e00615. doi:10.1016/j.btre.2021.e00615
88. Karami, E.; Behdani, M.; Kazemi-Lomedasht, F. *J. Drug Delivery Sci. Technol.* **2020,** *55,* 101471. doi:10.1016/j.jddst.2019.101471
89. Tao, H.-y.; Wang, R.-q.; Sheng, W.-j.; Zhen, Y.-s. *Int. J. Biol. Macromol.* **2021,** *187,* 24–34. doi:10.1016/j.ijbiomac.2021.07.080
90. Lima, T.; Bernfur, K.; Vilanova, M.; Cedervall, T. *Sci. Rep.* **2020,** *10,* 1129. doi:10.1038/s41598-020-57943-6
91. Vitali, M.; Casals, E.; Canals, F.; Colomé, N.; Puntes, V. *Nanoscale* **2020,** *12,* 15832–15844. doi:10.1039/d0nr02379e
92. Rabel, M.; Warncke, P.; Thürmer, M.; Grüttner, C.; Bergemann, C.; Kurland, H.-D.; Müller, F. A.; Koeberle, A.; Fischer, D. *Nanoscale* **2021,** *13,* 9415–9435. doi:10.1039/d0nr09053k
93. Elzoghby, A. O.; Samy, W. M.; Elgindy, N. A. *J. Controlled Release* **2012,** *157,* 168–182. doi:10.1016/j.jconrel.2011.07.031
94. Habibi, N.; Christau, S.; Ochyl, L. J.; Fan, Z.; Hassani Najafabadi, A.; Kuehnhammer, M.; Zhang, M.; Helgeson, M.; von Klitzing, R.; Moon, J. J.; Lahann, J. *Adv. Ther.* **2020,** *3,* 2000100. doi:10.1002/adtp.202000100
95. Pang, G.; Liu, Y.; Wang, Y.; Wang, Y.; Wang, F.; Zhao, J.; Zhang, L. W. *Wiley Interdiscip. Rev.: Nanomed. Nanobiotechnol.* **2022,** *14,* e1747. doi:10.1002/wnan.1747
96. Pulsipher, K. W.; Honig, S.; Deng, S.; Dmochowski, I. J. *J. Inorg. Biochem.* **2017,** *174,* 169–176. doi:10.1016/j.jinorgbio.2017.06.012
97. Bellini, M.; Riva, B.; Tinelli, V.; Rizzuto, M. A.; Salvioni, L.; Colombo, M.; Mingozzi, F.; Visioli, A.; Marongiu, L.; Frascotti, G.; Christodoulou, M. S.; Passarella, D.; Prosperi, D.; Fiandra, L. *Small* **2020,** *16,* 2001450. doi:10.1002/smll.202001450
98. Cai, Y.; Deng, T.; Pan, Y.; Zink, J. I. *Adv. Funct. Mater.* **2020,** *30,* 2002043. doi:10.1002/adfm.202002043
99. Tetter, S.; Hilvert, D. *Angew. Chem., Int. Ed.* **2017,** *56,* 14933–14936. doi:10.1002/anie.201708530
100. Matsumoto, R.; Kakuta, M.; Sugiyama, T.; Goto, Y.; Sakai, H.; Tokita, Y.; Hatazawa, T.; Tsujimura, S.; Shirai, O.; Kano, K. *Phys. Chem. Chem. Phys.* **2010,** *12,* 13904–13906. doi:10.1039/c0cp00556h

101. Godoy-Gallardo, M.; Labay, C.; Trikalitis, V. D.; Kempen, P. J.; Larsen, J. B.; Andresen, T. L.; Hosta-Rigau, L. *ACS Appl. Mater. Interfaces* **2017,** *9,* 15907–15921. doi:10.1021/acsami.6b16275
102. Wang, H.; Zhao, Z.; Liu, Y.; Shao, C.; Bian, F.; Zhao, Y. *Sci. Adv.* **2018,** *4,* eaat2816. doi:10.1126/sciadv.aat2816
103. Shao, M.; Lopes, D.; Lopes, J.; Yousefiasl, S.; Macário-Soares, A.; Peixoto, D.; Ferreira-Faria, I.; Veiga, F.; Conde, J.; Huang, Y.; Chen, X.; Paiva-Santos, A. C.; Makvandi, P. *Matter* **2023,** *6,* 761–799. doi:10.1016/j.matt.2023.01.012
104. Cheng, J.; Wang, X.; Yuan, X.; Liu, G.; Chu, Q. *Am. J. Cancer Res.* **2022,** *12,* 2226–2248.
105. Théry, C.; Witwer, K. W.; Aikawa, E.; Alcaraz, M. J.; Anderson, J. D.; Andriantsitohaina, R.; Antoniou, A.; Arab, T.; Archer, F.; Atkin-Smith, G. K.; et al. *J. Extracell. Vesicles* **2018,** *7,* 1535750. doi:10.1080/20013078.2018.1535750
106. Liang, Y.; Duan, L.; Lu, J.; Xia, J. *Theranostics* **2021,** *11,* 3183–3195. doi:10.7150/thno.52570
107. Wu, P.; Zhang, B.; Ocansey, D. K. W.; Xu, W.; Qian, H. *Biomaterials* **2021,** *269,* 120467. doi:10.1016/j.biomaterials.2020.120467
108. Li, P.; Kaslan, M.; Lee, S. H.; Yao, J.; Gao, Z. *Theranostics* **2017,** *7,* 789–804. doi:10.7150/thno.18133
109. Sharifi, F.; Sedighi, A.; Rehman, M. *Eng. Proc.* **2020,** *2,* 76. doi:10.3390/ecsa-7-08221
110. Pisano, S.; Pierini, I.; Gu, J.; Gazze, A.; Francis, L. W.; Gonzalez, D.; Conlan, R. S.; Corradetti, B. *Front. Cell Dev. Biol.* **2020,** *8,* 553576. doi:10.3389/fcell.2020.553576
111. Li, X.; Corbett, A. L.; Taatizadeh, E.; Tasnim, N.; Little, J. P.; Garnis, C.; Daugaard, M.; Guns, E.; Hoorfar, M.; Li, I. T. S. *APL Bioeng.* **2019,** *3,* 011503. doi:10.1063/1.5087122
112. Garg, A.; Dewangan, H. K. *Crit. Rev. Ther. Drug Carrier Syst.* **2020,** *37,* 183–204. doi:10.1615/critrevtherdrugcarriersyst.2020033273
113. Sokullu, E.; Soleymani Abyaneh, H.; Gauthier, M. A. *Pharmaceutics* **2019,** *11,* 211. doi:10.3390/pharmaceutics11050211
114. Dashti, N. H.; Abidin, R. S.; Sainsbury, F. *ACS Nano* **2018,** *12,* 4615–4623. doi:10.1021/acsnano.8b01059
115. Zhang, N.; Wu, H.; Liang, Y.; Ye, J.; Zhang, H.; Miao, Y.; Luo, Y.; Fan, H.; Yue, T. *Int. J. Nanomed.* **2021,** *16,* 7091–7102. doi:10.2147/ijn.s325282
116. Bao, W.; Ma, H.; Wang, N.; He, Z. *Mater. Technol. (Abingdon, U. K.)* **2021,** *36,* 308–316. doi:10.1080/10667857.2020.1758474
117. Fang, Z.; Sun, Y.; Cai, C.; Fan, R.; Guo, R.; Xie, D. *Int. J. Polym. Mater. Polym. Biomater.* **2021,** *70,* 27–36. doi:10.1080/00914037.2019.1685516
118. Delfi, M.; Sartorius, R.; Ashrafizadeh, M.; Sharifi, E.; Zhang, Y.; De Berardinis, P.; Zarrabi, A.; Varma, R. S.; Tay, F. R.; Smith, B. R.; Makvandi, P. *Nano Today* **2021,** *38,* 101119. doi:10.1016/j.nantod.2021.101119
119. Raj, S.; Khurana, S.; Choudhari, R.; Kesari, K. K.; Kamal, M. A.; Garg, N.; Ruokolainen, J.; Das, B. C.; Kumar, D. *Semin. Cancer Biol.* **2021,** *69,* 166–177. doi:10.1016/j.semcancer.2019.11.002
120. Zhang, Z.; Qian, H.; Huang, J.; Sha, H.; Zhang, H.; Yu, L.; Liu, B.; Hua, D.; Qian, X. *Int. J. Nanomed.* **2018,** *13,* 4961–4975. doi:10.2147/ijn.s170148
121. Chen, H.; Sha, H.; Zhang, L.; Qian, H.; Chen, F.; Ding, N.; Ji, L.; Zhu, A.; Xu, Q.; Meng, F.; Yu, L.; Zhou, Y.; Liu, B. *Int. J. Nanomed.* **2018,** *13,* 5347–5359. doi:10.2147/ijn.s165109
122. Feng, Y.; Liu, Q.; Li, Y.; Han, Y.; Liang, M.; Wang, H.; Yao, Q.; Wang, Y.; Yang, M.; Li, Z.; Gong, W.; Yang, Y.; Gao, C. *Bioact. Mater.* **2021,** *6,* 1528–1540. doi:10.1016/j.bioactmat.2020.11.014
123. Castro, F.; Martins, C.; Silveira, M. J.; Moura, R. P.; Pereira, C. L.; Sarmento, B. *Adv. Drug Delivery Rev.* **2021,** *170,* 312–339. doi:10.1016/j.addr.2020.09.001
124. Chai, Z.; Ran, D.; Lu, L.; Zhan, C.; Ruan, H.; Hu, X.; Xie, C.; Jiang, K.; Li, J.; Zhou, J.; Wang, J.; Zhang, Y.; Fang, R. H.; Zhang, L.; Lu, W. *ACS Nano* **2019,** *13,* 5591–5601. doi:10.1021/acsnano.9b00661
125. Branco, F.; Cunha, J.; Mendes, M.; Vitorino, C.; Sousa, J. J. *ACS Nano* **2024,** *18,* 16359–16394. doi:10.1021/acsnano.4c01790
126. Han, X.; Zhang, X.; Kang, L.; Feng, S.; Li, Y.; Zhao, G. *Int. J. Biol. Macromol.* **2025,** *299,* 140143. doi:10.1016/j.ijbiomac.2025.140143
127. Fu, S.; Liang, M.; Wang, Y.; Cui, L.; Gao, C.; Chu, X.; Liu, Q.; Feng, Y.; Gong, W.; Yang, M.; Li, Z.; Yang, C.; Xie, X.; Yang, Y.; Gao, C. *ACS Appl. Mater. Interfaces* **2019,** *11,* 1841–1854. doi:10.1021/acsami.8b18664
128. Fan, J.; Liu, B.; Long, Y.; Wang, Z.; Tong, C.; Wang, W.; You, P.; Liu, X. *Acta Biomater.* **2020,** *113,* 554–569. doi:10.1016/j.actbio.2020.06.025
129. Kim, M. W.; Lee, G.; Niidome, T.; Komohara, Y.; Lee, R.; Park, Y. I. *Front. Bioeng. Biotechnol.* **2020,** *8,* 133. doi:10.3389/fbioe.2020.00133
130. Zhang, M.; Cheng, S.; Jin, Y.; Zhang, N.; Wang, Y. *Clin. Transl. Med.* **2021,** *11,* e292. doi:10.1002/ctm2.292
131. Wang, H.; Liu, Y.; He, R.; Xu, D.; Zang, J.; Weeranoppanant, N.; Dong, H.; Li, Y. *Biomater. Sci.* **2020,** *8,* 552–568. doi:10.1039/c9bm01392j
132. Wang, X.; Mao, K.; Zhang, X.; Zhang, Y.; Yang, Y.-G.; Sun, T. *Interdiscip. Med.* **2024,** *2,* e20240014. doi:10.1002/inmd.20240014
133. Jin, J.; Bhujwalla, Z. M. *Front. Oncol.* **2020,** *9,* 1560. doi:10.3389/fonc.2019.01560
134. Liu, X.; Sun, Y.; Xu, S.; Gao, X.; Kong, F.; Xu, K.; Tang, B. *Theranostics* **2019,** *9,* 5828–5838. doi:10.7150/thno.34837
135. Shao, D.; Zhang, F.; Chen, F.; Zheng, X.; Hu, H.; Yang, C.; Tu, Z.; Wang, Z.; Chang, Z.; Lu, J.; Li, T.; Zhang, Y.; Chen, L.; Leong, K. W.; Dong, W.-f. *Adv. Mater. (Weinheim, Ger.)* **2020,** *32,* 2004385. doi:10.1002/adma.202004385
136. Kong, F.; He, H.; Bai, H.; Yang, F.; Ma, M.; Gu, N.; Zhang, Y. *Bioact. Mater.* **2022,** *18,* 526–538. doi:10.1016/j.bioactmat.2022.03.022
137. Ke, R.; Zhen, X.; Wang, H.-S.; Li, L.; Wang, H.; Wang, S.; Xie, X. *J. Colloid Interface Sci.* **2022,** *609,* 307–319. doi:10.1016/j.jcis.2021.12.009
138. Wang, M.; Hu, Q.; Huang, J.; Zhao, X.; Shao, S.; Zhang, F.; Yao, Z.; Ping, Y.; Liang, T. *J. Nanobiotechnol.* **2022,** *20,* 85. doi:10.1186/s12951-022-01282-3
139. Li, Z.; Cai, H.; Li, Z.; Ren, L.; Ma, X.; Zhu, H.; Gong, Q.; Zhang, H.; Gu, Z.; Luo, K. *Bioact. Mater.* **2023,** *21,* 299–312. doi:10.1016/j.bioactmat.2022.08.028
140. Zhao, X.; Xu, S.; Jiang, Y.; Wang, C.; ur Rehman, S.; Ji, S.; Wang, J.; Tao, T.; Xu, H.; Chen, R.; Cai, Y.; Jiang, Y.; Wang, H.; Ma, K.; Wang, J. *Chem. Eng. J.* **2023,** *454,* 140440. doi:10.1016/j.cej.2022.140440
141. Du, J.; Sun, J.; Liu, X.; Wu, Q.; Shen, W.; Gao, Y.; Liu, Y.; Wu, C. *Eur. J. Pharm. Sci.* **2023,** *180,* 106338. doi:10.1016/j.ejps.2022.106338
142. Gao, T.; Liu, H.; Xie, Z.; Zheng, M. *J. Colloid Interface Sci.* **2023,** *630,* 385–394. doi:10.1016/j.jcis.2022.10.003
143. Zheng, D.; Zhou, J.; Qian, L.; Liu, X.; Chang, C.; Tang, S.; Zhang, H.; Zhou, S. *Bioact. Mater.* **2023,** *22,* 567–587. doi:10.1016/j.bioactmat.2022.10.025

144. Chrastina, A.; Massey, K. A.; Schnitzer, J. E. *Wiley Interdiscip. Rev.: Nanomed. Nanobiotechnol.* **2011,** *3,* 421–437. doi:10.1002/wnan.143
145. Walweel, N.; Cinar, V.; Mersin, O.; Macit, S.; Yildiz, U.; Demirel, E.; Tunç, C. U.; Ulutabanca, H.; Hamurcu, Z.; Yuksel Durmaz, Y.; Aydin, O. *ACS Appl. Bio Mater.* **2025,** *8,* 2938–2953. doi:10.1021/acsabm.4c01778
146. Ma, N.; Ma, C.; Li, C.; Wang, T.; Tang, Y.; Wang, H.; Mou, X.; Chen, Z.; He, N. *J. Nanosci. Nanotechnol.* **2013,** *13,* 6485–6498. doi:10.1166/jnn.2013.7525
147. Huang, X.; Guo, H.; Wang, L.; Zhang, Z.; Zhang, W. *Drug Discovery Today* **2023,** *28,* 103514. doi:10.1016/j.drudis.2023.103514
148. Eksi, O. B.; Kutlu, A. U.; Yumuk, K.; Chatzi Memet, B.; Benk, R.; Kursunluoglu, G.; Aydin, O. Nanodelivery in Gene Therapy. In *Handbook of Cancer and Immunology;* Rezaei, N., Ed.; Springer International Publishing: Cham, Switzerland, 2024; pp 1–40. doi:10.1007/978-3-030-80962-1_410-1
149. Liu, Y.; Zou, Y.; Feng, C.; Lee, A.; Yin, J.; Chung, R.; Park, J. B.; Rizos, H.; Tao, W.; Zheng, M.; Farokhzad, O. C.; Shi, B. *Nano Lett.* **2020,** *20,* 1637–1646. doi:10.1021/acs.nanolett.9b04683
150. Lin, C.; Yang, X.; Li, H.; Zou, Y.; Mohammad, I. S.; Rong, H.; Rao, Y.; Song, J.; Leung, S. S. Y.; Hu, H. *Nanoscale* **2021,** *13,* 6605–6623. doi:10.1039/d1nr00032b
151. Li, K.; Qiu, Y.; Liu, X.; Huang, F. *Balk. Med. J.* **2022,** *39,* 178–186. doi:10.4274/balkanmedj.galenos.2022.2021-11-1
152. Wang, Y.; Ji, X.; Ruan, M.; Liu, W.; Song, R.; Dai, J.; Xue, W. *Small* **2018,** *14,* 1803002. doi:10.1002/smll.201803002
153. Hao, X.; Li, Q.; Wang, H.; Muhammad, K.; Guo, J.; Ren, X.; Shi, C.; Xia, S.; Zhang, W.; Feng, Y. *J. Mater. Chem. B* **2018,** *6,* 5975–5985. doi:10.1039/c8tb01789a
154. Zhang, L.; Deng, S.; Zhang, Y.; Peng, Q.; Li, H.; Wang, P.; Fu, X.; Lei, X.; Qin, A.; Yu, X. *Adv. Healthcare Mater.* **2020,** *9,* 1900772. doi:10.1002/adhm.201900772
155. Tunç, C. U.; Öztaş, D. Y.; Uzunoğlu, D.; Bayrak, Ö. F.; Çulha, M. *Hum. Gene Ther.* **2019,** *30,* 1547–1558. doi:10.1089/hum.2019.119
156. Gong, C.; Yu, X.; Zhang, W.; Han, L.; Wang, R.; Wang, Y.; Gao, S.; Yuan, Y. *J. Nanobiotechnol.* **2021,** *19,* 58. doi:10.1186/s12951-021-00805-8
157. Chen, M.; Chen, M.; He, J. *Artif. Cells, Nanomed., Biotechnol.* **2019,** *47,* 1635–1641. doi:10.1080/21691401.2019.1608219
158. Liu, B.; Hu, F.; Zhang, J.; Wang, C.; Li, L. *Angew. Chem.* **2019,** *131,* 8896–8900. doi:10.1002/ange.201903417
159. Xu, C.; Liu, W.; Hu, Y.; Li, W.; Di, W. *Theranostics* **2020,** *10,* 3325–3339. doi:10.7150/thno.41228
160. Mu, X.; Li, J.; Yan, S.; Zhang, H.; Zhang, W.; Zhang, F.; Jiang, J. *ACS Biomater. Sci. Eng.* **2018,** *4,* 3895–3905. doi:10.1021/acsbiomaterials.8b00858
161. Liang, L.; Cen, H.; Huang, J.; Qin, A.; Xu, W.; Wang, S.; Chen, Z.; Tan, L.; Zhang, Q.; Yu, X.; Yang, X.; Zhang, L. *Mol. Cancer* **2022,** *21,* 186. doi:10.1186/s12943-022-01651-4
162. Yang, L.; Lin, Y.; Zhang, J.; Huang, J.; Qin, A.; Miao, Y.; Wang, P.; Yu, X.; Wang, L.; Zhang, L. *J. Colloid Interface Sci.* **2022,** *625,* 532–543. doi:10.1016/j.jcis.2022.06.008
163. Liu, S.-Y.; Liang, Z.-S.; Gao, F.; Luo, S.-F.; Lu, G.-Q. *J. Mater. Sci.: Mater. Med.* **2010,** *21,* 665–674. doi:10.1007/s10856-009-3895-x
164. Xu, L.; Cheng, L.; Wang, C.; Peng, R.; Liu, Z. *Polym. Chem.* **2014,** *5,* 1573–1580. doi:10.1039/c3py01196h
165. Cheng, L.; Yang, K.; Chen, Q.; Liu, Z. *ACS Nano* **2012,** *6,* 5605–5613. doi:10.1021/nn301539m
166. Wu, P.; Gao, Y.; Zhang, H.; Cai, C. *Anal. Chem. (Washington, DC, U. S.)* **2012,** *84,* 7692–7699. doi:10.1021/ac3015164
167. Espinosa, A.; Silva, A. K. A.; Sánchez-Iglesias, A.; Grzelczak, M.; Péchoux, C.; Desboeufs, K.; Liz-Marzán, L. M.; Wilhelm, C. *Adv. Healthcare Mater.* **2016,** *5,* 1040–1048. doi:10.1002/adhm.201501035
168. Piao, J.-G.; Wang, L.; Gao, F.; You, Y.-Z.; Xiong, Y.; Yang, L. *ACS Nano* **2014,** *8,* 10414–10425. doi:10.1021/nn503779d
169. Ren, X.; Zheng, R.; Fang, X.; Wang, X.; Zhang, X.; Yang, W.; Sha, X. *Biomaterials* **2016,** *92,* 13–24. doi:10.1016/j.biomaterials.2016.03.026
170. Rao, L.; Cai, B.; Bu, L.-L.; Liao, Q.-Q.; Guo, S.-S.; Zhao, X.-Z.; Dong, W.-F.; Liu, W. *ACS Nano* **2017,** *11,* 3496–3505. doi:10.1021/acsnano.7b00133
171. Wu, P.; Jiang, X.; Yin, S.; Yang, Y.; Liu, T.; Wang, K. *J. Nanobiotechnol.* **2021,** *19,* 213. doi:10.1186/s12951-021-00949-7
172. Li, Y.; Fan, X.; Li, Y.; Chen, R.; Ni, H.; Zhang, Y.; Xia, Q.; Feng, Z.; Tang, B. Z.; Qian, J.; Lin, H. *bioRxiv* **2021**. doi:10.1101/2021.04.19.440457
173. Hussein, E. A.; Zagho, M. M.; Nasrallah, G. K.; Elzatahry, A. A. *Int. J. Nanomed.* **2018,** *13,* 2897–2906. doi:10.2147/ijn.s161031
174. He, C.; Duan, X.; Guo, N.; Chan, C.; Poon, C.; Weichselbaum, R. R.; Lin, W. *Nat. Commun.* **2016,** *7,* 12499. doi:10.1038/ncomms12499
175. Fang, X.; Wu, X.; Li, Z.; Jiang, L.; Lo, W.-S.; Chen, G.; Gu, Y.; Wong, W.-T. *Adv. Sci.* **2021,** *8,* 2003041. doi:10.1002/advs.202003041
176. Ming, J.; Zhang, J.; Shi, Y.; Yang, W.; Li, J.; Sun, D.; Xiang, S.; Chen, X.; Chen, L.; Zheng, N. *Nanoscale* **2020,** *12,* 3916–3930. doi:10.1039/c9nr09402d
177. Ng, C. W.; Li, J.; Pu, K. *Adv. Funct. Mater.* **2018,** *28,* 1870327. doi:10.1002/adfm.201870327
178. Wei, Y.; Wang, Z.; Yang, J.; Xu, R.; Deng, H.; Ma, S.; Fang, T.; Zhang, J.; Shen, Q. *J. Colloid Interface Sci.* **2022,** *606,* 1950–1965. doi:10.1016/j.jcis.2021.09.160
179. Shu, X.; Chen, Y.; Yan, P.; Xiang, Y.; Shi, Q.-Y.; Yin, T.; Wang, P.; Liu, L.-H.; Shuai, X. *J. Controlled Release* **2022,** *347,* 270–281. doi:10.1016/j.jconrel.2022.05.010
180. Liu, S.; Zhang, T.; Li, S.; Wu, Q.; Wang, K.; Xu, X.; Lu, M.; Shao, R.; Zhao, W.; Liu, H. *Small* **2023,** *19,* 2206503. doi:10.1002/smll.202206503
181. Zhao, Y.; Pan, Y.; Zou, K.; Lan, Z.; Cheng, G.; Mai, Q.; Cui, H.; Meng, Q.; Chen, T.; Rao, L.; Ma, L.; Yu, G. *Bioact. Mater.* **2023,** *19,* 237–250. doi:10.1016/j.bioactmat.2022.04.011
182. Zhou, S.; Dai, L.; Pan, L.; Shen, G.; Qian, Z. *Chem. Commun.* **2025,** *61,* 4595–4605. doi:10.1039/d4cc06730d
183. Liu, C.; Gao, J.; Cheng, Y.; Zhang, S.; Fu, C. *Regener. Biomater.* **2025,** *12,* rbae135. doi:10.1093/rb/rbae135
184. Wu, Q.; Chen, L.; Huang, X.; Lin, J.; Gao, J.; Yang, G.; Wu, Y.; Wang, C.; Kang, X.; Yao, Y.; Wang, Y.; Xue, M.; Luan, X.; Chen, X.; Zhang, Z.; Sun, S. *Int. J. Oral Sci.* **2023,** *15,* 9. doi:10.1038/s41368-022-00211-2
185. Zhang, F.; Hu, Q.; Li, B.; Huang, Y.; Wang, M.; Shao, S.; Tang, H.; Yao, Z.; Ping, Y.; Liang, T. *J. Controlled Release* **2023,** *354,* 835–850. doi:10.1016/j.jconrel.2023.01.007
186. Al-Jamal, A. N.; Al-Hussainy, A. F.; Mohammed, B. A.; Abbas, H. H.; Kadhim, I. M.; Ward, Z. H.; Mahapatra, D. K.; Joseph, T. M.; kianfar, E.; Thomas, S. *Health Sci. Rev.* **2025,** *14,* 100218. doi:10.1016/j.hsr.2025.100218

187. Van Straten, D.; Mashayekhi, V.; De Bruijn, H. S.; Oliveira, S.; Robinson, D. J. *Cancers* **2017,** *9,* 19. doi:10.3390/cancers9020019
188. Henderson, B. W.; Dougherty, T. J. *Photochem. Photobiol.* **1992,** *55,* 145–157. doi:10.1111/j.1751-1097.1992.tb04222.x
189. Foote, C. S. *Photochem. Photobiol.* **1991,** *54,* 659. doi:10.1111/j.1751-1097.1991.tb02071.x
190. Bacellar, I. O. L.; Tsubone, T. M.; Pavani, C.; Baptista, M. S. *Int. J. Mol. Sci.* **2015,** *16,* 20523–20559. doi:10.3390/ijms160920523
191. Igney, F. H.; Krammer, P. H. *Nat. Rev. Cancer* **2002,** *2,* 277–288. doi:10.1038/nrc776
192. Zhang, T.; Liu, H.; Li, L.; Guo, Z.; Song, J.; Yang, X.; Wan, G.; Li, R.; Wang, Y. *Bioact. Mater.* **2021,** *6,* 3865–3878. doi:10.1016/j.bioactmat.2021.04.004
193. Wu, H.; Du, X.; Xu, J.; Kong, X.; Li, Y.; Liu, D.; Yang, X.; Ye, L.; Ji, J.; Xi, Y.; Zhai, G. *Acta Biomater.* **2023,** *157,* 551–565. doi:10.1016/j.actbio.2022.12.010
194. Nowak, K. M.; Schwartz, M. R.; Breza, V. R.; Price, R. J. *Cancer Lett.* **2022,** *532,* 215592. doi:10.1016/j.canlet.2022.215592
195. Wang, P.; Li, C.; Wang, X.; Xiong, W.; Feng, X.; Liu, Q.; Leung, A. W.; Xu, C. *Ultrason. Sonochem.* **2015,** *23,* 116–127. doi:10.1016/j.ultsonch.2014.10.027
196. Zhang, D.; Lin, Z.; Zheng, Y.; Song, J.; Li, J.; Zeng, Y.; Liu, X. *ACS Nano* **2020,** *14,* 8985–8999. doi:10.1021/acsnano.0c03833
197. Lin, X.; He, T.; Tang, R.; Li, Q.; Wu, N.; Zhou, Y.; He, H.; Wan, L.; Huang, J.; Jiang, Q.; Zhong, Y.; Xie, Z.; Hu, Z.; Zhou, Y.; Li, P. *J. Nanobiotechnol.* **2022,** *20,* 80. doi:10.1186/s12951-022-01287-y
198. Aydin, O.; Kursunluoglu, G.; Akdeniz, M. *Cancer Res.* **2025,** *85,* 4479. doi:10.1158/1538-7445.am2025-4479
199. Feng, Q.; Yang, X.; Hao, Y.; Wang, N.; Feng, X.; Hou, L.; Zhang, Z. *ACS Appl. Mater. Interfaces* **2019,** *11,* 32729–32738. doi:10.1021/acsami.9b10948

License and Terms

BEILSTEIN JOURNAL OF NANOTECHNOLOGY

Bioinspired polypropylene-based functionally graded materials and metamaterials modeling the mistletoe–host interface

Lina M. Rojas González[1], Naeim Ghavidelnia[1,2], Christoph Eberl[1,2,3] and Max D. Mylo[*1,2]

Full Research Paper

Open Access

Address:
[1]Department of Microsystems Engineering, University of Freiburg, D-79110 Freiburg, Germany, [2]Cluster of Excellence livMatS @ FIT – Freiburg Center for Interactive Materials and Bioinspired Technologies, University of Freiburg, D-79110 Freiburg, Germany and [3]Fraunhofer Institute for Mechanics of Materials (IWM), Wöhlerstr. 11, D-79108 Freiburg, Germany

Email:
Max D. Mylo[*] - max.mylo@livmats.uni-freiburg.de

* Corresponding author

Keywords:
bioinspiration; digital image correlation; fiber-reinforced polypropylene; materials interface; programmable failure

Beilstein J. Nanotechnol. **2025,** *16,* 1592–1606.
https://doi.org/10.3762/bjnano.16.113

Received: 12 May 2025
Accepted: 26 August 2025
Published: 11 September 2025

This article is part of the thematic issue "Micro- and nanoscale effects in biological and bioinspired materials and surfaces".

Guest Editor: T. H. Büscher

Abstract

Biological systems and their structural and functional adaptations provide valuable insights into increasing the longevity of engineered materials. A striking example is the hemiparasitic European mistletoe (*Viscum album*), which forms a lifelong (over 20 years) connection with its host tree, providing physiological supply and mechanical anchorage. The V-shaped interface between mistletoe and host is characterized by a lignification and cell wall gradient that bridges the mechanical differences between the adjacent tissues. These characteristics of the mistletoe–host interface can be transferred to functionally graded polymeric materials. Using extrusion molding and hot pressing, we developed a material system that combines pure and glass-fiber-reinforced polypropylene and exhibits a continuously graded mistletoe-inspired V-shaped interface. Microtomographic analyses quantified the gradual transition of the glass fiber content along one specimen from 0 to 30%, further revealing the random fiber orientation in the polymer matrix. Tensile tests showed that both Young's modulus (by 38%) and ultimate tensile strength (by 62%) could be increased by introducing V-shaped interfaces. Digital image correlation analysis and the fracture images showed that the positioning of the area with the highest glass fiber content can lead to spatial control over local strain behavior and the failure point. Moreover, this phenomenon was transferred to metamaterial structures where the material gradient counteracts the geometric gradient (beam thickness). The results highlight the effective anchoring method of mistletoe through graded structuring of the interface with the host branch and provide a framework for creating bioinspired functionally graded material systems with programmable local strain and failure behavior.

Introduction

Longevity and the efficient use of resources are playing an increasingly important role in the development and production of engineering materials systems. In order to fully exploit the longevity potential, the robustness and resilience of materials and material composites and their structuring are of crucial importance to withstand severe conditions, prevent damage, and maintain their functionality [1]. Furthermore, damage control mechanisms can be used to enable the targeted and economical use of resources and the recyclability of individual parts or the entire materials system [2]. In addition to self-healing mechanisms for reusing damaged structures [3-5], the targeted and pre-programmed discard of non-functional parts can also be used to maintain the overall function or recyclability of the materials used [6]. In order to achieve this in a spatially controlled manner, predetermined failure locations can be introduced, which should have little or no effect on the overall mechanical properties in the regular product environment.

A class of materials characterized by a high degree of flexibility and distribution of material properties, which enables locally adapted behavior and, thus, allows for thermal and mechanical stresses to be controlled locally, is known as functionally graded materials (FGMs). By means of a gradual composition and microstructure, FGMs can reduce interfacial stress, allowing for precise tailoring of mechanical properties such as stiffness, strength, and toughness along a specific direction or within a defined volume [7]. By strategically varying the composition or morphology of the material, FGMs can be designed with enhanced performance characteristics tailored to specific application requirements. The gradient can be continuous or discontinuous, or step-wise [8]; also, it can be along the longitudinal, transverse, and cross-sectional axes [9]. In comparison to conventional homogeneous materials, polymeric FGMs offer several advantages, including improved load-bearing capacity, resistance to fracture and fatigue, and compatibility with diverse manufacturing processes [10,11].

Programming the mechanical properties and fracture behavior by combining FGMs and mechanical metamaterials represents an exciting frontier in materials engineering and computational design [12-14]. By embedding FGMs into the hierarchical architecture of mechanical metamaterials, even more complex and tailored mechanical properties can be achieved at multiple length scales [15]. This integration enables the creation of materials with unprecedented combinations of stiffness, strength, damping, and other mechanical characteristics, offering enhanced performance and versatility for a wide range of applications [16]. By strategically designing the gradient profiles within FGMs and integrating them into the hierarchical architectures of mechanical metamaterials, engineers can effectively program and manipulate the stiffness of the resulting structures at multiple length scales [17]. This approach allows for precise control over stiffness distributions, enabling the creation of materials with tailored mechanical responses that vary spatially or directionally to meet specific performance requirements. Recent advancements in additive manufacturing techniques have demonstrated the potential for creating functionally graded structures using multimaterial 3D printing [18-20]. However, these methods mainly focus on structural gradients [21] and face significant challenges in part integrity due to the layer-by-layer fabrication process, which results in poor adhesion between layers of different materials [22]. Thus, almost all functionally graded metamaterials are limited to structural gradients and do not feature material gradients.

Nature is one prime example of multihierarchical structuring and gradation, which can be found in various forms and on different scales [23], with its diverse plant and animal systems having developed over millions of years during the course of evolution. As such, the kingdom Plantae offers a wide range of functional principles that can be used as a source of bioinspiration to increase longevity and damage control potential [1,4]. Biological materials and their highly modified structure–function relationship are designed to enable organisms to survive and/or adapt to the environmental conditions in which they live [24,25]. The European mistletoe (*Viscum album*) is an excellent model of a long-lasting connection between two material systems with different mechanical properties. As a hemiparasite, it uses a modified organ called the “haustorium” with wedge-shaped, or simplified, V-shaped structures to penetrate the host and establish a physiological and mechanical connection (Figure 1) [26-28]. This allows it to take up water and nutrients and to maintain mechanical stability during joint growth for over 20 years, despite its ever-increasing weight and the additional loads caused by wind and snow [29]. Analyses of the tissue and cell structure have revealed a chemical lignification gradient along the V-shaped interface between the tissues of the two species. Moreover, a decrease in cell wall thickness from the interface to the inner parts of the mistletoe was found [30]. The material and geometric structuring of the interface increase the contact area and enable a smooth transition between the different mechanical properties of the softer mistletoe and the stiffer host tissue, preventing catastrophic failure of the mistletoe attachment.

The strong structural and mechanical similarity of multihierarchical biological systems and functionally graded (meta-)materials [31] has recently been exploited to create bioinspired nanocomposites [32], gyroid cellular sandwich structures [33], composites with functionally graded fibers for mechanical rein-

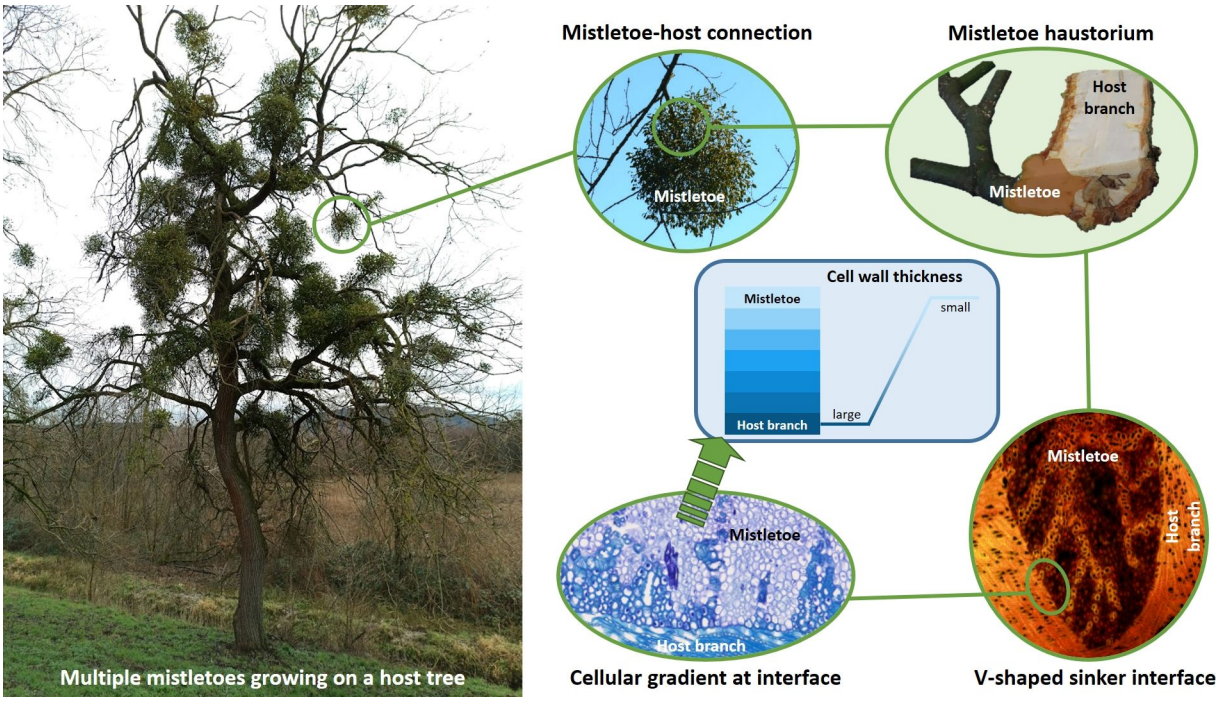

Figure 1: Multihierarchical representation of the connection between the parasitic mistletoe and its host tree, from the entire organism to sectioned specimen and stained histological sections. A cellular gradient extends along the V-shaped interface between the fully lignified host and the softer mistletoe tissue, resulting in a gradual transition in mechanical properties. This gradient, together with the V-shaped interface structure, forms the source of bioinspiration for this study. The histological images are adapted from [30] (© 2021 M. Mylo et al., published by Frontiers, distributed under the terms of the Creative Commons Attribution 4.0 Intational License, https://creativecommons.org/licenses/by/4.0).

forcement [34], radially graded metamaterials [35], and 3D-printed specimens with stepwise and continuous transitions [36,37]. In addition to the mostly rectilinear gradients, Saldívar and colleagues have also structured the interfaces of the gradients in their work on bioinspired 3D-printed fused deposition modeling materials, incorporating different patterns such as collagen-like triple helices into their geometric design, resulting in a 50% toughness increase compared to the non-graded control [38]. However, their work is limited to bimaterial structures, and they are unable to produce continuous graduated materials due to limitations in their manufacturing method.

This study aims to establish a polymer-based hot-compression FGM material system that overcomes the limitations of additive manufacturing. We intend to transfer the connection mechanisms of mistletoe to a bioinspired material system in which the interface between different materials is not only geometrically structured (V-shape), but also has continuous gradients along the geometry to enable smooth transition between materials. Additionally, we will examine how this structuring can be employed to model local failure behavior through material distribution. Furthermore, we will investigate the transferability of the FGM framework to mechanical metamaterials, with the aim of expanding their geometry-based properties through graded material behavior, and achieving even higher modularity through this geometry–material combination.

Materials and Methods

Specimen preparation

A polypropylene-based system was used to fabricate the polymeric FGMs. The base materials were Moplen HP500N polypropylene (hereafter abbreviated as PP) with a melt flow rate of 12 g/10 min and an indicated modulus of 1400 MPa and glass fiber-reinforced polypropylene MP2000 (hereafter abbreviated as PPGF) with 25% glass fiber content, a melt flow rate of 16 g/10 min and an indicated modulus of 4000 MPa (both LyondellBasell, Rotterdam, Netherlands). The reported moduli are manufacturer's data and were obtained by testing injection molded specimens. The polymer blends were extruded using a co-rotating twin-screw microcompounder (XPlore 15 mL, Sittard, Netherlands) at a screw speed of 120 rpm, a barrel temperature of 200 °C and a processing time of 90 s. Five different PP/PPGF blends (83/17, 66/34, 50/50, 34/66, and 17/83) were produced and labeled according to their PP content (e.g., PP/PPGF-83 for the 83/17 blend).

Laminates of homogeneous and graded materials were produced from these blends using a laboratory vacuum press

(200P, COLLIN Lab & Pilot Solutions GmbH, Ebersberg, Germany) with a mold size of 110 × 80 mm^2, resulting in a laminate thickness of about 1.5 mm. The compression parameters were adjusted in preliminary tests to provide good results for molding of the two homogeneous materials (PP and PPGF) and were kept constant for the preparation of all laminates. They consist of preheating for 5 min at a constant temperature of 200 °C, pressing for 8 min at a pressure of 0.8 MPa and cooling to room temperature for 20 min. The compression times had a marked effect on the feasibility of hot pressing and the mechanical properties of the resulting polymers.

To obtain laminates with either rectilinear or V-shaped sinker-inspired interfaces, two grids were 3D-printed using PLA polymeric filament, each with seven compartments and corresponding interface structures (Figure 2A,B). In both designs, the extruded polymer blends were distributed between the compartments (~2 g each) to create either a linear gradient (Figure 2C,D) or a bidirectional gradient (Figure 2E,F) with respect to the glass fiber content of the PP. For the bidirectional gradient, the glass fiber content (PP/PPGF of 0/100) was highest in the middle compartment and decreased towards the outside. Once the molding grids had been filled with the base material, they were carefully removed, and hot compression was carried out.

Tensile specimens were cut from the laminate using a laser cutter (MT-7050W100, Maitech, Milan, Italy) with a single cycle at a laser speed of 10 mm/s and a power of 30 W, ensuring that only areas without visible defects were cut out of the plates. For specimens with rectilinear interfaces, conventional dog bone specimens were prepared. For specimens with V-shaped interfaces, however, the geometry had to be slightly adapted (widened) so that a complete V-shape could be cut out of the laminate in the width. Figure 2 provides an overview of the tensile specimen designs and their respective fiber content distribution and dimensions.

Furthermore, two 2D metamaterials with triangular unit cell configurations were laser cut from the hot-pressed laminates of graded material with rectilinear interface. Triangular structures were selected for their isotropic properties, which help mini-

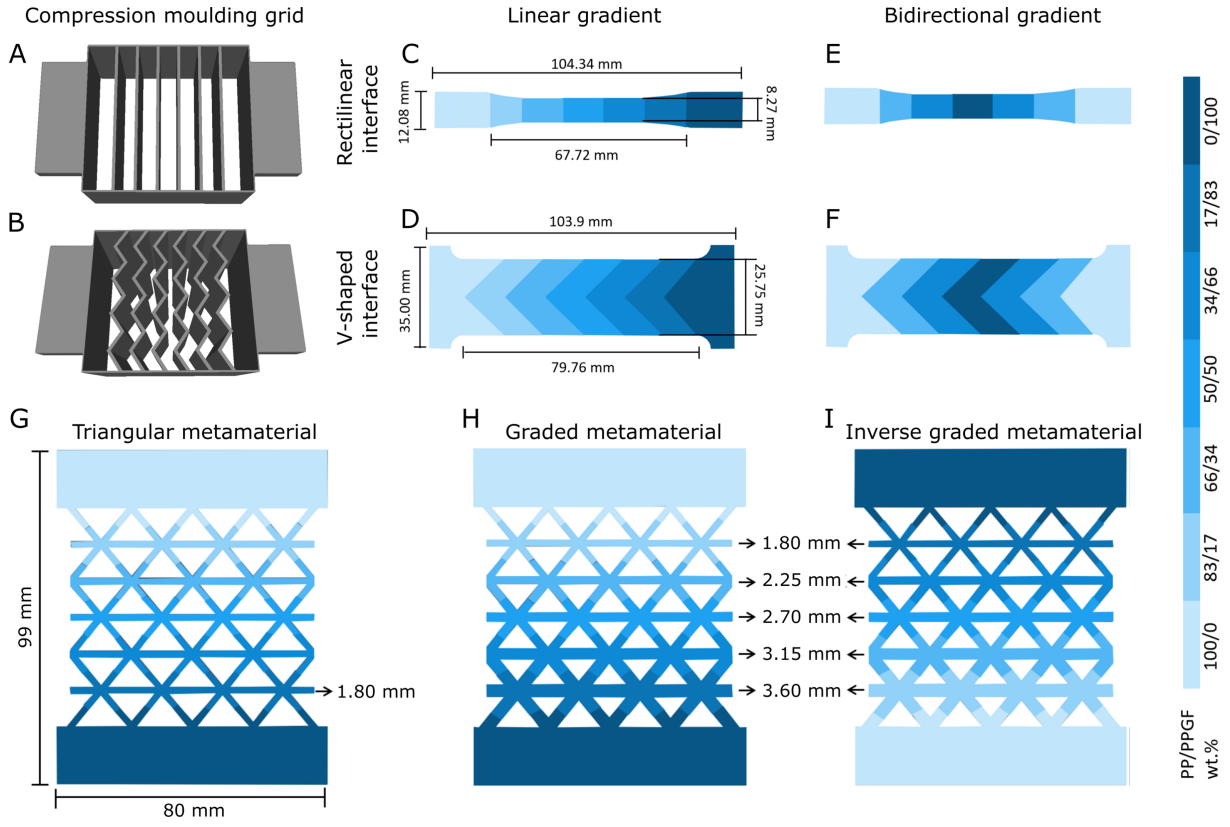

Figure 2: Fabrication of the graded tensile specimens. Geometry of the grids for compartmentalized hot compression molding with rectilinear (A) and V-shaped (B) interfaces. Sketches of tensile specimen geometries with glass fiber gradients (marked in shades of blue) with linear (C, D) and bidirectional gradients (E, F) and with straight (C, E) and V-shaped (D, F) interfaces as well as triangular (G), graded (H), and inverse (I) metamaterial geometries are shown.

mize the impact of loading direction deviations during testing. The metamaterial structure consisted of unit cells with a uniform beam thickness of 1.8 mm (Figure 2G).

The effective stiffness of elasticity (E_{eff}) of the triangular mechanical metamaterials was calculated using Equation 1, where E_s is the elastic modulus of the bulk material used for fabrication of the metamaterial, η is the slenderness ratio of the metamaterial beams, defined as the ratio of the length to the thickness of the unit cells beams ($\eta = L/t$) [39]. This equation was used to calculate the beam thicknesses of the three mechanical metamaterials configurations with different gradients of the base material. The triangular metamaterial had a beam length of L = 12.29 mm and a thickness of t =2.0 mm, resulting in η = 6.145. The mean value of the linearly graded materials, obtained experimentally from the stress–strain slopes of the elastic region, was used as the E_s value. In order to achieve a homogeneous strain distribution along the inversely graded metamaterial geometry, the beams of the two graded geometries had thicknesses with a geometrical gradient from 1.8 to 3.6 mm. This geometry was fabricated in two versions, namely, one with PP/PPGF-0 in the thinner beam section and PP/PPGF-100 in the thicker beam section (i.e., graded metamaterial; Figure 2H), and one with an inverse material gradient (i.e., inversely graded metamaterial, Figure 2I).

$$E_{\text{eff}} = \frac{2\sqrt{3}E_{\text{s}}\left(\eta^2+1\right)}{3\eta^3+\eta} \quad (1)$$

Glass fiber content analysis

X-ray microtomographic (μCT) scans were used to determine the glass fiber content along a linearly graded specimen with rectilinear interfaces and to estimate the heating effects of laser cutting at the specimen edges. Sections of about 13.50 × 8.00 mm^2 for each layer were cut from a tensile specimen with linear gradient and rectilinear interface using the laser cutter mentioned above, resulting in a total of seven specimens. Each specimen was scanned at a resolution of 4 μm, with a 360° scan and a rotation step of 0.3°, using a SkyScan 1272 CT scanner together with SkyScan software (version 1.1.10, both Bruker Corporation, Billerica, MA, United States). Data were reconstructed using NRecon software (version 1.6.10.1, Micro Photonics Inc., Allentown, PA, United States).

Image processing was performed using the image processing toolbox of the Matlab software (version R2023a, MathWorks Inc., Natick, MA, United States). First, all intensity values of the images were normalized. Only the area of the polypropylene matrix was considered, and the pixel area of the resulting binary image (A_t) was calculated. A second binary segmentation based on a threshold that differentiated between the pixel brightness of the glass fibers and the PP resulted in the fiber pixel area (A_f). The fiber content of each cross-sectional image was calculated as the ratio between A_f and A_t, and the values of the cross sections of each cut specimen were assembled accordingly with respect to the original specimen.

Tensile testing

For all tensile specimens, the end parts of pure PP or PPGF were firmly secured in the tensile clamps, and the initial distance between the clamps (L_0) was measured. Tensile tests were performed to failure under uniaxial loading at a speed of 1 mm/min at room temperature using a RetroLine universal testing machine (ZwickRoell GmbH & Co. KG., Ulm, Germany) equipped with a 10 kN load cell. Samples for which slippage was visible during tensile loading were excluded from further evaluation. Stress ($\sigma = F/A_0$) and strain ($\varepsilon = (l_i - l_0)/l_0 = \Delta l/l_0$) values were calculated from the resulting force and displacement data and specimen geometries. The Young's modulus ($E = \sigma/\varepsilon$) of the specimens was calculated within the linear region of the stress–strain curves, and the ultimate tensile strength (UTS) was calculated as the highest stress achieved before failure from the respective stress–strain curves. Table 1 provides an overview of the specimens tested and their respective sample sizes.

Table 1: Tensile specimen groups and the respective sample sizes.

Specimen group		Sample size
homogeneous PP		9
homogeneous PPGF		9
linearly graded	rectilinear interface	3
	V-shaped interface	4
bidirectionally graded	rectilinear interface	4
	V-shaped interface	2
metamaterial	triangular	5
	graded	2
	inversely graded	2

Digital image correlation

Digital image correlation (DIC) analysis was used to measure local strain progression during tensile loading of selected specimens for each group. To create a random, high-contrast speckle pattern, the surface of the dog bone and metamaterial specimens was sprayed with a white primer (5200 Permanentspray Premium-Acryllack, Edding International GmbH, Thalwil, Switzerland) before applying a black speckle pattern (Carbon black, Liquitex Spray Paint, Cincinnati, OH, United States). During the tensile test, the surface was captured at 25 fps using a Basler ace camera (acA2040; Basler AG, Ahrensburg,

Germany) equipped with a 35 mm lens (CCTV LM35HC; Kôwa, Nagoya, Japan).

The captured image stacks were imported into the GOM correlate software for DIC analysis (version 2018, GOM GmbH, Braunschweig, Germany). A facet size of 20 pixels and a point distance of 14 pixels was used for surface detection, using an image in the undeformed state as reference. The principal engineering strain in the direction of deformation was calculated by comparing all deformation images with the initial reference image over the entire surface between the clamps. A virtual section was placed in the center of the specimen over the entire gradient, across which a detailed strain analysis was conducted. The deformation images at 90% of the total deformation were selected for comparative strain pattern analysis.

Simulations

In order to determine the mechanical behavior and response of the triangular, graded, and inversely graded metamaterial structures in an idealized form, and thus highlight the possibilities of combining geometric and material gradients, finite element (FE) simulations were performed using small deformation implicit modeling. The linear solver of the ANSYS static structural module was used for the FE simulations. Due to the low thickness of the metamaterial structures, the plane stress 2D model (PLANE 183 elements) was chosen for the FE analysis. The quadratic elements were implemented to generate the mesh through the metamaterial geometry in order to obtain a better agreement in complex and difficult parts of the geometry, such as the sharp corners at the beam joints. The mesh size was chosen to have at least four elements along the thickness of the beams, in order to obtain sufficient accuracy in the results. The linear elastic material model was implemented based on the mechanical properties provided by the manufacturer to model the behavior of the PP (E_{PP} = 1400 MPa) and the PPGF (E_{PPFG} = 4000 MPa) materials, and the constant parameter of Poisson's ratio was set to $\nu = 0.3$ for both materials. The metamaterial geometry was divided vertically into seven subsections, as shown in Figure 2G–I. Each subsection was assigned distinct material properties based on a linear interpolation of the elastic modulus between PP and PPFG. The subsections were assumed to be bonded to one another through contact conditions. The bottom sides of the structure were considered as fixed (clamped) supports without any displacement and rotation, and the loading was applied as a ramped displacement from 0 to 5 mm at the top edge of the metamaterial structure upwards to apply 4.5% strain to the specimen similar to the experimental setup.

Results and Discussion

Material preparation

When testing a range of compression temperatures and times, 200 °C at 0.8 MPa for 8 min and a preheating time of 5 min at 200 °C proved to be the most suitable parameters for material fabrication with a gradient that could be produced as reliably as possible and that was spatially well defined, despite the intermixing of adjacent material compounds. Figure 3 shows the interfaces of hot-pressed specimens and laminates of the different specimens produced. It can be seen that unidirectional and bidirectional gradients can be produced with a straight or V-shaped material interface present. However, it is apparent

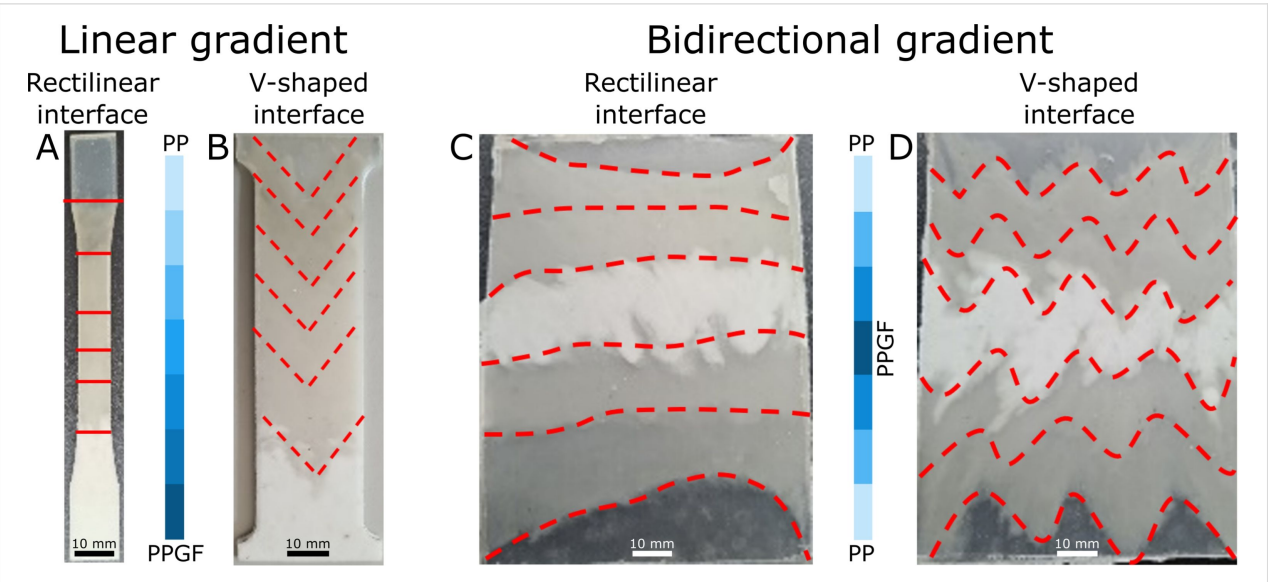

Figure 3: Results of material fabrication. Laser cut tensile specimens with rectilinear interface (A) and V-shaped interface (B) between sections of linearly graded glass fiber ratio. (C) and (D) show the hot-compressed laminates of the bidirectionally graded materials, with and without V-shape, from which the respective tensile specimens are cut. The red (dotted) lines indicate the approximate interfaces between adjacent polymer blends.

that, as the glass fiber content decreases, the polymer flow increases (Figure 3C, bottom and top part) [40], resulting in less clearly defined interfaces between the compounds. This can be explained by the reduction in heat transfer of polymer blends with higher glass fiber content [41] and needs to be considered when designing graded interfaces of fiber-reinforced polymers.

The results show that interface structuring of FGMs is possible using prefabricated molds for the hot compression technique. The diffusion differences at the interfaces impose a spatial limitation on the structural complexity, but it is conceivable to go beyond the possibilities presented here in terms of gradient direction (i.e., linear and bidirectional) and interface structuring (i.e., rectangular and V-shaped). The potential for 3D structuring using more complex, multilayered molds should be explored in future studies.

Glass fiber content

Seven µCT scans were obtained from sections along a linearly graded tensile specimen with rectilinear interfaces. Figure 4A shows representative cross-sectional µCT images for each scan. The relatively small difference in brightness between the PP matrix (dark grey) and the surrounding air (black) compared to the very bright appearing glass fibers can be explained by the large difference in density between the polymer and the glass fibers [42,43]. All scans reveal the random orientation of the glass fibers in the PP matrix, with small areas of identical orientation being explained by the fiber alignment in the raw pellets (Figure 4C). Some distinct bright areas are visible at the edges of the specimen (Figure 4B), where glass fibers have been burned by laser cutting. However, these were not visible inside the specimens and did not seem to affect the PP matrix, so it can be assumed that laser cutting does not have a marked effect on the inner fibers and, consequently, on the mechanical properties of the individual areas of different fiber content, which is in good agreement with the literature on laser cutting of fiber-reinforced plastics [44,45].

As expected, a gradually increasing volume fraction of glass fibers is visible along the graded specimen. This trend can be seen both qualitatively by comparing the cross sections of the individual scans (Figure 4A) and quantitatively over the course

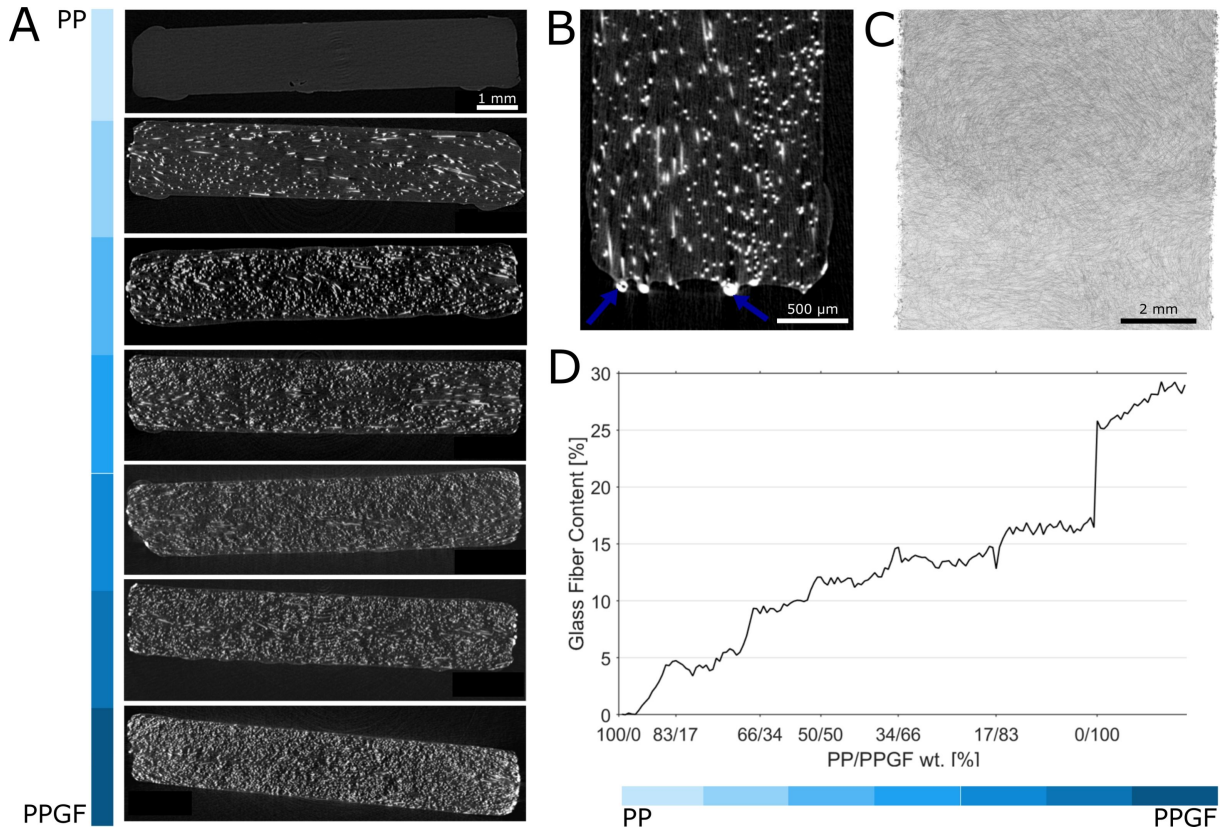

Figure 4: Analysis and quantification of fiber content and orientation using µCT images. (A) Representative cross sections of the scanned segments with different PP/PPGF ratios. (B) Detailed view of a specimen edge showing the burns of the outer glass fibers caused by laser cutting. (C) Frontal view of a raw image of a segment showing random fiber orientation. (D) Quantified glass fiber content along the length of a linearly graded PP/PPGF specimen.

of the entire specimen (Figure 4D). In addition to the slight variations within a specimen, the step changes at the cut intersections between the pieces are noticeable. These can be explained by the material removed during laser cutting and by slight differences between the CT scans (e.g., due to unavoidable ring artifacts that could only be partially corrected). The increase in glass fiber content at the interface to the PP/PPFG-0 section is particularly pronounced, which can be partly explained by the increased number of burnt glass fiber particles at the edges. In the sections with the highest glass fiber density, a volume fraction of between 25% and 30% was obtained, which is in good agreement with the 25% specified by the manufacturer (Figure 4D), demonstrating the validity of the fiber content analysis applied. The small deviation may be due to the volume reduction of PP during hot pressing, the burnt glass fibers at the edges, and inaccuracies in the post-processing threshold algorithms.

The good fusion of the individual compartments and the gradual increase in fiber concentration along the specimen indicate that the presented hot compression molding process is capable of producing FGMs with modulated interfaces and a continuous material gradient. This represents a methodological advantage over 3D printing processes, which are capable of producing complex graded structured and interfaces [18,20,38], as well as graded porosities [16,46,47], but are mostly not capable of achieving a continuous material gradient. Such a continuous gradient affects the global and local mechanical properties of the sample and prevents the risk of delamination along the interface compared to abrupt material transitions.

Mechanical properties and failure behavior

The homogeneous PPGF specimens (1499.8 ± 123.7 MPa) revealed a 9.3% higher Young's modulus than the non-reinforced PP specimens (1372.5 ± 156.2 MPa) (Figure 5A). A pronounced influence on the Young's modulus was observed for the interface structuring of the FGM specimens as the introduction of the gradient noticeably reduced the values for the rectilinear specimens by up to 27% compared to homogeneous PP and 33.5% compared to PPGF. The introduction of the mistletoe-inspired V-shaped interface negated this effect, and the measured values were again in the range of the homoge-

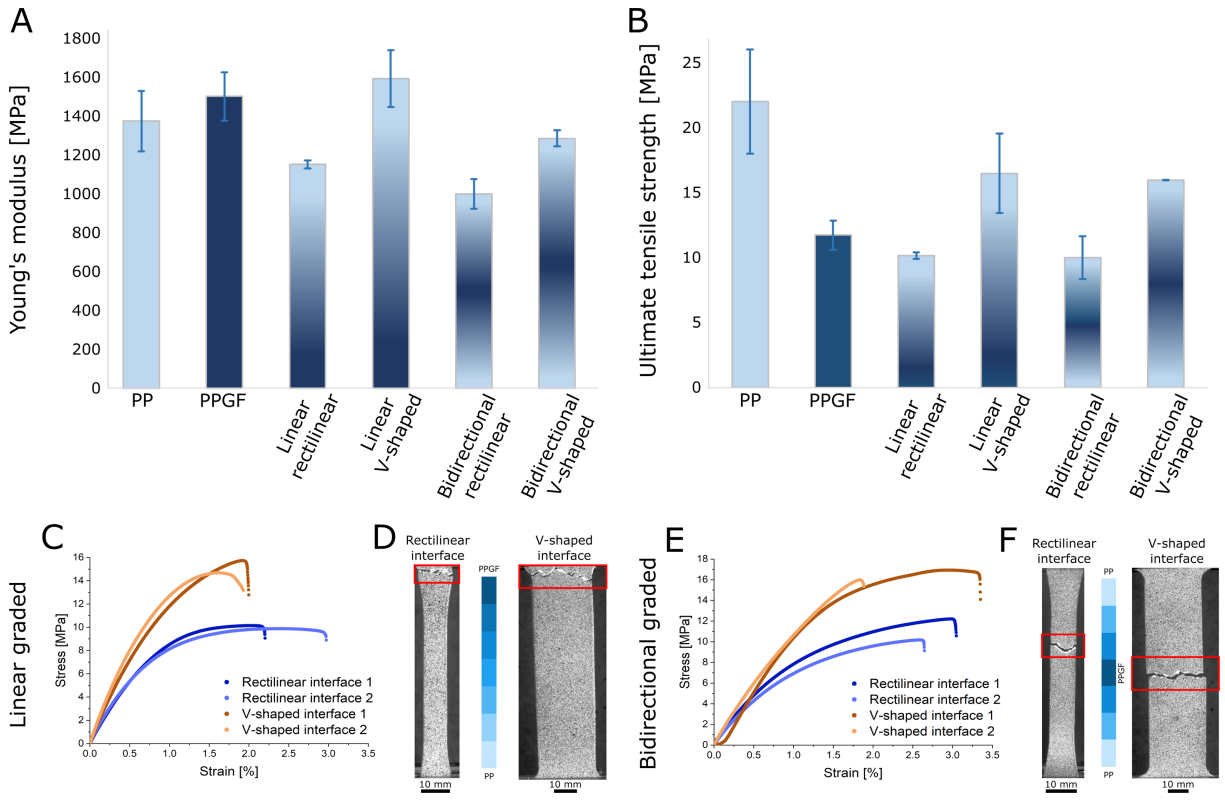

Figure 5: Mechanical properties from tensile tests of the homogeneous PP and PPGF specimens and the four groups of graded specimens. Data of (A) the Young's modulus and (B) UTS are shown as mean and standard deviation. Comparison of linearly graded specimens, showing exemplary (C) stress–strain curves and (D) failure patterns. Comparison of bidirectionally graded specimens, showing exemplary (E) stress–strain curves and (F) failure patterns.

neous base materials. For the linearly graded specimens, those with V-shaped interfaces had an increase in Young's modulus of about 38% compared to their counterparts with rectilinear interfaces (1590.6 ± 146.4 MPa against 1150.2 ± 21.1 MPa). This can be explained by the fact that, in the specimens with V-shaped interfaces, there is a better intermixing between the compartments with different glass fiber contents (Figure 3D). The large deviations between the measured Young's modulus values of PPGF and the values given by the manufacturer can be explained by the fact that the data sheet values were obtained by testing injection-molded test specimens, whereas our specimens were produced by hot pressing. Each method has an effect on the direction of the glass fibers; injection molding results in an anisotropic orientation of the fibers, whereas hot pressing results in isotropic orientations [48]. An anisotropic fiber orientation along the direction of tensile testing increases the Young's modulus compared to an isotropic alignment [49], which also explains why the difference between the pure PP and the glass fiber-reinforced polymer was rather small in our specimens.

The mean UTS values of the PP specimens (22.02 ± 4.01 MPa) were almost 88% higher than those of the homogeneous PPGF specimens (11.73 ± 1.14 MPa) (Figure 5B). This is in good agreement with similar studies on polymeric FGM [50] and can be explained by the fact that local residual stresses accumulate at the fiber–matrix interface [51], particularly in areas of imperfect fabrication, which can quickly become overcritical for crack initiation and, thus, lead to failure of the specimen at reduced stresses. Similar to the trend for the Young's modulus, the mean strength values for the linearly graded V-shaped specimen were about 62% higher than those for the rectilinear specimen (16.48 ± 3.07 MPa against 10.17 ± 0.25 MPa; Figure 5C).

The finding that the linearly graded specimens all failed at or along the PPGF gauge section of the dog bone with the highest fiber content was verified using a bidirectional fiber gradient. The mechanical properties of these specimens followed the same trend as the linearly graded specimens. Again, the Young's modulus of the specimens with a V-shaped interface was about 29% higher than that of their rectilinear counterparts (1284.3 ± 41.4 MPa against 998.1 ± 76.9 MPa) (Figure 5A). The bidirectionally graded specimens all failed in the middle of the dog bones (Figure 5F), at or along the location of the PPFG. Their UTS values followed the trend already described for the linearly graded specimens, with the V-shaped specimens showing a value about 60% higher than the rectilinear specimens (15.97 ± 0.01 against 10.00 ± 1.64 MPa) (Figure 5B,E). Hence, the UTS values for the specimen with a rectilinear interface are similar to those of homogeneous PPGF, whereas those of the groups with a V-shaped interface are between those of homogeneous PP and those of PPGF. This can be explained by the fact that, in the V-shaped specimens, there is no cross section in which only the strength-dominating PPGF is present. In contrast, such cross sections are present in the rectilinear specimens, resulting in strength values that correspond well to those of pure PPGF.

For the production of the bidirectional FGMs we used the same number of compartments in the hot-press mold as for the linearly graded specimens (Figure 2), resulting in a higher gradient difference between adjacent compartments. This may affect the uniform distribution of glass fibers and the slightly lower Young's modulus values of the bidirectionally graded specimens compared to the linearly graded specimens (reduction of about 15% for the linearly graded specimens and about 24% for the specimens with V-shaped interface). For UTS, both groups show almost identical values (differences of 2–3%), which again can be attributed to the fact that the tensile strength is mainly influenced by the stress concentration in the area of highest glass fiber content, which is identical in both groups. This is a good indication that the spatial failure behavior of the specimens can be controlled by positioning the area of highest fiber content.

Time and pressure during hot pressing also play a crucial role in the development of stable materials. The thermal conductivity is reduced by increasing the glass fiber content; thus, the molecular movement of the polymer is reduced, which affects the tensile modulus and the maximal strength of the material [41]. At the same time, pressure reduces the inter-atomic distance between polymer chains [52], which might also have been a factor regarding the rather low differences between the tensile properties of the two base materials. It can be concluded that the pressing time and pressure applied during hot pressing may have affected the integrity of the material and, therefore, its tensile properties. Hence, no significant difference was found for the Young's modulus between homogeneous PP and PPGF.

These results provide a good estimate of the expected stiffness of the polymeric FGMs, depending on the material properties of the base materials and the ratio at which the gradients are designed. At the same time, it has been shown that the stiffness can be increased, if desired, by interfacial structuring, so that there is very little difference to the base materials. The knowledge of the failure locations along the region of highest glass fiber concentration can be used to integrate predetermined failure sites into a multimaterial system. If this is not desired, or only to a limited extent, interface structuring can also help to tune the effect and increase the UTS compared to specimens with rectilinear interfaces.

Local strain patterns were determined for all material groups by DIC, a technique that has demonstrated its applicability for strain quantification at functional interfaces [29,36-38,53,54], predetermined failure sites [55], and for the comparison between biological and bioinspired material systems [56,57]. Figure 6 shows patterns of major strain, comparing the FGM specimen just before failure. The dotted red lines show the sections for detailed analysis, which is plotted alongside.

The linearly graded specimens showed the highest local strains (over 5%) in the PPGF parts. In the rectilinear specimen, these were distributed over a larger area (Figure 6A), whereas, in the V-shaped specimen, they were only found in the edge area of the specimen (Figure 6C). Strains in the remainder of the specimen ranged from 1% to 2% for the straight specimen to less than 1% for the V-shaped graded specimen. In the bidirectionally graded specimens, a wider distribution of strain was found, with the strain peaking again in the PPFG region and also reaching values between 4% and 5%. This suggests that there is a lower fiber content in the central area of the specimen, resulting in a highly localized initiation of failure. The values shown in the line plot are slightly lower as the largest strains occur at the edges of the specimen and are, therefore, offset from the center line. A more localized peak was found for the rectilinear interface specimen (Figure 6B), while an even broader distribution was found for the specimen with V-shaped interfaces (Figure 6D).

Functionally graded metamaterials

To analyze the mechanical metamaterials, three different geometries were tested under tension, one with a triangular metastructure and two with a graded PP–PPGF metastructure (Figure 2G–I). Figure 7 shows the stress–strain curves for all specimen analyzed. The five triangular geometry specimens tested showed fairly homogeneous behavior up to plastic deformation. The UTS values within this group were reasonably close to each other, while the strain at UTS showed greater differences of up to 80%, which, however, is not unusual for polymer specimens. The two replications of the graded and inversely graded metamaterials showed larger relative differences in UTS, which can be explained by the fact that smaller material differences or laser cutting inaccuracies in the area of the thinner beams have a greater effect (see also the strain distributions of the DIC analysis in Figure 8). Comparing the different metamaterial groups, it was observed that the presence of a gradient in the metamaterial structure affects the stress–strain behavior of the metamaterials. The graded metamaterials (mean UTS: 1.21 MPa) exhibited about 30% lower, and the inversely graded metamaterials (mean UTS: 1.00 MPa) about 40% lower, UTS values compared to the triangular metamaterials (mean

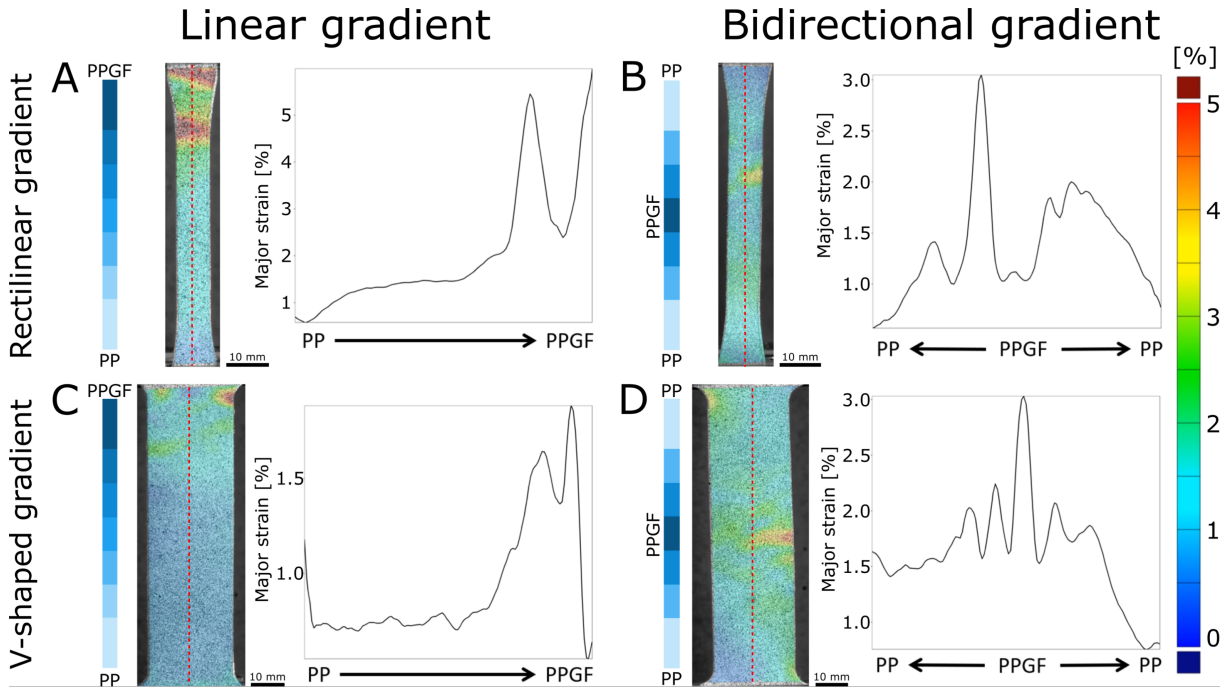

Figure 6: Overview of the major strain analyses of the linear (A, C) and bidirectionally graded (B, D) materials obtained by DIC. For all specimens, the pre-failure stage was selected for visualization. In addition to the respective full-field major strain patterns, the values of a line passing through the center of the specimen (dotted red) are shown in detail.

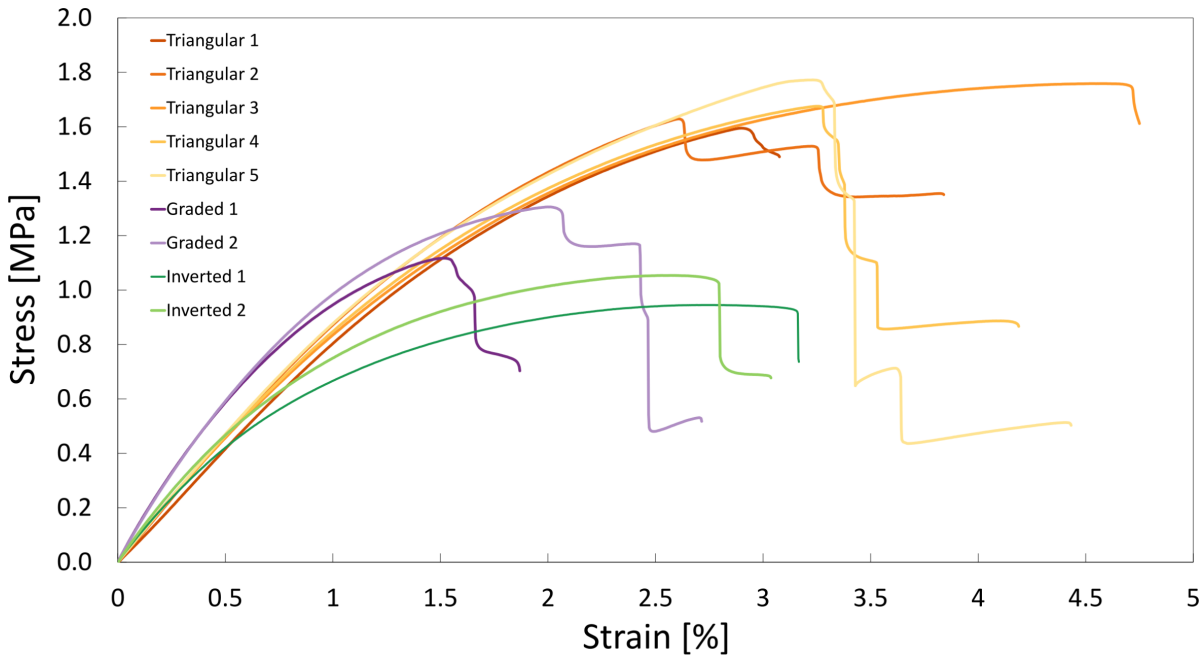

Figure 7: Stress–strain curves of the specimens from the three metamaterial geometries under tensile load until failure.

UTS: 1.69 MPa). Most specimens showed a step-down failure with successive failure of individual beams. Notably, the graded metamaterials exhibited markedly lower strain values at first failure than the triangular metamaterials.

This step-down failure can also be observed in Figure 8, where, after the failure of the first beam, the metamaterials continued to deform under tensile loading until catastrophic failure with additional failure of (mostly adjacent) beams. DIC analysis revealed clear differences in the local strain distribution among the three metamaterial geometries (Figure 8). The triangular metamaterial showed a strain distribution with values up to 5% at the failure of the first beam and even higher values further on before complete failure over large parts of the specimen. For the graded and inversely graded metamaterials, a significant strain concentration in a similar range was observed in the area of the 1–2 thinnest layers of the beams (graded metamaterial) and the 2–3 thinnest layers of the beams (inversely graded metamaterial). Overall, the diagonal beams exhibited higher strains than the horizontal beams, and it was the diagonal beams that failed first in all specimens due to the alignment of these beams to the vertical loading direction of the specimens. In the triangular metamaterial, the PPGF beams broke first, while, in the graded materials, it was the thinner beams that initiated failure and then led to complete failure. From the graded to the inversely graded metamaterial, there was a shift from the very thin beams at the very edge to the second row where the beams were already somewhat thicker. This shows that, although there is an effect of the PP/PPGF distribution along the specimen, due to the rather small mechanical differences between the two base materials, this effect was not large enough to fully compensate for the effects of the structural grading and other important effects such as non-periodic boundary conditions for the metamaterial structures at the gripping points and free sides.

To better illustrate the effect of the opposing structural and material gradients, we performed idealized FE simulations using the PP and PPGF material properties provided by the manufacturer. These show strain accumulation along the notches at the beam joints for all three geometries (Figure 9). In the triangular metamaterial geometry without geometric gradients, the strains are highest in the region of the material with low Young's modulus and gradually decrease toward the end of the material with high Young's modulus. This effect is further enhanced when a geometric gradient is introduced in addition to the material gradient (graded metamaterial) and the thinner beams are located in the region of the low Young's modulus. The resulting strain concentrations are much more pronounced and encompass a larger area. However, if the orientation of the material gradient is reversed so that the thin beams are in the region with high Young's modulus (inversely graded metamaterial), the strain gradient almost completely disappears, and an almost homogeneous strain distribution is obtained along the metamaterial.

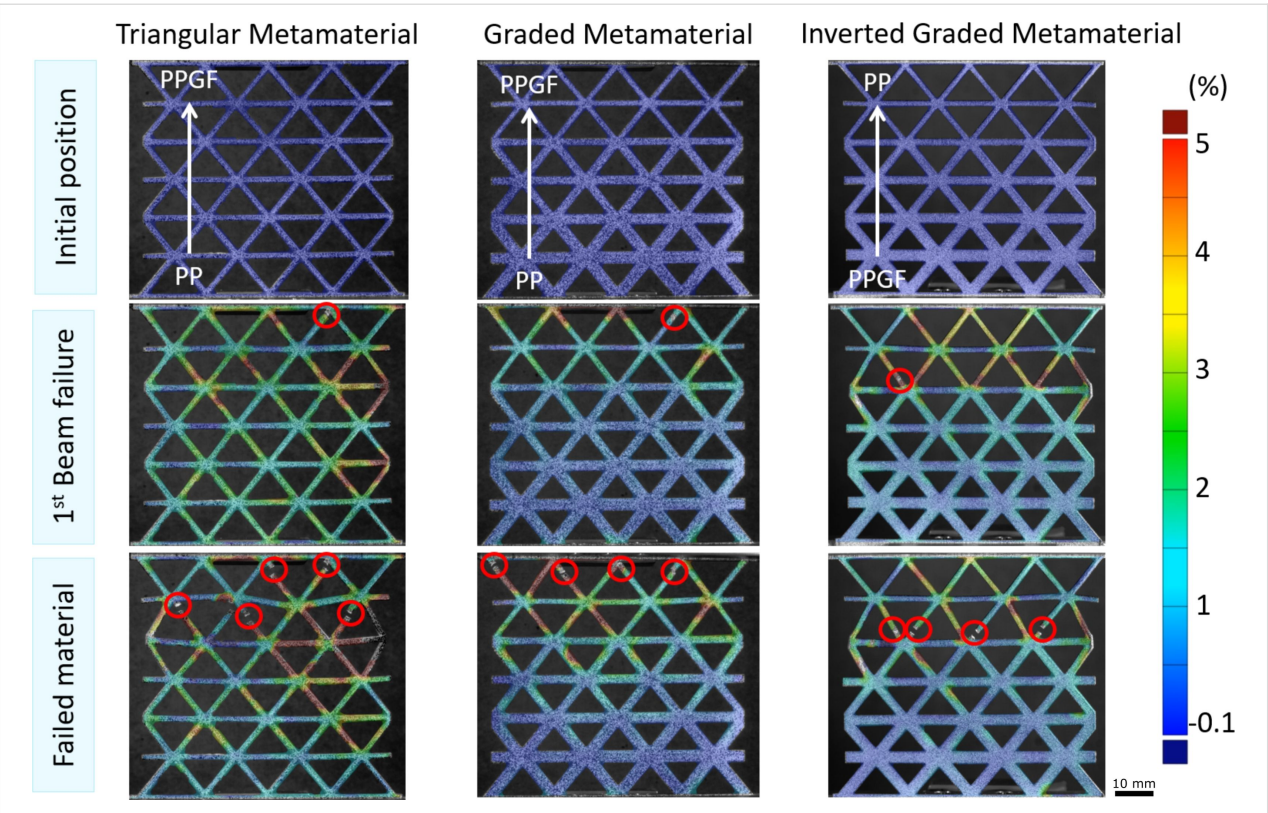

Figure 8: Digital image correlation analysis to reveal local strain distributions of the three metamaterial specimens at three stages during the tensile test: before loading, after first beam failure, after catastrophic failure of the specimens. The red circles indicate the failure locations.

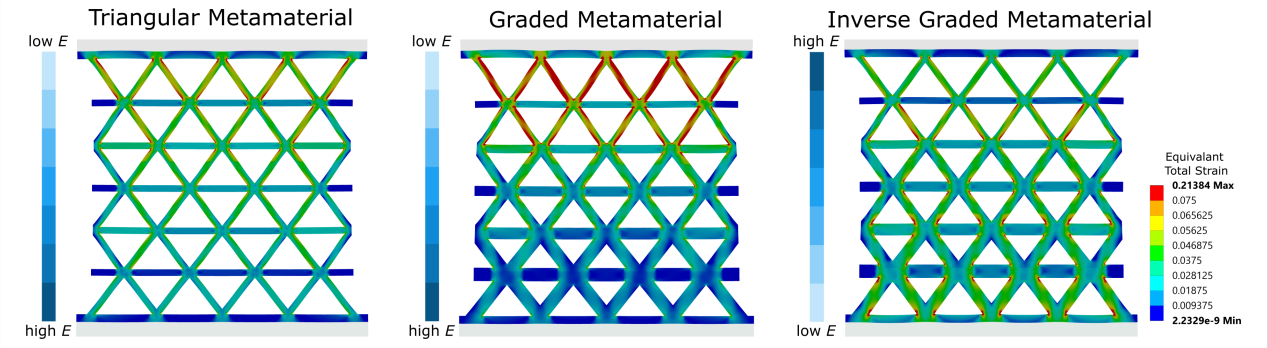

Figure 9: FE simulation results of the strain distributions of the three metamaterial geometries with a linear mechanical gradient from low to high Young's modulus (*E*).

Conclusion

Using a material system of polymeric FGMs made of reinforced polypropylene with graded glass fiber content, we were able to demonstrate the two-part attachment mechanism of European mistletoe with its V-shaped interfacial structure and the gradual progression of mechanical properties along it. Using extrusion and hot compression molding, we were able to extend the existing bimaterial FGM fabrication techniques, to produce continuous fiber gradients along the geometrically structured interface. From a design perspective, we demonstrated that considerably better mechanical results could be achieved in the production of continuously graded FGMs by adapting the interface geometry to resemble a mistletoe sinker. This applies to both unidirectional and bidirectional gradients. Our approach of processing glass fiber-reinforced polypropylene is only one of many possible material systems and can be extended by suitable combinations of materials with different mechanical properties but similar melting temperatures. In order to contribute to

more sustainable material use, the transferability to bio-based or biodegradable material combinations (such as cellulose plastic) should be explored.

The introduction of a V-shaped interface instead of rectilinear interfaces in graded materials showed a noticeable improvement in the mechanical properties of the FGM, highlighting the importance of the graded interface structuring of mistletoe and host for their durability. Naturalistic FE simulations should be used in future studies to systematically investigate this functional mechanism and its relevance to plant material systems, thus laying an even broader foundation for mistletoe-inspired composites. The knowledge of the different failure behavior of PP and PPGF was also used to program the failure locations. For example, DIC showed a wider strain distribution for the specimens with a V-shaped interface, but all specimens failed in the area with the highest glass fiber density. This makes it possible to introduce predetermined failure points into material systems and program the stiffness and local behavior via the selected fiber density. This is not limited to a seven-step grading with a linear or bidirectional gradient; more complex geometries or gradients can be generated as desired. It should be noted, however, that the spatial separation of the individual compartments is not as high as in additive manufacturing processes due to the mixing behavior of the polymer matrix.

To demonstrate the versatility of the material system, it has been extended to include graded mechanical metamaterials. These are typically fabricated using structural gradients. Our approach offers an extension by adding a material gradient that can either enhance or counteract the gradient effect, opening up even more possibilities for advanced programmable metamaterials, which could find applications, for example, in crash-resistant components to selectively absorb impact energy or in material systems for targeted separation and recycling of individual components after their service life.

Acknowledgements

We are grateful to Rene Reiser for help with selecting and providing the polymers, to Ulrich Matthes for providing the equipment for fabricating the polymer composites, and to the Freiburg Materials Research Center (FMF) for the use of the technical equipment.

Funding

This research was funded by the Deutsche Forschungsgemeinschaft (DFG, German Research Foundation) under Germany's Excellence Strategy–EXC 2193/1–390951807 and by the Carl-Zeiss-Stiftung "Grundlagenforschung mit Anwendungsbezug".

Author Contributions

Lina M. Rojas González: data curation; investigation; visualization; writing – original draft. Naeim Ghavidelnia: investigation; supervision; visualization; writing – original draft. Christoph Eberl: conceptualization; funding acquisition; supervision; writing – review & editing. Max D. Mylo: conceptualization; project administration; supervision; visualization; writing – original draft.

ORCID® iDs

Lina M. Rojas González - https://orcid.org/0009-0004-4740-5977
Naeim Ghavidelnia - https://orcid.org/0000-0003-0473-0070
Christoph Eberl - https://orcid.org/0000-0001-9449-9583
Max D. Mylo - https://orcid.org/0000-0001-5744-9069

Data Availability Statement

Data generated and analyzed during this study is available from the corresponding author upon reasonable request.

References

1. Mylo, M. D.; Speck, O. *Biomimetics* **2023,** *8,* 173. doi:10.3390/biomimetics8020173
2. Speck, O.; Langer, M.; Mylo, M. D. *Anthropocene Rev.* **2022,** *9,* 220–236. doi:10.1177/20530196211018489
3. Cremaldi, J. C.; Bhushan, B. *Beilstein J. Nanotechnol.* **2018,** *9,* 907–935. doi:10.3762/bjnano.9.85
4. Speck, O.; Speck, T. *Biomimetics* **2019,** *4,* 26. doi:10.3390/biomimetics4010026
5. Ghavidelnia, N.; Slesarenko, V.; Speck, O.; Eberl, C. *Adv. Mater. (Weinheim, Ger.)* **2024,** *36,* 2313125. doi:10.1002/adma.202313125
6. Kiakojouri, F.; De Biagi, V.; Abbracciavento, L. *Biomimetics* **2023,** *8,* 95. doi:10.3390/biomimetics8010095
7. Naebe, M.; Shirvanimoghaddam, K. *Appl. Mater. Today* **2016,** *5,* 223–245. doi:10.1016/j.apmt.2016.10.001
8. Miyamoto, Y.; Kaysser, W. A.; Rabin, B. H.; Kawasaki, A.; Ford, R. G., Eds. *Functionally Graded Materials;* Materials Technology Series, Vol. 5; Springer: New York, NY, USA, 1999. doi:10.1007/978-1-4615-5301-4
9. Claussen, K. U.; Scheibel, T.; Schmidt, H.-W.; Giesa, R. *Macromol. Mater. Eng.* **2012,** *297,* 938–957. doi:10.1002/mame.201200032
10. Luo, Y. *Results Mater.* **2023,** *17,* 100375. doi:10.1016/j.rinma.2023.100375
11. Gao, Y.; Xie, Q.; Gao, T.; Yang, W.; Chen, Q.; Tian, Z.; Li, L.; Liang, Y.; Wang, B. *J. Mater. Res. Technol.* **2023,** *23,* 258–267. doi:10.1016/j.jmrt.2023.01.016
12. Kim, T. Y.; Park, S.-H.; Park, K. *Addit. Manuf.* **2021,** *47,* 102254. doi:10.1016/j.addma.2021.102254
13. Boggarapu, V.; Gujjala, R.; Ojha, S.; Acharya, S.; Venkateswara babu, P.; Chowdary, S.; kumar Gara, D. *Compos. Struct.* **2021,** *262,* 113596. doi:10.1016/j.compstruct.2021.113596
14. Kuang, X.; Wu, J.; Chen, K.; Zhao, Z.; Ding, Z.; Hu, F.; Fang, D.; Qi, H. J. *Sci. Adv.* **2019,** *5,* eaav5790. doi:10.1126/sciadv.aav5790

15. Salem, T.; Xie, X.; Jiao, P.; Lajnef, N. *Thin-Walled Struct.* **2021,** *159,* 107264. doi:10.1016/j.tws.2020.107264
16. Chen, D.; Gao, K.; Yang, J.; Zhang, L. *Thin-Walled Struct.* **2023,** *191,* 111046. doi:10.1016/j.tws.2023.111046
17. Boccaccio, A.; Uva, A. E.; Fiorentino, M.; Mori, G.; Monno, G. *PLoS One* **2016,** *11,* e0146935. doi:10.1371/journal.pone.0146935
18. Li, Y.; Feng, Z.; Hao, L.; Huang, L.; Xin, C.; Wang, Y.; Bilotti, E.; Essa, K.; Zhang, H.; Li, Z.; Yan, F.; Peijs, T. *Adv. Mater. Technol. (Weinheim, Ger.)* **2020,** *5,* 1900981. doi:10.1002/admt.201900981
19. Shaukat, U.; Rossegger, E.; Schlögl, S. *Polymers (Basel, Switz.)* **2022,** *14,* 2449. doi:10.3390/polym14122449
20. Nian, Y.; Wan, S.; Avcar, M.; Yue, R.; Li, M. *Int. J. Mech. Sci.* **2023,** *258,* 108580. doi:10.1016/j.ijmecsci.2023.108580
21. Alkunte, S.; Gupta, M.; Rajeshirke, M.; More, N.; Cheepu, M.; Gupta, A.; Lakal, N.; Shingare, K.; Alifui-Segbaya, F.; Fidan, I. *Processes* **2024,** *12,* 2252. doi:10.3390/pr12102252
22. Lopes, L. R.; Silva, A. F.; Carneiro, O. S. *Addit. Manuf.* **2018,** *23,* 45–52. doi:10.1016/j.addma.2018.06.027
23. Wegst, U. G. K.; Bai, H.; Saiz, E.; Tomsia, A. P.; Ritchie, R. O. *Nat. Mater.* **2015,** *14,* 23–36. doi:10.1038/nmat4089
24. Wang, Y.; Naleway, S. E.; Wang, B. *Bioact. Mater.* **2020,** *5,* 745–757. doi:10.1016/j.bioactmat.2020.06.003
25. Speck, O.; Speck, T. *New Phytol.* **2021,** *231,* 950–956. doi:10.1111/nph.17396
26. Yoshida, S.; Cui, S.; Ichihashi, Y.; Shirasu, K. *Annu. Rev. Plant Biol.* **2016,** *67,* 643–667. doi:10.1146/annurev-arplant-043015-111702
27. Teixeira-Costa, L. *Braz. J. Bot.* **2021,** *44,* 165–178. doi:10.1007/s40415-021-00704-0
28. Teixeira-Costa, L.; Wiese, L.; Speck, T.; Mylo, M. D. *J. Exp. Bot.* **2025,** *76,* 3412–3426. doi:10.1093/jxb/eraf129
29. Mylo, M. D.; Hofmann, M.; Balle, F.; Beisel, S.; Speck, T.; Speck, O. *J. Exp. Bot.* **2022,** *73,* 1204–1221. doi:10.1093/jxb/erab518
30. Mylo, M. D.; Hofmann, M.; Delp, A.; Scholz, R.; Walther, F.; Speck, T.; Speck, O. *Front. Plant Sci.* **2021,** *12,* 715711. doi:10.3389/fpls.2021.715711
31. Ren, L.; Wang, Z.; Ren, L.; Han, Z.; Liu, Q.; Song, Z. *Composites, Part B* **2022,** *242,* 110086. doi:10.1016/j.compositesb.2022.110086
32. Nepal, D.; Kang, S.; Adstedt, K. M.; Kanhaiya, K.; Bockstaller, M. R.; Brinson, L. C.; Buehler, M. J.; Coveney, P. V.; Dayal, K.; El-Awady, J. A.; Henderson, L. C.; Kaplan, D. L.; Keten, S.; Kotov, N. A.; Schatz, G. C.; Vignolini, S.; Vollrath, F.; Wang, Y.; Yakobson, B. I.; Tsukruk, V. V.; Heinz, H. *Nat. Mater.* **2023,** *22,* 18–35. doi:10.1038/s41563-022-01384-1
33. Peng, C.; Tran, P. *Composites, Part B* **2020,** *188,* 107773. doi:10.1016/j.compositesb.2020.107773
34. Chen, M.; Li, Z.; Yuan, Z.; Ke, L.-L. *Compos. Sci. Technol.* **2022,** *228,* 109675. doi:10.1016/j.compscitech.2022.109675
35. Kouhi-Lakeh, K.; Teimouri, M.; Asgari, M. *Compos. Struct.* **2024,** *346,* 118435. doi:10.1016/j.compstruct.2024.118435
36. Mirzaali, M. J.; Herranz de la Nava, A.; Gunashekar, D.; Nouri-Goushki, M.; Doubrovski, E. L.; Zadpoor, A. A. *Materials* **2019,** *12,* 2735. doi:10.3390/ma12172735
37. Mirzaali, M. J.; Herranz de la Nava, A.; Gunashekar, D.; Nouri-Goushki, M.; Veeger, R. P. E.; Grossman, Q.; Angeloni, L.; Ghatkesar, M. K.; Fratila-Apachitei, L. E.; Ruffoni, D.; Doubrovski, E. L.; Zadpoor, A. A. *Compos. Struct.* **2020,** *237,* 111867. doi:10.1016/j.compstruct.2020.111867
38. Saldívar, M. C.; Tay, E.; Isaakidou, A.; Moosabeiki, V.; Fratila-Apachitei, L. E.; Doubrovski, E. L.; Mirzaali, M. J.; Zadpoor, A. A. *Nat. Commun.* **2023,** *14,* 7919. doi:10.1038/s41467-023-43422-9
39. Karathanasopoulos, N.; Dos Reis, F.; Reda, H.; Ganghoffer, J.-F. *Comput. Mater. Sci.* **2018,** *154,* 284–294. doi:10.1016/j.commatsci.2018.07.044
40. Stanek, M.; Manas, D.; Manas, M.; Skrobak, A.; Janostik, V.; Senkerik, V. *MATEC Web Conf.* **2016,** *76,* 02020. doi:10.1051/matecconf/20167602020
41. Hamlaoui, O.; Klinkova, O.; Elleuch, R.; Tawfiq, I. *Polymers (Basel, Switz.)* **2022,** *14,* 17. doi:10.3390/polym14010017
42. Nguyen Thi, T. B.; Morioka, M.; Yokoyama, A.; Hamanaka, S.; Yamashita, K.; Nonomura, C. *J. Mater. Process. Technol.* **2015,** *219,* 1–9. doi:10.1016/j.jmatprotec.2014.11.048
43. Hessman, P. A.; Riedel, T.; Welschinger, F.; Hornberger, K.; Böhlke, T. *Compos. Sci. Technol.* **2019,** *183,* 107752. doi:10.1016/j.compscitech.2019.107752
44. Choudhury, I. A.; Shirley, S. *Opt. Laser Technol.* **2010,** *42,* 503–508. doi:10.1016/j.optlastec.2009.09.006
45. Bhaskar, V.; Kumar, D.; Singh, K. K. *Aust. J. Mech. Eng.* **2017,** *17,* 95–108. doi:10.1080/14484846.2017.1363989
46. Hindy, A.; Farahmand, F.; Pourdanesh, F.; Torshabi, M.; Al Janabi, A. H.; Rasoulianboroujeni, M.; Tayebi, L.; Tabatabaei, F. S. *J. Mater. Sci.* **2020,** *55,* 9082–9094. doi:10.1007/s10853-020-04645-z
47. Balakrishnan, H. K.; Dumée, L. F.; Merenda, A.; Aubry, C.; Yuan, D.; Doeven, E. H.; Guijt, R. M. *Small Struct.* **2023,** *4,* 2200314. doi:10.1002/sstr.202200314
48. Walkare, A.; Solanki, B. S.; Singh, H.; Sheorey, T. *Mater. Today: Proc.* **2023,** *72,* 3017–3022. doi:10.1016/j.matpr.2022.08.270
49. Meng, Q.; Wang, T. J. *Appl. Mech. Rev.* **2019,** *71,* 040801. doi:10.1115/1.4044018
50. Singh, S.; Dwivedi, U. K.; Shukla, S. C. *Mater. Today: Proc.* **2021,** *47,* 3001–3005. doi:10.1016/j.matpr.2021.05.324
51. Yamamoto, G.; Onodera, M.; Koizumi, K.; Watanabe, J.; Okuda, H.; Tanaka, F.; Okabe, T. *Composites, Part A* **2019,** *121,* 499–509. doi:10.1016/j.compositesa.2019.04.011
52. Shamloo, A.; Fathi, B.; Elkoun, S.; Rodrigue, D.; Soldera, A. *J. Appl. Polym. Sci.* **2018,** *135,* 46176. doi:10.1002/app.46176
53. Mylo, M. D.; Hoppe, A.; Pastewka, L.; Speck, T.; Speck, O. *Front. Plant Sci.* **2022,** *13,* 950860. doi:10.3389/fpls.2022.950860
54. Hu, S.; Li, C.; Wang, H.; Mylo, M. D.; Becker, J.; Cao, B.; Müller, C.; Eberl, C.; Yin, K. *Mater. Des.* **2024,** *241,* 112960. doi:10.1016/j.matdes.2024.112960
55. Fischer, M.; Mylo, M. D.; Lorenz, L. S.; Böckenholt, L.; Beismann, H. *Biomimetics* **2024,** *9,* 191. doi:10.3390/biomimetics9030191
56. Correa, D.; Poppinga, S.; Mylo, M. D.; Westermeier, A. S.; Bruchmann, B.; Menges, A.; Speck, T. *Philos. Trans. R. Soc., A* **2020,** *378,* 20190445. doi:10.1098/rsta.2019.0445
57. Mylo, M. D.; Poppinga, S. *Front. Plant Sci.* **2024,** *14,* 1335445. doi:10.3389/fpls.2023.1335445

BEILSTEIN JOURNAL OF NANOTECHNOLOGY

Beyond the bilayer: multilayered hygroscopic actuation in pine cone scales

Kim Ulrich*[1,2], Max David Mylo[1,3], Tom Masselter[2], Fabian Scheckenbach[4], Sophia Fischerbauer[2], Martin Nopens[5], Silja Flenner[6], Imke Greving[6], Linnea Hesse[1,4] and Thomas Speck[1,2]

Full Research Paper

Open Access

Address:
[1]Cluster of Excellence livMatS @ FIT—Freiburg Center for Interactive Materials and Bioinspired Technologies, University of Freiburg, Freiburg im Breisgau, Germany, [2]Plant Biomechanics Group @ Botanic Garden, University of Freiburg, Freiburg im Breisgau, Germany, [3]Department of Microsystems Engineering—IMTEK, University of Freiburg, Freiburg im Breisgau, Germany, [4]Biomimetics Group, Institute for Wood Sciences, University of Hamburg, Hamburg, Germany, [5]Thünen Institute of Wood Research, Hamburg, Germany and [6]Institute of Materials Physics, Helmholtz-Zentrum Hereon, Geesthacht, Germany

Email:
Kim Ulrich* - ki.ul@icloud.com

* Corresponding author

Keywords:
digital volume correlation (DVC); finite element analysis; hygroscopic bending; plant biomechanics; sorption measurements

Beilstein J. Nanotechnol. **2025,** *16,* 1695–1710.
https://doi.org/10.3762/bjnano.16.119

Received: 06 June 2025
Accepted: 11 September 2025
Published: 29 September 2025

This article is part of the thematic issue "Micro- and nanoscale effects in biological and bioinspired materials and surfaces".

Guest Editor: T. H. Büscher

Abstract

The anisotropic hygroscopic behavior of pine cone scales and its effect on bending motion, with implications for bioinspired actuation, is investigated. Using gravimetric water uptake measurements, synchrotron radiation-based nano-holotomography, and digital volume correlation analysis, inter- and intra-tissue variations of hygroscopic swelling/shrinkage were observed. In addition, the moisture content of pine cone scale tissues was measured as a function of relative humidity. There were distinct differences between tissues and a pronounced hysteresis between sorption and desorption. Finite element analysis was performed on geometries ranging from simplified bilayer models to complex remodeled scales. Simulation results showed an underestimation of the bending of bilayer geometries due to an overestimated contribution of sclerenchyma fiber stiffness. Geometries with discrete fibers embedded in a brown tissue matrix more accurately reproduced the bending angles observed in experiments. This highlights the importance of the chosen material properties and tissue arrangements for predicting pine cone scale bending in silico. By contributing to a deeper understanding of pine cone scale biomechanics, these results also support the development of bioinspired technical applications. Future studies should refine tissue mechanical properties and integrate high-resolution computed tomography-based geometries to further elucidate the mechanisms underlying hygroscopic actuation. This integrative approach will bridge experimental findings with computational modeling and advance plant biomechanics and biomimetic transfer.

Introduction

In recent years, the hygroscopic motion of plant structures has attracted increasing attention from researchers and engineers, both for fundamental biological research and bioinspired technical applications [1-4]. Of particular interest are, for example, *Banksia* seed pods [5,6], *Hakea* fruits [7,8], and scales of pine cones [9-12], which passively respond to changes in ambient relative humidity by shape morphing to facilitate seed dispersal. In the case of pine cones, winged seeds are blocked and protected by the scales under wet conditions and released under dry conditions for wind dispersal. The inspiration provided by such biological motion principles has driven innovation in a variety of fields, including wood elements for weather-responsive and self-forming building parts [13], ceramic bilayer actuators [14], and 4D-printed weather-responsive façade shading elements [15]. The underlying principle in these biological examples is often compared to a thermally actuated "bimetal" mechanism [16,17]. The differential expansion or shrinkage of adjacent tissues drives the bending motion. However, current research on pine cones is increasingly revealing more complex, multilayered systems than simple bilayer analogies suggest. For instance, isolated pine cone scale tissues can bend independently, highlighting the complexity and resilience of the system despite delamination or cracking [18,19]. Additionally, research concerning the initial cone opening [20] and scale opening orchestration [21] has been conducted, highlighting the functional robustness and resilience [22] of pine cones. A better understanding of the pine cone scale and how its tissue properties and arrangement impact the bending motion, can therefore benefit the development and improvement of novel bioinspired technical applications.

At present, some characteristics of pine cones have been described that help to explain how their individual tissues can deform under desiccation/hydration and thus lead to the bending motion of the scale. One crucial influencing factor is the difference within or between tissues, as Eger et al. [23] highlighted. The authors measured the relative change of moisture content as a function of relative humidity by gravimetric water uptake measurements of the sclereid cells, the brown tissue, and the sclerenchyma fibers of a *Pinus wallichiana* pine cone scale. However, as their water uptake measurements consisted of only one measurement per tissue, being limited to the range of 30–80% RH, and their equilibrium criterion being one hour of exposure instead of a mass change threshold, a more nuanced study of the differences in water uptake between tissues is required to gain a better understanding of motion actuation. Quan et al. [24] also measured the gravimetric water uptake, revealing a hysteresis between uptake and evaporation, but without distinguishing between the scale tissues. Furthermore, they described a porosity gradient in the sclereid cell layer, without distinguishing between the sclereid cell layer and the brown tissue layer. The more porous adaxial sclereid cells they described are consistent with the earlier description of the brown tissue between the sclereid layer and the sclerenchyma fibers [12]. Other approaches have also observed a gradient in the cross-sectional shape of the prosenchymatous cells of sclerenchyma fibers of *Pinus elliottii* cones and higher tensile strength of the abaxial compared to the adaxial side of the sclerenchyma fibers [18].

Although recent advances in the study of pine cone scales have revealed the involvement of more than two tissue layers (sclereid cells, brown tissue, and sclerenchyma fibers) that may themselves contain a gradient [18,19,23,24], the relationship between these gradients and the resulting axis-dependent hygroscopic expansion of the tissues is still not described. To date, the hygroscopic expansion of pine cone scale tissues was often described under the assumption of isotropic expansion. Dawson et al. [11] measured the hygroscopic expansion coefficient of *Pinus radiata* cone scale tissues, but since then, an axis-dependent description of the hygroscopic expansion has remained omitted. This axial dependence of hygroscopic expansion has been an important research topic in wood research for years [25-27], but has so far been widely neglected in research on hygroscopic plant movements.

Recent advancements in the application of digital volume correlation (DVC) [28] in combination with synchrotron radiation-based nano-holotomography enable the study of axially dependent hygroscopic expansion and shrinkage of tissues [29]. This approach overcomes previous limitations related to the use of only affine registration or the previously neglected longitudinal (along the cell length axis) expansion of the measured cells [26,27]. By scanning tissue samples in a moist and a dry state using nano-holotomography, a DVC-based analysis of the two states becomes possible, which results in a displacement field representing the deformation from one state to the other. Using this displacement field allows for the calculation of a strain tensor field, which describes the axis-dependent hygroscopic expansion [29].

Incorporating the anisotropic swelling and shrinkage behavior into in silico models of the pine cone scale system further facilitates a more precise description of the bending motion. When simulating and analyzing the hygroscopic bending of pine cone scales using finite element analysis (FEA), as has already been done for a bilayer system [23,30], some geometrical simplifications and assumptions have to be made. For example, the cross-sectional shape of the tissues is simplified to rectangular shapes and modeled solely as a bilayer, which hardly mimics the

scales. With these simplifications, a bending motion can be simulated, but the conclusions that can be drawn, for example, regarding the impact of the tissue involved and their arrangement, are very limited.

The aim of this work is to characterize the anisotropic hygroscopic behavior of pine cone scale tissues and its effect on the bending motion. To this end, we first characterize their sorption behavior using gravimetric water uptake measurements. Furthermore, we apply synchrotron radiation-based nano-holotomography paired with DVC analysis to measure the axial dependent dimensional changes of cell size level tissue samples while shrinking. Finally, we compare measurements of the opening angle of pine cone scales with FEA models of different abstraction levels of a pine cone scale cross-sectional geometry incorporating the DVC-estimated hygroscopic expansion coefficients. This will answer the questions of (1) whether an intra-tissue gradient of the hygroscopic strain can be observed, (2) whether this measured hygroscopic strain can be used in a FEA to reproduce a comparable bending motion, and (3) whether this will allow us to properly describe and explore the effect of the cross-sectional shape and arrangement of the tissues on the bending motion.

Experimental

Sample preparation

All four pine cones used in our experiments originated from a *Pinus jeffreyi* tree growing in the Botanical Garden in Freiburg im Breisgau, Germany, and were collected from the ground in February 2022, after they had already opened and dispersed most of their seeds. Following collection, the cones were stored in a climate-controlled environment at room temperature. If individual cone scales were required for experiments, a pine cone was submerged in water overnight and then the scales were removed from the central axis by hand.

Gravimetric water uptake

The following three tissues were isolated from ten scales of the first cone: (1) the sclereid cell layer with the abaxial epidermis, (2) the brown tissue, and (3) the sclerenchyma fibers (Figure 1).

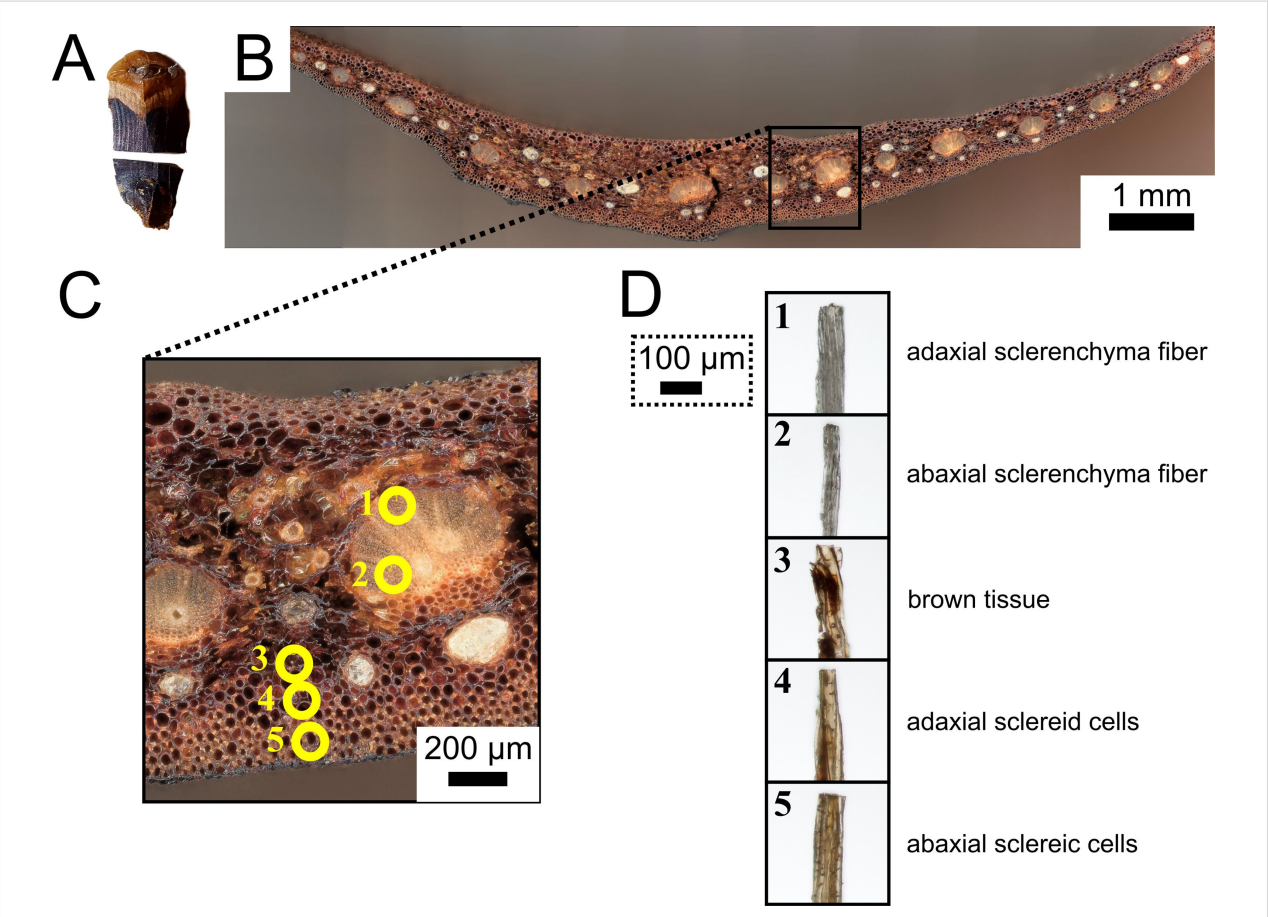

Figure 1: Tissue sample extraction from a *Pinus jeffreyi* cone scale. (A) The position of the cross section along the longitudinal axis of the scale, where the tissue samples were prepared from. (B) The respective scale cross section at the sampling location. (C) Close-up of the exact sampling locations within the tissues. (D) Microscopic images of the upper end of the respective tissue sample pillars.

Each scale was first saturated with water to facilitate subsequent separation with a razor blade. Saturating the scales with water prior to the sorption experiments prevents measuring a biased scanning isotherm due to the unknown sorption history of the sample [31]. We then divided the total amount of separated tissue material equally into five sample dishes each. The gravimetric water uptake of the extracted samples was then measured using a sorption test system (SPSx-1µ-High-Load, ProUmid, Germany) and a temperature and humidity sensor (HC2A-S Ambient Air Probe, ROTRONIC, Germany). At a controlled temperature of 20.0 °C, the samples were exposed to different steps of relative humidity, starting at 90%, dropping to 0% in increments of 15%, and returning to 90%, respectively. During this time, the samples were weighed every 20 min until all samples reached equilibrium. Equilibrium was defined as a change of mass of less than 0.01% over a period of 40 min. The 0% RH climate step was maintained for at least 96 h to ensure an equilibrium when measuring the dry mass of the samples. During the measurements, an error occurred in one sample of sclerenchyma fiber tissue, resulting in a pronounced mass shift from one weighing step to the next, making it unsuitable for further analysis. The relative mass change of the samples with respect to the measured dry mass was calculated and used for further analysis.

Axially dependent hygroscopic tissue shrinkage

The general imaging and analysis protocol followed the procedure presented in Ulrich and colleagues [29]. A pine cone scale was isolated from the second of the collected cones and transported to Hamburg, Germany, where the scale was soaked in water overnight to improve its cutability. Tissue samples were prepared of the ab- and adaxial parts of the sclereid cell layer and the sclerenchyma fibers, and the brown tissue (Figure 1). Each sample was cut into small pillars (length: ~800 µm, width: ~50 µm) by hand using a microscope (Olympus BX51, Evident Europe GmbH, Hamburg, Germany) and a razor blade. One end of the pillars was then glued to special sample holders using a UV-cured liquid plastic welding system (Bondic BC4000, VIKO UG, Kranzberg, Germany). Each tissue sample was then imaged at a special synchrotron radiation-based nano-holotomography setup at the imaging beamline P05 operated by Helmholtz-Zentrum Hereon at PETRA III (DESY Deutsches Elektronen Synchrotron, Hamburg, Germany). Phase contrast-based near-field holotomography was used to image our samples, utilizing a 300 µm gold Fresnel zone plate to focus the monochromatic beam with an energy of 11 keV [32]. For the in situ nano-holotomography, a climate chamber [33] was used to image the specimen in a moist (90% RH) and a dry (<3% RH) state. A binning factor of two was applied to the images. The phase retrieval was performed using the Holowizard framework [34,35]. The sample volumes were reconstructed using the GridRec algorithm [36] with a Shepp–Logan filter, implemented in TomoPy [37] with the P05 reconstruction pipeline. The resulting voxel size was 127 nm.

Prior to the DVC analysis, some preprocessing was performed using FIJI (ver. 1.54f) [38]. Since the sample expanded in vertical direction, the imaged sample area is not exactly the same in both scans. Therefore, the images were cropped to the same sample region for comparability. Additionally, the bit type of the images was reduced to 8-bit for computational efficiency, which reduced the computational time with negligible loss of information.

DVC was performed using the image registration software Elastix with its implemented B-spline transformation (ver. 5.1.0) [39]. The images were aligned in a two-step process, first with an affine transformation and then with a B-spline transformation. For both steps, a pyramidal approach with five resolution levels using a Gaussian filter was applied. The number of iterations per resolution level was set to 1000 for the affine transformation and 2000 for the B-spline transformation. Advanced normalized correlation was chosen as the correlation metric. The detailed parameter files, “Affine_parameters.txt” and “BSpline_parameters.txt” can be found in Supporting Information File 1. Based on the resulting displacement field, the Green–Lagrangian strain was calculated using the Insight Toolkit strain filter extension (ITK: ver. 5.3.0, itk-strain: ver. 0.4.0) [40] in Python (ver. 3.11.9) [41]. Finally, for each sample, the median of the axial strain components across all sample bulk voxel entries was calculated.

Hygroscopic bending motion

The scales of the last two pine cones were isolated, and two of the scale rows organized in steep spirals along the central axis were randomly selected for both cones. From each spiral, five scales were prepared for measurement, starting with the first basal scale whose adaxial epidermis was not blocked by another scale. For each experiment, one set of ten scales from one cone was then mounted in two rows of five in a sample holder inside a climate chamber (CTC-265, Memmert GmbH + Co.KG, Schwabach, Germany), with the rows representing one of the cone spirals. The most basal scale was mounted on the left and the most apical scale on the right (Figure 2). For further analysis, the position along the scale axis was assigned to an ordinal scale, with 1 being most basal and 5 being most apical. The scales were mounted by clamping the leftover part of the central cone axis at the basal end of the scale. The basal and apical parts of these scales facing the window were marked with a larger white dot with a black dot in the center to improve visibility and traceability.

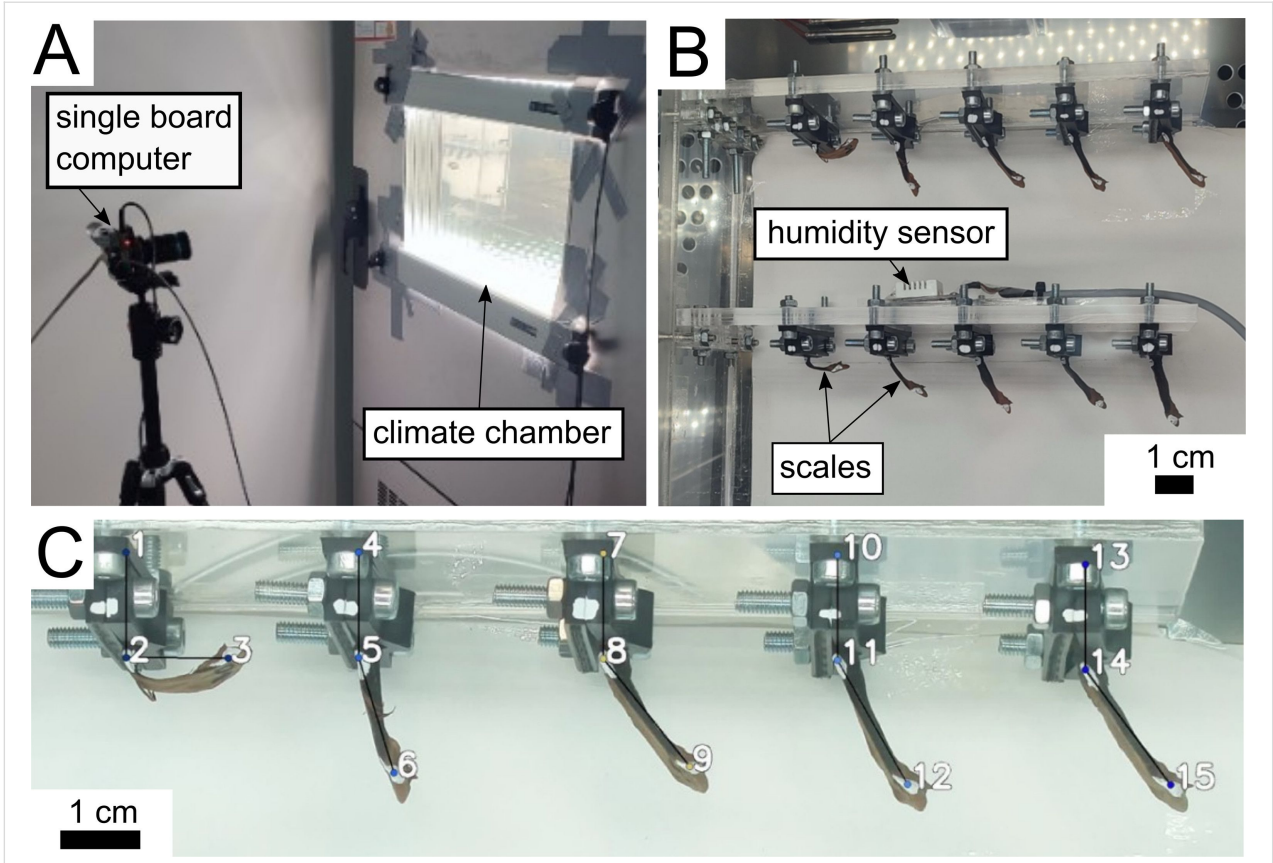

Figure 2: Characterization of the scale bending angle as a function of relative humidity and temperature. (A) Single board computer with camera module in front of the climate chamber. (B) Ten *Pinus jeffreyi* cone scales fixed in a sample holder inside the climate chamber. A row of scales of one cone is sorted from more basal (left) to more apical (right) based on the original position along the central cone axis. (C) Single frame of the first scale row during the automated point tracking for calculating the bending angle.

To test how long it takes for the scale bending motion to equilibrate, we set the climate chamber to run for 48 h, with the first 24 h at 31.7 ± 0.2% RH and the second 24 h at 73.9 ± 0.9% RH. The time to equilibrium was then calculated for each climate step. Equilibrium was defined as an angular change of less than 0.01° over 60 min. In a second run, the climate chamber was programmed to start at 30% RH and remain there for 24 h, then increased to 75% RH in four ~12% increments. Each incremental climate step was held for 12 h. After remaining at the highest humidity level for 24 h, the RH was again lowered back to 30% in four 12 h long decrements. Due to the limitations of the climate chamber and the required large volume of the interior, the equilibration steps achieved could vary between the incremental increases and decreases in humidity. The temperature and humidity in close proximity to our samples inside the chamber, as well as a side view of the samples, were recorded externally every 10 min using a single-board computer (Raspberry Pi 4 Model B, Raspberry Pi Foundation, Cambridge, UK) connected to a temperature and humidity sensor (DHT22, Sertronics GmbH, Berlin, Germany) and a camera module (Raspberry Pi HQ Camera V1.0, Raspberry Pi Foundation). The captured images were then analyzed using the adapted tracking script by Cheng et al. [15] to measure the opening angle of the scales. This was done by calculating the angle between a vertical line passing through the base of a scale and the connecting line between the base and apical points. The average of the last five angles measured for each climate step was then used for further analysis. The angle attained at equilibrium during the initial drying step was used as the baseline for normalizing all angle measurements.

Scale bending simulation

Based on a CT scan of a *P. jeffreyi* cone scale bending zone (basal third), five CAD geometries were created (Figure 3). The geometries were kept within the same dimensions (length: 11.5 mm, width: 11.5 mm, and thickness: 1.6 mm), to compare the resulting bending motion with the bending of the natural scales. The first geometry was a bilayer consisting of the sclereid layer and the sclerenchyma fiber layer, both being modeled with rectangular cross sections. The second geometry was a trilayer with the addition of a (thinner) intermediate brown tissue layer. The third geometry was a trilayer with the scle-

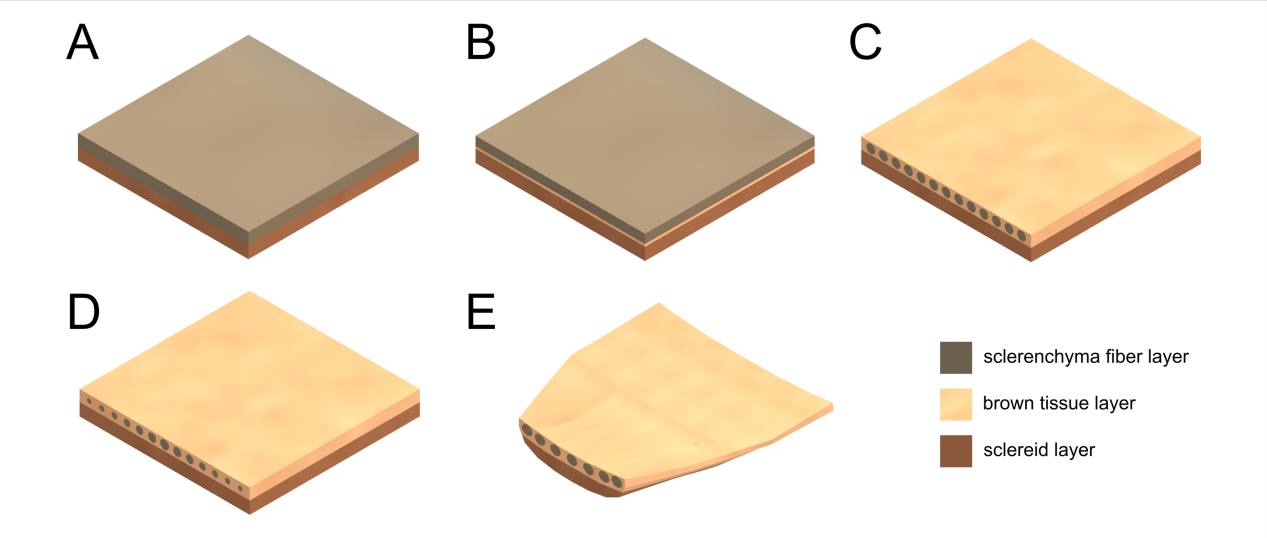

Figure 3: Geometries used for finite element analysis. (A) Bilayer. (B) Trilayer. (C) Trilayer with uniform fibers. (D) Trilayer with varying fibers. (E) Remodeled scale ("scale-like").

renchyma fibers being modeled as uniform tubes within the brown tissue layer. The fourth geometry was similar to the third, but with the diameter of the sclerenchyma fiber tubes gradually decreasing from 0.6 mm medial to 0.3 mm lateral. The last geometry resembled the natural anatomy of the pine cone scale the most as the geometry was modeled on the basis of five sketches of corresponding CT cross sections from five distinguished locations with defined distance along the longitudinal scale axis. Starting with a cross section from the basal part of the bending zone, the following cross sections were taken from positions 2.5, 5.5, 7.5, and 11.5 mm more apical. These five cross-sectional positions were then used as control points with the same longitudinal spacing between them to extrude the volume model. Since the sclerenchyma fibers branch along the longitudinal axis of a scale, they were simplified by allowing branching only at the cross sections used as control points (Figure S1, Supporting Information File 2).

The response of the involved tissues of the five scale-derived geometries during expansion and the influence of the involved tissues were characterized by simulative FEA in Ansys (ver. 2024 R2, Ansys, Inc., Canonsburg, PA, USA). Expansion was modeled using thermal stress analysis (a combination of the steady-state thermal and static structural solvers). The thermal expansion coefficients of the three tissues involved (sclereid layer, sclerenchyma fibers, and brown tissue) were defined to be orthotropic and derived from the hygroscopic shrinkage of the individual tissues measured in section "Axially dependent hygroscopic tissue shrinkage". The average value of the respective ab- and adaxial values was used for the sclereid layer and the sclerenchyma fibers. For the *X*- and *Y*-directions (spanning the cross section of each model), the mean value of the two measured values was used, while the *Z*-value (from the basal to the apical end of the models) was derived directly. The same coefficients were used in all simulations. A linear elastic material model was applied for all tissues, with Young's moduli of 30 MPa for the sclereid layer, 500 MPa for the sclerenchyma fibers, and 50 MPa for the brown tissue, and a Poisson's ratio of 0.3 for all tissues (all values derived from Eger et al. [23]). These five simulations will be referred to as the standard simulations in the following. To analyze the influence of the mechanical properties, in another simulation of the bilayer, the value of the Young's modulus of the sclerenchyma fibers was adjusted to that of the brown tissue (from 500 to 50 MPa). To analyze the influence of the Young's modulus of the brown tissue also in the scale-like model, another simulation was performed in which the Young's modulus was reduced below the Young's modulus of the sclereid layer from 50 to 10 MPa.

The imported geometries were converted into a volume mesh in Ansys (quadratic tetrahedrons; Tet10 elements) with edge lengths of 0.10 to 0.15 mm, resulting in meshes of 772,934 to 1,234,185 nodes (500,074 to 808,140 elements; Figure S1, Supporting Information File 2). To avoid highly deformed elements near the fixed plane, non-linear adaptive remeshing based on the skewness values of the elements was included where necessary. At the basal end of the geometry, a fixed support was applied over the entire cross-sectional area to suppress movement at this end and mimic experimental conditions. Expansion was induced by a temperature change of 150 °C in all volumes and simulated nonlinearly, accounting for large deformations. This temperature should be noted as being used only as an analogue for the hygroscopic expansion actuation, with no relation to the physical effect that an actual temperature would have on

the scales. The choice of 150 °C was determined iteratively to produce a bending of the geometries in the range of the natural scale. Initially, the chosen expansion coefficients were determined so that a temperature change of 100 °C corresponds to the results of the tissue shrinkage experiment. However, it is known from preliminary experiments that the influences of individual materials in multimaterial systems affect each other and that the actuation temperature must therefore be adapted. The results of all five geometries were compared in terms of their maximum total displacement at the apical tip and the observed double curvature. For this purpose, the maximum displacement in the *Y*-direction was quantified at three points. These were located at the two adaxial apical corners of each geometry and at the adaxial apical center (Figure S2, Supporting Information File 2). In order to assess the sensitivity of the FE analyses with respect to the expansion coefficients in the measured ranges, two comparative simulations were performed on the geometry with graded fiber size. In these simulations, the expansion coefficient of the brown tissue was set to the reciprocal of the minimum or maximum measured median strains (−5.8% and −10.5%, respectively) determined by DVC.

Statistical analysis

Data management, statistical analyses, and visualization were done with Python (ver. 3.12.8) using the packages pandas (ver. 2.2.3) [42], scipy (ver. 1.14.1) [43] and seaborn (ver. 0.13.2) [44]. The threshold of statistical significance was set at $p < 0.05$.

Results

Gravimetric water uptake

The gravimetric water uptake measurements allowed us to make precise analyses of the moisture content (Figure 4A). The behavior of the sclereid cells and the brown tissue revealed marked differences particularly above 50% RH. During absorption at 60% RH, the moisture content of the brown tissue is 0.37 percentage points lower than that of the sclereid cells, when looking at absolute differences. At 90% RH, the moisture content of the brown tissue is 2.13 percentage points lower. The sclerenchyma fibers have a lower moisture content than the other two tissues even at lower RHs. At 30% RH during absorption, their moisture content is 0.43 percentage points lower than the brown tissue and 0.55 percentage points lower than the sclereid cell moisture content. In the high RH range, it is particularly striking that the sclerenchyma fibers absorb the least percentage of water, the sclereid cells the most, and the brown tissue in between. At 90% RH, the sclereid cells achieve a moisture content of 27.7 ± 0.4% for desorption and 26.8 ± 0.4% for absorption. In comparison, the sclerenchyma fibers achieve a moisture content of 23.7 ± 0.6% for desorption and 23.0 ± 0.5% for absorption. In terms of the hysteresis observed, the difference in moisture content between desorption and absorption at 60% RH is in the range of 2.4–2.5 percentage points for each of the three tissues, with moisture content being higher during desorption than during absorption.

Axially dependent hygroscopic tissue shrinkage

Geometric differences between the tissue samples were observed using DVC to analyze the axial shrinkage from moist to dry state (Table 1). In the following, radial shrinkage (ε_{xx} and ε_{yy}) corresponds to shrinkage along both the abaxial–adaxial and the lateral–medial axis of a pine cone scale, since differentiation is not possible based on our tissue samples No statistical testing was performed to compare axial strains of individual tissue samples. The large number of observed voxels (>10^7) could produce misleading significant results, even for negligible biological differences (see the Supplementary information in [29] for an example).

The radial shrinkage of the cell samples ranged from the lowest of −5.8% for the brown tissue *y*-axial shrinkage to the highest of −11.0% for the sclerenchyma fiber *x*-axial shrinkage. The *x*- and *y*-axial shrinkage of the samples differed most for the brown tissue sample with the median *y*-axial shrinkage being 45% lower than the *x*-axial shrinkage (4.7 percentage points). On average, the radial shrinkage (average across sampling position and *x*- and *y*-axis for each tissue) of the sclerenchyma fibers was −9.3%, of the brown tissue −8.2%, and of the sclereid cells −7.6%. For longitudinal shrinkage (ε_{zz}), the lowest value was measured for the abaxial and adaxial sclerenchyma fibers, with higher shrinkage in the abaxial fiber (abaxial: −3.1%; adaxial: −1.8%). The highest longitudinal shrinkage was measured for the sclereid cells, with the adaxial shrinking more than the adaxial (abaxial: −8.1%; adaxial: −8.8%). The brown tissue sample showed higher longitudinal shrinkage (−7.6%) closer to the sclereid cell layer than to the sclerenchyma fibers. The radial shrinkage of the adaxial sclerenchyma fibers is, for example, 4.8–5.0 times higher than the longitudinal shrinkage. Whereas for the radial shrinkage of the abaxial sclereid cells is 0.8–1.1 times the longitudinal shrinkage.

Hygroscopic bending motion

The ten scales took 9.1 ± 1.6 h to reach their bending angle plateau from laboratory conditions to low RH (Figure 4B). From low RH to high RH, they took 10.0 ± 1.4 h to reach a plateau with a maximum measured angle of 17.8°. Regarding a correlation between their respective position along the central cone axis and their time until equilibrium, we cannot assume a normal distribution (Shapiro–Wilk test for high RH results: $W = 0.936$, $p > 0.05$, $n = 10$). Therefore, we calculated the

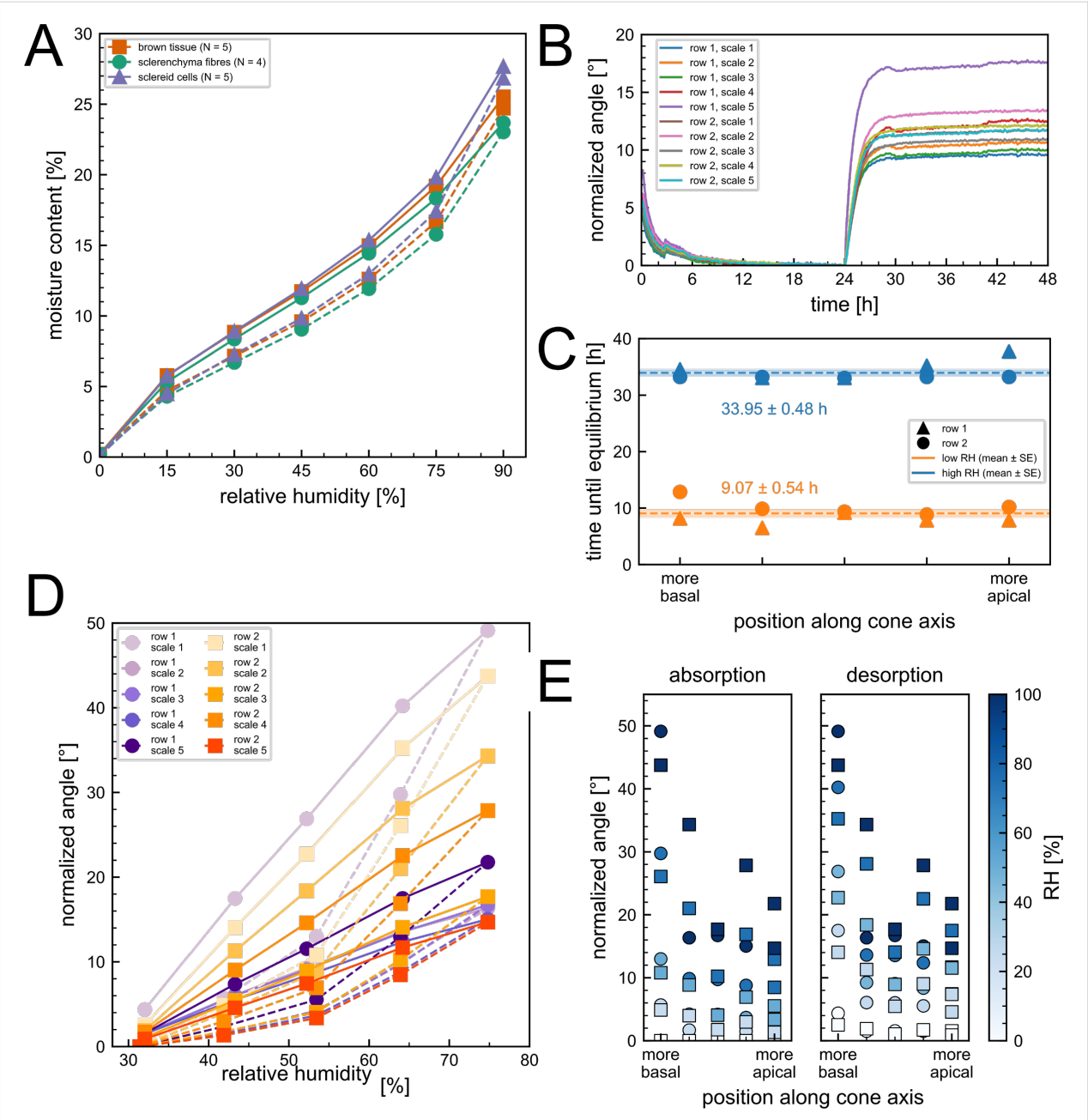

Figure 4: Results of the sorption measurements and the bending angle characterization. (A) The average moisture content of the scale tissues as a function of relative humidity. The desorption is shown as a solid line, the absorption as a dashed line. Violet: sclereid cells, orange: brown tissue, green: sclerenchyma fibers. (B) Ten pine cone scales where exposed to first a low, then a high relative humidity. Their bending angle normalized to the angle before changing conditions after 24 h is shown as a function of time. (C) The time it took the scales to reach equilibrium is plotted as a function of their position along the longitudinal central cone axis. Orange: low RH, blue: high RH. Circle: scales of first row, square: scale of second row. (D) Incremental measurements of the scale bending angle as a function of RH. The desorption is shown as a solid line, the absorption as a dashed line. The rows of scales are separated by color scheme. Violet: first row, orange: second row. The scales position along the central cone axis is shown by saturation. High saturation: more apical, low saturation: more basal. (E) The measured angle during absorption and desorption depicted in (D) is shown as a function of the scales position along the central cone axis. The respective RH is indicated by color. The first row of scales is depicted as circles, the second row as squares.

Spearman's rank correlation coefficient and found no significant correlation neither at low RH (rho = −0.161, $p > 0.05$) nor high RH (rho = 0.283, $p > 0.05$, $n = 10$). Comparing the linear model with an intercept-only (constant) model using AICc indicated a marginal preference for the constant model ($\Delta AICc = AICc_{linear} - AICc_{constant}$; low RH: $\Delta AICc = 1.38$; high RH: $\Delta AICc = 0.09$). As both $\Delta AICc$ values are ≤2 (i.e., models have comparable support), we chose the more parsimonious repre-

Table 1: Measured median axial strain across all evaluated voxels of the sample bulk.

tissue sample	sampling position	median axial strain with IQR			number of evaluated voxels
		ε_{xx} [%]	ε_{yy} [%]	ε_{zz} [%]	
sclerenchyma fiber	adaxial	–8.6 (–14.0, –2.4)	–9.0 (–14.1, –2.9)	–1.8 (–7.8, 3.3)	125,594,142
sclerenchyma fiber	abaxial	–11.0 (–17.7, –2.9)	–8.6 (–16.4, 0.5)	–3.1 (–10.1, 3.9)	38,983,712
brown tissue	—	–10.5 (–14.4, –6.1)	–5.8 (–9.8, –1.4)	–7.6 (–10.8, –3.1)	56,858,642
sclereid cells	adaxial	–7.5 (–12.7, –2.5)	–7.6 (–12.9, –2.4)	–8.8 (–12.6, –5.4)	125,224,286
sclereid cells	abaxial	–6.7 (–14.3, 2.2)	–8.7 (–15.3, –1.5)	–8.1 (–13.0, –2.9)	145,464,169

sentation and report the mean and standard deviation (Figure 4C).

Measuring the opening angle as a function of relative humidity (Figure 4D) shows a dependence of the bending on the direction of the humidity change, and a difference in the angle obtained with respect to the position along the central axis. In particular, the opening angles are smaller for absorption than for desorption for the same observed climatic conditions. The difference between the angles is greatest in the range between 50% and 60% RH, reaching, for example, 11.9° for one of the most basal scales. When the angle is considered as a function of the position along the central axis, basal scales reach an angle of ~50°, while apical scales sometimes reach only ~20° (Figure 4E). For both ab- and desorption and all RH steps, we calculated the Spearman's rank correlation between the normalized angle and the position along the central axes. We found significant correlation for all combinations (rho < −0.6, $p < 0.05$).

Scale bending simulation

The simulations of all five models resulted in a bending along the *Z*-direction of the geometry (Figure 5, Supporting Information Files 3–9). The largest bendings of the standard simulations were achieved by the trilayer with uniform fibers (maximum total displacement: 4.56 mm), the trilayer with varying fiber diameters (4.58 mm) and the scale-like geometry (5.57 mm). In the fiberless trilayer, a medium bending magnitude was achieved (4.11 mm), and the standard bilayer geometry bent the least (2.90 mm). By reducing the Young's modulus of the sclerenchyma fiber layer in the bilayer, the maximum total displacement was increased to 5.10 mm. A similar trend was found for the scale-like geometry in which the Young's modulus of the brown tissue was reduced, with an increased maximum displacement of 5.33 mm, and thus the highest value measured in any of the simulations. Looking at the change in curvature of the lateral axis of the geometries, a bending was particularly evident in the trilayer geometry with graded fibers and both scale-like geometries, while it was only slightly prominent in the other geometries (Figure S2b, Supporting Information File 2). In the case of the trilayer geometry with graded fiber diameters, the adaxial surface visibly bulged upwards. The pre-curved adaxial surface of the scale-like geometry flattens. This lateral curvature is influenced by the chosen radial expansion coefficient of the simulations, as highlighted in the comparative simulations of the geometry with graded fiber size (Figure S3, Supporting Information File 2). A lower expansion coefficient resulted in negligible lateral curvature, while a higher expansion coefficient resulted in increased lateral curvature.

To validate the FE simulations, a mesh sensitivity analysis was performed based on the trilayer geometry with fibers. Further mesh refinement with an increased number of nodes by a factor of ~3 resulted in a relative change in maximum deformation of only around 0.1% (For the mesh sensitivity analysis, elements sizes were changed from 0.15 mm (fibers) and 0.1 mm (sclereid layer and brown tissue) to 0.1 and 0.067 mm, respectively. The resulting mesh comprised 3,927,014 nodes and 2,681,955 elements. The maximum deformation of the scale changed from 4.5617 to 4.5574 mm, corresponding to a relative change of about 0.1%). Thus, mesh convergence can be assumed. Additional analysis of the impact of expansion coefficient variance based on the "trilayer with fibers" model showed the highest impact on bending for the *z*-axial hygroscopic expansion coefficient of the sclereid layer. More detailed results can be found in Table S1, Supporting Information File 2.

Discussion

Our analysis of axis-dependent swelling and shrinkage revealed inter- and intra-tissue gradients of the hygroscopic strain. We observed the lowest longitudinal shrinkage (median: −1.8%) for the adaxial sclerenchyma fiber tissue. Additionally, we found a difference between the adaxial and abaxial sides concerning the extent of longitudinal shrinkage, with the abaxial side exhibiting about 70% greater median shrinkage (Table 1). This gradient is consistent with spiral secondary cell wall thickenings only being observed on the abaxial side, leading to a differ-

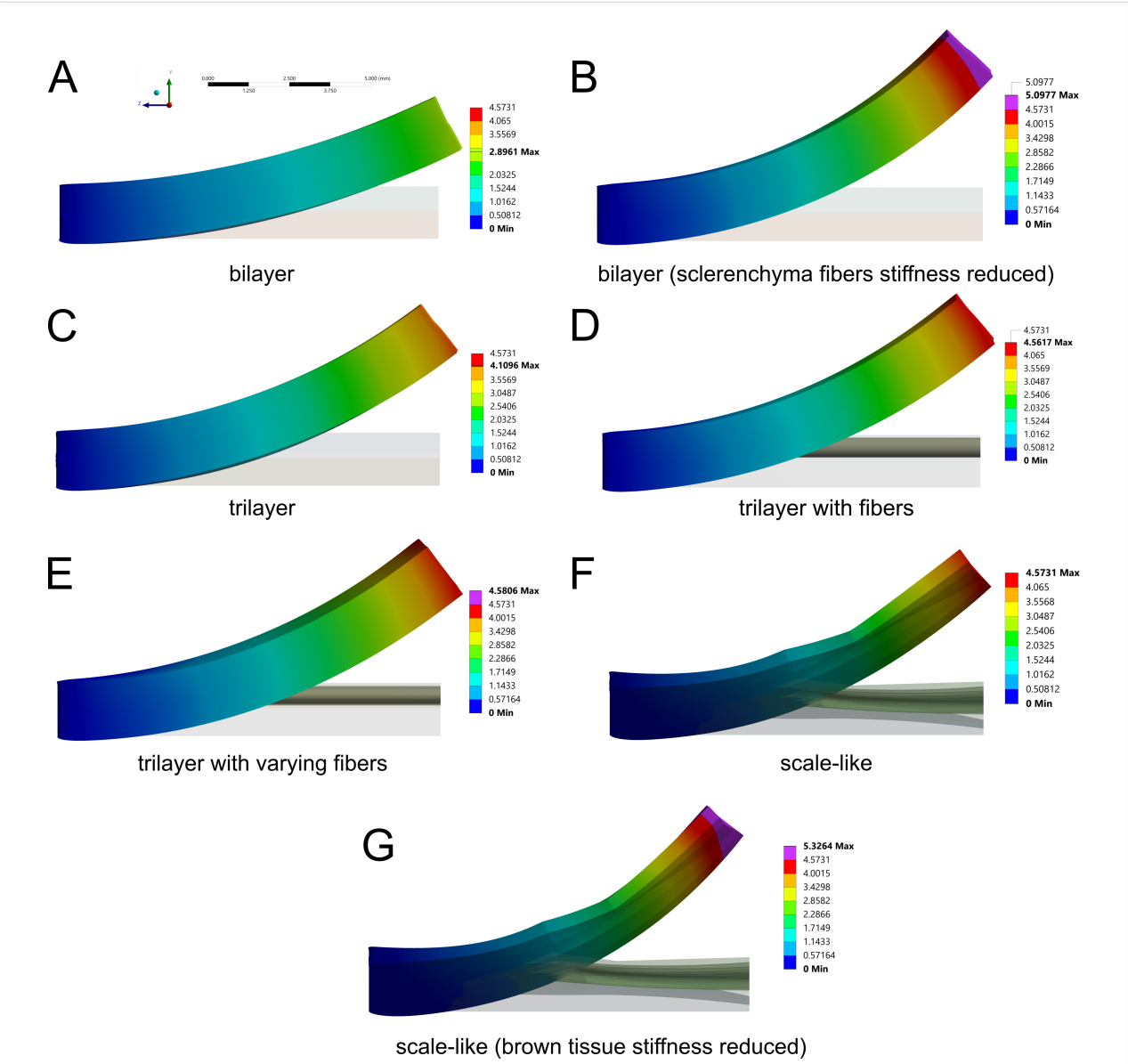

Figure 5: Results of the FE analysis. Obtained bending of (A) the bilayer, (B) the bilayer with reduced stiffness of the sclerenchyma fiber layer, (C) the trilayer, (D) the trilayer with fibers, (E) the trilayer with fibers with varying diameter, (F) the remodeled scale-like geometry, and (G) the remodeled scale-like geometry with reduced stiffness of the brown tissue. All results share the same coordinate system and scale depicted in (A). The colors indicate the total displacement.

ential longitudinal extension rate within the sclerenchyma fibers measured using environmental scanning electron microscopy (abaxial: 9%, adaxial: 1%, [18]). Although their exact values of measured longitudinal expansion may differ from ours due to differences in methodology and pine species studied, our results do support the ability of individual fibers to bend independently in response to moisture changes due to an intra-tissue gradient. In contrast, the longitudinal shrinkage measured in the abaxial and adaxial sides of the sclereid layer was more uniform, with about 0.7 percentage points higher values for the adaxial side, likely being within the measurement noise. The brown tissue exhibited lower hygroscopic shrinkage than the sclereid layer, although not as low as that observed in the sclerenchyma fibers. The boundary between the sclereid layer and the brown tissue is gradual rather than discrete [24], suggesting a continuous gradient in hygroscopic behavior. This gradual transition also hinders identification of specific tissues during sample preparation, leading to the sample labeled as “brown tissue” possibly partially reflecting the characteristics of the adaxial sclereid layer. Additionally, our analysis was limited by the measurement of only a single sample per internal tissue sampling location. In order to refine our understanding of the

hygroscopic material properties of tissue samples, future studies should include larger sample sizes. Nevertheless, the use of DVC-assisted sample evaluation has proven to be a very useful complementary method to classical ways for analyzing and comparing the hygroscopic shrinking behavior of lignocellulosic tissue samples.

When examining the radial tissue shrinkage (along the abaxial–adaxial and lateral–medial axes), we observed the intrinsic anisotropy of cell wall shrinkage [25,29,45]. Considering the *x*-axial shrinkage within the *x*–*y*-plane, cell walls oriented parallel to this axis have a lower *x*-axial shrinkage than perpendicularly oriented cell walls. The same can be observed for the *y*-axial shrinkage. This observation explains the variance between *x*- and *y*-axial shrinkage. Although under ideal sample preparation, the proportion of parallel and perpendicular cell wall sections should be similar (see adaxial sclerenchyma fibers), this is not always the case under real conditions. The porous brown tissue is a good example for this issue, showing high variance between the median *x*- (−10.5%) and *y*-axial (−5.8%) shrinkage. Therefore, future measurements should include more cells to avoid conflicting results for the radial shrinkage. In addition, the original orientation during specimen preparation and imaging should remain traceable in order to differentiate between ab-/adaxial and lateral directions in the resulting images. The tissue average radial shrinkage is highest for the sclerenchyma fibers and lowest for the sclereids, which can be explained by the microfibril angle. The angle of the microfibrils can not only limit cell expansion along its longitudinal direction, but also constrict radial shrinkage like a belt [46,47]. Since the microfibril angle is highest in sclereid cells, their longitudinal expansion is higher and their radial expansion is lower. The sclerenchyma fibers, in contrast, have a lower microfibril angle and expand less longitudinally and more radially.

Like the inter-tissue gradient of the hygroscopic strain, we also observed a clear hierarchy between the three tissues in terms of moisture content as a function of relative humidity (Figure 4). At the initial 90% RH before drying, the sclereid layer exhibited the highest moisture content (27.7%), followed by the brown tissue at a slightly lower level (25.5%), and the sclerenchyma fibers with the lowest moisture content (23.7%). This resulted in a moisture uptake profile that diverges notably from that reported by Eger and colleagues [23]. Comparing the water uptake measured by us in the range of 30–80% RH with that reported by Eger et al. [23], the behavior of the sclerenchyma fibers is comparable. However, both the sclereid layer and the brown tissue in our study exhibit a 1.5–2 times higher relative water uptake, a discrepancy that may arise from differences in the equalization criterion or inherent species-specific characteristics. It is important to note that different species were studied in each case, which may indicate that the water uptake of the tissues differs markedly between pine cones of different species.

Furthermore, our measurements reveal a pronounced hysteresis between absorption and desorption cycles in all three tissue types, indicating that the moisture content, and consequently the swelling behavior, is strongly dependent on the sample's exposure history. A comparable hysteresis was also indicated in previous studies [23,24], but has not yet been investigated further. This path-dependency may affect the repeatability of hygroscopic behavior under fluctuating environmental conditions. The same phenomenon can be observed when measuring the bending angle of the cone scales during absorption and desorption (Figure 4). Within the 50–60% RH range, the bending angle varied markedly depending on the pre-conditioning of the scale: Scales that were drier prior to exposure achieved up to ~12° smaller bending angles than those that were previously moistened. This observed hysteresis of the scale bending angle is closely related to the sorption hysteresis of the scale tissues and may also have biological implications. Considering a cone has just opened and is releasing its seeds, it would be disadvantageous for the cone scales to "overreact" and close due to every slight rain shower or increase in humidity. In this context, the hysteresis might act as an additional buffer besides the general slow speed of the closure. Delayed closure relative to humidity after a dry state ensures that the cone does not respond abruptly to transient increases in humidity, thereby stabilizing the seed dispersal process. A similar mechanism may apply to closed cones, where it has already been described that the initial opening is influenced by resin at the apophysis and is therefore dependent on temperature and humidity being within a certain range [20]. After the initial opening, a delayed response to humidity changes could additionally prevent inadvertent responses to transient humidity decreases, ensuring that the cone only opens when environmental conditions consistently favor seed dispersal. This should also be taken into account and further investigated in the case of future studies, not only to enhance the understanding of the ecological importance of the pine cone opening and closure, but also to improve the design of bioinspired systems. Controlled, delayed responses to environmental changes may be desirable for various engineering and architectural systems, such as adaptive façade shading systems [15].

The achievable bending angle also varied with the position of the scales along the central cone axis. Scales from the apical part achieve an up to ~30° lower opening angle than those from the basal part. This may be attributed to variations in tissue composition or mechanical and hygroscopic properties along

the cone. In the case of basal scales, our measured opening angle is underestimated due to the chosen method of angle calculation and the strong curvature of the scales. Interestingly, we found that the time required for the scales' bending motion to reach an equilibrium was consistent across different positions along the cone. This uniformity suggests that the time until equilibrium may be independent of local structural variations, potentially ensuring coordinated movement across the cone. In this case, if evaporation through the apophysis were the primary driver of moisture loss in a closed cone, all scales would be expected to open simultaneously. In *Pinus jeffreyi*, however, the orchestration occurs successively. This supports the conclusions drawn by Horstmann et al. [21], who attributed the successive orchestration to the overlapping arrangement of scales and the constrained evaporation through the apophysis. This coordinated opening mechanism may facilitate seed dispersal since not all seeds are released at the same time. It also provides valuable insights for the design of bioinspired systems that mimic such controlled, sequential responses and actuations.

The results of the simulations clearly show that we can use the measured values of hygroscopic expansion to achieve a bending angle in the range of biological specimens (Figure 5). However, the chosen material properties of the tissues, and in particular the cross-sectional area of the more rigid sclerenchyma fiber layer, play a crucial role. For example, the simulation of the bilayer geometry showed that a considerably lower bending is achieved compared to other geometries. This is due to the cross-sectional geometry and the shape and proportion of the stiffer sclerenchyma fiber layer. When the cross-sectional geometry is simplified to a bilayer with the sclerenchyma fibers as a rectangular layer, the resulting area moment of inertia increases compared to a layer consisting of multiple fibers. Thus, the sclerenchyma fiber layer contributes more to the structural Young's modulus of the cone scale model, and the resulting bending is less than that observed in nature. Since previous simulations of the pine cone scale have used the bilayer model as a simplified geometry [23,30], the obtained results must be taken with caution. However, if the sclerenchyma fibers' Young's modulus is decreased, or if they are considered as discrete fiber elements embedded in an intermediate tissue, higher bending angles can be achieved with the same material properties and more closely represent the biological model.

As part of these considerations of the relevance of Young's modulus, it was also noted that the indentation measurements by Eger et al. [23] used as the basis for our simulations may reflect a cellular rather than a structural Young's modulus of the tissue. In their measurements, the Young's modulus of the brown tissue is in the same range as that of the sclereid layer. This is despite the fact that in cone scales of *P. jeffreyi* and other species, for example, the brown tissue is significantly more porous [24] than the sclereid layer and can be easily deformed and bent by hand, while the sclereid layer remains relatively rigid. This porosity can also be seen in the cross sections we prepared (Figure 1) and in the CT images (Figure S4, Supporting Information File 2). Since the choice of probe tip for nanoindentation measurements of hierarchically structured biological samples is very important in relation to what one wants to measure [48,49], it is possible that a tip that is too small was used. It is also possible that the gradual transition between sclereid cells and brown tissue may have caused the indentation to sample predominantly the adaxial sclereid cells rather than the brown tissue.

Our simulations not only extend the geometric complexity of previous bilayer models [23,30]; they also take into account the measured axial swelling instead of assuming isotropy. This leads not only to curvature along the longitudinal axis, but also to lateral curvature, albeit less pronounced. In contrast to the biologically observed opening motion [12], the lateral curvature we observe is inverted. This effect can be explained by the higher average radial shrinkage/swelling of brown tissue compared to sclereid cells. This may be due to the higher measurement variance of the DVC analysis due to the porous structure of the brown tissue. When the simulations are performed with the lower y-axis shrinkage, this lateral curvature is negligible, whereas when the higher x-axis shrinkage is chosen, the inverted movement becomes even more pronounced (Figure S3, Supporting Information File 2). This illustrates the influence of the radial shrinkage/swelling properties of the motions involved and the measurement errors on the radial curvature. Furthermore, only a single parameter was varied in the comparative simulation, so it can be assumed that the biological curvature can be reproduced by further variations. However, the aim of this work was not to adjust the individual parameters of the simulation to achieve the best possible agreement between experiment and simulation, but rather to set up a simulation based on the experimentally determined values and to use it to characterize the influence of the underlying geometries and tissue distributions. Our analysis of the impact of parameter variation on achieved bending highlighted the importance of z-axial hygroscopic expansion of the sclereid layer. This finding further supports the results of our simulations based on DVC-estimated hygroscopic expansion coefficients. While the simulations are sensitive to changes in the z-axial hygroscopic expansion coefficient, their results are comparable to those of biological samples. However, further refinements to the DVC-based estimation are essential to strengthen the predictive reliability of upcoming simulations. For the analysis of the motion mechanism of the scale, for example, to show the multiphase nature of the motion [12], future simulation approaches could

use transient heat transfer simulations incorporating diffusion models.

The comparative simulations in this work, together with previously published bilayer models, show that the analytical analysis of such a complex drying movement is a sensitive system of selected expansion coefficients, mechanical properties, and geometric models. It should be noted that the modeling of sorption/desorption of water via thermal expansion/contraction is common for plant structures due to the limitations of FEA software [23,50], but it involves an artificial detour. We have shown that the assignment of mechanical properties in multimaterial systems plays a crucial role in the extent of actuation; hence, the best possible data base is crucial for the accuracy and thus the informative value of the simulation. It should also be mentioned that most simulations assume clear boundaries between individual tissues/components and thus can only partially represent the natural models and their complex, often graded interfaces. Furthermore, our work has demonstrated the influence of the complexity of the simulated geometry. The geometries recently used to simulate plant systems range from highly simplified 2D geometries for complex damage analysis [51,52], to rather simplified rod-like structures [53] and 3D shell models [50,54], and ultimately to highly detailed geometries based on segmented computed tomography images [55,56]. No general guideline can be given for the level of detail required for FEA of plant systems as this depends on the complexity of the system, the available data, and, most importantly, the research question to be answered. The data presented should demonstrate the importance of considering geometries. It should be noted that simplifying each tissue as a homogeneous layer still does not fully represent biological samples. Our approach does not consider internal gradients and gradual interfaces, which can be observed in the samples. However, these features should be included when creating highly detailed virtual twins of the pine scales. Considering all of the above factors and the associated uncertainties, FEA analysis can have an ever-increasing impact on the biomechanical analysis and characterization of plant motion. To better describe and analyze the pine cone scale in silico in the future, the material properties of the tissues should be re-measured, focusing on their structural rather than cellular properties. A detailed mesh of a pine cone scale based on a segmented CT scan could also be the next step to overcome the limitations of the currently used simplifications.

Conclusion

In summary, returning to our initial research questions, we were able to observe and further investigate inter- and intra-tissue gradients of hygroscopic swelling/shrinkage and moisture content. In addition, we observed hysteresis both at the tissue level with respect to moisture content and in the measurements of the bending angle of the scales as a function of relative humidity. The measured hygroscopic expansion coefficients were used for FEA of various geometries resembling simplified pine cone scale bending zones. This analysis highlighted the importance of the tissue material properties and raises some questions about previous Young's modulus measurements. Furthermore, the achievable bending angle can be increased by avoiding a simple bilayer geometry and modeling the sclerenchyma layer as discrete fibers embedded in a brown tissue matrix. Therefore, the use of more complex geometries, such as a remodeled scale, is recommended for a more accurate study of the biological system in silico.

Supporting Information

Supporting Information File 1

Detailed parameter files for digital volume correlation. The ZIP archive contains two txt files, that is, "Affine_parameters.txt", the parameter file for affine registration, and "BSpline_parameters.txt", the parameter file for B-spline registration.
[https://www.beilstein-journals.org/bjnano/content/supplementary/2190-4286-16-119-S1.zip]

Supporting Information File 2

Additional experimental data.
[https://www.beilstein-journals.org/bjnano/content/supplementary/2190-4286-16-119-S2.pdf]

Supporting Information File 3

Bending simulation result of the bilayer model.
[https://www.beilstein-journals.org/bjnano/content/supplementary/2190-4286-16-119-S3.mp4]

Supporting Information File 4

Bending simulation result of the trilayer model.
[https://www.beilstein-journals.org/bjnano/content/supplementary/2190-4286-16-119-S4.mp4]

Supporting Information File 5

Bending simulation result of the fiber model.
[https://www.beilstein-journals.org/bjnano/content/supplementary/2190-4286-16-119-S5.mp4]

Supporting Information File 6

Bending simulation result of the fiber model with a gradient.
[https://www.beilstein-journals.org/bjnano/content/supplementary/2190-4286-16-119-S6.mp4]

Supporting Information File 7
Bending simulation result of the scale-like model.
[https://www.beilstein-journals.org/bjnano/content/supplementary/2190-4286-16-119-S7.mp4]

Supporting Information File 8
Bending simulation result of the bilayer model with reduced E-modulus.
[https://www.beilstein-journals.org/bjnano/content/supplementary/2190-4286-16-119-S8.mp4]

Supporting Information File 9
Bending simulation result of the scale-like model with reduced E-modulus.
[https://www.beilstein-journals.org/bjnano/content/supplementary/2190-4286-16-119-S9.mp4]

Acknowledgements
We thank Gerald Koch, Noah Knorr, Joel Gust, Simon Poppinga, Heike Beismann, Moses Gereon Wullweber und Matthias Fischer for support during our Desy Beamtime in November 2023. We thank Sergej Kaschuro for sample preparation. This research was supported in part through the Maxwell computational resources operated at DESY.

Funding
KU, MDM, TM and TS are grateful for funding by the Deutsche Forschungsgemeinschaft (DFG, German Research Foundation) under Germany's Excellence Strategy [EXC-2193/1–390951807]. LH and FS thank the Deutsche Forschungsgemeinschaft (DFG, German Research Foundation) [HE 9048/1-1] and DESY for support. LH additionally thanks the European Social Fund and the Ministry of Science, Research and the Arts Baden-Württemberg within the framework of the "Margarete von Wrangell Habilitation Programme". This work was supported by the Deutsche Forschungsgemeinschaft (DFG, German Research Foundation) through the Cluster of Excellence EXC3120 BlueMat: Water-Driven Materials.

Author Contributions
Kim Ulrich: conceptualization; data curation; formal analysis; investigation; methodology; project administration; software; validation; visualization; writing – original draft; writing – review & editing. Max David Mylo: conceptualization; data curation; formal analysis; investigation; methodology; software; writing – original draft; writing – review & editing. Tom Masselter: conceptualization; supervision; writing – review & editing. Fabian Scheckenbach: data curation; methodology; writing – review & editing. Sophia Fischerbauer: data curation; investigation; methodology; software; writing – review & editing. Martin Nopens: methodology; writing – review & editing. Silja Flenner: data curation; formal analysis; investigation; methodology; software; writing – review & editing. Imke Greving: data curation; methodology; writing – review & editing. Linnea Hesse: funding acquisition; resources; supervision; writing – review & editing. Thomas Speck: conceptualization; funding acquisition; resources; supervision; writing – review & editing.

ORCID® iDs
Kim Ulrich - https://orcid.org/0000-0002-4196-8814
Max David Mylo - https://orcid.org/0000-0001-5744-9069
Tom Masselter - https://orcid.org/0000-0001-5465-8252
Fabian Scheckenbach - https://orcid.org/0009-0009-9481-4083
Sophia Fischerbauer - https://orcid.org/0009-0006-3832-6964
Linnea Hesse - https://orcid.org/0000-0001-9308-5776
Thomas Speck - https://orcid.org/0000-0002-2245-2636

Data Availability Statement
Data generated and analyzed during this study is openly available in Mendeley Data at https://doi.org/10.17632/phyx35hcy6.1. Due to imaging data size, additional research data generated and analyzed is available from the corresponding author upon reasonable request.

References
1. Elbaum, R.; Gorb, S.; Fratzl, P. *J. Struct. Biol.* **2008,** *164,* 101–107. doi:10.1016/j.jsb.2008.06.008
2. Poppinga, S.; Correa, D.; Bruchmann, B.; Menges, A.; Speck, T. *Integr. Comp. Biol.* **2020,** *60,* 886–895. doi:10.1093/icb/icaa028
3. Tahouni, Y.; Krüger, F.; Poppinga, S.; Wood, D.; Pfaff, M.; Rühe, J.; Speck, T.; Menges, A. *Bioinspiration Biomimetics* **2021,** *16,* 055002. doi:10.1088/1748-3190/ac0c8e
4. Luo, D.; Maheshwari, A.; Danielescu, A.; Li, J.; Yang, Y.; Tao, Y.; Sun, L.; Patel, D. K.; Wang, G.; Yang, S.; Zhang, T.; Yao, L. *Nature* **2023,** *614,* 463–470. doi:10.1038/s41586-022-05656-3
5. Huss, J. C.; Schoeppler, V.; Merritt, D. J.; Best, C.; Maire, E.; Adrien, J.; Spaeker, O.; Janssen, N.; Gladisch, J.; Gierlinger, N.; Miller, B. P.; Fratzl, P.; Eder, M. *Adv. Sci.* **2018,** *5,* 1700572. doi:10.1002/advs.201700572
6. Reppe, F.; Guiducci, L.; Elbaum, R.; Werner, P.; Dunlop, J. W. C.; Merritt, D. J.; Fratzl, P.; Eder, M. *Adv. Funct. Mater.* **2025,** *35,* 2418592. doi:10.1002/adfm.202418592
7. Fischer, M.; Beismann, H. *Flora (Jena)* **2022,** *289,* 152035. doi:10.1016/j.flora.2022.152035
8. Fischer, M.; Mylo, M. D.; Lorenz, L. S.; Böckenholt, L.; Beismann, H. *Biomimetics* **2024,** *9,* 191. doi:10.3390/biomimetics9030191
9. Shaw, G. R. *The Genus Pinus;* Roverside Press: Cambridge, MA, USA, 1914. doi:10.5962/bhl.title.26194
10. Harlow, W. M.; Côté, W. A.; Day, A. C. *J. For.* **1964,** *62,* 538–540. doi:10.1093/jof/62.8.538
11. Dawson, C.; Vincent, J. F. V.; Rocca, A.-M. *Nature* **1997,** *390,* 668. doi:10.1038/37745

12. Correa, D.; Poppinga, S.; Mylo, M. D.; Westermeier, A. S.; Bruchmann, B.; Menges, A.; Speck, T. *Philos. Trans. R. Soc., A* **2020,** *378,* 20190445. doi:10.1098/rsta.2019.0445
13. Wood, D.; Vailati, C.; Menges, A.; Rüggeberg, M. *Constr. Build. Mater.* **2018,** *165,* 782–791. doi:10.1016/j.conbuildmat.2017.12.134
14. Van Opdenbosch, D.; Fritz-Popovski, G.; Wagermaier, W.; Paris, O.; Zollfrank, C. *Adv. Mater. (Weinheim, Ger.)* **2016,** *28,* 5235–5240. doi:10.1002/adma.201600117
15. Cheng, T.; Tahouni, Y.; Sahin, E. S.; Ulrich, K.; Lajewski, S.; Bonten, C.; Wood, D.; Rühe, J.; Speck, T.; Menges, A. *Nat. Commun.* **2024,** *15,* 10366. doi:10.1038/s41467-024-54808-8
16. Timoshenko, S. *J. Opt. Soc. Am. Rev. Sci. Instrum.* **1925,** *11,* 233–255. doi:10.1364/josa.11.000233
17. Palacios, A.; Chiriatti, L.; Poppinga, S.; Speck, T.; Le Houérou, V. *Adv. Intell. Syst.* **2025,** *7,* 2400396. doi:10.1002/aisy.202400396
18. Zhang, F.; Yang, M.; Xu, X.; Liu, X.; Liu, H.; Jiang, L.; Wang, S. *Nat. Mater.* **2022,** *21,* 1357–1365. doi:10.1038/s41563-022-01391-2
19. Ulrich, K.; Genter, L.; Schäfer, S.; Masselter, T.; Speck, T. *Bioinspiration Biomimetics* **2024,** *19,* 046009. doi:10.1088/1748-3190/ad475b
20. Horstmann, M.; Buchheit, H.; Speck, T.; Poppinga, S. *Front. Plant Sci.* **2022,** *13,* 982756. doi:10.3389/fpls.2022.982756
21. Horstmann, M.; Speck, T.; Poppinga, S. *Plants* **2024,** *13,* 2078. doi:10.3390/plants13152078
22. Mylo, M. D.; Speck, O. *Biomimetics* **2023,** *8,* 173. doi:10.3390/biomimetics8020173
23. Eger, C. J.; Horstmann, M.; Poppinga, S.; Sachse, R.; Thierer, R.; Nestle, N.; Bruchmann, B.; Speck, T.; Bischoff, M.; Rühe, J. *Adv. Sci.* **2022,** *9,* 2200458. doi:10.1002/advs.202200458
24. Quan, H.; Pirosa, A.; Yang, W.; Ritchie, R. O.; Meyers, M. A. *Acta Biomater.* **2021,** *128,* 370–383. doi:10.1016/j.actbio.2021.04.049
25. Rafsanjani, A.; Stiefel, M.; Jefimovs, K.; Mokso, R.; Derome, D.; Carmeliet, J. *J. R. Soc., Interface* **2014,** *11,* 20140126. doi:10.1098/rsif.2014.0126
26. Patera, A.; Van den Bulcke, J.; Boone, M. N.; Derome, D.; Carmeliet, J. *Wood Sci. Technol.* **2018,** *52,* 91–114. doi:10.1007/s00226-017-0960-3
27. Patera, A.; Carl, S.; Stampanoni, M.; Derome, D.; Carmeliet, J. *Adv. Struct. Chem. Imaging* **2018,** *4,* 1. doi:10.1186/s40679-018-0050-0
28. Bay, B. K.; Smith, T. S.; Fyhrie, D. P.; Saad, M. *Exp. Mech.* **1999,** *39,* 217–226. doi:10.1007/bf02323555
29. Ulrich, K.; Scheckenbach, F.; Wong, T. M.; Masselter, T.; Flenner, S.; Visconti, A.; Nopens, M.; Krause, A.; Kaschuro, S.; Mietner, J. B.; Speck, T.; Greving, I.; Zeller-Plumhoff, B.; Hesse, L. *Front. Plant Sci.* **2025,** *16,* 1572745. doi:10.3389/fpls.2025.1572745
30. Lin, S.; Xie, Y. M.; Li, Q.; Huang, X.; Zhou, S. *Soft Matter* **2016,** *12,* 9797–9802. doi:10.1039/c6sm01805j
31. Nopens, M.; Riegler, M.; Hansmann, C.; Krause, A. *Sci. Rep.* **2019,** *9,* 10309. doi:10.1038/s41598-019-46381-8
32. Flenner, S.; Storm, M.; Kubec, A.; Longo, E.; Döring, F.; Pelt, D. M.; David, C.; Müller, M.; Greving, I. *J. Synchrotron Radiat.* **2020,** *27,* 1339–1346. doi:10.1107/s1600577520007407
33. Nopens, M.; Greving, I.; Flenner, S.; Hesse, L.; Lüdtke, J.; Altgen, M.; Koch, G.; Beruda, J.; Heldner, S.; Köhm, H.; Kaschuro, S.; Olbrich, A.; Mietner, J. B.; Scheckenbach, F.; Sieburg-Rockel, J.; Krause, A. *J. Synchrotron Radiat.* **2025,** *32,* 1354–1360. doi:10.1107/s1600577525006484
34. A Python framework for the online reconstruction of X-ray near-field holography data, version 1.3.1. https://zenodo.org/records/14024980 (accessed Sept 11, 2025). doi:10.5281/zenodo.14024980
35. Dora, J.; Möddel, M.; Flenner, S.; Schroer, C. G.; Knopp, T.; Hagemann, J. *Opt. Express* **2024,** *32,* 10801–10828. doi:10.1364/oe.514641
36. Dowd, B. A.; Campbell, G. H.; Marr, R. B.; Nagarkar, V. V.; Tipnis, S. V.; Axe, L.; Siddons, D. P. *Proc. SPIE* **1999,** *3772,* 224–236. doi:10.1117/12.363725
37. Gürsoy, D.; De Carlo, F.; Xiao, X.; Jacobsen, C. *J. Synchrotron Radiat.* **2014,** *21,* 1188–1193. doi:10.1107/s1600577514013939
38. Schindelin, J.; Arganda-Carreras, I.; Frise, E.; Kaynig, V.; Longair, M.; Pietzsch, T.; Preibisch, S.; Rueden, C.; Saalfeld, S.; Schmid, B.; Tinevez, J.-Y.; White, D. J.; Hartenstein, V.; Eliceiri, K.; Tomancak, P.; Cardona, A. *Nat. Methods* **2012,** *9,* 676–682. doi:10.1038/nmeth.2019
39. Klein, S.; Staring, M.; Murphy, K.; Viergever, M. A.; Pluim, J. P. W. *IEEE Trans. Med. Imaging* **2010,** *29,* 196–205. doi:10.1109/tmi.2009.2035616
40. N-Dimensional Computation of Strain Tensor Images in the Insight Toolkit. http://hdl.handle.net/10380/3573 (accessed Sept 11, 2025). doi:10.54294/1wtpo8
41. Van Rossum, G.; Drake, F. L. *Python 3 Reference Manual;* CreateSpace: Scotts Valley, CA, USA, 2009.
42. McKinney, W. Data Structures for Statistical Computing in Python. In *Proceedings of the 9th Python Science Conference,* van der Walt, S.; Millman, J., Eds.; 2010; pp 56–61. doi:10.25080/majora-92bf1922-00a
43. Virtanen, P.; Gommers, R.; Oliphant, T. E.; Haberland, M.; Reddy, T.; Cournapeau, D.; Burovski, E.; Peterson, P.; Weckesser, W.; Bright, J.; van der Walt, S. J.; Brett, M.; Wilson, J.; Millman, K. J.; Mayorov, N.; Nelson, A. R. J.; Jones, E.; Kern, R.; Larson, E.; Carey, C. J.; Polat, İ.; Feng, Y.; Moore, E. W.; VanderPlas, J.; Laxalde, D.; Perktold, J.; Cimrman, R.; Henriksen, I.; Quintero, E. A.; Harris, C. R.; Archibald, A. M.; Ribeiro, A. H.; Pedregosa, F.; van Mulbregt, P.; SciPy 1.0 Contributors. *Nat. Methods* **2020,** *17,* 261–272. doi:10.1038/s41592-019-0686-2
44. Waskom, M. L. *J. Open Source Software* **2021,** *6,* 3021. doi:10.21105/joss.03021
45. Arzola-Villegas, X.; Lakes, R.; Plaza, N. Z.; Jakes, J. E. *Forests* **2019,** *10,* 996. doi:10.3390/f10110996
46. Burgert, I.; Eder, M.; Gierlinger, N.; Fratzl, P. *Planta* **2007,** *226,* 981–987. doi:10.1007/s00425-007-0544-9
47. Fratzl, P.; Elbaum, R.; Burgert, I. *Faraday Discuss.* **2008,** *139,* 275–282. doi:10.1039/b716663j
48. Ebenstein, D. M.; Pruitt, L. A. *Nano Today* **2006,** *1,* 26–33. doi:10.1016/s1748-0132(06)70077-9
49. Oyen, M. L.; Shean, T. A. V.; Strange, D. G. T.; Galli, M. *J. Mater. Res.* **2012,** *27,* 245–255. doi:10.1557/jmr.2011.322
50. Sachse, R.; Westermeier, A.; Mylo, M.; Nadasdi, J.; Bischoff, M.; Speck, T.; Poppinga, S. *Proc. Natl. Acad. Sci. U. S. A.* **2020,** *117,* 16035–16042. doi:10.1073/pnas.2002707117
51. Bidhendi, A. J.; Lampron, O.; Gosselin, F. P.; Geitmann, A. *Nat. Commun.* **2023,** *14,* 8275. doi:10.1038/s41467-023-44075-4
52. Striet, L.; Mylo, M. D.; Speck, O.; Dondl, P. W. *J. Mech. Phys. Solids* **2025,** *196,* 105965. doi:10.1016/j.jmps.2024.105965
53. Hone, T.; Mylo, M.; Speck, O.; Speck, T.; Taylor, D. *J. R. Soc., Interface* **2021,** *18,* 20201023. doi:10.1098/rsif.2020.1023
54. Mylo, M. D.; Hoppe, A.; Pastewka, L.; Speck, T.; Speck, O. *Front. Plant Sci.* **2022,** *13,* 950860. doi:10.3389/fpls.2022.950860
55. Ali, S. A.; Sonego, M.; Salavati, M.; Fleck, C. *Adv. Eng. Mater.* **2024,** *26,* 2300723. doi:10.1002/adem.202300723
56. Levavi, L.; Bar-On, B. *PNAS Nexus* **2024,** *3,* pgae501. doi:10.1093/pnasnexus/pgae501

BEILSTEIN JOURNAL OF NANOTECHNOLOGY

Self-assembly and adhesive properties of *Pollicipes pollicipes* barnacle cement protein cp19k: influence of pH and ionic strength

Shrutika Sawant[1,2], Anne Marie Power[3] and J. Gerard Wall[*1,2]

Full Research Paper

Open Access

Address:
[1]Microbiology, School of Biological and Chemical Sciences, University of Galway, University Rd, Galway H91 TK33, Ireland, [2]CÚRAM Research Ireland Centre for Medical Devices, University of Galway H91 TK33, Ireland and [3]Ryan Institute, School of Natural Sciences, University of Galway H91 TK33, Ireland

Email:
J. Gerard Wall[*] - gerard.wall@universityofgalway.ie

* Corresponding author

Keywords:
adhesive; amyloid fibre; barnacle cement protein; surface coating; transmission electron microscopy

Beilstein J. Nanotechnol. **2025,** *16,* 1863–1872.
https://doi.org/10.3762/bjnano.16.129

Received: 01 July 2025
Accepted: 19 September 2025
Published: 23 October 2025

This article is part of the thematic issue "Micro- and nanoscale effects in biological and bioinspired materials and surfaces".

Guest Editor: T. H. Büscher

Abstract

Marine organisms such as barnacles rely on a complex underwater adhesive system, driven by self-assembly and intermolecular associations between cement proteins, for permanent attachment to a variety of surface types. In this study, we investigated the influence of environmental parameters on the self-assembly of recombinant cp19k, a key adhesive protein in *Pollicipes pollicipes*. Using TEM imaging, a low pH (4.0) and high salt concentration (600 mM NaCl) environment, mimicking *P. pollicipes* gland conditions, was identified to promote the formation of extended, needle-like fibrils by the cp19k protein. The β-amyloid nature of fibrils formed under these conditions and at high pH/low salt concentration was confirmed by Thioflavin T assay. Non-fibrillar cp19k adhered most effectively to hydrophilic and hydrophobic surfaces under low pH/low salt concentration conditions, while preformed fibrils retained their adhesion ability upon switching to a high pH/high salt concentration environment, which was designed to mimic the change in the protein environment upon secretion in vivo. These findings support the hypothesis that fibril formation occurs in the acidic, iso-osmotic gland of the barnacle, with delayed cement curing enabling fibril secretion for sustained adhesion of the organism. The study provides insight into the environmental sensitivity of cp19k structure–function dynamics and may support the design of bioinspired adhesives and biomaterials.

Introduction

Marine adhesives are naturally occurring substances secreted by a variety of organisms to attach themselves to submerged surfaces such as rocks, ship hulls, and even other organisms [1]. These bioadhesives function under challenging aquatic conditions, including high and fluctuating salinity, and constant turbulence. Unlocking the molecular mechanisms behind their

ability to achieve robust, long-term adhesion under wet and dynamic conditions may help to inform the design of eco-friendly adhesives for application in biomedicine, industry, and underwater engineering [2,3].

Mussel adhesive proteins are the most extensively studied of marine bioadhesives. Mussels anchor to submerged surfaces using a byssus, a bundle of proteinaceous threads secreted by the foot [4]. Each thread ends in an adhesive plaque composed of mussel foot proteins (Mfps), which are rich in the modified amino acid L-3,4-dihydroxyphenylalanine (DOPA) [5]. DOPA is formed via post-translational hydroxylation of tyrosine and mediates wet surface adhesion through hydrogen bond formation, metal chelation, and covalent interactions [6]. The byssal threads display a mechanical gradient, with regions proximal to the animal more elastic and distal regions stiffer and tougher [7]. This design allows for effective dissipation of hydrodynamic forces and maintains attachment of the threads under wave-induced stress, thereby allowing the byssus to function as both an adhesive and a shock-absorbing tether [7].

Mussel adhesives are difficult to re-create either synthetically or recombinantly [8], the latter due largely to difficulties associated with post-translational modifications in recombinant protein expression systems [9]. Cell-Tak™ is a commercial mixture of mussel foot proteins Mfp-1 and Mfp-2 from *Mytilus edulis* [10] but purification of Mfp-based adhesives necessitates harvesting and chemical processing of large quantities of mussels, raising ecological and scalability concerns [10]. Additionally, *M. edulis* Mfp exhibits optimal adhesion under acidic conditions [11], potentially limiting its biomedical application. Meanwhile, synthetic sealants based on DOPA functionalisation of natural or synthetic polymers have shown promise in biomedical applications, but their formulation, biocompatibility, long-term stability, and clinical efficacy still require significant investigation [12,13].

Barnacles are sessile marine organisms which employ a different strategy for underwater adhesion: they secrete a multicomponent proteinaceous cement that facilitates robust, permanent attachment to a wide range of natural and synthetic surfaces [1,14,15]. Notably, the absence of DOPA means that several barnacle cement proteins have been produced in *E. coli*, providing an advantage over mussel adhesive proteins in terms of reproducibility and scalability [16-22].

Studies on barnacle cement proteins have predominantly focused on acorn barnacles with calcareous (calcium carbonate) bases (e.g., *Balanus albicostatus*) to date. The goose barnacle *Pollicipes pollicipes* is a sessile crustacean with body parts encased in calcified plates and a cuticle-covered stalk (peduncle) that anchors it to a surface [23]. Structural and biochemical analyses revealed that the cuticle is primarily composed of α-chitin, with indications of elastin-like proteins and collagen [23], and stiffness values comparable to those found in elastomers and in the soft cuticles of crustaceans following molting [23]. This flexibility of the cuticle allows for attachment in environments where rigid adhesion would fail, such as on soft tissues, polymers, or dynamic interfaces [23,24]. Stalked barnacles exhibit significant evolutionary divergence (200–250 million years) from acorn barnacles [25] and inhabit different ecological niches, suggesting potentially distinct biochemical properties in their adhesive systems [14]. Most functional studies on *P. pollicipes* cement proteins to date have been limited to in silico analyses [26,27] or basic characterisation under seawater-like (basic pH with high salt concentration) or proposed gland-like (acidic pH with low salt concentration) conditions [28-31], however, with much still unknown about their structural properties or mechanical function under varied environmental conditions.

Among *P. pollicipes* cement proteins, cp19k has emerged as a key contributor to underwater adhesion [16,32]. We previously described recombinant production of the 19 kDa *P. pollicipes* cement protein (rPpolcp19k) and its adhesion on various substrate chemistries [21]. The protein self-assembled into intertwined amyloid fibres [22] and has the potential to form amyloid-like fibrillar aggregates, a structural motif increasingly implicated in barnacle adhesion [33,34]. Amyloid fibres are characterised by their β-sheet-rich architecture and have been linked to increased cohesive strength and durability in marine adhesives [35,36].

In the present work, we expressed recombinant *P. pollicipes* cp19k (rPpolcp19k) in *E. coli* and identified key environmental modulators of fibril formation by the protein. Transmission electron microscopy (TEM) was used to study the rate of fibril formation and morphology under varied pH and salt concentration conditions, while Thioflavin T was utilised to detect β-sheet content and provide insight into the amyloidogenic nature of the assembled structures. Finally, the adhesive properties of monomeric and fibrillar rPpolcp19k-his were investigated to better understand the relationship between structural conformation and adhesion in the protein.

Results

Protein expression and fibril formation

Co-expression of rPolcp19k-his with *E. coli* GroEL-GroES chaperones to improve folding was performed as described previously [21]. Purified rPolcp19k-his protein yields of 1.8 to 2 mg per litre of *E. coli* culture were achieved (Supporting Information File 1, Figure S1). Purified protein was dialysed

into 10 mM sodium acetate (pH 4.0) or 10 mM sodium phosphate (pH 8.0) buffer, with NaCl concentrations ranging from 0 to 600 mM.

Transmission electron microscopy

TEM analysis identified the formation of fibril structures by rPolcp19k-his under a variety of conditions analysed. Fibre networks were clearly more extensive in the presence of low pH/high salt concentration and high pH/low salt concentration than under the other tested conditions. Fibrils appeared as early as day 0 (Figure 1a) or day 3 (Supporting Information File 1, Figure S2) in these samples and became more abundant by day 11 (Figure 1b). Fibril formation was most pronounced at pH 4.0 in the presence of 600 mM NaCl, with highly abundant and well-dispersed structures clearly visible throughout the sample after 21 days of incubation (Figure 1c). By day 21 also (Figure 1c), apparent morphological differences were evident between fibrils formed at pH 4.0 (needle-like and extended) and those formed at pH 8.0 (more coiled and entangled) (Figure 2).

Thioflavin (ThT) binding assay

The ThT assay showed the greatest increase in fluorescence intensity over 21 days in rPolcp19k-his protein samples that had been incubated at pH 8.0 with no NaCl, followed by rPolcp19k-his at pH 4.0 and 600 mM NaCl or 150 mM NaCl (Figure 3). This is indicative of the occurrence of β-amyloid in the samples and, combined with the TEM analysis (Figure 1 and Figure 2), indicates that the cp19k protein forms amyloid fibres, potentially with diverse morphologies, under a variety of physicochemical conditions. Lysozyme and BSA (negative controls) and heat-denatured lysozyme (positive control) were used to validate the assay (Supporting Information File 1, Figure S3).

Adhesion analysis

rPpolcp19k-his protein samples were analysed for adhesion after prior incubation for 21 days under a variety of pH and salt concentration conditions to allow for fibre formation, or without any pre-incubation. Protein samples that had not been incubated prior to the adhesion assay to enable fibre formation (0 day) demonstrated relatively homogeneous staining on both hydrophilic and hydrophobic materials, indicating adhesion to the relevant surfaces (Figure 4a,b). Staining was noticeably more intense for protein samples incubated at pH 4.0 and 150 mM NaCl, followed by samples incubated at pH 8.0 and 0 mM NaCl (Figure 4a,b). Additionally, denser staining in a heterogenous, granulated pattern, thought to correspond to clusters of aggregated proteins, was observed to occur on both surfaces in samples that had been incubated for 21 days at pH 4.0, 150 mM NaCl (Figure 4c), whereas these were not evident in either pH 8.0 environment. No significant change in staining was observed when samples that had been incubated for 21 days at pH 4.0, 150 mM NaCl to allow fibres to form were switched to pH 8.0, 600 mM NaCl (to mimic seawater) prior to carrying out the adhesion analysis (Figure 4a,b).

Discussion

This study investigates the physicochemical conditions of fibril formation by recombinant *P. pollicipes* cp19k, a key protein involved in barnacle underwater adhesion. The results identify a combination of low pH and high salt concentration as optimal for fibril formation, whereas previous reports with cp19k homologues from other barnacle species reported that fibres predominantly formed under either “gland-like” (low pH, low salt concentration) [29] or seawater-mimicking (high pH, high salt concentration) conditions [31].

We hypothesise that the combination of low pH and high ionic strength mimics the osmotic conditions pertaining in the *P. pollicipes* adhesive glands. As barnacles are osmoconformers rather than osmoregulators [37], their internal fluid environment is iso-osmotic to seawater. While species such as *Balanus improvisus* can adapt to brackish conditions, *P. pollicipes* is an open-coast barnacle optimally adapted to full-strength seawater [38]. Thus, although the adhesive glands are acidic [14,39], their osmolarity is likely comparable to that of seawater. Our findings suggest, therefore, that fibril formation is favoured in the gland environment in *P. pollicipes*. As this process is slow, apparently requiring days to several weeks, this likely prevents premature cement curing within the gland – this is the post-secretion process of enzymatic and oxidative cross-linking of adhesive proteins to transform them into a hardened, insoluble matrix that enables permanent underwater adhesion of the barnacle [1].

While fibrils also formed under high pH and low salt concentration conditions in this study, these appeared more curled and tangled than the extended, needle-like conformations observed in the low pH/high salt concentration environment. Both fibril forms (needle-like and curled) tested positive in the ThT assay, indicating that, despite the difference in morphology, they contain a β-sheet-rich architecture characteristic of amyloid structures, which is increasingly implicated in enhancing cohesive strength in marine adhesives [33]. rPolcp19k-his fibrils formed in the high pH/low salt concentration environment exhibited the highest fluorescence, though more detailed investigation using methods such as attenuated total reflectance-Fourier transform infrared (ATR-FTIR) spectroscopy or circular dichroism (CD) will be necessary to confirm an elevated β-sheet content in these fibrils. A similar curled-fibril morphology has been reported for cp19k homologues from other barnacle species, but at the low pH/low salt concentration conditions noted above, and these fibrils did not exhibit fluores-

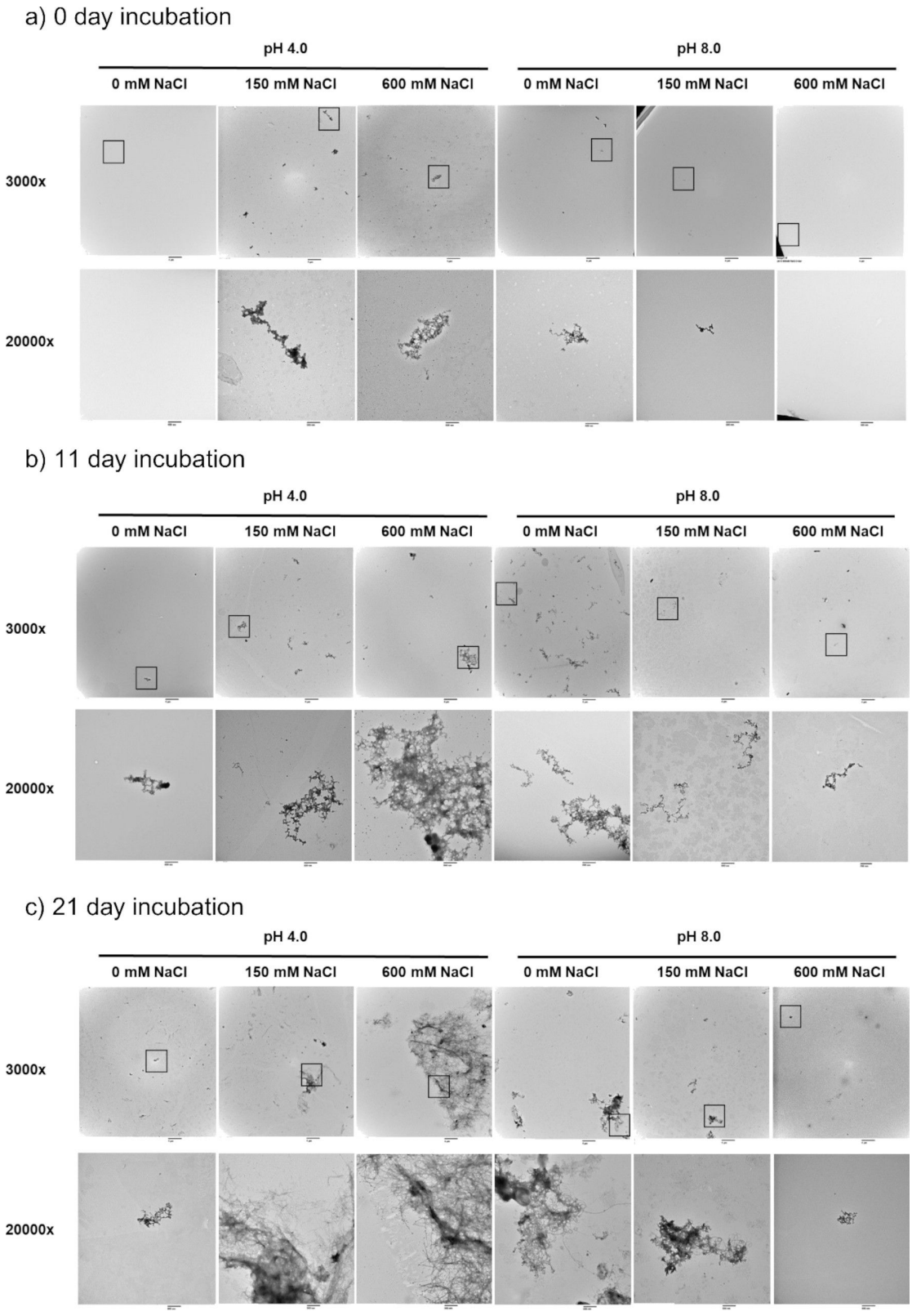

Figure 1: TEM images of rPolcp19k-his protein samples after incubation under the indicated pH and salt concentration conditions for (a) 0 days, (b) 11 days, and (c) 21 days. Squares in 3000× magnification images represent areas shown at 20000× magnification in the corresponding panels below. The scale bar represents 4 µm (3000× magnification images) or 600 nm (20000× magnification images).

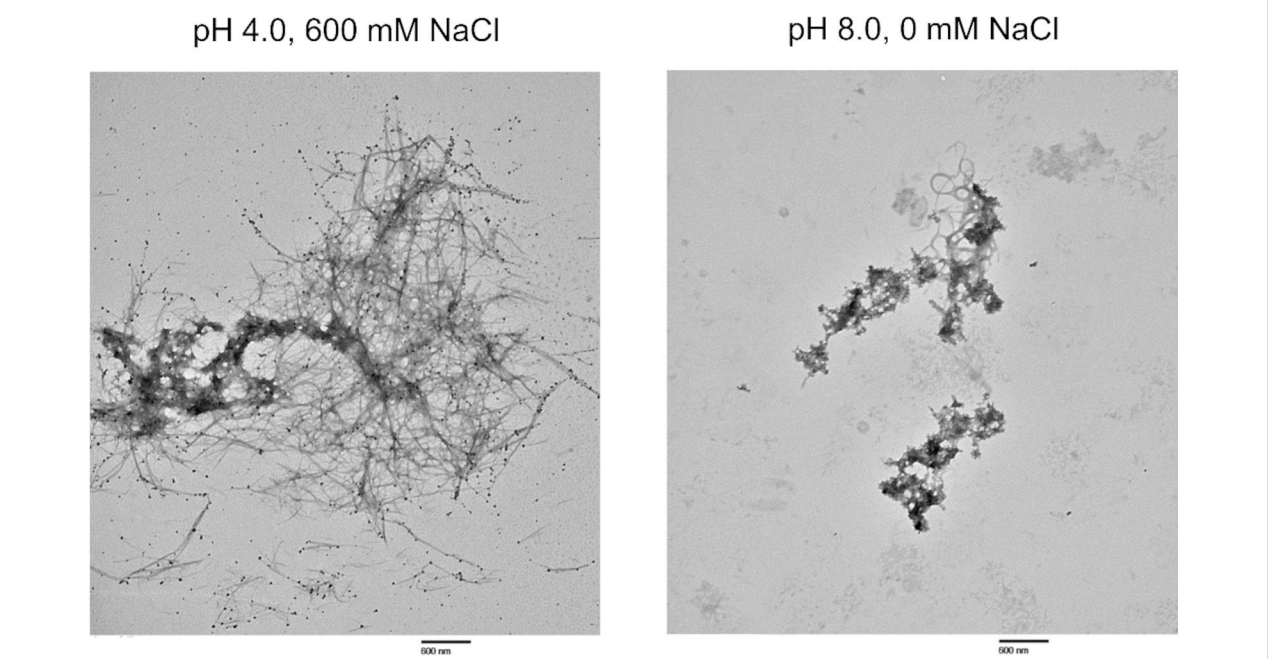

Figure 2: TEM images of rPolcp19k-his protein samples after incubation for 21 days. Fibres formed under pH 4.0, 600 mM NaCl (left) and pH 8.0, 0 mM NaCl (right) conditions, at 20000× magnification are shown. The scale bar represents 600 nm.

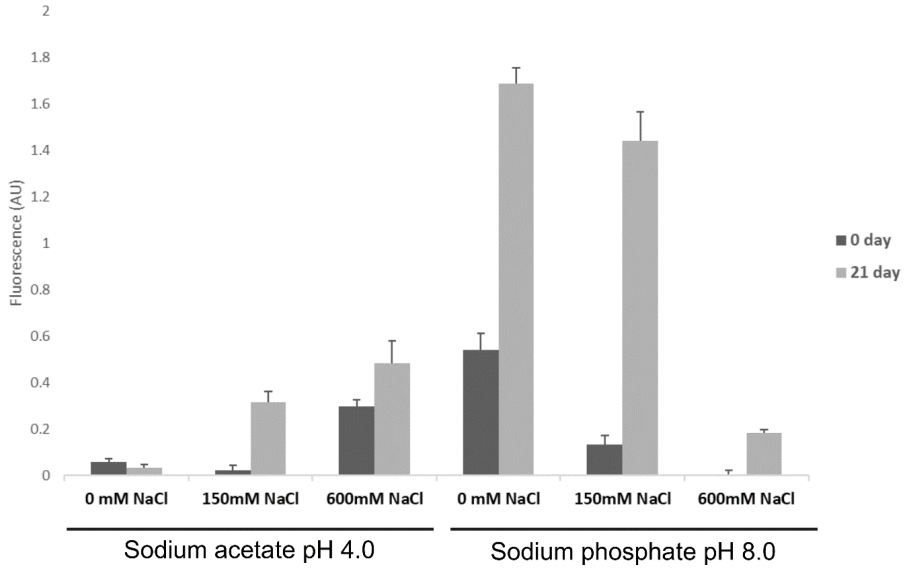

Figure 3: ThT assay analysis of rPolcp19k-his protein samples incubated for 0 and 21 days in the indicated buffers. Assay results are presented in arbitrary units (AU) of fluorescence and as mean ± standard deviation; $n = 3$.

cence in ThT assays and were instead proposed to be largely non-amyloid and α-helical in content [29]. Moreover, no fibrils were observed at pH 8.0–9.9, 150 mM NaCl in the previous study [29], in contrast with our present observations, though the authors did not investigate the pH 4.0, 600 mM NaCl conditions in which fibril formation was most pronounced in our work [29-31].

A study of a recombinantly produced *Balanus albicostatus* cp19k protein from which cysteine residues had been removed reported the formation of fibrils only under seawater-mimicking conditions (pH 8.0, high salt concentration) and not in an acidic environment [31]. While the modified amino acid sequence may have impacted the protein morphology, the differences from both other published results with cp19k homo-

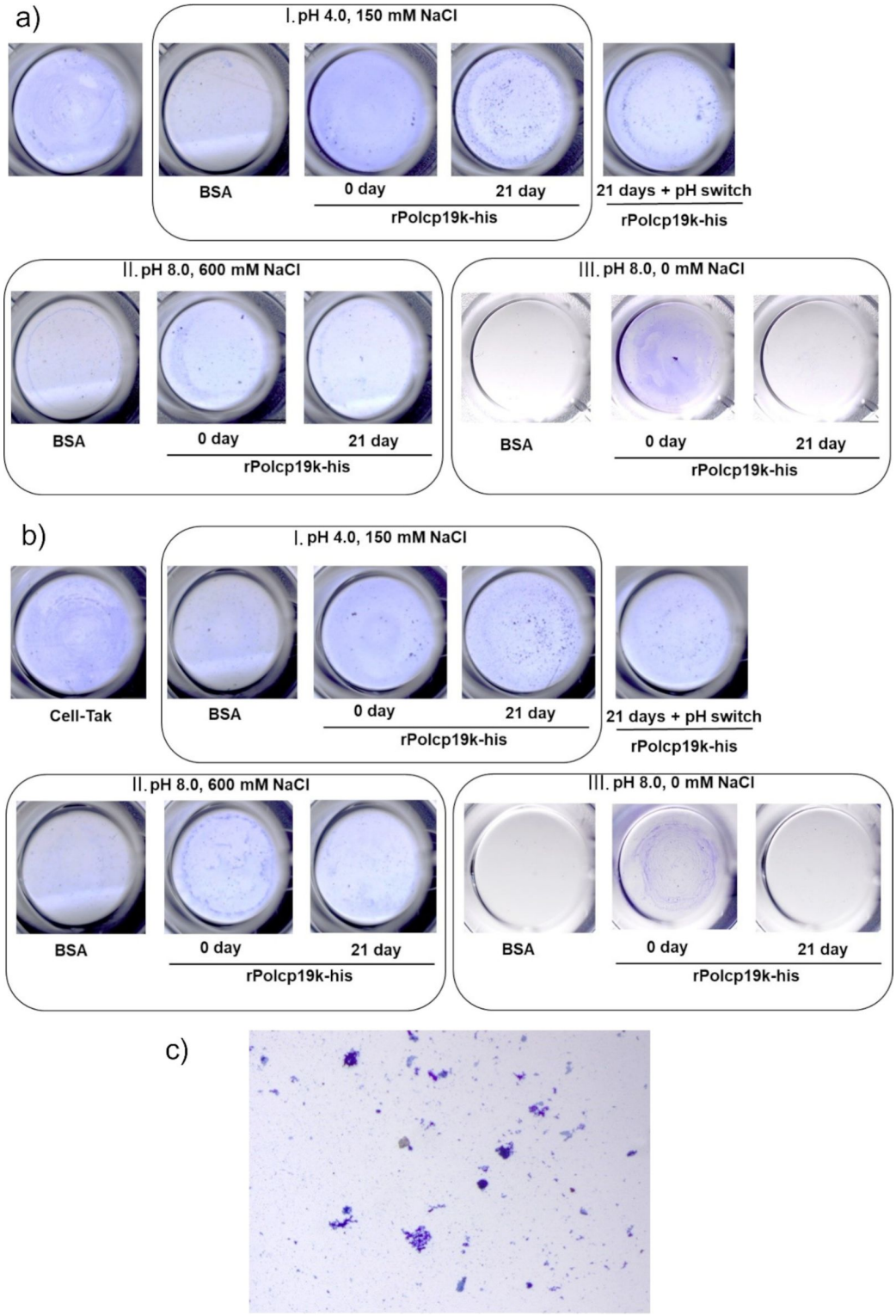

Figure 4: Analysis of adhesion of rPolcp19k-his protein to (a) hydrophilic and (b) hydrophobic polystyrene surfaces in the presence of (I.) pH 4.0, 150 mM NaCl; (II.) pH 8.0, 600 mM NaCl; and (III.) pH 8.0, 0 mM NaCl. 21 days + pH switch: rPolcp19k-his incubated in pH 4.0, 150 mM NaCl for 21 days, followed by switching to pH 8.0, 600 mM NaCl prior to adhesion analysis. Wells are 6.5 mm in diameter, viewed at 6.5× magnification. 0 day: protein samples were not pre-incubated for fibre formation before adhesion analysis. 21 day: protein samples were pre-incubated under the indicated conditions for 21 days before adhesion analysis. (c) rPolcp19k-his incubated at pH 4.0, 150 mM NaCl for 21 days, on hydrophilic surface, at 11.5× magnification.

logues [29] and the present study underscore the importance of protein construct design as well as environmental parameters in determining the self-assembly behaviour of cp19k.

We also investigated the adhesive properties of the rPpolcp19k-his protein, in its unassembled and fibrillar forms. The unassembled or 0-day incubated protein molecules exhibited greater and homogenous adhesion in a low pH/low salt concentration than in a high pH/high salt concentration environment, which is consistent with a previous report that monomeric cp19k lost adhesion at high pH/high salt concentration [29]. The same authors reported that pre-assembled aggregates of cp19k were more stable and exhibited enhanced adhesion at high pH [29], while in our work, samples that were incubated for 21 days under native gland-like conditions forming thin needle like fibres were observed to form clusters of apparently aggregated protein which exhibited surface binding. This supports the hypothesis that unstructured or partially assembled cp19k fibrils may maximise surface interaction prior to curing and becoming stained by Coomassie homogenously, whereas fibrillar aggregates formed under gland-like conditions, though structurally robust, may offer less surface contact, resulting in the granular Coomassie staining. The curled fibres formed in low pH and low salt concentration conditions were also tested for surface adhesion, resulting in no homogenous or even no granular staining. We hypothesise that these curled fibres formed under non-native like conditions hold no adhesion value.

In order to mimic the natural process by which cp19k protein is synthesised and possibly forms fibrils in a low pH/high salt concentration gland environment, before secretion into the higher pH/similar salt concentration seawater, rPpolcp19k-his samples that had undergone assembly into fibrils for 21 days at pH 4.0, 150 mM NaCl were transferred into a pH 8.0, 600 mM NaCl environment prior to investigation of adhesion. Similar aggregates of proteinaceous material were observed before and after the pH switch, and no observable difference in adhesion was noted, suggesting that cp19k fibrils remain stable and retain their adhesion ability after the pH switch. To further correlate these observations with the natural life cycle of barnacle adhesion, more detailed AFM- or quartz crystal microbalance-dissipation (QCM-D)-based studies of the adhesive properties of rPolcp19k-his monomers and fibres formed under different physicochemical conditions, as well as after a similar pH switch, are planned.

Conclusion

This study identifies a low pH and high salt concentration environment as optimal for formation of β-amyloid-containing fibrils by recombinant *P. pollicipes* cp19k (rPpolcp19k). We hypothesise that these conditions reflect the acidic, iso-osmotic environment of the adhesive glands in *P. pollicipes*, an open-coast species adapted to full-strength seawater. The different morphologies and β-amyloid content of fibrils formed under different pH and salt concentration conditions demonstrate the conformational plasticity of cp19k in response to its environment, with its self-assembly into elongated fibrils favoured under low pH/high salt concentration conditions, and the prolonged timescale of fibrillogenesis likely preventing premature adhesive curing within the gland prior to secretion. Overall, our findings support a model in which cp19k undergoes pH- and salt concentration-dependent self-assembly into fibrils in the cement gland, with implications for the mechanism and timing of underwater curing in barnacle bioadhesion. While monomeric cp19k exhibited apparently stronger surface adhesion than fibrillar protein, differences in structure, β-amyloid composition, and adhesive properties between the monomeric and the fibrillar protein, as well as between fibrils assembled under different conditions, will be further investigated through a detailed macro- and nanoscale study designed to understand the relationship between structural transitions and function of the protein in vivo.

Experimental

Recombinant protein expression and purification

rPpolcp19k-his protein was expressed in *E. coli* BL21 (DE3) cells as previously described [21] and purified by two step purification, that is, immobilised metal affinity chromatography (IMAC) followed by ion exchange chromatography (IEC). For IMAC, the Co-IDA resin column was washed with 25 mM Tris-HCl buffer (pH 8.0) containing 150 mM NaCl and 0.1% Triton, and eluted using the same buffer containing 150 mM imidazole. Elution fractions containing rPpolcp19k-his protein were pooled and dialysed against 25 mM Tris-HCl (pH 8.0) buffer overnight at 4 °C and passed through an ion exchange UNO-S resin that had been equilibrated with 25 mM Tris-HCl (pH 8.0). The column was washed using equilibration buffer containing 100 mM NaCl, and bound protein was eluted in equilibration buffer containing 300 mM NaCl. Eluted fractions from both columns were analysed by SDS-PAGE and immunoblotting, as described in Supporting Information File 1, Figure S1.

Formation of protein fibrils

Purified rPpolcp19k-his protein was concentrated to 500 µg/mL using an Amicon® Ultra Centrifugal Filter, 10 kDa MWCO (Merck). The protein was reconstituted at 500 µg/mL in 10 mM sodium acetate buffer (pH 4.0) or 10 mM sodium phosphate buffer (pH 8.0) with NaCl concentrations from 0–600 mM, using a Slide-A-Lyzer™ MINI dialysis device, 10K MWCO

(Thermo Fisher Scientific). Samples were incubated at 25 °C for up to 21 days, removed at intervals, snap frozen in liquid nitrogen, and stored at −80 °C for further analysis

Transmission electron microscopy

A 10 µL aliquot of rPpolcp19k-his protein (500 µg/mL), incubated for 0, 3, 11, or 21 days under varying pH and NaCl conditions, was applied to 200 mesh Cu formvar/carbon-coated grids (Agar Scientific) and allowed to settle for 5 min. Grids were washed three times in phosphate-buffered saline for 5 min each, followed by three washes in dH_2O. Negative staining with uranyl acetate was performed by incubating 5 µL of R1000 UA-Zero EM stain (Agar Scientific) on grids for 3 min. Grids were washed five times with dH_2O and air-dried overnight. Bright-field TEM imaging was carried out using a Hitachi H7000 microscope operated at an accelerating voltage of 80 kV, and images were acquired at 3000× and 20000× magnifications. Each sample was initially scanned throughout at 3000× magnification to identify proteinaceous material; 10–15 TEM fields were then captured at 20000× magnification, and representative images containing protein, if present, were selected. Analysis of pH 8.0, 600 mM NaCl 21 day, pH 8.0, 0 mM NaCl 21 day, pH 8.0, 0 mM NaCl 11 day, and pH 4.0, 150 mM NaCl 11 day samples was repeated to confirm initial observations.

ThT

ThT, a dye that selectively binds to β-sheet-rich regions in amyloid fibrils and exhibits enhanced fluorescence with a redshift in emission upon binding [5], was used to investigate β-amyloid fibril formation by the rPpolcp19k-his protein. Protein samples (0.5 mg/mL) were incubated at 25 °C under varying pH and NaCl conditions, and analysed after 0 and 21 days for the presence of amyloid. Protein samples (100 µL) were mixed with 100 µL of 40 µM ThT prepared in the sample buffer at the same pH and incubated at room temperature for 5 min. Fluorescence emission was recorded at 482 nm using a Varioskan Flash spectrofluorometer in a black polystyrene 96-well plate, with excitation at 440 nm and a bandwidth of 12 nm. Spectra were plotted after subtracting the fluorescence values of the respective buffers. Negative controls (bovine serum albumin (BSA; lyophilised powder, Merck) and hen egg white lysozyme (Fluka)) and a positive control (hen egg white lysozyme denatured at 60 °C for 48 h in 0.1 M HCl-KCl buffer, pH 2.0) were included in the assay.

Surface adhesion assay

The adhesion of rPpolcp19k-his in both monomeric and fibril form was studied by surface coating assay using surfaces typical of cell culture experiments, namely, hydrophilic 96-well polystyrene tissue culture-treated plates (Sarstedt), and hydrophobic Nunc™ MicroWell™ 96-well untreated plates (Thermo Scientific™). Cell-Tak (Corning® Cell-Tak™, Fisher Scientific), containing a mixture of *Mytilus edulis* adhesive proteins mfp-1 and -2, and BSA were used as positive and negative controls, respectively.

Cell-Tak was prepared in 5% acetic acid according to the manufacturer's instruction and investigated at 10 µg/cm^2. Unassembled rPpolcp19k-his and rPpolcp19k-his incubated for 21 days for fibril formation and BSA were coated at 30 µg/cm^2. In addition, rPpolcp19k-his samples incubated for 21 days at pH 4.0, 600 mM NaCl and subsequently switched to pH 8.0, 600 mM NaCl were analysed at 30 µg/cm^2 as above.

BSA was tested under the same conditions as rPpolcp19k-his. Cell-Tak was mixed with a threefold volume of 0.1 M sodium bicarbonate buffer (pH 8.3), according to the manufacturer's instructions, followed by incubation in wells at 25 °C for 48 h. After all incubations, the protein solution was aspirated, wells were washed three times with dH_2O water for 5 min each, and Coomassie Blue stain was added for 15 min, followed by three destaining steps for 5 min each. Experiments were performed in triplicate, and wells were viewed on an Olympus SZX16 Stereo Microscope at 6.5× magnification.

Supporting Information

Supporting Information File 1

Additional figures.
[https://www.beilstein-journals.org/bjnano/content/supplementary/2190-4286-16-129-S1.pdf]

Acknowledgements

The authors acknowledge the facilities of the Anatomy Imaging and Microscopy Facility at the University of Galway (https://imaging.universityofgalway.ie/imaging/) and the scientific and technical assistance of Dr. Éadaoin Timmins in TEM imaging.

Funding

This publication was supported by Taighde Éireann – Research Ireland (Science Foundation Ireland) and co-funded under the European Regional Development Fund grant number 13/RC/2073_P2.

Author Contributions

Shrutika Sawant: conceptualization; investigation; methodology; visualization; writing – original draft; writing – review & editing. Anne Marie Power: conceptualization; funding acquisition; project administration; supervision; visualization; writing – original draft; writing – review & editing. J. Gerard Wall:

conceptualization; funding acquisition; project administration; supervision; visualization; writing – original draft; writing – review & editing.

ORCID® iDs

Shrutika Sawant - https://orcid.org/0009-0005-9222-8225
Anne Marie Power - https://orcid.org/0000-0001-7351-2451
J. Gerard Wall - https://orcid.org/0000-0003-4603-4276

Data Availability Statement

Data generated and analyzed during this study is available from the corresponding author upon reasonable request.

References

1. Power, A. M.; Klepal, W.; Zheden, V.; Jonker, J.; McEvilly, P.; von Byern, J. Mechanisms of Adhesion in Adult Barnacles. In *Biological Adhesive Systems;;* von Byern, J.; Grunwald, I., Eds.; Springer: Vienna, Austria, 2010; pp 153–168. doi:10.1007/978-3-7091-0286-2_9
2. Claverie, M.; McReynolds, C.; Petitpas, A.; Thomas, M.; Fernandes, S. C. M. *Polymers (Basel, Switz.)* **2020,** *12,* 1002. doi:10.3390/polym12051002
3. Xue, B. *Adv. Healthcare Mater.* **2025,** 2402019. doi:10.1002/adhm.202402019
4. Waite, J. H.; Tanzer, M. L. *Science* **1981,** *212,* 1038–1040. doi:10.1126/science.212.4498.1038
5. Yu, M.; Hwang, J.; Deming, T. J. *J. Am. Chem. Soc.* **1999,** *121,* 5825–5826. doi:10.1021/ja990469y
6. Waite, J. H. *Integr. Comp. Biol.* **2002,** *42,* 1172–1180. doi:10.1093/icb/42.6.1172
7. Waite, J. H. *J. Exp. Biol.* **2017,** *220,* 517–530. doi:10.1242/jeb.134056
8. Endrizzi, B. J.; Stewart, R. J. *J. Adhes.* **2009,** *85,* 546–559. doi:10.1080/00218460902996457
9. Zhu, J.; Ruan, Y.; Fu, X.; Zhang, L.; Ge, G.; Wall, J. G.; Zou, T.; Zheng, Y.; Ding, N.; Hu, X. *Front. Bioeng. Biotechnol.* **2020,** *8,* 313. doi:10.3389/fbioe.2020.00313
10. Hwang, D. S.; Gim, Y.; Kang, D. G.; Kim, Y. K.; Cha, H. J. *J. Biotechnol.* **2007,** *127,* 727–735. doi:10.1016/j.jbiotec.2006.08.005
11. Maier, G. P.; Bernt, C. M.; Butler, A. *Biomater. Sci.* **2018,** *6,* 332–339. doi:10.1039/c7bm00884h
12. Jain, R.; Wairkar, S. *Int. J. Biol. Macromol.* **2019,** *137,* 95–106. doi:10.1016/j.ijbiomac.2019.06.208
13. Annabi, N.; Yue, K.; Tamayol, A.; Khademhosseini, A. *Eur. J. Pharm. Biopharm.* **2015,** *95,* 27–39. doi:10.1016/j.ejpb.2015.05.022
14. Jonker, J.-L.; von Byern, J.; Flammang, P.; Klepal, W.; Power, A. M. *J. Morphol.* **2012,** *273,* 1377–1391. doi:10.1002/jmor.20067
15. Kamino, K. *Mar. Biotechnol.* **2008,** *10,* 111–121. doi:10.1007/s10126-007-9076-3
16. Kamino, K. Barnacle Underwater Attachment. In *Biological Adhesives;* Smith, A. M., Ed.; Springer International Publishing: Cham, Switzerland, 2016; pp 153–176. doi:10.1007/978-3-319-46082-6_7
17. Urushida, Y.; Nakano, M.; Matsuda, S.; Inoue, N.; Kanai, S.; Kitamura, N.; Nishino, T.; Kamino, K. *FEBS J.* **2007,** *274,* 4336–4346. doi:10.1111/j.1742-4658.2007.05965.x
18. Mori, Y.; Urushida, Y.; Nakano, M.; Uchiyama, S.; Kamino, K. *FEBS J.* **2007,** *274,* 6436–6446. doi:10.1111/j.1742-4658.2007.06161.x
19. Kamino, K.; Nakano, M.; Kanai, S. *FEBS J.* **2012,** *279,* 1750–1760. doi:10.1111/j.1742-4658.2012.08552.x
20. Kamino, K.; Inoue, K.; Maruyama, T.; Takamatsu, N.; Harayama, S.; Shizuri, Y. *J. Biol. Chem.* **2000,** *275,* 27360–27365. doi:10.1016/s0021-9258(19)61519-x
21. Tilbury, M. A.; McCarthy, S.; Domagalska, M.; Ederth, T.; Power, A. M.; Wall, J. G. *Philos. Trans. R. Soc., B* **2019,** *374,* 20190205. doi:10.1098/rstb.2019.0205
22. Tilbury, M. A.; Tran, T. Q.; Shingare, D.; Lefevre, M.; Power, A. M.; Leclère, P.; Wall, J. G. *J. R. Soc., Interface* **2023,** *20,* 20230332. doi:10.1098/rsif.2023.0332
23. Almeida, M.; Fernandes, E. M.; Marques, C. F.; Lobo, F. C. M.; Sousa, R. O.; Reis, R. L.; Silva, T. H. *Mar. Drugs* **2023,** *21,* 96. doi:10.3390/md21020096
24. Troy, E.; Tilbury, M. A.; Power, A. M.; Wall, J. G. *Polymers (Basel, Switz.)* **2021,** *13,* 3321. doi:10.3390/polym13193321
25. Pérez-Losada, M.; Harp, M.; Høeg, J. T.; Achituv, Y.; Jones, D.; Watanabe, H.; Crandall, K. A. *Mol. Phylogenet. Evol.* **2008,** *46,* 328–346. doi:10.1016/j.ympev.2007.10.004
26. Davey, P. A.; Power, A. M.; Santos, R.; Bertemes, P.; Ladurner, P.; Palmowski, P.; Clarke, J.; Flammang, P.; Lengerer, B.; Hennebert, E.; Rothbächer, U.; Pjeta, R.; Wunderer, J.; Zurovec, M.; Aldred, N. *Biol. Rev.* **2021,** *96,* 1051–1075. doi:10.1111/brv.12691
27. Cruz, T.; Jacinto, D.; Fernandes, J. N.; Seabra, M. I.; Syoc, R. J. V.; Power, A. M.; Macho, G.; Sousa, A.; Castro, J. J.; Hawkins, S. J. Pedunculate Cirripedes of the Genus Pollicipes: 25 Years After Margaret Barnes' Review. *Oceanography and Marine Biology: An Annual Review;* CRC Press: Boca Raton, FL, USA, 2022; Vol. 60, pp 19–168. doi:10.1201/9781003288602-3
28. Liang, C.; Li, Y.; Liu, Z.; Wu, W.; Hu, B. *PLoS One* **2015,** *10,* e0136493. doi:10.1371/journal.pone.0136493
29. Liang, C.; Ye, Z.; Xue, B.; Zeng, L.; Wu, W.; Zhong, C.; Cao, Y.; Hu, B.; Messersmith, P. B. *ACS Appl. Mater. Interfaces* **2018,** *10,* 25017–25025. doi:10.1021/acsami.8b04752
30. Liang, C.; Bi, X.; Gan, K.; Wu, J.; He, G.; Xue, B.; Ye, Z.; Cao, Y.; Hu, B. *Biomacromolecules* **2022,** *23,* 2019–2030. doi:10.1021/acs.biomac.2c00031
31. Liu, X.; Liang, C.; Zhang, X.; Li, J.; Huang, J.; Zeng, L.; Ye, Z.; Hu, B.; Wu, W. *Biochem. Biophys. Res. Commun.* **2017,** *493,* 654–659. doi:10.1016/j.bbrc.2017.08.136
32. Kamino, K. *Biofouling* **2013,** *29,* 735–749. doi:10.1080/08927014.2013.800863
33. Mostaert, A. S.; Higgins, M. J.; Fukuma, T.; Rindi, F.; Jarvis, S. P. *J. Biol. Phys.* **2006,** *32,* 393–401. doi:10.1007/s10867-006-9023-y
34. Mostaert, A. S.; Crockett, R.; Kearn, G.; Cherny, I.; Gazit, E.; Serpell, L. C.; Jarvis, S. P. *Arch. Histol. Cytol.* **2009,** *72,* 199–207. doi:10.1679/aohc.72.199
35. Sawaya, M. R.; Sambashivan, S.; Nelson, R.; Ivanova, M. I.; Sievers, S. A.; Apostol, M. I.; Thompson, M. J.; Balbirnie, M.; Wiltzius, J. J. W.; McFarlane, H. T.; Madsen, A. Ø.; Riekel, C.; Eisenberg, D. *Nature* **2007,** *447,* 453–457. doi:10.1038/nature05695
36. Li, J.; Zhu, Y.; Yu, H.; Dai, B.; Jun, Y.-S.; Zhang, F. *ACS Nano* **2021,** *15,* 11843–11853. doi:10.1021/acsnano.1c02944
37. Sundell, K.; Wrange, A.-L.; Jonsson, P. R.; Blomberg, A. *Front. Physiol.* **2019,** *10,* 877. doi:10.3389/fphys.2019.00877

38. Gómez-del Campo, V.; Arrontes, J.; Cruz, T.; Vázquez, E.; Macho, G.; Thiébaut, E.; Geiger, K.; Fernandes, J. N.; Jacinto, D.; Aguión, A.; Silva, T.; Mateus, D.; Román, S.; Herrero, A.; Iván-Baragaño, Y.; Broudin, C.; Perrier, L.; Davoult, D.; Fernández, C.; Rico, J. M.; Sostres, J.; Guardado, C.; Castro, J. J.; Acuña, J. L. *Rev. Fish Biol. Fish.* **2025,** *35,* 279–296. doi:10.1007/s11160-024-09900-z
39. Jonker, J.-L.; Abram, F.; Pires, E.; Varela Coelho, A.; Grunwald, I.; Power, A. M. *PLoS One* **2014,** *9,* e108902. doi:10.1371/journal.pone.0108902

License and Terms

BEILSTEIN JOURNAL OF NANOTECHNOLOGY

The cement of the tube-dwelling polychaete *Sabellaria alveolata*: a complex composite adhesive material

Emilie Duthoo[1], Aurélie Lambert[1], Pierre Becker[1], Carla Pugliese[1], Jean-Marc Baele[2], Arnaud Delfairière[1], Matthew J. Harrington[3] and Patrick Flammang[*1]

Full Research Paper

Open Access

Address:
[1]Biology of Marine Organisms and Biomimetics Unit, Research Institute for Biosciences, University of Mons, Place du Parc 23, B-7000 Mons, Belgium, [2]Department of Geology, Faculty of Engineering, University of Mons, 7000 Mons, Belgium and [3]Department of Chemistry, McGill University, 801 Sherbrooke Street West, Montreal, Quebec H3A 0B8, Canada

Email:
Patrick Flammang[*] - Patrick.Flammang@umons.ac.be

* Corresponding author

Keywords:
adhesive protein; Annelida; biological material; Polychaeta; protein phosphorylation

Beilstein J. Nanotechnol. **2025,** *16,* 1998–2014.
https://doi.org/10.3762/bjnano.16.138

Received: 11 June 2025
Accepted: 16 October 2025
Published: 11 November 2025

This article is part of the thematic issue "Micro- and nanoscale effects in biological and bioinspired materials and surfaces".

Guest Editor: T. H. Büscher

Abstract

Adhesives produced by marine organisms offer remarkable performance and serve as a major source of inspiration for developing biomimetic adhesives. However, a thorough understanding of their composition and operating mechanism is essential for advancing such applications. Sabellariid tubeworms are model organisms in bioadhesion research, and their adhesive system has been characterized in several studies. However, some aspects of cement formation are still poorly understood and several differences have been pointed out between the two main model species. This study aims to investigate the adhesive system of *Sabellaria alveolata* by identifying new potential adhesive proteins, as well as describing the ultrastructure and elemental composition of the cement cells and their secretion. Different adhesive proteins are packaged in one or the other of two types of cement cells, namely, those containing homogeneous granules and those containing heterogeneous granules with lamellar inclusions. Phosphoserine has been identified as one of the main modified amino acids in tubeworm cement and, using in situ hybridization, we propose that FAM20C kinases would be the enzymes responsible for the phosphorylation of serine residues in adhesive proteins. Comparison between the ultrastructure of the granules and that of the cement suggests that the inclusions of the heterogeneous granules would inflate through a still unexplained process to form hollow spheroids dispersed in the cement matrix, leading to the formation of a complex composite material.

Introduction

Many invertebrate marine organisms have adhesive mechanisms that allow them to firmly attach to various substrates in a wet and salty environment [1,2]. This remarkable ability has raised the interest of scientists in developing bio-inspired underwater adhesive materials for various applications, particularly in the industrial and biomedical fields [3,4]. Polychaetes of the

family Sabellariidae are one of the model organisms that have been studied extensively for their adhesion and have fascinated researchers since the 18th century [5]. Two species in particular have been the subject of numerous studies focused on the microstructure and composition of their adhesive secretion, namely, the North American species *Phragmatopoma californica* Krøyer in Mörch, 1863 and the European species *Sabellaria alveolata* (Linnaeus, 1767). Sabellariids are tube-dwelling worms that build their tube using a specialized building organ located near the mouth. The two finger-like lobes of this organ allow them to manipulate sand grains or shell fragments and to glue them together with several spots of a strong proteinaceous cement [6-9]. The building organ is the external part of an extended glandular system comprising two types of cement cells located in the parathoracic region of the worm, around the digestive tract and at the base of parapodia. The two types of cells can be distinguished by the morphology of their secretory granules, which are either homogeneous or heterogeneous containing inclusions [6,10-12]. The adhesive proteins are packaged into secretory granules via a process called complex coacervation, which involves the aggregation of oppositely charged proteins along with a sulfated polysaccharide and significant amounts of Mg^{2+} and Ca^{2+} ions [8,9,12,13]. The two types of secretory granules are secreted separately and intact, but rapidly fuse to form a porous cement spot whose pores would derive from the heterogeneous granule inclusions [9,12,13].

In *P. californica*, the cement would consist of up to 25 proteins, but only five, referred to as Pc-1 to -5, have been partially characterized [8,12,14-16]. Pc-1 and Pc-2 are basic proteins that contain glycine-rich peptide repeats [14,15]. A fraction of their tyrosine residues are post-translationally hydroxylated to form 3,4-dihydroxyphenylalanine (DOPA) residues, which may facilitate bonding to mineral surfaces and play a role in quinone-mediated cross-linking during cement hardening [14,15]. Pc-3 exists in at least two major isoforms, Pc-3A and Pc-3B. Both isoforms are exceptionally rich in serine (72.9 mol %), with up to 90% of these residues undergoing post-translational phosphorylation [15]. As a result, Pc-3 is an unusually acidic protein. Pc-4 and Pc-5 are histidine-rich basic proteins. In the adhesive secretion of *S. alveolata*, only three adhesive proteins have been identified [17], although a differential transcriptomic study suggested the existence of many others [18]. The proteins Sa-1, Sa-2, Sa-3A, and Sa-3B share the same physico-chemical characteristics as their homologues in *P. californica* [17]. In both species, the polyphosphorylated proteins appear to be segregated exclusively in the inclusions within the heterogeneous granules [9,17].

Despite the remarkable abundance of phosphoserine (pSer) residues in the Sabellariid worm adhesive system, the identity of the kinase involved in the maturation of adhesive proteins is not well understood. Sagert et al. [19] proposed that the phosphorylation of cement proteins is catalyzed by a casein kinase, but its sequence could not be retrieved [12,16]. Since then, casein kinases have been identified as FAM20C kinases [20-22]. FAM20C is a secreted protein that is responsible for phosphorylating S-x-E/pS motifs but also polyserine stretches within proteins in the secretory pathway [20,23]. It is involved in various biological processes, including mineral formation as it phosphorylates extracellular proteins that regulate biomineralization [20,24]. This enzyme could therefore be a candidate kinase for the modification of adhesive proteins in *S. alveolata*.

This study aims at better characterization of the adhesive system of *S. alveolata* through the ultrastructural and chemical characterization of the two types of adhesive cells and the cement they produce, as well as the identification of new adhesive protein candidates. Another goal is to address the gap in knowledge about adhesive protein maturation by identifying and localizing the kinases phosphorylating adhesive proteins using in silico analyses and in situ hybridization techniques. The results may provide new insights into the composition and biosynthesis of the adhesive secretion, which is crucial to the honeycomb worm's survival.

Methods

Collection of honeycomb worms and samples preparation

Reef fragments of *S. alveolata* were collected at low tide in Champeaux, Bay of Mont Saint-Michel, France (48°43′50″N, 01°33′05″W). Additionally, some reef fragments were obtained from the Biological Sample Collection Service of the Station Biologique de Roscoff in Brittany, France. Animals were transported to the laboratory of Biology of Marine Organisms and Biomimetics (University of Mons, Belgium), where they were kept in a re-circulating aquarium chilled at 13 °C and filled with artificial seawater of 33 psu salinity. Animals used in our experiments were maintained and treated in compliance with the guidelines specified by the Belgian Ministry of Trade and Agriculture.

Individual tubes containing an individual worm were isolated from the reef fragment and placed in a petri dish. The distal third of each tube was then sectioned, fixed in 4% paraformaldehyde in phosphate-buffered saline, rinsed, and air-dried. Worms were left in the remaining proximal part of the tube and were provided with glass beads (425–600 µm in diameter; Sigma) to reconstruct the missing part [25].

Scanning electron microscopy and elemental composition analyses

For secondary electron imaging, the anterior parts of a few worms as well as some reconstructed tube fragments were fixed in Bouin's fluid for 24 h, dehydrated in graded ethanol, dried by the critical-point method, and mounted on aluminium stubs using carbon adhesive tabs. The samples were then coated with gold–palladium in a sputter-coater and observed using a JEOL JSM-7200F field-emission scanning electron microscope.

To observe the organization of natural tubes, air-dried tube fragments were placed vertically in 2.5 cm cylindrical brass molds, and embedded with petrographic epoxy resin (Hillquist inc., USA). After curing for 1 h at 80 °C, a transverse section of the mounted tubes was finely ground with SiC grit 800 abrasive suspensions on a high-flatness cast-iron lapping plate. The sections were then polished in three steps on textile cloths soaked with diamond suspensions of 6, 3, and 1 µm, respectively. Transverse sections through the tubes could be imaged with high resolution in SEM (JEOL JSM-7200F), showing the arrangement of cement spots binding mineral particles together. The epoxy resin embedding technique provided excellent preservation of the cement spot structure. Honeycomb worms embedded in Spurr resin (TEM samples) were used for the observation of cement gland secretory granules. All SEM images were acquired in low vacuum mode (50 Pa), with the backscattered electron detector.

X-ray microanalysis and elemental mapping were performed using an Oxford X-Max^N energy-dispersive spectrometer (EDS) equipped with an 80 mm^2 silicon drift detector. Acquisition conditions on the SEM were 15 kV, 10 mm working distance, and 10 s live time acquisition at approximately 30–40% dead time. The spectra were acquired with an AZtec (Oxford Instrument) EDS data processing software.

Transmission electron microscopy

The anterior part of *S. alveolata* individuals and single glass beads bearing cement spots were fixed for 3 h at 4 °C in a solution of 3% glutaraldehyde in cacodylate buffer (0.1 M, pH 7.8; osmolarity adjusted to 1030 mOsm·L^{-1} with NaCl). They were then rinsed three times for 10 min in a solution of cacodylate buffer (0.2 M, pH 7.8, adjusted to 1030 mOsm·L^{-1}), and post-fixed for 1 h in 1% osmium tetroxide in cacodylate buffer (0.1 M, pH 7.8, adjusted to 1030 mOsm·L^{-1}) in the dark. After a final rinse in cacodylate buffer, the cement spots were decalcified for 24 h in a 10% EDTA solution (pH ≈8). All the samples were then dehydrated in a series of ethanol baths of increasing strength (25%, 50%, 70%, 90%, and 100%) and embedded in Spurr resin. Semi-thin sections of 1 µm thickness were cut using a Reichert Om U2 ultramicrotome. They were then stained with a 1:1 mixture of 1% aqueous solution of methylene blue in 1% sodium tetraborate and 1% aqueous solution of azur II. Ultrathin sections, 70 nm thick, were then obtained using a Leica Ultracut UCT ultramicrotome fitted with a diamond knife. These sections were contrasted with uranyl acetate and lead citrate and observed using a Zeiss LEO 906E transmission electron microscope.

Identification and characterization of new adhesive protein and kinase candidates

Local basic local alignment search tool (BLAST) searches were performed in the transcriptome of the anterior part of *S. alveolata* [26] using the adhesive protein sequences of *P. californica* from the study by Endrizzi and Stewart [16] as queries. Additional searches were also performed using different FAM20C sequences retrieved from the NCBI database (NCBI accession numbers: AVI57681.1 (*Pinctada fucata*), XP_033744735.1 (*Pecten maximus*), CAD7192288.1 (*Sepia pharaonic*), XP_035824787.1 (*Aplysia californica*), Q5MJS3.1 (*Mus musculus*), and Q8IXL6.2 (*Homo sapiens*)) (retrieved in January 2021).

All the obtained transcripts, as well as previously identified adhesive protein sequences from *S. alveolata* (NCBI accession numbers: Sa-1 – HE599563; Sa-2 – HE599584; Sa-3A – HE599605; Sa-3B – HE599626), were translated and analyzed in silico. Molecular weight and theoretical pI were computed using the ProtParam tool (https://web.expasy.org/protparam/) [27], and amino acid composition was analyzed using SAPS (https://www.ebi.ac.uk/jdispatcher/seqstats/saps) [28]. The presence of a signal peptide was predicted using SignalP 6.0 (https://services.healthtech.dtu.dk/services/SignalP-6.0/) [29]. Finally, the sequences were used in a reciprocal tBLASTn search against the NCBI non-redundant protein database to confirm identification.

Total RNA extraction and cDNA construction

Total RNA was extracted from different parts of three honeycomb worms using TRIzol^{TM} Reagent kit (Thermofisher). The parts selected were the head, parathoracic, abdominal, and caudal regions. Concentration and purity of the extracted RNA were measured with a UV–vis spectrophotometer (DENOVIX DS-11). A cDNA library was synthesized from the RNA extracted by reverse transcription polymerase chain reaction (RT-PCR) using the Reverse transcription kit (Roche).

Amplification by PCR

Double-stranded DNA templates were amplified by PCR using the Q5 High-Fidelity DNA Polymerase kit method (New England BioLabs), with primer designed by Open Primer 3 (bioinfo.ut.ee/primer3/) with an optimal amplicon length be-

tween 700 and 900 bp (Supporting Information File 1, Table S4). For the previously reported adhesive proteins, the primers were designed using the first clone of each cement precursor protein available on NCBI [17]. For in situ hybridization probe synthesis, a second PCR was done with a T7 promoter binding site (5′-GGATCCTAATACGACTCACTATAGG-3′) added to reverse strand PCR primers. After quality and size check by gel electrophoresis, PCR products were purified using the Wizard SV Gel and PCR clean-up system kit (Promega). The purified products were used for RNA probe synthesis after sequencing to check if the amplified sequence corresponds to the desired transcript.

Localization of the candidates using in situ hybridization

A few worms were retrieved from their tubes, and their anterior part was dissected and fixed in a 4% paraformaldehyde solution in phosphate-buffered saline (pH 7.4). The samples were then dehydrated through graded ethanol series and embedded in paraffin wax. Sections of 14 µm in thickness were cut with a Microm HM 340 E microtome and mounted on Superfrost Ultra Plus (Thermo Scientific) microscope slides using a Milli-Q water drop.

Antisense digoxigenin (DIG)-labelled RNA probes were synthesized with DIG RNA Labelling Kit (Roche) with T7 RNA polymerase and DIG–dUTP. In situ hybridization was performed according to the protocol of Lengerer and colleagues [30]. The RNA probes were used at a concentration of 0.2 ng·µL^{-1} on dewaxed sections of *S. alveolata* and detected with anti digoxigenin-AP Fab fragments (Roche) at a dilution of 1:2000. The signal was developed using the NBT/BCIP substrate (Roche) at 37 °C. The sections were observed using a Zeiss Axio Scope A1 light microscope with a 100× objective to distinguish both types of cement glands based on their secretory granule morphology, and images were taken with an AxioCam 305 digital camera (Carl Zeiss MicroImaging).

Results

Tube structure

As described by Vovelle [6], the tubes of *S. alveolata* are generally rectilinear and cylindrical, measuring up to 12 cm in length (Figure 1A,C) and up to 4 mm in diameter (Figure 1B,D). These tubes are made up of sand grains and shell fragments arranged obliquely to the tube's long axis in a funnel-like pattern, giving their upper part a flared appearance (Figure 1A,B). Internally, the tube is lined by a layer of flat mineral components covered with a thin, smooth organic layer (Figure 1D).

Tube reconstruction was induced by placing amputated tubes containing worms in a Petri dish filled with glass beads. Within less than 24 h, a newly formed tube made of glass beads could be observed (Figure 1E, Figure 2A).

Ultrastructure of the cement

SEM observations of the tubes made up of glass beads show that the beads are connected one to another by four to five cement spots with diameters ranging from 100 to 160 µm (Figure 2A–C). Cement spots display a smooth outer skin both at their margin and at the interface with the glass beads, while their inner core is porous (Figure 2C–E). The pores revealed by the cohesive failure of the cement present diameters varying from approximately 0.25 to 4 µm (Figure 2C–E). Pores are larger in the center of the cement spot and decrease in size towards the edges (Figure 2C). In an unfixed, air-dried tube fragment that was subsequently broken, SEM imaging and microanalysis of a fractured cement spot showed one NaCl crystal within each of the pores (Figure 2E, Supporting Information File 1, Figure S1).

A decalcified cement spot that held two glass beads together was also observed in TEM (Figure 2F,G). The cement matrix is homogeneous and of medium electron density. It encloses hollow spheroids of various sizes, as well as small electron-dense granules and small lacunae (Figure 2F). The exception is the periphery of the cement spot, which is made up entirely of the matrix, giving it a smooth appearance. The hollow spheroids, measuring about 0.3–6.8 µm in diameter, appear empty at their centers. Their cortex is electron-dense and possesses a concentric lamellar structure. The thickness of this cortex also seems to increase with the spheroid size and can measure up to 400 nm. The sizes of the electron-dense granules and lacunae are 50–700 nm and 50–1400 nm in diameter, respectively. They are homogeneously distributed in the matrix between the hollow spheroids (Figure 2F,G).

Morphology and ultrastructure of the adhesive glands

The body of *S. alveolata* measures approximately three to four centimeters in length and is divided into four regions, namely, the head, parathorax, abdomen, and cauda (Figure 3A). The parathoracic region comprises three segments preceding the abdomen, which forms the bulk of the body, and the cauda, an unsegmented, smooth tube terminating at the anus (Figure 3A). Anteriorly, the operculum caps approximately 250 oral tentacles involved in capturing mineral and food particles (Figure 1F, Figure 3A,B). Partially surrounding the mouth, the building organ (a horseshoe (or U)-shaped structure) is located in the thoracic area, immediately below the tentacles (Figure 1F, Figure 3B,C). Its surface is covered with cilia, which are especially numerous at the tip of the lobes (Figure 3D). A pit-like opening that allows for the release of

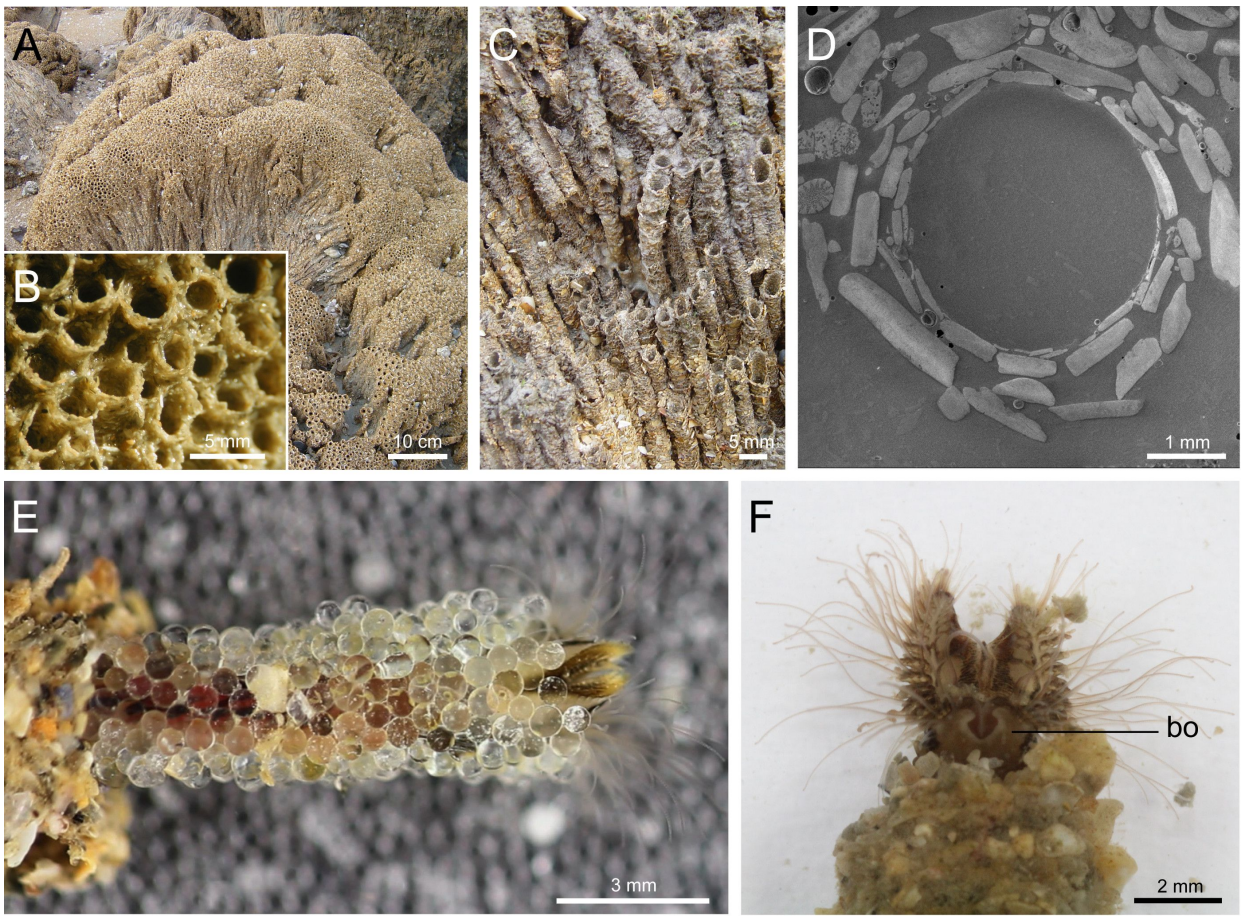

Figure 1: Structure of the tubes of *Sabellaria alveolata*. Picture of a reef fragment (Champeaux, Bay of Mont Saint-Michel) (A), with detailed views of the natural tubes (B, C). SEM image of an epoxy-embedded tube in cross section showing the arrangement of mineral particles (D). Individual of *S. alveolata* which extended its tube using provided glass beads (E). Another individual in its natural tube showing its building organ (F). Abbreviation: bo – building organ.

secretory granules is visible on the inner face of each lobe, slightly below its tip (Figure 3E,F).

The two lobes of the building organ form the external part of a complex secretory organ made up of clusters of cement cells located deep within the parathoracic segments of the worm [6,17]. Using transmission electron microscopy, two main types of cement cells can be distinguished based on the ultrastructure of their secretory granules, that is, cells with homogeneous granules and cells with heterogeneous granules (Figure 3G,H, Figure 4A,B). Both types of granules have a size between 2.5 and 4.0 µm in diameter. Homogeneous granules have a uniform electron density with no internal structure (Figure 4A,C). In contrast, heterogeneous granules contain conspicuous inclusions of various shapes within a matrix that is less electron-dense and resembles the contents of homogeneous granules (Figure 4B,D). These inclusions, which vary in size from 100–1500 nm, appear as spherical to elliptical and are made up of electron-dense concentric lamellae (Figure 4D). In a few samples, some inclusions, particularly the larger ones, show an apparently empty cavity in their center (Figure 4B; Supporting Information File 1, Figure S2). The granules occupy most of the cytoplasm of the cement cells, with the nucleus and the rough endoplasmic reticulum being the only visible organelles in the cell bodies. Granules also fill the cellular processes that extend up to the building organ (Figure 3E, Figure 4F). Granules are secreted through pores in the pit-like opening of the building organ, an area where epidermal cells are densely ciliated (Figure 3D,E, Figure 4G). Newly secreted granules can still be easily identified (Figure 4H). Their contents appear to gradually expand and coalesce to form a structure reminiscent of a cement spot (Figure 4H).

Elemental composition of the secretory granules and cement

To investigate the elemental composition of cement cell granules, we used energy-dispersive X-ray spectroscopy (EDS) coupled with scanning electron microscopy (SEM). Elemental

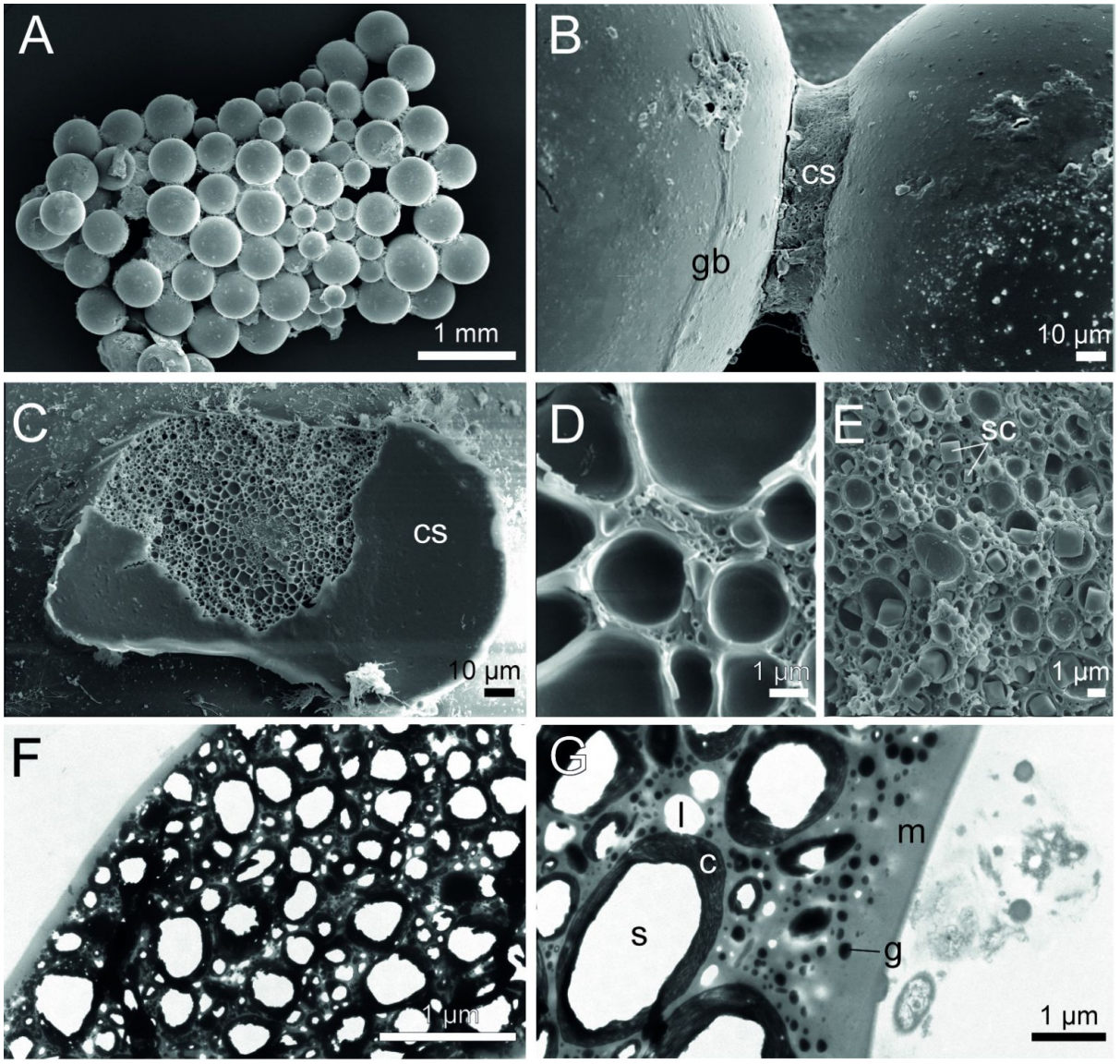

Figure 2: Ultrastructure of the cement in *Sabellaria alveolata*. SEM images of a glass bead tube (A), with a closer view of a spot of cement connecting two beads (B). A cohesive failure in the cement spot reveals pores of varying diameters (C–E), with some dry salt crystals found inside a pore (E). TEM images reveal the complex ultrastructure of the cement spot (F, G). Abbreviations: c – cortex; sc – salt crystal; cs – cement spot; g – electron-dense granule; gb – glass bead; l – lacunae; m – matrix; s – spheroid.

composition was measured on four secretory granules of both types of cement cells in the parathoracic part of worms embedded in Spurr resin (TEM blocks). Using the backscattered electron detector, the secretory granules could be easily distinguished. The heterogeneous granules exhibited high concentrations of phosphorus (7.3% ± 1.2%), sodium (2.6% ± 0.5%), magnesium (2.4% ± 1.0%), and calcium (0.9% ± 0.3%) (Figure 5A, Supporting Information File 1, Table S1). In contrast, the homogeneous granules (Figure 5B) presented much smaller quantities of these elements: 1.7% ± 0.4% for phosphorus, 1.1% ± 0.1% for sodium, 0.6% ± 0.2% for magnesium, and no detectable amounts of calcium (Figure 5B, Table S2). Figure 5C shows two spectra taken at the level of the heterogeneous and homogeneous granules on a transverse section of the worm's parathorax, as indicated in Figure 5B. The P, Mg and, Na signals are mostly present in the heterogeneous granules. These observations were confirmed by the mapping of these elements over the entire samples (Figure 5A,B).

We also conducted an elemental analysis on six cement spots from natural tubes embedded in epoxy resin (Figure 5D). Our

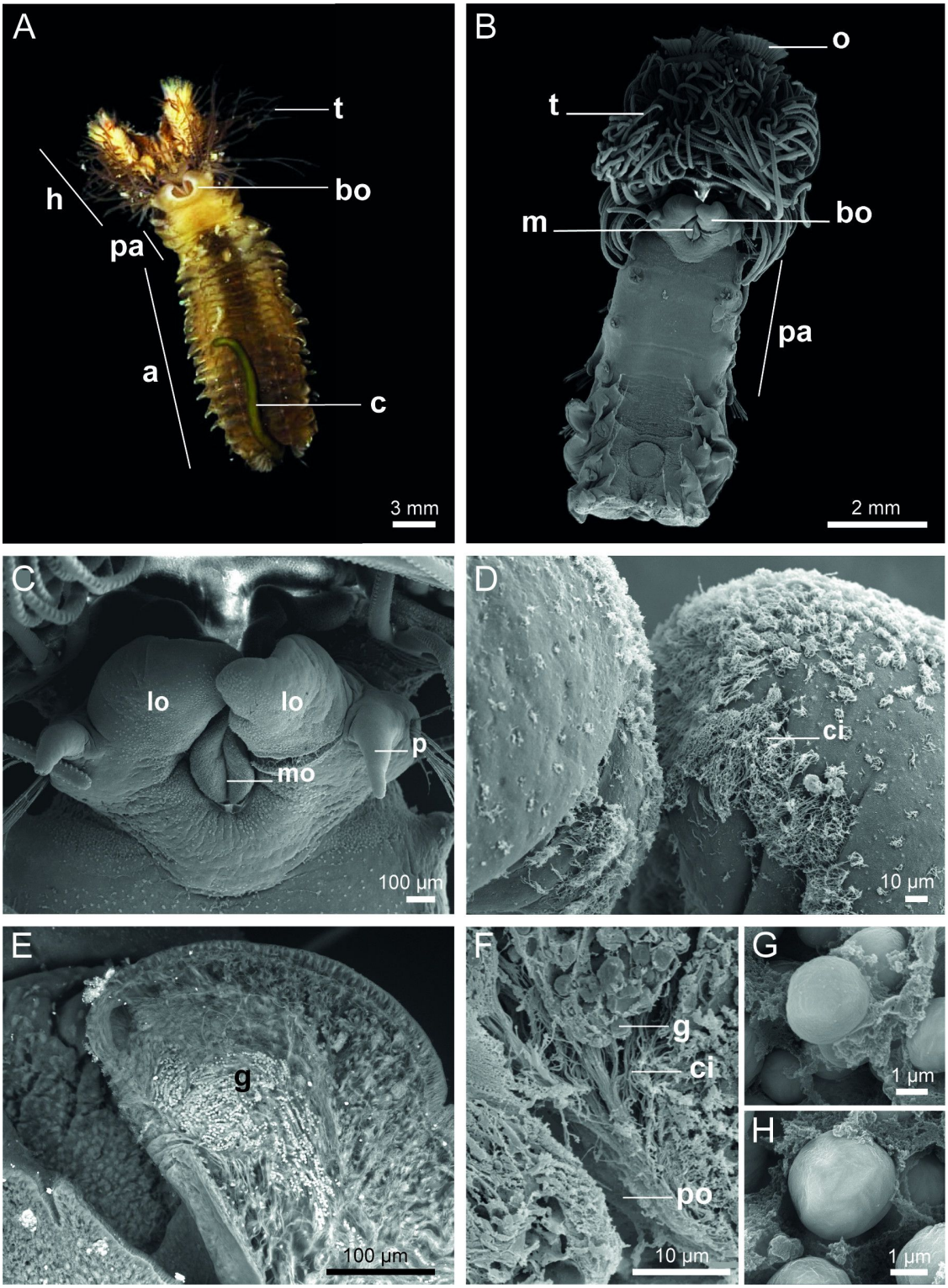

Figure 3: Morphology of *Sabellaria alveolata*. General ventral view of an individual (A) and SEM images showing the location and structure of the building organ (B, C). Detail of the tips of the lobes of the building organ showing cilia (D). Backscattered electron image of a longitudinal section through one building organ lobe showing secretory granules travelling towards the pit-like opening (E). Detail of the pit-like opening (F). Backscattered electron images of the two types of cement granules found in the adhesive glands: homogeneous granules (G) and heterogeneous granules (H). Abbreviations: a – abdomen; bo - building organ; c – cauda; ci – cilia; g – granule; h – head; lo - building organ lobe; mo – mouth; o – operculum; p – palp; po - pit-like opening; pa – parathorax; t – tentacle.

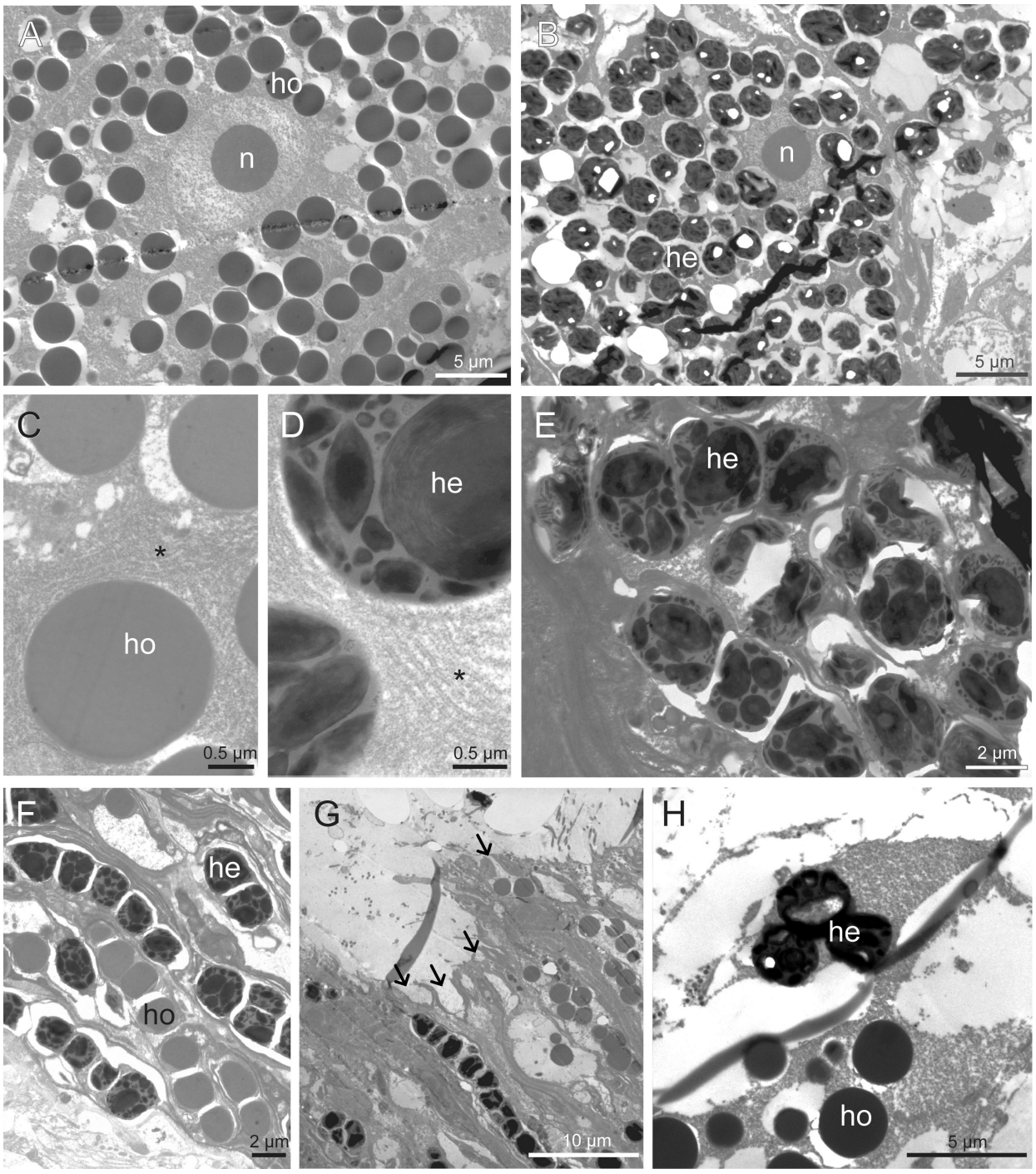

Figure 4: TEM images of the two types of cement cells. Cement glands with homogeneous granules (A, C) and with heterogeneous granules (B, D, E). Asterisks indicate the rough endoplasmic reticulum. The secretory granules are transported through long cell processes (F) towards the building organ where they are released through pores leading to the pit-like openings (G). Arrows indicate the pores. Granules are released intact and then gradually expand and coalesce (H). Abbreviations: he – heterogeneous granules; ho – homogeneous granules; n – nucleus.

measurements revealed that, in addition to carbon and oxygen, the cement primarily consisted of calcium (15.5% ± 4.5%) and phosphorus (3.7% ± 1.1%). Additionally, we detected smaller amounts of sulfur (0.6% ± 0.1%), magnesium (0.6% ± 0.2%), and sodium (0.2% ± 0.1%) (Supporting Information File 1, Table S3). Again, the mapping of Ca and P over the entire samples confirmed the results of the spectra (Figure 5D).

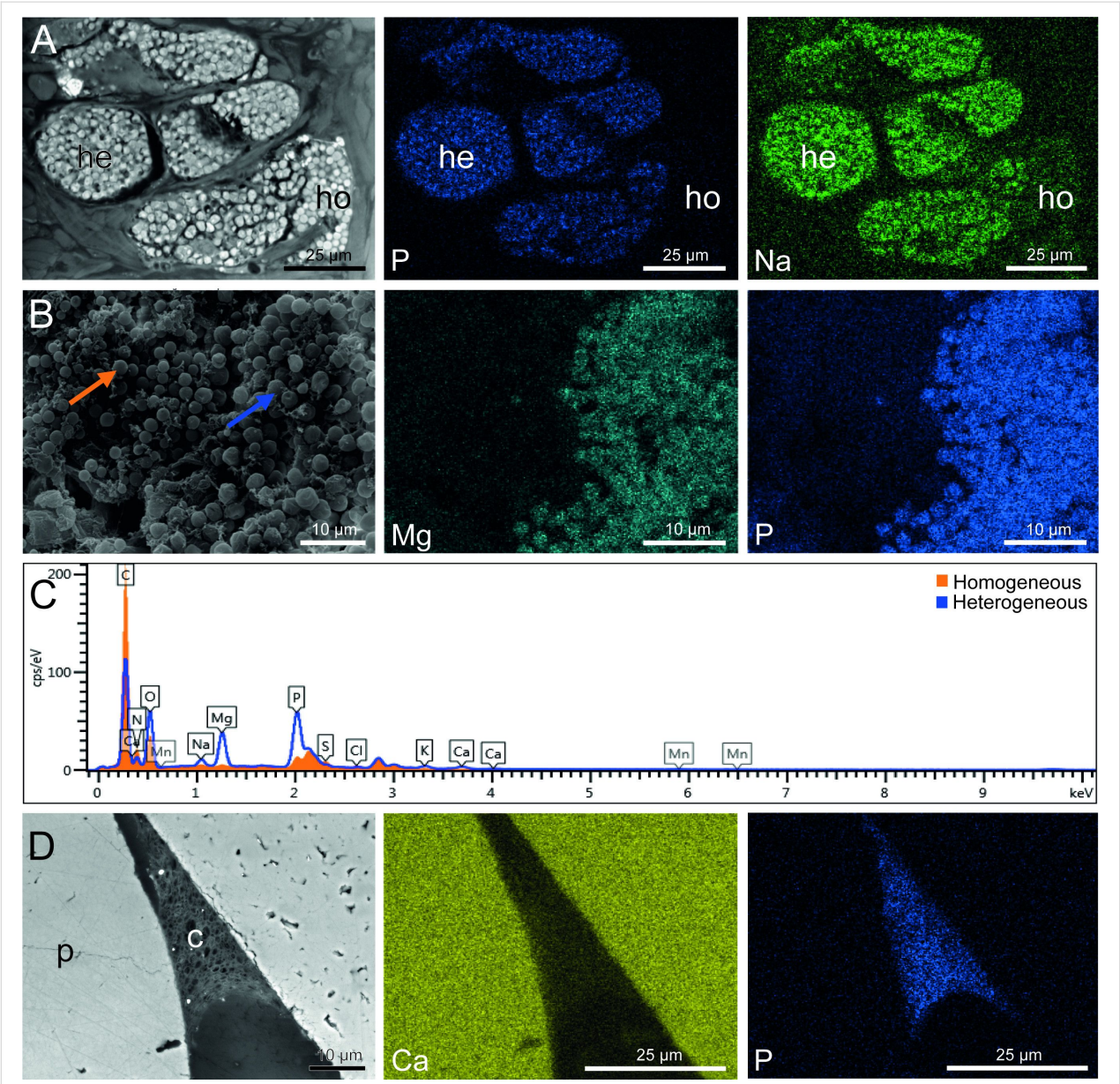

Figure 5: Elemental composition of the secretory granules and cement in *Sabellaria alveolata*. (A) SEM backscattered electron image with EDS spatial maps for phosphorus and sodium for the two types of cement cells. (B) SEM secondary electron image with EDS spatial maps for magnesium and phosphorus for the two types of cement cells. (C) Representative EDS spectra from the homogeneous granules (orange-filled peaks) and from the heterogeneous granules (open blue curve), as indicated in (B). (D) SEM backscattered electron image with EDS spatial maps for calcium and phosphorus for a cement spot sticking two mineral particles together in a natural tube. Abbreviations: c – cement; he – heterogeneous granules; ho – homogeneous granules; p – particles constituting the worm's tube.

Identification of new adhesive protein and kinase candidates

It has already been suggested that *P. californica* would possess up to 26 distinct cement proteins classified into four main groups, that is, (I) GY-rich adhesive proteins, (II) H-repeat adhesive proteins, (III) SY-rich proteins, and finally (IV) a miscellaneous category of diverse proteins that do not fit into the first three groups [12,16]. The sequences from *P. californica* proteins were used as queries for BLAST searches in the transcriptome of *S. alveolata* to identify new adhesive proteins. However, as previous studies have shown, limited percentages of identity in the alignment of these proteins made it difficult to find homologues [7,31]. Despite this, one transcript encoding a protein showing similarity to Pc-5 and one transcript showing similarity to Pc-3 were identified (Table 1; Supporting Information File 1, Table S5). The adhesive protein Sa-5, encoded by the transcript comp278784_c3_seq5, has 45% identity with Pc-5 and is a H-repeat protein. This protein is polybasic, with

Table 1: List of adhesive protein and kinase candidates identified in the tubeworm *Sabellaria alveolata* after transcriptomic analyses. Indicated are the name of the protein (and NCBI accession number of the transcript if available), the transcript ID from the transcriptome of the anterior part of the worm, the normalized expression level of the transcript in the transcriptome (FPKM), the differential expression of the transcript between the parathoracic part of the worm and the rest of its body (log2-FoldChange reported in Buffet et al. [18]), the amino acid length, presence of a signal peptide, the conserved domain, and the top reciprocal BLAST hit (name of the protein, species, accession number).[a]

Protein candidate	ID transcripts	FPKM	Differential expression	Length (aa)	Signal peptide	CDD	Reciprocal BLASTP hit
Sa-1 (CCD57419)	comp225468_c0_seq2	30403.9	–4.25	231	Y	NA	cement precursor protein 1 *Sabellaria alveolata* CCD57419.1
Sa-2 (CCD57440)	comp271660_c3_seq1	23866.7	–3.95	234	Y	NA	cement precursor protein 2 *Sabellaria alveolata* CCD57440.1
Sa-3A (CCD57461)	comp282003_c2_seq7	3233.6	–4.88	228	Y	NA	cement precursor protein 3A *Sabellaria alveolata* CCD57471.1
Sa-3B (CCD57482)	comp267107_c0_seq4	1867.6	–4.96	216	Y	NA	cement precursor protein 3B *Sabellaria alveolata* CCD57482.1
Sa-3C	comp199754_c0_seq1 Contig3247[b]	252	–4.07	405	Y	NA	NA
Sa-5	comp278784_c3_seq5	3880.1	–4.02	128	Y	NA	NA
SaFAM20C-1	comp253537_c0_seq2	1.3	NDE	545	Y	Fam20C-like superfamily	hypothetical protein partial mRNA *Helobdella robusta* XM_009033198.1
SaFAM20C-2	comp288995_c0_seq4	5.5	–	635	Y	Fam20C	extracellular serine/threonine protein kinase FAM20C-like *Octopus sinensis* XM_029780782.2
SaFAM20C-3	comp284991_c0_seq1	4.1	NDE	577	Y	Fam20C	extracellular serine/threonine protein kinase FAM20C-like *Octopus sinensis* XM_029780782.2
SaFAM20C-4	comp280217_c0_seq2	2.22	–	433	Y	Fam20C-like Superfamily	glycosaminoglycan xylosylkinase *Crassostrea gigas* XM_011454801.3
SaFAM20C-5	comp278295_c0_seq4	3.65	NDE	465	N	Fam20C-like Superfamily	hypothetical protein partial mRNA *Helobdella robusta* XM_009033198.1

[a]NA not applicable; NDE not differentially expressed; [b]All the indicated parameters are for transcript Contig3247 from Buffet et al. [18], except for the FPKM value, which corresponds to the proportion of transcript comp199754_c0_seq1 within the transcriptome of the anterior part of *S. alveolata*.

8.6% of its amino acid composition corresponding to histidine (Supporting Information File 1, Table S5). Its corresponding mRNA is highly expressed in the transcriptome (Table 1). Another adhesive protein was also identified, encoded by transcript comp199754_c0_seq1. This transcript was incomplete, but a full-length version (contig3247) was found in the differential transcriptome of Buffet and colleagues [18]. This protein, that we named Sa-3C, has 77% identity with Pc-3B and is unique as it starts with an SY-rich region and ends with a GY-rich region (Supporting Information File 1, Table S5). It contains a signal peptide and has a molecular weight of 38.4 kDa (Table 1). Both Sa-5 and Sa-3C are overexpressed in the worm's parathoracic region at the mRNA level (Table 1).

In this study, we hypothesized that FAM20C kinases might be the enzymes responsible for the phosphorylation of serine residues in the adhesive proteins of the honeycomb worm. Tagliabracci et al. [21] showed that there is a high protein sequence homology in the FAM20 family across different species. A BLAST search in the transcriptome of *S. alveolata* with different FAM20C sequences from other species retrieved from the NCBI database was therefore conducted. From this analysis, five transcripts were obtained, and their translated protein sequences, named SaFAM20C-1 to -5 (Table 1), were analyzed to look for the signature amino acid features characteristic of FAM20 kinases [22]. These features include a glycine-rich loop that covers the ATP-binding pocket, a highly conserved

DRHHYE motif characteristic of the enzyme active site, and another highly conserved motif (a variant motif of DFG) binding a divalent cation required for catalysis (Supporting Information File 1, Figure S3) [20,22,32]. Of the five candidates we selected, two do not meet these criteria. SaFAM20C-1 (encoded by transcript comp253537) lacks the glycine-rich loop and the DRHHYE motif (Supporting Information File 1, Figure S4). SaFAM20C-5 (encoded by transcript comp278295) does not contain a signal peptide or any features of the FAM20C enzymes (Supporting Information File 1, Figure S4). The reciprocal BLAST hits revealed similarities between these two sequences and sequences that are not described as FAM20C sequences (Table 1); they were not selected for further experiments. SaFAM20C-2 (encoded by transcript comp288995), SaFAM20C-3 (encoded by transcript comp284991), and SaFAM20C-4 (encoded by transcript comp280217) contain a signal peptide, a FAM20C domain, and the active site features of the enzyme (Supporting Information File 1, Figure S3 and Figure S4). Their reciprocal BLAST hit corresponds to sequences described as belonging to the FAM20C family, making them good candidates. However, these proteins are not differentially expressed in the parathorax of the worm (Table 1) and RT-PCR experiments showed that their corresponding mRNAs are expressed in all regions of the body (Supporting Information File 1, Figure S5).

Localization of new adhesive protein and kinase candidates

The localization of cells synthesizing the main adhesive proteins of *S. alveolata* (Sa-1, Sa-2, Sa-3A/B/C, and Sa-5) was carried out using in situ hybridization to see if this localization corresponds to that of their homologues in *P. californica*. Using DIG-labelled RNA probes, we labelled the mRNAs encoding the adhesive proteins on a section of the worm's parathoracic part that displayed the cement cells. Control experiments were conducted with sense RNA probes, without probes, and without antibody (Supporting Information File 1, Figure S6). Sa-1 and Sa-2 proteins were expressed in cement cells with heterogeneous granules and in cells with homogeneous granules, respectively (Figure 6A,B). These expression sites are similar to those observed for Pc-1 and Pc-2. Like Sa-1, all three variants of Sa-3 were expressed in cement cells with heterogeneous granules (Figure 6C–E), consistent with the distribution pattern observed for *P. californica* [12]. Unfortunately, Sa-5 could not be localized. The localization of the three FAM20C candidates was done using the same method (Figure 6 and Supporting Information File 1, Figure S6). The results show that all the sequences are mostly expressed in both types of cement cells, but a faint signal was also detected in the epithelium of the digestive tract after a prolonged exposure time (Supporting Information File 1, Figure S6).

Discussion

Sabellaria alveolata and *Phragmatopoma californica* are two tube-dwelling marine polychaetes of the family Sabellariidae. They are called honeycomb worms and sandcastle worms, respectively, because they are gregarious and the tubes of all individuals are closely imbricated to form large reef-like mounds in the intertidal zone. As they belong to sister genera [33], their adhesive systems are remarkably similar although some differences have been noted such as the absence of sulfated polysaccharides in *S. alveolata* [31].

Production of a solid composite material forming highly resistant cement spots

The ultrastructural study (SEM and TEM) of the adhesive system of *S. alveolata* definitively confirms the presence of two types of cement cells in *S. alveolata*, namely, cement cells containing homogeneous granules and those containing heterogeneous granules (Figure 7). These cells are located in the three parathoracic segments, around the digestive tract and at the base of the parapodia of the honeycomb worm. Both types of granules have the same spherical shape and size, and they are very similar to those described in *P. californica* [11]. In *S. alveolata*, the use of TEM added some details. Homogeneous granules have a uniform content with no internal substructure, while heterogeneous granules contain very electron-dense inclusions formed by concentric lamellae that are embedded in a homogeneous matrix.

TEM observation of the cement spot revealed a homogeneous matrix containing three types of structures, that is, hollow spheroids of variable sizes, small dense granules, and small lacunae (Figure 7). The secretory granules from both types of cement cells are excreted simultaneously through individual pores on the epidermal surface of the building organ. There, the homogeneous material from the granules of the two types of cement cells appears to coalesce to form the matrix of the cement spot. The inclusions of the heterogeneous granules disperse in this matrix to form dense granules and hollow spheroid structures. Among these, the largest spheroids (with diameters exceeding the size of a cement gland secretory granule) appear to originate from a remarkable swelling of the inclusions of the heterogeneous granules occurring through a still unknown process. This swelling was also suggested in *P. californica* based on the similar bright appearance of heterogeneous granule inclusions and spheroid cortex under scanning electron microscopy using backscattered electrons, as well as their high phosphorus content [9]. In *S. alveolata*, TEM revealed an identical lamellar structure between inclusions and spheroids. The link between these two structures is also corroborated by simple volume calculations (i.e., the volume of the largest inclusions equals the volume of the cortex in the largest

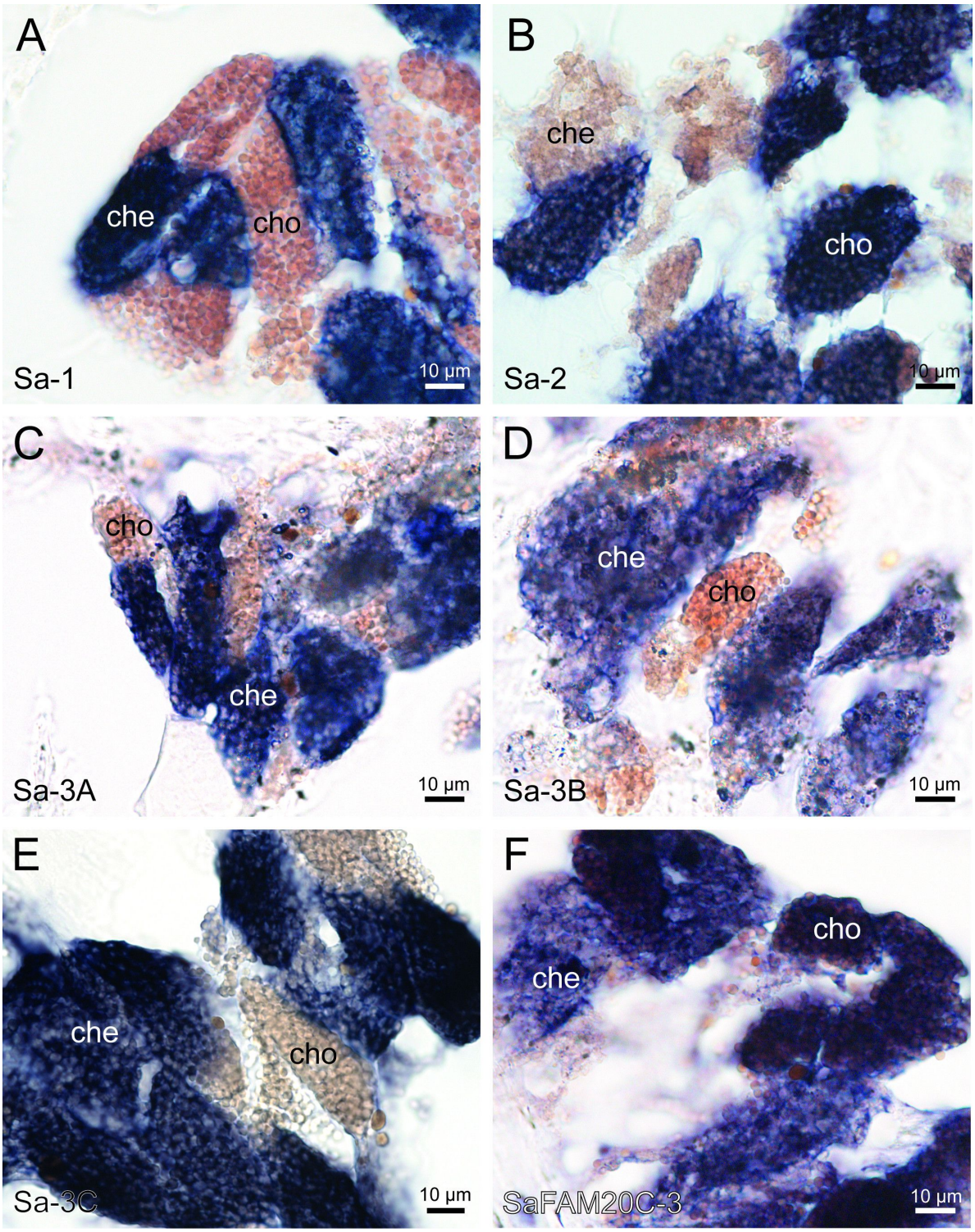

Figure 6: Localization of adhesive protein (A–E) and kinase (F) transcripts in *Sabellaria alveolata* using in situ hybridization. Abbreviations: che – cement cell with heterogeneous granules; cho – cement cell with homogeneous granules.

spheroids). The occurrence of expanded inclusions in some samples, although it may be an artifact of preparation, could mimic intermediate states between inclusions and hollow spheroids. Time-lapse experiments on extracted secretory granules could help decipher the mechanisms behind the expansion of heterogeneous granule inclusions [9,34].

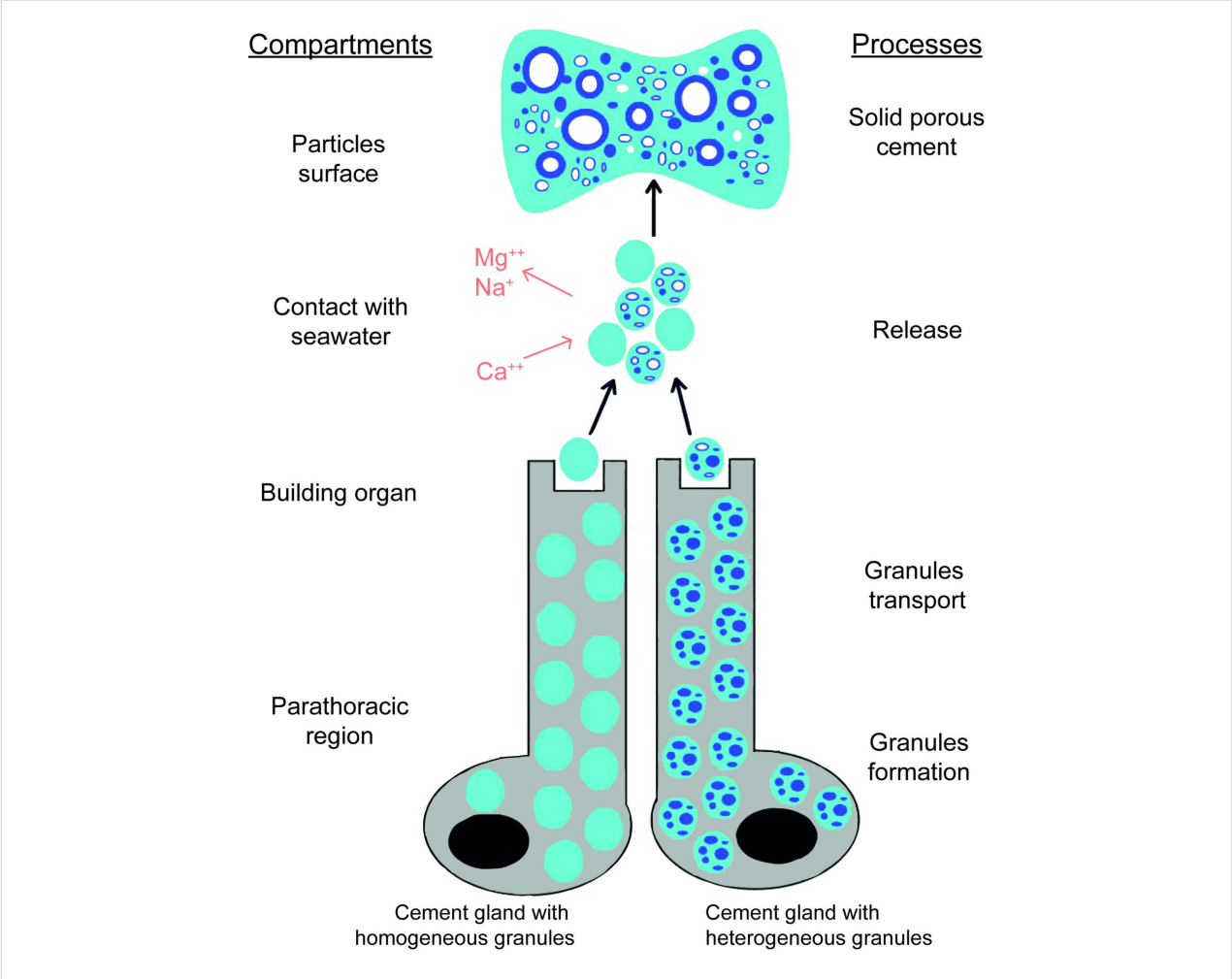

Figure 7: Schematic model of honeycomb worm cement formation. Granules from both types of cement cells are secreted simultaneously through individual pores, and their contents coalesce to form the matrix of the cement spot. Upon secretion, some elements might be replaced by others to facilitate complexation with the negatively charged phosphoserine residues of the adhesive proteins. Additionally, a pH shift could trigger changes in bonding, leading to spheroid hardening. Finally, the cement spot is cured through quinonic cross-linking.

In the cement, hollow spheroids could function as microdashpots, absorbing shocks and constraints [35], or act as stiff reinforcements in a softer matrix (see below). In both cases, the composite nature of the cement would allow *S. alveolata* to live in high-energy environments. During the secretion process, pockets of seawater could be trapped in the adhesive secretion, giving rise to the lacunae visible in TEM, as was suggested for the cement of *P. californica* [35]. Alternatively, these lacunae could be filled with a non-cross-linked adhesive protein condensate like the pores in the mussel byssal plaque [36]. This material would be dissolved during sample preparation. After secretion, intermolecular quinone bonds form between adhesive proteins, involving the oxidation of DOPA residues by catechol oxidase enzymes produced by both types of cement cells [13,15,26]. These bonds allow the adhesive to solidify within a few hours, potentially explaining the porosity gradient observed in the cement spots. Curing would prevent the spheroids from expanding further. As it likely begins at the free edge of the adhesive spot and progresses toward its center, more time is available for the formation of larger spheroids at the center of the cement spot.

The inorganic content of the cement is modified during secretion

Both the European and Californian species have heterogeneous granules with inclusions that contain phosphorus and magnesium. In *P. californica*, the concentration of magnesium is sufficient to balance the negative charges of the phosphates [9]. This high magnesium concentration is indicative of the presence of an ATP-dependent H^+/Mg^+ antiporter in the granule membrane [9]. In *S. alveolata*, the heterogeneous granules also contain a significant amount of phosphorus and magnesium, but also sodium and calcium. Like in *P. californica*, the divalent ions Mg^{2+} and Ca^{2+}, as well as Na^+, can also contribute to the neu-

tralization of negative charges in the granules. However, the composition of the granules can vary according to the fixative used, as shown by Gruet et al. [10], and this could also explain the differences reported between studies. It is worth noting that a previous study conducted on *S. alveolata* found small amounts of iron and manganese in the glands' periphery [10]. However, these metals were not detected in this study.

The elemental analysis was also conducted on cement spots. In our samples, the phosphorus content is two-fold lower in the cement spots than in the heterogeneous granules, presumably because of the mixing of heterogeneous granules with homogeneous granules in similar quantities. We observed that the amount of calcium was 15 times higher in the cement than in the heterogeneous granules. In contrast, the magnesium and sodium content strongly decreased. Moreover, the observation of NaCl crystals in open spheroids of a fractured air-dried cement spot suggests spheroids might be filled with a solution enriched in sodium and chloride ions. All this suggests that, upon secretion, Mg^{2+} and Na^{+} might be replaced by Ca^{2+} for complexation with the negatively charged phosphoserine residues of the adhesive proteins (Figure 7). The Na^{+} ions might be released in the center of the growing spheroids. Our findings align with previous studies that have emphasized the presence of calcium and magnesium in the structure of cement spots [10,37]. Deias et al. [38] analyzed the elemental composition of the cement spots from different *S. alveolata* reef sites and found that while the concentrations of most trace elements were similar to those in seawater, those of Ca^{2+} and Mg^{2+} were significantly higher than the mean seawater composition. The elemental composition of the cement secreted by *P. californica* shows more magnesium and less calcium than what we measured in *S. alveolata* [8].

In *P. californica*, it was suggested that secretion is accompanied by a jump in pH from 5 in the secretory granule to 8.2 in seawater that could trigger a change from electrostatic to ionic bonds between divalent cations and phosphate, the effect of which would be to harden spontaneously and solidify the hollow spheroids [19]. This could explain why it is important to use an EDTA treatment for decalcification of the cement spots prior to sectioning, while the cement cells did not require decalcification despite the presence of divalent cations. SEM analyses conducted on *P. californica* revealed a distortion of the spheroids in cement spots treated with EDTA compared to untreated spots [39]. Moreover, EDTA treatment had a strong effect on the mechanical properties of the cement [39].

Proteins involved in the adhesive system

In *S. alveolata*, the localization of the adhesive proteins Sa-1 and Sa-3 in cement cells with heterogeneous granules and of Sa-2 in cells with homogeneous granules correspond to what has been described in *P. californica* for Pc-1 to Pc-3. In the Californian species, two additional adhesive proteins (Pc-4 and Pc-5) located in the heterogeneous and homogeneous granules, respectively, have been identified, and other putative adhesive proteins (Pc-6 to Pc-26) have been reported [12,16]. By comparing all putative *P. californica* adhesive proteins with the transcriptome of the honeycomb worm, a potential Sa-5 and a new Sa-3 adhesive proteins were identified. However, no other homologues have been retrieved in the European species as there are limited percentages of identity in the alignment of their adhesive proteins with those of *P. californica*.

Sa-5 is overexpressed in the worm's parathoracic region but it could not be localized by in situ hybridization. Its involvement in the cement therefore remains hypothetical. Sa-5 has 8.6% of its amino acid composition as histidine. It has been shown that some histidine-containing adhesive proteins may function as metal-binding proteins, as observed in the mussel byssus. Mussels actively uptake metal ions from seawater, which they then incorporate into their byssus [40]. For instance, His residues in the His-rich terminal domains of preCols, the collagenous proteins that make up over 95% of the byssal threads core, can form metal coordination cross-links with zinc ions [41,42]. In the byssal plaque, mfp-4, the protein linking the plaque to the thread, contains His-rich blocks that can form cross-links with transition metal ions, particularly copper ions [43]. These metals were not detected in this study, however.

Another candidate, Sa-3C, was also identified through the in silico analyses. This candidate has a diblock copolymer structure containing a N-terminal SY-rich region and a C-terminal GY-rich region. It was found to be expressed in cement cells containing heterogeneous granules where its block structure could help anchor the inclusions in the matrix.

Enzymes responsible for the phosphorylation of serine residues in adhesive proteins

The occurrence of protein phosphorylation in biological adhesion has been reported in various organisms such as sandcastle worms, sea cucumbers, and mussels, and proposed to be an important component for their adhesion [19,44]. For example, mfp-5, an adhesive protein found in the mussel foot, has been shown to contain phosphoserine residues that can bind to calcareous mineral surfaces [45]. But it is in Sabellariid tubeworms that this post-translationally modified amino acid seems to be the most important. In sandcastle worms, more than 25% of the cement was found to be composed of phosphoserine [15]. In this organism, it may play a role in the condensation of the

adhesive proteins in the secretory granules through complex coacervation [8]. As mentioned above, it also participates in the hardening of the spheroids through ionic bonding with calcium ions [19]. Despite the important roles of phosphorylated amino acids in adhesion, the enzymes involved in phosphorylation are not fully understood.

In a previous study, researchers attempted to identify and locate a serine kinase responsible for phosphorylating the serine residues of the Pc-3 adhesive proteins in *P. californica*, but the sequence could not be found [12]. In this study, we hypothesized that FAM20C could be the serine kinase involved in this modification. It is a secreted protein kinase that phosphorylates the polyserine motifs within secreted proteins [20]. This protein is part of the FAM20 family, which also includes FAM20A, FAM20B, and is found in both vertebrates and invertebrates with elevated protein sequence homology across different species [21,22,24]. Three FAM20C variants were retrieved from the transcriptome of *S. alveolata*, which contained the glycine-rich loop, the conserved DRHHYE motif, and the DFG motif characteristic of FAM20C kinases. To confirm their involvement in adhesive protein maturation, we localized their mRNAs using in situ hybridization on paraffin sections of the parathoracic part of the worm. All three candidates were expressed in both types of cement cells, supporting the hypothesis that these enzymes might indeed be involved in the maturation of adhesive proteins. However, these FAM20C kinases were also found to be expressed in other parts of *S. alveolata*, as shown by PCR results from other body parts of the worm (Supporting Information File 1, Figure S5). This is not unexpected as it has already been shown that FAM20C kinases are involved in a wide range of biological processes and that they generate the majority of the secreted phosphoproteome in humans, suggesting several roles for these enzymes in honeycomb worms [46]. Additional in situ hybridization experiments to localize FAM20C kinases in other parts of the worm coupled with immunohistochemical labelling using anti-pSer antibodies should allow for the identification of the secretory cells other than cement cells producing polyphosphoproteins.

The kinase candidates are expressed in both types of cement glands in *S. alveolata*, but we showed that the polyphosphoserine adhesive proteins are localized exclusively in the cells with heterogeneous granules. This raises questions about why the kinases are also present in cells with homogeneous granules of *S. alveolata*. Our elemental composition analysis of the granules of the adhesive glands revealed the presence of phosphorus in the heterogeneous granules, as expected, but a small amount of this element was also found in the homogeneous granules. Becker et al. [17] showed that anti-pSer antibodies labelled the inclusions present in the heterogeneous granules, but also the homogeneous granules, though with a lower signal. Moreover, transcriptomic analysis conducted by Buffet et al. [18] identified a large diversity of cement-related proteins, with over 68% of the overexpressed transcripts assigned to the Poly(S) category. These findings suggest that other unidentified polyphosphoproteins could be present in the homogeneous granules.

Conclusion

The findings of this study highlight the complexity of the adhesive system in *S. alveolata* but also demonstrate the need for further research into the composition and formation of this cement. At least five different adhesive proteins are segregated between two types of cement cells, with different polyphosphoproteins and cations concentrated in the inclusions of heterogeneous granules. After secretion, these inclusions would inflate through a still unexplained process possibly involving ion exchange, to form hollow spheroids dispersed in the cement matrix. A better understanding of this complex composite material would provide valuable insights into the physical and chemical processes that underline the assembly of biological materials, which could inspire the design and fabrication of innovative hierarchical materials with diverse applications in various fields.

Supporting Information

Supporting Information File 1

Detailed experimental results.
[https://www.beilstein-journals.org/bjnano/content/supplementary/2190-4286-16-138-S1.pdf]

Supporting Information File 2

Sabellaria alveolata adhesive proteins and FAM20C kinases candidates identified through in silico analyses. Complete list of *Sabellaria alveolata* adhesive proteins and FAM20C kinases candidates identified through in silico analyses. Indicated are the NCBI accession number of the transcript if available, the transcript ID from the transcriptome of the anterior part of the worm, the amino acid length, proportion of transcripts in the transcriptome, completeness of the ORF, presence of a signal peptide, molecular weight, isoelectric point, the conserved domain, the top reciprocal BLAST hit, and the amino acid composition, with color coding indicating lower or higher amino acid concentrations.
[https://www.beilstein-journals.org/bjnano/content/supplementary/2190-4286-16-138-S2.xlsx]

Funding

ED was supported by a FRIA doctoral fellowship from the Fund for Scientific Research of Belgium (F.R.S.-FNRS). PF is Research Director from the F.R.S.-FNRS. This study contributes to the Biosciences Research Institute from the University of Mons and the "Centre Interuniversitaire de Biologie Marine" (CIBIM). PF acknowledges funding from the F.R.S.-FNRS (PDR T.088.20). MJH acknowledges funding from the Natural Sciences and Engineering Research Council of Canada (NSERC Discovery Grant RGPIN-2018−05243).

Author Contributions

Emilie Duthoo: conceptualization; data curation; investigation; visualization; writing – original draft; writing – review & editing. Aurélie Lambert: investigation; writing – review & editing. Pierre Becker: investigation; writing – original draft; writing – review & editing. Carla Pugliese: investigation; writing – review & editing. Jean-Marc Baele: resources; writing – review & editing. Arnaud Delfairière: investigation; writing – review & editing. Matthew J. Harrington: conceptualization; funding acquisition; supervision; writing – review & editing. Patrick Flammang: conceptualization; funding acquisition; project administration; supervision; validation; writing – original draft; writing – review & editing.

ORCID® iDs

Emilie Duthoo - https://orcid.org/0000-0003-1053-1617
Pierre Becker - https://orcid.org/0000-0001-6158-102X
Patrick Flammang - https://orcid.org/0000-0001-9938-1154

Data Availability Statement

All data that supports the findings of this study is available in the published article and/or the supporting information of this article.

References

1. Hennebert, E.; Maldonado, B.; Ladurner, P.; Flammang, P.; Santos, R. *Interface Focus* **2015,** *5,* 20140064. doi:10.1098/rsfs.2014.0064
2. Delroisse, J.; Kang, V.; Gouveneaux, A.; Santos, R.; Flammang, P. Convergent Evolution of Attachment Mechanisms in Aquatic Animals. In *Convergent Evolution;* Bels, V. L.; Russell, A. P., Eds.; Fascinating Life Sciences; Springer International Publishing: Cham, Switzerland, 2023; pp 523–557. doi:10.1007/978-3-031-11441-0_16
3. Modaresifar, K.; Azizian, S.; Hadjizadeh, A. *Polym. Rev. (Philadelphia, PA, U. S.)* **2016,** *56,* 329–361. doi:10.1080/15583724.2015.1114493
4. Almeida, M.; Reis, R. L.; Silva, T. H. *Mater. Sci. Eng., C* **2020,** *108,* 110467. doi:10.1016/j.msec.2019.110467
5. Réaumur, R.-A.. *Mémoires de mathématique et de physique de l'Académie royale des sciences, Académie royale des sciences* **1711,** ffads-00121334.
6. Vovelle, J. *Arch. Zool. Exp. Gen.* **1965,** *106,* 1–187.
7. Hennebert, E.; Maldonado, B.; Van De Weerdt, C.; Demeuldre, M.; Richter, K.; Rischka, K.; Flammang, P. From Sand Tube to Test Tube: The Adhesive Scretion From Sabellariid Tubeworms. In *Bioadhesion and Biomimetics;* Bianco-Peled, H.; Davidovich-Pinhas, M., Eds.; Jenny Stanford Publishing: New York, NY, USA, 2015; pp 109–128. doi:10.1201/b18095-8
8. Stewart, R. J.; Weaver, J. C.; Morse, D. E.; Waite, J. H. *J. Exp. Biol.* **2004,** *207,* 4727–4734. doi:10.1242/jeb.01330
9. Stewart, R. J.; Wang, C. S.; Song, I. T.; Jones, J. P. *Adv. Colloid Interface Sci.* **2017,** *239,* 88–96. doi:10.1016/j.cis.2016.06.008
10. Gruet, Y.; Vovelle, J.; Grasset, M. *Can. J. Zool.* **1987,** *65,* 837–842. doi:10.1139/z87-133
11. Wang, C. S.; Svendsen, K. K.; Stewart, R. J. Morphology of the Adhesive System in the Sandcastle Worm, Phragmatopoma californica. In *Biological Adhesive Systems;* von Byern, J.; Grunwald, I., Eds.; Springer: Vienna, Austria, 2010. doi:10.1007/978-3-7091-0286-2_10
12. Wang, C. S.; Stewart, R. J. *J. Exp. Biol.* **2012,** *215,* 351–361. doi:10.1242/jeb.065011
13. Wang, C. S.; Stewart, R. J. *Biomacromolecules* **2013,** *14,* 1607–1617. doi:10.1021/bm400251k
14. Waite, J. H.; Jensen, R. A.; Morse, D. E. *Biochemistry* **1992,** *31,* 5733–5738. doi:10.1021/bi00140a007
15. Zhao, H.; Sun, C.; Stewart, R. J.; Waite, J. H. *J. Biol. Chem.* **2005,** *280,* 42938–42944. doi:10.1074/jbc.m508457200
16. Endrizzi, B. J.; Stewart, R. J. *J. Adhes.* **2009,** *85,* 546–559. doi:10.1080/00218460902996457
17. Becker, P. T.; Lambert, A.; Lejeune, A.; Lanterbecq, D.; Flammang, P. *Biol. Bull. (Chicago, IL, U. S.)* **2012,** *223,* 217–225. doi:10.1086/bblv223n2p217
18. Buffet, J.-P.; Corre, E.; Duvernois-Berthet, E.; Fournier, J.; Lopez, P. J. *Acta Biomater.* **2018,** *72,* 316–328. doi:10.1016/j.actbio.2018.03.037
19. Sagert, J.; Sun, C.; Waite, J. H. Chemical Subtleties of Mussel and Polychaete Holdfasts. In *Biological Adhesives;* Smith, A. M.; Callow, J. A., Eds.; Springer: Berlin, Heidelberg, 2006; pp 125–143. doi:10.1007/978-3-540-31049-5_7
20. Tagliabracci, V. S.; Engel, J. L.; Wen, J.; Wiley, S. E.; Worby, C. A.; Kinch, L. N.; Xiao, J.; Grishin, N. V.; Dixon, J. E. *Science* **2012,** *336,* 1150–1153. doi:10.1126/science.1217817
21. Tagliabracci, V. S.; Pinna, L. A.; Dixon, J. E. *Trends Biochem. Sci.* **2013,** *38,* 121–130. doi:10.1016/j.tibs.2012.11.008
22. Tagliabracci, V. S.; Xiao, J.; Dixon, J. E. *Biochem. Soc. Trans.* **2013,** *41,* 1061–1065. doi:10.1042/bst20130059
23. Cozza, G.; Moro, E.; Black, M.; Marin, O.; Salvi, M.; Venerando, A.; Tagliabracci, V. S.; Pinna, L. A. *FEBS J.* **2018,** *285,* 4674–4683. doi:10.1111/febs.14689
24. Du, J.; Liu, C.; Xu, G.; Xie, J.; Xie, L.; Zhang, R. *Sci. Rep.* **2018,** *8,* 3563. doi:10.1038/s41598-018-21797-w
25. Jensen, R. A.; Morse, D. E. *J. Comp. Physiol., B* **1988,** *158,* 317–324. doi:10.1007/bf00695330
26. Duthoo, E.; Delroisse, J.; Maldonado, B.; Sinot, F.; Mascolo, C.; Wattiez, R.; Lopez, P. J.; Van de Weerdt, C.; Harrington, M. J.; Flammang, P. *iScience* **2024,** *27,* 111443. doi:10.1016/j.isci.2024.111443
27. Gasteiger, E.; Hoogland, C.; Gattiker, A.; Duvaud, S.; Wilkins, M. R.; Appel, R. D.; Bairoch, A. Protein Identification and Analysis Tools on the ExPASy Server. In *The Proteomics Protocols Handbook;* Walker, J. M., Ed.; Humana Press: Totowa, NJ, USA, 2005; pp 571–607. doi:10.1385/1-59259-890-0:571

28. Madeira, F.; Madhusoodanan, N.; Lee, J.; Eusebi, A.; Niewielska, A.; Tivey, A. R. N.; Lopez, R.; Butcher, S. *Nucleic Acids Res.* **2024,** *52,* W521–W525. doi:10.1093/nar/gkae241
29. Nielsen, H.; Teufel, F.; Brunak, S.; von Heijne, G. SignalP: The Evolution of a Web Server. In *Protein Bioinformatics;* Lisacek, F., Ed.; Methods in Molecular Biology, Vol. 2836; Humana Press: New York, NY, USA, 2024; pp 331–367. doi:10.1007/978-1-0716-4007-4_17
30. Lengerer, B.; Algrain, M.; Lefevre, M.; Delroisse, J.; Hennebert, E.; Flammang, P. *Philos. Trans. R. Soc., B* **2019,** *374,* 20190195. doi:10.1098/rstb.2019.0195
31. Hennebert, E.; Gregorowicz, E.; Flammang, P. *Biol. Open* **2018,** *7,* bio037358.
32. Bossemeyer, D. *Trends Biochem. Sci.* **1994,** *19,* 201–205. doi:10.1016/0968-0004(94)90022-1
33. Capa, M.; Hutchings, P.; Peart, R. *Zool. J. Linn. Soc.* **2012,** *164,* 245–284. doi:10.1111/j.1096-3642.2011.00767.x
34. Renner-Rao, M.; Jehle, F.; Priemel, T.; Duthoo, E.; Fratzl, P.; Bertinetti, L.; Harrington, M. J. *ACS Nano* **2022,** *16,* 20877–20890. doi:10.1021/acsnano.2c08410
35. Stevens, M. J.; Steren, R. E.; Hlady, V.; Stewart, R. J. *Langmuir* **2007,** *23,* 5045–5049. doi:10.1021/la063765e
36. Valois, E.; Mirshafian, R.; Waite, J. H. *Sci. Adv.* **2020,** *6,* eaaz6486. doi:10.1126/sciadv.aaz6486
37. Sanfilippo, R.; Rosso, A.; Mastandrea, A.; Viola, A.; Deias, C.; Guido, A. *J. Morphol.* **2019,** *280,* 1839–1849. doi:10.1002/jmor.21069
38. Deias, C.; Guido, A.; Sanfilippo, R.; Apollaro, C.; Dominici, R.; Cipriani, M.; Barca, D.; Vespasiano, G. *Water* **2023,** *15,* 1549. doi:10.3390/w15081549
39. Sun, C.; Fantner, G. E.; Adams, J.; Hansma, P. K.; Waite, J. H. *J. Exp. Biol.* **2007,** *210,* 1481–1488. doi:10.1242/jeb.02759
40. Priemel, T.; Palia, G.; Förste, F.; Jehle, F.; Sviben, S.; Mantouvalou, I.; Zaslansky, P.; Bertinetti, L.; Harrington, M. J. *Science* **2021,** *374,* 206–211. doi:10.1126/science.abi9702
41. Qin, X.-X.; Coyne, K. J.; Waite, J. H. *J. Biol. Chem.* **1997,** *272,* 32623–32627. doi:10.1074/jbc.272.51.32623
42. Waite, J. H.; Vaccaro, E.; Sun, C.; Lucas, J. M. *Philos. Trans. R. Soc., B* **2002,** *357,* 143–153. doi:10.1098/rstb.2001.1025
43. Zhao, H.; Waite, J. H. *Biochemistry* **2006,** *45,* 14223–14231. doi:10.1021/bi061677n
44. Flammang, P.; Lambert, A.; Bailly, P.; Hennebert, E. *J. Adhes.* **2009,** *85,* 447–464. doi:10.1080/00218460902996358
45. Waite, J. H.; Qin, X. *Biochemistry* **2001,** *40,* 2887–2893. doi:10.1021/bi002718x
46. Tagliabracci, V. S.; Wiley, S. E.; Guo, X.; Kinch, L. N.; Durrant, E.; Wen, J.; Xiao, J.; Cui, J.; Nguyen, K. B.; Engel, J. L.; Coon, J. J.; Grishin, N.; Pinna, L. A.; Pagliarini, D. J.; Dixon, J. E. *Cell* **2015,** *161,* 1619–1632. doi:10.1016/j.cell.2015.05.028

License and Terms

BEILSTEIN JOURNAL OF NANOTECHNOLOGY

Molecular and mechanical insights into gecko seta adhesion: multiscale simulations combining molecular dynamics and the finite element method

Yash Jain*[1], Saeed Norouzi[1], Tobias Materzok[1], Stanislav N. Gorb[2] and Florian Müller-Plathe[1]

Full Research Paper

Open Access

Address:
[1]Eduard-Zintl-Institut für Anorganische und Physikalische Chemie, Technische Universität Darmstadt, Peter-Grünberg-Str. 8, D-64287 Darmstadt, Germany and [2]Zoological Institute Functional Morphology and Biomechanics, Kiel University, Am Botanischen Garten 1–9, D-24118 Kiel, Germany

Email:
Yash Jain* - y.jain@theo.chemie.tu-darmstadt.de

* Corresponding author

Keywords:
finite element method; gecko adhesion; hybrid modeling; molecular dynamics; multiscale simulations; seta; spatula

Beilstein J. Nanotechnol. **2025,** *16,* 2055–2076.
https://doi.org/10.3762/bjnano.16.141

Received: 31 May 2025
Accepted: 21 October 2025
Published: 14 November 2025

This article is part of the thematic issue "Micro- and nanoscale effects in biological and bioinspired materials and surfaces".

Associate Editor: P. Leiderer

Abstract

Gecko adhesion, enabled by micro- and nanoscale structures known as setae and spatulae, has prompted extensive research. We present a concurrent multiscale computational model of a seta that integrates molecular dynamics to capture molecular interactions at the spatula–substrate interface and finite element method to simulate the mechanical behavior of the larger setal shaft. This hybrid approach enables synchronized simulations that resolve both fine-scale interfacial dynamics and overall structural deformation. The model reproduces key aspects of spatula behavior during adhesion and detachment, showing that spatula–substrate contact evolves through a combination of bending, sliding, and peeling, depending on the spatula's initial orientation. Our results further demonstrate that lateral sliding can delay detachment, thereby enhancing adhesion strength. The computed pull-off forces and observed mechanisms are consistent with atomic force microscopy measurements and previous simulations. These results align with existing experimental and computational studies. They also overcome scale and resolution limitations inherent in single-scale models.

Introduction

Geckos possess the ability to adhere to a variety of substrates, a trait attributed to specialized micro- and nanoscale structures on their feet [1,2]. This bioadhesion mechanism has been studied extensively, especially for biomimetic adhesive applications [3-9]. Understanding these interactions presents a formidable challenge in biophysics and materials science due to the extremely small length and time scales involved.

In previous research, we used molecular dynamics simulations to explore various aspects of gecko adhesion [10-13]. We found

that humidity increases the force required to pull a spatula off from a substrate [10,12], a phenomenon also observed in high-humidity atomic force microscopy (AFM) experiments. Our investigation into how gecko keratin interacts with hydrophilic and hydrophobic substrates [12] supported the importance of the water-mediating effect [10] and elucidated mechanistic differences depending on surface chemistry. A particle-based mesoscale model of a single gecko spatula was then used to bridge molecular interactions and macroscopic adhesion behavior. This mesoscale model accurately simulated spatula detachment from various substrates and matched experimental pull-off forces observed in AFM studies and pull-off pressures from united atom simulations of gecko keratin [11]. It also helped clarify other aspects of humidity-enhanced adhesion, revealing that keratin softening due to water uptake accounts for only a minor part of the increase in adhesion on very smooth surfaces [13]. The present paper builds on our previous research and extends the treatment to an entire seta with multiple spatulae.

Since purely particle-based simulation techniques are limited by the number of atoms (or coarse-grained beads), it becomes computationally unfeasible to model an entire seta at molecular resolution. A back-of-the-envelope calculation gives an estimate of around 10^{14} atoms for a single gecko seta. Coarse-graining [14,15] can improve the situation, but not by more than 1–2 orders of magnitude. Consequently, multiscale approaches combining continuum methods like the finite element method (FEM) [16-18] with particle-based molecular dynamics (MD) [19,20] are necessary to capture both large-scale geometry and local molecular interactions at the adhesive interface. There have been several pure finite element studies of gecko adhesion, which examine mechanisms like peeling from and pushing (loading) onto a substrate [21-28]. While there have been a few sequential multiscale studies [29-31], there have been no concurrent simulations in which micrometer-scale seta mechanics and molecular spatula–substrate interactions feed into each other at runtime. This work concurrently couples MD and FEM in a single simulation to model multiple spatulae in parallel, all connected to a larger setal shaft. Forces and displacements are exchanged at each iteration, ensuring that spatula-level phenomena (e.g., van der Waals contact, slight sliding at the substrate, and spatula bending) feed back into the global deformation. The continuum and particle domains exchange information through a handshake region using our coupling algorithm, which will be detailed in Section "Methods". The simulations presented in this paper visualize the mechanical response of whole seta and the peeling of spatulae during pull-off from a dry, smooth, and hydrophobic substrate at a loading rate of 1.88×10^{12} pN/s. We also examined adhesion forces and quantified spatula–substrate contacts, while comparing with qualitative and quantitative experimental results where available.

We synchronously simulated 16 spatula–substrate contact sites via molecular dynamics, each coupled through its own bridging domain to a single seta described by finite elements. In this way, forces were transmitted between different spatulae as they would in real life. At the same time, molecular processes between spatulae and substrate under these forces were covered at molecular resolution. This two-way, concurrent coupling turns adhesion from a prescribed boundary condition into an emergent, geometry- and state-dependent response: Local spatula-level peeling, sliding, and contact reorientation feed back into the global branched seta, which, in turn, reshapes the local interface state at the next iteration. Practically, it exposes cross-scale observables that pure MD or pure FEM cannot provide, that is, redistribution of forces across branches (anchor-point loads), spatula-resolved contact maps and sliding velocities during seta preloading/pull-off, and detachment order as a function of branch position and seta deformation. The simultaneous use of multiple MD regions coupled to an FEM model is new. Although 16 spatulae are fewer than the thousands found on a real gecko seta [3,32-35], this number was chosen to align with Sauer and colleagues [22]. Scaling to more spatula–substrate sites is straightforward but would increase runtime.

Models

Multiscale seta–spatula model

A seta branches into spatulae as seen in scanning electron microscopy (SEM) images of gecko setae (Figure 1). A single seta on a gecko's foot can have dozens of sub-branches, which further branch into hundreds to thousands of spatulae [32-35]. Our seta geometry (Figure 2) was inspired by the branching geometry in Sauer et al. [21], which simplified the seta into distinct branching levels. While this captured key structural features, it did not fully represent the intricate natural hierarchy of real gecko setae, which includes finer branches, varying cross sections, and region-specific material anisotropy. Real setae possess complex cross-sectional shapes and non-uniform branching angles, which could lead to variations in force distributions. Nonetheless, this idealized geometry was sufficient as a first step in validating our concurrent MD–FEM approach and extracting fundamental insights about contact formation, load transfer, and spatula detachment mechanisms.

Simulating each spatula in its own MD simulation, while coupling them all with the seta FEM model, becomes computationally expensive as the number of spatulae increases. Therefore, we limited the model to 16 spatulae per seta. The model can be modified to accommodate different seta morphologies with more spatulae if needed. Figure 2 shows how the setal shaft was

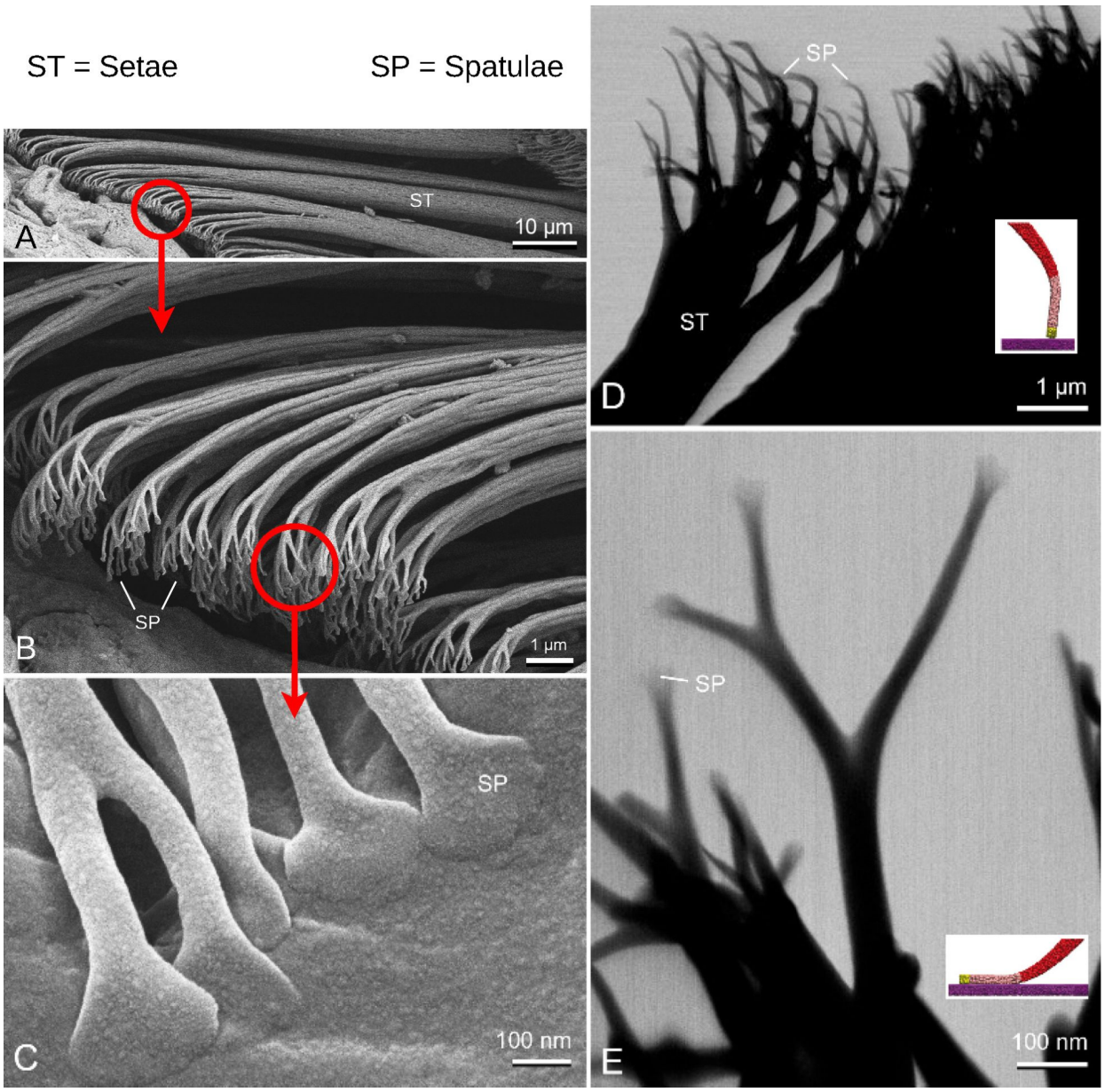

Figure 1: Electron microscopy images of the gecko setae. (A–C) Three hierarchical levels in the scanning electron microscope: A, setae; B, branches of setae (setulae) with the spatulae at the tips; C, spatulae in contact with the surface. The red circles highlight a region while the corresponding arrow points towards a higher resolution (zoomed-in) image of a similar region. (D, E) Setae in contact with the surface with different orientations in the transmission electron microscope. The inset images show corresponding orientations of the spatula molecular model.

simulated with FEM, whereas the spatulae in alternating orientations with their substrates were simulated in 16 parallel MD calculations.

The skeleton of our multiscale seta was created by distributing branching points along two parabolas (Figure 3) as described by Sauer and colleagues [21]. Figure 3 illustrates the construction of the seta FE mesh. The seta was modeled with a height H_0 of 22.8 µm and an inclination angle α_{se} of 30°. The multiscale seta was constructed by modeling a main shaft that branched four times into 16 tips, each connecting to a molecular spatula. The overall seta geometry was bound by the positive legs of the two parabolas (red lines, Figure 3) given by Equation 1 [21],

$$\frac{x^2}{C_1^2}-\frac{y^2}{C_2^2}=1, \qquad x,y>0, \tag{1}$$

where $C_1 = 0.5D_0$ and $1.5D_0$ for the two boundary parabolas, and $C_2 = C_1\tan(\alpha_{se})$. The horizontal line segment between the

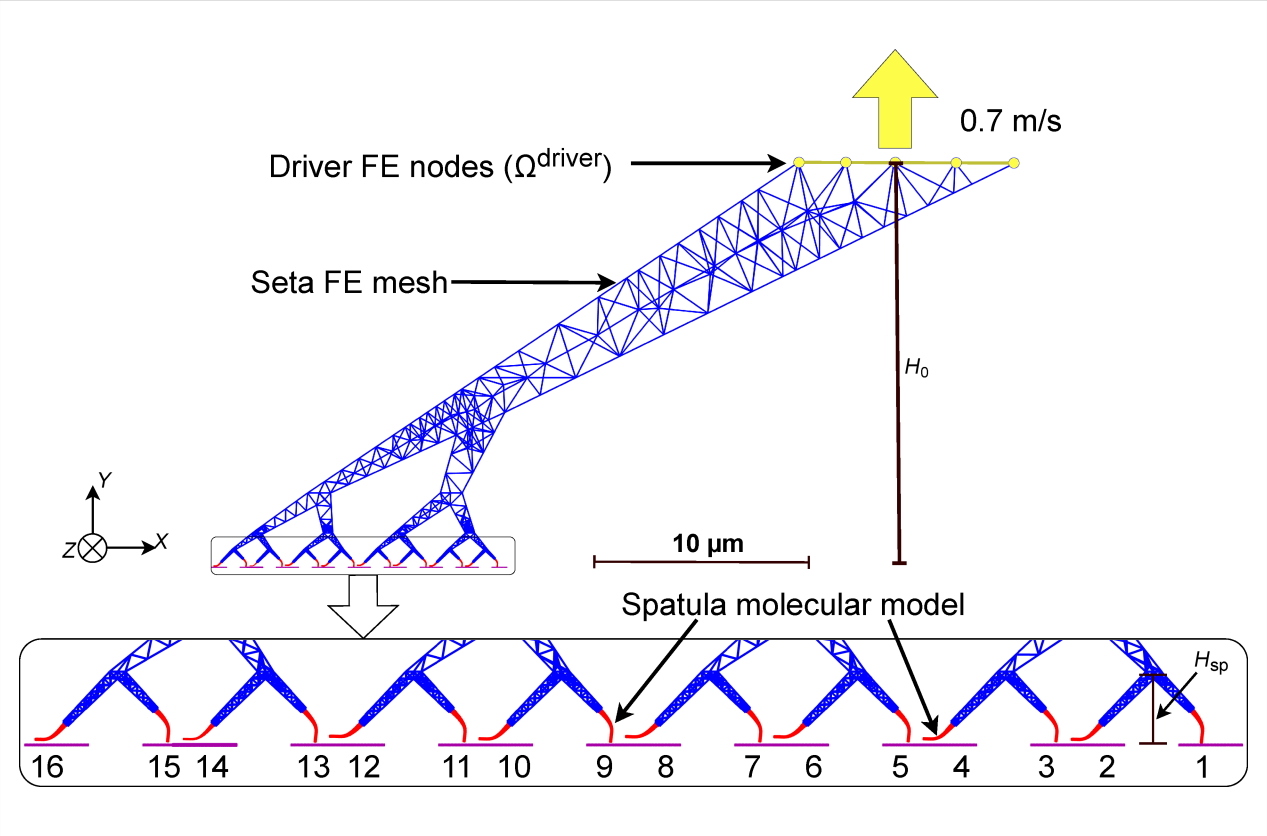

Figure 2: Illustration of the entire multiscale seta model. The red spatulae are modeled using beads, while the rest of the larger blue seta is modeled using a finite element mesh. The driver FE nodes (Ω^{driver}) at the top of the seta are subject to an incremental displacement of 1 nm per load step for more than 500 load steps, or until all spatulae are completely detached from the substrate. H_{sp} is the height of the spatula including both the final FE branch and the spatula molecular model; H_0 is the total height of the multiscale seta.

parabolas at each branching height H_i (where i = 1,2,3,4) was divided into 2^{i-1} equidistant intervals, and the x-coordinate of each branching point was the midpoint of one of these intervals. The height of each branching point, starting from the first (highest) branching level, decreased progressively according to Equation 2:

$$H_i = \eta^{4-i} H_{sp}, \qquad i = 0,1,2,3,4, \tag{2}$$

where i represents the branching level, H_{sp} is the total spatula height, including both the final tiny FE branch that connects to the molecular spatula and the molecular spatula itself (see Figure 2), and η is a scaling parameter. The bottom tips of the final branches are at i = 5. Joining these branching points with lines formed the skeleton of the multiscale seta (blue lines, Figure 3).

Seta: finite elements

From the seta skeleton, we constructed a three-dimensional finite element mesh using C3D10 tetrahedral elements [36]. The seta's cross-sectional width W_i (see Figure 4) was determined based on the molecular spatula shaft diameter R_{sp} and a scaling parameter γ as given by Equation 3:

$$W_i = \gamma^{(5-i)} R_{sp}, \qquad i = 0,1,2,3,4,5. \tag{3}$$

After the mesh was constructed, the top portion of the seta above a height (H_0) of 22.8 µm was removed. The 45 FE nodes on this cross-sectional area received the prescribed displacement for preloading and pull-off during simulations. They effectively drove the simulation and are referred to as driver FE nodes. Portions of the mesh at the end of the spatulae were also removed to be replaced by molecular spatulae models. Table 1 lists the parameters and values used to construct the continuum part of the model.

The finite element mesh response was governed by linear isotropic elasticity, with the stress–strain relationship given by Hooke's law [36,37]:

$$\boldsymbol{\sigma} = \lambda \mathrm{tr}(\boldsymbol{\varepsilon})\mathbf{I} + 2\mu\boldsymbol{\varepsilon}, \tag{4}$$

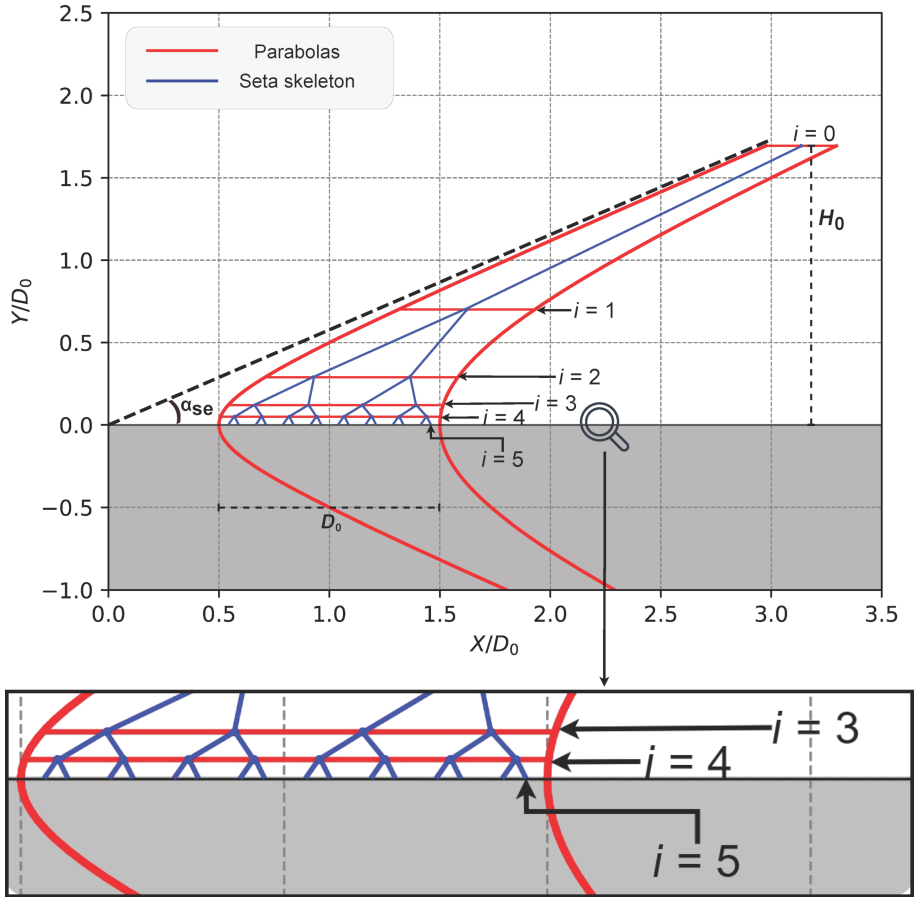

Figure 3: Schematic for constructing the skeleton of our multiscale model. The dimensions of the figure have been normalized with respect to the seta base width D_0 = 13.5 µm. The red lines are the two guiding parabolas that helped construct the seta's skeleton (blue). A magnified image of the portion with branching points i = 3,4,5 shows the final 16 branches that represent our spatulae.

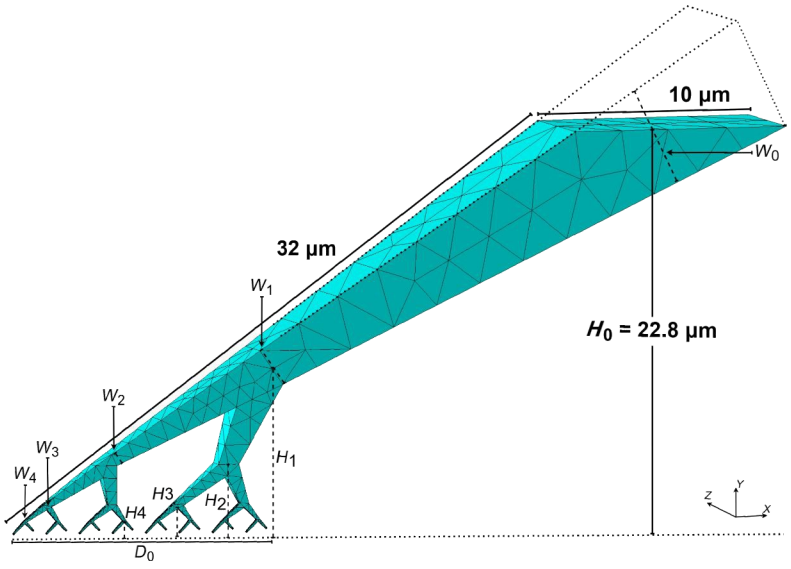

Figure 4: The finite element mesh of the setal shaft in our model. The dotted lines at the top of the seta show the portion that was removed above a height (H_0) of 22.8 µm. Portions of the final tiny FE branches (i = 5) were also removed to enable connections to molecular spatulae (here hidden for clarity). A horizontal dotted line shows where the missing portion of the final branches would be, and serves as the reference for displaying heights H_i.

Table 1: Geometric parameters for the finite element portion of the seta.

Parameter	Value
H_0	22.8 μm
D_0	13.5 μm
α_{se}	30°
R_{sp}	50 nm
η	2.417
γ	$\sqrt[4]{40}$
H_{sp}	0.67 μm

where **σ** is the Cauchy stress tensor, **ε** is the infinitesimal strain tensor, tr(**ε**) denotes the trace of the strain tensor, **I** is the second-order identity tensor, and λ and μ are the Lamé parameters defined as:

$$\lambda = \frac{E\nu}{(1+\nu)(1-2\nu)} \tag{5}$$

$$\mu = \frac{E}{2(1+\nu)} \tag{6}$$

with E being Young's modulus and ν Poisson's ratio.

The real seta material may exhibit anisotropy and viscoelastic or even plastic behavior, especially under rapid loading. Our FE mesh is presently limited to a linear-elastic, isotropic constitutive law, with parameters E and ν matching those of our molecular keratin spatula model [11,12]. These values were derived in a bottom-up manner from atomistic simulations that reproduced experimental data [8,38,39]. For each of our simulations, we sampled E and ν from normal distributions with the same mean and standard deviations as our mesoscale spatula model. Table 2 summarizes the material parameters used for our FE mesh.

Table 2: Mechanical parameters for the finite element portion of the seta model. [a]

Parameter	Value
constitutive law	isotropic linear elasticity
Young's modulus (E)	4.518 ± 0.036 GPa
Poisson's ratio (ν)	0.401 ± 0.002

[a]For every simulation, we sampled Young's modulus and Poisson's ratio from normal distributions with these means and standard deviations.

Spatulae and substrate: particles

Mesoscale spatula model

The mesoscale spatula model was derived from prior research. Its shape is based on SEM images [23], and the force field was derived bottom-up from united-atom gecko keratin simulations [12]. The keratin proteins in gecko seta and spatulae form a structure similar to a fiber-reinforced elastomer, with a fibrillar nature that leads to anisotropic mechanical properties [40-42]. Rather than explicitly resolving individual fibers and the surrounding amorphous matrix, we represented the spatula with a coarse-grained bead network whose anisotropic fibrillar structure was encoded through direction-dependent bond stiffnesses. Figure 5a shows the molecular spatula with beads colored according to different regions (tip/pad/shaft). Each bead, representing approximately five keratin molecules or 2.5 keratin dimers (65228 Da), was connected to 30 neighboring beads via harmonic bonds,

$$V(r) = \frac{1}{2}K(r-b_0)^2, \tag{7}$$

where r is the distance between the two beads, and b_0 is the initial (equilibrium) distance between them. Their force constants K increased when the bonds aligned with the local keratin fibril direction,

$$K = k + k_b \cdot |\cos\theta|, \tag{8}$$

where k is the base isotropic force constant identical for all bonds, k_b is an additional force constant in the fibril direction, and θ is the angle between the bond vector and the fibril direction. We systematically tuned the parameters k and k_b so that the resulting coarse-grained network reproduced the spatula's key mechanical properties, specifically, its Young's modulus and Poisson's ratio, as derived from atomistic simulations and experimental data [11]. We generated ten such spatula models with differing bead positions and bond constants, yielding a Young's modulus of 4.518 ± 0.036 GPa and a Poisson's ratio of 0.401 ± 0.002. Details can be found in our previous work [11]. These spatula models were coupled to the FE seta in two orthogonal orientations as shown in Figure 5 and Figure 2b.

Smooth substrate

We employed a simple particle-based model of a nonpolar (hydrophobic), smooth substrate as a baseline to remain consistent with the previously validated parametrization of our coarse-grained potential against united-atom simulations of gecko

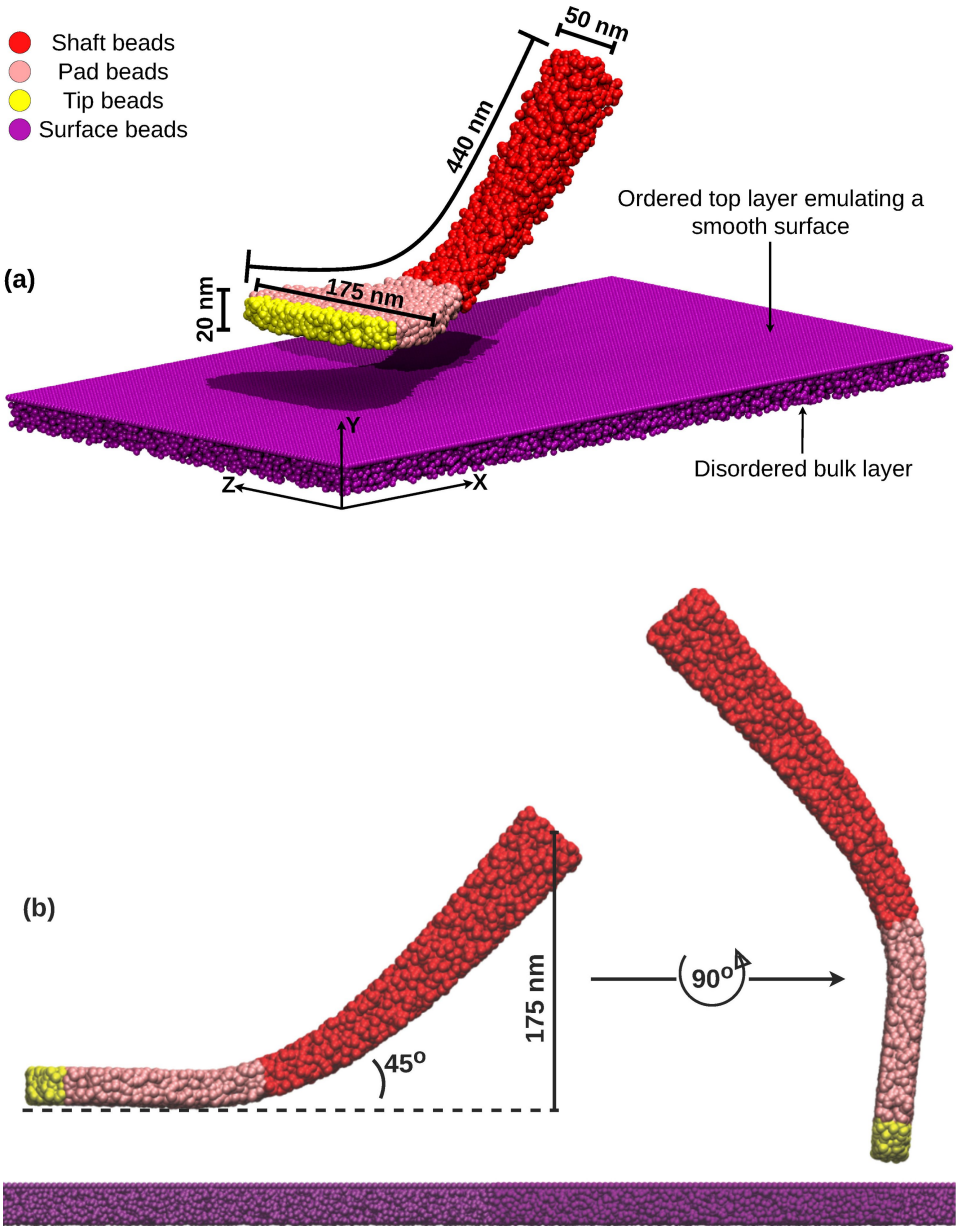

Figure 5: Geometry of the molecular spatula and substrate. (a) A spatula interacting with the dual-layered smooth substrate and (b) the two orthogonal orientations of the spatula in our seta model.

keratin on nonpolar surfaces [10]. Hydrophilic substrates, roughness, and humidity, which introduce additional mechanisms such as keratin softening and capillary forces, have been addressed in our previous spatula-scale studies [12,13] and will be treated in future multiscale work. In our previous work [10], we only investigated spatula detachment in a direction normal to the substrate, so a fully random bead arrangement posed no risk of the spatula beads sliding into frozen/immobile substrate pores. In the present simulations, the spatula was free to slide laterally, which could have risked "locking" if the substrate was entirely disordered, contained random voids, and was inflexible. To prevent this, we introduced a two-layer substrate, that is, a lattice-like monolayer of beads on top, forming a smooth, cavity-free surface, and a 13 nm thick amorphous bulk below, which matched the same bead density as our previous random-substrate model. All substrate beads had identical interactions with the spatula, and both layers were held fixed in space. Since the regular top monolayer differed from the fully random arrangement used previously, we re-parameterized the spatula–substrate Lennard-Jones interactions:

$$V(r) = 4\epsilon\left[\left(\frac{\sigma}{r}\right)^{12} - \left(\frac{\sigma}{r}\right)^{6}\right], \quad r < r_{\text{cutoff}}, \tag{9}$$

so that the new surface would have the same pull-off (adhesion) pressure as before. Specifically, several parameter combinations were tested in pull-off simulations against our reference data for gecko keratin [12], and the parameter set that reproduced the target adhesion (ϵ = 290 kJ/mol, σ = 4 nm, and r_{cutoff} = 12 nm) was selected. The relatively large σ value reflects the coarse graining, and $r_{\text{cutoff}} = 3\sigma$ retains most of the attractive tail of the LJ potential. Any surface bead deeper than the cutoff (12 nm) does not interact with the spatula beads; therefore, any substrate thicker than the spatula–substrate potential cutoff ($r_{\text{cutoff}} \leq$ thickness $\leq \infty$) would result in identical dynamics and forces. Our substrate (1 monolayer + 13 nm amorphous bulk) exceeds the cutoff, fully representing all interactions while avoiding unnecessary computational cost. We note that the substrate model is an idealized approximation chosen for consistency with our prior work [10,12] and computational efficiency. Modeling biologically realistic interfaces will require extending the present model to include stratification, surface roughness, substrate deformability, and explicit long-range electrostatics for hydrophilic systems, which will necessitate thicker substrate models.

The coupling between each molecular spatula and the FE seta was handled via a bridging domain (BD), described in section "Methods".

Methods

Multiscale coupling algorithm

The coupling algorithm connects three distinct domains, each governed by different physical principles and simulation techniques: (1) The particle domain, that is, the set of all particles simulated using molecular dynamics (MD). This domain captures molecular interactions, structures, and processes at the spatula–substrate interface. (2) The continuum domain, that is, the set of all nodes and elements simulated using the finite element method (FEM). This domain models large-scale mechanical behavior. (3) The bridging domain (BD), that is, a handshake region that incorporates elements of both MD and FEM. It facilitates synchronous information exchange between the particle and continuum domains through the coupling algorithm.

Figure 6 illustrates these three domains. The pink region, consisting of MD particles, is the particle domain; the blue region, composed of a finite element mesh with nodes, is the continuum domain; and the overlapping grey region, which includes coupling components such as anchor points (APs) and

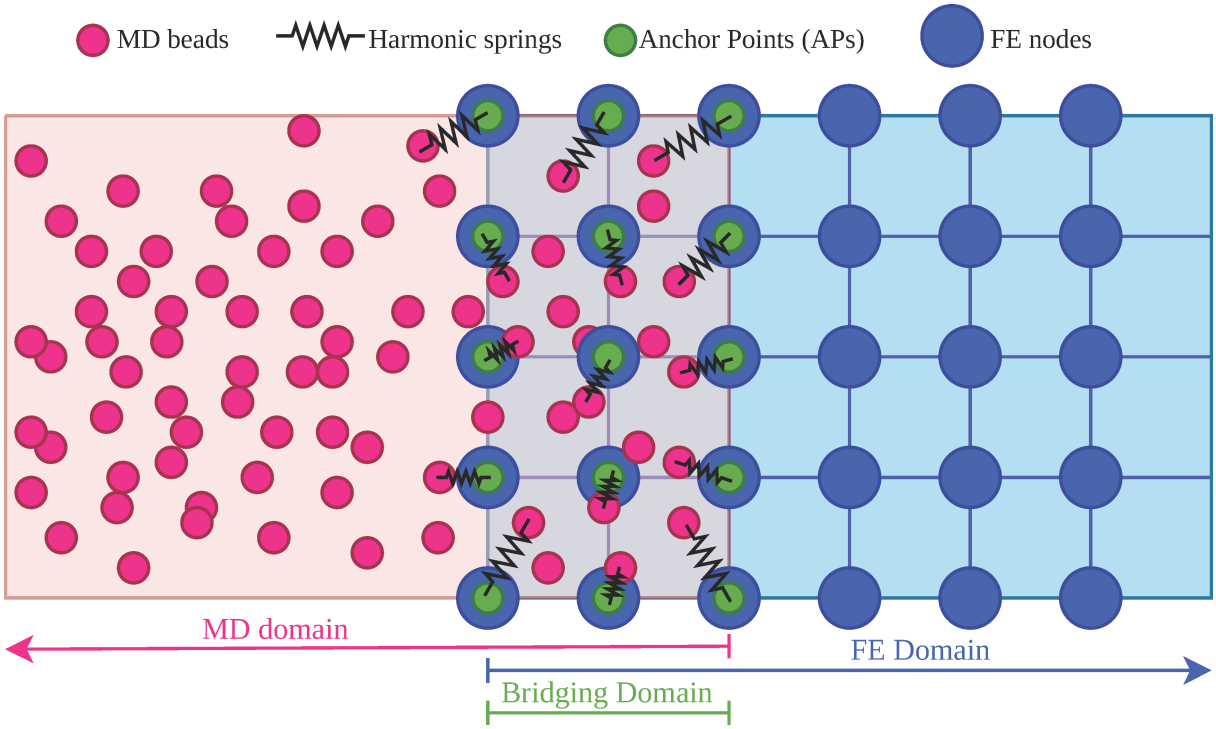

Figure 6: Illustration of the three domains: particle (MD), continuum (FE), and bridging domain (BD). Also shown are the FE nodes, MD beads, anchor points (APs), and harmonic bonds connecting APs to MD beads.

harmonic springs, is the bridging domain. Calculations alternate between MD and FEM. The finite element mesh and anchor points (see subsection "Anchor points and force transfer") are held fixed while MD runs for several hundred picoseconds (140 ps or 7000 time steps in our case). Then, the MD particles are frozen and the FEM is solved. These alternations are continued until the process of interest is complete.

Anchor points and force transfer

To connect the particle and continuum domains, APs are placed in the bridging domain. The APs are virtual particles fixed in space that coincide with the positions of FE nodes in the bridging domain. Each AP is connected to a nearby MD bead (not already linked to another AP) via a harmonic spring. The initial AP–MD bead distance serves as the equilibrium length of the harmonic spring. Figure 6 shows the APs as green particles in the bridging domain. Each green AP coincides with a blue FE node and is connected to a pink MD bead by a black harmonic spring. A suitable choice of the MD-coupling spring constant produces forces of the same order of magnitude as the forces among MD beads. In our simulations, the same force constant as for bonds within the molecular model was used. During each MD iteration, forces exerted on the APs by the MD system are recorded, averaged over the final portion of the trajectory (typically 30–50%), and then transferred to the corresponding FE nodes.

Controlling FEM deformation

In the FEM calculation, forces transferred through the APs are applied as external loads on the corresponding FE nodes. These loads cause deformation of the FE mesh. However, since they remain constant during each FEM run, the mesh deformation may not fully reflect interactions where forces evolve dynamically based on spatula behavior. In particular, during loading simulations such as multiscale seta pull-off, this can lead to excessive FE mesh deformation due to missing dynamic contributions from the spatulae.

To mitigate excessive deformation or drift, harmonic springs connect the FE nodes in the bridging domain to their initial positions at the start of each FEM iteration. These springs have a stiffness referred to as the FE-coupling spring constant. These FE-coupling harmonic springs are not shown in Figure 6. By providing a restoring force, they ensure controlled deformation of the FEM mesh and prevent overshooting beyond equilibrium. Additional theoretical details on how the FE-coupling springs act as a penalty term in the FEM calculation can be found in our previous work, which used this multiscale approach to simulate crystalline and amorphous polymers [43]. Once the FEM calculation is complete, the updated positions of the FE nodes in the bridging domain, and hence of the APs, are passed back to the particle domain. The FE-coupling spring constant was optimized, starting from the same value as the MD-coupling spring constant and then reduced until forces across the domains matched [43]. Further discussion on the choice of the spring constants is provided in Supporting Information File 1. The FE calculation is static (no inertia), and the MD employs thermostats; accordingly, strict global momentum conservation across both domains is not enforced. Instead, the appropriate consistency criterion is traction–displacement matching at the interface. Traction–displacement consistency refers to enforcing both displacement continuity and traction equilibrium in the bridging domain between a continuum domain and a particle domain. In practice, this means that the FE and MD domains share matching deformations at their boundary (no jump in displacements), and the forces/stresses transmitted across the interface are balanced (no net traction mismatch) [44-47]. The reactions of the FE-coupling springs remain internal to the FE solver; their influence on MD enters only via the updated positions of bridging domain FE nodes, which serve as the new AP positions for the subsequent MD run.

Iterative workflow and load steps

After the FE calculation, the MD system evolves under the external potential of the updated AP positions, and the averaged forces on the APs are then calculated and transferred back to the FEM simulation. This cycle of FEM and MD simulations constitutes a single FEM–MD iteration.

Synchronization of the domains requires multiple iterations, not only due to deformation control from the FE-coupling spring but also due to interplay between molecular and continuum forces. The number of required iterations depends on the FE-coupling spring constant and should be considered during their optimization. A smaller FE-coupling spring constant leads to greater mesh deformation and, thus, represents a larger step towards the final FEM solution. This requires fewer iterations but also increases the risk of numerical instabilities. Conversely, a larger spring constant results in smaller steps towards equilibrium but requires more iterations.

External loading (e.g., displacement or force) on the full system, such as moving the entire seta, is applied in increments called load steps. Each load step consists of (1) applying a portion of the total load (a displacement of 1 nm in our case) to the driver nodes and (2) running multiple FEM–MD iterations (ten in our case) under the applied load until the required loading rate is matched (for non-equilibrium simulations), or system energies and AP forces converge (for quasi-static equilibrium simulation).

For instance, a total displacement of 10 nm is applied in ten load steps of 1 nm each, with several FEM–MD iterations at each step. The maximum loading rate that can be imposed and the number of iterations per load step depend on the system size and dynamics. Since the FEM calculation is static and lacks time information, the time corresponding to a load step, Δt^{ls}, is estimated using the MD time step, Δt^{MD}, the number of MD steps per iteration, n^{MD}, and the number of iterations per load step, n^{iter}:

$$\Delta t^{\mathrm{ls}} = n^{\mathrm{iter}} n^{\mathrm{MD}} \Delta t^{\mathrm{MD}}. \tag{10}$$

Using this time and the imposed strain per load step $\varepsilon^{\mathrm{ls}}$, the pull-off velocity is set as

$$\dot{\varepsilon}^{\mathrm{ls}} = \frac{\varepsilon^{\mathrm{ls}}}{\Delta t^{\mathrm{ls}}}. \tag{11}$$

In our previous work [46-50] on bulk polymer models, we found that prescribing a displacement of around 0.004–0.1% of the system size per load step was effective. For our seta model, a 1 nm displacement is 0.004% of the initial height. Furthermore, a parameter study for our polymer models [47] showed that $\dot{\varepsilon}^{\mathrm{ls}}$ should be small enough (50–100% of a polymer bond length) to avoid a excessively large strain on the MD domain. A displacement of 1 nm corresponded to 33% of the shortest bond (3 nm) and 14% of the average bond length (7.33 ± 2.16 nm) in our molecular spatula model.

In pull-off experiments, the loading rate is defined as the rate at which adhesion forces increase during pull-off. The spatula–substrate MD force field was parametrized to match atomistic keratin pull-off simulations at a loading rate of 1.66×10^{12} pN/s [10,12,13], and so we aimed to match the same rate. Preliminary pull-off tests identified a pull-off velocity of 0.7 m/s which yielded a loading rate of 1.88×10^{12} pN/s. For a displacement ($\varepsilon^{\mathrm{ls}}$) of 1 nm and a velocity ($\dot{\varepsilon}^{\mathrm{ls}}$) of 0.7 m/s, our load step time (Δt^{ls}) then corresponded to 1.4 ns according to Equation 11.

The parameter study for our previous multiscale polymer models [47] showed that such an approach, in general, is robust with respect to the number of iterations per load step (n^{iter}). This observation holds for our current simulations as well. Different choices of n^{iter} between one and ten are explored in Supporting Information File 1. Our choice of $n^{\mathrm{iter}} = 10$ is large enough for agreement between pre-detachment forces in different domains, while remaining computationally feasible. If instead a quasi-static equilibrium simulation is desired, then Δt^{iter} and n^{iter} must both be high enough (thereby also increasing Δt^{ls} in Equation 10) for the multiscale system to be in equilibrium at the end of every load step.

Seta–spatula bridging domain

In the multiscale model, there were 16 bridging domains (BDs), one for each spatula. Each BD needed to be of a size that could be described by both (MD and FEM) methods. The FE portion of each BD was roughly $79 \times 75 \times 50$ nm^3 in size, and the overlapping MD portion was roughly $40 \times 36 \times 39$ nm^3 (Figure 7).

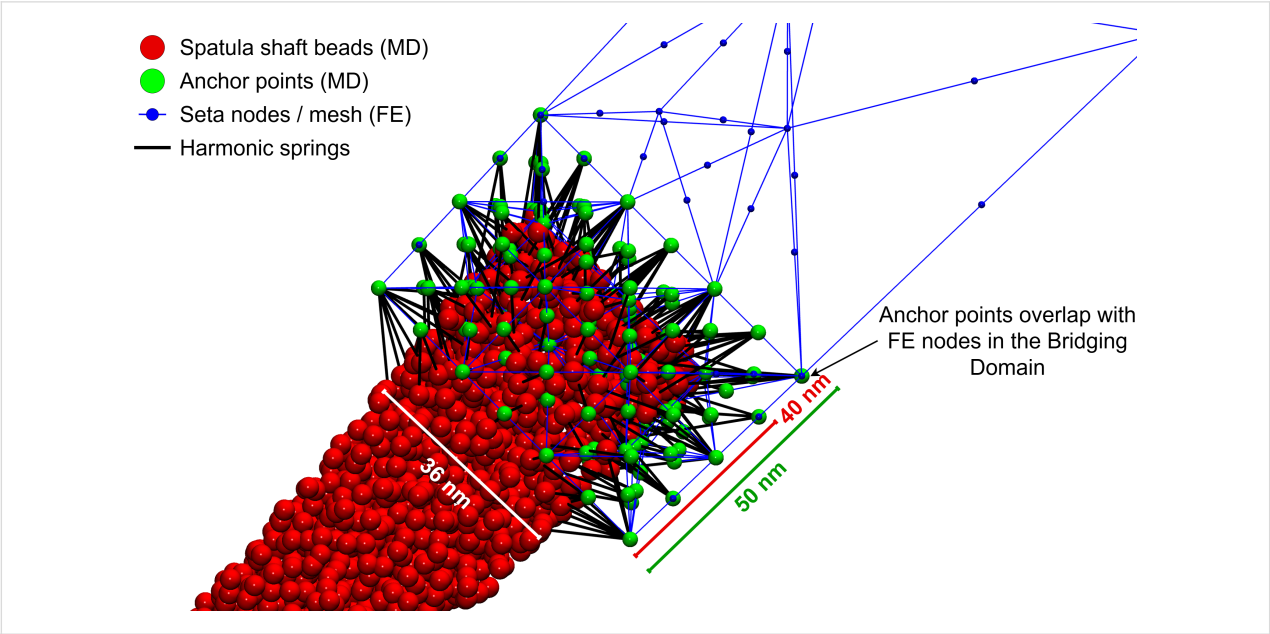

Figure 7: A bridging domain connects one of the spatulae (modeled using molecular dynamics) to the setal shaft (modeled using finite elements).

The number of APs per BD averaged 395 ± 9.9, depending slightly on the local FE mesh geometry. Each AP coincided with a FE node and was linked to a nearby MD bead via a harmonic spring with stiffness (MD-coupling spring constant) 0.28 nN/nm. FE nodes in the BD were also coupled to their initial positions via springs with stiffness (FE-coupling spring constant) 0.08 nN/nm. Figure 7 illustrates a typical BD configuration, showing the overlapping domains, anchor points, and harmonic spring connections.

Simulation Details and Parameters

Iteration details

Molecular dynamics

We used the velocity-Verlet algorithm [51] under canonical (NVT) ensemble to perform time integration of the spatula beads and update their positions and velocities. A velocity rescaling thermostat [52] with a coupling time of 2 ps acting only outside the BD maintained the temperature of the spatulae at 300 K, similar to our previous work [11,13]. Since the simulation assumed a frictionless vacuum environment, thermostats like dissipative particle dynamics and Langevin [53,54], which introduce implicit friction, are inherently unsuitable. In particular, Langevin dynamics led to unphysical effects such as loss of spatula jump-to-contact (snap-in) when near the substrate and absence of post-detachment wiggling. Consequently, a weak Berendsen thermostat [55] with a coupling time of 10 ps proved sufficient to maintain the temperature of the bridging domain while dissipating the kinetic energy introduced by load steps. Each AP experienced a force due to its harmonic bond with a connected MD bead. This force was averaged over the final 50% (70 ps) of the MD trajectory ($\bar{\mathbf{f}}_{\text{ap}}$) and then applied as an external boundary condition to the next FEM iteration as per Equation 12. The MD iterations were conducted with LAMMPS [56]. Table 3 lists further details and parameters of the MD simulations.

Table 3: Molecular dynamics iteration parameters.

Parameter	Value
ensemble	NVT
thermostat outside the bridging domain	velocity rescaling [52]
thermostat inside the bridging domain	Berendsen [55]
thermostat temperature	300 K
velocity rescaling thermostat coupling time	2 ps
Berendsen thermostat coupling time	10 ps
time step	20 fs
non-bonded interaction cutoff	120 Å
total time per iteration	140 ps
force-averaging period	last 70 ps

Finite element iterations

In the FEM part, boundary conditions were applied on two distinct node groups, namely, the driver group (Ω^{driver}) and the bridging domain (Ω^{BD}) group. The 45 driver nodes (Ω^{driver}) located on the top end of the seta (Figure 2) were subjected to Dirichlet boundary conditions: In the first iteration of each load step, a prescribed displacement of 1 nm was applied in the *Y*-direction (negative for preload; positive for pull-off), with motion in *X*- and *Z*-directions fully constrained. In all subsequent iterations within the same load step, the driver nodes were fully constrained in all three directions.

The BD nodes (Ω^{BD}) were subjected to Neumann boundary conditions, where averaged forces on the anchor points $\bar{\mathbf{f}}_{\text{ap}}$ computed from the MD iteration were applied as external forces on the BD nodes:

$$\mathbf{f}_{\text{ext}} = \bar{\mathbf{f}}_{\text{ap}} \quad \text{on } \Omega^{\text{BD}} \quad \text{(all iterations)}. \tag{12}$$

As discussed in subsection “Controlling FEM deformation”, we attached linear elastic springs to all nodes in Ω^{BD}, anchoring them to their initial reference positions. These springs introduced a restoring force proportional to the node displacement $\mathbf{u}$:

$$\mathbf{f}_{\text{spring}} = -k^{\text{FE}}\mathbf{u} \quad \text{on } \Omega^{\text{BD}}, \tag{13}$$

where k^{FE} is the FE-coupling spring constant. Therefore, the final external force on these nodes becomes

$$\left(\mathbf{K} + \mathbf{K}^{\text{FE}}\right)\mathbf{u} = \mathbf{f}_{\text{ext}}. \tag{14}$$

Here, $\mathbf{K}^{\text{FE}}$ is a diagonal matrix representing spring contributions assembled over Ω^{BD}.

The remaining nodes of the finite element mesh adjusted their positions in response to the displacement of the top and the forces transmitted from the molecular dynamics domain at the bottom by solving Equation 14 as prescribed by the constitutive law discussed in subsection “Seta: finite elements”. At the end of the FEM iteration, positions of nodes in Ω^{BD} ($\mathbf{r}_{\text{bdfe}}$) were set as new anchor point positions for the next MD iteration. The FEM iterations were conducted with ABAQUS [36].

Simulation protocol

We aimed to replicate the protocol used in AFM experiments on gecko spatulae and setae as reported in [23,57]: (1) Initially, all spatulae were positioned at a minimum distance of 13 nm above the substrate, which is higher than the non-bonded interaction cutoff of 12 nm. (2) In the preloading phase, a 1 nm downward displacement towards the substrate was applied to the driver FE nodes at the start of each load step. Each load step consisted of ten FEM–MD iterations. During this phase, the 16 spatulae were gradually pushed onto the substrate by the moving seta. This process continued until a total preload (spatula–substrate) force of 320 nN combined from all spatulae was reached, ensuring that all spatulae established contact with the substrate. This preload force is similar to the average 18–20 nN per spatula imposed in AFM experiments [23,58]. (3) Following preloading, a set of 10 FEM–MD iterations (1.4 ns) was conducted without any applied displacement. Unlike in typical AFM experiments, where the seta is pulled sideways (sheared) to increase the contact area, we did not actively shear. However, spontaneous sliding of the spatulae was observed during preloading. (4) After relaxation, during the pull-off (loading) phase, the seta top was moved upwards by reversing the direction of the applied displacement, again using 1 nm per load step. This eventually led to detachment of the spatulae from the substrate. The pull-off was continued until all spatulae were outside the interaction range of the substrate.

To ensure statistical robustness, we conducted five simulation runs using independently generated multiscale seta models. The same seta FE mesh, with slightly perturbed Young's modulus and Poisson's ratio (see subsection "Seta: finite elements"), was attached to 16 spatulae. Each spatula was randomly selected from the set of ten uniquely generated spatula models (see subsection "Spatulae and substrate: particles").

Results and Discussion

Forces, contacts, and displacement profiles

AFM experiments measure forces exerted by the cantilever tip during pull-off, with the maximum pulling force representing the adhesion force between the spatula and the substrate [57]. These experiments typically report the force required to detach a spatula, but they are limited to measuring forces at the cantilever tip and cannot directly resolve molecular-scale interactions at the spatula–substrate interface. In contrast, our hybrid MD–FE model enables us to compute forces at multiple locations throughout the system and to track the dynamics of individual spatulae during preloading and pull-off. To analyze adhesion behavior, we plotted force, contact, and displacement profiles, which provide complementary perspectives on the detachment process.

Force profiles

We calculated forces at three points in the system: (1) Spatula–substrate adhesion forces, that is, the total force exerted by the substrate on the spatulae through their interactions. These were averaged over the last 3500 time steps or 70 ps of the final MD iteration of a load step. (2) Anchor point forces, also averaged over the last 3500 time steps or 70 ps of the final MD iteration of a load step. (3) Driver FE node forces, which were not time-averaged and were computed directly at the end of each load step.

In all force profiles presented in this study, compressive forces, where two entities press against each other, are reported as positive, while tensile forces, which represent adhesion during pull-off, are negative. When reporting an "adhesion (pull-off) force" in the text, we quote the magnitude of the minimum force, that is, $|F_{\min}|$, unless stated otherwise.

Contact profiles

We tracked the number of spatula–substrate contact points throughout the simulation. A contact point is defined as the distance between a spatula bead and a substrate bead being less than 12 nm. So long as any spatula bead was interacting with any substrate bead (i.e., any bead–bead distance smaller than the cutoff), the spatula was considered to be in contact with the substrate. The number of such interactions is referred to as the number of contact points. The contact profiles provide a measure of how many spatulae, and through how many contact points, adhered to the substrate at any point in the simulation, helping us understand the detachment sequence and the extent of adhesion loss during pull-off.

Displacement profiles

To further investigate how individual spatulae detach, we tracked the displacement of spatula tips and pads over time. The tip refers to the distal end of the spatula, which is typically the last point of contact during detachment, while the pad represents the main surface of interaction between the spatula and the substrate. Figure 5 shows the "tip" and "pad" beads in our spatula models, colored yellow and pink, respectively. We defined the X-axis as parallel to the substrate and the Y-axis as perpendicular (normal) to it (see Figure 2). The $+X$ direction points toward spatula no. 1 in Figure 2 (i.e., along the elevation of the setal shaft), while the $+Y$ direction follows the applied pulling force. The displacement profiles for each group of beads (tip or pad) were computed by averaging the positions of all beads in that group. These displacement profiles help distinguish between peeling, shearing, and other modes of detachment, and enable correlating displacement trends with force and contact loss.

Seta behavior

Forces during preloading and pull-off

Once preloading began (Figure 8) and the spatulae made initial contact with the substrate, further load pressed the spatulae against the substrate. The added spatula–substrate forces reached 320 nN after 224 ns (load step 160), marking the end of the preloading phase. In Figure 8, the relaxation phase is the single data point at 225.4 ns (load step 161) consisting of ten FEM–MD iterations (1.4 ns), and the transition to pull-off is identified by a reversal in the force direction from positive (compression) to negative (adhesion). As the pull-off continued, we crossed a point at 364 ns (load step 260) where the seta and substrate remained in contact but the net spatula–substrate force was zero. Beyond this point, the attractive force became more negative, reaching a minimum of −(284.5 ± 14) nN at 526 ns (load step 376). If all 16 spatulae were to detach simultaneously, this would give a naive average spatula adhesion force of ≈18 nN per spatula (reported as $|F_{\min}|$), an averaging method previously found in AFM experiments [57]. Spatula contact analysis (detailed in the following subsection "Spatula behavior") revealed that, at this moment, 14 of 16 spatulae were still in contact with the substrate (i.e., only spatulae 1 and 3 had de-

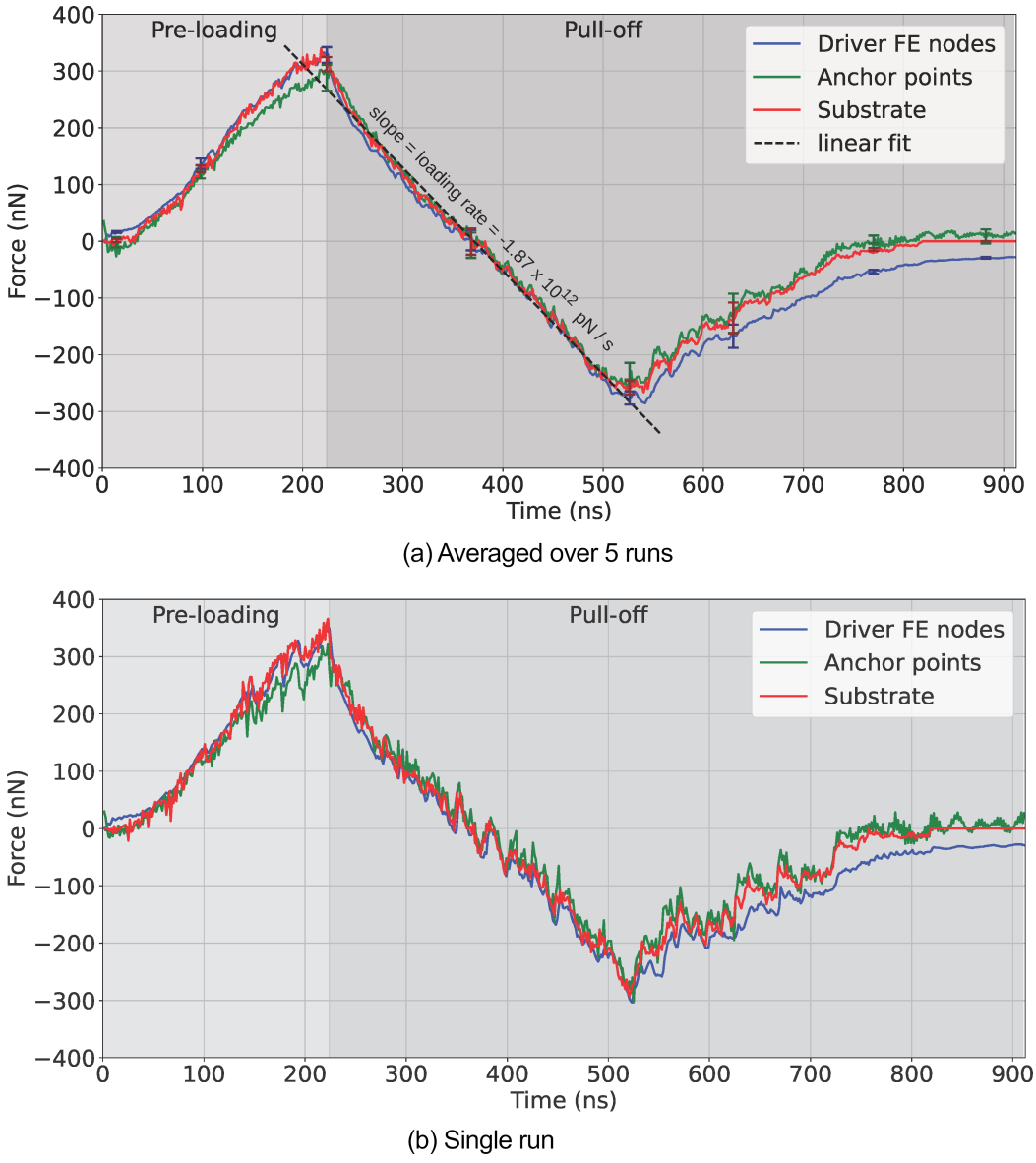

Figure 8: Reaction forces experienced by the substrate (red), anchor points (green), and the driver FE nodes (blue) in the pull-off simulations of entire gecko setae. (a) Averaged over five runs using different realisations of the spatulae. Error bars with darker colors have been plotted at interesting points in the curve. (b) For a single run. By convention, compression during preloading is positive, and adhesion during pull-off is negative; the adhesion peak corresponds to the minimum of the curves.

tached) and several pad-dominant spatulae achieved their own force minima later. Consequently, dividing the seta-level minimum by 16 (≈18 nN) underestimates the per-spatula adhesion force. A more accurate calculation involves averaging the force of each individual spatula at its own force minima, which yielded an average adhesion force of $|F_{min}| = 33.2 \pm 4.7$ nN. This matches the adhesive force of ≈35 nN reported in our previous work for the same molecular spatula model at a similar loading rate [10,13]. In the previous work, we conducted molecular simulations at various loading rates and extrapolated the adhesion forces down to rates which are typical in AFM measurements. At those lower loading rates, we saw extrapolated adhesion forces in the range of 12–25 nN, which matched the range of 8–20 nN observed in AFM experiments [35,57,59]. As detachment progressed, spatulae peeled off one by one, causing a gradual return of the force toward zero. The bumps in this detachment regime of Figure 8b result from a rise in the spatula–substrate adhesion force just before a spatula detaches and then the subsequent return due to detachment. Complete seta detachment occurred when the substrate reaction force dropped to zero due to all spatulae detaching at around 840–860 ns (load steps 600–615).

Despite discrepancies arising from the energy exchange via thermostats in the MD domain and differences in how each force is computed and averaged, the three different forces in Figure 8a remain closely aligned until detachment begins. Beyond this point, the curves begin to diverge. This divergence is not primarily due to the physical mechanics of detachment, but rather due to the limited number of FEM–MD iterations per load step in our runs (i.e., we mimic non-equilibrium AFM pulling), which prevented the system from fully equilibrating after rapid detachment events. Further discussion and simulations showing the effect of varying the number of FEM–MD iterations per load step on the force profiles are presented in Supporting Information File 1.

As individual spatulae detached, some slightly before and many after the seta-level force minima (peak adhesion) at ≈526 ns, they released stored elastic energy and accelerated rapidly. This sudden increase in velocity caused wiggling and rapid configurational changes within the MD domain. Due to the limited number of FEM–MD iterations per load step, the FE mesh did not have sufficient opportunity to adapt to these fast dynamics. As a result, the anchor point and driver FE node forces retained residual mismatches that were not fully dissipated, even after the substrate reaction force (red curve) dropped to zero. In the single-run results of Figure 8b, this manifests itself as persistent fluctuations around non-zero values in the AP and driver FE forces beyond ≈840 ns, when all spatulae are fully detached. These fluctuations arise from post-detachment wiggling of the spatulae. However, the concerning aspect is that these forces oscillate around non-zero values even after the substrate force has vanished. In Supporting Information File 1, we provide additional tests where load steps were extended up to 400 FEM–MD iterations. They confirm that the force divergence seen in the post-detachment phase is significantly reduced, or even eliminated, if sufficient iterations are allowed. However, such high iteration counts are not only computationally unfeasible with our available hardware but also go against a fast loading rate of 10^{12} pN/s. Therefore, while force and contact behaviors before detachment are well resolved and converged, the post-detachment region (after ≈526 ns or load step 376) should be interpreted with caution in terms of exact force magnitudes.

Seta–substrate contacts

The contact profile in Figure 9a was calculated by summing the number of contact points over all spatulae and then averaging over the five runs, while Figure 9b is the contact profile for a single run. They follow a similar trend to the seta–substrate force profiles (Figure 8). During preloading, contacts increased as spatulae were pressed against the substrate. In the pull-off phase, the number of contact points decreased gradually as the seta retracted, until individual spatulae started to detach completely (at ≈526 ns). This is marked by the sudden increase in the rate of contact loss (negative slope). Eventually, all spatulae completely detached from the substrate. Furthermore, the curve for a single run (Figure 9b) shows discrete steps when the final few spatulae detach one by one between 500 and 850 ns. Animations of the entire multiscale seta are available in Supporting Information File 2.

Spatula behavior

Since all spatulae share the same coarse-grained spatula–substrate potential, differences in adhesion originate from structure and geometry rather than interface chemistry. We analyzed the 16 spatulae individually. Figure 10, Figure 11, and Figure 12 report, respectively, their force, contact, and displacement profiles in a representative run. Across runs, orientation (pad- vs tip-dominant contact), branch position along the hierarchy (Figure 2), and transient shear/sliding modulate the peak adhesion force ($|F_{min}|$) and detachment order (Table 4, below).

Pre-loading phase

As the spatulae were pressed against the substrate, the compressive force increased (positive in Figure 10). The contact and displacement profiles provide additional insights: Odd-numbered spatulae (1,3,5,…,15) approached the substrate tip-first. Upon initial contact, their contact number increased, but as loading continued, the spatula bent slightly, causing the tip to tilt. This reduced the number of contacts as only the edge of the

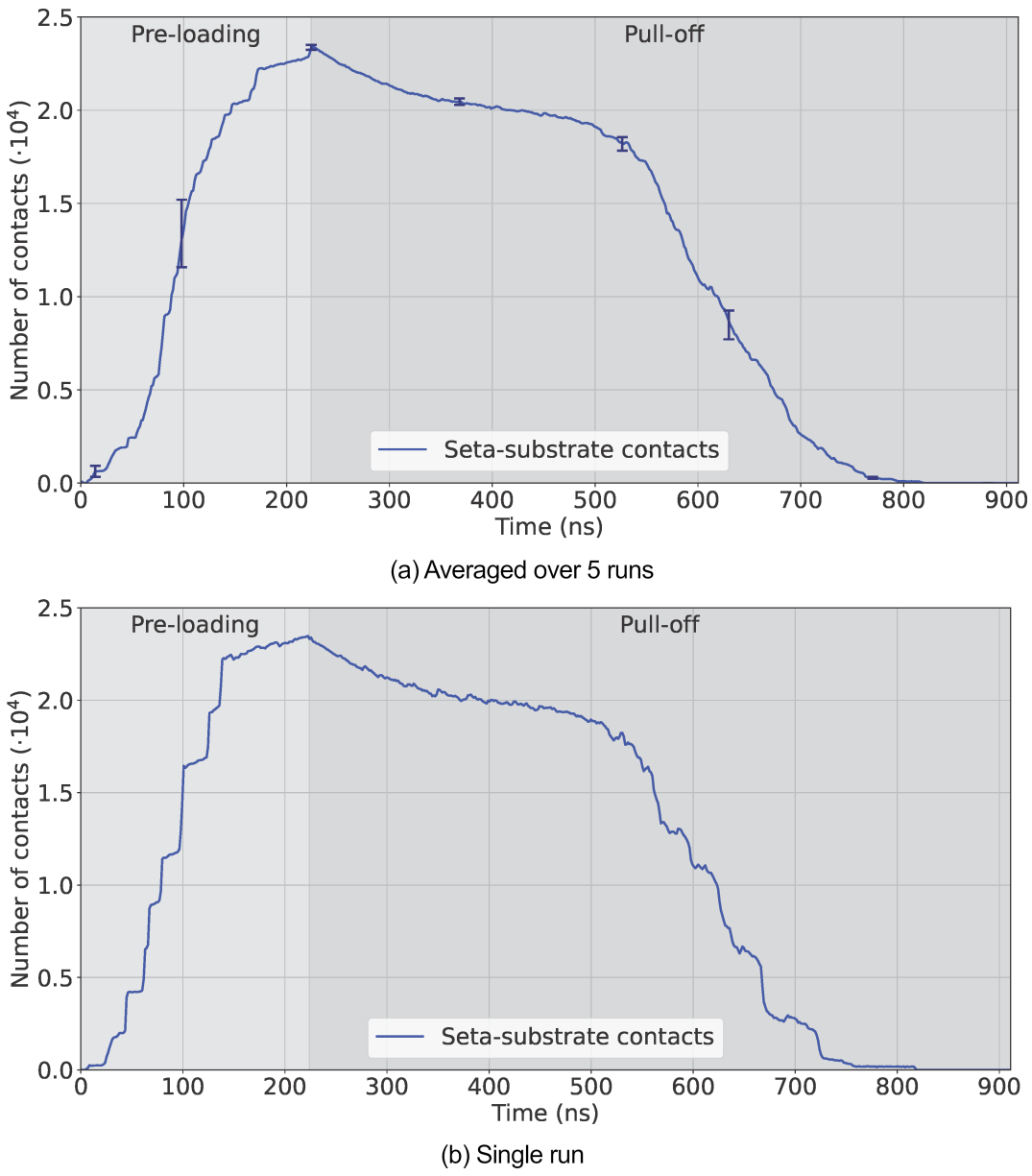

Figure 9: Number of seta–substrate contacts. (a) Averaged over five runs with error bars in a darker blue color at interesting points. (b) For a single run.

tip remained in contact. In terms of displacement, the tip's *X*- and *Y*-coordinates remained nearly unchanged, while the pad's *X*-coordinate increased slightly due to bending. The extent of bending decreased progressively from spatula 1 to 16, as shown by the increasing *X*-displacement of the pad while the tip displacement remained close to zero in Figure 12. In some cases, such as spatula 1, the tip tilted so far that parts of the pad came into contact with the substrate, causing an increase in the contact number (Figure 11). Spatula 3 exhibited a different behavior; its tip slid during preload and slipped at the end of it, which is evident in the tip displacement profile (Figure 12). Here, we use the term "sliding" to refer to gradual lateral movement of the spatula tip or pad across the substrate, and "slipping" to describe a sudden loss of contact followed by lateral motion. The contact profile for spatula 3 shows a zig-zag pattern, initial contact loss from tip tilting, followed by recovery from sliding and re-tilting, and finally a sharp drop due to tip slippage. Figure 13 shows snapshots of spatula 3 just before and after this tip slip event. Full animations of all spatulae are available in Supporting Information File 3. In contrast, Even-numbered spatulae (2,4,6,…,16) approached the substrate with their pads nearly parallel, leading to a classic jump-to-contact (snap-in in

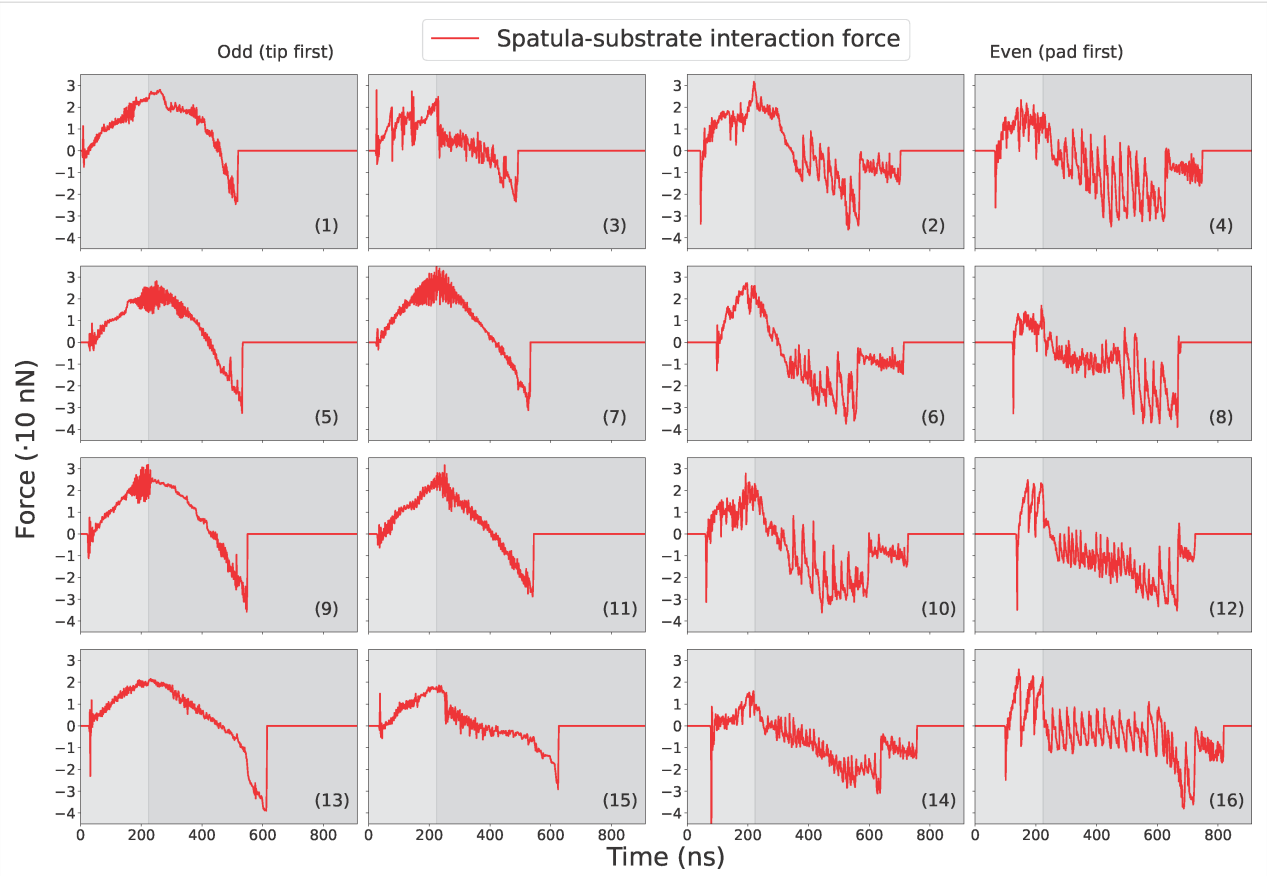

Figure 10: Spatula–substrate force profiles for every spatula for a typical pull-off run. For numbering of spatulae, see Figure 2. Sign convention as in Figure 8: positive = compression, negative = adhesion.

AFM terminology) upon first entering the attractive range. This transition from no-contact to intimate contact is visible in the animations in Supporting Information File 3. This resulted in a sharp, immediate increase in contact number, approximately ten times higher than that of odd-numbered spatulae, and a sharp negative spike in the adhesion force as seen in Figure 11 and Figure 10, respectively. Further loading gradually increased the number of contacts as more spatula beads came within the substrate's interaction range. The displacement profiles in Figure 12 show that, during preload, both the tip and pad X-coordinates start decreasing at a certain point, indicating sliding toward the $-X$-direction. Higher-numbered spatulae initiated sliding earlier and underwent greater displacement, indicating that sliding became more pronounced farther from the pulling point.

This behavior is clearly visible for a few example spatulae in the first two rows of Figure 14, that is, the moment of first contact, and the end of the preloading phase. The animations of individual spatulae provided in Supporting Information File 3 show these behaviors with more clarity. Figure 14 shows that odd-numbered spatulae maintained contact primarily through their tips, while even-numbered spatulae achieved full pad contact without requiring shearing.

Pull-off phase

During pull-off, spatulae experienced bending, shearing, and detachment, depending on their orientation and distance from the pulling point: As pull-off began, odd-numbered spatulae (tip-dominated contact) unbent (Figure 12), restoring the tip to a more perpendicular orientation. This resulted in a temporary increase in contact number before reaching a plateau. The compressive force gradually decreased, reaching zero before transitioning to a tensile (adhesive) force (negative in Figure 10). This force increased in magnitude until complete detachment occurred. Just before detachment, the tip's and pad's X-coordinates decreased slightly, suggesting a minor slide towards $-X$ before the spatula completely detached. At detachment, there was a sudden increase in the tip's Y-coordinate, marking separation from the substrate. After detachment, the spatula exhibited post-detachment oscillations, visible in fluctuations of its Y-coordinate, due to the release of stored elastic energy. The most negative force (peak adhesion) occurred just before the spatula tip fully detached from the substrate. Aver-

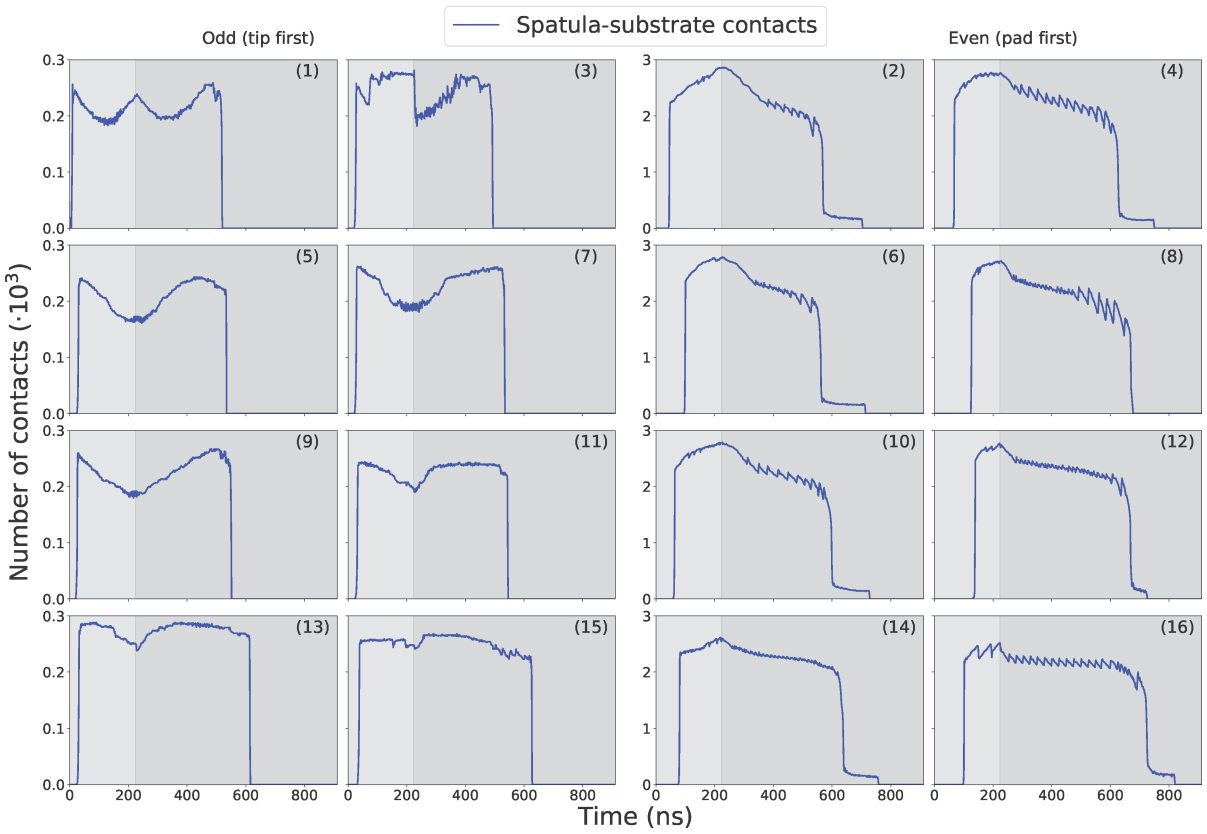

Figure 11: Spatula-substrate contact profiles of every spatula for a typical pull-off run. For numbering of spatulae, see Figure 2

aged across all tip-dominant spatulae, this adhesion magnitude was 30.5 ± 4.9 nN. This behavior is visible in the third row of Figure 14. It shows the moment of last contact for odd-numbered spatulae when the tip adhered to the substrate just before final detachment. In contrast, even-numbered spatulae (pad-dominated contact) underwent peeling and shearing simultaneously. Initially, as pull-off began, the tip's and pad's Y-coordinates remained nearly unchanged, but their X-coordinates increased, indicating sliding in $+X$, as the spatula moved back towards its original position. Just before detachment, the pad lost contact with the substrate, causing a sudden increase in its Y-coordinate, while the tip remained adhered to the substrate. The tip continued to slide in X even after the pad lifted, meaning that the spatula detached partially, while the tip remained in contact and underwent additional sliding. Finally, once the tip also detached, both the tip and pad moved away together, with post-detachment oscillations due to stored elastic energy being released. For these spatulae, the most negative (peak adhesion) force typically occurred earlier, specifically, when the pad detached from the substrate. After this, the spatula continued to adhere via its tip, but the corresponding force magnitudes were lower. The average adhesion magnitude across all pad-dominant spatulae was 35.9 ± 2.3 nN. The third row of Figure 14 illustrates the moment of last contact for even-numbered spatulae, when the pad had detached but the tip remained in contact just before final detachment. This two-stage detachment mechanism, where the pad peels off first, followed by the tip, is clearly visible in the contact profile, where the number of contacts sharply dropped to a non-zero plateau before eventually dropping to zero.

The animations in Supporting Information File 2 provide a clear visualization of the detachment sequence and mechanisms of individual spatulae. For the run used in our Figures Figure 10–Figure 14 and in the discussion so far, Table 4 lists the spatula detachment time in the order of detachment. The table confirms that the odd-numbered spatulae detached before even-numbered ones and that spatulae closer to the pulling force (i.e., lower-numbered) detached earlier.

Sliding and friction

Since our force field was never intended to reproduce macroscopic friction forces (see Subsection "Spatulae and substrate: particles"), and our substrate model is exceedingly smooth compared to real surfaces, agreement with experimental friction values at comparable sliding velocities was not a goal of this

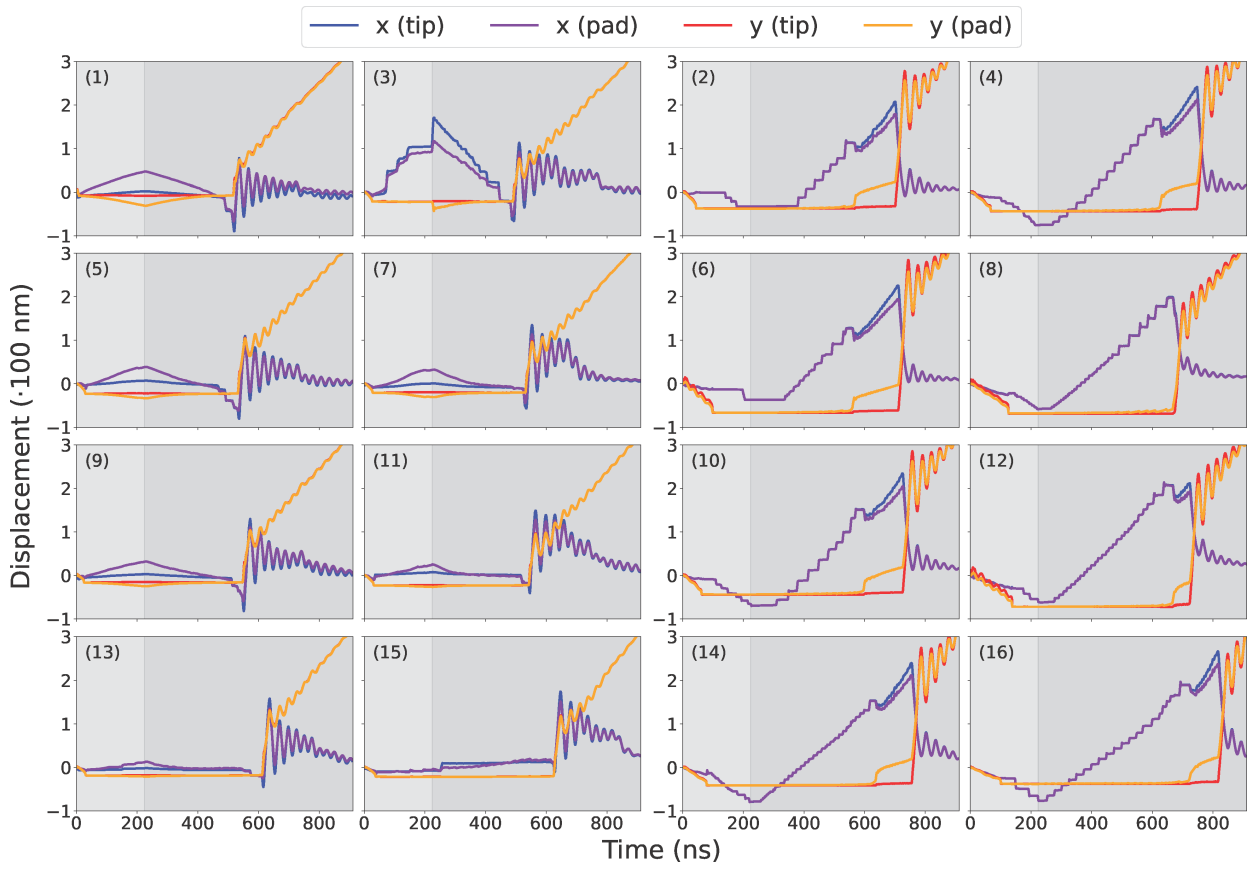

Figure 12: Spatula tip and pad displacement profiles along *X*-axis (along the surface in the direction of seta inclination) and *Y*-axis (surface normal) of every spatula for a typical pull-off run. For numbering of spatulae, see Figure 2; for the designation of tip and pad beads, see Figure 5.

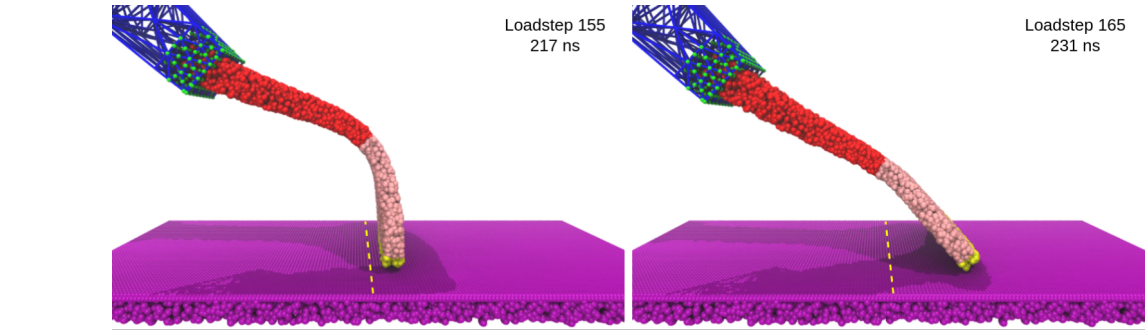

Figure 13: Snapshots of spatula 3 just before (load step 155; 217 ns) and after (load step 165; 231 ns) a tip slip event that occurred at the end of the preloading phase (load step 160; 224 ns). Yellow beads = spatula tip, pink beads = spatula pad, red beads = spatula shaft, green = anchor points, and blue = FE mesh. The yellow dashed line on the substrate is a marker near the initial spatula contact point.

study. Nonetheless, our simulations revealed significant spatula sliding, particularly among the pad-dominant (even-numbered) spatulae (Figure 2). During the 400–600 ns time interval, as visible in the pad displacement profiles (Figure 12), the in-plane displacement (*X*) of both the tips and pads increased nearly linearly, while the normal position (*Y*) remained constant. This indicates a sliding regime during which the contact numbers steadily decreased (Figure 11) and the adhesive forces increased (became more negative) (Figure 10). We estimated the sliding velocity in this regime by averaging the slopes of the pad displacements of all even-numbered (pad-dominant) spatulae, arriving at 0.66 ± 0.11 m/s. By contrast, shear speeds in AFM experiments range from 0.5 µm/s to 0.1 m/s [8,9,60], meaning our simulated shear speeds exceeded even the fastest

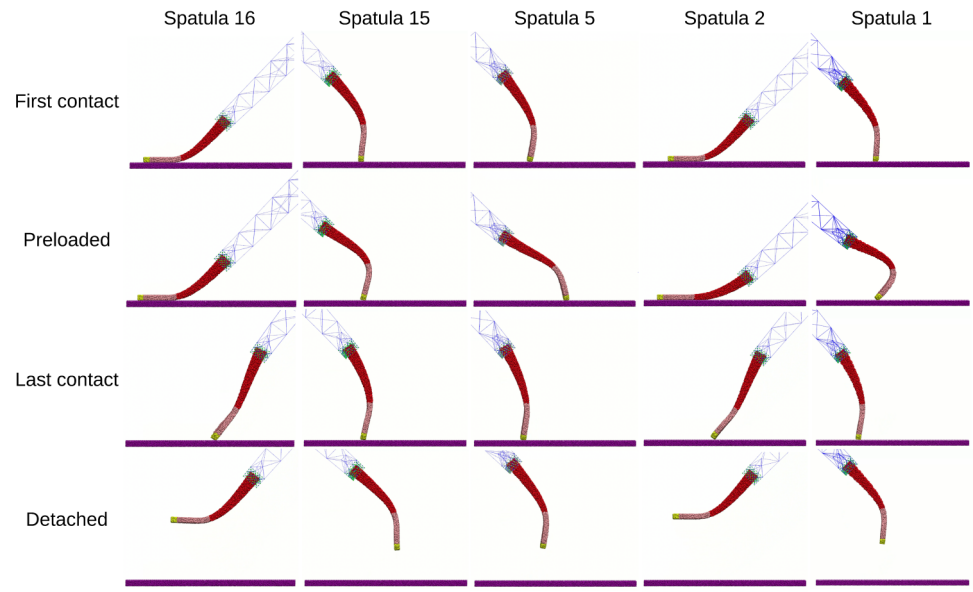

Figure 14: Snapshots of different spatulae at interesting stages during pull-off simulations. Yellow = spatula tip, pink = spatula pad, red = spatula shaft, green = anchor points, and blue = FE mesh.

Table 4: Load steps at which spatulae detached in the order of detachment for a typical pull-off run.

Spatula no.	Detachment load step	Detachment time (ns)
3	352	492.8
1	371	519.4
7	381	533.4
5	382	534.8
11	389	544.6
9	393	550.2
13	439	614.6
15	448	627.2
8	484	677.6
2	502	702.8
6	510	714.0
12	518	725.2
10	520	728.0
4	535	749.0
14	541	757.4
16	585	819.0

experimental rates several times. This is probably due to a much higher loading rate and a defect-free, smooth substrate in the simulations.

The friction coefficient μ is the unitless ratio of frictional force to normal force. Friction coefficients in gecko adhesion studies vary widely depending on anatomical scale. At the whole-foot or whole-toe level, shear-supported adhesion often yields μ values between 1 and 10, depending on the shear speed [9,60]. However, experiments using isolated gecko setal arrays, more comparable in scale to our model, report values in the range of 0.3–0.7 on smooth glass substrates at low shear speeds (0.1 mm/s) [60,61]. We conducted supplementary pure MD simulations of individual pad-dominant spatula–substrate systems subjected to preloading (up to 20 nN) followed by shear at 0.1, 1, 10, and 100 m/s. These simulations displaced the APs in the normal direction for preload, and then in the $+X$ direction for shear, while constraining the other two dimensions. Each simulation was repeated three times with different spatula–substrate systems. At the highest shear speed (100 m/s), the spatula deformed unphysically rather than sliding. At the lower speeds, however, we observed clear sliding and recorded both adhesion and lateral forces to compute friction coefficients. These were 0.30 ± 0.05, 0.19 ± 0.02, and 0.16 ± 0.01 for shear speeds of 0.1, 1, and 10 m/s, respectively. This downward trend is consistent with experimental observations, where the friction coefficient is known to decrease with increasing shear velocity.

In the seta pull-off simulations, the apparent friction coefficient (averaged over forty instances, i.e., five runs times eight pad-dominant spatulae) was 0.55 ± 0.13, likely elevated compared to the pure MD shear simulations because sliding was overlayed with peel-off. Notably, this value falls within the 0.3–0.7 range measured for isolated setal arrays, despite our simulated shear velocity (0.66 m/s) being orders of magnitude higher than in those experiments.

Comparison to literature

Our seta geometry and loading process were designed to closely follow the pure finite element model of a branched seta developed by Sauer and colleagues [21]. As with their model, ours represents an idealization of the natural geometry of gecko setae [57,62]. Sauer et al.'s simulations demonstrated how the peeling of spatulae upon retraction could extend the distance over which adhesion forces act before detachment, effectively increasing the "range" of adhesion. Their model also captured the sequential detachment of spatulae, a feature consistent with experimental observations [58]. However, their reported spatula pull-off force of 7.9 nN was not a predicted outcome of the simulation, but a prescribed input. In their contact formulation, the adhesive force was applied at a single point and defined by user input. In contrast, our model calculated the pull-off force as an emergent result of molecular interactions distributed over the entire spatula pad. This distinction between localized point contact and distributed area contact led to differences in detachment behavior and force response. In their model, detachment was instantaneous, with no further interaction following separation. In our simulations, detachment proceeded gradually via peeling, and interactions continued as long as some spatula beads remained within the non-bonded interaction range (12 nm) of the substrate. Their seta model used a Young's modulus of 2 GPa and Poisson's ratio of 0.2, values that were selected without direct experimental validation. These parameters resulted in a more compliant seta capable of greater deformation, which increased adhesion range but reduced the peak pull-off force. Our material parameters were ultimately derived from atomistic keratin simulations [12], which resulted in a stiffer response. The mesoscale spatula geometry in our model was based on SEM images from Xu and colleagues [23]. Our spatula was modeled using coarse-grained particles, whereas theirs used finite elements. Sauer et al. simulated spatula–substrate adhesion through a Lennard-Jones potential parameterized in earlier work [29]. Although their framework allowed for the inclusion of tangential sticking forces, this aspect was not explored in detail. Our model also used a potential (see Subsection "Spatulae and substrate: particles") parameterized against pull-off pressures from atomistic simulations. Like them, we did not explicitly account for frictional forces, and our substrate was atomically smooth, which affected sliding behavior. Additionally, their simulations are equilibrium in nature, while we perform non-equilibrium simulations with high loading rates. Consequently, our computed average spatula peak pull-off force was higher, at 33.2 ± 2.6 nN.

Our simulation approach followed the general protocol used in atomic force microscopy (AFM) experiments, particularly those by Huber et al. [58] and Niederegger and colleagues [63]. Our computed spatula peak pull-off force (≈33 nN) was higher than the 8–10 nN reported by Huber et al., and the 4–20 nN range observed in humidity-controlled studies by Huber et al. and Sun and colleagues [35,57,59]. Note that our geometry led to perfect contact of an ideal spatula with an ideal substrate, whereas in experiment, roughnesses and defects on both sides will lower the effective adhesion. Despite these systematic differences, our results fell within the broader range of experimental observations and captured behaviors such as bending, sliding, and peeling.

Conclusion

This paper presented a coupled multiscale molecular dynamics (MD) and finite element method (FEM) technique for simulating gecko seta adhesion on substrates. By adopting a hybrid approach, we avoided key limitations of purely MD-based or purely FEM-based simulations. Our study built on the seta geometry of Sauer et al. [21,22], as well as on multiscale MD–FEM simulations in polymer research, where they have been shown to be successful [43,47,48,50].

At the core of our work was a gecko seta-spatula model that integrated mesoscale molecular dynamics for the spatula–substrate interface with finite element calculations for the larger, micrometer-scale seta. It employed a spatula–substrate force field derived from atomistic (united-atom) simulations of gecko keratin. Even with an idealized seta geometry and the linear-elastic FE model, the multiscale simulations revealed a wider array of detachment mechanisms, including peeling, sliding, and bending. The study underscored how relatively small changes in spatula orientation could significantly alter load distribution and contact evolution. The results aligned with experimental AFM observations and prior computational findings, reproducing pull-off forces within the reported ranges. Additionally, the model captured mechanisms, such as spatula bending and sliding on the substrate, behaviors not permitted in earlier computational models and still inaccessible to current experimental methods. Furthermore, the results demonstrated that the MD–FEM non-equilibrium coupling scheme could reproduce key features and force magnitudes consistent with pure non-equilibrium MD simulations. Animations illustrating these behaviors are available in the Supporting Information File 1. Taken together, our results indicate that, at fixed interface chemistry, the realized pull-off is governed by geometry and load sharing through the branched seta, features captured by the concurrent MD–FEM coupling.

In future work, further refinements could incorporate more realistic substrates and seta structures, including hierarchical branching, rough substrates, or chemical patterning, ultimately bringing simulations closer to biological reality. We therefore view this concurrent MD–FE method as a stepping stone

for more comprehensive studies of gecko adhesion, as well as an adaptable platform for exploring other bioadhesive phenomena.

Supporting Information

Supporting Information File 1

Discussion around the effects and choice of parameters.
[https://www.beilstein-journals.org/bjnano/content/supplementary/2190-4286-16-141-S1.pdf]

Supporting Information File 2

Animations of the entire multiscale seta and a zoomed version focusing on all 16 spatulae.
[https://www.beilstein-journals.org/bjnano/content/supplementary/2190-4286-16-141-S2.zip]

Supporting Information File 3

16 Animations focusing on individual spatulae; adjacent spatulae have been omitted for clarity.
[https://www.beilstein-journals.org/bjnano/content/supplementary/2190-4286-16-141-S3.zip]

Acknowledgements

We acknowledge Prof. Dr. Hossein Eslami and Dr.-Ing. Sebastian Pfaller for helpful discussions related to method development and analysis of simulation results.

ORCID® iDs

Yash Jain - https://orcid.org/0000-0002-5980-6813
Saeed Norouzi - https://orcid.org/0009-0002-2390-278X
Stanislav N. Gorb - https://orcid.org/0000-0001-9712-7953

Data Availability Statement

Simulation files, scripts, and code to reproduce all results from this paper are available at: https://tudatalib.ulb.tu-darmstadt.de/handle/tudatalib/4618

References

1. Arzt, E.; Quan, H.; McMeeking, R. M.; Hensel, R. *Prog. Mater. Sci.* **2021,** *120,* 100823. doi:10.1016/j.pmatsci.2021.100823
2. Cross, R. *Chem. Eng. News* **2017,** *95* (4), 4. doi:10.1021/cen-09504-notw3
3. Autumn, K.; Liang, Y. A.; Hsieh, S. T.; Zesch, W.; Chan, W. P.; Kenny, T. W.; Fearing, R.; Full, R. J. *Nature* **2000,** *405,* 681–685. doi:10.1038/35015073
4. Zhang, W.; Wang, R.; Sun, Z.; Zhu, X.; Zhao, Q.; Zhang, T.; Cholewinski, A.; Yang, F. (Kuo).; Zhao, B.; Pinnaratip, R.; Forooshani, P. K.; Lee, B. P. *Chem. Soc. Rev.* **2020,** *49,* 433–464. doi:10.1039/c9cs00285e
5. Yu, X.; Tan, W.; Wang, R.; Zhang, Y.; Yang, L.; Gu, Y.; Zhang, C. Design, fabrication and characterization of gecko inspired micro-fibrillar adhesive materials for wall climbing robots. In *2022 IEEE International Conference on Cyborg and Bionic Systems (CBS),* IEEE, 2023; pp 110–115. doi:10.1109/cbs55922.2023.10115372
6. Prasad, A.; Mahato, K.; Chandra, P.; Srivastava, A.; Joshi, S. N.; Maurya, P. K. *J. Mol. Eng. Mater.* **2016,** *04,* 1640004. doi:10.1142/s2251237316400049
7. Lee, Y. B.; Shin, Y. M.; Kim, E. M.; Lee, J.-y.; Lim, J.; Kwon, S. K.; Shin, H. *J. Mater. Chem. B* **2016,** *4,* 6012–6022. doi:10.1039/c6tb01057a
8. Huber, G.; Orso, S.; Spolenak, R.; Wegst, U. G. K.; Enders, S.; Gorb, S. N.; Arzt, E. *Int. J. Mater. Res.* **2008,** *99,* 1113–1118. doi:10.3139/146.101750
9. Gravish, N.; Wilkinson, M.; Sponberg, S.; Parness, A.; Esparza, N.; Soto, D.; Yamaguchi, T.; Broide, M.; Cutkosky, M.; Creton, C.; Autumn, K. *J. R. Soc., Interface* **2010,** *7,* 259–269. doi:10.1098/rsif.2009.0133
10. Materzok, T.; Gorb, S.; Müller-Plathe, F. *Soft Matter* **2022,** *18,* 1247–1263. doi:10.1039/d1sm01232k
11. Materzok, T.; De Boer, D.; Gorb, S.; Müller-Plathe, F. *Small* **2022,** *18,* 2201674. doi:10.1002/smll.202201674
12. Materzok, T.; Canestraight, A.; Gorb, S. N.; Müller-Plathe, F. *ACS Nano* **2022,** *16,* 19261–19270. doi:10.1021/acsnano.2c08627
13. Materzok, T.; Eslami, H.; Gorb, S. N.; Müller-Plathe, F. *Small* **2023,** *19,* 2206085. doi:10.1002/smll.202206085
14. Joshi, S. Y.; Deshmukh, S. A. *Mol. Simul.* **2021,** *47,* 786–803. doi:10.1080/08927022.2020.1828583
15. Rudd, R. E.; Broughton, J. Q. *Phys. Rev. B* **1998,** *58,* R5893–R5896. doi:10.1103/physrevb.58.r5893
16. Liu, W. K.; Li, S.; Park, H. S. *Arch. Comput. Methods Eng.* **2022,** *29,* 4431–4453. doi:10.1007/s11831-022-09740-9
17. Logan, D. L. *A first course in the finite element method,* 4th ed.; Thomson, 2011.
18. Zienkiewicz, O. C.; Taylor, R. L.; Zhu, J. Z. *The finite element method: its basis and fundamentals,* 6th ed.; Butterworth-Heinemann: Oxford, UK, 2005.
19. Frenkel, D.; Smit, B. *Understanding Molecular Simulation: From Algorithms to Applications;* Academic Press: London, UK, 2002. doi:10.1016/b978-0-12-267351-1.x5000-7
20. Alder, B. J.; Wainwright, T. E. *J. Chem. Phys.* **1959,** *31,* 459–466. doi:10.1063/1.1730376
21. Sauer, R. A. *Comput. Methods Biomech. Biomed. Eng.* **2009,** *12,* 627–640. doi:10.1080/10255840902802917
22. Sauer, R. A.; Holl, M. *Comput. Methods Biomech. Biomed. Eng.* **2013,** *16,* 577–591. doi:10.1080/10255842.2011.628944
23. Xu, Q.; Wan, Y.; Hu, T. S.; Liu, T. X.; Tao, D.; Niewiarowski, P. H.; Tian, Y.; Liu, Y.; Dai, L.; Yang, Y.; Xia, Z. *Nat. Commun.* **2015,** *6,* 8949. doi:10.1038/ncomms9949
24. Zhao, B.; Pesika, N.; Zeng, H.; Wei, Z.; Chen, Y.; Autumn, K.; Turner, K.; Israelachvili, J. *J. Phys. Chem. B* **2009,** *113,* 3615–3621. doi:10.1021/jp806079d
25. Han, Q.; Wang, W.; Shen, H.; Feng, X.; Zhang, H.; Li, Q.; Sun, Y.; Wu, H.; Ji, A. *J. Bionic Eng.* **2024,** *21,* 707–717. doi:10.1007/s42235-023-00460-9
26. Sauer, R. A. *J. Adhes. Sci. Technol.* **2014,** *28,* 240–255. doi:10.1080/01694243.2012.691792
27. Gouravaraju, S.; Sauer, R. A.; Gautam, S. S. *J. Adhes.* **2021,** *97,* 1234–1254. doi:10.1080/00218464.2020.1746652

28. Hu, C.; Alex Greaney, P. *J. Appl. Phys.* **2014,** *116,* 074302. doi:10.1063/1.4892628
29. Sauer, R. A.; Li, S. *Int. J. Numer. Methods Eng.* **2007,** *71,* 931–962. doi:10.1002/nme.1970
30. Hu, S.; Jiang, H.; Xia, Z.; Gao, X. *ACS Appl. Mater. Interfaces* **2010,** *2,* 2570–2578. doi:10.1021/am100409s
31. Hu, S.; Xia, Z.; Gao, X. *ACS Appl. Mater. Interfaces* **2012,** *4,* 1972–1980. doi:10.1021/am201796k
32. Zhang, Q. K.; Li, L. X. *J. Adhes.* **2020,** *96,* 1449–1465. doi:10.1080/00218464.2019.1615466
33. Liu, S. Y.; Tang, M. M.; Soh, A. K.; Hong, L. *J. Nano Res.* **2013,** *22,* 85–93. doi:10.4028/www.scientific.net/jnanor.22.85
34. Kim, T. W.; Bhushan, B. *J. Adhes. Sci. Technol.* **2007,** *21,* 1–20. doi:10.1163/156856107779976097
35. Sun, W.; Neuzil, P.; Kustandi, T. S.; Oh, S.; Samper, V. D. *Biophys. J.* **2005,** *89,* L14–L17. doi:10.1529/biophysj.105.065268
36. Smith, M. *ABAQUS/standard user's manual, version 6.9;* Dassault Systèmes Simulia Corp., 2009.
37. Bower, A. F. *Applied mechanics of solids;* CRC Press: Boca Raton, FL, USA, 2009. doi:10.1201/9781439802489
38. Prowse, M. S.; Wilkinson, M.; Puthoff, J. B.; Mayer, G.; Autumn, K. *Acta Biomater.* **2011,** *7,* 733–738. doi:10.1016/j.actbio.2010.09.036
39. Taylor, A. M.; Bonser, R. H. C.; Farrent, J. W. *J. Mater. Sci.* **2004,** *39,* 939–942. doi:10.1023/b:jmsc.0000012925.92504.08
40. Hallahan, D. L.; Keiper-Hrynko, N. M.; Shang, T. Q.; Ganzke, T. S.; Toni, M.; Dalla Valle, L.; Alibardi, L. *J. Exp. Zool., Part B* **2009,** *312B,* 58–73. doi:10.1002/jez.b.21242
41. Alibardi, L. *Tissue Cell* **2013,** *45,* 231–240. doi:10.1016/j.tice.2013.01.002
42. Rizzo, N. W.; Gardner, K. H.; Walls, D. J.; Keiper-Hrynko, N. M.; Ganzke, T. S.; Hallahan, D. L. *J. R. Soc., Interface* **2006,** *3,* 441–451. doi:10.1098/rsif.2005.0097
43. Norouzi, S.; Furge, R.; Eslami, H.; Müller-Plathe, F. *J. Chem. Theory Comput.* **2025,** *21,* 358–373. doi:10.1021/acs.jctc.4c01332
44. Saether, E.; Yamakov, V.; Glaessgen, E. H. *Int. J. Numer. Methods Eng.* **2009,** *78,* 1292–1319. doi:10.1002/nme.2529
45. Davydov, D.; Pelteret, J.-P.; Steinmann, P. *Comput. Methods Appl. Mech. Eng.* **2014,** *277,* 260–280. doi:10.1016/j.cma.2014.04.013
46. Pfaller, S.; Rahimi, M.; Possart, G.; Steinmann, P.; Müller-Plathe, F.; Böhm, M. C. *Comput. Methods Appl. Mech. Eng.* **2013,** *260,* 109–129. doi:10.1016/j.cma.2013.03.006
47. Zhao, W.; Steinmann, P.; Pfaller, S. *Int. J. Numer. Methods Eng.* **2021,** *122,* 7431–7451. doi:10.1002/nme.6836
48. Pfaller, S.; Kergaßner, A.; Steinmann, P. *Multiscale Sci. Eng.* **2019,** *1,* 318–333. doi:10.1007/s42493-019-00028-y
49. Rahimi, M.; Karimi-Varzaneh, H. A.; Böhm, M. C.; Müller-Plathe, F.; Pfaller, S.; Possart, G.; Steinmann, P. *J. Chem. Phys.* **2011,** *134,* 154108. doi:10.1063/1.3576122
50. Jain, Y.; Ries, M.; Pfaller, S.; Müller-Plathe, F. *J. Chem. Theory Comput.* **2022,** *18,* 2375–2387. doi:10.1021/acs.jctc.1c00940
51. Verlet, L. *Phys. Rev.* **1967,** *159,* 98–103. doi:10.1103/physrev.159.98
52. Bussi, G.; Donadio, D.; Parrinello, M. *J. Chem. Phys.* **2007,** *126,* 014101. doi:10.1063/1.2408420
53. Dünweg, B.; Paul, W. *Int. J. Mod. Phys. C* **1991,** *02,* 817–827. doi:10.1142/s0129183191001037
54. Grønbech-Jensen, N.; Farago, O. *Mol. Phys.* **2013,** *111,* 983–991. doi:10.1080/00268976.2012.760055
55. Berendsen, H. J. C.; Postma, J. P. M.; van Gunsteren, W. F.; DiNola, A.; Haak, J. R. *J. Chem. Phys.* **1984,** *81,* 3684–3690. doi:10.1063/1.448118
56. Thompson, A. P.; Aktulga, H. M.; Berger, R.; Bolintineanu, D. S.; Brown, W. M.; Crozier, P. S.; in 't Veld, P. J.; Kohlmeyer, A.; Moore, S. G.; Nguyen, T. D.; Shan, R.; Stevens, M. J.; Tranchida, J.; Trott, C.; Plimpton, S. J. *Comput. Phys. Commun.* **2022,** *271,* 108171. doi:10.1016/j.cpc.2021.108171
57. Huber, G.; Mantz, H.; Spolenak, R.; Mecke, K.; Jacobs, K.; Gorb, S. N.; Arzt, E. *Proc. Natl. Acad. Sci. U. S. A.* **2005,** *102,* 16293–16296. doi:10.1073/pnas.0506328102
58. Huber, G.; Gorb, S. N.; Spolenak, R.; Arzt, E. *Biol. Lett.* **2005,** *1,* 2–4. doi:10.1098/rsbl.2004.0254
59. Huber, G.; Gorb, S. N.; Hosoda, N.; Spolenak, R.; Arzt, E. *Acta Biomater.* **2007,** *3,* 607–610. doi:10.1016/j.actbio.2007.01.007
60. Autumn, K.; Dittmore, A.; Santos, D.; Spenko, M.; Cutkosky, M. *J. Exp. Biol.* **2006,** *209,* 3569–3579. doi:10.1242/jeb.02486
61. Tao, D.; Wan, J.; Pesika, N. S.; Zeng, H.; Liu, Z.; Zhang, X.; Meng, Y.; Tian, Y. *Biosurface Biotribology* **2015,** *1,* 42–49. doi:10.1016/j.bsbt.2015.02.002
62. Holler, K. R.; Rasmussen, M. A.; Baio, J. E.; Jaye, C.; Fischer, D. A.; Gorb, S. N.; Weidner, T. *J. Phys. Chem. Lett.* **2022,** *13,* 2193–2196. doi:10.1021/acs.jpclett.2c00004
63. Niederegger, S.; Gorb, S.; Jiao, Y. *J. Comp. Physiol., A* **2002,** *187,* 961–970. doi:10.1007/s00359-001-0265-7

License and Terms

BEILSTEIN JOURNAL OF NANOTECHNOLOGY

Optical bio/chemical sensors for vitamin B_{12} analysis in food and pharmaceuticals: state of the art, challenges, and future outlooks

Seyed Mohammad Taghi Gharibzahedi[1] and Zeynep Altintas[*1,2]

Review

Open Access

Address:
[1]Division of Bioinspired Materials and Biosensor Technologies, Institute of Materials Science, Faculty of Engineering, Kiel University, 24143, Kiel, Germany and [2]Kiel Nano, Surface and Interface Science (KiNSIS), Kiel University, 24118, Kiel, Germany

Email:
Zeynep Altintas[*] - zeynep.altintas@tf.uni-kiel.de

* Corresponding author

Keywords:
carbon dots; cobalamin; energy transfer; fluorescence sensor; molecularly imprinted polymers (MIPs); nanobiosensor

Beilstein J. Nanotechnol. **2025,** *16,* 2207–2244.
https://doi.org/10.3762/bjnano.16.153

Received: 27 June 2025
Accepted: 13 November 2025
Published: 05 December 2025

This article is part of the thematic issue "Micro- and nanoscale effects in biological and bioinspired materials and surfaces".

Guest Editor: M. Rebora

Abstract

Vitamin B_{12} (VB_{12}) is an essential Co^{2+}-containing nutrient for neurological function, DNA synthesis, and red blood cell formation. Accurate and efficient VB_{12} quantification in food and pharmaceutical products is crucial due to its animal-derived dietary sources and the significant health implications of VB_{12} deficiency. Traditional methods for VB_{12} analysis, such as high-performance liquid chromatography and enzyme-linked immunosorbent assay, are often troublesome and time-consuming, and require high-tech laboratory setups. The current overview highlights the latest optical biosensing platforms in detecting Co^{2+} ions and VB_{12} using RNA aptamer–gold nanoparticles colorimetric sensors, surface plasmon resonance sensors, chemiluminescence and electrochemiluminescence biosensors, and fluorescence biosensors (i.e., chemosensors, nanoclusters/nanoparticles-based sensors, and carbon dot (CD)- and quantum dot (QD)-based sensors). The advent of optical biosensing technologies has resulted in a new era for VB_{12} analysis, characterized by the development of innovative CD- and QD-based sensors. These nanomaterials offer several advantages over conventional methods, including enhanced sensitivity, specificity, rapid detection, and the ability for real-time analysis. CD- and QD-based biosensors with excellent optical properties such as photoluminescence enable the detection of VB_{12} at negligible concentrations and in real-world samples with complex matrices. Furthermore, integrating these biosensors into cellular bioimaging and the potential for non-invasive in vitro and in vivo analysis demonstrate their versatility and applicability across a broad spectrum of biomedical research, diagnostics, and nutrient analysis.

Introduction

Micronutrients including vitamins and minerals play key roles in modulating body growth, preventing a wide range of diseases and disorders, and maintaining general health and wellness [1,2]. Apart from vitamin D, which the body can synthesize under sunlight exposure, all other micronutrients must be obtained via dietary intake [3]. Vitamins are classified into two

distinct categories, namely, water-soluble (e.g., vitamin C and vitamin B group) and fat-soluble (e.g., vitamins A, D, E, and K). Vitamin B_{12} (VB_{12}) is among B-group vitamins and cannot be absorbed through plant sources. This vitamin should be provided by consuming animal-derived products such as milk and dairy products, meat and meat products (e.g., liver, poultry, beef, pork, and ham), eggs, fish (e.g., tuna, trout, sardine, and salmon), and shellfish [2]. Recently, the presence of this vitamin in some plant sources such as microalgae (e.g., *Spirulina* and *Chlorella*) and mushrooms (e.g., shiitake, maitake, black trumpet, and golden chanterelle) species and Asian fermented soy products (e.g., tempeh and miso) has been reported [2,4,5]. Since these plant sources and their derived products cannot provide adequate amounts of active VB_{12} for the human body, the supplementation of plant products such as breakfast cereals and nondairy milk is considered a possible dietary strategy for preventing its deficiency among vegetarians and vegans [2,6,7]. The deficiency of VB_{12} can lead to several health issues such as pernicious anemia (PA), anemia, fatigue, nausea, and weight loss [2,8]. In contrast, excessive intake of VB_{12} may contribute to conditions like liver disease, neurotoxicity, kidney failure, or myeloproliferative disorders [2,9,10]. Consequently, monitoring the levels of VB_{12} in foods and pharmaceuticals is crucial for health management and disease prevention.

VB_{12} is also known as cobalamin due to the presence of a central cobalt ion (Co^{2+}) within the structure of its modified tetrapyrrole ring (Figure 1). A unique feature of the tetrapyrrole-derived ring in VB_{12} is that it has experienced a process called ring contraction. In this change, one of the carbon atoms that usually links the four pyrrole rings together is removed. This alteration results in a tighter and unevenly shaped large ring (corrin), making it different from the broader and more symmetrical rings found in heme and chlorophyll [2,11]. The structure of VB_{12} also includes a nucleotide loop that contains a unique base known as dimethylbenzimidazole (DMB). This nucleotide loop is attached to one of the propionate side chains of the corrin ring via an aminopropanol linker and stretches out below the corrin ring's plane. This particular arrangement allows the DMB base to act as a secondary ligand for the central cobalt ion (Co^{2+}), playing a crucial role in the molecule's structural integrity and biological activity. Within the structure of VB_{12}, Co^{2+} is capable of binding to an upper ligand, which can vary among different biochemical forms (–R, Figure 1), including hydroxy (OH–, OHCbl), cyanide (CN–, CNCbl), methyl (CH_3–, MeCbl), and adenosyl (AdoCbl) [2]. Nonetheless, CNCbl is the main form of this vitamin, as cyanide is commonly used to extract and purify the vitamin during the isolation process [2,12].

Quality control measures in the industry include the analysis of VB_{12} concentrations in serum extracted from blood plasma, pharmaceutical products such as tablets and injections, and fermentation-derived products [13]. The most common techniques to determine the VB_{12} content in different food and pharma formulations include high-performance liquid chromatography (HPLC) [14], HPLC coupled with inductively coupled plasma-mass spectrometry (ICP-MS) [15], and a diode array detector [16], atomic absorption spectroscopy [17], surface-en-

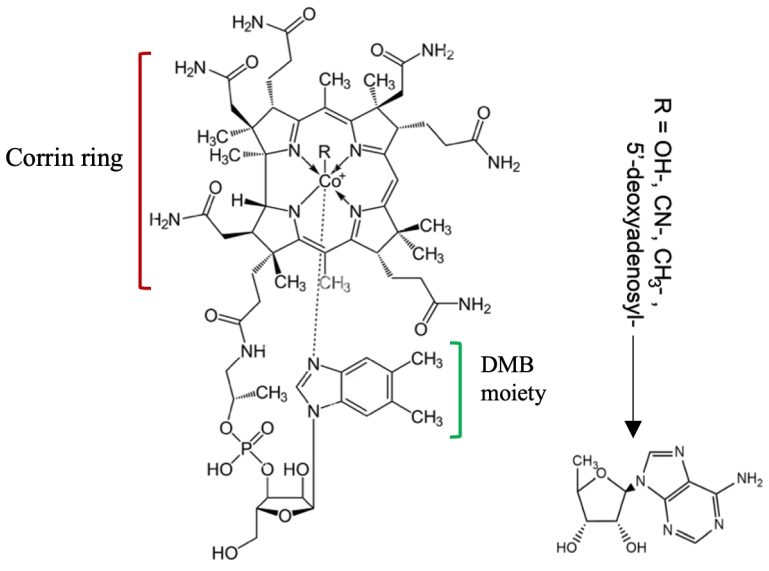

Figure 1: The chemical structure of VB_{12} ($C_{63}H_{88}CoN_{14}O_{14}P$; 1355.388 g/mol). Figure 1 was adapted from [2] (© 2023 S. M. T. Gharibzahedi et al., published by MDPI, distributed under the terms of the Creative Commons Attribution 4.0 International License, https://creativecommons.org/licenses/by/4.0).

hanced Raman spectroscopy [18,19], capillary electrophoresis [20], chemiluminescence [21-24], enzyme-linked immunosorbent assay (ELISA) [25,26], and electrochemical assays [2,27]. However, these methods involve complex procedures with long preparation times, poor selectivity, expensive equipment, and relatively costly or environmentally harmful reagents, which restrict their practical applications [2,13,28]. Consequently, there is a growing need to develop simple, rapid analytical systems such as biosensors to tackle these challenges by highly selective and sensitive detection of VB_{12} without requiring specialized skills.

Nowadays, electrochemical and optical biosensing platforms are one of the best approaches to detect VB_{12}. Various electrochemical methods have been employed for the effective detection of VB_{12}, focusing on its electroactive nature and the redox chemistry of the cobalt atom, primarily utilizing the Co^{3+}/Co^{2+} and Co^{2+}/Co^{+} redox reactions [2,27]. Although Antherjanam et al. reviewed different electrochemical sensing strategies for VB_{12} [27], to the best of our knowledge, the utilization of optical sensing platforms for detecting VB_{12} has not been yet reviewed. Optical sensing involves generating an optical signal as the output, utilizing the optical properties of the signal such as fluorescence, absorbance, refractive index, and Raman scattering for quantification and evaluation. The most prevalent types of optical sensing include colorimetric, plasmonic, fluorescence, and spectrophotometric methods due to their ease of use, affordability, and enhanced performance [29,30]. The current study critically reviews the newest findings on the mechanisms and designing principles of different optical sensing systems for sensitive and selective detection of VB_{12} in various media and real-world samples. Present limitations and emerging trends in a wide range of optical sensing systems of VB_{12} in analyzing food and pharmaceutical products are also highlighted.

Review

Nutritional requirements of vitamin B_{12}

The recommended daily intakes (RDIs) of VB_{12} in the UK and the US are 2.4 μg and 1.5 μg, respectively, which should be obtained by consuming animal-derived products, fortified foods, and vitamin supplements [2,31-34]. However, a higher dietary intake of VB_{12} for pregnancy and lactation is recommended. The RDIs of VB_{12} during lactation in the UK and the US are 2.0 and 2.8 μg, respectively. However, the RDI of VB_{12} for adults in the European Union is 4.0 μg [32,33]. The bioavailability of VB_{12} in food sources for healthy adults with typical absorption efficiency is roughly estimated to be 50%. In contrast, crystalline VB_{12} incorporated into supplements and fortified foods shows an absorption rate ranging from 55% to 74%. Hence, it is important to note that the absorption rates vary greatly depending on the specific food items; for instance, egg products, fish, and lean meat have an absorption rate of 24% to 36% (VB_{12} dose 0.30–0.94 μg), 42% (dose 1.95–2.18 μg), and 65% (dose 0.95 μg), respectively [34,35]. This water-soluble micronutrient is essential for improving brain and nervous system functions, blood cell development, bone health improvement, energy and DNA production, fertility and embryo development, control of neurological symptoms (e.g., stress, depression, dementia, and visual disturbances), and fatigue reduction [2,36]. VB_{12} deficiency represents a significant global public health concern, impacting approx. 6% of the global population and 1.6% to 10% of European communities [37]. The different demographic data showed that the most vulnerable groups to VB_{12} deficiency comprise geriatric populations, vegetarians and vegans, pregnant women, and breastfeeding infants of VB_{12}-deficient mothers, particularly in developing countries [10,38-40]. VB_{12} has a pivotal role in the development of the fetal and neonatal brain. Therefore, mothers with vegetarian and vegan diets should significantly increase the intake rate of this vitamin during pregnancy and lactation as VB_{12} deficiency can cause some fully reversible damage to newborns' brain and nervous system health [41,42]. A recent study revealed that VB_{12} deficiency should be considered one of the most important parameters in infants with hypotonia or neurodevelopmental retardation accompanied by thinning of the corpus callosum, cortical atrophy, and retardation in myelination [43]. The inadequate intake of VB_{12} from daily diets becomes clinically apparent after several years because of the substantial hepatic storage capacity (1–5 mg) and minimal losses via enterohepatic circulation [44]. Yet, this nutritional deficiency can quickly appear with VB_{12} malabsorption in patients with PA, celiac disease, inflammatory bowel disease, Whipple's disease, food-bound VB_{12} malabsorption, chronic alcoholism, patients taking antidiabetic medications (e.g., metformin) and bile acid sequestrants (e.g., cholestyramine), and patients with inherited disorders such as deficiency of the non-glycosylated protein of transcobalamin II (TC-II) [2,10,45-48].

Pathways of vitamin B_{12} absorption and metabolism

Two principal mechanisms exist for the absorption of VB_{12} (Figure 2), namely, passive diffusion and active transport [34,44]. In passive diffusion, a minor fraction (1–2%) of oral VB_{12} dose can be directly absorbed via the intestinal mucosa and the gastrointestinal tract surface without the need for the intrinsic factor (IF). If the active transport of VB_{12} is impossible, a high dose of oral VB_{12} (like 1.0 mg daily) is essential for ensuring an "adequate" intake of this vitamin in the body [34,49]. Accordingly, this IF-independent pathway is less efficient and becomes more significant in individuals with a defi-

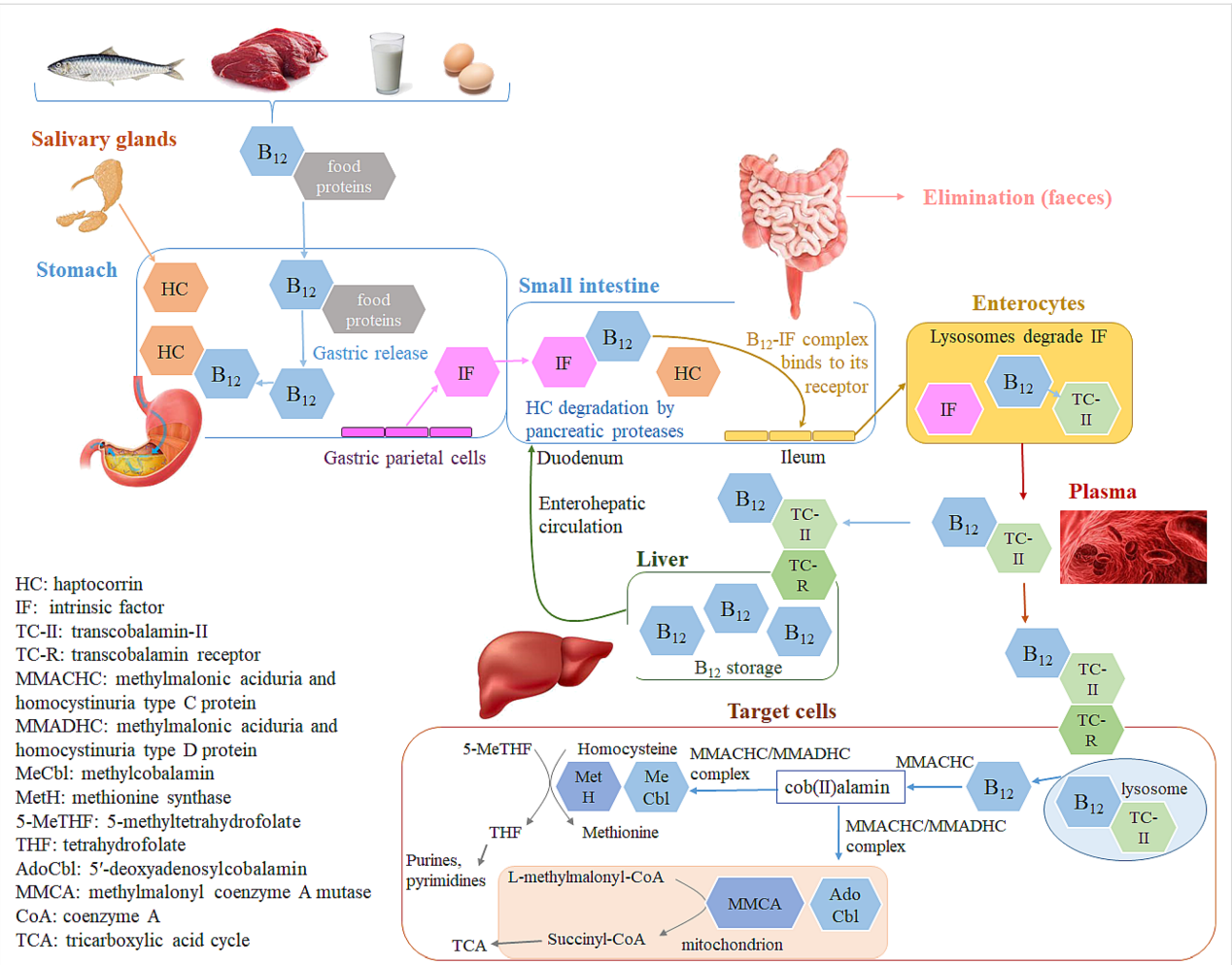

Figure 2: Graphical illustration of the ADME (absorption, distribution, metabolism, excretion) pathways for VB_{12}, including its enterohepatic recycling, as well as the mechanisms regulating its cellular absorption and physiological roles. Figure 2 was reproduced from [47] (© 2022 Ž. Temova Rakuša et al., published by MDPI, distributed under the terms of the Creative Commons Attribution 4.0 International License, https://creativecommons.org/licenses/by/4.0).

ciency or absence of IF, or when the capacity of the IF system is exceeded [50]. In the active transport pathway, the absorption of VB_{12} through receptors commences following its liberation from the dietary source. Food proteins act as carriers for dietary VB_{12}. The acidic conditions within the gastric lumen enable the liberation of this vitamin from food matrices, initiating its active absorption into the body. A glycoprotein known as haptocorrin (HC; transcobalamin-I or R-binder), secreted by salivary and esophageal glands, binds to the released VB_{12} and shields it against the acidic environment of the stomach [47,51,52]. Nevertheless, proteases present in the duodenum are capable of breaking down the VB_{12}–HC complex under alkaline conditions, allowing the liberated VB_{12} to easily link to the IF that is secreted from the stomach's parietal cells [12,44,47,48]. The VB_{12}–IF complex moves to the distal ileum, the primary location for its absorption. Here, it attaches to a specific receptor (Cubam) on the ileal enterocyte membrane and is internalized into the enterocytes via endocytosis. Meanwhile, lysosomes break down IF, freeing VB_{12}. This allows VB_{12} to bind to TC-II (HoloTC), facilitating its transport in the bloodstream and delivery to target cells [47,53,54].

The VB_{12}–TC-II complex is absorbed by cells through receptor-specific endocytosis. Once inside, it undergoes degradation in the lysosomes, resulting in the release of VB_{12}. This vitamin inside the target cell is transformed into its two active coenzyme forms (AdoCbl and MeCbl), via a complicated intracellular process involving various chaperone proteins and transporters, regardless of its form when ingested [34,47,50,55]. Acting as the main chaperone, the methylmalonic aciduria and homocystinuria type-C protein (MMACHC) captures VB_{12} exiting the lysosomes in a distinct base-off conformation. In this process, the protein replaces the 5,6-dimethylbenzimidazole ligand of VB_{12} with one of its histidine residues. Furthermore,

MMACHC plays a pivotal role in converting all variants of VB_{12} into the cob(II)alamin intermediate. This crucial step includes the decyanation of CNCbl and the dealkylation of alkylcobalamins (alkylCbls). These biochemical transformations are contingent upon the enzymatic action of glutathione S-transferase [47,56,57]. The subsequent transformation of cob(II)alamin into AdoCbl and MeCbl is facilitated by a complex of enzymes (i.e., MMACHC, methylmalonic aciduria and homocystinuria type-D protein (MMADHC), and methionine synthase reductase). The physiological functions of AdoCbl and MeCbl are activated when they bind to their respective target enzymes like methionine synthase (MetH) and methylmalonyl-CoA mutase (MCM) [58,59]. Accordingly, MeCbl emerges as the prevalent form of VB_{12} in plasma, while AdoCbl is dominant across all tissues [47,60]. MeCbl plays a crucial role in the remethylation of homocysteine (Hcy) to methionine, a process catalyzed by methionine synthase. In this reaction, 5-methyltetrahydrofolate (5-MTHF) donates the methyl group and is thereafter transformed into tetrahydrofolate. Methionine is then converted into S-adenosylmethionine (SAM), which serves as a vital methyl donor for the methylation of proteins, phospholipids, neurotransmitters, RNA, and DNA. In contrast, Ado-Cbl acts as a cofactor for MCM, facilitating the transformation of methylmalonyl-CoA into succinyl-CoA, with methylmalonyl-CoA being a byproduct of propionate metabolism. In the majority of mammals, propionate is generated through the catabolism of specific amino acids (e.g., Ile, Met, Thr, Thy, and Val), cholesterol, and the β-oxidation of odd-chain fatty acids [34]. This function of Ado-Cbl in the body supports energy production by facilitating the conversion of methylmalonyl-CoA to succinyl-CoA, a key step in the Krebs cycle, which is central to cellular energy generation [61]. The metabolic pathway of VB_{12} in the body concludes with its primary excretion via bile. The liver then reabsorbs and keeps the excreted VB_{12}, finishing its cycle in the body. Excess amounts of this vitamin are also expelled from the body via urine [2,62].

Monitoring methods of vitamin B_{12} deficiency

In clinical assessments, the deficiency level of VB_{12} can be measured based on the following biomarkers: (i) high levels of corpuscular volume of erythrocytes, (ii) low serum levels of VB_{12}, (iii) high plasma levels of total Hcy and methylmalonic acid (MMA), and (iv) decreased serum levels of VB_{12}–TC-II complex [10,32,43,47,63]. Cutoff values for target metabolites from literature reports or standard clinical values (SCVs) are as follows: total plasma VB_{12} (i.e., protein-bound VB_{12} and free VB_{12}) < 148 pmol/L or 200 ng/L (SCVs) [64-66], HoloTC < 35 pmol/L [65-67], Hcy > 12.6–13.0 μmol/L [65,67], MMA > 350 nmol/L [68,69], erythrocyte folate < 160 μg/L (SCVs) [65], and creatinine > 97 μmol/L (>1.1 mg/dL) for women as well as >124 μmol/L (>1.4 mg/dL) for men (SCVs) [32,65]. In an intriguing review, Aparicio-Ugarriza et al. highlighted the varying cut-off levels for defining VB_{12} deficiency used in studies from different countries, organized by the VB_{12} concentration threshold [70].

Initially, labs used microbiological tests to determine VB_{12} levels because of their favorable accuracy. These tests did not measure VB_{12} directly. Instead, microbiological analyses examined how certain bacteria consume this water-soluble vitamin, especially *Lactobacillus leichmannii* (ATCC 7830). Meanwhile, radioisotope dilution methods also came into use. But now, automated tests, owing to their higher speed and lower labor intensity, are the top choice for determining VB_{12}. Since the early 1990s, assays based on competitive-binding luminescence have been used to measure total VB_{12}. They include immunoassays such as electrochemiluminescence, chemiluminescence, enzyme-linked fluorescent, or colorimetric methods [71]. Immunoassays are the most common method to determine the total plasma VB_{12}. However, this technique can also produce inaccurately normal readings due to interference from anti-intrinsic factor (IF-Ab) or variables like heterophilic antibodies [72,73]. However, Zhang et al. have recently collected VB_{12} through solid-phase extraction and analyzed it using an LC tandem mass spectrometry (LC-MS/MS) method. They showed that the LC-MS/MS assay can efficiently contribute to distinguishing false-normal VB_{12} results reported by immunoassays [72]. ELISA, as well as electrochemiluminescent and chemiluminescent immunoassays, are usually applied to test HoloTC in clinical labs [26]. Not only does the accuracy of HoloTC tests still depend on the specific method but some rare genetic variations in the TC gene may also cause falsely low HoloTC results, even when no real deficiency exists and other lab markers are normal. HoloTC measurements are usually not affected by high IF-Ab levels. However, HoloTC levels in a few cases (particularly with PA) might misleadingly appear normal [26,71]. Looking back, techniques like paper chromatography, thin-layer chromatography, spectrophotometry, and ELISA were employed to measure MMA concentrations. However, mass spectrometry methods, particularly LC-MS/MS, have gradually gained popularity for their enhanced sensitivity and specificity [26]. Currently, automated enzyme immunoassays, GC-MS, LC-MS, and HPLC with either fluorescent or electrochemical detection are utilized to assess the total HCY level [26,71,74].

Optical biosensing techniques of vitamin B_{12}

RNA aptamer-based AuNP colorimetric biosensors

In this sensing system, the recognition material is the RNA aptamer, the indicator material is the gold nanoparticle (AuNP), and the sensing signal is colorimetric. The excellent optical-electronic characteristics of AuNPs have been recently considered in point-of-care (POC) diagnostics for different disorders

and diseases. Resonance among the free electrons at the surface of colloidal AuNPs, induced by the interaction with light energy, causes the light to be absorbed in the blue-green and red parts of the visible spectrum. Consequently, the appearance of colors in AuNP suspensions is substantially influenced by their particle size and dispersion speed. 10–20 nm AuNPs with a narrow size distribution tend to absorb light from the blue-green spectrum and reflect red light. In contrast, their aggregation leads to a light absorption shift to longer wavelengths, resulting in reflecting light ranging from pale blue to purple [75,76].

Selvakumar and Thakur developed a colorimetric sensor for detecting VB_{12} using AuNPs and a stable modified RNA aptamer. The RNA aptamer, which attaches to VB_{12}, triggers the aggregation of AuNPs, resulting in a color shift from red to purple. The sensor's effectiveness was confirmed with a limit of detection (LOD) of 0.1 μg/mL and a recovery rate (RR) of 92.0–95.3% for VB_{12}, equivalent in accuracy to ultraviolet–visible (UV–vis) spectrometry. Since the sensor's LOD for VB_{12} was above the recommended dietary allowance level (0.02–0.03 μg/mL in food), they emphasized performing an optimization study to reach a lower acceptable LOD for the regulatory standard [77]. Kumudha et al. characterized the HPLC peak of extracts of VB_{12} obtained from the green microalgae *Chlorella vulgaris* using MS/MS, selected ion recording, and multiple reaction monitoring. They found that MeCbl was the main constituent of the extracted VB_{12} and analyzed by chemiluminescence, AuNPs-based RNA aptamers, and microbiological techniques. The corresponding amounts of MeCbl were 26.84, 28.02, and 29.87 μg/100 g dry weight, respectively. Accordingly, there was no significant difference in the detected amounts of MeCbl among the utilized diagnostic assays [78].

Small-molecule-based colorimetric chemosensors for cobalt/VB_{12} detection

In this class, the recognition material is a small-molecule receptor (chemosensor), the indicator material is its intrinsic chromophore or fluorophore scaffold, and the sensing signal is primarily colorimetric, with some examples also producing dual colorimetric/fluorescent outputs.

The absence of Co^{2+} in the body can increase the PA risk, as the central Co^{2+} in the corrin ring of VB_{12} plays a pivotal role in iron metabolism to synthesize hemoglobin. Conversely, excessive absorption of Co^{2+} causes some negative impacts on health, including asthma, reduced cardiac output, and heart and lung diseases [79].

A new colorimetric chemosensor fabricated from a pyridyl moiety and a 2-chloro-*N*-(2-((3-nitro-2-oxo-2*H*-chromen-4-yl)amino)phenyl)acetamide group was developed to detect Co^{2+} ions in water with high selectivity. Here, the small molecule served as the recognition receptor, its coumarin scaffold acted as the indicator chromophore, and the sensing signal was a visible change from colorless to pale violet [80]. When anchored to silica, this sensor could effectively oxidize Co^{2+} to Co^{3+} in almost entirely aqueous environment. Na et al. also showed that this chemosensor had a superb capacity to be an optical solid sensor [80]. Maity and Govindaraju earlier reported a colorimetric coumarin-conjugated thiocarbanohydrazone-based chemosensor, which could selectively detect Co^{2+}. In this system, the coumarin–thiocarbanohydrazone acted as the recognition element, the coumarin moiety provided the indicator, and the sensing signal was a colorimetric shift from light-yellow to deep-pink with a minimum LOD of 1.0 μM. Furthermore, this sensor also showed potential for bioimaging *Escherichia coli* cells due to its fluorescence response when exposed to Co^{2+} [81].

A new fluorescent–colorimetric chemosensor was designed based on 1,8-bis{2-{*N*-[2′-(8′-hydroxy-9,10-anthraquinon-1-yloxy) ethyl] benzimidazoliumyl} ethoxy}-9′,10′ anthraquinone hexafluorophosphate to detect Co^{2+}, in which the benzimidazolium–anthraquinone scaffold acted as the recognition unit, the anthraquinone moiety as the indicator, and the signals included a visible color change from orange to red together with fluorescence quenching. A hypochromatic shift of about 27 nm and a new absorption peak at 487 nm were found in the absorption spectrum. Utilizing this chemosensor in integrating with a smartphone resulted in an LOD of 0.47 μM for Co^{2+} [82]. A coumarin platform was utilized to fabricate a new ratiometric and colorimetric chemosensor for Co^{2+}, where the coumarin scaffold functioned as both the recognition unit and the chromophoric indicator, while the sensing response was expressed through ratiometric spectral variation. Upon interacting with this cation, a significant 44 nm shift in its absorption spectra by altering color from yellow to red was recorded, which could be easily seen with the naked eye. Using both standard and ratiometric absorption spectrometry techniques, the linear range of detecting Co^{2+} was found to be 0–10 μM with an LOD of less than 0.31 μM [83].

An innovative biosensing platform (i.e., a thiosemicarbazide-based Schiff-base chemosensor containing a naphthalene moiety (TSNCS)) has been recently designed for the colorimetric detection of Ni^{2+} and Co^{2+} ions, in which the Schiff-base provided the recognition site, the naphthalene group served as the chromophoric indicator, and the detection relied on a distinct colorimetric response. Upon exposure to these ions within aqueous solutions of acetonitrile, TSNCS visibly shifted from colorless to dark yellow, enabling instant and accurate de-

termination with low LODs for Ni^{2+} (0.0114 μM) and Co^{2+} (0.0168 μM). This study also successfully applied paper strips coated with TSNCS for swift ion detection in water environments. Moreover, it was utilized for both quantifiable and descriptive evaluation of Co^{2+} in commercial VB_{12} and real-water samples [84]. Kim et al. employed a new chelated-type Schiff base for creating a colorimetric chemosensor to detect Co^{2+} (0.66 μM LOD) and Cu^{2+} (0.88 μM LOD) ions in water, where the Schiff-base acted as the recognition moiety, the ligand framework functioned as the indicator, and the response was monitored through a straightforward colorimetric change from colorless to yellow [85]. Another dual chemosensor composed of a fluorophore (quinoline) and a hydrophilic functional group (N^1,N^1-dimethylethane-1,2-diamine) was fabricated to detect Zn^{2+} (0.01 μM LOD) and Co^{2+} (6.89 μM LOD) in both biological systems and aqueous environments, with the diamine serving as the recognition unit, quinoline as the indicator scaffold, and the outputs expressed as fluorescence enhancement for Zn^{2+} and a visible chromatic shift for Co^{2+}. An increase in the fluorescence intensity and a color transition from colorless to yellow led to the determination of these cations, respectively [86]. Alhalafi [87] has currently explored that the reaction of 3-amino-2-styrylquinazolin-4(3*H*)-one with phenols in a diazotization-like process produced a range of azo derivatives, 3-(diazenyl)-2-(styryl)quinazolin-4(3*H*)-one for detecting metal ions of Co^{2+} and Fe^{2+}, where the azo-quinazolinone acted as the recognition material, the azo chromophore acted as the indicator, and the sensing readout was a distinct spectral absorption response. Specifically, the derived compound of 3-((2-hydroxynaphthalen-1-yl)diazenyl)-2-(styryl)quinazolin-4(3*H*)-one emerged as a rapid tool for the determination of Co^{2+} (λ_{max} = 582 nm) and Fe^{2+} (λ_{max} = 566 nm) in water.

Surface plasmon resonance-based biosensors

Surface plasmon resonance (SPR) sensors operate through a simple and effective mechanism in five key steps: (i) An electromagnetic field at the metal–dielectric interface excites coherent electron oscillations in the metal; (ii) this leads to the generation of surface plasmon polaritons (SPPs; i.e., oscillating charge densities), (iii) SPPs produce a decaying electric field that extends into the surrounding medium; (iv) the evanescent field is highly sensitive to changes in the medium's refractive index; and (v) during resonance, incident light absorption at a specific angle or wavelength results in a signal peak, which shifts with any refractive index changes due to the analyte [88,89].

Gao et al. applied biomolecular interaction analysis based on SPR to assess B-group vitamins such as VB_{12} enriched into infant formulas based on milk, whey protein concentrate, lactose-free milk protein isolate, or partially hydrolyzed nonfat milk, where the recognition was mediated by VB_{12}-binding proteins, the SPR sensor chip acted as the indicator surface, and the sensing signal was generated through resonance shifts. To prepare the extraction buffer, a 0.2% sodium cyanide solution was diluted with a phosphate–citrate buffer at pH 4.5. This buffer was then added to an infant formula sample, which was subsequently autoclaved at 121 °C for 25 min. The purpose of this step was to denature the VB_{12} binding protein present in the sample and liberate the vitamin for the subsequent analysis. Low repeatability based on relative standard deviation (RSD < 2%) with a high RR (94.7–109.1%) was reported for all B-group vitamins [90]. This study was in the continuation of works performed by Indyk et al. [91] and Cannon and colleagues [92]. Indyk et al. applied a similar technique to measure VB_{12} in various foods (i.e., dried and fluid milk, infant formula, cereal-based foods, baby food composite, meat, and liver) using a non-labeled inhibition protein-binding assay, in which the recognition relied on protein–vitamin binding, the sensor surface acted as the indicator, and the signal was measured by resonance response. The quantitation range and RR were 0.08–2.40 ng/mL and 89–106%, respectively [91]. Cannon et al. employed SPR to indirectly detect VB_{12} by observing the interactions between this vitamin and its specific binding proteins, with the protein interaction acting as the recognition step, the SPR chip as the indicator, and the resonance change as the output signal. This method achieved an LOD of approximately 1 mg/mL for VB_{12} [92]. In the Association of Official Agricultural Chemists (AOAC) international meeting on June 29, 2011, the committee eventually decided to collaboratively assess VB_{12} by SPR, specifically for infant formula and adult nutritionals through the Biacore Q™ biosensor and Qflex™ Kit (RSD of 1.59–27.8%). They confirmed that the method satisfies the performance requirements set by the stakeholder panel on infant formula and adult nutritionals for infant and pediatric nutritional formulas [93].

SPR sensors were also applied to determine VB_{12} in ten commercial milk powders in less than 6 h, where covalently immobilized VB_{12} on a CM5 chip acted as the recognition element, the chip surface itself served as the indicator platform, and the sensing signal was derived from resonance changes. The vitamin chip was stable, with an RSD of less than 10% over 50 cycles. Also, the LOD for VB_{12} was 0.006 μg/100 g with an RR of 92.1–104.1% [94]. Çimen and Denizli have recently developed a plasmonic nanosensor for the real-time detection of B-group vitamins (i.e., B_2, B_9, and B_{12}) in infant formula and milk samples using molecular imprinted polymers (MIPs), where the MIP cavities served as the recognition sites, the SPR chip surface as the indicator, and the resonance shift as the sensing signal. For SPR chip surface modification, they initially added allyl groups to the SPR chip surface using allyl

mercaptan. To eliminate any unattached allyl mercaptan, the chip underwent washing with distilled water and ethanol, followed by drying under vacuum at 200 mmHg and 25 °C. The determined LOD for vitamins B_2, B_9, and B_{12} were 1.6×10^{-4}, 13.5×10^{-4}, and 2.5×10^{-4} ng/mL, respectively. Not only was a remarkably excellent selectivity, reproducibility, and storage stability for the SPR sensor recorded, but a strong association between the SPR sensor and LC-MS/MS findings was found [95].

Recently, Bareza et al. have reported that graphene nanostructures, which can confine mid-infrared plasmons at the nanoscale, serve as an advanced spectroscopic platform for improved molecular identification. They highlighted graphene's potential in biosensing owing to its capability to be functionalized with dissimilar biomolecules such as enzymes and DNA. In their study, they presented a quantitative bioassay leveraging mid-IR plasmon resonance in graphene nanostructures to detect VB_{12}, where functionalized graphene nanoribbons provided the recognition sites, the nanostructured graphene surface acted as the plasmonic indicator, and the sensing signal was a mid-IR resonance shift. This approach achieved an LOD of 53.5 ng/mL using graphene nanoribbons modified with specific recognition elements [96]. Moreover, Bareza et al. demonstrated the scalability and industrial applicability of this bioassay through the use of large-area nanostructured graphene films, proving the promising future of graphene-based mid-IR localized SPR (LSPR) biosensing platforms [96].

Chemiluminescence and electrochemiluminescence biosensors

Chemiluminescence (CL) sensors detect light emissions released from the chemical reaction process. After the reaction of certain chemicals, CL sensors produce light without requiring an external light source. In such systems, the recognition is usually provided by specific reactive molecules, the luminophore acts as the indicator, and the sensing signal is the emitted light. This chemical process involves the excitation of molecules to higher energy states during the reaction, and then they emit photons (light) when they return to their ground state [97]. In contrast, electrochemiluminescence (ECL) sensors integrate electrochemical and chemiluminescent principles. The light-emitting reaction is started by applying an electrical voltage that triggers redox reactions on the electrode surface. Here, the recognition relies on analyte–electrode interactions, the electrode or surface-bound luminophore acts as the indicator, and the signal is the electrochemically induced light emission. These reactions generate excited states that emit light as they relax back to lower energy levels [98]. Therefore, the main difference between CL and ECL is how the excited states are generated: The light production in CL and ECL is based on chemical energy and electrochemical reactions, respectively. Table 1 shows a summary of analytical features for CL-based assessment of Co^{2+} and VB_{12} [99-114].

Qin et al. designed a CL sensor to detect VB_{12}, incorporating flow injection analysis, where the catalytic activity of Co^{2+} released from the VB_{12} structure acted as the recognition element, luminol served as the indicator luminophore, and the sensing signal was the chemiluminescent emission triggered by H_2O_2. The sensor operates according to the catalytic action of Co^{2+}, which is released from the VB_{12} structure through acid treatment, on the CL reaction involving luminol (which is electrostatically immobilized on an anion-exchange column) and hydrogen peroxide (H_2O_2). The H_2O_2 is electrochemically produced in real-time by utilizing a negative bias to an electrode, which converts dissolved oxygen in the flow cell. The linear range, LOD, and RSD for the detection of VB_{12} were 0.001–10 mg/L, 0.0035 mg/L, and less than 3.5%, respectively [102]. Also, Kumar et al. could well detect VB_{12} in multivitamin capsules, VB_{12} tablets, and VB_{12} injections by fabricating a sensitive CL sensor based on the reaction of VB_{12} and luminol under alkaline conditions using the carbonate enhancement effect, where VB_{12} acted as the recognition analyte, luminol as the indicator, and the CL light emission as the signal. Linear range, LOD, RSD, and RR were 5 pg/mL, 10 pg/mL to 1.0 µg/mL, 0.30–1.09%, and 97.0–99.2%, respectively. The developed approach suggested remarkable benefits, including simplicity, lower reagent use, improved sensitivity and analytical efficiency, and ease of implementation [22]. Moreover, Lok et al. assessed VB_{12} doses in a continuous-flow lab-on-a-chip system based on luminol-peroxide CL tests to monitor Co^{2+} in the molecular structure of VB_{12} [24], where the released Co^{2+} acted as the recognition target, luminol as the indicator luminophore, and the CL detected in the microchannels as the sensing output. The device includes two micromixers and a double spiral microchannel for optical detection, operating in two modes, namely, "mode I" with direct in-chip acidification and "mode II" with pre-detection external acidification. In mode I, the VB_{12} sample undergoes direct acidification within the microfluidic device. Through separate inlets (A, B, C, D, and E), the system receives, respectively, the VB_{12} sample, HCl, NaOH, luminol, and H_2O_2. The process begins with mixing the VB_{12} sample with diluted HCl in a designated acidification channel to release Co^{2+}. Subsequently, NaOH is added to neutralize the acid mix. This neutralized sample is then integrated with luminol and H_2O_2 in a reaction channel, where the resulting CL signal is detected. In mode II, acidification happens outside the device. Inlets A and B are closed off, and the externally acidified VB_{12} sample and luminol and H_2O_2 are introduced, respectively, via inlets C, D, and E. These components mix in the reaction channel, initiating the CL detection process. Mode I

Table 1: Analytical features of CL-based sensing platforms of CO^{2+} and VB_{12}.

Sample type/Ref.	Analyte(s)	Flow technique[a]	Sample throughput (1/h)	Reagents[c]	Total flow rate (mL/min)
	CL response time (s)	linear range	LOD	RSD (%)	RR (%)
pharmaceutical preparations [99]	Co^{2+}/VB_{12}	FIA	–	luminol–H_2O_2	7
	–	1–100 mg/L Co^{2+}	0.02 mg/L Co^{2+}	2.9	95.3–103.1
degradation studies of CNCbl [100]	Co^{2+}	MSFIA	>180	luminol–H_2O_2	25
	–	0.015–5.0 µg/L	0.015 µg/L	–	–
high-purity iron sample [101]	Co^{2+}	FIA	<15	luminol–H_2O_2	2.8
	–	0.5–100 µg/L	0.5 µg/L	4.0	–
pharmaceutical preparations [102]	Co^{2+}/VB_{12}	r-FIA	60	luminol immobilized on an anion exchanger and H_2O_2 electrogenerated	14
	–	1.0×10^{-3}–10 mg/L	3.5×10^{-4} mg/L VB_{12}	<3.5	–
human serum, fish tissue, egg yolk, pharmaceuticals [103]	Co^{2+}/VB_{12}	FIA	100	luminol-O_2	6
	1.5–5.0	2.0×10^{-10}–1.2×10^{-6} g/L VB_{12}	5.0×10^{-11} g/L VB_{12}	<5.0	92.0–107.8
pharmaceutical injections [104]	VB_{12}	FIA	–	luminol–H_2O_2	3
	10	8.68–86.9 ng/mL	0.89 ng/mL	2.5	94.8–102.6
pharmaceutical (VB12) injections [105]	Co^{2+}	FIA	60	$(1,10\text{-phenanthroline})_3$ complex on the lucigenin-periodate reaction	2.45
	–	1.0×10^{-9}–3.0×10^{-7} g/mL	4.4×10^{-10} g/mL	2.3	–
injection ampoules [106]	VB_{12}	FBL (silicon photodiode detector)	72	luminol–H_2O_2	11.33–11.88
	–	2.4–12.0 µg/L	0.11 µg/L	<2.2	97.8–102.1
injections, tablets [107]	Co^{2+}/VB_{12}	FIA	–	luminol–percarbonate (H_2O_2 source)	10
	2	10 –5,000 µg/L Co^{2+}	9.3 µg/L	2.2–4.4	95.8, 97.7
pharmaceuticals (ampoules, tablets) [108]	Co^{2+}	continuous FIA with CCD photodetector	–	luminol–percarbonate (H_2O_2 source)	19.8
	2	4.0–300 µg/L	0.42 µg/L	2.2, 4.2	94.7–103.5

Table 1: Analytical features of CL-based sensing platforms of CO^{2+} and VB_{12}. (continued)

20 µg VB_{12} tablets, multivitamin tablets [110]	VB_{12}	microfluidics (chip fabricated by a soft-lithographic procedure using PDMS)	–	AuNPs-enhanced luminol-$AgNO_3$	0.03
	–	0.25–100 ng/mL	0.04 ng/mL	1.56	93.0–105.5 (VB_{12} tablets), 98.5–103.7 (multivitamin tablets)
egg yolk [111]	Co^{2+}/VB_{12}	–[b]	–	DBS, LDHs, H_2O_2	–
	4.0–4.5	1.0 ng/mL–5.0 µg/mL VB_{12}	0.57 ng/mL VB_{12}	2.8	96.0–103.0
pharmaceutical preparations [112]	VB_{12}	bead injection with multicommutation	11	luminol, H_2O_2, Dowex 1 × 8 beads	2.6
	–	1.7–50 µg/L	0.5 µg/L	5.3	92.0–103.2
pharmaceuticals, human serum, egg yolk, fish tissue [113]	Co^{2+}/VB_{12}	liquid system, chitosan membrane adsorption	–	luminol–H_2O_2	–
	–	0.4 pg/L–40 µg/L	4.0 fg/L Co^{2+}	–	–
energy drinks [114]	VB_{12}	dipstick-based immunochemiluminescence	–	VB_{12} antibody, VB_{12}–alkaline phosphatase conjugate, CDP-Star substrate, Tween-20, EDC-NHS, XAD-2 amberlite	–
	5	1–500 ng/mL	1.0 ng/mL	<0.2	90.0–99.3

[a]r-FIA: reversed-flow injection analysis, MSFIA: multisyringe flow injection analysis, FBL: flow–batch luminometer, CCD: charge-coupled device, PDMS: polydimethyl siloxane; [b]the primary focus is on the novel CL amplifier (DBS–LDHs) for enhancing the detection of Co^{2+} released from VB_{12}, improving selectivity and sensitivity without specifying the flow system involved in sample delivery and reaction; [c]DBS: dodecylbenzene sulfonate, LDHs: layered double hydroxides, CDP-Star: disodium 2-chloro-5-(4-methoxyspiro{1,2-dioxetane-3,2′-5-chlorotricyclo[3.3.1.1^{3,7}]decan}-4-yl)-1-phenyl phosphate, NHS: *N*-hydroxysuccinimide, EDC: ethyl-3-(3-dimethylaminopropyl)carbodiimide.

achieved a linear range of 1.0 ng/mL to 10 µg/mL and an LOD of 0.368 pg/mL, requiring 30 µL samples and 3.6 s for analysis. Mode II extended the linear range to 0.10 ng/mL with an LOD of 0.576 pg mL, requiring 50 µL samples and 6 s. Mode II could effectively detect VB_{12} in nutritional supplements and egg yolks [24].

Another research group earlier introduced a CL technique for VB_{12} measurement, utilizing the Co^{2+}-enhanced CL reaction between luminol and dissolved oxygen within a flow injection setup, in which Co^{2+} released from VB_{12} acted as the recognition element, luminol acted as the indicator, and the increased CL intensity represented the sensing signal. The increase in CL intensity matched the VB_{12} concentration, showing a linear response from 2.0×10^{-10} to 1.2×10^{-6} g/L and a low LOD (5.0×10^{-11} g/L). The results were obtained within 0.5 min at a 2.0 mL/min flow rate and displayed less than 5.0% RSD. This biosensing platform was effectively employed to analyze VB_{12} in various samples, including pharmaceuticals, human serum, egg yolk, and fish tissue [103]. Akbay and Gök also assessed CL intensities via a flow injection system for quantifying VB_{12}. This technique utilized the catalytic role of Co^{2+} present in VB_{12} to facilitate the CL reaction between luminol and H_2O_2 under alkaline conditions, where Co^{2+} functioned as the recognition target, luminol acted as the indicator luminophore, and the CL emission served as the output signal. The enhancement in CL intensity is directly linked to the VB_{12} concentration, with an LOD of 0.89 ng/mL. CL measurements using a flow rate of 3.0 mL/min were rapid (10 s) and showed high precision (RSD < 2.5%). This method could be effectively utilized to measure VB_{12} levels in pharmaceutical injections [104]. A flow injection CL technique to detect Co^{2+} was also developed by

Du et al. [105] based on the significant catalytic impact of a Co^{2+}–(1,10-phenanthroline)$_3$ complex on the lucigenin-periodate reaction within an alkaline environment, where the Co^{2+} complex acted as the recognition unit, lucigenin served as the indicator, and the chemiluminescent response was the sensing signal. The CL emission under optimal conditions exhibited a direct linear relationship with Co^{2+} concentrations from 1.0×10^{-9} to 3.0×10^{-7} g/mL and an LOD of 4.4×10^{-10} g/mL with 2.3% RSD [105]. Andrade et al. designed a flow–batch methodology paired with a large-area silicon photodiode instead of a photomultiplier tube, resulting in a convenient and automated luminometer for CL analysis. In this platform, VB_{12} served as the recognition analyte, luminol acted as the indicator, and the detected CL emission represented the signal. This system was applied to measure VB_{12} in injection ampoules, achieving detection and quantification limits of 0.11 and 0.36 µg/L, respectively. The RR, RSD, and sample measuring capacity were 97.8–102.1%, less than 2.2%, and 72 samples per hour, respectively. The authors claimed that this system featured straightforward design, adaptability, and multifunctionality, coupled with reduced usage of reagents and samples, and generated minimal waste [106].

In two distinct studies, Murillo Pulgarín et al. evaluated the chemiluminescent determination of VB_{12} [107,108]. First, a charge-coupled device (CCD) photodetector alongside UV persulfate oxidation within a streamlined continuous flow system was employed for the catalytic enhancement of Co^{2+} in the reaction between luminol and percarbonate (H_2O_2 source) in an alkaline setting, where Co^{2+} released from VB_{12} acted as the recognition element, luminol served as the indicator, and the CL emission intensity represented the sensing signal. UV irradiation in the persulfate environment led to the liberation of Co^{2+} from the VB_{12} structure, and the CCD detector integrated into the flow cell captured comprehensive spectral data of the Co^{2+}-enhanced luminol–percarbonate reaction. A remarkable correlation between VB_{12} concentration and emission intensity was observed by achieving an LOD of 9.3 µg/L [107]. Second, the authors utilized the enhancing effect of Co^{2+} extracted with microwave assistance on the CL reaction between luminol and percarbonate, in which Co^{2+} again functioned as the recognition target, luminol acted as the indicator, and the measurable light output was the signal. Spectral analysis of the Co^{2+}-catalyzed luminol–percarbonate reaction was conducted using a CCD photodetector connected to a straightforward continuous flow system. The optimal operating conditions to attain peak CL emission included 8.0 mM luminol in a 0.075 M carbonate buffer (pH 10.0), 0.15 M sodium percarbonate, a flow rate of 0.33 mL/s, and an integration time of 2 s. Not only an LOD of 0.42 µg/L for Co^{2+} concentration was obtained, but the authors also reported that this method was effectively used to quantify VB_{12} in pharmaceutical (ampoules and tablets) products formulated with OHCbl and CNCbl [108]. Kumudha and Sarada assessed the total content of VB_{12} (42 µg/100 g; Ado-Cbl as the main isomer) purified from the halotolerant green alga, *Dunaliella salina* V-101 using a luminometer and in a polystyrene cuvette, where VB_{12} served as the recognition analyte, the luminol-based reaction acted as the indicator system, and the recorded chemiluminescence was the sensing output. The results showed a high association with the value determined by the AuNPs-based RNA aptamer (40 µg/100 g) and the microbiological method (49 µg/100 g) [109].

An advanced CL system integrated with a microfluidic platform was engineered for the quantification of VB_{12}, utilizing the chemiluminescent reaction between luminol and $AgNO_3$, catalyzed by AuNPs, where VB_{12} served as the recognition analyte, luminol acted as the indicator luminophore, and the strong CL emission revealed the sensing signal. In this system, Ag^+ served as a chemiluminescent oxidant, facilitating luminol oxidation in the catalytic presence of AuNPs, thereby generating a potent CL emission. The catalytic action of AuNPs enables the conversion of luminol to luminol radicals via interaction with $AgNO_3$, which subsequently reacts with dissolved oxygen to produce CL emission. This innovative CL technique was successfully applied to ascertain VB_{12} doses in pharmaceutical tablets and multivitamin formulations [110]. To overcome the low selectivity of VB_{12} detection because of metal ion interference in the luminol system, Zhang et al. utilized the dodecylbenzene sulfonate-modified layered double hydroxide to catalyze a Fenton-like, ultraweak CL reaction for specifically detecting VB_{12} in egg yolk [111], where the surfactant-modified catalyst served as the recognition site, the peroxide reaction acted as the indicator system, and the ultraweak CL emission was the analytical signal. They determined the linear range (from 1.0 ng/mL to 5.0 µg/mL) and the LOD (0.57 ng/mL) for VB_{12} detection, which could be effectively used to measure its content in egg yolk. The accuracy of this novel CL method without relying on luminol was validated against the standard inductively coupled plasma-MS (ICP-MS), indicating a highly selective VB_{12} determination [111]. Domínguez-Romero et al. introduced a novel application of bead injection within multicommutation-based flow systems, featuring a surface-renewable CL flow sensor that utilizes the CL reaction between luminol and H_2O_2, in which Co^{2+} released from VB_{12} acted as the recognition element, luminol served as the indicator, and the Co^{2+}-enhanced CL emission was the sensing signal. This technique was implemented for three commercial mineral water samples spiked with Co^{2+}. The method's effectiveness was also demonstrated by detecting VB_{12} in injectable pharmaceuticals through Co^{2+}-induced CL signal enhancement in an alkaline medium, after mineralization to release Co^{2+}. This biosensing

platform showed a linear range of 1.7 to 50 µg/L, an LOD of 0.5 µg/L, and a sampling rate of 11 samples per hour. The data acquired through this method were rigorously validated against ICP-MS results [112]. The CL potential of luminol for the determination of Co^{2+}adsorbed on a chitosan membrane was assessed based on the catalytic effect of these ions on the luminol–H_2O_2 CL reaction, where the chitosan membrane provided the recognition surface, luminol acted as the indicator, and the detected CL light emission was the sensing output. Linear range and LOD of Co^{2+} were found to be 0.4 pg/L to 40 µg/L and 4.0 fg/L, respectively. The membrane/liquid CL system demonstrated analytical performance comparable to the liquid-only CL system. The pre-concentration of Co^{2+} on chitosan membranes had potential for biomedical and food applications for VB_{12} determination in pharmaceuticals, human serum, egg yolk, and fish tissue [113].

Selvakumar and Thakur utilized a dipstick-based immuno-CL biosensor to detect VB_{12} in two different energy drinks, where the antibody–antigen interaction provided the recognition event, the chemiluminescent substrate (CDP-Star) acted as the indicator, and the sensing signal was the measured photon emission. In this competitive assay, VB_{12} antibodies were fixed onto a nitrocellulose membrane, then exposed to both VB_{12} and its enzyme-bound form for competitive binding. The detection principle was based on the utilization of CDP-Star, with the generated light being inversely proportional to the VB_{12} levels. The LOD and RR of VB_{12} using this sensor were 1.0 ng/mL and 90–99.4%, respectively. Results obtained from the dipstick technique coupled with CL showed a high association with the ELISA findings [114]. Lee et al. developed NutriPhone as a quick tool to check VB_{12} levels in blood within 15 min using a smartphone, where VB_{12} acted as the recognition analyte, the AuNP–antibody conjugates and chemiluminescent reaction served as the indicator system, and the measurable optical/CL response was the sensing signal. It consisted of a special phone attachment, an app, and a test strip that could detect very low levels of VB_{12}. A unique part of the test is a "spacer pad" to make the results clearer. The NutriPhone was also used in a study with twelve people, accurately determining their VB_{12} blood levels from just a tiny drop of blood from a finger prick. For this work, the serum after a 1 h incubation was separated by centrifugation (2,000 rpm, 10 min), and serum VB_{12} levels were evaluated using a chemiluminescence immunoassay. The Siemens VB_{12} kit indicated that the normal range for VB_{12} levels was between 142 and 724 pmol/L, with an LOD of 92 pmol/L [115]. The customized VB_{12} test strip detailed in Figure 3A is engineered for a lateral flow assay incorporating a blood filtration membrane, a pad for AuNP–anti-VB_{12} conjugates, a spacer pad to extend sample–conjugate interaction, a nitrocellulose membrane for VB_{12}–bovine serum albumin (BSA) conjugation, secondary antibodies as test and control

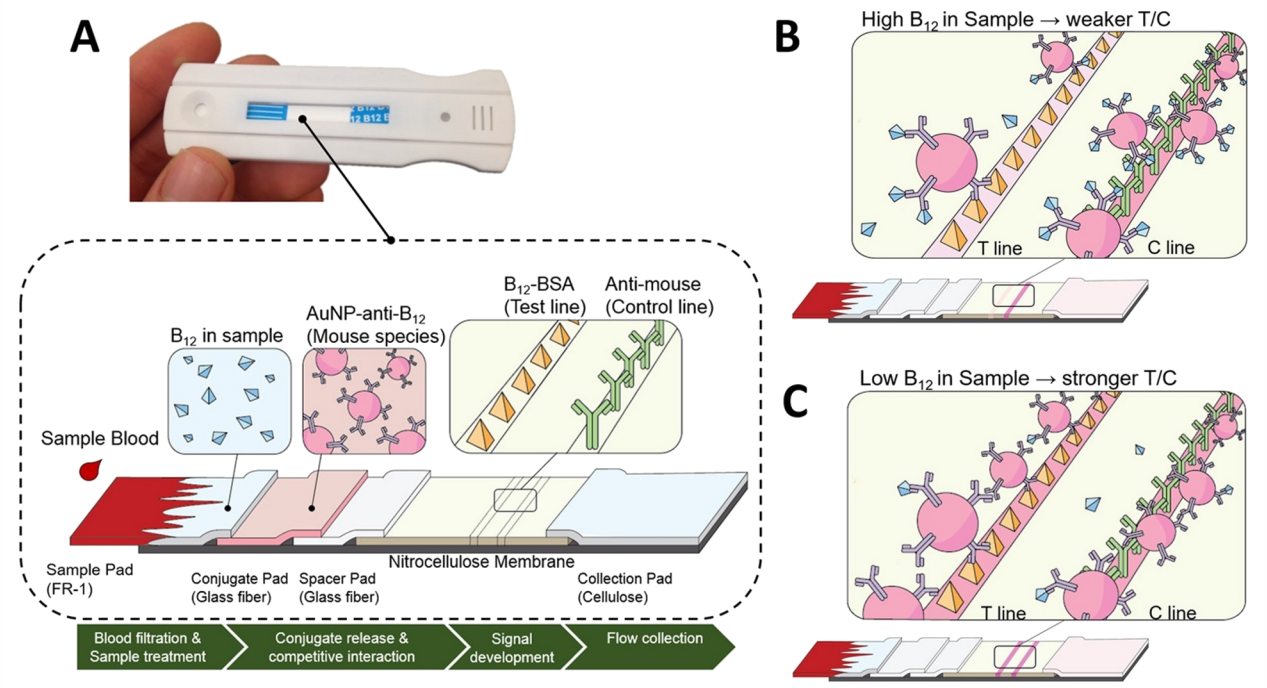

Figure 3: VB_{12} lateral flow test. (A) Visualization and structure of the VB_{12} test strip design and elements, (B) competitive dynamics at the test line between VB_{12} in the sample and anchored BSA-VB_{12} for restricted binding zones on AuNP-anti-VB_{12}, yielding low T/C signal intensity with elevated VB_{12} levels, and (C) high T/C signal intensity with low VB_{12} doses. Figure 3 was reproduced from [115] (© 2016 S. Lee et al., published by Springer Nature, distributed under the terms of the Creative Commons Attribution 4.0 International License, https://creativecommons.org/licenses/by/4.0).

lines, and an absorbent pad for waste. Designed for the small molecular size of VB_{12}, this structure ensures its competitive binding to antibodies. A crucial step involves the sample's interaction with AuNP–anti-VB_{12} on the conjugate pad, significantly enhanced by the spacer pad that delays the flow to the nitrocellulose membrane, crucial for detecting low VB_{12} concentrations. With high VB_{12} levels, most conjugates bind to VB_{12} in the sample, resulting in a minimal color change at the test line (T) but a strong control line (C), leading to low T/C ratios (Figure 3B). In contrast, low VB_{12} levels yield an intense color at the test line and a weak control signal, indicating fewer conjugates reach the control line, thus high T/C ratios (Figure 3C) [115].

In a recent observational cohort study involving 11,549 pregnant women, researchers investigated the correlation between imbalances in serum folate and VB_{12}, measured by chemiluminescent immunoassays, and adverse pregnancy outcomes, where folate and VB_{12} acted as the recognition analytes, the chemiluminescent immunoassay kit served as the indicator platform, and the photon emission intensity was the recorded signal. Per the manufacturer's guidelines, the LODs of serum folate and VB_{12} were under 2 μg/L and below 50 ng/L, respectively, while the corresponding normal ranges for a healthy population were considered 5.9–24.8 μg/L and 180–914 ng/L, respectively [116]. Wiesholler et al. developed a self-assembled nanoengineered interface to facilitate direct detection of VB_{12} in serum through a simple luminescence method. Here, VB_{12} in serum was the recognition target, thulium (Tm^{3+})-doped sodium yttrium fluoride ($NaYF_4$) upconversion nanoparticles (UCNPs) on gold nanotriangle arrays acted as the indicator system, and the enhanced near-infrared (NIR)-excited UV luminescence was the sensing signal. This approach relied on the synergistic effects of Tm^{3+}-doped $NaYF_4$ UCNPs on gold nanotriangle arrays created via nanosphere lithography on a glass slide. It greatly improved the conversion of near-NIR light to UV light, achieving a notable increase in UV light intensity (i.e., six times higher at 344 nm) when stimulated with a NIR light at 980 nm using a low power density of about 13 W/cm^2. The process optimization was particularly advantageous for luminescence-based sensing in biological samples, as it minimized autofluorescence through NIR excitation. This methodology enabled the measurement of VB_{12} levels in serum with an LOD as low as 3.0 nmol/L from a small sample volume of 200 μL [117].

In general, there are fewer and newer studies on the ECL sensors compared to CL sensors to detect VB_{12}. Bhaiyya et al. have recently fabricated a novel laser-induced graphene (LIG)-based ECL system with two and three channels to detect H_2O_2, VB_{12}, and vitamin C (VC) from real samples. VB_{12} and VC acted as the recognition analytes, the luminophore–graphene interface served as the indicator platform, and the smartphone-captured ECL light emission was the sensing signal. This system, made from polyimide sheets capable of producing graphitized areas in one step, utilized a CO_2 IR laser with optimized settings to construct closed bipolar electrodes (C-BPEs) and driving electrodes (DEs). A compact, 3D-printed setup was designed to support the device and integrated a smartphone, transforming it into a self-contained ECL detection platform. The smartphone captured the ECL signals and also powered the device via a DC-to-DC buck-boost converter. LIG-C-BPE-ECL-based devices with two and three channels were created to detect either single analytes or two analytes simultaneously. Linear range and LOD of H_2O_2, VB_{12}, and VC in a two-channel LIG-C-BPE-ECL system were 0.5–100 μM and 0.303 μM, 0.5–1000 nM and 0.109 nM, and 1–1000 μM and 0.96 μM, respectively. The concurrent determination of VB_{12} and VC was possible using a three-channel version of this portable and versatile system [118]. These researchers, in another study, reported ECL sensing of VB_{12} using LIG-based BPE and single electrodes (SEs) in a 3D-printed portable system, where VB_{12} acted as the recognition target, the graphene electrode served as the indicator, and the electrochemically triggered luminescence resulted in the output signal. Similar to the previous investigation, they utilized an Android smartphone for data acquisition, including operation of the DC-to-DC buck-boost converter and the capture of ECL images. Linear range and LOD of VB_{12} in BPE and SE modes were 0.5–700 nM and 107 pM, and 0.5–1000 nM and 94 pM, respectively [119].

Fluorescence-based biosensors

Small-molecule-based fluorescent chemosensors

Fluorescence-based chemosensors are highly sensitive, specific, and rapid tools to detect B-group vitamins [84,120]. Xu et al. prepared an innovative strategy by integrating Förster resonance energy transfer (FRET) and flow injection analysis to assess VB_{12} based on its fluorescence quenching (FQ) on the acridine orange/rhodamine 6G system. In this assay, VB_{12}, the dye pair acridine orange/rhodamine 6G, and fluorescence quenching acted as the recognition analyte, the indicator, and the sensing signal, respectively. Energy transfer between acridine orange and rhodamine 6G within dodecyl benzene sodium sulfonate was effectively facilitated using a 454 nm argon laser as the light source, significantly enhancing rhodamine 6G's fluorescence emission. However, the presence of VB_{12} was observed to drastically reduce fluorescence in this setup. Utilizing a combined solution of acridine orange, rhodamine 6G, and dodecyl benzene sodium, and introducing VB_{12} into this mixture, resulted in distinctive negative peaks useful for VB_{12} determination. Linear range and LOD of VB_{12} were assessed to be

0.04–2.0 μM and 1.65 μM, respectively. This fluorescent chemosensor could be successfully employed to detect VB_{12} in injections [121]. A new fluorescent probe composed of 7-nitrobenzo-2-oxa-1, 3-diazole (HINBD) skeleton was also developed to measure VB_{12} in medical drugs. Here, VB_{12} was the target molecule, fluorescence of HINBD represented the indicator, while its suppression provided the output signal. This soluble probe in water showed a robust emission within the visible spectrum (excitation wavelength λ_{ex} = 479 nm and emission wavelength λ_{em} = 545 nm) and maintained stability across various pH levels. The presence of VB_{12} was observed to significantly suppress HINBD's fluorescence, with the degree of suppression directly correlating to the VB_{12} dose. Under ideal conditions, a linear detection span from 0 to 24 nmol/L was established, with an LOD of 83 pmol/L. Scholars also reported reliable outcomes in analyzing the concentration of this water-soluble vitamin in pharmaceutical products [122]. In a distinct work, Chakravarty et al. designed a real-time, label-free opto-electrical (fluorescence and impedance) sensing system of VB_{12} using silk fibroin protein from *Bombyx mori*. The recognition was based on VB_{12} binding, micropatterned silk fibroin films functioned as the indicator, and fluorescence/impedance variations were the readout signals. The solution and films' inherent autofluorescence led to an LOD of 3.0 pg/μL, while the impedance-based detection resulted in an LOD of 17.8 ppm and 0.25 ppm of VB_{12} in aqueous solutions and human blood serum, respectively [123]. Wang et al. introduced a new approach for synthesizing fluorescent nanowires from nanoscale diamonds. In their FRET-based sensor, VB_{12} served as the analyte, sulfur-modified diamond nanowires acted as the indicator, and the fluorescence response was recorded as the signal. These nanomaterials are recognized for their exceptional chemical capabilities alongside their dependence on size, shape, and constituent materials. Using a thermal process that combined oxidized nanoscale diamonds with dibenzyl disulfide at 900 °C, researchers successfully fabricated sulfur-modified nanoscale diamonds. A method involving porous anodic aluminum oxide templates and cathodic electrophoretic deposition was utilized to fabricate the sulfur-modified nanoscale diamond nanowires. Eventually, an optical sensor based on the sulfur-modified nanoscale diamond nanowires was developed, demonstrating exceptional sensitivity and specificity in detecting VB_{12} through the FRET mechanism [124]. In an intriguing work, Ahmad et al. applied FRET-based genetically encoded nanosensors, dubbed SenVitAL ("Sensor for Vitamin Anemia Linked"), as a refined approach for real-time monitoring of metabolite levels of VB_{12} directly within live cells using a construct that combines the VB_{12} binding protein (BtuF) with cyan (CFP) and yellow (YFP) fluorescent protein variants. In this design, BtuF served as the recognition element, CFP/YFP functioned as the indicator pair, and changes in FRET efficiency represented the measurable signal. Transferred into various expression vectors, SenVitAL demonstrated high specificity for VB_{12}, maintained stability across pH variations, and quantified its concentrations in a dose-dependent manner, with an apparent affinity of ≈157 μM [125].

Nanocluster/nanoparticle-based fluorescent sensors

The utilization of nanocluster-based sensors in measuring VB_{12} is pivotal for improving sensitivity and specificity in food and pharmaceutical analysis. These sensors exploit the unique optical and electronic properties of these nanostructures to achieve low LODs and high accuracy, which are necessary in ensuring the nutritional adequacy and safety of biofunctional products [126-130]. A highly sensitive approach was successfully designed based on the FQ of BSA-stabilized gold nanoclusters (AuNCs) for the rapid determination of VB_{12}, where VB12, AuNCs, and the quenched fluorescence were the recognition analyte, indicator, and signal, respectively. The system worked within the concentration range of 0.16–38.5 μg/mL with an LOD of 0.1 μg/mL. A 97.7–102% RR with an RSD of 2.0–5.9% was obtained when this sensor was utilized to analyze VB_{12} in commercially available injectable dosage products [126]. A new fluorescent sensing probe without using toxic organic solvents was developed based on a histidine-stabilized copper nanocluster for the detection of VB_{12}. A remarkable reduction in the emission intensity of the fabricated probe with the addition of VB_{12} was found. This quenching occurred because of FRET between the analyte and probe. This method could selectively assess VB_{12} with an LOD of 3.30×10^{-9} mol/L amid other potentially interfering vitamins [127]. Another study was performed to find a response to how metal ions interact with AuNCs, causing structural alterations in the clusters that manifest as changes in fluorescence, enabling the detection of heavy metals like cobalt and cadmium. Here, the bound metal ions acted as the recognition elements, BSA-derived AuNCs provided the indicator, and the fluorescence modulation via intersystem crossing and FRET was the measurable signal. This mechanism facilitated the sensitive detection of cobalt and cadmium within a concentration range of 5–165 ng/mL and 20–1000 ng/mL, respectively. Furthermore, this technique was effectively utilized to quantify VB_{12} in commercial injections [128]. Silver nanoclusters emitting red light within lysozyme structures were fabricated through the reduction of dithiothreitol and utilized to detect copper ions and VB_{12}. The quenching mechanism induced by VB_{12} was based on the inner filter effect (IFE) and FRET. These homogenous nanoclusters with excellent water solubility and photoluminescence (PL) potential could be applied to detect VB_{12} in real samples [129]. Qu et al. also reported that VB_{12}, via the IFE mechanism, quenched fluorescence induced by silver nanoclusters (AgNCs) capped by hyperbranched polyethyleneimine

(HBPEI) with various molecular weights and terminal groups. Analyte, indicator, and signal were VB_{12}, HBPEI-stabilized AgNCs, and fluorescence quenching, respectively. Silver nanoclusters templated by a 600 kDa HBPEI as a sensitive probe could be used to monitor VB_{12} in a linear range of 0.005–70 μM and an LOD of 0.00262 μM. The sensing potential was also validated by detecting this vitamin with desired RRs in tablets (97.13–102.58%) and injections (99.09–105.09%) [130]. Recently, Zhang et al. evaluated the capability of stable histidine-modified silver nanoclusters as a blue fluorescence emission probe for measuring VB_{12}. Histidine and ascorbic acid were utilized as capping and reducing agents, respectively. Linear range and LOD of VB_{12}, respectively, were 0.5–200 μM and 0.038 μM under optimized conditions of histidine (5 mL) and ascorbic acid (200 μL) volumes, pH (5.0), temperature (55 °C), and incubation time (5 h). The successful application of this nanoprobe in real-sample analysis and temperature measurement confirmed its performance for effective VB_{12} assessment, highlighting an innovative strategy with excellent sensitivity, selectivity, and practical utility [131].

Yu et al. created a fluorescent probe based on water-soluble copper nanoclusters shielded by PEI through the synergistic process of UV radiation and microwave heating. The sensor's FQ mechanism relied on the integration of FRET and IFE, where VB_{12} acted as the recognition analyte, the PEI–Cu nanoclusters served as the indicator, and the quenching of fluorescence provided the measurable signal. It was applied to monitor tetracycline hydrochloride and VB_{12} within linear concentration ranges of 0.33–66.67 μmol/L and 0.33–53.33 μmol/L, respectively. The LOD and limit of quantification were estimated to be 55.50 and 56.34 nmol/L as well as 184.82 and 187.61 nmol/L for tetracycline hydrochloride and VB_{12}, respectively. This probe, compared to HPLC analysis, presented satisfactory results for measuring VB_{12} in oral liquid or tablets [132]. Through a single-step wet chemical synthesis process, Hu et al. also produced an AuNC-based fluorescent sensor by combining silver addition and dual ligands (thiosalicylic acid (TSA) and BSA). These ligands were mixed drop by drop into a vial at 80 °C for 2 h. They studied the effect of various aromatic thiols and the molar ratio of gold (Au) to silver (Ag) on the nanoclusters' PL efficiency. These alloy nanoclusters proved their potential as effective fluorescent sensors for assaying VB_{12} and chlortetracycline hydrochloride (CCH), as the fluorescence induced by these nanoclusters could be quenched upon adding the investigated analytes due to the combined effects of FRET and IFE. The LOD for VB_{12} and CCH were, respectively, determined to be 0.071 μmol/L and 0.064 nmol/L within the linear range of 0.33–60 μmol/L. They pointed out that this fluorescent sensor was capable of effectively detecting VB_{12} in mineral water and tablets, as well as CCH in veterinary medications and topical creams [133]. It was mentioned that histidine-modified silver nanoclusters [131], copper nanoclusters protected by PEI [132], and TSA/BSA-Au/AgNCs [133] can also be considered highly efficient temperature sensors.

Chau et al. have recently designed a fluorescent assessment for VB_{12} detection through the IFE of 1,3-propanedithiol-functionalized silver nanoparticles (PDT-AgNPs). Here, VB_{12} served as the recognition target, PDT-AgNPs acted as the fluorescent indicator, and the IFE quenching was the sensing output. The authors initially synthesized AgNPs via the reduction of Ag^+ to Ag^0 by applying $NaBH_4$. The fluorescence intensity (λ_{ex} = 360 nm and λ_{em} = 410 nm) could be substantially enhanced by functionalizing AgNPs with PDT for 2 h, resulting in a significant FQ in the presence of VB_{12} due to spectral overlap. Here, VB_{12} served as the recognition target, PDT-AgNPs acted as the fluorescent indicator, and the IFE quenching was the sensing output. Linear range and LOD of VB_{12} were determined to be 1–50 μM and 0.5 μM, respectively. The favorable sensitivity and selectivity of the developed PDT-AgNPs-based fluorescent probes were also affirmed by accurately quantifying VB_{12} in pharmaceutical tablets [134]. In another study, researchers made a composite from silicon NPs (SiNPs) and AuNPs as a selective fluorescent probe (λ_{ex} = 420 nm and λ_{em} = 520 nm) to sensitively detect Co^{2+} and VB_{12} by integrating selective aggregation and IFE. Green-emitting SiNPs were prepared using a one-pot hydrothermal method and then functionalized with thioglycolic acid and cetyltrimethylammonium bromide. Selective aggregation of AuNPs occurred in the presence of Co^{2+} and VB_{12}, enhancing the LSPR absorption at 520 nm and significantly quenching the green fluorescence of SiNPs through IFE. A linear FQ efficiency with Co^{2+} doses was recorded in the range of 0.1 to 80 μM, achieving an LOD of 60 nM, which was lower than the guideline value of Co^{2+} in drinking water (1.7 μM). Also, linear range and LOD for VB_{12} were assessed to be 0.1–100 μM and 69 nM, respectively [135].

Gholami et al. also synthesized a graphene oxide (GO) nanolayer for the label-free detection of VB_{12} using fluorescence spectroscopy. The developed nanolayer showed high selectivity as it could specifically interact with VB_{12} to discriminate it from some vitamins (such as vitamins B_1, B_6, and B_9, and VC), as well as other substances (i.e., lauric acid, glucose, urea, and uric acid). The detection mechanism was based on the quenching effect of VB_{12} on the nanolayer's fluorescence emission. In this case, the selective interaction of VB_{12} with GO represented the recognition event, the intrinsic fluorescence of the GO nanolayer was the indicator, and the quenching effect constituted the signal. Linear range and LOD of VB_{12} were 2.5×10^{-7}–2.81×10^{-5} M and 3.2×10^{-7} M, respectively [136].

Carbon dot-based fluorescent biosensors for vitamin B_{12}

Fluorimetric assays using organic dyes [137-139], semiconductor quantum dots (scQDs) [138,140], and metallic nanoclusters [131,141] were earlier suggested to analyze VB_{12}. However, there are some significant concerns in utilizing organic dyes (e.g., photobleaching, limited photostability, and environmental sensitivity) [142-144], scQDs (e.g., toxicity, use in size-sensitive applications, low solubility, and batch-to-batch variations in biological environments) [145-148], and metallic nanoclusters (e.g., high reactivity and cytotoxicity in biological applications, difficulties in precise size control, low quantum yield, and low-purity synthesis) [149,150] in biosensing of VB_{12}. Carbon dots (CDs), as practical substitutes for these fluorescent components, are characterized by sizes ranging from less than 10 nm to around 60 nm [151]. While CDs typically display dot-like structures, scientists have successfully engineered these fluorescent NPs in various sizes and shapes, including triangles, ribbons, and rods, by carefully selecting precursors and designing the reaction process [152,153]. There are four different classes of CDs, including carbon quantum dots (CQDs), carbon nanodots (CNDs), graphene quantum dots (GQDs), and carbonized polymer dots (CPDs). CQDs are typically spherical and characterized by distinct crystal lattices and chemical groups on their surface, contributing to their unique optical and chemical properties. CNDs exhibit a high degree of carbonization along with the presence of some chemical groups on their surface. Unlike other carbon-based nanomaterials, they typically do not display an obvious crystal lattice structure and are characterized by the absence of polymer features. GQDs are tiny fragments of graphene, composed of a single layer or a few layers of graphene sheets, featuring distinct graphene lattice structures and chemical groups positioned along the edges or within interlayer defects. Last, CPDs feature a hybrid structure of polymer and carbon, consisting of abundant functional groups or polymer chains on the surface and a carbonized core [154-156]. CDs possess remarkable characteristics to boast versatile applications, extending from biomedical fields (e.g., bioimaging, drug delivery, and gene delivery) to various other domains (e.g., photocatalysis, photovoltaic cells, CL, ECL, optical sensors, fluorescent inks, and light-emitting diodes) [157,158]. The wide applicability of CDs is due to the superior electron conductivity, resilience against photobleaching and photoblinking, high photoluminescent quantum yield, tunable fluorescence, resistance to photodecomposition, adjustable excitation and emission, enhanced electrocatalytic activity, high aqueous solubility, excellent biocompatibility, enduring chemical stability, low cost, negligible toxicity, and a significant surface area-to-volume ratio [152,159,160].

In recent years, more attention has been directed towards CQDs due to their advantageous features, including excellent PL properties, straightforward and economical synthesis routes, affordability of starting materials, high water solubility and chemical stability, minimal toxicity, and ease of functionalization [158,161]. CQD-based sensors and biosensors operate through a variety of mechanisms including FQ (both static and dynamic), energy transfer, IFE, photoinduced electron transfer (PET), and FRET, enabling their application in detecting a wide range of analytes such as metal ions, acids, proteins and polypeptides, DNA and miRNA, water pollutants, hematin, drugs, and vitamins [158]. There is an intense tendency to utilize CDs, especially CQDs, in biosensing and cell bioimaging studies of water-soluble vitamins such as VC [162-166] and B-group vitamins [166-170]. Table 2 summarizes a list of QD-based fluorescent sensors, their synthesis methods, sensing mechanisms, as well as optical and physical properties for detecting VB_{12} in different food and pharmaceutical samples.

Carbon dot-based fluorescent sensors

CDs that emit light at longer wavelengths have recently attracted growing interest regarding their potential applications in biology. Huang et al. studied the Schiff base crosslinking reaction between methyl-*p*-benzoquinone and triethylenetetramine to prepare orange-emitting CDs with a quantum yield of 6.56% at ambient temperature. These nanoscale materials (5 nm) revealed a robust excitation-dependent emission [171]. Thanks to the strong IFE of the as-synthesized CDs, they could effectively be applied for the sensitive determination of VB_{12} concentrations in the linear range of 50–200 μM with an LOD of 0.01 μM. Here, VB_{12} acted as the recognition analyte, the CDs were the fluorescent indicator, and IFE fluorescence quenching served as the signal. The designed fluorescent sensor by introducing various VB_{12} doses (1, 10, and 50 μM) into CDs was successfully applied to detect VB_{12} in lake water, fetal bovine serum, and milk samples. The ranges of RR and RSD values for the corresponding samples were 98.0–108.8% and 1.54–2.76%, 98.9–102.0% and 1.94–3.56%, as well as 97.9–108.0% and 1.87–3.41%, respectively. Accordingly, these nanoprobes would be promising sensing tools for measuring VB_{12} in complex sample matrices [171]. The CDs exhibited two pronounced absorption peaks near 278 and 445 nm. These peaks correspond to π–π^* transitions among aromatic sp^2 carbon atoms and the n–π^* transitions among C=O/C=N bonds, respectively [171,172]. The emission characteristics of these CDs are generally linked to the quantum confinement effect or the states of their surfaces. The CDs' modest crystallinity suggested that their fluorescence primarily originated from surface states. The CDs display an excitation-dependent fluorescence, with λ_{em} exhibiting a redshift when λ_{ex} was increased from 320 to 520 nm. At an excitation of 460 nm, the peak λ_{em} for the CDs was iden-

Table 2: A summary of QDs-based fluorescent biosensors for the detection of VB_{12} in food and pharmaceutical products.

VB_{12}-containing sample type/Ref.	Precursors[a]	Synthesis method	QD type[b]	Quantum yield (%)	Average size (nm)
	λ_{ex} (nm)	λ_{em} (nm)	sensing mechanism[c]	linear range (μM)	LOD (μM)
commercial injections [206]	DAN, GO	citric acid pyrolysis	GQDs	–	35–40
	328	423	IFE-based FQ	–	6.37×10^{-6}
Tap/(Commercial) drinking water (Co^{2+} ions) [208]	citric acid, cysteamine·HCl	hydrothermal (160 °C, 4 h)	N,S-GQDs	–	3
	345	425	FQ by Co^{2+}–ligand complexation	0–40	1.25
injection, saliva, fetal bovine serum [210]	TCBQ, EDA	Schiff base condensation	CPDs	2.96	0.6–2.1
	350	440	IFE-based FQ	25–100	0.14
tablets, human urine [213]	glycerol, trisodium citrate, APTES	microwave process (400 W, 180 °C, 10 min)	SiQDs	10.5	4–5
	360	460	IFE-based FQ	0.5–16	0.158
drug tablets [214]	sodium oxalate, citric acid, DAMO (Si source), catechol, thiourea	microwave-assisted hydrothermal	SiQDs	25	6–8
	420	520	IFE-based FQ	0.05–30	0.05
Water (Co^{2+} ions) [221]	PVP, AEAPDMMS	hydrothermal (100 °C, 3 h)	SiQDs	2.36	4.1
	370	435	SQE-based FQ	1–120	0.37
milk powder [222]	curryberries juice	ultrasonication	nCQDs	10.24	2–8
	360	510	PL quenching	1–40	0.04
Milk [226]	milkcap mushroom (*Lactarius hatsudake*)	hydrothermal (200 °C, 12 h)	nCQDs	22.88	3
	324	408	IFE-based FQ	0–20	36.9
drug tablets [182]	*O*-phenylenediamine, 4-aminobenzoic acid	hydrothermal (190 °C, 3 h)	nCQDs	32	2.22
	390	567	IFE-based FQ	0–90, 140–250	0.119
drug tablets [229]	*Saccharomyces*, ethanediamine (N source)	microwave-assisted hydrothermal (200 °C, 3 h)	N,nCQDs	16	2.9
	380	460	FRET-based FQ	0–100	2.19

Table 2: A summary of QDs-based fluorescent biosensors for the detection of VB_{12} in food and pharmaceutical products. (continued)

water (Co^{2+} ions) [230]	Kelp (C source) EDA (N dopant)	microwave irradiation (200 °C, 10 min, 800 W)	N,nCQDs	23.5	≈3.7
	370	450	IFE-based FQ	1–200	0.39
water (Co^{2+} ions) [231]	biomass quinoa saponin powder (C source), EDA (N dopant)	hydrothermal (220 °C, 10 h)	N,nCQDs	22.2	≈2.25
	390	470	FQ by Co^{2+} interaction	2–150	0.49
water (Co^{2+} ions), serum and milk (VB_{12}) [232]	*Weissella* sp. KI-3 (Gram-positive bacteria), ampicillin sodium	hydrothermal (200 °C, 6 h)	N,nCQDs	8.96	5.2
	346	424	IFE-based FQ	0–25 (VB_{12}), 0–50 (Cr^{6+})	0.0515 (VB_{12}), 0.10657 (Cr^{6+})
human serum [233]	bird's nest, distilled water	hydrothermal (180 °C, 5 h)	nCQDs	–	–
	386	471	dynamic electron transfer	0–100	0.24
drug tablets [176]	CDPC, EDA	hydrothermal (160 °C, 10 h)	BCQDs	22.3	2.84
	350	450	Co^{2+} ion-induced CQD aggregation and electron transfer	0.5–3.0	<0.081
VB_{12} injection (0.5 mg/mL) [181]	L-tartaric acid, urea	solvothermal (180 °C, 4 h)	N-doped yellow-emitting CDs	16.7	≈8.2
	450	550	IFE-based FQ	0–200	2.045
VB_{12} powders (CNCbl, Sigma), VB_{12} injections and tablets [177]	citric acid monohydrate, nicotinamide	microwave-assisted hydrothermal (80 W, 160 °C, 20 min)	NA-CQDs	–	<10
	366	444	IFE-based FQ	0.1–60	0.0317
VB_{12} tablets, vitamin drink, human serum [178]	citric acid	hydrothermal (170 °C, 6 h)	CQDs	15.2 (liquid), 39.9 (solid)	34.03
	595	560	IFE-based FQ	0.5–100	0.06078
VB_{12} powders [179]	citric acid, sodium hydrate, quinine sulfate	thermal (300 °C, 2 h), sonication (30 min, 60 W, 40 kHz)	t-QDs	16.28	6
	330	420	FRET-based FQ	1–12[d]	<0.1[d]

Table 2: A summary of QDs-based fluorescent biosensors for the detection of VB_{12} in food and pharmaceutical products. (continued)

VB_{12} powders [180]	hydroquinone, EDA	self-exothermic reaction driving the formation of the nanocrystalline core (dissolution-oxidation-carbonization)	CQDs	24.6	≈4
	370	525	IFE-based FQ	0.75–100	0.2
VB_{12} tablets, other cobalt-containing medicines [183]	citric acid, DETA	hydrothermal (200 °C, 5 h)	NCQDs	58	2.3
	391	438	PET-based FQ	0–90	0.4
lake water, fetal bovine serum, milk [171]	methyl-*p*-benzoquinone, triethylenetetramine	Schiff base crosslinking reaction	orange-emitting CDs	6.56	5
	460	580	IFE-based FQ	0.05–200	0.01
VB_{12} powders [173]	Safranine T, ethanol	salvothermal (200 °C, 6 h)	orange-emitting CDs	7.6	2.04
	545	595	IFE-based FQ	1–65, 70–140	0.62
pharmaceutical injections [234]	*Cannabis sativa* paste, EDA, glutathione	hydrothermal (180 °C, 16 h)	N,nCQDs	14	4–6
	320	384	SQE-based FQ	20–100[d]	7.87[d]
VB_{12} tablets and injections [174]	ammonium citrate	hydrothermal (160 °C, 6 h)	CDs	–	3.03
	350	446	IFE-based FQ	0.3–15	0.093
VB_{12} tablets, natural water (Co^{2+} ions) [175]	L-cysteine	hydrothermal (300 °C, 2 h)	CDs	13.2	3.6
	325	395	PL quenching	0.01–100	0.01
tap water (Co^{2+} ions) [184]	PEI	hydrothermal (-)	CQDs	8.68	2.82
	340	462	IFE-based FQ	0.05–11	0.048
VB_{12} tablets (Co^{2+} ions) [185]	glycine (N and C source), PEI	hydrothermal (4 h at 200 °C)	NCQDs	57	2–2.5
	360	464	IFE, SQE, aggregation, complex formation between N-CQDs (amino group) and Co^{2+}	0.5–3.0	0.12
VB_{12} powders (CNCbl, Sigma) [186]	TSA, DETA	hydrothermal (160 °C, 6 h)	NCQDs	43	2.7
	390	450	FRET-based FQ	0.001–20	0.00021

Table 2: A summary of QDs-based fluorescent biosensors for the detection of VB_{12} in food and pharmaceutical products. (continued)

VB_{12} tablets, human serum, energy drink [187]	L-aspartic acid, 3,6-diaminoacridine hydrochloride	hydrothermal (170 °C, 5 h)	NCQDs	22.7	3.8
	360	450	IFE-based FQ	0–70	0.05628
veterinary VB_{12} injection (0.5 mg/mL) [188]	L-tartaric acid, urea, DMF	hydrothermal (180 °C, 4 h)	NCQDs	15.9	3.8
	450	550	IFE-based FQ	0–200	2.101
milk, two kinds of vitamin drinks [190]	thiamine nitrate (N and S source)	hydrothermal (180 °C, 10 h)	N,S-CQDs	10.4	1.5
	338	416	FRET-based FQ	0.33–28.30, 28.30–74.85	0.0156
VB_{12} tablets and injections [191]	*O*-phenylenediamine, thiourea	hydrothermal (180 °C, 12 h)	N,S-CQDs	14.3	≈2.9
	420	565	IFE-based FQ	0.25–20	0.775
tap water, lake water (Co^{2+} ions) [192]	L-cysteine	hydrothermal (180°C, 12 h)	N,S-CQDs	27	≈6
	340	420	SQE + electron transfer	1–50	0.026
VB_{12} injections [195]	cystamine, pomegranate juice	hydrothermal (180 °C, 8 h)	N,S-CQDs	–	2–3
	340	414	–	0–110	0.082
tap water (Co^{2+} ions) [198]	freeze-dried tofu, EDA, phosphoric acid	hydrothermal (210 °C, 4 h)	N,P-CQDs	64	2.9
	360	460	SQE + IFE-based FQ	0–0.5	0.058
VB_{12} tablets, blood serums [200]	L-arginine, phosphoric acid	hydrothermal (240 °C, 12 h)	N,P-CQDs	18.38	2.4
	340	444	IFE-based FQ	1.99–98.6, 98.6–176	0.059
VB_{12} tablets, vitamin drink, mineral water [8]	phenylboronic acid	hydrothermal (200 °C, 10 h)	BCDs	12	3.3
	247	323	IFE + FRET-based FQ	0.2–30	0.008
VB_{12} tablets and injections (Co^{2+} ions and VB_{12}) [199]	phosphoric acid (85%), sucrose, 1,2-EDA	hydrothermal (-)	N,P-CQDs	6.88	3.44
	365	451	SQE + IFE-based FQ	2–31 (VB_{12}), 1.7–12 and 28–141 (Co^{2+})	0.003 (VB_{12}), 0.0294 (Co^{2+})

Table 2: A summary of QDs-based fluorescent biosensors for the detection of VB_{12} in food and pharmaceutical products. (continued)

pharmaceutical injections (1,000 and 100 μg/mL of VB_{12}) [202]	tellurium powder, sodium borohydride ($NaBH_4$), cadmium chloride hydrate ($CdCl_2{\cdot}2.5H_2O$), TGA	hydrothermal (90 °C, 3 h)	CdS QDs	0.23[e]	3.6
	390	523	IFE-based FQ	0.02–0.4, 1.5–70.0	0.002
blood serum, urine, pharmaceuticals (multivitamin injections) [201]	cadmium chloride hydrate ($CdCl_2{\cdot}H_2O$), sodium sulfide (Na_2S), MPA	mix, adjust pH, deaerate, add reactants, stir overnight, dilute, store	CdS QDs	–	1.72
	370	532	photoinduced charge transfer by nonradiative FRET	0.5–100[d]	6.91[d]
tap water (Co^{2+} ions) [203]	SQDs, Co^{2+}, norfloxacin	mixing and reacting for 10 min at room temperature	SQDs	–	5.36
	360	≈410	ACQ-based FQ	0–90	0.02
VB_{12} powders (CNCbl, Sigma) [204]	zinc acetate dihydrate, sodium sulphide flakes, manganese acetate tetrahydrate	thermal (refluxing; 100 °C, 3 h) and mechanical (sonication)	Mn^{2+}-doped ZnS QDs	0.07	4
	320	587	FRET-based FQ	4.9×10^{-6}–29.4×10^{-6}	1.15×10^{-6}
several commercial health beverages, Milk, VB_{12} tablets [235]	aegle marmelos fruit juice (for CQDs), lemon juice (for surface functionalization)	ultrasound-assisted hydrothermal	N-, K-, and Ca-doped nCQDs	4.10	≈4.4
	250	290–750 (pH-dependent)	adsorption + FRET between VB_{12} and CQDs	0.01–100	9.16×10^{-4}

[a]DAN: 1,8-diaminonaphthalene, GO: graphene oxide, APTES: (3-aminopropyl)triethoxysilane, DAMO: *N*-[3-(trimethoxysilyl)propyl]ethylenediamine, PVP: poly(vinylpyrrolidone), EDA: ethylenediamine, AEAPDMMS: 3(2-aminoethylamino)propyldimethoxymethylsilane, CDPC: cytidine diphosphate choline, TCBQ: tetrachlorobenzoquinone, DETA: diethylenetriamine, PEI: polyethyleneimine, TSA: thiosalicylic acid, DMF: dimethylformamide, TGA: thioglycolic acid, MPA: mercaptopropionic acid; [b]GQDs: graphene quantum dots, N,S-GQDs: nitrogen and sulfur co-doped GQDs, SiQDs: silicon quantum dots, BCDs: boron quantum dots, CPDs: carbonized polymer dots, nCQDs: natural carbon-based quantum dots, NCQDs: nitrogen-doped NCQD, N,nCQDs: nitrogen-doped nCQDs, Mn^{2+}-doped ZnS: manganese-doped zinc sulfide, BCQDs: biomimetic carbon quantum dots, NA-CQDs: nicotinamide-functionalized CQDs, t-QDs: thermally reduced quantum dots, N,S-CQDs: nitrogen and sulfur co-doped CQDs, N,P-CQDs: nitrogen and phosphorus co-doped CQDs, TGA-CdS QDs: cadmium telluride quantum dots, SQDs: sulfur quantum dots; [c]FQ: fluorescence quenching, IFE: inner filter effect, SQE: static quenching effect, PL: photoluminescence quenching; PET: photoinduced electron transfer, ACQ: aggregation-caused quenching; [d]in μg/mL; [e]0.28 relative to fluorescein (as reference dye) with a quantum yield of 0.93 at 490 nm and in sodium borate buffer (pH 9.5).

tified at 580 nm. Furthermore, when compared to rhodamine 6G (as a standard), the relative quantum yield of the CDs is approximately 6.56%. This results in a vibrant orange fluorescence when observed under UV light [171]. Meng et al. also developed orange-emitting CDs for the label-free identification of VB_{12}. These excitation-independent CDs were synthesized from safranine T and ethanol through a simplified hydrothermal procedure. The ability of VB_{12} could well quench the fluorescence produced by CDs via the IFE mechanism, within two distinct linear detection ranges of 1–65 μM and 70–140 μM, with an LOD of 0.62 μM [173]. In another study, a new CD-based fluorescent sensor from ammonium citrate as precursor in a hydrothermal process was developed for sensing VB_{12} (LOD of 93 nM). The IFE was the main mechanism due to the overlap between the UV–vis absorption spectrum of VB_{12} and the emission/excitation spectra of the CDs. Monitoring VB_{12} in

injection and tablet samples using these sensors resulted in RR and RSD values of 93.3–109.2% and 0.67–1.62%, respectively [174]. Li et al. synthesized QDs (3.6 nm) from L-cysteine via a hydrothermal method at 300 °C for 2 h in order to detect Co^{2+} across a range from 0.01 to 100 μM via PL quenching [175].

Carbon quantum dot-based fluorescent sensors

Novel biomimetic CQDs for the VB_{12} analysis were also synthesized from cytidine diphosphate choline and ethylenediamine (EDA) through a pyrolysis process. A strong luminescence at 450 nm by these CQDs demonstrated ultrasensitive and highly selective detection capabilities for VB_{12} (LOD < 81 nM). In this assay, VB_{12} functioned as the recognition molecule, the biomimetic CQDs acted as the fluorescent indicator, and the observed fluorescence attenuation represented the signal. The fluorescence of the biomimetic CQDs also remained constant across various pH levels, salt concentrations, and under UV light exposure [176]. Dadkhah et al. have recently evaluated VB_{12} concentrations by developing a triple-mode nanosensor based on nicotinamide (NA)-functionalized CQDs through a microwave-assisted hydrothermal process. Linear range and LOD were determined to be 0.1–60 μM and 0.0317 μM, respectively. Interestingly, VB_{12}-induced color shifts in NA-CQDs could be captured using a UV–vis spectrophotometer and a custom smartphone app for simultaneous signal reading. When integrated into a smartphone, the NA-CQDs acted as a colorimetric sensor by presenting a reliable linear detection range (4.16–66.6 μM) for VB_{12} with an LOD of 1.40 μM. An RR of 96.52–105.10% with an RSD of 1.32–3.44% for pharmaceutical supplements (i.e., injections and tablets) showed a minimized cross-activity [177]. He et al. synthesized high-yield orange-emitting CQDs using citric acid as precursor in a hydrothermal process. In addition, VB_{12} in tablets, vitamin-infused drinks, and human serum effectively attenuated the CDs' fluorescence intensity through the IFE, confirming high specificity towards VB_{12} with an LOD of 60.78 nM [178]. Figure 4A shows the clear absorption peak at 530 nm for the CQDs solution, with λ_{ex} = 560 nm and maximum λ_{em} = 520 nm. A vivid orange fluorescence was observed in photos obtained under both daylight and 365 nm UV light exposure. However, there was no dependency between λ_{ex} and λ_{em} of the CDs (λ_{ex} = 360–540 nm; Figure 4B). Figure 4C depicts that, when the solid-state CQDs were exposed to both daylight and 365 nm UV light, they emitted a fluorescence similar to that of CQDs in solution under UV light, with a peak λ_{em} of 595 nm exhibiting a redshift. This indicates the potential application of these CQDs in optoelectronic devices. The fluorescence lifetimes of CQDs in both solid state and aqueous solution were measured, resulting in lifetimes of 3.446 ns and 3.535 ns for the solid state and the aqueous solution, respectively (Figure 4D) [178].

Thermally reduced CDs-based FRET optical sensors were also applied to assess VB_{12} in an aqueous solution within a concentration range from 1 to 12 μg/mL with an LOD of less than 0.1 μg/mL. This approach is highlighted for its simplicity, affordability, sensitivity, and selectivity in detecting biologically important vitamin VB_{12} [179]. Chen et al. [180] in a large-scale produced core–shell CQDs using hydroquinone and EDA as precursors. The rapid formation of the nanocrystalline core was facilitated with the intense exothermic nature of this reaction. Furthermore, these CQDs exhibited green photoluminescence at approximately 525 nm when excited between 320 and 420 nm. A noticeable decrease in the fluorescence intensity was observed after adding VB_{12} to the CQD solution, accompanied by a blueshift in their emission spectrum. The fluorescence intensity ratio at 525 nm of the developed CQDs was proportionally to the VB_{12} level (0.75–100 μM), with an LOD of 0.2 μM. Incremental VB_{12} concentrations significantly diminished the CQDs' green fluorescence. The FQ of CQDs by VB_{12} demonstrated remarkable specificity, as other studied vitamins and metal ions did not affect their fluorescence. The high selectivity level in detecting VB_{12} led to the development of an easy, visual paper sensor for analyzing VB_{12} fluorescence. Researchers also fabricated a CQD-based fluorescent paper sensor for detecting VB_{12}. A strong green fluorescence under UV light was observed when a solution of CQDs was applied to the filter paper. The CQDs' fluorescence intensity was significantly quenched by increasing the concentration of VB_{12} from 50 to 1000 μM. The authors claimed high specificity of the sensor as FQ through VB_{12} was more noticeable than those through other examined vitamins [180]. In this assay, VB_{12} acted as the recognition analyte, the CQDs functioned as the fluorescent indicator, and fluorescence quenching (observed both in solution and on paper) represented the measurable signal.

There are many studies on CQD-based fluorescent sensing platforms to detect VB_{12} due to their great luminescent potential. Sun et al. synthesized yellow-emitting CDs with a high quantum yield (16.7%) based on L-tartaric acid and urea as precursors in a solvothermal technique. The developed CQDs with excellent photostability and dispersibility could detect VB_{12} in water (LOD of 2.045 μM), manifesting a "turn off" response in their fluorescence. There was a direct linear correlation between the CQDs' fluorescence intensity and the concentration of VB_{12} (0–200 μM). The IFE-based FQ was identified to be the main mechanism according to detailed microscopic and spectroscopic analyses [181]. The excitation-dependent emission of these yellow-emitting CDs was likely due to the presence of various luminescent centers or emissions arising from surface states. A noticeable shift in color from yellow to red with rising concentration was visible to the naked eye. This

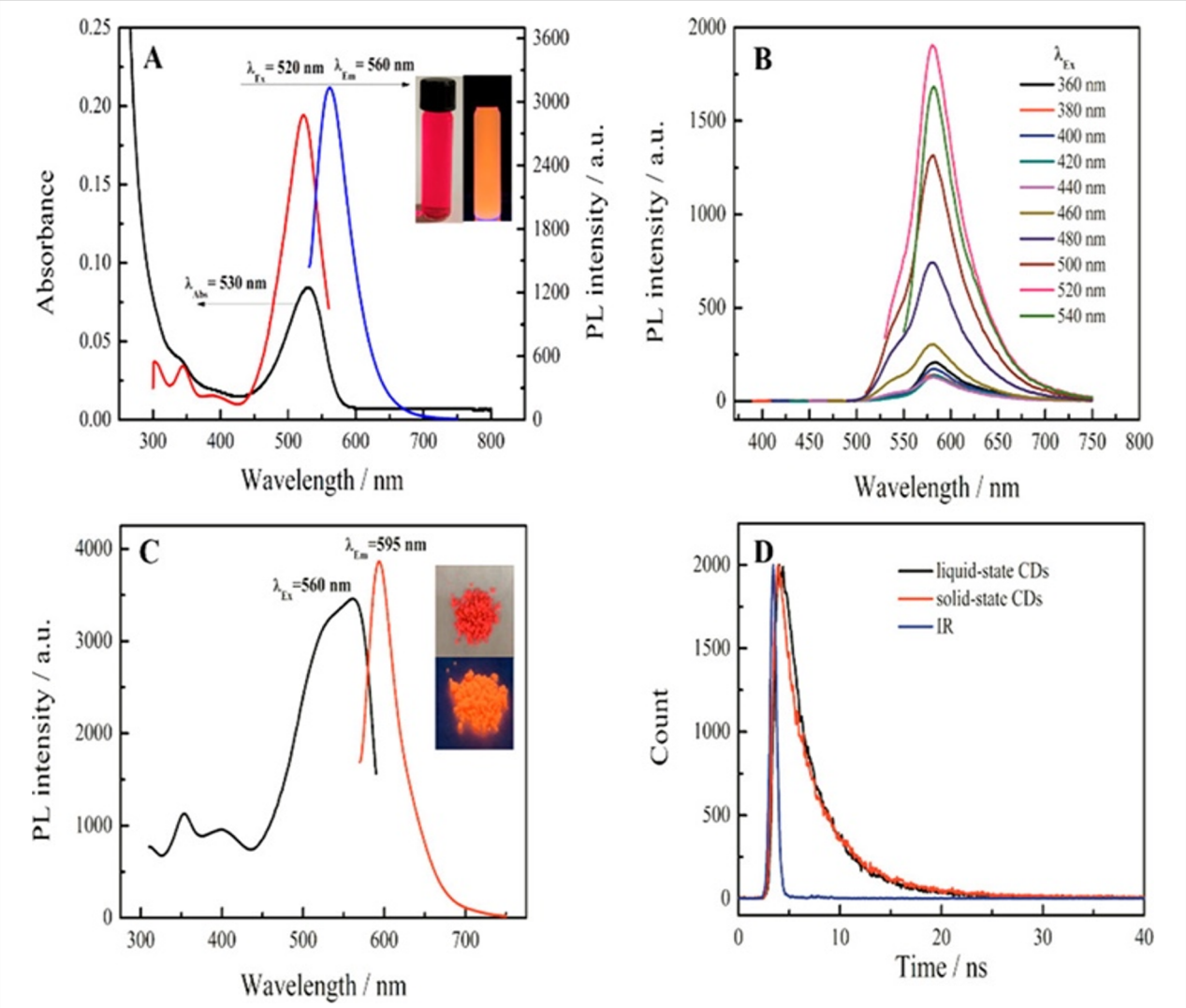

Figure 4: (A) Spectral characteristics including UV–vis absorption, fluorescence excitation, and emission of CDs in water (inset: daylight and 365 nm UV light exposure visuals of CDs). (B) Emission profiles of water-based CDs across excitation wavelengths from 360 to 540 nm. (C) Excitation and emission spectral data for CDs in solid form (inset: visual representation of solid-state CDs under natural and 365 nm UV illumination). (D) Comparative fluorescence lifetime traces for CDs in both solid and liquid mediums. Figure 4 was reprinted with permission from [178], Copyright 2020 American Chemical Society. This content is not subject to CC BY 4.0.

trend was also evident in the graphs depicting the ethanol solutions of CQDs at different doses from 2.5 to 150 μM under 450 nm excitation [181]. In this sensing system, VB_{12} was the recognition analyte, the yellow-emitting CQDs acted as the fluorescent indicator, and fluorescence quenching ("turn off" response) was recorded as the signal. As well, Zhao et al. synthesized bright yellow fluorescent nitrogen-doped CDs (N-CQDs) with a quantum yield of 32% via a hydrothermal process with *O*-phenylenediamine and 4-aminobenzoic acid as precursors. They stated that when these QDs were excited at 390 nm, a pronounced decrease in their fluorescence intensity at 567 nm was observed upon interaction with VB_{12}. A fluorescence sensor based on these QDs was developed in an aqueous medium, indicating a linear response to two different concentration ranges of VB_{12} (0 to 90 μM and 140 to 250 μM), with a low LOD of 0.119 μM [182]. Another hydrothermal process in the presence of citric acid and diethylenetriamine (DETA), respectively, as carbon and nitrogen sources, was performed to prepare blue-emitting N-CQDs (λ_{ex} = 391 nm and λ_{em} = 438 nm) with a size of 2.3 nm and an exceptional quantum yield of 58%. The presence of Co^{2+} ions in water with very low cross-reactivity with other metal ions could quench the fluorescence of the developed CDs, confirming the high sensor selectivity. A linear range of 0–90 μM and a LOD of less than 0.4 μM were recorded to monitor these metal ions, which can be particularly used to track the presence of VB_{12} or Co^{2+}-based medications [183]. Zhang et al. reported the synthesis of onion-derived CQDs via a hydrothermal technique and their subse-

quent functionalization with PEI. The findings revealed that the 2.82 nm PEI-CQDs with hydroxy and amino groups on their surface exhibited excitation and emission peaks at 340 nm and 462 nm, respectively, with a fluorescence quantum yield of 8.68%. The fluorescence of PEI-CQDs was selectively quenched by Co^{2+} ions, making them effective for the detection and quantification of Co^{2+} in various samples such as VB_{12}. The LOD and linear range for detecting Co^{2+} were determined to be 0.048 μM and 0.05–11 μM, respectively. An RR of 97.0–100.64% showed that PEI-CQDs could be effectively utilized in monitoring Co^{2+} levels in tap water [184].

Nitrogen-doped carbon quantum dot-based fluorescent sensors

N-CQDs are particularly practical for fluorescent sensing of VB_{12}, owing to their synergistic properties, including enhanced fluorescence, precise target interaction, high quantum yield, biocompatibility, stability, and cost-effective production. The integration of nitrogen atoms not only increases their fluorescence intensity but also reinforces targeted interactions with Co^{2+} and VB_{12}, revealing significant changes in fluorescence signals. These modifications are based on the nitrogen contribution to the dots' quantum yield, ensuring the detection of very low concentrations of Co^{2+} and VB_{12}. Their compatibility with biological samples allows for their use without affecting detection quality or creating health risks. Furthermore, the resilience of N-CQDs to different environmental conditions ensures reliable sensing across diverse sample matrices. Coupled with their economical and simple synthesis process, N-CQDs would be potent and promising nanomaterials for the sensitive and selective detection of Co^{2+} and VB_{12}, with widely ranging implications for healthcare diagnostics and nutritional analysis [185,186].

Bano et al. synthesized fluorescent N-CQDs with a high quantum yield of 57%. These nanomaterials showed a robust blue emission. These N-CQDs also demonstrated resilience to high salt concentrations and maintained their photostability for over six months. Utilizing N-CQDs as a sensor for the selective "turn off" detection of Co^{2+} proved an LOD of lower than 0.12 μM within a linear range of 0.5–3.0 μM. Different mechanisms were involved in detecting Co^{2+}, including IFE, static quenching effect (SQE), aggregation, and the formation of complexes with the N-CQDs' amino groups. The fluorescence quenched by Co^{2+} could be "turned on" again by adding chemical compounds such as glutathione, ascorbic acid, cysteine, and ethylenediaminetetraacetic acid (EDTA), proving the N-CQDs' potential as a reversible probe for Co^{2+} determination. The standard recovery test of Co^{2+} spiked into VB_{12} samples showed that N-CQDs were an efficient detection tool with 96.0–105.5% RR and 1.34–2.54% RSD [185].

Kalaiyarasan and Joseph assessed VB_{12} through pH-dependent (2.0–9.0) FRET quenching of N-CQDs prepared by a hydrothermal process (160 °C, 6 h) in the presence of TSA and DETA. N-CQDs had a polycrystalline structure under acidic conditions, whereas a mixed crystalline structure was observed for N-CQDs in basic media. The authors also indicated that VB_{12} could strongly quench the fluorescence of the developed N-CQDs through the FRET mechanism. High-resolution transmission electron microscopy analysis showed CQDs with diameters of 2.1–3.5 nm embedded in an amorphous carbon matrix, while dynamic light scattering indicated a dominant size of 10.8 nm. Aggregated particles were likely due to nitrogen-induced hygroscopic effects. Lattice spacings of 0.229, 0.334, and 0.186 nm matched the (100), (006), and (105) planes of graphite. The XRD pattern showed a broad peak at 25°, consistent with disordered carbon and the (006) graphite plane. The LOD and linear range of VB_{12} were ≈210 pM and 1 nM–20 μM, respectively [186]. Nandi et al. [187] and Yu et al. [188] also produced fluorescent NCQDs with high optical stability from different precursors via hydrothermal synthesis (Table 2). Compared to Yu et al.'s work, Nandi et al. obtained a higher quantum yield (22.7% vs 15.9%; Table 2). Nandi et al. reported that the developed NCQDs had good potential to measure bilirubin and VB_{12} through FRET- and IFE-based FQ, respectively. The efficacy of this kind of fluorescent nanosensors (λ_{ex} = 360 nm, λ_{em} = 450 nm) was confirmed in real samples such as VB_{12} tablets, human serum, and energy drinks with an RR of 95.06–112.48% [187]. Yu et al. found that NCQDs prepared from the precursors L-tartaric acid, urea, and dimethylformamide could detect VB_{12} with an LOD of 2.101 μM; also, they maintained their photostability under diverse pH levels, temperatures, and ionic strengths [188].

Nitrogen and sulfur co-doped carbon quantum dot-based fluorescent sensors

Nitrogen and sulfur co-doped CQDs (N,S-CQDs) present a remarkable advancement in the field of molecular sensing due to their enhanced properties over quantum dots doped solely with nitrogen. The combined doping with nitrogen and sulfur not only increases the photoluminescence of the CQDs for brighter and more stable fluorescence but also improves their sensitivity and selectivity towards target molecules. This can be attributed to the synergistic effect of nitrogen and sulfur doping, which introduces more active sites and facilitates selective binding to specific molecules (such as VB_{12}). Moreover, N,S-CQDs demonstrate superior chemical and photostability, broadening their application beyond sensing to bioimaging, drug delivery, and photocatalysis [189].

Li et al. synthesized N,S-CQDs with a quantum yield of 10.4% from thiamine nitrate via a hydrothermal process. VB_{12} and the

synthetic lemon-yellow azo dye tartrazine (acceptor) could well quench N,S-CQDs' fluorescence (donor) via FRET. Energy transfer rate and efficiency between donor and acceptor compounds were increased by increasing acceptor concentrations and varied with different excitation wavelengths (338–408 nm). VB_{12} and tartrazine were selectively and sensitively detected using the N,S-CQD-based probe with LODs of 0.0156 and 0.018 μM, respectively. High RRs of 97.5–104.2% for VB_{12} (RSD = 0.11–2.08%) and 91.0–110.6% for tartrazine (RSD = 0.09–3.35%) in milk and two types of vitamin drinks demonstrated the sensor's performance [190]. Orange-emitting N,S-CQDs with good stability and quantum yield were also developed for label-free monitoring of VB_{12} through a hydrothermal reaction between the precursors *o*-phenylenediamine and thiourea. The nanomaterials exhibited a unique photoluminescent signature, with emission peaks at 420 nm and 565 nm, remaining constant regardless of the excitation wavelength. This feature enabled the identification of VB_{12} based on IFE, as its absorption spectrum extensively overlaps with the emission peaks of the nanomaterials. Under optimal reaction conditions (at 25 °C in a pH 6.0 methylethanesulfonate buffer for 5 min), there was a linear relationship between the VB_{12} concentration and the fluorescence quenching ratio at 565 nm (0.25–20 μM), with an LOD of 77.5 nM [191]. In this sensing model, VB_{12} functioned as the recognition analyte, the N,S-CQDs acted as the fluorescent indicator, and the quenching of orange emission provided the detectable signal.

Similar nanomaterials based on L-cysteine as precursor were prepared for the selective and visual determination of Co^{2+} ions within a linear range of 1–50 μM and an LOD of 0.026 μM [192]. Sun et al. found that the addition of H_2O_2 or EDTA can restore (turn on) the fluorescence of N,S-CDs that was previously quenched (turned off) by Co^{2+} ions. The quenching was attributed to an SQE mechanism, which involves electron transfer through the creation of a complex between Co^{2+} and the functional groups present on the N,S-CDs [192]. Luo and Jiang earlier explained that the robust oxidizing capabilities of H_2O_2 could make the fluorescence system based on N,S-CDs a promising "on–off–on" fluorescent switch sensor for the detection of H_2O_2 [193]. The fluorescence of the combination of N,S-CDs, and Co^{2+} was also rejuvenated with EDTA. This chemical, due to its strong chelating ability, can simply form stable complexes with metal ions and does not alter the fluorescence intensity of N,S-CDs. Thus, the presence of EDTA reduces the impact of Co^{2+} on the N,S-CDs, facilitating the recovery of the quenched fluorescence [194]. In a similar procedure, Mohammadi et al. hydrothermally synthesized N,S-CQDs by utilizing pomegranate juice as the carbon source and cystamine for both sulfur and nitrogen in order to sensitively detect VB_{12} in the concentration range of 0–110 μM with an LOD of 0.082 μM. To demonstrate the practicality of this approach, a VB_{12} ampoule was analyzed as a real-world sample. The obtained high RR confirmed the effectiveness and applicability of N,S-CQDs for pharmaceutical and biological purposes [195].

Nitrogen and phosphorus co-doped carbon quantum dot-based fluorescent sensors

Nitrogen and phosphorus co-doped CQDs (N,P-CQDs) represent a significant advancement in the field of nanomaterial-based sensing, offering enhanced capabilities compared to their N-CQDs. By introducing both nitrogen and phosphorus into the carbon lattice, N,P-CQDs exhibit modified electronic structures and surface chemistries, leading to excellent photoluminescence properties that can be finely tuned for specific sensing applications [196]. This co-doping approach not only enhances the sensitivity and selectivity of these QCDs towards various analytes but also improves their solubility and stability across different environments. The presence of nitrogen and phosphorus allows for the introduction of diverse functional groups on the CQDs' surface, facilitating specific interactions with target molecules. These interactions can induce changes in the QDs' luminescence, serving as a basis for detecting a wide range of substances [197].

Wen et al. hydrothermally prepared N,P-CQDs with a 64% yield using a blend of frozen tofu, EDA, and phosphoric acid. This N,P-CQDs-based sensor could selectively and sensitively detect Co^{2+} ions with an LOD of 0.058 μM by fluorescence quenching [198]. Similar to the work of Sun et al. [192] on N,S-CDs-based fluorescent sensors in detecting Co^{2+} ions, Wen et al. reported that the fluorescence quenching can be reversed by adding EDTA. Accordingly, the LOD of 0.098 μM for the concentration of EDTA in solutions was determined. This dual functionality establishes that these CQDs as an effective "off–on" fluorescence sensor for both Co^{2+} ions and EDTA. The practical application of this method was validated by accurately measuring Co^{2+} levels in tap water (96.3–103.3% RR, 1.78–3.03% RSD) and EDTA in contact lens solutions (98.6–104.3% RR, 1.87–2.64% RSD) [198]. Zhang et al. also designed a new N,P-CQDs with good water solubility and favorable biocompatibility, which were hydrothermally synthesized using a mixture of sucrose (C source), 85% phosphoric acid (P source), and 1,2-EDA (N source). The excitation/emission peaks are at 365/451 nm, and bright blue, green, or red emission was found depending on whether the excitation wavelengths of the laser were set to 408, 488, or 543 nm, respectively. The authors found that the fluorescence could be quenched by both VB_{12} and Co^{2+} ions by a combination of SQE and IFE mechanisms. The linear range for the VB_{12} concentration was assessed to be 2.0–31 μM, whereas the linear response to Co^{2+} ions occurred in two ranges of 1.7–12 μM and 28–141 μM. The

LOD of VB_{12} and Co^{2+} were 3.0 nM and 29.4 nM, respectively. In this sensing model, VB_{12} or Co^{2+} served as the recognition analytes, the N,P-CQDs acted as the fluorescent indicators, and the quenching of multicolor emissions provided the measurable signals. To validate the sensor's performance, the nanoprobe was successfully applied to analyze VB_{12} (96–108% RR and 2.7–8.1%) and Co^{2+} (112–132% RR and <3.0%) in tablets/injections and spiked water samples, respectively [199]. In another study done by Wang et al., N,P-CDs with an 18.38% quantum yield as well as excellent water solubility and luminescent qualities were successfully synthesized through a one-step hydrothermal method using L-arginine and phosphoric acid as precursors [200]. They pointed out that the optimal emission could be observed at 444 nm upon excitation at 340 nm. The developed N,P-CDs could efficiently and selectively monitor VB_{12} via the IFE mechanism. This highly fluorescent sensor responded to VB_{12} concentrations within two linear ranges of 1.99–98.6 μM and 98.6–176 μM, with a very low LOD of 0.059 μM. Moreover, the sensor's efficacy was affirmed by analyzing VB_{12} in various vitamin tablet formulations (99.6–109.0% RR and 0.66–1.06%) and blood serum (82.1–102.1% RR and 0.37–4.66%) samples [200].

Fluorescent sensors based on other chemically doped quantum dots

Cadmium sulfide (CdS) and cadmium telluride (CdTe) QDs have unique optical properties and applications. CdS QDs are primarily utilized in optoelectronics and photocatalysis, benefiting from their strong UV–visible absorption and photoluminescence. In contrast, CdTe QDs are favored in medical imaging and biosensing, owing to their tunable emission across a broader visible to near-infrared spectrum, which is particularly advantageous for biological applications requiring deep tissue penetration. While both types serve in sensing technologies, their inherent differences in emission range and stability make each suitable for specific tasks, with CdTe QDs being especially valuable in the food and pharmaceutical industries for sensitive and selective detection of metabolites and molecules, such as VB_{12} analysis [201,202]. Gore et al. fabricated an innovative FRET probe to measure VB_{12} in aqueous environments through mercaptopropionic acid (MPA)-functionalized CdS QDs, made from cadmium chloride and sodium sulfide. In the range of 5.0–100 μg/mL, there was a linear relation between CdS QDs' fluorescence intensity and VB_{12} level, while an LOD of 6.91 μg/mL was recorded. High selectivity was determined for this fluorescent sensor in the presence of many interfering substances such as metal ions (e.g., K^+, Ca^{2+}, and Mg^{2+}), ammonium cations (NH^{4+}), sugars (e.g., starch, maltose, glucose, fructose, sucrose, lactose, and dextrose), ascorbic acid, tyrosine, urea, and thiourea. In this platform, VB_{12} functioned as the recognition analyte, MPA-functionalized CdS QDs served as the fluorescent indicator, and the FRET-induced fluorescence quenching provided the sensing signal. The MPA-functionalized CdS QDs could be efficiently applied to monitor VB_{12} in blood serum, urine, and multivitamin injections without any sample pretreatment (97.15–99.49% RR, 0.63–2.16% RSD) [201]. Shamsipur et al. developed a selective and sensitive IFE-based method using thioglycolic acid (TGA)-capped CdTe QDs in order to monitor VB_{12} in aqueous media. The fluorescence quenching rate of the prepared TGA-CdTe QDs (λ_{ex} = 390 nm and λ_{em} = 523 nm) under optimum conditions had a linear correlation with VB_{12} dose within concentration ranges of 0.02–0.4 and 1.5–70.0 μM VB_{12} with an LOD of 0.002 μM. The sensor potential was confirmed by determining VB_{12} in pharmaceutical injections (95–105% RR, 2.4–4.5% RSD) [202]. Wang et al. developed fluorescence sensors based on 5.36 nm sulfur quantum dots (SQDs) to detect Co^{2+} ions. They introduced a novel assay leveraging aggregation-caused quenching of SQDs for detecting these ions with a linear concentration range of 0–9 μM, with an LOD of 0.02 μM [203]. A new fluorescent sensor was also synthesized based on Mn^{2+}-doped ZnS QDs, using zinc acetate dihydrate, sodium sulfide flakes, and manganese acetate tetrahydrate as precursors, through an integrated thermal and mechanical treatment [204]. Jia et al. hydrothermally produced 3.3 nm boron-doped carbon dots (BCDs) using phenylboronic acid as the precursor. These nanomaterials with a quantum yield of 12% exhibited excitation and emission wavelengths of 247 nm and 323 nm, respectively. The fluorescence of BCDs could be quenched by sorbate and VB_{12} through IFE and FRET mechanisms. Linear range and LOD of VB_{12} were determined to be 0.20–30 μM and 0.008 μM, respectively [8].

Graphene quantum dot-based fluorescent sensors

This type of sensor is considered an innovative approach to VB_{12} detection due to the exceptional surface area, conductivity, and biocompatibility of graphene and GO. These characteristics facilitate rapid, reliable assays, critical for monitoring VB_{12} levels in complex matrices and promoting the quality control and efficacy of dietary supplements and fortified foods [205]. A new fluorescent probe, 1,8-diaminonaphthalene (DAN)-functionalized GQDs (DAN-GQDs), designed by Ravi et al. [206], could sensitively detect negligible levels of vitamin B_9 (LOD = 1.73×10^{-15} M) and MeCbl (LOD = 6.37×10^{-12} M) in water using absorption and fluorescence methods. This technique utilized IFE due to the overlap between the absorption spectra of vitamin B_9 and VB_{12} and the emission spectrum of DAN-GQDs. The derived association constant values indicated that DAN–GQD interacts with vitamin B_9 and MeCbl at stoichiometric ratios of 1:2 and 1:1, respectively. Investigation into the time-resolved fluorescence decay patterns (λ_{ex} = 328 nm, λ_{em} = 338 nm) validated that the

reduction in fluorescence intensity of DAN–GQD, triggered by the addition of vitamin B_9 and MeCbl, is a consequence of the non-radiative dissipation of energy from excited electron states. In this biosensing setup, MeCbl served as the recognition analyte, DAN–GQDs acted as the fluorescent indicator, and the IFE fluorescence quenching constituted the sensing signal. They also reported that the DAN-GQDs-based sensor revealed a desirable performance with commercial FA and MeCbl in water [206]. Co-doping GQDs with heteroatoms (e.g., nitrogen or sulfur) enhances their electronic and optical properties, enhancing fluorescence efficiency for better performance in sensing, bioimaging, and optoelectronics. This approach modifies the GQDs' bandgap, increases PL yield, and improves stability and surface functionality, enabling more selective and sensitive interactions in applications like sensors and catalysis [207-209]. Boonta et al. assessed the fluorescence detection of Co^{2+} ions in water via synthesized nitrogen and sulfur co-doped GQDs (N,S-GQDs). The prepared N,S-GQDs could be quenched by Co^{2+} through interactions between the metal ions and the surface functional groups of the fluorescent probe. Furthermore, the aggregation of N,S-GQDs was induced by the addition of Co^{2+}, leading to an enhancement of UV–vis absorption at 430 nm and a color transition to yellow-brown within 3 min. Linear range and LOD for Co^{2+} were determined to be 0–40 μM and 1.25 μM, respectively. Also, the authors successfully evaluated the fluorescent sensor probe's potential to measure Co^{2+} in real water samples [208]. Martins et al. monitored multivitamins (LOD_{VB12} = 0.32 nM) in classic and fruit-based energy drinks using electrodes functionalized with N,S-GQDs [209].

Carbonized polymer dot-based fluorescent sensors

Gao et al. prepared CPDs using a facile, one-pot method with tetrachlorobenzoquinone and EDA as precursors, catalyzed by a Schiff base condensation reaction. These CPDs are characterized by their unique dual-emission properties, with blue emission at 445 nm and yellow emission at 575 nm, demonstrating exceptional photostability and antioxidant capabilities. The authors also developed a ratiometric fluorescent nanoprobe for the accurate detection of VB_{12}, achieving a sensitive assay within a linear range of 0.25–100 μM and a very low LOD of 0.14 μM. The researchers claimed that the applied innovation not only simplified the CPDs fabrication process with lower cost and complexity but also signified a significant step forward in the field of biosensing, offering a potent tool for the design of advanced fluorescent nanoprobes for a wide array of analytical and biomedical applications [210].

Silicon quantum dot-based fluorescent sensors

Silicon-based nanomaterials, including nanoparticles, nanowires, and nanorods, due to their negligible toxicity and inherent biocompatibility, can be utilized for biomedical applications. The unique optical properties of these materials, along with their non-toxic nature and controllable surface functionalization, have rendered them intriguing substances for fabricating advanced fluorescent sensors [211]. Silicon quantum dots (SiQDs) as zero-dimensional fluorescent silicon nanomaterials have acceptable water solubility for biological applications such as photoluminescent sensing and bioimaging of different ions and biomarkers [212].

Long et al. designed label-free SiQD-based fluorescent sensors using microwave-assisted synthesis under normal pressure to detect VB_{12}. This micronutrient, owing to the IFE, could quench the SiQDs' fluorescence. The authors applied quercetin and doxorubicin as controls thanks to the alignment of their absorption peaks with SiQDs' excitation or emission peaks, which aided in elucidating the quenching mechanism. The quenching efficiency was found to depend on the overlap extent between the quencher's absorption peak and the SiQDs' excitation or emission peaks, with a greater overlap leading to increased quenching efficiency. A linear increase in fluorescence quenching efficiency was observed within a VB_{12} concentration range from 0.5 to 16 μM, while an LOD of 0.158 μM was obtained. In this sensing system, VB_{12} acted as the recognition analyte, SiQDs were the fluorescent indicator, and fluorescence quenching via the IFE mechanism provided the signal. Furthermore, the performance of SiQDs-based fluorescent sensors for VB_{12} quantification was affirmed by evaluating a RR between 97.7% and 101.1% in tablets and human urine samples [213]. In another research, green luminescent SiQDs were used for the assessment of VB_{12} and as antibacterial agent [214]. Zhao et al. synthesized them using thiourea and catechol via a microwave-assisted hydrothermal process. The developed SiQDs showed a linear range of 0.05–30 μM and an LOD of 0.05 μM for VB_{12}. The authors also realized that these nanomaterials had good antimicrobial activity against *Staphylococcus aureus* with a minimum inhibitory concentration of 250 μg/mL. However, they pointed out that at least 1.3 mg/mL is needed to inhibit the biofilm growth of this bacterium. The SiQDs–lysozyme complex effectively inactivated *S. aureus*, achieving a low MIC of 10 μg/mL and hindering biofilm growth at 62.5 μg/mL, thanks to singlet oxygen, charge effects, and peptidoglycan hydrolysis [214]. In general, the antibacterial mechanism of SiQDs can be due to (i) their small particle size, facilitating easy penetration through bacterial walls and membranes, thus inducing bacterial death, (ii) electrostatic interactions, where SiQDs disrupt membrane structures via electrostatic adsorption, leading to bacterial death, and (iii) the generation of reactive oxygen species, which can damage microbial external membranes and proteins, ultimately causing bacterial death [215-220]. *S. aureus* displayed bright orange, green, and blue fluorescence when excited by

lasers at 557, 493, and 353 nm, respectively. The visible distinct spherical structure of *S. aureus* suggested the bacteria cells successfully absorbed the SiQDs [214]. Sullam et al. developed a new fluorescence probe based on SiQDs to measure Co^{2+} in a linear range of 1–120 μM and an LOD of 0.37 μM. Highly water-soluble and stable SiQDs were hydrothermally produced by mixing 3(2-aminoethylamino)propyldimethoxymethylsilane and poly(vinylpyrrolidone) for detecting Co^{2+} through static quenching. The authors also developed a cheap SiQD-based test paper with excellent selectivity and sensitivity and minimized cross-activity, and successfully utilized it to quantify Co^{2+} levels in natural water samples. The FQ was notably intensified by raising the concentration of Co^{2+}, aligning closely with the outcomes obtained in the absence of interfering ions [221].

Fluorescent sensing with natural carbon-based quantum dots

The use of fluorescent sensing with natural carbon-based quantum dots (nCQDs) is crucial not only for ensuring food safety and quality but also for the pharmaceutical industry, as it provides a highly sensitive, non-toxic, and eco-friendly method for detecting contaminants, nutrients, and active pharmaceutical ingredients. This innovative approach enables the rapid, accurate monitoring and quality control of food products and pharmaceuticals, which is essential for preventing health hazards, adhering to rigorous regulatory standards, and enhancing consumer preference in both the food supply chain and pharmaceutical products [29,222-224].

Recently, a lot of natural resources have been used to synthesize CQDs as cost-effective and eco-friendly sensing materials by carbonation and hydrothermal methods. Preethi et al. obtained a fluorescent biosensor via ultrasound-assisted green synthesis of CQDs from curry berries (*Murrayakoenigii* L.) for VB_{12} quantification (LOD = 0.04 μM). The fluorescent intensity was progressively diminished in the presence of VB_{12} because a significant reduction in this parameter was observed from 0 to 0.40 μM. In this biosensing design, VB_{12} was the recognition molecule, CQDs acted as the fluorescent indicator, and the fluorescence attenuation due to coordination with Co^{2+} ions served as the measurable signal [222]. The presence of oxygen-containing groups on the CQDs' surface allowed for the formation of complexes with Co^{2+} ions via coordination interaction, facilitating electron transition from the CQDs to the Co^{2+} ions [225]. The complex formed between CQDs and Co^{2+} ions resulted in a substantial reduction in the CQDs' fluorescence. Researchers also confirmed the sensor efficiency by calculating the RR (93.0–97.6%) in milk powders at pH 7.0 with three concentrations of 0.1, 0.2, and 0.3 μM VB_{12} [222].

Xiang et al. developed innovative nCQDs obtained from the edible mushroom *Lactarius hatsudake* as fluorescent sensors for detecting VB_{12}. In a hydrothermal process at 200 °C for 12 h, they successfully synthesized new 3 nm nCQDs with a quantum yield of 22.88% to detect VB_{12} concentrations within a linear range of 0–20 μM and an LOD of 36.9 μM. They evaluated the selective performance of nCQDs was validated by analyzing the content of VB_{12} in three different milk samples with an RR of 91.50–100.40% and an RSD as low as 2.08% [226]. A comparison in the RR and RSD of these nCQDs with other analytical methods, such as HPLC-ICP-MS (81.3–103.6% RR and 0.4–4.6% RSD) [227] and HPLC-MS/MS (75.2–89.5% RR and 3.6–5.9% RSD) [228], showed acceptable performance of the sensors based on *L. hatsudake*-derived CQDs. Yu et al. also synthesized N-doped nCQDs for sensing pH and VB_{12}. The precursor and nitrogen source were *Saccharomyces* and ethanediamine, respectively. The fluorescence intensity and lifetime of N-doped nCQDs were increased by shifting the pH value from 14 to 2. Furthermore, the fluorescence intensity revealed a highly reversible capability from pH 13 to 2, maintaining its strength without a meaningful decrease after ten consecutive cycles. These sensors, according to the FRET mechanism, could also detect VB_{12} with an LOD of 2.19 μM [229]. Likewise, Zhao et al. prepared new N-doped nCQDs for Co^{2+} ions and pH sensing based on the precursors of seaweed kelp and EDA under 800 W microwave irradiation at 200 °C for 10 min. The luminescence of CDs displayed a consistent linear correlation across a pH spectrum of 3 to 8 and was utilized for visually identifying Co^{2+} ions. They mentioned that adding Co^{2+} visibly changed the solution's color from clear to brownish-yellow under normal light and from bright blue to dark blue under UV light. Linear range and LOD of Co^{2+} concentration were 1–200 μM and 0.39 μM, respectively. This fluorescent sensor was effectively used to monitor these ions in samples of water collected from a river [230]. Another study on the hydrothermal synthesis of N-doped nCQDs using biomass quinoa saponin powders and EDA was performed. A high quantum yield (22.2%) with a small particle size (≈2.25 nm) was recorded for these fluorescent materials, which showed excitation wavelength-dependent blue light emission. The developed N-doped nCQDs detected Co^{2+} ions within the linear range of 20–150 μM with an LOD of 0.49 μM [231]. Ji et al. also synthesized bright-blue photoluminescent CDs from the bacterium *Weissella* sp. Kl-3 through a hydrothermal technique. CDs sensitized by ampicillin sodium with multicolor fluorescence emission characteristics were efficiently utilized as a fluorescence nanosensor to detect Cr^{6+} and VB_{12} via the IFE mechanism. Linear range and LOD for Cr^{6+} and VB_{12} concentrations were determined to be 0–50 μM and 0–25 μM, as well as 0.10657 μM and 0.0515 μM, respectively. This nanosensor was able to detect Cr^{6+} ions in water and VB_{12} in serum and milk

samples [232]. In a recent research by Chen et al., nCQDs using edible bird's nest, a traditional Chinese delicacy, and distilled water have been hydrothermally prepared to analyze VB_{12} in serum [233]. These nanomaterials represented excellent features such as high water solubility, fluorescence efficacy, biocompatibility, and stability across a wide pH spectrum (3.0–11.0) and in solutions of high ionic strength. The interaction of nCQDs with VB_{12} led to a remarkable reduction in the fluorescence intensity of nCQDs with increasing VB_{12} doses. Linear range and LOD were 0–100 μM and 0.24 μM, respectively. An RR of 96.2–100.3% of VB_{12} in human serum revealed that the developed nCQDs can be used for clinical applications [233]. Tiwari et al. fabricated CDs derived from *Cannabis sativa*, co-doped with nitrogen (10.71%) and sulfur (1.94%; N–S@CsCD), which were able to serve as highly efficient nanosensing platforms for temperature and VB_{12}. These 4–6 nm CDs showed an excitation-independent emission with a peak λ_{em} at ≈414 nm. N–S@CsCDs maintained excellent stability over time and at different salt and pH levels. Besides, N–S@CsCD in the presence of VB_{12} exhibited selective FQ, achieving an LOD of 7.87 μg/mL. The unchanged fluorescence lifetimes of N–S@CsCD in the absence and presence of VB_{12} indicated a static mechanism for the sensing behavior. Eventually, the selectivity of these sensors was determined by assessing the content of VB_{12} in pharmaceutical injections. RR and RSD values were 93.75–98.20% and 0.28–1.09%, respectively [234].

Kansay et al. fabricated a novel solid-state fluorescence nanosensor based on CQDs obtained from *Aegle marmelos* fruit extract and doped with N, K, and Ca, integrated into a bioplastic nanocomposite, enabling the precise and sensitive quantification of VB_{12}. The nanosensor facilitated dual on-site VB_{12} monitoring through fluorescence and a visible color change, captured and analyzed by a smartphone camera using a custom Android app for real-time, quantitative feedback. Linear range and LOD of VB_{12} were obtained to be 0.01–100 μM and 0.00916 μM, respectively. A combined process involving adsorption and FRET between VB_{12} and the CQDs was the main fluorescence quenching mechanism (Figure 5A) [235]. Similar quenching phenomena have been reported in studies using a variety of luminescent QD-based nanoprobes for VB_{12} detection [8,123,176,186,204]. Figure 5B illustrates cost-effective and simple tools for detecting VB_{12} through fluorescence in POC scenarios. Digital shots display a custom protective enclosure for a conventional ultraviolet C (UVC) light tube (11 W, 254 nm), equipped with a compartment for inserting samples and a viewing hole to utilize a smartphone's rear camera. Once the test sample is positioned within the UV chamber, a digital image can be captured using specialized Android smartphone applications. These apps proceed to analyze the image in RGB (red, green, and blue) format and subsequently report the VB_{12} concentration in the sample. Figure 5C illustrates an economical packaging approach for the novel nanosensors, further increasing their applicability in POC settings. The effectiveness of the newly created nanosensor compared to a standard reference method (i.e., immunoassay technique based on electrochemiluminescence (ECL) technology) was examined by employing Pearson's correlation test (r = 0.96; Figure 5D). The authors could successfully apply these nanomaterials to assess VB_{12} contents in commercial beverages and pharmaceutical supplements (98.6–106.4% RR). This proposed that the newly developed fluorescent nanosensor, which utilized CQDs embedded in bioplastic nanocomposites, was effective for the quantitative analysis of VB_{12} [235].

VB_{12}-specific quantum dot fluorescent sensors for cell-bioimaging applications

The genetically encoded fluorescent nanosensor (SenVitAL) has been successfully utilized to measure the intracellular VB_{12} content in *E. coli* cells under in vivo conditions. Exposing *E. coli* cells to VB_{12} led to a notable enhancement in FRET efficiency [125]. Bogner et al. [236] and Zhang et al. [237] earlier found that genetically encoded FRET-based sensors could be applied to evaluate the kinetics of the accumulation of plant/microbial metabolites in the cells. Ahmad et al. reported that the SenVitAL sensor measured VB_{12} concentrations within the cytosol of yeast and mammalian cells, demonstrating its non-destructive real-time monitoring potential of this vitamin in eukaryotic systems. Therefore, this sensor emerged as a novel tool to scrutinize VB_{12} import and metabolism, potentially aiding in exploring their intricate roles in biological processes. The sensor's in vivo specificity was confirmed by adding ascorbic acid and vitamin B_1 to the bacterial cells expressing the sensor for 35 min. The addition of these metabolites did not lead to any notable shifts in the FRET ratio over this period, as compared to the initial FRET ratio measurements at 0 min. Nevertheless, a significant alteration in the FRET ratio was only detected in the presence of VB_{12} [125].

Meng et al. [173] initially assessed the toxicity of orange-emitting CDs using the MTT (3-(4,5-dimethylthiazol-2-yl)-2,5-diphenyltetrazolium bromide) assay on the PC-12 cell line (derived from a rat's adrenal medulla tumor or pheochromocytoma) and found that these cells had a survival rate of above 80% after exposure to various concentrations of the CDs (0–300 μg/mL), confirming their suitability for applications in bioimaging. Here, VB_{12} functioned as the recognition molecule, the CDs acted as fluorescent indicators, and the gradual attenuation of cytoplasmic orange fluorescence represented the measurable signal. The authors then evaluated the potential of orange-emitting CDs in tracking VB_{12} in live cells. Incubating

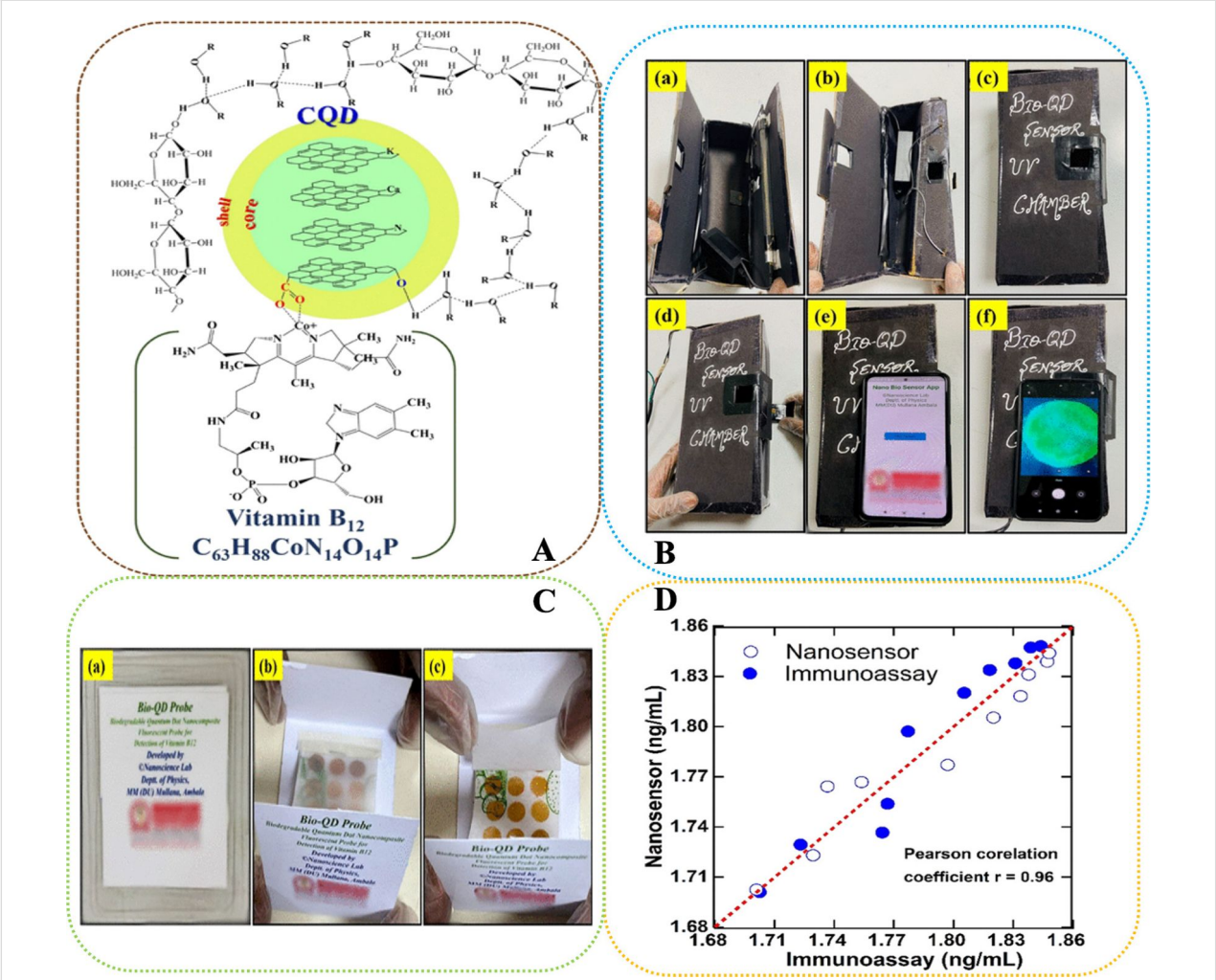

Figure 5: (A) Potential pathways for the reduction in fluorescence of VB_{12} within a bioplastic polymer matrix. (B) Proof-of-concept testing setups for CQDs in bioplastic nanocomposite-based nanosensor with real samples for affordable POC uses. (a–c) Digital images of tailored UV chamber for sample analysis, including UVC tube (11 W, 254 nm) assembly and adapter circuit configuration. (d) Procedure for loading samples and (e, f) RGB (red, green, and blue) format image acquisition via specialized smartphone applications. (C) Digital photographs of (a–c) customized packaging of *A. marmelos*-derived CQDs in bioplastic nanocomposite-based fluorescence nanosensors for low-cost POC applications, and (D) Pearson's correlation analysis of bioplastic nanocomposite nanosensor versus standard reference method for VB_{12} detection. Figure 5 was adapted with permission from [235], Copyright 2024 American Chemical Society. This content is not subject to CC BY 4.0.

PC-12 cells with 0.25 mg/mL CDs for 30 min resulted in a pronounced orange fluorescence within the cytoplasm, indicating successful internalization and dispersion of CDs throughout the cytoplasmic area. Upon adding VB_{12} to the PC-12 cells' nutrient solution, a gradual decrease in orange fluorescence was observed, confirming the ability of CDs to monitor the presence of VB_{12} in living cells [173].

Wang et al. also employed the standard MTT assay to investigate the cytotoxicity of biomimetic CQDs on the human cervical cancer cell line HeLa before their biological application. Results showed that the cell viability exceeded 85% after a two-day incubation with these CQDs at 100 µg/mL. Green and red fluorescence of the biomimetic CQDs was measured after excitation at wavelengths of 488 and 543 nm, respectively. The merged images, appearing gold, combine both green and red signals. Cells were first incubated with the CQDs for 4 h for 2D imaging. The 3D images demonstrated precise imaging of HeLa cells, with these CQDs visibly entering the cytoplasm and nucleus, confirming their internalization within the cells, rather than superficial attachment. To assess the intracellular colocalization of CQDs and VB_{12}, cells in 3D culture pretreated with CQDs were subsequently incubated with VB_{12} for 5 h and then imaged. The 3D cell reconstructions showed a notable decrease in fluorescence intensity after introducing VB_{12} to the CQDs-treated HeLa cells, suggesting that VB_{12} not only penetrated the cells but also interacted with CQDs inside the cells, leading to the quenching of CQD fluorescence. This

observation demonstrated the significant potential of the synthesized CDs as optical nanoprobes for detecting VB_{12} within cells [176].

Liu et al. claimed that the selective and sensitive determination of Co^{2+} by the CDs would be promising for biological labeling, meeting the need for tracking the distribution of VB_{12} or other cobalt-containing medications within cells or organisms. They showed the bioimaging potential of the synthesized CDs in HeLa cells under in vitro conditions. The photoluminescent CDs, using inverted fluorescence microscopy, were monitored within the membrane and cytoplasmic regions of HeLa cells at λ_{ex} = 391 nm, indicating the CDs' ability for efficient penetration of the cells. The authors assessed the impact of Co^{2+} on fluorescence cellular imaging when the cells were treated with 100 μM Co^{2+} and incubated for 20 min at room temperature. Results showed a meaningful quenching of cellular fluorescence, proposing that these CDs could be effectively used for bioimaging living cells at different doses of Co^{2+} and VB_{12} [183]. Nitrogen-doped CDs synthesized from L-aspartic acid and 3,6-diaminoacridine hydrochloride demonstrated minimal cytotoxicity and excellent biocompatibility in in vitro studies conducted on HeLa cells using the MTT assay. The viability of HeLa cells decreased gradually as the concentration of N-doped CDs increased. However, the overall cell viability remained above 80% even at a high concentration of 500 μg/mL N-doped CDs. Upon incubating HeLa cells with 200 μg/mL N-doped CDs, they display a vivid blue fluorescence under 405 nm laser excitation in confocal laser scanning microscopy (CLSM). The fluorescence intensity of NCD-treated HeLa cells significantly decreased with 24 μM VB_{12} and was nearly extinguished at 60 μM VB_{12} concentration. This indicates that N-doped CDs could be effective fluorescent nanoprobes to detect VB_{12} within living cells [187].

Wang et al. also evaluated the bioimaging potential of fluorescent N,P co-doped CDs on HeLa cells. The MTT assay showed that cell viability could be maintained at 0.8 mg/mL N,P co-doped CDs. These nanoprobes were then introduced into HeLa cells via pipetting and incubated for 0.5 h to facilitate entry into the cells. Cells were subsequently washed with phosphate-buffered saline (PBS), and a remarkable alteration in cell morphology was observed using a laser confocal microscope. Subsequent addition of VB_{12} to the culture and a 1 h incubation followed by triple washing reduced background noise. Adding 500 μL of PBS to the culture medium led to a marked reduction in blue fluorescence, suggesting these CDs would be promising tools to be utilized in cell imaging [200]. Gao et al. also demonstrated that dual-emitting CPDs had a high ability in cell bioimaging. Bright blue fluorescence and yellow fluorescence were observed within the HeLa cells, indicating efficient entry of CPDs via endocytosis. In this setup, CPDs acted as the fluorescent probe, VB_{12} served as the recognition molecule, and the selective quenching of blue emission constituted the measurable output. The blue fluorescence of CPDs was significantly quenched upon the addition of VB_{12}, while the yellow fluorescence showed only slight changes [210]. In another study, *Cannabis sativa*-derived N,S co-doped CDs exhibited high viability towards HeLa cells at a concentration range of 20–1,200 μg/mL, indicating very low toxicity and high biocompatibility. MTT results revealed that the cell viability could be kept over 90% at the maximum dose of 1,200 μg/mL. Images with a blue fluorescence signal were taken after incubating HeLa cells with these nanomaterials for 3 h using the CLSM at the λ_{ex} of 405 nm, affirming the internalization of N,S co-doped CDs via endocytosis, owing to their nanoscale size and hydrophilic characteristics [234].

He et al. assessed the biological potential of CDs by determining their cytotoxicity and potential for cell imaging. A low toxicity of CDs with only a slight reduction in cell activity (lower than 20%) was observed by increasing the CD concentration from 200 to 1000 μg/mL. The MDA-MB-231 human breast cancer cell line, initially non-fluorescent in bright field, exhibited intense orange fluorescence after being stimulated with a 488 nm laser following incubation with 600 μg/mL CDs. The overlay image in 15e (D) confirms the complete internalization of CDs by the cells, which also retained good morphological integrity. Since VB_{12} could quench fluorescence induced by these CDs, they could be potentially utilized for intracellular VB_{12} detection. Introducing various concentrations of VB_{12} to the cells led to a consistent decrease in cellular fluorescence intensity, while still enabling effective imaging. Therefore, CDs proved to be a viable fluorescent probe for VB_{12} detection within cells [178]. Yu et al. also assessed the toxicity of N-doped yellow fluorescent CDs towards MDA-MB-231 cells using the cell counting kit-8 (CCK-8) assay. After a 4 h co-culture with various N-doped CD concentrations, it was revealed that the survival rate of these cells exceeded 90% at a concentration of 20 mg/mL of N-doped CDs. Nonetheless, a gradual decrease in cell survival was observed at concentrations of more than 20 mg/mL. Accordingly, the authors selected a dose of 20 mg/mL of these CDs for subsequent cell imaging experiments. The results demonstrated that these nanomaterials were able to penetrate the cell nucleus over time, evidenced by increased yellow fluorescence after incubation [188].

Zhang et al. evaluated the potential of P,N co-doped CQDs as sensitive fluorescent nanoprobes for the detection and cellular imaging of VB_{12} and Co^{2+}. The cytotoxicity results of P,N co-doped CQDs using MTT assays on PC12, human liver cancer (SMMC7721), human bronchial epithelial (BEAS-2B),

and human lung cancer (A549) cell lines showed over 87% cell viability at an 800 μg/mL concentration of the nanomaterial. In this sensing design, P,N co-doped CQDs acted as the fluorescent probe, VB_{12}/Co^{2+} functioned as the recognition molecules, and the fluorescence quenching in cytoplasm and nucleus provided the measurable signal. A significant decrease in fluorescence upon VB_{12} addition was found in SMMC7721 and BEAS-2B cells, indicating the P,N co-doped CQDs' ability to detect VB_{12} in living cells. Besides, A549 and PC12 cells were utilized to monitor intracellular Co^{2+} levels, with fluorescence reduction observed shortly after Co^{2+} addition. In these experiments, P,N co-doped CQDs were not only distributed throughout the cytoplasm but also entered the nucleus of four different cell models [199]. Furthermore, Yu et al. reported blue fluorescence from *Saccharomyces*-derived N-doped CDs in A549 cells at λ_{ex} = 405 nm and pH 6.0, with a noticeable fluorescence reduction at higher pH levels. Comparative pH sensing in the human liver cell line LO2 and the human liver cancer cell line HepG2 cells revealed a decrease in the fluorescence intensity with rising pH across all tested cell types, confirming *Saccharomyces*-derived N-doped CDs as effective probes for intracellular pH monitoring. HepG2 cells displayed brighter fluorescence at pH 6.0 at λ_{ex} = 405 nm than LO2 cells [229], likely due to tumor cells' slightly acidic microenvironment and enhanced phagocytosis [238]. This investigation explored the potential of specialized CDs in targeted biological sensing [229].

Conclusions, Current Limitations, and Prospects

The exploration of optical biosensing technologies for VB_{12} detection has highlighted a significant shift from traditional analytical approaches toward more innovative, efficient, and sensitive methods. Central to this shift is the emergence of CD- and QD-based sensors, which have demonstrated unparalleled capabilities in terms of sensitivity, specificity, and the ability to operate in complex matrices. These advancements not only facilitate accurate and rapid VB_{12} quantification in food and pharmaceutical products but also extend to cutting-edge applications in cellular bioimaging and in vitro/in vivo monitoring, thus offering a multifaceted tool for biomedical research and diagnostics. The utility of CDs and QDs in optical biosensing is grounded in their unique photoluminescent properties, allowing for the detection of VB_{12} at nanomolar concentrations, far surpassing the capabilities of conventional methods. This sensitivity is crucial for early detection of VB_{12} deficiency, which can have profound health implications, including neurological disorders and anemia. Moreover, the ability of these nanomaterials to be functionalized for specific target recognition further enhances their specificity, ensuring that VB_{12} quantification is not confounded by the presence of similar biomolecules or interfering substances commonly found in biological samples. The integration of these nanosensors into cellular bioimaging represents a notable advancement, providing insights into the intracellular dynamics of VB_{12}. This application not only furthers our understanding of VB_{12}'s biological roles but also opens new avenues for investigating its therapeutic potentials and mechanisms of action within live cells. Furthermore, the exploration of non-invasive in vitro and in vivo analysis through these biosensors introduces the possibility of real-time monitoring of VB_{12} levels in organisms, a development that could revolutionize nutritional assessments and disease diagnostics.

Despite these promising advancements, the path toward widespread adoption of CD- and QD-based biosensors in clinical and nutritional science is fraught with challenges. The synthesis and functionalization of these nanomaterials often result in heterogeneity in sensor performance, posing significant hurdles to standardization and reproducibility. Additionally, the complexity of biological matrices in which VB_{12} detection is required demands sensors with improved robustness and selectivity, a goal that remains a work in progress. Moreover, concerns surrounding the biocompatibility and potential toxicity of these nanomaterials, especially for in vivo applications, necessitate further research to ensure their safe use. The translation of these advanced biosensing technologies into practical, user-friendly devices for point-of-care or at-home use also requires overcoming significant engineering, scalability, and cost barriers.

Looking ahead, the field of biosensing, particularly for VB_{12} detection using QDs and CDs, is ripe with opportunities for advancement and innovation. The continued exploration in advanced material engineering promises to refine the optical properties, stability, and biocompatibility of these nanomaterials, enhancing their efficacy as biosensors. The development of multiplexed and integrated sensing systems that can concurrently detect VB_{12} alongside other vital nutrients or biomarkers is another promising avenue, which could revolutionize comprehensive nutritional assessments and diagnostics. Moreover, the integration of these biosensors into smart platforms through digital technologies and the "Internet of Things" presents an exciting opportunity for real-time monitoring, data analysis, and personalized health management. Last, a focus on sustainable and green biosensing technologies emphasizes the importance of environmentally friendly materials and manufacturing processes, aligning with the principles of green chemistry and addressing environmental concerns associated with nanomaterials. Together, these future directions not only promise to overcome existing challenges but also unlock new possibilities in the realm of biosensing.

Funding

The authors acknowledge the German Research Foundation (Project numbers: 428780268, 541301469, INST 257/739, and INST 257/742-1), the Aventis Foundation (Project number: 80304368), Joachim Herz Foundation (Project number: 803043) and the European Union (Project number: 101097989) for their financial support. The authors also acknowledge the support of the Alexander von Humboldt Foundation for SMTG via the Georg Forster Research Fellowship.

Conflict of Interest

The authors declare no conflicts of interest.

Author Contributions

Seyed Mohammad Taghi Gharibzahedi: conceptualization; investigation; writing – original draft. Zeynep Altintas: funding acquisition; project administration; resources; supervision; writing – review & editing.

ORCID® iDs

Seyed Mohammad Taghi Gharibzahedi - https://orcid.org/0000-0001-6280-8361
Zeynep Altintas - https://orcid.org/0000-0002-5461-3289

Data Availability Statement

Data sharing is not applicable as no new data was generated or analyzed in this study.

References

1. Gharibzahedi, S. M. T.; Jafari, S. M. *Trends Food Sci. Technol.* **2017,** *62,* 119–132. doi:10.1016/j.tifs.2017.02.017
2. Gharibzahedi, S. M. T.; Moghadam, M.; Amft, J.; Tolun, A.; Hasabnis, G.; Altintas, Z. *Molecules* **2023,** *28,* 7469. doi:10.3390/molecules28227469
3. Hashemifesharaki, R.; Gharibzahedi, S. M. T. *Nutrire* **2020,** *45,* 19. doi:10.1186/s41110-020-00122-4
4. Singh, M. P.; Rai, S. N.; Dubey, S. K.; Pandey, A. T.; Tabassum, N.; Chaturvedi, V. K.; Singh, N. B. *Crit. Rev. Biotechnol.* **2022,** *42,* 913–930. doi:10.1080/07388551.2021.1964431
5. Durdakova, M.; Kolackova, M.; Janova, A.; Krystofova, O.; Adam, V.; Huska, D. *Crit. Rev. Food Sci. Nutr.* **2024,** *64,* 3091–3102. doi:10.1080/10408398.2022.2130156
6. Kumar, R.; Singh, U.; Tiwari, A.; Tiwari, P.; Sahu, J. K.; Sharma, S. *Process Biochem. (Oxford, U. K.)* **2023,** *127,* 44–55. doi:10.1016/j.procbio.2023.02.002
7. Marques de Brito, B.; Campos, V. d. M.; Neves, F. J.; Ramos, L. R.; Tomita, L. Y. *Crit. Rev. Food Sci. Nutr.* **2023,** *63,* 7853–7867. doi:10.1080/10408398.2022.2053057
8. Jia, Y.; Hu, Y.; Li, Y.; Zeng, Q.; Jiang, X.; Cheng, Z. *Microchim. Acta* **2019,** *186,* 84. doi:10.1007/s00604-018-3196-5
9. Pourreza, N.; Mirzajani, R.; Burromandpiroze, J. *Anal. Methods* **2017,** *9,* 4052–4059. doi:10.1039/c7ay01297g
10. Green, R.; Allen, L. H.; Bjørke-Monsen, A.-L.; Brito, A.; Guéant, J.-L.; Miller, J. W.; Molloy, A. M.; Nexo, E.; Stabler, S.; Toh, B.-H.; Ueland, P. M.; Yajnik, C. *Nat. Rev. Dis. Primers* **2017,** *3,* 17040. doi:10.1038/nrdp.2017.40
11. Osman, D.; Cooke, A.; Young, T. R.; Deery, E.; Robinson, N. J.; Warren, M. J. *Biochim. Biophys. Acta, Mol. Cell Res.* **2021,** *1868,* 118896. doi:10.1016/j.bbamcr.2020.118896
12. Froese, D. S.; Fowler, B.; Baumgartner, M. R. *J. Inherited Metab. Dis.* **2019,** *42,* 673–685. doi:10.1002/jimd.12009
13. Du, F.; Cheng, Z.; Kremer, M.; Liu, Y.; Wang, X.; Shuang, S.; Dong, C. *J. Mater. Chem. B* **2020,** *8,* 5089–5095. doi:10.1039/d0tb00443j
14. Wongyai, S. *J. Chromatogr. A* **2000,** *870,* 217–220. doi:10.1016/s0021-9673(99)01200-5
15. Gharibzahedi, S. M. T.; Altintas, Z. *Food Chem.* **2024,** *448,* 139069. doi:10.1016/j.foodchem.2024.139069
16. Fan, D.; Zhang, Y.; Wu, H. *Anal. Methods* **2021,** *13,* 4920–4925. doi:10.1039/d1ay01118a
17. Li, Y.; Gill, B. D.; Grainger, M. N. C.; Manley-Harris, M. *Int. Dairy J.* **2019,** *99,* 104543. doi:10.1016/j.idairyj.2019.104543
18. Radu, A. I.; Kuellmer, M.; Giese, B.; Huebner, U.; Weber, K.; Cialla-May, D.; Popp, J. *Talanta* **2016,** *160,* 289–297. doi:10.1016/j.talanta.2016.07.027
19. Jafari, M.; Mousavi, M.; Shirzad, K.; Hosseini, M.-A.; Badiei, A.; Pourhakkak, P.; Ghasemi, J. B. *Microchem. J.* **2022,** *181,* 107813. doi:10.1016/j.microc.2022.107813
20. Wang, X.; Li, K.; Yao, L.; Wang, C.; Van Schepdael, A. *J. Pharm. Biomed. Anal.* **2018,** *147,* 278–287. doi:10.1016/j.jpba.2017.07.030
21. Harrington, D. J.; Stevenson, E.; Sobczyńska-Malefora, A. *Ann. Clin. Biochem.* **2025,** *62,* 22–33. doi:10.1177/00045632241292432
22. Kumar, S. S.; Chouhan, R. S.; Thakur, M. S. *Anal. Biochem.* **2009,** *388,* 312–316. doi:10.1016/j.ab.2009.02.029
23. Chen, X.; Ren, F.; Xu, J.; Yu, Z.; Lin, X.; Bai, Z.; Gong, F. *Clin. Lab. (Mainz, Ger.)* **2020,** *66,* 277–286. doi:10.7754/clin.lab.2019.190604
24. Lok, K. S.; Muttalib, S. Z. b. A.; Lee, P. P. F.; Kwok, Y. C.; Nguyen, N.-T. *Lab Chip* **2012,** *12,* 2353–2361. doi:10.1039/c2lc00037g
25. Kong, D.; Liu, L.; Song, S.; Kuang, H.; Xu, C. *Food Anal. Methods* **2017,** *10,* 10–18. doi:10.1007/s12161-016-0543-1
26. Harrington, D. J. Methods for Assessment of Vitamin B_{12}. In *Laboratory Assessment of Vitamin Status;* Harrington, D. J., Ed.; Elsevier: Amsterdam, Netherlands, 2019; pp 265–299. doi:10.1016/b978-0-12-813050-6.00012-7
27. Antherjanam, S.; Saraswathyamma, B.; Krishnan, R. G.; Gopakumar, G. M. *Chem. Pap.* **2021,** *75,* 2981–2995. doi:10.1007/s11696-021-01574-2
28. Gharibzahedi, S. M. T.; Altintas, Z. *Trends Food Sci. Technol.* **2025,** *163,* 105147. doi:10.1016/j.tifs.2025.105147
29. Gharibzahedi, S. M. T.; Altintas, Z. *TrAC, Trends Anal. Chem.* **2024,** *170,* 117473. doi:10.1016/j.trac.2023.117473
30. Kumari, A.; Vyas, V.; Kumar, S. *ISSS J. Micro Smart Syst.* **2022,** *11,* 329–341. doi:10.1007/s41683-021-00084-3
31. Padonou, S. W.; Houngbédji, M.; Hounhouigan, M. H.; Chadare, F. J.; Hounhouigan, D. J. *J. Food Sci.* **2023,** *88,* 3155–3188. doi:10.1111/1750-3841.16697
32. EFSA Panel on Dietetic Products, Nutrition, and Allergies (NDA). *EFSA J.* **2015,** *13,* 4150. doi:10.2903/j.efsa.2015.4150

33. Institute of Medicine. *Dietary reference intakes: thiamin, riboflavin, niacin, vitamin B_6, folate, vitamin B_{12}, pantothenic acid, biotin, and choline;* National Academies Press (US): Washington, DC, USA, 2000.
34. Sobczyńska-Malefora, A.; Delvin, E.; McCaddon, A.; Ahmadi, K. R.; Harrington, D. J. *Crit. Rev. Clin. Lab. Sci.* **2021,** *58,* 399–429. doi:10.1080/10408363.2021.1885339
35. Doets, E. L.; in 't Veld, P. H.; Szczecińska, A.; Dhonukshe-Rutten, R. A. M.; Cavelaars, A. E. J. M.; van 't Veer, P.; Brzozowska, A.; de Groot, L. C. P. G. M. *Ann. Nutr. Metab.* **2013,** *62,* 311–322. doi:10.1159/000346968
36. Fidaleo, M.; Tacconi, S.; Sbarigia, C.; Passeri, D.; Rossi, M.; Tata, A. M.; Dini, L. *Nanomaterials* **2021,** *11,* 743. doi:10.3390/nano11030743
37. Azzini, E.; Raguzzini, A.; Polito, A. *Int. J. Mol. Sci.* **2021,** *22,* 9694. doi:10.3390/ijms22189694
38. Nalder, L.; Zheng, B.; Chiandet, G.; Middleton, L. T.; de Jager, C. A. *J. Nutr., Health Aging* **2021,** *25,* 287–294. doi:10.1007/s12603-020-1489-y
39. Desmond, M. A.; Sobiecki, J. G.; Jaworski, M.; Płudowski, P.; Antoniewicz, J.; Shirley, M. K.; Eaton, S.; Książyk, J.; Cortina-Borja, M.; De Stavola, B.; Fewtrell, M.; Wells, J. C. K. *Am. J. Clin. Nutr.* **2021,** *113,* 1565–1577. doi:10.1093/ajcn/nqaa445
40. Behere, R. V.; Deshmukh, A. S.; Otiv, S.; Gupte, M. D.; Yajnik, C. S. *Front. Endocrinol.* **2021,** *12,* 619176. doi:10.3389/fendo.2021.619176
41. Goraya, J. S.; Kaur, S. *Paediatr. Int. Child Health* **2023,** *43,* 50–56. doi:10.1080/20469047.2023.2171767
42. Gramer, G.; Hoffmann, G. F. *Curr. Med. Sci.* **2020,** *40,* 801–809. doi:10.1007/s11596-020-2260-7
43. El Hasbaoui, B.; Mebrouk, N.; Saghir, S.; El Yajouri, A.; Abilkassem, R.; Agadr, A. *Pan Afr. Med. J.* **2021,** *38,* 237.
44. Guéant, J.-L.; Guéant-Rodriguez, R.-M.; Alpers, D. H. Vitamin B12 absorption and malabsorption. *Vitamins and Hormones;* Academic Press: Cambridge, MA, USA, 2022; Vol. 119, pp 241–274. doi:10.1016/bs.vh.2022.01.016
45. Langan, R. C.; Goodbred, A. J. *Am. Fam. Physician* **2017,** *96,* 384–389.
46. Gharibzahedi, S. M. T.; Hasabnis, G. K.; Akin, E.; Altintas, Z. *Sens. Bio-Sens. Res.* **2025,** *47,* 100759. doi:10.1016/j.sbsr.2025.100759
47. Temova Rakuša, Ž.; Roškar, R.; Hickey, N.; Geremia, S. *Molecules* **2022,** *28,* 240. doi:10.3390/molecules28010240
48. Andres, E.; Dali-Youcef, N. Cobalamin (vitamin B_{12}) Malabsorption. In *Molecular Nutrition;* Patel, V. B., Ed.; Academic Press: Cambridge, CA, USA, 2020; pp 367–386. doi:10.1016/b978-0-12-811907-5.00014-2
49. Kiryukhin, M. V.; Lim, S. H.; Chia, C. Y. Design and Use of Microcarriers for the Delivery of Nutraceuticals. In *Materials Science and Engineering in Food Product Development;* Lai, W.-F., Ed.; John Wiley & Sons: Hoboken, NJ, USA, 2023; pp 93–116. doi:10.1002/9781119860594.ch6
50. Brito, A.; Habeych, E.; Silva-Zolezzi, I.; Galaffu, N.; Allen, L. H. *Nutr. Rev.* **2018,** *76,* 778–792. doi:10.1093/nutrit/nuy026
51. Fedosov, S. N.; Nexo, E. *Nutrients* **2024,** *16,* 648. doi:10.3390/nu16050648
52. Bahardoust, M.; Mousavi, S.; Ziafati, H.; Alipour, H.; Haghmoradi, M.; Olamaeian, F.; Tayebi, A.; Tizmaghz, A. *Eur. J. Cancer Prev.* **2024,** *33,* 208–216. doi:10.1097/cej.0000000000000838
53. Kozyraki, R.; Cases, O. *Curr. Med. Chem.* **2020,** *27,* 3123–3150. doi:10.2174/0929867325666181008143945
54. Hu, X.; Yang, G.; Chen, S.; Luo, S.; Zhang, J. *Biomater. Sci.* **2020,** *8,* 1020–1044. doi:10.1039/c9bm01378d
55. Mascarenhas, R.; Li, Z.; Gherasim, C.; Ruetz, M.; Banerjee, R. *J. Biol. Chem.* **2020,** *295,* 9630–9640. doi:10.1074/jbc.ra120.014094
56. Kim, J.; Hannibal, L.; Gherasim, C.; Jacobsen, D. W.; Banerjee, R. *J. Biol. Chem.* **2009,** *284,* 33418–33424. doi:10.1074/jbc.m109.057877
57. Guéant, J.-L.; Guéant-Rodriguez, R.-M.; Kosgei, V. J.; Coelho, D. *Crit. Rev. Biochem. Mol. Biol.* **2022,** *57,* 133–155. doi:10.1080/10409238.2021.1979459
58. Plesa, M.; Kim, J.; Paquette, S. G.; Gagnon, H.; Ng-Thow-Hing, C.; Gibbs, B. F.; Hancock, M. A.; Rosenblatt, D. S.; Coulton, J. W. *Mol. Genet. Metab.* **2011,** *102,* 139–148. doi:10.1016/j.ymgme.2010.10.011
59. McCorvie, T. J.; Ferreira, D.; Yue, W. W.; Froese, D. S. *J. Inherited Metab. Dis.* **2023,** *46,* 406–420. doi:10.1002/jimd.12593
60. Gimsing, P. *Br. J. Haematol.* **1995,** *89,* 812–819. doi:10.1111/j.1365-2141.1995.tb08419.x
61. Ge, Y.; Zadeh, M.; Mohamadzadeh, M. *Nutrients* **2022,** *14,* 2825. doi:10.3390/nu14142825
62. Mikkelsen, K.; Apostolopoulos, V. Vitamin B_{12}; Folic Acid; and the Immune System. In *Nutrition and Immunity;* Mahmoudi, M.; Rezaei, N., Eds.; Springer: Cham, Switzerland, 2019; pp 103–114. doi:10.1007/978-3-030-16073-9_6
63. Devalia, V.; Hamilton, M. S.; Molloy, A. M.; the British Committee for Standards in Haematology. *Br. J. Haematol.* **2014,** *166,* 496–513. doi:10.1111/bjh.12959
64. Shipton, M. J.; Thachil, J. *Clin. Med. (London. Online)* **2015,** *15,* 145–150. doi:10.7861/clinmedicine.15-2-145
65. Miller, J. W.; Garrod, M. G.; Rockwood, A. L.; Kushnir, M. M.; Allen, L. H.; Haan, M. N.; Green, R. *Clin. Chem.* **2006,** *52,* 278–285. doi:10.1373/clinchem.2005.061382
66. Woo, K.-S.; Kim, K.-E.; Park, J.-S.; Park, J.-I.; Han, J.-Y. *Korean J. Lab. Med.* **2010,** *30,* 185–189. doi:10.3343/kjlm.2010.30.2.185
67. Herrmann, W.; Obeid, R.; Schorr, H.; Geisel, J. *Clin. Chem. Lab. Med.* **2003,** *41,* 1478–1488. doi:10.1515/cclm.2003.227
68. Clarke, R.; Refsum, H.; Birks, J.; Evans, J. G.; Johnston, C.; Sherliker, P.; Ueland, P. M.; Schneede, J.; McPartlin, J.; Nexo, E.; Scott, J. M. *Am. J. Clin. Nutr.* **2003,** *77,* 1241–1247. doi:10.1093/ajcn/77.5.1241
69. Dib, M.-J.; Gumban-Marasigan, M.; Yoxall, R.; Andrew, T.; Harrington, D. J.; Sobczyńska-Malefora, A.; Ahmadi, K. R. *Front. Nutr.* **2022,** *8,* 789357. doi:10.3389/fnut.2021.789357
70. Aparicio-Ugarriza, R.; Palacios, G.; Alder, M.; González-Gross, M. *Clin. Chem. Lab. Med.* **2015,** *53,* 1149–1159. doi:10.1515/cclm-2014-0784
71. Kósa, M.; Galla, Z.; Lénárt, I.; Baráth, Á.; Grecsó, N.; Rácz, G.; Bereczki, C.; Monostori, P. *Metabolites* **2022,** *12,* 1104. doi:10.3390/metabo12111104
72. Zhang, R.; Ma, X.; Zou, Y.; Qiu, L.; Wang, D.; Tang, Y.; Cao, Y.; Yu, S.; Cheng, X. *Clin. Chem. Lab. Med.* **2023,** *61,* 86–92. doi:10.1515/cclm-2022-0523
73. Knoepfel, C.; Michel Blanco, M.; Nydegger, U.; Risch, L.; Renz, H.; Risch, M. *J. Lab. Med. (Berlin, Ger.)* **2018,** *42,* 141–147. doi:10.1515/labmed-2018-0023
74. Alam, S. F.; Kumar, S.; Ganguly, P. *J. Clin. Biochem. Nutr.* **2019,** *65,* 171–177. doi:10.3164/jcbn.19-49
75. Savas, S.; Gharibzahedi, S. M. T. *Biosensors* **2025,** *15,* 574. doi:10.3390/bios15090574

76. Elghanian, R.; Storhoff, J. J.; Mucic, R. C.; Letsinger, R. L.; Mirkin, C. A. *Science* **1997,** *277,* 1078–1081. doi:10.1126/science.277.5329.1078
77. Selvakumar, L. S.; Thakur, M. S. *Anal. Biochem.* **2012,** *427,* 151–157. doi:10.1016/j.ab.2012.05.020
78. Kumudha, A.; Selvakumar, S.; Dilshad, P.; Vaidyanathan, G.; Thakur, M. S.; Sarada, R. *Food Chem.* **2015,** *170,* 316–320. doi:10.1016/j.foodchem.2014.08.035
79. Patil, A.; Salunke-Gawali, S. *Inorg. Chim. Acta* **2018,** *482,* 99–112. doi:10.1016/j.ica.2018.05.026
80. Na, Y. J.; Choi, Y. W.; You, G. R.; Kim, C. *Sens. Actuators, B* **2016,** *223,* 234–240. doi:10.1016/j.snb.2015.09.098
81. Maity, D.; Govindaraju, T. *Inorg. Chem.* **2011,** *50,* 11282–11284. doi:10.1021/ic2015447
82. Liu, Q.-X.; Hu, Z.-L.; Zhao, Z.-X. *New J. Chem.* **2018,** *42,* 20049–20055. doi:10.1039/c8nj04983a
83. Liu, Z.; Wang, W.; Xu, H.; Sheng, L.; Chen, S.; Huang, D.; Sun, F. *Inorg. Chem. Commun.* **2015,** *62,* 19–23. doi:10.1016/j.inoche.2015.10.017
84. Azizi Khereshki, N.; Mohammadi, A.; Zavvar Mousavi, H.; Alizadeh, N. *Supramol. Chem.* **2021,** *33,* 513–526. doi:10.1080/10610278.2022.2085105
85. An Kim, P.; Lee, H.; So, H.; Kim, C. *Inorg. Chim. Acta* **2020,** *505,* 119502. doi:10.1016/j.ica.2020.119502
86. Park, G. J.; Lee, J. J.; You, G. R.; Nguyen, L.; Noh, I.; Kim, C. *Sens. Actuators, B* **2016,** *223,* 509–519. doi:10.1016/j.snb.2015.09.129
87. Alhalafi, M. H. *J. Saudi Chem. Soc.* **2023,** *27,* 101685. doi:10.1016/j.jscs.2023.101685
88. Gharibzahedi, S. M. T.; Savas, S. *Foods* **2025,** *14,* 3411. doi:10.3390/foods14193411
89. Zeng, S.; Yu, X.; Law, W.-C.; Zhang, Y.; Hu, R.; Dinh, X.-Q.; Ho, H.-P.; Yong, K.-T. *Sens. Actuators, B* **2013,** *176,* 1128–1133. doi:10.1016/j.snb.2012.09.073
90. Gao, Y.; Guo, F.; Gokavi, S.; Chow, A.; Sheng, Q.; Guo, M. *Food Chem.* **2008,** *110,* 769–776. doi:10.1016/j.foodchem.2008.03.007
91. Indyk, H. E.; Persson, B. S.; Caselunghe, M. C. B.; Moberg, A.; Filonzi, E. L.; Woollard, D. C. *J. AOAC Int.* **2002,** *85,* 72–81. doi:10.1093/jaoac/85.1.72
92. Cannon, M. J.; Myszka, D. G.; Bagnato, J. D.; Alpers, D. H.; West, F. G.; Grissom, C. B. *Anal. Biochem.* **2002,** *305,* 1–9. doi:10.1006/abio.2002.5647
93. Vyas, P.; O'Kane, A. A.; Dowell, D. *J. AOAC Int.* **2012,** *95,* 329–334. doi:10.5740/jaoacint.cs2011_16
94. Sun, M.; Chen, Y.; Zheng, X.; Chen, Q. J. *Food Saf. Qual.* **2014,** *5,* 3891–3897.
95. Çimen, D.; Denizli, A. *Photonic Sens.* **2020,** *10,* 316–332. doi:10.1007/s13320-020-0578-1
96. Bareza, N. J.; Wajs, E.; Paulillo, B.; Tullila, A.; Jaatinen, H.; Milani, R.; Dore, C.; Mihi, A.; Nevanen, T. K.; Pruneri, V. *Adv. Mater. Interfaces* **2023,** *10,* 2201699. doi:10.1002/admi.202201699
97. Zhu, H.; Huang, X.; Deng, Y.; Chen, H.; Fan, M.; Gong, Z. *TrAC, Trends Anal. Chem.* **2023,** *158,* 116879. doi:10.1016/j.trac.2022.116879
98. Garebaghi, S.; Gharibzahedi, S. M. T.; Altintas, Z. *Electrochim. Acta* **2025,** *543,* 147470. doi:10.1016/j.electacta.2025.147470
99. Zhou, Y. K.; Li, H.; Liu, Y.; Liang, G. Y. *Anal. Chim. Acta* **1991,** *243,* 127–130. doi:10.1016/s0003-2670(00)82550-7
100. Pizà, N.; Miró, M.; de Armas, G.; Becerra, E.; Estela, J. M.; Cerdà, V. *Anal. Chim. Acta* **2002,** *467,* 155–166. doi:10.1016/s0003-2670(02)00196-4
101. Economou, A.; Clark, A. K.; Fielden, P. R. *Analyst* **2001,** *126,* 109–113. doi:10.1039/b007685f
102. Qin, W.; Zhang, Z.; Liu, H. *Anal. Chim. Acta* **1997,** *357,* 127–132. doi:10.1016/s0003-2670(97)00546-1
103. Song, Z.; Hou, S. *Anal. Chim. Acta* **2003,** *488,* 71–79. doi:10.1016/s0003-2670(03)00665-2
104. Akbay, N.; Gök, E. *J. Anal. Chem.* **2008,** *63,* 1073–1077. doi:10.1134/s1061934808110105
105. Du, J.; Lu, J.; Zhang, X. *Microchim. Acta* **2006,** *153,* 21–25. doi:10.1007/s00604-005-0452-2
106. Andrade, R. A. N.; Andrade, S. I. E.; Martins, V. L.; Moreira, P. N. T.; Costa, D. J. E.; Lyra, W. S.; Araújo, M. C. U. *Microchem. J.* **2013,** *108,* 151–155. doi:10.1016/j.microc.2012.10.009
107. Murillo Pulgarín, J. A.; García Bermejo, L. F.; Nieves Sánchez García, M. *Luminescence* **2011,** *26,* 536–542. doi:10.1002/bio.1266
108. Murillo Pulgarín, J. A.; García Bermejo, L. F.; Sánchez García, M. N. *Anal. Lett.* **2011,** *44,* 2593–2605. doi:10.1080/00032719.2011.553005
109. Kumudha, A.; Sarada, R. *J. Food Sci. Technol.* **2016,** *53,* 888–894. doi:10.1007/s13197-015-2005-y
110. Kamruzzaman, M.; Alam, A.-M.; Kim, K. M.; Lee, S. H.; Kim, Y. H.; Kabir, A. N. M. H.; Kim, G.-M.; Dang, T. D. *Biomed. Microdevices* **2013,** *15,* 195–202. doi:10.1007/s10544-012-9716-x
111. Zhang, L.; Rong, W.; Lu, C.; Zhao, L. *Talanta* **2014,** *129,* 126–131. doi:10.1016/j.talanta.2014.05.041
112. Domínguez-Romero, J. C.; Gilbert-López, B.; Beneito-Cambra, M.; Molina-Díaz, A. *Talanta* **2018,** *182,* 267–272. doi:10.1016/j.talanta.2018.01.091
113. Khadro, B.; Leca-Bouvier, B. D.; Lagarde, F.; Barbier, F.; Blum, L. J.; Martelet, C.; Marcotte, L.; Tabrizian, M.; Jaffrezic-Renault, N. *Sens. Lett.* **2009,** *7,* 833–838. doi:10.1166/sl.2009.1158
114. Selvakumar, L. S.; Thakur, M. S. *Anal. Chim. Acta* **2012,** *722,* 107–113. doi:10.1016/j.aca.2012.02.006
115. Lee, S.; O'Dell, D.; Hohenstein, J.; Colt, S.; Mehta, S.; Erickson, D. *Sci. Rep.* **2016,** *6,* 28237. doi:10.1038/srep28237
116. Yuan, X.; Han, X.; Zhou, W.; Long, W.; Wang, H.; Yu, B.; Zhang, B. *Front. Nutr.* **2022,** *9,* 947118. doi:10.3389/fnut.2022.947118
117. Wiesholler, L. M.; Genslein, C.; Schroter, A.; Hirsch, T. *Anal. Chem. (Washington, DC, U. S.)* **2018,** *90,* 14247–14254. doi:10.1021/acs.analchem.8b03279
118. Bhaiyya, M.; Pattnaik, P. K.; Goel, S. *Sens. Actuators, A* **2021,** *331,* 112831. doi:10.1016/j.sna.2021.112831
119. Bhaiyya, M.; Pattnaik, P. K.; Goel, S. *Microfluid. Nanofluid.* **2021,** *25,* 41. doi:10.1007/s10404-021-02442-x
120. Chen, J.; Huang, X.; Tang, H.; Guo, H.; Yang, F. *Dyes Pigm.* **2022,** *207,* 110705. doi:10.1016/j.dyepig.2022.110705
121. Xu, H.; Li, Y.; Liu, C.; Wu, Q.; Zhao, Y.; Lu, L.; Tang, H. *Talanta* **2008,** *77,* 176–181. doi:10.1016/j.talanta.2008.06.022
122. Shang, Z. B.; Wen, Y. J.; Yan, X. Q.; Sun, H. H.; Wang, Y.; Jin, W. J. *Luminescence* **2014,** *29,* 598–602. doi:10.1002/bio.2588
123. Chakravarty, S.; Gogoi, B.; Mandal, B. B.; Bhardwaj, N.; Sarma, N. S. *Biosens. Bioelectron.* **2018,** *112,* 18–22. doi:10.1016/j.bios.2018.03.057
124. Wang, J.; Su, S.; Qiu, J.; Wang, S. *Nano* **2019,** *14,* 1950084. doi:10.1142/s179329201950084x

125. Ahmad, M.; Mohsin, M.; Iqrar, S.; Manzoor, O.; Siddiqi, T. O.; Ahmad, A. *Sens. Actuators, B* **2018,** *257,* 866–874. doi:10.1016/j.snb.2017.11.030
126. Samari, F.; Hemmateenejad, B.; Rezaei, Z.; Shamsipur, M. *Anal. Methods* **2012,** *4,* 4155–4160. doi:10.1039/c2ay25196e
127. Shanmugaraj, K.; Sasikumar, T.; Ilanchelian, M. *J. Anal. Test.* **2018,** *2,* 168–174. doi:10.1007/s41664-018-0054-8
128. Akshath, U. S.; Bhatt, P.; Singh, S. A. *J. Fluoresc.* **2020,** *30,* 537–545. doi:10.1007/s10895-020-02509-y
129. Sarkar, P.; Saha, M.; Nandi, N.; Sahu, D. K.; Sahu, K. *ACS Appl. Nano Mater.* **2022,** *5,* 7670–7678. doi:10.1021/acsanm.1c04496
130. Qu, F.; Song, Q.; You, J. *Anal. Methods* **2016,** *8,* 4324–4327. doi:10.1039/c6ay00088f
131. Zhang, S.; Wang, X.; Wang, Y.; Dong, J.; Zhang, Y.; Zhao, M. *Microchem. J.* **2024,** *199,* 109985. doi:10.1016/j.microc.2024.109985
132. Yu, W.; Qin, Y.; Fan, Y.; Wang, Z.; Cheng, Z. *ChemistrySelect* **2021,** *6,* 10889–10897. doi:10.1002/slct.202102951
133. Hu, Y.; Yu, W.; Liao, Y.; Jiang, X.; Cheng, Z. *Spectrochim. Acta, Part A* **2021,** *263,* 120194. doi:10.1016/j.saa.2021.120194
134. Chau, P. B. K.; Vu, T. H.; Kim, M. I. *Nanomaterials* **2023,** *13,* 2444. doi:10.3390/nano13172444
135. Huang, M.; Tong, C. *Spectrochim. Acta, Part A* **2022,** *268,* 120706. doi:10.1016/j.saa.2021.120706
136. Gholami, J.; Manteghian, M.; Badiei, A.; Javanbakht, M.; Ueda, H. *Fullerenes, Nanotubes Carbon Nanostruct.* **2015,** *23,* 878–884. doi:10.1080/1536383x.2015.1012583
137. Sun, J.; Zhu, X.; Wu, M. *J. Fluoresc.* **2007,** *17,* 265–270. doi:10.1007/s10895-007-0168-2
138. Vaishnavi, E.; Renganathan, R. *Spectrochim. Acta, Part A* **2013,** *115,* 603–609. doi:10.1016/j.saa.2013.06.068
139. Liu, B.; Liu, Z.; Jing, G. *Anal. Lett.* **2005,** *38,* 1367–1377. doi:10.1081/al-200062182
140. Ding, L.; Yang, H.; Ge, S.; Yu, J. *Spectrochim. Acta, Part A* **2018,** *193,* 305–309. doi:10.1016/j.saa.2017.12.015
141. Ren, J.; Wu, W.; Chen, T.; Guo, H.; Xu, C.; Ma, J.; Wang, L.; Wang, J.; Li, L. *Spectrochim. Acta, Part A* **2024,** *304,* 123438. doi:10.1016/j.saa.2023.123438
142. Bian, X.; Wen, X.; Huang, Y.; Fan, Z. *Microchim. Acta* **2025,** *192,* 494. doi:10.1007/s00604-025-07374-9
143. Zhu, T.; Du, J.; Cao, W.; Fan, J.; Peng, X. *Ind. Eng. Chem. Res.* **2016,** *55,* 527–533. doi:10.1021/acs.iecr.5b04214
144. Demchenko, A. P. *Methods Appl. Fluoresc.* **2020,** *8,* 022001. doi:10.1088/2050-6120/ab7365
145. Filali, S.; Pirot, F.; Miossec, P. *Trends Biotechnol.* **2020,** *38,* 163–177. doi:10.1016/j.tibtech.2019.07.013
146. Chang, J. C.; Kovtun, O.; Blakely, R. D.; Rosenthal, S. J. *Wiley Interdiscip. Rev.: Nanomed. Nanobiotechnol.* **2012,** *4,* 605–619. doi:10.1002/wnan.1186
147. McHugh, K. J.; Jing, L.; Behrens, A. M.; Jayawardena, S.; Tang, W.; Gao, M.; Langer, R.; Jaklenec, A. *Adv. Mater. (Weinheim, Ger.)* **2018,** *30,* 1706356. doi:10.1002/adma.201706356
148. Hildebrandt, N. *ACS Nano* **2011,** *5,* 5286–5290. doi:10.1021/nn2023123
149. Sun, J.; Jin, Y. *J. Mater. Chem. C* **2014,** *2,* 8000–8011. doi:10.1039/c4tc01489h
150. Li, J.; Zhu, J.-J.; Xu, K. *TrAC, Trends Anal. Chem.* **2014,** *58,* 90–98. doi:10.1016/j.trac.2014.02.011
151. Sagbas, S.; Sahiner, N. Carbon Dots: Preparation; Properties; and Application. In *Nanocarbon and its Composites;* Khan, A.; Jawaid, M.; Inamuddin; Asiri, A. M., Eds.; Woodhead Publishing: Duxford, U.K., 2019; pp 651–676. doi:10.1016/b978-0-08-102509-3.00022-5
152. Wang, B.; Cai, H.; Waterhouse, G. I. N.; Qu, X.; Yang, B.; Lu, S. *Small Sci.* **2022,** *2,* 2200012. doi:10.1002/smsc.202200012
153. Liang, T.; Liu, E.; Li, M.; Ushakova, E. V.; Kershaw, S. V.; Rogach, A. L.; Tang, Z.; Qu, S. *ACS Nano* **2021,** *15,* 1579–1586. doi:10.1021/acsnano.0c09053
154. Li, G.; Xu, J.; Xu, K. *Nanomaterials* **2023,** *13,* 2684. doi:10.3390/nano13192684
155. Xia, C.; Zhu, S.; Feng, T.; Yang, M.; Yang, B. *Adv. Sci.* **2019,** *6,* 1901316. doi:10.1002/advs.201901316
156. Singh, P.; Arpita; Kumar, S.; Kumar, P.; Kataria, N.; Bhankar, V.; Kumar, K.; Kumar, R.; Hsieh, C.-T.; Khoo, K. S. *Nanoscale* **2023,** *15,* 16241–16267. doi:10.1039/d3nr01966g
157. Armăşelu, A.; Jhalora, P. Application of Quantum Dots in Biomedical and Biotechnological Fields. In *Quantum Dots;* Ameta, R.; Bhatt, J. P.; Ameta, S. C., Eds.; Elsevier: Amsterdam, Netherlands, 2023; pp 245–276. doi:10.1016/b978-0-12-824153-0.00011-2
158. Molaei, M. J. *Anal. Methods* **2020,** *12,* 1266–1287. doi:10.1039/c9ay02696g
159. Dinç, S.; Tjardts, T.; Maschkowitz, G.; Lukaszczuk, V.; Taghi Gharibzahedi, S. M.; Altintas, Z. *Microchem. J.* **2025,** *208,* 112301. doi:10.1016/j.microc.2024.112301
160. Ji, C.; Zhou, Y.; Leblanc, R. M.; Peng, Z. *ACS Sens.* **2020,** *5,* 2724–2741. doi:10.1021/acssensors.0c01556
161. Zhu, S.; Song, Y.; Zhao, X.; Shao, J.; Zhang, J.; Yang, B. *Nano Res.* **2015,** *8,* 355–381. doi:10.1007/s12274-014-0644-3
162. Wang, T.; Luo, H.; Jing, X.; Yang, J.; Huo, M.; Wang, Y. *Molecules* **2021,** *26,* 1246. doi:10.3390/molecules26051246
163. Li, J.; Xu, O.; Zhu, X. *RSC Adv.* **2021,** *11,* 34107–34116. doi:10.1039/d1ra05656e
164. Msto, R. K.; Othman, H. O.; Al-Hashimi, B. R.; Salahuddin Ali, D.; Hassan, D. H.; Hassan, A. Q.; Smaoui, S. *J. Food Qual.* **2023,** 5555608. doi:10.1155/2023/5555608
165. Zhu, Y.; Deng, X.; Chen, J.; Hu, Z.; Wu, F. *Food Chem.* **2023,** *429,* 136957. doi:10.1016/j.foodchem.2023.136957
166. Li, X.; Wang, C.; Li, P.; Sun, X.; Shao, Z.; Xia, J.; Liu, Q.; Shen, F.; Fang, Y. *Food Chem.* **2023,** *409,* 135243. doi:10.1016/j.foodchem.2022.135243
167. Sathyan, B.; Banerjee, G.; Jagtap, A. A.; Verma, A.; Cyriac, J. *ACS Appl. Bio Mater.* **2024,** *7,* 1191–1203. doi:10.1021/acsabm.3c01072
168. Irfan; Soleja, N.; Mohsin, M. *Anal. Biochem.* **2023,** *679,* 115285. doi:10.1016/j.ab.2023.115285
169. Dadkhah, S.; Mehdinia, A.; Jabbari, A.; Manbohi, A. *Sci. Rep.* **2022,** *12,* 18276. doi:10.1038/s41598-022-23055-6
170. Kundu, A.; Nandi, S.; Das, P.; Nandi, A. K. *J. Colloid Interface Sci.* **2016,** *468,* 276–283. doi:10.1016/j.jcis.2016.01.070
171. Huang, X.; Liu, Z.; Huang, Y.; Zong, Y.; Yang, X.; Hu, Z.; Zeng, C. *Spectrochim. Acta, Part A* **2022,** *276,* 121239. doi:10.1016/j.saa.2022.121239
172. Huang, Y.; Huang, X.; Lin, H.; Liu, Z.; Zong, Y. *Opt. Mater. (Amsterdam, Neth.)* **2021,** *114,* 110967. doi:10.1016/j.optmat.2021.110967
173. Meng, Y.; Jiao, Y.; Zhang, Y.; Lu, W.; Wang, X.; Shuang, S.; Dong, C. *J. Hazard. Mater.* **2021,** *408,* 124422. doi:10.1016/j.jhazmat.2020.124422

174. Sun, X. Y.; Yuan, M. J.; Liu, B.; Shen, J. S. *RSC Adv.* **2018,** *8,* 19786–19790. doi:10.1039/c8ra03070g
175. Li, C.-L.; Huang, C.-C.; Periasamy, A. P.; Roy, P.; Wu, W.-C.; Hsu, C.-L.; Chang, H.-T. *RSC Adv.* **2015,** *5,* 2285–2291. doi:10.1039/c4ra11704b
176. Wang, M.; Liu, Y.; Ren, G.; Wang, W.; Wu, S.; Shen, J. *Anal. Chim. Acta* **2018,** *1032,* 154–162. doi:10.1016/j.aca.2018.05.057
177. Dadkhah, S.; Mehdinia, A.; Jabbari, A.; Manbohi, A. *J. Fluoresc.* **2022,** *32,* 681–689. doi:10.1007/s10895-021-02863-5
178. He, W.; Weng, W.; Sun, X.; Pan, Y.; Chen, X.; Liu, B.; Shen, J. *ACS Appl. Nano Mater.* **2020,** *3,* 7420–7427. doi:10.1021/acsanm.0c01003
179. Wang, J.; Wei, J.; Su, S.; Qiu, J. *New J. Chem.* **2015,** *39,* 501–507. doi:10.1039/c4nj00538d
180. Chen, B. B.; Liu, Z. X.; Deng, W. C.; Zhan, L.; Liu, M. L.; Huang, C. Z. *Green Chem.* **2016,** *18,* 5127–5132. doi:10.1039/c6gc01820c
181. Sun, Z.; Chen, Z.; Luo, J.; Zhu, Z.; Zhang, X.; Liu, R.; Wu, Z.-c. *Dyes Pigm.* **2020,** *176,* 108227. doi:10.1016/j.dyepig.2020.108227
182. Zhao, X.; Du, Q.; Qiu, H.; Zhao, Y.; Wang, S.; Li, J.; Dong, C. *J. Fluoresc.* **2025,** *35,* 693–700. doi:10.1007/s10895-023-03558-9
183. Liu, X.; Wei, S.; Diao, Q.; Ma, P.; Xu, L.; Xu, S.; Sun, Y.; Song, D.; Wang, X. *Microchim. Acta* **2017,** *184,* 3825–3831. doi:10.1007/s00604-017-2367-0
184. Zhang, Y.; Zhu, C.; Zhang, Y.; Jing, N.; Wang, Y. *J. Nanosci. Nanotechnol.* **2021,** *21,* 2099–2108. doi:10.1166/jnn.2021.19034
185. Bano, D.; Kumar, V.; Chandra, S.; Singh, V. K.; Mohan, S.; Singh, D. K.; Talat, M.; Hasan, S. H. *Opt. Mater. (Amsterdam, Neth.)* **2019,** *92,* 311–318. doi:10.1016/j.optmat.2019.04.045
186. Kalaiyarasan, G.; Joseph, J. *Microchim. Acta* **2017,** *184,* 3883–3891. doi:10.1007/s00604-017-2421-y
187. Nandi, N.; Gaurav, S.; Sarkar, P.; Kumar, S.; Sahu, K. *ACS Appl. Bio Mater.* **2021,** *4,* 5201–5211. doi:10.1021/acsabm.1c00371
188. Yu, G.; Cheng, Y.; Duan, Z. *Materials* **2022,** *15,* 9057. doi:10.3390/ma15249057
189. Somaraj, G.; Mathew, S.; Abraham, T.; Ambady, K. G.; Mohan, C.; Mathew, B. *ChemistrySelect* **2022,** *7,* e202200473. doi:10.1002/slct.202200473
190. Li, Y.; Jia, Y.; Zeng, Q.; Jiang, X.; Cheng, Z. *Spectrochim. Acta, Part A* **2019,** *211,* 178–188. doi:10.1016/j.saa.2018.12.002
191. Fan, P.; Liu, C.; Hu, C.; Li, F.; Lin, X.; Xiao, F.; Liang, H.; Li, L.; Yang, S. *New J. Chem.* **2022,** *46,* 877–882. doi:10.1039/d1nj04706j
192. Sun, L.; Liu, Y.; Wang, Y.; Xu, J.; Xiong, Z.; Zhao, X.; Xia, Y. *Opt. Mater. (Amsterdam, Neth.)* **2021,** *112,* 110787. doi:10.1016/j.optmat.2020.110787
193. Luo, K.; Jiang, X. *J. Fluoresc.* **2019,** *29,* 769–777. doi:10.1007/s10895-019-02395-z
194. Ramezani, Z.; Qorbanpour, M.; Rahbar, N. *Colloids Surf., A* **2018,** *549,* 58–66. doi:10.1016/j.colsurfa.2018.04.006
195. Mohammadi, N.; Samadi, N.; Akhgari, F. *Chem. Res.* **2021,** *3,* 177–185.
196. Li, R.; Yue, J.; Zhu, F.; Zhou, J.; Liu, X. *J. Food Sci.* **2025,** *90,* e70299. doi:10.1111/1750-3841.70299
197. Kou, X.; Jiang, S.; Park, S.-J.; Meng, L.-Y. *Dalton Trans.* **2020,** *49,* 6915–6938. doi:10.1039/d0dt01004a
198. Wen, X.; Wen, G.; Li, W.; Zhao, Z.; Duan, X.; Yan, W.; Trant, J. F.; Li, Y. *Mater. Sci. Eng., C* **2021,** *123,* 112022. doi:10.1016/j.msec.2021.112022
199. Zhang, L.; Wang, H.; Hu, Q.; Guo, X.; Li, L.; Shuang, S.; Gong, X.; Dong, C. *Microchim. Acta* **2019,** *186,* 506. doi:10.1007/s00604-019-3617-0
200. Wang, D.; Mei, X.; Wang, S.; Li, J.; Dong, C. *New J. Chem.* **2021,** *45,* 3508–3514. doi:10.1039/d0nj05597b
201. Gore, A. H.; Kale, M. B.; Anbhule, P. V.; Patil, S. R.; Kolekar, G. B. *RSC Adv.* **2014,** *4,* 683–692. doi:10.1039/c3ra42553c
202. Shamsipur, M.; Nasirian, V.; Barati, A.; Rafienia, M.; Sheikh Arabi, M. *Adv. Nanochem.* **2019,** *1,* 1–5. doi:10.22126/anc.2019.3146.1002
203. Wang, S.; Bao, X.; Gao, B.; Li, M. *Dalton Trans.* **2019,** *48,* 8288–8296. doi:10.1039/c9dt01186b
204. Pramanik, S.; Roy, S.; Bhandari, S. *Nanoscale Adv.* **2020,** *2,* 3809–3814. doi:10.1039/d0na00540a
205. Sharma, A. S.; Ali, S.; Sabarinathan, D.; Murugavelu, M.; Li, H.; Chen, Q. *Compr. Rev. Food Sci. Food Saf.* **2021,** *20,* 5765–5801. doi:10.1111/1541-4337.12834
206. Ravi, P. V.; Thangadurai, T. D.; Nataraj, D. *J. Photochem. Photobiol., A* **2020,** *400,* 112691. doi:10.1016/j.jphotochem.2020.112691
207. Denis, P. A. *ACS Omega* **2022,** *7,* 45935–45961. doi:10.1021/acsomega.2c06010
208. Boonta, W.; Talodthaisong, C.; Sattayaporn, S.; Chaicham, C.; Chaicham, A.; Sahasithiwat, S.; Kangkaew, L.; Kulchat, S. *Mater. Chem. Front.* **2020,** *4,* 507–516. doi:10.1039/c9qm00587k
209. Martins, E. C.; Santana, E. R.; Spinelli, A. *Talanta* **2023,** *252,* 123836. doi:10.1016/j.talanta.2022.123836
210. Gao, Y.-T.; Chen, B.-B.; Jiang, L.; Lv, J.; Chang, S.; Wang, Y.; Qian, R.-C.; Li, D.-W.; Hafez, M. E. *ACS Appl. Mater. Interfaces* **2021,** *13,* 50228–50235. doi:10.1021/acsami.1c12993
211. Wang, H.; He, Y. *Sensors* **2017,** *17,* 268. doi:10.3390/s17020268
212. Zhang, Y.; Cai, N.; Chan, V. *Biosensors* **2023,** *13,* 311. doi:10.3390/bios13030311
213. Long, Y.; Zhang, L.; Yu, Y.; Lin, B.; Cao, Y.; Guo, M. *Luminescence* **2019,** *34,* 544–552. doi:10.1002/bio.3651
214. Zhao, D.; Liu, H.; Zhang, Z.; Xiao, X.; Li, J. *Colloids Surf., B* **2022,** *220,* 112868. doi:10.1016/j.colsurfb.2022.112868
215. Chai, S.; Zhou, L.; Pei, S.; Zhu, Z.; Chen, B. *Micromachines* **2021,** *12,* 1116. doi:10.3390/mi12091116
216. Gharibzahedi, S. M. T.; Mohammadnabi, S. *J. Mol. Liq.* **2016,** *224,* 1332–1340. doi:10.1016/j.molliq.2016.10.120
217. Gharibzahedi, S. M. T. *J. Mol. Liq.* **2017,** *234,* 240–248. doi:10.1016/j.molliq.2017.03.094
218. Han, J.-F.; Lou, Q.; Ding, Z.-Z.; Zheng, G.-S.; Ni, Q.-C.; Song, R.-W.; Liu, K.-K.; Zang, J.-H.; Dong, L.; Shen, C.-L.; Shan, C.-X. *Light: Sci. Appl.* **2023,** *12,* 104. doi:10.1038/s41377-023-01149-8
219. Van Acker, H.; Coenye, T. *Trends Microbiol.* **2017,** *25,* 456–466. doi:10.1016/j.tim.2016.12.008
220. Chai, S.; Chi, Y.; Sun, W.; Pei, X.; Pei, S.; Sun, C.; Luo, K.; Yao, B. *J. Anal. Test.* **2024,** *8,* 218–227. doi:10.1007/s41664-023-00289-5
221. Sullam, E. M.; Adam, K. M.; Liu, J.; Chen, H.; Xiao, J. *Chin. Chem. Lett.* **2024,** *35,* 108476. doi:10.1016/j.cclet.2023.108476
222. Preethi, M.; Viswanathan, C.; Ponpandian, N. *Mater. Lett.* **2021,** *303,* 130521. doi:10.1016/j.matlet.2021.130521
223. Gharibzahedi, S. M. T.; Barba, F. J.; Zhou, J.; Wang, M.; Altintas, Z. *Biosensors* **2022,** *12,* 356. doi:10.3390/bios12050356
224. Gharibzahedi, S. M. T.; Barba, F. J.; Mofid, V.; Altintas, Z. Biosensing Technology in Food Production and Processing. In *Advanced Sensor Technology;* Barhoum, A.; Altintas, Z., Eds.; Elsevier: Amsterdam, Netherlands, 2023; pp 743–824. doi:10.1016/b978-0-323-90222-9.00023-6

225. Schneider, J.; Reckmeier, C. J.; Xiong, Y.; von Seckendorff, M.; Susha, A. S.; Kasák, P.; Rogach, A. L. *J. Phys. Chem. C* **2017,** *121,* 2014–2022. doi:10.1021/acs.jpcc.6b12519
226. Xiang, Y.; Song, F.; Jiang, L.; Liu, Z.; Tu, Y. *J. AOAC Int.* **2022,** *105,* 1350–1359. doi:10.1093/jaoacint/qsac033
227. Tang, S.; Chen, X.; Wang, J. *Sci. Sin.: Chim.* **2010,** *40,* 711–716. doi:10.1360/zb2010-40-6-711
228. Szterk, A.; Roszko, M.; Małek, K.; Czerwonka, M.; Waszkiewicz-Robak, B. *Meat Sci.* **2012,** *91,* 408–413. doi:10.1016/j.meatsci.2012.02.023
229. Yu, Y.; Li, C.; Chen, C.; Huang, H.; Liang, C.; Lou, Y.; Chen, X.-B.; Shi, Z.; Feng, S. *Talanta* **2019,** *195,* 117–126. doi:10.1016/j.talanta.2018.11.010
230. Zhao, C.; Li, X.; Cheng, C.; Yang, Y. *Microchem. J.* **2019,** *147,* 183–190. doi:10.1016/j.microc.2019.03.029
231. Zhou, C.; Wu, S.; Qi, S.; Song, W.; Sun, C. *J. Anal. Methods Chem.* **2021,** 9732364. doi:10.1155/2021/9732364
232. Ji, X.; Wang, S.; Luo, Y.; Yuan, X.; Wei, Y.; Zhang, Q.; Qin, K.; Tu, Y. *Dyes Pigm.* **2021,** *184,* 108818. doi:10.1016/j.dyepig.2020.108818
233. Chen, J.; Mao, C.; Ye, H.; Gao, X.; Zhao, L. *Spectrochim. Acta, Part A* **2024,** *305,* 123459. doi:10.1016/j.saa.2023.123459
234. Tiwari, P.; Kaur, N.; Sharma, V.; Kang, H.; Uddin, J.; Mobin, S. M. *New J. Chem.* **2019,** *43,* 17058–17068. doi:10.1039/c9nj04061g
235. Kansay, V.; Sharma, V. D.; Chandan, G.; Srivastava, V.; Batra, N.; Mittal, A.; Chakrabarti, S.; Bera, M. K. *ACS Appl. Electron. Mater.* **2024,** *6,* 1971–1981. doi:10.1021/acsaelm.3c01843
236. Bogner, M.; Ludewig, U. *J. Fluoresc.* **2007,** *17,* 350–360. doi:10.1007/s10895-007-0192-2
237. Zhang, C.; Wei, Z.-H.; Ye, B.-C. *Appl. Microbiol. Biotechnol.* **2013,** *97,* 8307–8316. doi:10.1007/s00253-013-5121-5
238. Babu, P. J.; Raichur, A. M.; Doble, M. *Sens. Actuators, B* **2018,** *258,* 1267–1278. doi:10.1016/j.snb.2017.11.148

License and Terms